



國立中央大學天文研究所
鹿林天文台年報

2017

No.15

國立中央大學天文研究所 編

目錄

研究論文

Multiband variability studies and novel broadband SED modeling of Mrk 501 in 2009, M. L. Ahnen, S. Ansoldi, L. A. Antonelli, et al., A&A 603, A31 (2017)	4
Multiwavelength Stellar Polarimetry of the Filamentary Cloud IC5146. I. Dust Properties, Jia-Wei Wang , Shih-Ping Lai , Chakali Eswaraiah, et al., The Astrophysical Journal, 849:157 (18pp), 2017 November 10	34
Confirmation of Large Super-fast Rotator (144977) 2005 EC127, Chan-Kao Chang, Hsing-Wen Lin, Wing-Huen Ip, et al., The Astrophysical Journal Letters, 840:L22 (6pp), 2017 May 10	52
Study of Molecular Clouds, Variable Stars and Related Topics at NUU and UBAI, Hojaev, A. S., ASP Conference Series, Vol. 511. San Francisco: Astronomical Society of the Pacific, 2017, p.116, 07/2017	58
MAXI J1807+132: Lulin observations find substantial optical variability during the X-ray fading phase, ATel #10245; A. K. H. Kong (NTHU & Oxford), R. Jin, C.-H. Tseng, E.-T. Lin (NTHU) on 6 Apr 2017; 08:09 UT	59
Dissecting the long-term emission behaviour of the BL Lac object Mrk 421, M. I. Carnerero, C. M. Raiteri, M. Villata, , et al., MNRAS 472, 3789–3804 (2017)	60
Synchrotron emission from the blazar PG 1553+113. An analysis of its flux and polarization variability, C. M. Raiteri, F. Nicastro, A. Stamerra, et al., MNRAS 466, 3762–3774 (2017)	76
Blazar spectral variability as explained by a twisted inhomogeneous jet C. M. Raiteri, M. Villata1, J. A. Acosta-Pulido, et al., 374 NATURE VOL 552 21/28 DECEMBER 2017	89
Long-term Periodicities of Cataclysmic Variables with Synoptic Surveys, Michael Ting-Chang Yang, Yi Chou, Chow-Choong Ngeow, et al., Publications of the Astronomical Society of the Pacific, 129:094202 (15pp), 2017 September	102
Recent work on sprite spectrum in Taiwan, Min-Ruey Lu, Pei-Yu Chen, Cheng-Ling Kuo, et al., Terr. Atmos. Ocean. Sci., Vol. 28, No. 4, 625-636, August 2017	117

工作報告

鹿林天文台觀測時數統計(2003-2017).....	130
鹿林天文台LOT 觀測研究計畫統計 (2017).....	132
鹿林天文台工作報告2017, 林宏欽、張明新、張永欣等.....	137
鹿林天文台團體參觀及觀測教學2017.....	147
SSP-4 近紅外光度計(NIR-photometer)於鹿林一米望遠鏡(LOT)上測試與觀測工作簡報, 羅烜玟.....	149
Rotationally Resolved Polarization Observations of the M-type Asteroid 16 Psyche, Kang-Shian Pan, Yu-Chi Cheng, Wing-Huen Ip.....	152
Synchronous Surveillances of Meteor Events using the Taiwan Meteor Detection System, Bo-Hao Wang ¹ , Jun-You Liu ² , Zong-yi Lin.....	156
中美掩星計畫I·II, 陳筱琪.....	163

新聞報導

新聞報導.....	168
-----------	-----

研究論文

Multiband variability studies and novel broadband SED modeling of Mrk 501 in 2009

M. L. Ahnen¹, S. Ansoldi², L. A. Antonelli³, P. Antoranz⁴, A. Babic⁵, B. Banerjee⁶, P. Bangale⁷, U. Barres de Almeida^{7,24}, J. A. Barrio⁸, J. Becerra González^{9,25}, W. Bednarek¹⁰, E. Bernardini^{11,26}, A. Berti^{2,27}, B. Biasuzzi², A. Biland¹, O. Blanch¹², S. Bonnefoy⁸, G. Bonnoli¹, F. Borracci⁷, T. Bretz^{13,28}, S. Buson¹⁴, A. Carosi³, A. Chatterjee⁶, R. Clavero⁹, P. Colin⁷, E. Colombo⁹, J. L. Contreras⁸, J. Cortina¹², S. Covino³, P. Da Vela⁴, F. Dazzi⁷, A. De Angelis¹⁴, B. De Lotto², E. de Oña Wilhelmi¹⁵, F. Di Pierro³, M. Doert^{16,*}, A. Domínguez⁸, D. Dominis Prester⁵, D. Dorner¹³, M. Doró¹⁴, S. Einecke¹⁶, D. Eisenacher Glawion¹³, D. Elsaesser¹⁶, M. Engelkemeier¹⁶, V. Fallah Ramazani¹⁷, A. Fernández-Barral¹², D. Fidalgo⁸, M. V. Fonseca⁸, L. Font¹⁸, K. Frantzen¹⁶, C. Fruck⁷, D. Galindo¹⁹, R. J. García López⁹, M. Garczarczyk¹¹, D. Garrido Terrats¹⁸, M. Gaug¹⁸, P. Giammaria³, N. Godinović⁵, A. González Muñoz¹², D. Gora¹¹, D. Guberman¹², D. Hadasch²⁰, A. Hahn⁷, Y. Hanabata²⁰, M. Hayashida²⁰, J. Herrera⁹, J. Hose⁷, D. Hrupec⁵, G. Hughes¹, W. Idec¹⁰, K. Kodani²⁰, Y. Konno²⁰, H. Kubo²⁰, J. Kushida²⁰, A. La Barbera³, D. Lasas⁵, E. Lindfors¹⁷, S. Lombardi³, F. Longo^{2,27}, M. López⁸, R. López-Coto^{12,29}, P. Majumdar⁶, M. Makariev²¹, K. Mallot¹¹, G. Maneva²¹, M. Manganaro⁹, K. Mannheim¹³, L. Maraschi³, B. Marcote¹⁹, M. Mariotti¹⁴, M. Martínez¹², D. Mazin^{7,30}, U. Menzel⁷, J. M. Miranda⁴, R. Mirzoyan⁷, A. Moralejo¹², E. Moretti⁷, D. Nakajima²⁰, V. Neustroev¹⁷, A. Niedzwiecki¹⁰, M. Nieves Rosillo⁸, K. Nilsson^{17,31}, K. Nishijima²⁰, K. Noda⁷, L. Nogués¹², A. Overkemping¹⁶, S. Paiano¹⁴, J. Palacio¹², M. Palatiello², D. Paneque^{7,*}, R. Paoletti⁴, J. M. Paredes¹⁹, X. Paredes-Fortuny¹⁹, G. Pedalletti¹¹, M. Peresano², L. Perri³, M. Persic^{2,32}, J. Poutanen¹⁷, P. G. Prada Moroni²², E. Prandini^{1,33}, I. Puljak⁵, I. Reichardt¹⁴, W. Rhode¹⁶, M. Ribó¹⁹, J. Rico¹², J. Rodríguez García⁷, T. Saito²⁰, K. Satalecka¹¹, S. Schröder¹⁶, C. Schultz¹⁴, T. Schweizer⁷, S. N. Shore²², A. Sillanpää¹⁷, J. Sitarek¹⁰, I. Snidarić⁵, D. Sobczynska¹⁰, A. Stamerra³, T. Steinbring¹³, M. Strzys⁷, T. Suric⁵, L. Takalo¹⁷, F. Tavecchio³, P. Temnikov²¹, T. Terzić⁵, D. Tescaro¹⁴, M. Teshima^{7,30}, J. Thaele¹⁶, D. F. Torres²³, T. Toyama⁷, A. Treves², G. Vanzo⁹, V. Verguillov²¹, I. Vovk⁷, J. E. Ward¹², M. Will⁹, M. H. Wu¹⁵, R. Zanin^{19,29},
(The MAGIC collaboration)
A. U. Abeysekara³⁵, S. Archambault³⁶, A. Archer³⁷, W. Benbow³⁸, R. Bird³⁹, M. Buchovecky⁴⁰, J. H. Buckley³⁷, V. Bugaev³⁷, M. P. Connolly⁴¹, W. Cui^{42,43}, H. J. Dickinson⁴⁴, A. Falcone⁴⁵, Q. Feng⁴², J. P. Finley⁴², H. Fleischhack¹¹, A. Flinders³⁵, L. Fortson⁴⁶, G. H. Gillanders⁴¹, S. Griffin³⁶, J. Grube⁴⁷, M. Hütten¹¹, D. Hanna³⁶, J. Holder⁴⁸, T. B. Humensky⁴⁹, P. Kaaret⁵⁰, P. Kar³⁵, N. Kelley-Hoskins¹¹, M. Kertzman⁵¹, D. Kieda³⁵, M. Krause¹¹, F. Krennrich⁴⁴, M. J. Lang⁴¹, G. Maier¹¹, A. McCann³⁶, P. Moriarty⁴¹, R. Mukherjee⁵², D. Nieto⁴⁹, S. O'Brien³⁹, R. A. Ong⁴⁰, N. Otte⁵⁷, N. Park⁵³, J. Perkins²⁵, A. Pichel⁵⁴, M. Pohl^{55,25}, A. Popkow⁴⁰, E. Pueschel³⁹, J. Quinn³⁹, K. Ragan³⁶, P. T. Reynolds⁵⁶, G. T. Richards⁵⁷, E. Roache³⁸, A. C. Rovero⁵⁴, C. Rulten⁴⁶, I. Sadeh¹¹, M. Santander⁵², G. H. Sembroski⁴², K. Shahinyan⁴⁶, I. Telezhinsky^{55,25}, J. V. Tucci⁴², J. Tyler³⁶, S. P. Wakely⁵³, A. Weinstein⁴⁴, P. Wilcox⁵⁰, A. Wilhelm^{55,25}, D. A. Williams⁵⁸, B. Zitzer⁵⁹,
(the VERITAS Collaboration)
S. Razaque⁶⁰, M. Villata⁶¹, C. M. Raiteri⁶¹, H. D. Aller⁶², M. F. Aller⁶², V. M. Larionov^{63,64}, A. A. Arkharov⁶⁴, D. A. Blinov^{63,65,66}, N. V. Efimova⁶⁴, T. S. Grishina⁶³, V. A. Hagen-Thorn⁶³, E. N. Kopatskaya⁶³, L. V. Larionova⁶³, E. G. Larionova⁶³, D. A. Morozova⁶³, I. S. Troitsky⁶³, R. Ligustri⁶⁷, P. Calciolone⁶⁸, A. Berdyugin¹⁷, O. M. Kurtanidze^{69,70}, M. G. Nikolashvili⁶⁹, G. N. Kimeridze⁶⁹, L. A. Sigua⁶⁹, S. O. Kurtanidze⁶⁹, R. A. Chigladze⁶⁹, W. P. Chen⁷², E. Koptelova⁷², T. Sakamoto⁷³, A. C. Sadun⁷⁴, J. W. Moody⁷⁵, C. Pace⁷⁵, R. Pearson III⁷⁵, Y. Yatsu⁷⁶, Y. Mori⁷⁶, A. Carraminyana⁷⁷, L. Carrasco⁷⁷, E. de la Fuente⁷⁸, J. P. Norris⁷⁹, P. S. Smith⁸⁰, A. Wehrle⁸¹, M. A. Gurwell⁸², A. Zook⁸³, C. Pagani⁸⁴, M. Perri^{85,86}, M. Capalbi⁸⁵, A. Cesarini⁸⁷, H. A. Krimm^{25,88,89}, Y. Y. Kovalev^{90,91}, Yu. A. Kovalev⁹⁰, E. Ros^{91,92,93}, A. B. Pushkarev^{90,94}, M. L. Lister⁴², K. V. Sokolovsky^{90,95,96}, M. Kadler¹³, G. Piner⁹⁷, A. Lähteenmäki⁹⁸, M. Tornikoski⁹⁸, E. Angelakis⁹¹, T. P. Krichbaum⁹¹, I. Nestoras⁹¹, L. Fuhrmann⁹¹, J. A. Zensus⁹¹, P. Cassaro⁹⁹, A. Orlati¹⁰⁰, G. Maccaferri¹⁰⁰, P. Leto¹⁰¹, M. Giroletti¹⁰⁰, J. L. Richards⁴², W. Max-Moerbeck⁹¹, and A. C. S. Readhead¹⁰²

(Affiliations can be found after the references)

Received 17 August 2016 / Accepted 7 December 2016

ABSTRACT

Aims. We present an extensive study of the BL Lac object Mrk 501 based on a data set collected during the multi-instrument campaign spanning from 2009 March 15 to 2009 August 1, which includes, among other instruments, MAGIC, VERITAS, *Whipple* 10 m, and *Fermi*-LAT to cover the γ -ray range from 0.1 GeV to 20 TeV; RXTE and *Swift* to cover wavelengths from UV to hard X-rays; and GASP-WEBT, which provides coverage of radio and optical wavelengths. Optical polarization measurements were provided for a fraction of the campaign by the Steward and St. Petersburg observatories. We evaluate the variability of the source and interband correlations, the γ -ray flaring activity occurring in May 2009, and interpret the results within two synchrotron self-Compton (SSC) scenarios.

Methods. The multiband variability observed during the full campaign is addressed in terms of the fractional variability, and the possible correlations are studied by calculating the discrete correlation function for each pair of energy bands where the significance was evaluated with dedicated Monte Carlo simulations. The space of SSC model parameters is probed following a dedicated grid-scan strategy, allowing for a wide range of models to be tested and offering a study of the degeneracy of model-to-data agreement in the individual model parameters, hence providing a less biased interpretation than the “single-curve SSC model adjustment” typically reported in the literature.

Results. We find an increase in the fractional variability with energy, while no significant interband correlations of flux changes are found on the basis of the acquired data set. The SSC model grid-scan shows that the flaring activity around May 22 cannot be modeled adequately with a one-zone SSC scenario (using an electron energy distribution with two breaks), while it can be suitably described within a two (independent) zone SSC scenario. Here, one zone is responsible for the quiescent emission from the averaged 4.5-month observing period, while the other one, which is spatially separated from the first, dominates the flaring emission occurring at X-rays and very-high-energy (>100 GeV, VHE) γ rays. The flaring

* Corresponding author: e-mail: marlene.doert@tu-dortmund.de, dpaneque@mppmu.mpg.de

activity from May 1, which coincides with a rotation of the electric vector polarization angle (EVPA), cannot be satisfactorily reproduced by either a one-zone or a two-independent-zone SSC model, yet this is partially affected by the lack of strictly simultaneous observations and the presence of large flux changes on sub-hour timescales (detected at VHE γ rays).

Conclusions. The higher variability in the VHE emission and lack of correlation with the X-ray emission indicate that, at least during the 4.5-month observing campaign in 2009, the highest energy (and most variable) electrons that are responsible for the VHE γ rays do not make a dominant contribution to the ~ 1 keV emission. Alternatively, there could be a very variable component contributing to the VHE γ -ray emission in addition to that coming from the SSC scenario. The studies with our dedicated SSC grid-scan show that there is some degeneracy in both the one-zone and the two-zone SSC scenarios probed, with several combinations of model parameters yielding a similar model-to-data agreement, and some parameters better constrained than others. The observed γ -ray flaring activity, with the EVPA rotation coincident with the first γ -ray flare, resembles those reported previously for low frequency peaked blazars, hence suggesting that there are many similarities in the flaring mechanisms of blazars with different jet properties.

Key words BL Lacertae objects: individual: Markarian 501 – methods: data analysis

1. Introduction

The BL Lac type object Markarian (Mrk) 501 is among the most prominent members of the class of blazars. Owing to its brightness, almost the entire broadband spectral energy distribution (SED) of Mrk 501 can be measured accurately with the current instrumentation. It is also known as one of the most active blazars, showing very strong and fast variability on timescales as short as a few minutes (Albert et al. 2007a). Moreover, because of its low redshift of $z = 0.034$, even the multi-TeV γ rays are influenced only weakly by the absorption on the extragalactic background light (EBL). Altogether, this makes Mrk 501 an excellent candidate source to study flux and spectral variability in the broadband emission of blazars.

Mrk 501 was the second extragalactic object to be detected in very high energy (>100 GeV, hereafter VHE) γ rays (Quinn et al. 1996; Bradbury et al. 1997), and it has been the subject of extensive studies in the different accessible energy bands over the last two decades. Based on its SED, it has been classified as a high frequency peaked BL Lac-type source (HBL) according to Padovani & Giommi (1995), or high-synchrotron peaked BL Lac (HSP) if following the classification given in Abdo et al. (2010b).

In 1997 Mrk 501 was found to be in an exceptionally high state, with the emission at VHE energies being up to 10 times the flux of the Crab Nebula (Protheroe et al. 1997; Djannati-Atai et al. 1999). During this large flare, the synchrotron bump appeared to peak at or above 100 keV, indicating a shift of the peak position from quiescent state by at least two orders of magnitude (Catanesi et al. 1997; Pian et al. 1998; Villata & Raiteri 1999; Tavecchio et al. 2001a). Over the following years, the source was intensively monitored at X-rays and VHE γ rays (e.g. Kataoka et al. 1999; Quinn et al. 1999; Sambruna et al. 2000; Aharonian et al. 2001; Massaro et al. 2004), and additional studies were done with the collected data a posteriori (e.g. Gliozzi et al. 2006). The observations could be well reproduced in the scope of one-zone synchrotron self-Compton (SSC) models. In 2005, the source showed another strong flaring event, for which flux-doubling times down to two minutes were measured at VHE (Albert et al. 2007a). This fast variability is a strong argument for a comparatively small emission region (with $R \approx 10^{15}$ cm), while the typical activity of the source could still be accommodated in models assuming a radius of the emission region which is larger by one to two orders of magnitude (e.g. Abdo et al. 2011a). Throughout the observations, the SED at the highest energies appeared to be harder in higher flux states (e.g. Albert et al. 2007a). Together with the observed shift of the synchrotron peak during the 1997 event, this suggests a change in the electron energy distribution as the cause for flaring events (Pian et al. 1998), but long-term changes in the

Doppler factor or the size of the emission region are also being discussed as a possibility (Mankuzhiyil et al. 2012).

High-resolution radio images revealed a comparatively slow moving jet that features a limb brightening structure (Piner et al. 2008, 2009; Giroletti et al. 2008). The radio core position of Mrk 501 has been found to be stationary within 2 parsec (pc), using observations from the observing campaign in 2011 with the VLBI Exploration of Radio Astrometry (VERA, Koyama et al. 2015a), although variations in its location on year timescales cannot be excluded. High-resolution Global mm-VLBI Array (GMVA) observations at 86 GHz during the observing campaign in 2012 detected a new feature in the jet of Mrk 501, located 0.75 milliarcseconds (mas) southeast of the radio core (which corresponds to ~ 0.5 pc de-projected distance), and one order of magnitude dimmer than the core (Koyama et al. 2015b). This radio feature is consistent with the one reported in Giroletti et al. (2008) using GMVA data from 2005. This confirms that there are several distinct regions in the jet of Mrk 501, possibly stationary on year timescales, with the presence of high-energy electrons which could potentially produce optical, X-ray, and γ -ray emission, in addition to the emission detected with these high-resolution radio instruments.

Even though Mrk 501 has been studied over a comparatively long time, clear constraints on the properties of the highest activity regions, and on the particle populations involved, are still to be set. In this paper we present an extensive multi-instrument campaign on Mrk 501 that was conducted in 2009 in order to shed light on some of these open questions. This paper is a sequel to Abdo et al. (2011a), where, among other things, the averaged broadband SED from the campaign was studied in detail. A study focused on the flaring activity of May 1 (MJD 54952), which includes very fast variability detected with the *Whipple* 10 m telescope, VERITAS light curves and spectra, and some measurements of the optical polarization performed by the Steward Observatory are reported in Pichel & Paneque (2011) and Aliu et al. (2016). In the work presented here, we address the variability seen during the full campaign, possible interband correlation of flux changes, and the characterization of the measured SED during two states of increased activity. While Aliu et al. (2016) looks at the average X-ray spectrum for a low state covering three weeks and a high state covering three days of the first VHE enhancement, we perform a detailed investigation characterizing the X-ray spectra for each pointing available for the campaign, hence providing a better quantification of the X-ray spectral variability. Furthermore, we consider an expanded data set, which also includes radio observations performed with the Very Long Baseline Array (VLBA), measuring the radio flux coming from the entire source and the radio flux from the compact core region only, and additional measurements of the optical

polarization performed by the Steward and St. Petersburg observatories before and after the flaring activity of May 1.

This paper is structured as follows. In Sect. 2 an overview of the multi-instrument campaign is given, and updates with respect to the information provided in [Abdo et al. \(2011a\)](#) are discussed. In Sect. 3 the collected light curves and spectra are assessed for variability and interband correlation. The discussion of the broadband spectral energy distributions and a quantification of these measured spectra within synchrotron self-Compton scenarios by means of a novel technique based on a scan over the full parameter range is reported in Sect. 4. Finally, the results are discussed in Sect. 5, and a short summary and concluding remarks are given in Sect. 6.

2. Multi-instrument observing campaign performed in 2009

The presented multiwavelength (MWL) campaign was conducted over 4.5 months in 2009. The aim of this campaign was to sample the SED over all wavelengths every ~ 5 days. This way, the intrinsic flux variability of the source could be probed during non-flaring activity, hence reducing the observational bias towards states of high activity, which are the main focus of target of opportunity (ToO) campaigns. The covered frequency range spans from radio to VHE γ rays, including data from ~ 30 different instruments. The campaign took place from 2009 March 15 (MJD 54905) to 2009 August 1 (MJD 55044). Good coverage was achieved, while the sampling density varies among the different wavelengths because of different duty cycles and observational constraints of the participating instruments. The individual data sets and the data reduction are described in detail in Table 1 and Sect. 5 of [Abdo et al. \(2011a\)](#), and are not reported again in this paper. In this section we only briefly mention the various observations performed, and report on the updates of some data analyses and on extended data sets.

In the radio band, several single-dish instruments were used, namely the Effelsberg 100 m radio telescope, the 32 m Medicina radio telescope, the 14 m Metsähovi radio telescope, the 32 m Noto radio telescope, the Owens Valley Radio Observatory (OVRO) 40 m telescope, the 26 m University of Michigan Radio Astronomy Observatory (UMRAO), and the 600 m ring radio telescope RATAN-600. The mm-interferometer Submillimeter Array (SMA) and the Very Long Baseline Array (VLBA) were also used during the campaign. These single-dishes and the SMA monitored the total flux of Mrk 501 as a point-like unresolved source at frequencies between 2.6 GHz and 225 GHz. The VLBA took data ranging from 5 GHz to 43 GHz through various programs (BP143, BK150, and MOJAVE). Owing to the better angular resolution of MOJAVE, in addition to the total flux of the source, measurements of the flux from the compact ($\sim 10^{-3}$ pc) core region of the jet could be obtained through two-dimensional Gaussian fits to the observed data.

Observations in optical frequency ranges have been performed by numerous instruments distributed all over the globe. In the *R* band, the Abastumani, Lulin, Roque de los Muchachos (Kungliga Vetenskapliga Akademien, KVA), St. Petersburg, Talmassons, and Valle d'Aosta observatories performed observations as part of GASP-WEBT, the GLAST-AGILE Support Program of the Whole Earth Blazar Telescope (e.g. [Villata et al. 2008, 2009](#)). Additional data with several optical filters were provided by the Goddard Robotic Telescope (GRT), the Remote Observatory for Variable Object Research (ROVOR), and the Multicolor Imaging Telescopes for Survey

and Monstrous Explosions (MITSuME). At near-infrared wavelengths, measurements performed by the Guillermo Haro Observatory (OAGH) have been included in the data set. Also within the GASP-WEBT program, the Campo Imperatore took measurements in near-infrared frequencies (*JHK* bands). The data obtained in the optical and near-infrared regime used the calibration stars reported in [Villata et al. \(1998\)](#), and have been corrected for Galactic extinction following [Schlegel et al. \(1998\)](#).

Through various observing proposals related to this extensive MWL campaign, 29 pointing observations were performed with the *Rossi-X-ray Timing Explorer* (RXTE), and 44 pointing observations performed with the *Swift* satellite¹. These observations provided coverage in the ultraviolet frequencies with the *Swift* Ultraviolet/Optical Telescope (UVOT), and in the X-ray regime with the RXTE Proportional Counter Array (PCA) and the *Swift* X-ray Telescope (XRT). *Swift*/XRT performed 41 snapshot observations in Windowed Timing (WT) mode throughout the whole campaign, and three observations in Photon Counting (PC) mode around MJD 54952. The PC observations had not been used in [Abdo et al. \(2011a\)](#). For PC mode data, events for the spectral analysis were selected within a circle of 20 pixel (~ 46 arcsec) radius, which encloses about 80% of the point spread function (PSF), centered on the source position. The source count rate was above ~ 5 counts s^{-1} and data were significantly affected by pile-up in the inner part of the PSF. After comparing the observed PSF profile with the analytical model derived by [Moretti et al. \(2005\)](#), pile-up effects were removed by excluding events within a 4 pixel radius circle centered on the source position, and an outer radius of 30 pixels was used. Occasionally, during the first ~ 100 s of a WT mode observation, *Swift*/XRT data can display a deviation in the light curve that is not due to the source variability, but is instead due to the settling of the spacecraft pointing causing a hot column to come in and out of either the source or background region. We inspected these data for any such deviations that could significantly impact our analysis, and none were found.

While Mrk 501 can be significantly detected with XRT and PCA for each single observation (~ 0.3 h), integration times of ~ 30 days are required in order to obtain significant detections with the RXTE All-Sky Monitor (ASM) and the *Swift* Burst Alert Telescope (BAT). The advantage of “all-sky instruments” like RXTE/ASM and *Swift*/BAT is that they can observe Mrk 501 without specifically pointing to the source, and hence provide a more uniform and continuous coverage than pointed instruments like *Swift*/XRT and RXTE/PCA. Details on the analysis of the RXTE/ASM and *Swift*/BAT data were given in [Abdo et al. \(2011a\)](#).

The range of high-energy γ rays was covered with the *Fermi* Large Area Telescope (*Fermi*-LAT). As is the case with RXTE/ASM and *Swift*/BAT, the sensitivity of *Fermi*-LAT is quite moderate, but it provides a more uniform temporal coverage than the pointing instruments; to detect Mrk 501 typically it is necessary to integrate over ~ 15 – 30 days in order to have significant detections. In addition to the observations from the coordinated MWL campaign, here we also report on the X-ray/ γ -ray activity of Mrk 501 measured with RXTE/ASM, *Swift*/BAT, and *Fermi*-LAT for a time interval spanning from MJD 54800 to MJD 55100, which exceeds the time span of the campaign.

¹ Several *Swift* observations took place thanks to a ToO proposal which concentrates on the states of increased activity of the source.

The *Fermi*-LAT data were reanalyzed using the Pass 8 SOURCE class events, and the ScienceTools software² package version v10r1p1. We used all events (from MJD 54 800 to MJD 55 100) with energies from 200 MeV to 300 GeV and within a 10° region of interest (RoI) centered at the position of Mrk 501. In order to avoid contamination from the Earth limb γ rays, only events with zenith angles below 100° were used. We used the *P8R2_SOURCE_V6* instrument response functions, and the *gll_iem_v06* and *iso_P8R2_SOURCE_V6_v06* models to parameterize the Galactic and extragalactic diffuse emission (Acero et al. 2016)³. Given that Mrk 501 is a relatively hard source, we only used events above 300 MeV for the spectral analysis, as was done in Abdo et al. (2011a). All point sources in the third *Fermi*-LAT source catalog (3FGL, Acero et al. 2015) located in the 10° RoI and an additional surrounding 5° wide annulus (called “source region”) were modeled in the fits, with the spectral parameters set to the values from the 3FGL, and the normalization parameters kept free only for the nine sources identified as variable (in the 3FGL) and located within 10° of Mrk 501. The normalization parameters for the two diffuse components were also kept free. The spectral analysis performed on 15- and 30-day time intervals from MJD 54 800 to MJD 55 100 led to spectra successfully described by a power-law (PL) function with an index compatible⁴ with $\Gamma = 1.75$. For the determination of the light curves in the two energy bands 0.2–2 GeV and >2 GeV that are reported in Sect. 3.1, we decided to fix the value of the PL index to $\Gamma = 1.75$.

MAGIC observations were carried out with a single telescope, as the second telescope was under construction during the campaign period. Owing to a scheduled upgrade, no data were taken with MAGIC between MJD 54 948 and MJD 54 960. All observations were carried out in “wobble” mode (Fomin et al. 1994). For the work presented here, the data underwent a revised quality check and were reanalyzed with an improved analysis pipeline with respect to the one presented in Abdo et al. (2011a). Compared to the analysis presented in the first publication, the data set has been expanded by several nights (MJD 54 937, 54 941, 54 944, 54 945, 54 973, 54 975, 55 035, 55 038). Three nights were rejected because of revised quality criteria (MJD 54 919, 54 977, 55 026). After all data selection and analysis cuts, the effective observation time covered by the data comprises 17.4 h, while the first analysis yielded 16.2 h of selected data.

VERITAS observed Mrk 501 with different telescope configurations over the duration of this campaign. The data presented here amounts to 9.7 h of effective time, and are identical to those presented in Abdo et al. (2011a). However, the work in this paper presents the VERITAS light curve for the first time.

The *Whipple* 10 m telescope observed Mrk 501 for 120 h throughout the campaign, separately from the VERITAS array. The data taken with the *Whipple* 10 m were not used in the first publication which focused on the average state of the source throughout the campaign (Abdo et al. 2011a). However, the *Whipple* 10 m data over a flaring period around May 1 have been recently reported in a separate paper (Aliu et al. 2016). For better comparison to the other VHE instruments, *Whipple* 10 m fluxes, originally computed as flux in Crab Units (C.U.) above

² <http://fermi.gsfc.nasa.gov/ssc/data/analysis/software/>

³ <http://fermi.gsfc.nasa.gov/ssc/data/access/lat/BackgroundModels.html>

⁴ The power-law index light curve can be fitted with a constant, yielding average power-law indices of 1.75 ± 0.03 and 1.76 ± 0.03 respectively for the 15- and 30-day time intervals.

400 GeV, were converted into fluxes above 300 GeV using the Crab flux above 300 GeV of $F_{>300\text{ GeV}} = 1.2 \times 10^{-10} \text{ cm}^{-2} \text{ s}^{-1}$ (Aleksić et al. 2012).

For more details on the observation strategy, list of instruments, and analysis procedures performed for the different instruments, the reader is referred to Abdo et al. (2011a) and references therein.

In addition to the MWL observations conducted as part of the campaign, the data set was expanded with measurements of the optical polarization performed by the Steward (Bok telescope) and St. Petersburg (LX-200) observatories from February to September 2009. The LX-200 polarization measurements were obtained from *R*-band imaging polarimetry, while the measurements from the Steward Observatory were derived from spectropolarimetry between 4000 and 75 00 Å with a resolution of ~ 15 Å, and the reported values are constructed from the median Q/I and U/I in the 5000–7000 Å band. The effective wavelength of this bandpass is similar to the Kron-Cousins *R* band, and the wavelength dependence in the polarization of Mrk 501 seen in the spectro-polarimetry is small and does not significantly affect the results. The details related to the observations and analysis of the polarization data is reported in Larionov et al. (2008) and Smith et al. (2009). The Steward observations are part of the public Steward Observatory program to monitor γ -ray bright blazars during the *Fermi*-LAT mission⁵, and a fraction of these polarization observations have been recently reported in Aliu et al. (2016).

3. Multi-instrument flux and spectral variability

During the 4.5-month MWL campaign, Mrk 501 was observed with numerous instruments covering the entire broadband SED. In the following section, we report the measured multiband flux and spectral variability, as well as multiband correlations.

3.1. Multi-instrument light curves

The light curves which were derived from pointed observations in the different energy bands, spanning from radio to VHE γ rays, are shown in Fig. 1. Figure 2 presents the X-ray and γ -ray activity as measured with the all-sky instruments RXTE/ASM, *Swift*/BAT and *Fermi*-LAT.

The light curves obtained during pointing observations in the radio regime exhibit a nearly constant flux at a level of ~ 1.2 Jy. The well-sampled light curve taken with the OVRO telescope shows constant emission of 1.158 ± 0.003 Jy.

The measurements performed with the VLBA at a frequency of 43 GHz are presented in Fig. 3. A constant fit delivers a reduced χ^2 of 8.4/3 for the total flux and 15.6/3 for the core flux, yielding a probability for the data points to be well described by a constant fit of 3.8% and 0.14%, respectively. Although marginally significant, this suggests an increase in the radio flux in May 2009 (dominated by the core emission) in comparison to that measured during the other months.

For the near-infrared observations in Fig. 1, flux levels of ~ 40 – 50 mJy (*J* and *K* bands) and ~ 50 – 60 mJy (*H* band) were measured. Only small variations can be seen, even though the sampling is less dense and the uncertainties of the measurements are comparatively large. For the extensive data sample in the optical regime, a nearly constant flux was measured at flux levels of ~ 6 mJy (*B* band), 11 mJy (*V*), ~ 16 mJy (*R*), and 24–29 mJy

⁵ <http://james.as.arizona.edu/~psmith/Fermi>

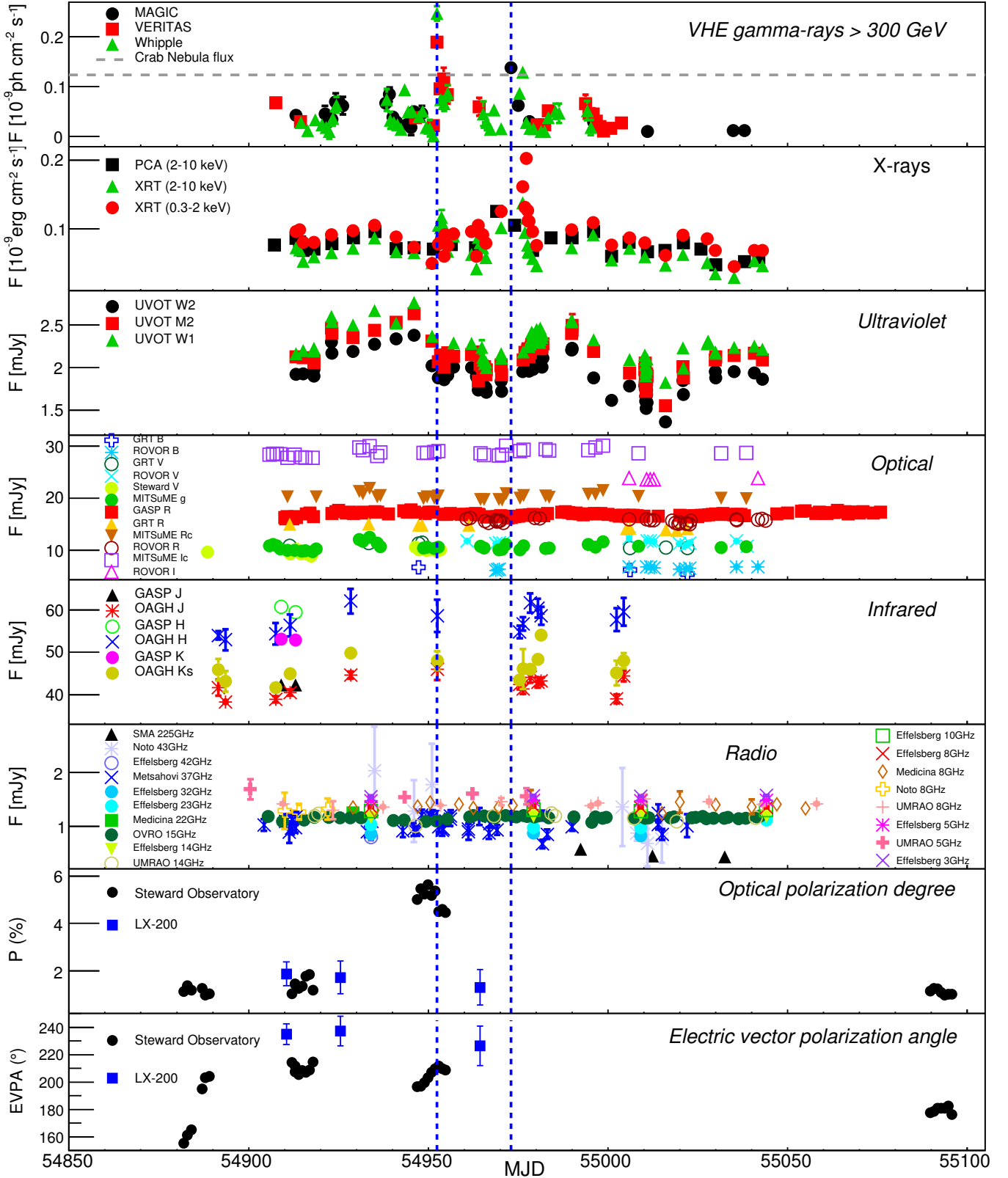


Fig. 1. Light curves compiled based on pointing observations in various energy bands. The *lowest two panels* show measurements of the optical polarization. The two vertical blue lines indicate the location of the two VHE γ -ray flares at MJD 54952 and MJD 54973 that are discussed in Sects. 4.2 and 4.3.

(*l/lc*). No correction for emission by the host galaxy was applied. At ultraviolet frequencies, a flux level of ~ 2 mJy with flux variations of about 25% over timescales of about 25 to 40 days can be seen.

The average *Swift*/XRT measured fluxes during the entire campaign are $F_{0.3-2\text{keV}} = (9.2 \pm 0.3) \times 10^{-11} \text{ erg cm}^{-2} \text{ s}^{-1}$ in the energy range between 0.3 and 2 keV and $F_{2-10\text{keV}} = (7.2 \pm 0.3) \times 10^{-11} \text{ erg cm}^{-2} \text{ s}^{-1}$ in the range 2–10 keV, while RXTE/PCA,

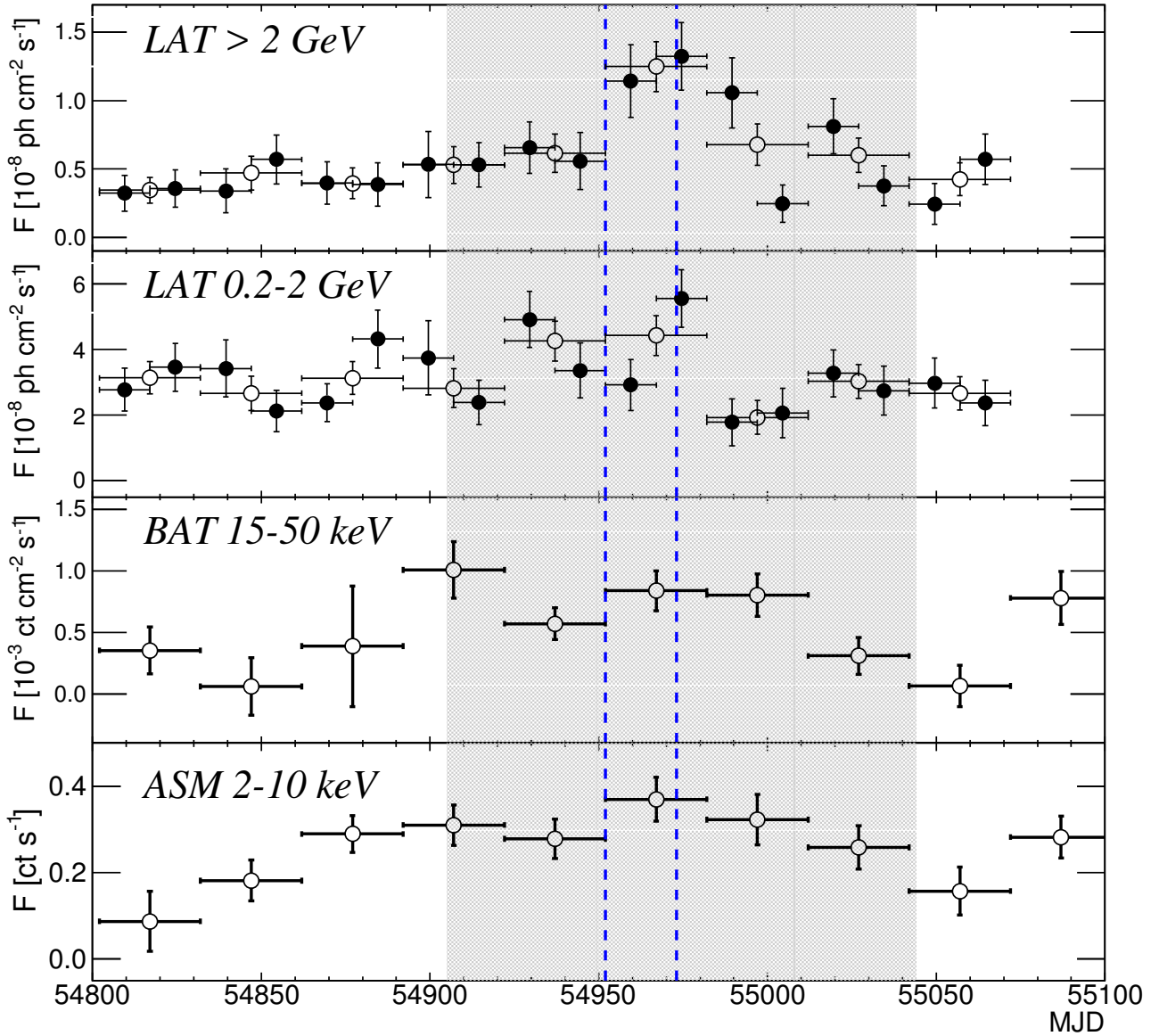


Fig. 2. Light curves of instruments with longer integration times. *From top to bottom: Fermi-LAT above 2 GeV, Fermi-LAT 0.2-2 GeV, Swift/BAT, and RXTE/ASM.* Flux points with integration times of 30 days are shown as open markers, while for *Fermi-LAT* flux points integrated over 15 days have also been derived and are added with filled markers. The gray shaded area depicts the time interval related to the multi-instrument campaign. The two vertical blue lines indicate the location of the two VHE γ -ray flares at MJD 54952 and MJD 54973 that are discussed in Sects. 4.2 and 4.3.

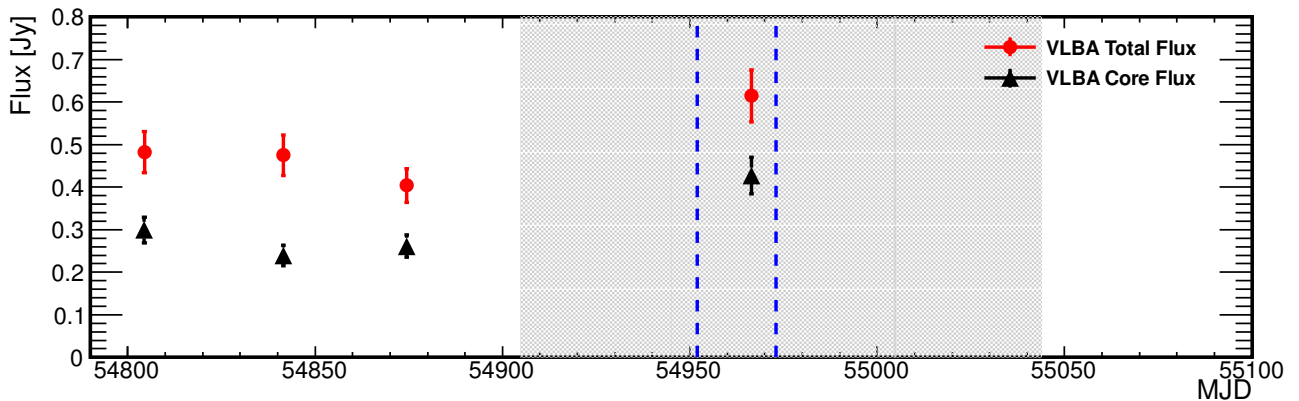


Fig. 3. Light curves obtained with the VLBA at 43 GHz. The total flux and the flux from the core region are shown. The gray shaded area depicts the time interval related to the multi-instrument campaign. The two vertical blue lines indicate the location of the two VHE γ -ray flares at MJD 54952 and MJD 54973 that are discussed in Sects. 4.2 and 4.3.

due to a slightly different temporal coverage, measured an average 2–10 keV flux of $F_{2-10\text{keV}} = (7.8 \pm 0.2) \times 10^{-11} \text{ erg cm}^{-2} \text{ s}^{-1}$.

The *Fermi*-LAT measured a variable flux in the two probed γ -ray bands, with an average flux of $F_{0.2-2\text{GeV}} = (2.75 \pm 0.14) \times 10^{-8} \text{ ph cm}^{-2} \text{ s}^{-1}$ between 200 MeV and 2 GeV and $F_{>2\text{GeV}} = (5.3 \pm 0.4) \times 10^{-9} \text{ ph cm}^{-2} \text{ s}^{-1}$ at energies above 2 GeV (shown in Fig. 2). The highest emission is seen in the 15-day time interval between MJD 54967 and MJD 54982.

The VHE γ -ray light curves are shown in the upper panel of Fig. 1. The average flux above 300 GeV of Mrk 501 during the campaign, including the flaring activities, is about $5 \times 10^{-11} \text{ ph cm}^{-2} \text{ s}^{-1}$ ($\sim 0.4 \text{ C.U.}$)⁶. Flux variability is evident throughout the VHE light curve, in addition to flaring episodes of a few days occurring in MJD 54952 (2009 May 1) and MJD 54973 (2009 May 22).

In the following paragraphs we review the first VHE flare in a MWL context, and include additional details specifically on the X-ray data. We then provide details on the second VHE flare.

3.1.1. VHE γ -ray flaring event starting at MJD 54952

On 2009 May 1, the *Whipple* 10 m telescope observed Mrk 501 for 2.3 h and detected a VHE flux ($>300 \text{ GeV}$) increase from ~ 1.0 – 1.5 C.U. to $\sim 4.5 \text{ C.U.}$ in the first 0.5 h (from MJD 54952.35 to MJD 54952.37), which implies a flux increase of about one order of magnitude with respect to the average VHE flux level recorded during the full campaign. Following the alert by the *Whipple* 10 m, VERITAS started to observe Mrk 501 after 1.4 h (at MJD 54952.41) and detected the source at a VHE flux of 1.5 C.U. without statistically significant flux variations during the full observation (from MJD 54952.41 to MJD 54952.48). This VHE flux level was also measured by the *Whipple* 10 m telescope in approximately the same time window (from MJD 54952.41 to MJD 54952.47), and corresponds to a VHE flux ~ 4 times larger than the typical flux level of 0.4 C.U. measured during the full campaign. The peak of the flare (which occurred at MJD 54952.37) was caught only by the *Whipple* 10 m. Still, the Mrk 501 VHE γ -ray flux remained high for the rest of the night and the following two nights (until MJD 54955), which was measured by VERITAS and the *Whipple* 10 m with very good agreement. Further details about the VERITAS and *Whipple* 10 m intra-night variability measured on 2009 May 1, and about the enhanced activity during the first days of May, can be found in Pichel & Paneque (2011) and Aliu et al. (2016).

During the period of the considered VHE γ -ray flare, no substantial increase in the X-ray regime can be claimed based on the *Swift*/XRT observations: the 0.3–2 keV and the 2–10 keV fluxes during this flaring episode are about $\sim 8 \times 10^{-11} \text{ erg cm}^{-2} \text{ s}^{-1}$ and $\sim 1 \times 10^{-10} \text{ erg cm}^{-2} \text{ s}^{-1}$, which are about $\sim 10\%$ lower and $\sim 30\%$ higher than the average X-ray flux values reported above. However, the *Swift*/XRT observations started seven hours after the *Whipple* 10 m and VERITAS observations of this very high VHE state on MJD 54952. The reason is that the XRT observations were taken within a ToO activated by the enhanced VHE activity measured by the *Whipple* 10 m and VERITAS unlike most of

the planned X-ray observations from the MWL campaign which were coordinated with the VHE observations.

In the two lowest panels in Fig. 1, the evolution of the optical polarization degree and orientation are shown. The degree of polarization during the few days around the first VHE flaring activity is measured at 5% compared to a 1% measurement during several observations before and after this flaring activity. There is also a rotation of the EVPA by 15 degrees, which comes to a halt at the time of the VHE outburst when the degree of polarization drops from 5.4% to 4.5% (see further details in Pichel & Paneque 2011; Aliu et al. 2016).

3.1.2. VHE γ -ray flaring event starting at MJD 54973

The MAGIC telescope observed Mrk 501 for 1.7 h on 2009 May 22 (MJD 54973) and measured a flux of 1.2 C.U., which corresponds to ~ 3 times the low flux level. At the next observation on May 24 (MJD 54975.00 to MJD 54975.12), the flux had already decreased to a level of $\sim 0.5 \text{ C.U.}$ The *Whipple* 10 m observed Mrk 501 later on the same date (from MJD 54975.25) and measured a flux of $\sim 0.7 \text{ C.U.}$, while the following day (from MJD 54976.23) it measured a flux increase to 1.1 C.U. No VERITAS observations of Mrk 501 took place at this time, due to scheduled telescope maintenance.

The MAGIC data of the flaring night were probed for variations on timescales down to minutes, but no significant intra-night variability was found. Moreover, tests for spectral variability during the night in terms of hardness ratios vs. time in different energy bands showed no significant variations either.

Unfortunately, there are no X-ray observations that are strictly simultaneous with the MAGIC observations on MJD 54973. The closest RXTE/PCA observations took place on MJD 56969 and MJD 54974, and the closest *Swift*/XRT observations are from MJD 54970 and MJD 54976, all of which show a flux increase (up to a factor of ~ 2) with respect to the average X-ray flux measured during the campaign.

Under the assumption that no unobserved intra-day variability occurred in the X-ray band, it can be inferred that Mrk 501 was in a state of increased X-ray and VHE activity over a period of up to 5 days. During this period there were no flux changes observed at optical or radio frequencies.

3.2. Spectral variability in individual energy bands

In this section we report on the spectral variability observed during the two VHE flaring episodes around the peaks of the two SED bumps, namely at X-ray and γ rays, where most of the energy is being emitted and where the flux variability is highest.

3.2.1. VHE γ rays

The VHE spectra measured with MAGIC and VERITAS, averaged over the entire campaign between 2009 March 15 (MJD 54905) and 2009 August 1 (MJD 55044), were reported in Abdo et al. (2011a). Only the time span MJD 54952–54955, where VERITAS recorded VHE flaring activity, was excluded for the average spectrum and was presented as a separate high-state spectrum (see Fig. 8 of Abdo et al. 2011a). The resulting average spectra relate to a VHE flux of about 0.3 C.U., which is the typical non-flaring VHE flux level of Mrk 501. Additionally, two spectra were obtained with the *Whipple* 10 m for that night: a very-high-state spectrum spanning MJD 54952.35–54952.41, which seems to cover the peak of

⁶ The average fluxes measured with MAGIC, VERITAS, and *Whipple* during the observing campaign are somewhat different because of the distinct temporal coverage of these instruments. The average VHE flux with MAGIC is $F_{>300\text{GeV}} = (4.6 \pm 0.4) \times 10^{-11} \text{ ph cm}^{-2} \text{ s}^{-1}$, with VERITAS is $F_{>300\text{GeV}} = (5.3 \pm 0.7) \times 10^{-11} \text{ ph cm}^{-2} \text{ s}^{-1}$, and with *Whipple* is $F_{>300\text{GeV}} = (4.4 \pm 0.5) \times 10^{-11} \text{ ph cm}^{-2} \text{ s}^{-1}$.

the flare, and a high-state spectrum derived from the time interval MJD 54 952.41–54 955.00, which is simultaneous with the observations performed with VERITAS. These spectra were reported in Pichel & Paneque (2011) following the general *Whipple* analysis technique described in Horan et al. (2007), and further details from these spectra are reported in Aliu et al. (2016).

The reanalysis of the MAGIC data (see Sect. 2), which contains some additional data compared to the analysis presented in Abdo et al. (2011a), revealed a flaring state on MJD 54 973, for which a dedicated spectrum was computed. An averaged spectrum was derived based on the remaining data set. The energy distribution of the differential photon flux can be well described by a PL function of the form

$$\frac{dN}{dE} = F_0 \times (E/1 \text{ TeV})^{-\Gamma}, \quad (1)$$

yielding $F_0 = (9.3 \pm 0.4) \times 10^{-8} \text{ ph m}^{-2} \text{ s}^{-1} \text{ TeV}^{-1}$ and $\Gamma = 2.40 \pm 0.05$. This new MAGIC averaged spectrum was found to be in agreement with the previously presented value where a power-law fit gave $F_0 = (9.0 \pm 0.5) \times 10^{-8} \text{ ph m}^{-2} \text{ s}^{-1} \text{ TeV}^{-1}$ and $\Gamma = 2.51 \pm 0.05$ (Abdo et al. 2011a). Here we only quote statistical uncertainties of the measurements. The systematic errors affecting data taken by the MAGIC telescope at the time of the presented campaign are discussed in Albert et al. (2008) and are valid for both analyses. They are estimated as an energy scale error of 16%, a systematic error on the flux normalization of 11%, and an error on the obtained spectral slope of ± 0.2 . In the following, the more recent analysis result are used.

All the VHE γ -ray spectra described above are presented in Fig. 4. The spectra shown in the figure were corrected for absorption by the EBL using the model from Franceschini et al. (2008). Given the proximity of Mrk 501, the impact of the EBL on the spectrum is relatively weak: the attenuation of the flux reaches 50% at an energy of 5 TeV. Many other EBL models (e.g. Finke et al. 2010; Domínguez et al. 2011) provide compatible results at energies below 5 TeV, hence the results do not depend significantly on the EBL model used. The power-law fit parameters (see Eq. (1)) of the measured spectra (i.e. the spectra not corrected for EBL) can be found in Table 1. For spectra measured with MAGIC, the presented fits also take into account the correlation between the individual spectral points which is introduced by the unfolding of the spectrum, while no explicit unfolding has been applied for the other instruments. The average-state spectra measured by the three instruments (after subtracting the time intervals with strong flaring activity in the VHE) agree very well, despite the somewhat different observing periods. This suggests that these VHE spectra are a good representation of the typical VHE spectrum of Mrk 501 during this MWL campaign. The high-state spectra show a spectral slope that is harder than that from the non-flaring state, hence indicating a “harder when brighter” behavior, as has been reported previously (e.g. Albert et al. 2007a).

3.2.2. GeV γ rays

The two short VHE flaring episodes discussed in this paper occurred within the time interval MJD 54 952–54 982, which is the 30-day time interval with the highest flux and hardest GeV γ -ray spectrum reported in Abdo et al. (2011a). The flux above 300 MeV $F_{>300 \text{ MeV}}$ and photon index Γ for this 30-day time interval computed using the ScienceTools software package version v9r15p6 and the *P6_V3_DIFFUSE* instrument response functions are $F_{>300 \text{ MeV}} = (3.6 \pm 0.5) \times 10^{-8} \text{ ph cm}^{-2} \text{ s}^{-1}$

and $\Gamma = 1.64 \pm 0.09$, while values for the *Fermi*-LAT spectrum averaged for the entire MWL campaign are $F_{>300 \text{ MeV}} = (2.8 \pm 0.2) \times 10^{-8} \text{ ph cm}^{-2} \text{ s}^{-1}$ and $\Gamma = 1.74 \pm 0.05$ (for further details, see Abdo et al. 2011a). Performing the analysis with the ScienceTools software package version v10r1p1 and the Pass 8 data (which implies somewhat different photon candidate events), as described in Sect. 2, led to a photon flux (above 300 MeV) of $F_{>300 \text{ MeV}} = (4.2 \pm 0.5) \times 10^{-8} \text{ ph cm}^{-2} \text{ s}^{-1}$ and a PL index of $\Gamma = 1.68 \pm 0.07$ for the time interval MJD 54 952–54 982, and a flux (above 300 MeV) of $F_{>300 \text{ MeV}} = (3.0 \pm 0.2) \times 10^{-8} \text{ ph cm}^{-2} \text{ s}^{-1}$ and a PL index of $\Gamma = 1.75 \pm 0.04$ for the entire campaign. The spectral results derived with Pass 6 and Pass 8 are compatible, and show a marginal increase in the flux and the hardness of the spectra during the time interval MJD 54 952–54 982 with respect to the full campaign period.

The Pass 8 *Fermi*-LAT data analysis is more sensitive than the Pass 6 data analysis, and allows us to detect Mrk 501 significantly (TS > 25)⁷ and to determine the spectra around these two flares in time intervals as short as 2 days centered at MJD 54 952 and 54 973. Additionally, for comparison purposes, we also computed the spectra for 7-day time intervals centered at MJD 54 952 and 54 973⁸. The *Fermi*-LAT spectral results for the various time intervals in May 2009 are reported in Table 2. For the first flare, for both the 2-day and 7-day time intervals, the LAT analysis yields a signal with TS ~ 40 . This shows that increasing the time interval from 2 days to 7 days did not increase the γ -ray signal, and hence indicates that the 2-day time interval centered at MJD 54 952 dominates the γ -ray signal from the 7-day time interval. The spectrum is marginally harder than the average spectrum from the time interval MJD 54 952–54 982. For the second flare, the 7-day time interval yields a signal significance ($\sim\sqrt{\text{TS}}$) 2.6 times larger than that of the 2-day time interval, showing that, contrary to the first flare, increasing the time interval from 2 days to 7 days enhanced the γ -ray signal considerably. The *Fermi*-LAT spectrum around the second flare is very similar to the average spectrum obtained for the 30-day time interval MJD 54 952–54 982.

For the MWL SEDs presented in Fig. 9, we show the *Fermi*-LAT spectral results for these two flares performed on three and five differential energy bins (starting from 300 MeV). Here, the shape of the spectrum was fixed to that obtained for the full range for each temporal bin. Upper limits at 95% confidence level were computed whenever the TS value (for the γ -ray signal of the bin) was below six and/or the uncertainty was equal to or larger than the energy flux value.

3.2.3. X-rays

In the X-ray band, individual spectra could be derived for each pointing of the two instruments *Swift*/XRT and RXTE/PCA. Both indicated significant variability in flux and spectral index during the course of the campaign. Figure 5 shows the XRT and PCA spectra around the times of the first and second flux increase in the VHE range. For the first flare, the variability in flux and spectral shape is greater for XRT than for PCA, but mostly because many of the XRT observations were performed within

⁷ “TS” stands for test statistic from the maximum likelihood fit. A TS value of 25 corresponds to an estimated $\sim 4.6\sigma$ (Mattox et al. 1996).

⁸ A one-week period is a natural time interval that is also used, for instance, in the LAT public light curves http://fermi.gsfc.nasa.gov/ssc/data/access/lat/msl_lc/. The spectral results would not change if we had used a 5-day or 10-day time interval.

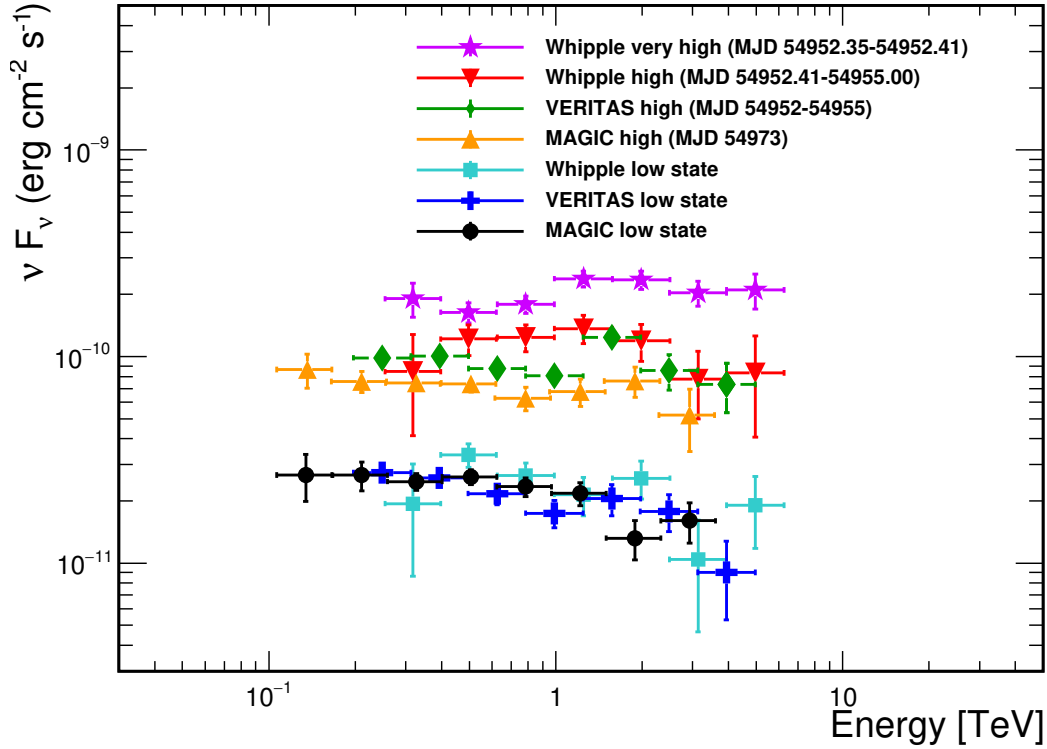


Fig. 4. Spectral energy distributions measured by MAGIC, VERITAS, and the *Whipple* 10 m during the low state of the source and two states of increased VHE flux. The spectra have been corrected for EBL absorption using the model of Franceschini et al. (2008).

Table 1. Fit parameters and goodness of fit describing the power-law function for the measured VHE γ -ray spectra.

Instrument	Flux state	MJD	F_0 [10^{-7} ph m^{-2} s^{-1} TeV^{-1}]	Γ	χ^2/ndf
<i>Whipple</i>	very high	54 952.35–54 952.41	16.1 ± 0.4	2.10 ± 0.05	13.5/8
<i>Whipple</i>	high	54 952.41–54 955	5.6 ± 0.4	2.31 ± 0.11	3.1/8
VERITAS	high	54 952.41–54 955	4.17 ± 0.24	2.26 ± 0.06	6.3/5
MAGIC	high	54 973	3.1 ± 0.2	2.28 ± 0.06	1.9/6
<i>Whipple</i>	low	54 936–54 951	1.16 ± 0.09	2.61 ± 0.11	3.4/8
VERITAS	low	54 907–55 004	0.88 ± 0.06	2.48 ± 0.07	3.8/5
MAGIC	low	54 913–55 038	0.93 ± 0.04	2.40 ± 0.05	8.4/6

Notes. For low-state spectra, the stated flaring time intervals have been excluded from the data. Spectral fits for the *Whipple* 10 m and VERITAS are listed as presented in Pichel & Paneque (2011).

Table 2. Spectral parameters describing the measured power-law spectra with *Fermi*-LAT during several temporal intervals in May 2009.

Temporal interval	MJD range	$F_{>300 \text{ MeV}}$ [10^{-8} ph m^{-2} s^{-1}]	Γ	TS
May 2009, 30 days	54 952–54 982	4.2 ± 0.5	1.68 ± 0.07	595
First Flare, 2 days	54 951–54 953	2.5 ± 1.3	1.2 ± 0.3	43
First Flare, 7 days	54 948.5–54 955.5	1.7 ± 0.8	1.4 ± 0.2	41
Second Flare, 2 days	54 972–54 974	4.0 ± 1.7	1.8 ± 0.3	39
Second Flare, 7 days	54 969.5–54 976.5	5.3 ± 1.0	1.6 ± 0.1	263

a ToO program, and so they provide a better characterization of the enhanced activity (see Sect. 2).

Around the first VHE flare, the XRT spectra tend to be much harder and appear to show an upward curvature towards higher energies. The hardening of the spectrum is confirmed by a spectral analysis performed using a power-law spectral model with the hydrogen density N_H fixed to the Galactic value. Figure 6 shows the spectral index light curve (see also Table 3) and the reduced χ^2 of the individual fits. Based on the reduced χ^2 values,

the representation by a simple power-law function is sufficient for most spectra. Around MJD 54 952–54 953, which roughly corresponds to the time of the first VHE flare, a peak in the hardness of the spectrum can be seen.

Around the second flux increase in the VHE γ -ray band, variability was seen by both *Swift*/XRT and RXTE/PCA, with flux changes of up to a factor of 2 with respect to the flux average of $\sim(7-8) \times 10^{-11}$ erg cm^{-2} s^{-1} in the 2–10 keV band (see Fig. 1).

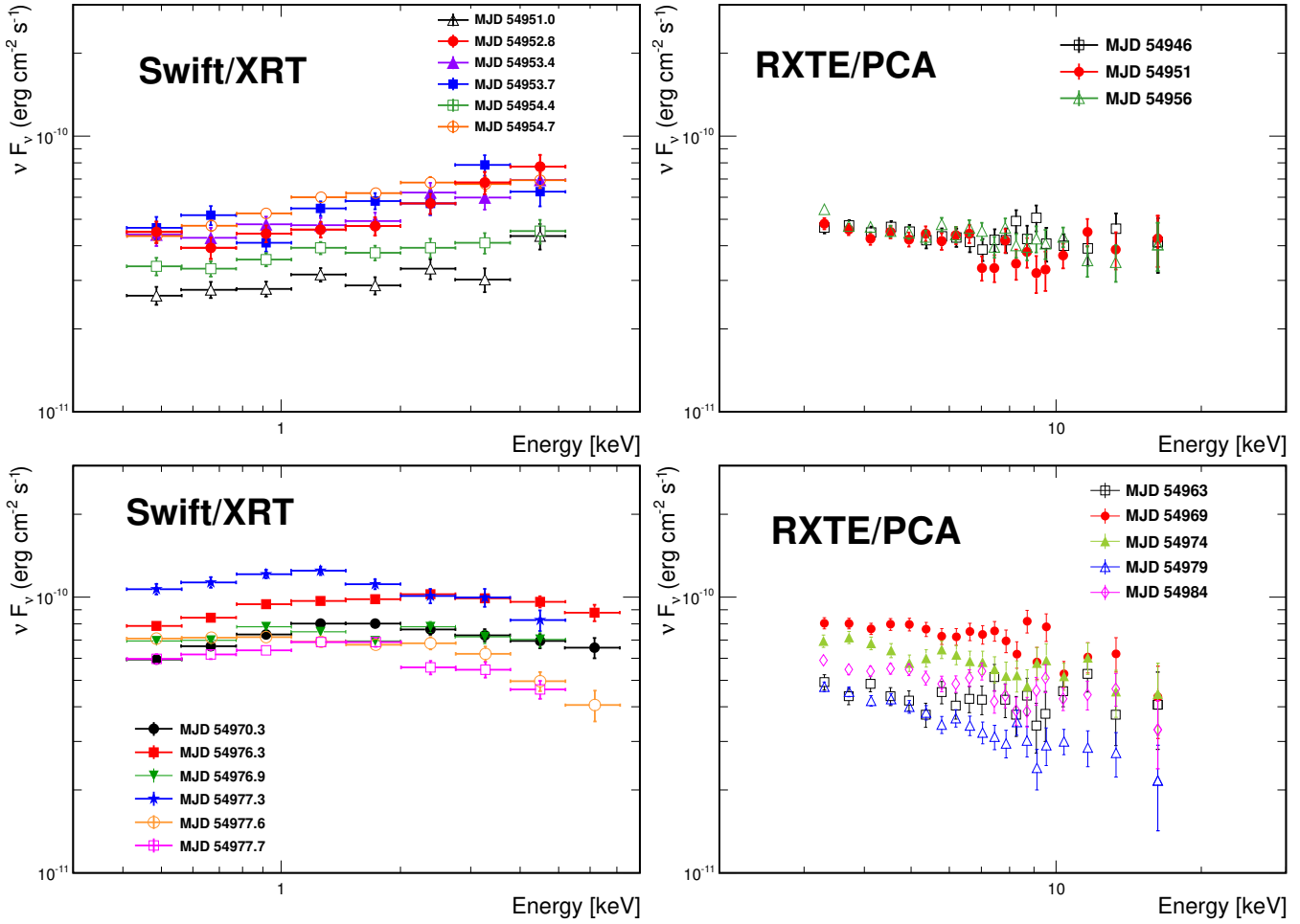


Fig. 5. X-ray spectra from single pointings. *Left:* Swift/XRT. *Right:* RXTE/PCA. *Upper panels:* spectra around the first flare (MJD 54952); *lower panels:* spectra around the second flare (MJD 54973).

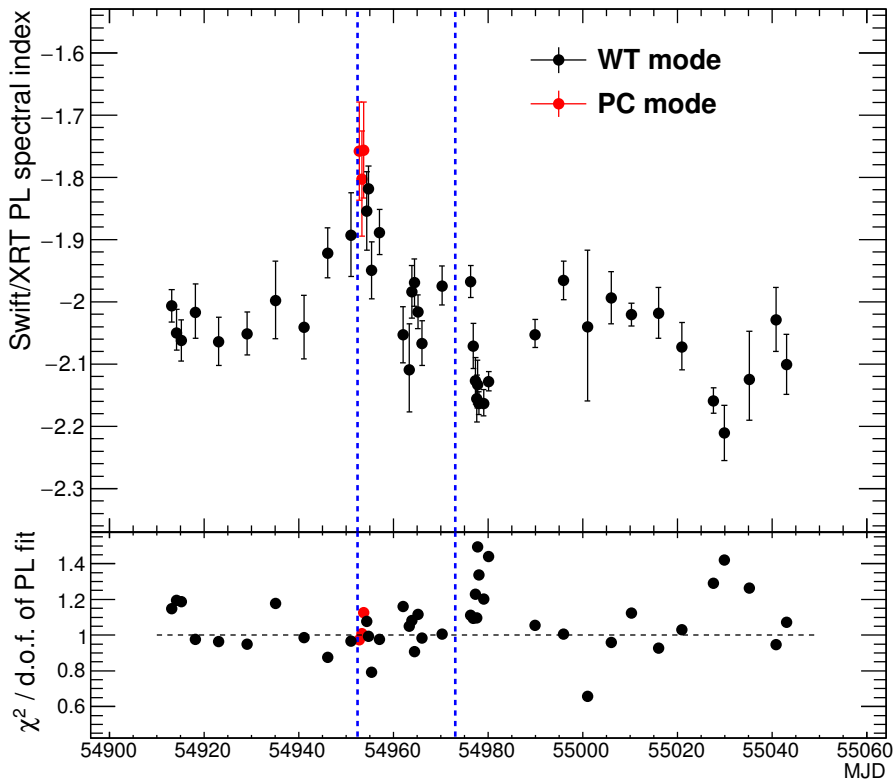


Fig. 6. *Upper panel:* spectral index obtained from a power-law fit to the Swift/XRT spectra vs. observation date. *Lower panel:* reduced χ^2 of the power-law fit to the X-ray spectra. The two vertical blue lines indicate the location of the two VHE γ -ray flares at MJD 54952 and MJD 54973 that are discussed in Sects. 4.2 and 4.3.

Table 3. Spectral results from the power-law (PL) fit to the measured *Swift*/XRT spectra.

MJD	Obs Mode	PL Index	$\chi^2/\#d.o.f.$	MJD	Obs Mode	PL Index	$\chi^2/\#d.o.f.$
54 913.1	WT	$-2.01^{+0.03}_{-0.03}$	246/214	54 966.0	WT	$-2.07^{+0.04}_{-0.04}$	180/183
54 914.2	WT	$-2.05^{+0.04}_{-0.03}$	246/206	54 970.2	WT	$-1.97^{+0.03}_{-0.03}$	200/199
54 915.2	WT	$-2.06^{+0.03}_{-0.03}$	200/168	54 976.3	WT	$-1.97^{+0.03}_{-0.03}$	271/244
54 918.2	WT	$-2.02^{+0.05}_{-0.04}$	130/133	54 976.9	WT	$-2.07^{+0.04}_{-0.04}$	201/184
54 923.1	WT	$-2.06^{+0.04}_{-0.04}$	160/166	54 977.3	WT	$-2.13^{+0.04}_{-0.04}$	171/139
54 929.1	WT	$-2.05^{+0.03}_{-0.03}$	179/189	54 977.6	WT	$-2.16^{+0.04}_{-0.04}$	178/162
54 935.0	WT	$-2.00^{+0.06}_{-0.06}$	88/75	54 977.7	WT	$-2.13^{+0.04}_{-0.04}$	245/164
54 941.1	WT	$-2.04^{+0.05}_{-0.05}$	111/113	54 978.0	WT	$-2.16^{+0.02}_{-0.02}$	424/317
54 946.1	WT	$-1.92^{+0.04}_{-0.04}$	139/159	54 979.0	WT	$-2.16^{+0.02}_{-0.02}$	359/298
54 951.0	WT	$-1.89^{+0.07}_{-0.07}$	62/64	54 980.1	WT	$-2.13^{+0.02}_{-0.01}$	497/345
54 952.8	PC	$-1.76^{+0.08}_{-0.08}$	56/58	54 989.9	WT	$-2.05^{+0.02}_{-0.02}$	303/287
54 953.4	PC	$-1.80^{+0.08}_{-0.09}$	57/56	54 995.9	WT	$-1.97^{+0.03}_{-0.03}$	197/196
54 953.7	PC	$-1.76^{+0.08}_{-0.08}$	66/59	55 001.0	WT	$-2.04^{+0.10}_{-0.10}$	14/21
54 954.4	WT	$-1.85^{+0.06}_{-0.06}$	84/78	55 006.0	WT	$-1.99^{+0.04}_{-0.04}$	152/159
54 954.7	WT	$-1.82^{+0.04}_{-0.04}$	165/166	55 010.3	WT	$-2.02^{+0.02}_{-0.02}$	331/295
54 955.4	WT	$-1.95^{+0.05}_{-0.05}$	100/126	55 015.9	WT	$-2.02^{+0.04}_{-0.04}$	147/158
54 957.1	WT	$-1.89^{+0.04}_{-0.03}$	163/167	55 020.9	WT	$-2.07^{+0.04}_{-0.04}$	180/175
54 962.0	WT	$-2.05^{+0.05}_{-0.04}$	125/108	55 027.6	WT	$-2.16^{+0.02}_{-0.02}$	377/292
54 963.4	WT	$-2.11^{+0.07}_{-0.07}$	79/75	55 029.9	WT	$-2.21^{+0.04}_{-0.04}$	144/101
54 963.9	WT	$-1.98^{+0.04}_{-0.04}$	140/129	55 035.2	WT	$-2.12^{+0.08}_{-0.07}$	89/70
54 964.4	WT	$-1.97^{+0.04}_{-0.04}$	141/155	55 040.8	WT	$-2.03^{+0.05}_{-0.05}$	101/107
54 965.1	WT	$-2.02^{+0.03}_{-0.03}$	269/241	55 043.0	WT	$-2.10^{+0.05}_{-0.05}$	109/102

Notes. For all spectra where the PL fit does not deliver a satisfactory result (fit probability $P < 0.3\%$ (3σ)), additional results from a log-parabola fit are quoted in the following: MJD 54 977.7: $\alpha = 2.01^{+0.05}_{-0.06}$, $\beta = 0.4^{+0.1}_{-0.1}$, $\chi^2/d.o.f. = 214/163$; MJD 54 978.0: $\alpha = 2.05^{+0.03}_{-0.03}$, $\beta = 0.32^{+0.06}_{-0.06}$, $\chi^2/d.o.f. = 335/316$; MJD 54 980.1: $\alpha = 2.03^{+0.02}_{-0.02}$, $\beta = 0.312^{+0.05}_{-0.05}$, $\chi^2/d.o.f. = 373/344$; MJD 55 027.6: $\alpha = 2.04^{+0.03}_{-0.03}$, $\beta = 0.33^{+0.06}_{-0.06}$, $\chi^2/d.o.f. = 293/291$.

However, no particular hardening of the spectrum was found (see Fig. 6), as was observed for the first flare.

3.3. Quantification of the multi-instrument variability

As a quantitative study of the underlying variability seen at different wavelengths, the fractional variability F_{var} was determined for each instrument according to Eq. (10) in Vaughan et al. (2003),

$$F_{\text{var}} = \sqrt{\frac{S^2 - \langle \sigma_{\text{err}}^2 \rangle}{\langle F_{\gamma} \rangle^2}}, \quad (2)$$

where S^2 represents the variance, $\langle \sigma_{\text{err}}^2 \rangle$ specifies the mean square error stemming from measurement uncertainties, and $\langle F_{\gamma} \rangle$ is the arithmetic mean of the measured flux. The term under the square root is also known as the normalized excess variance σ_{NXS}^2 .

The uncertainty of F_{var} is calculated following the prescription in Poutanen et al. (2008), as described in Aleksić et al. (2015a), so that they are also valid in the case when $\Delta F_{\text{var}} \sim F_{\text{var}}$,

$$\Delta F_{\text{var}} = \sqrt{F_{\text{var}}^2 + \text{err}(\sigma_{\text{NXS}}^2)} - F_{\text{var}}, \quad (3)$$

with the error of the normalized excess variance $\text{err}(\sigma_{\text{NXS}}^2)$ as defined in Eq. (11) in Vaughan et al. (2003).

This method for quantifying the variability comes with the caveat that the resulting F_{var} and related uncertainty depend very much on instrument sensitivity and the observing sampling, which is different for the different energy bands. In other words, a densely sampled light curve with small uncertainties in the flux measurements may allow us to see flux variations that are hidden otherwise, and hence may yield a larger F_{var} and/or smaller uncertainties in the calculated values of F_{var} . Some practical issues in the application of this methodology in the context of multi-wavelength campaigns are elaborated in Aleksić et al. (2014, 2015b,a).

For *Swift*/XRT and RXTE/PCA in the X-ray band, and MAGIC, VERITAS, and the *Whipple* 10 m in the VHE regime, the fractional variability has been calculated for the full data set and also after removal of the temporal intervals related to the two flaring episodes (MJD 54 952–54 955, MJD 54 973–54 978). The fractional variability specifically computed for the period around the first flaring episode has been recently reported in Aliu et al. (2016). For measurements in the optical *R* band, F_{var} has additionally been calculated for optical fluxes corrected for the host galaxy emission as derived in Nilsson et al. (2007). For data sets containing fewer than five data points, no F_{var} was calculated. The results are presented in Fig. 7.

A negative excess variance was obtained for data sets from the following instruments: UMRAO (at 5 GHz and 8 GHz), Noto (at 8 GHz and 43 GHz), Medicina (at 8 GHz), Effelsberg (all bands), and the near-IR measurements within the GASP-WEBT program (all bands). Such a negative excess variance is

interpreted as an absence of flux variability within the sensitivity range of the instrument. These data sets have not been included in Fig. 7.

At low frequencies, from radio to optical, no substantial variability was detected, with F_{var} ranging from ≈ 0.02 – 0.06 in radio to 0.01 – 0.1 in optical. In the X-ray band, we find $F_{\text{var}} \approx 0.3$, indicating substantial variation in the flux during the probed time interval. After removal of the flaring times, variabilities of $F_{\text{var}} \approx 0.2$ – 0.25 are still seen. The fractional variability in the γ -ray band covered by *Fermi*-LAT is on the order of $F_{\text{var}} \approx 0.3$ – 0.4 ; yet the *Fermi*-LAT F_{var} values are not directly comparable to the other instruments, as GeV variability on day timescales, which could be higher than that computed (separately) for the 15-day and the 30-day timescales, cannot be probed. Strong variability can be noted at VHE with $F_{\text{var}} \geq 0.4$ for the data sets without the flares and $F_{\text{var}} \geq 0.6$ (0.9 for *Whipple* 10 m) for observations including the flaring episodes.

All in all, Mrk 501 showed a large increase in variability with increasing energy, ranging from an almost steady behavior at the lowest frequencies to the highest variability observed in the VHE band.

3.4. Multi-instrument correlations

To study possible cross-correlations of flux changes between the different wavelengths, we determined the discrete correlation functions (DCF), following [Edelson & Krolik \(1988\)](#), based on the light curves obtained by the various instruments. The DCF allows a search for correlations with possible time lags, which could result for example from a spatial separation of different emission regions. We probed time lags in steps of 5 days up to a maximum shift of 65 days. The step size corresponds to the overall sampling of the light curve and thus to the objective of the MWL campaign itself, which was to probe the source activity and spectral distribution every ≈ 5 days. The maximum time span is governed by the duration of the campaign, as a good fraction of the light curve should be available for the calculation of cross-correlations. We chose a maximum of 65 days, which corresponds to roughly half the time span of the entire campaign. Because of the uneven sampling and varying exposure times, the significance of the correlations derived from the prescription given in [Edelson & Krolik \(1988\)](#) might be overestimated ([Uttley et al. 2003](#)). We derived an independent assessment of the significance of the correlation by means of dedicated Monte Carlo simulations as described in [Arévalo et al. \(2009\)](#) and [Aleksić et al. \(2015b,a\)](#).

In this study, possible cross-correlations between instruments of different wavelengths were examined. As already suggested by the low level of variability in the radio and optical band throughout the campaign, no correlations with any other wavelengths were found for these instruments. A correlation with flux changes in the MeV–GeV range could not be probed on timescales of days due to the integration time of 15–30 days required by *Fermi*-LAT for a significant detection. A similar situation occurs in the X-ray bands from *Swift*/BAT and RXTE/ASM, which also need integration times of the same order, and are thus also neglected for day-scale correlation studies.

Therefore, the study focuses on the highly sensitive X-ray and VHE γ -ray observations, namely the ones performed with *Swift*/XRT, RXTE/PCA, MAGIC, VERITAS, and *Whipple* 10 m, which are also the ones that report the highest variability (see Fig. 7). In the VHE γ -ray band, the number of observations is relatively small (in comparison to the number of X-ray observations performed with *Swift* and RXTE), and hence we compile a single

light curve with a dense temporal sampling of Mrk 501, including the measured flux points from all three participating VHE γ -ray telescopes. This procedure is straightforward as VERITAS and MAGIC both measured the flux above 300 GeV and the *Whipple* 10 m measurements have been scaled to report a flux in the same energy range (see Sect. 2). We also combined measurements by *Swift*/XRT in the 2–10 keV band and data points from RXTE/PCA to a single light curve, as the same energy range is covered by the two instruments. The light curve in the 0.3–2 keV band only consists of measurements performed by *Swift*/XRT. The DCF vs. time-shift distributions for the two X-ray bands and the VHE γ -ray measurements are shown on the left-hand side of Fig. 8.

At a time lag $\Delta T = (T_{\text{VHE}} - T_{\text{X-ray}})$ on the order of -20 to -25 days, a hint of correlation at the level of 2σ between fluxes in the soft X-ray band and the VHE γ -ray band is seen in the top left panel of Fig. 8. This feature is dominated by the two flaring events, as the dominant flare in VHE γ rays occurred around MJD 54 952, while the largest flux increase in soft X-rays was seen around MJD 54 977, with a separation of 24–25 days. The right-hand side of Fig. 8 reports the evaluation of the correlations after the flaring episodes have been excluded from the X-ray and VHE γ -ray light curves. The above-mentioned feature at 20–25 days is no longer present.

The large growth of the confidence intervals apparent at time shifts of $\Delta T \approx 40$ days are caused by sparsely populated regions in the VHE γ -ray light curve, mainly towards the end of the campaign. When the light curves are shifted by ≈ 40 days with respect to each other, these regions overlap with densely populated regions in the X-ray light curves, which results in a larger uncertainty of the determined DCF.

Overall, no significant correlation between X-ray and VHE γ -ray fluxes is found for any of the combinations probed.

4. Evolution of the spectral energy distribution

The time-averaged broadband SED measured during this MWL campaign (from MJD 54 905 to MJD 55 044) was reported and modeled satisfactorily in the context of a one-zone synchrotron self-Compton (SSC) scenario ([Abdo et al. 2011a](#)). In this model, several properties of the emission region are defined, such as the size of the region R , the local magnetic field B , and the Doppler factor δ , which describes the relativistic beaming of the emission towards the observer. Furthermore, the radiating electron population is described by a local particle density n_e and the spectral shape. For the averaged data set of this campaign, the underlying spectrum of the electron population was parameterized with a power-law distribution from a minimum energy γ_{min} to a maximum energy γ_{max} , with two spectral breaks $\gamma_{\text{break},1}$ and $\gamma_{\text{break},2}$. The two breaks in the electron energy distribution (EED) were required in order to properly model the entire broadband SED. Because of the relatively small multiband variability during the 4.5-month observing campaign (once the first VHE flare was removed) and the large number of observations performed with all the instruments, the average SED could be regarded as a high-quality representation of the typical broadband emission of Mrk 501 during the time interval covered by the campaign, and hence the one-zone SSC model was constrained to describe all the data points (including 230 GHz SMA and interferometric 43 GHz VLBA observations).

In this work, we focus on the characterization of the broadband SED during the two flaring episodes occurring in May 2009. As reported in Sect. 3.1, these two flaring episodes start on

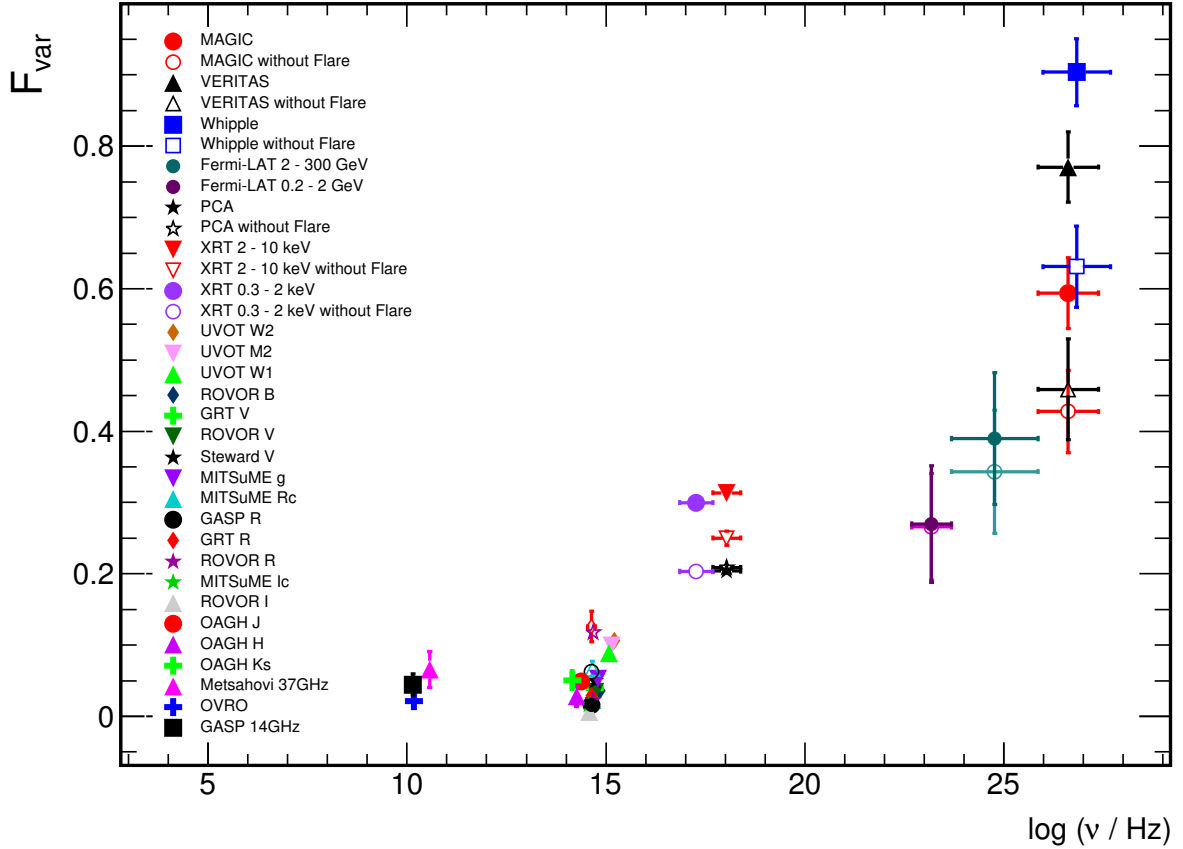


Fig. 7. Fractional variability at different frequencies. All the F_{var} values are computed with the single observations shown in Fig. 1, with the exception of the F_{var} values related to *Fermi*-LAT which were computed with 15-day and 30-day time intervals, and depicted with full circles and open circles, respectively. Open symbols for optical bands indicate the fractional variability after subtracting the host galaxy contribution, as determined in Nilsson et al. (2007). For the X-ray and the VHE γ -ray band, open markers depict the variability after removal of flaring episodes from the light curves as described in the text.

Table 4. SSC model parameters that characterize the average emission over the entire MWL campaign.

Parameter	γ_{min}	γ_{max}	$\gamma_{\text{break},1}$	$\gamma_{\text{break},2}$	α_1	α_2	α_3	n_e	B/mG	$\log\left(\frac{R}{\text{cm}}\right)$	δ
Av. state	600	1.5×10^7	4×10^4	9×10^5	2.2	2.7	3.65	635	15	17.11	12

Notes. The parameters apply to a one-zone model defined by Eq. (4) and are retrieved from the modeling presented in Abdo et al. (2011a).

MJD 54 952 and MJD 54 973, and last for approximately three and five days, respectively. There is some flux and spectral variability throughout these two flaring episodes, but for the sake of simplicity in this section we attempt to model only the SEDs related to the VHE flares on MJD 54 952 and 54 973, which are the first days of these two flaring activities. We try to model these two SEDs with the simplest leptonic scenarios, namely a one-zone SSC and a two-independent-zone SSC model. In the latter we assume that the quiescent or slowly changing emission is dominated by one region that is described by the SSC model parameters used for the average/typical broadband emission from the campaign (see Abdo et al. 2011a), while the flaring emission (essentially only visible in the X-ray and γ -ray bands) is dominated by a second independent and spatially separated region.

The assumption of a theoretical scenario consisting of one (or two) steady-state homogenous emission zone(s) could be an oversimplification of the real situation. The blazar emission may be produced in inhomogeneous regions, involving stratification of the emitting plasma both along and across a relativistic outflow, and the broadband SED may be the superposition

of the emission from all these different regions, characterized by different parameters and emission properties, as reported by various authors (e.g. Ghisellini et al. 2005; Graff et al. 2008; Giannios et al. 2009; Chen et al. 2011; Zhang et al. 2014; Chen et al. 2015). In this paper we decided to continue using the same theoretical scenario used in Abdo et al. (2011a), which we adopted as the reference paper for this data set. We also kept the discussion of the model parameters at a basic level, and did not attempt to perform a profound study of the implications of these parameters.

In this work we used the SSC model code described in Takami (2011), which is qualitatively the same as the one used in Abdo et al. (2011a), with the difference that the EED is parameterized as

$$\frac{dN}{d\gamma} = \begin{cases} n_e \cdot \gamma^{-\alpha_1}, & (\gamma_{\text{min}} < \gamma < \gamma_{\text{break},1}) \\ n_e \cdot \gamma_{\text{break},1}^{\alpha_2 - \alpha_1} \cdot \gamma^{-\alpha_2}, & (\gamma_{\text{break},1} < \gamma < \gamma_{\text{break},2}) \\ n_e \cdot \gamma_{\text{break},1}^{\alpha_2 - \alpha_1} \cdot \gamma_{\text{break},2}^{\alpha_3 - \alpha_2} \cdot e^{\left(\frac{\gamma_{\text{break},2}}{\gamma_{\text{max}}}\right)} \cdot \gamma^{-\alpha_3} \cdot e^{\left(-\frac{\gamma}{\gamma_{\text{max}}}\right)}, & (\gamma_{\text{break},2} < \gamma), \end{cases}$$

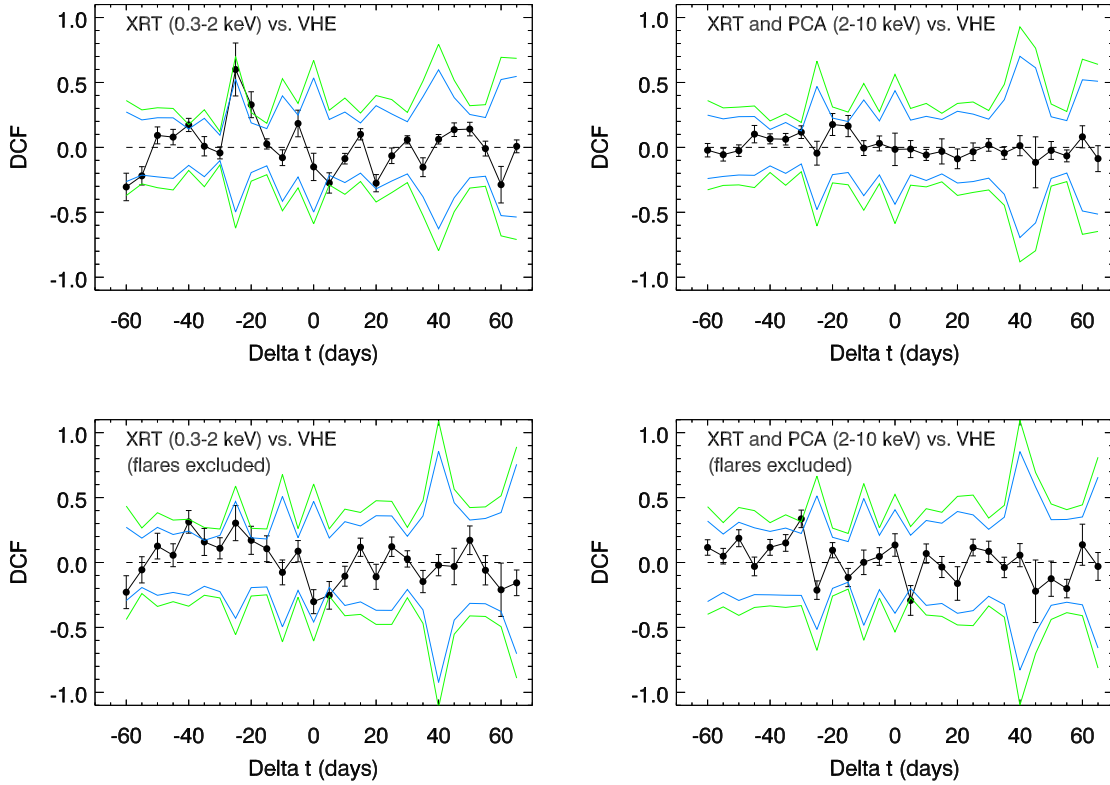


Fig. 8. DCF derived for VHE γ rays (combined from MAGIC, VERITAS, and *Whipple* measurements) and two X-ray bands (*Swift*/XRT measurements within the 0.3–2 keV band; *Swift*/XRT and RXTE/PCA combined within the 2–10 keV band). The blue (green) lines depict the 95% (99%) confidence intervals derived from Monte Carlo generated light curves (see text for detailed explanation). *Left*: DCF of complete data sets. *Right*: DCF derived with the data sets after subtracting the two flaring periods (excluded time windows as explained in the text).

(4)

where n_e is the electron number density. For reasons of comparability, only this definition is applied in all the SED modeling results in this section, including that of the quiescent, averaged SED obtained over the full MWL campaign. The corresponding one-zone SSC model parameter values defining the averaged SED from the full 2009 multi-instrument campaign are listed in Table 4. The parameter values are identical to those from the “Main SSC fit” reported in Table 2 of [Abdo et al. \(2011a\)](#), with the only difference being the usage of the electron number density n_e , instead of the equipartition parameter. The contribution of starlight from the host galaxy can be approximately described with the template from [Silva et al. \(1998\)](#), as was done in [Abdo et al. \(2011a\)](#).

For the characterization of the SEDs collected during the two flaring states, we allow for an EED with two spectral breaks in the case of one-zone SSC models. For the second zone in the two-zone SSC scenario, we keep the somewhat simpler description of the electron energy distribution as a power law with only one spectral break (i.e. $\alpha_2 \equiv \alpha_1$ in Eq. (4)).

4.1. Grid-scan strategy for modeling the SED

In contrast to the commonly used method of adjusting the model curve to the measured SED data points (e.g. [Tavecchio et al. 1998, 2001b](#); [Albert et al. 2007a](#)), in this study we applied a novel variation on the *grid-scan* approach in the space of model parameters. Given a particular theoretical scenario (e.g. the one-zone or two-zone SSC model), we make a multi-dimensional grid with the N model parameters that we want to sample. For each parameter, we define a range of allowed values and a step size for

the variation within this range. Theoretical (SSC) model curves are calculated for each point on the grid, i.e. for each combination of the N parameter values. Subsequently, the goodness of the resulting model curves in reconstructing the data points is quantified by means of the χ^2 between data and model, which takes into account the statistical uncertainties of the individual measurements. At the moment, systematic uncertainties are not considered for the evaluation of the agreement. This would require performing the entire procedure for various shifts in the flux and energy scale for each instrument, as well as for possible distortions in the individual spectra. The net impact of including systematic uncertainties in the single-instrument spectra would be a larger tolerance for the agreement between the experimental data and the theoretical model curves, which would yield a larger degeneracy in the parameter values that can model the data. While this will be investigated in the future, it is beyond the scope of this paper. Therefore, the data-model agreements reported in this manuscript, which are based on the χ^2 analysis using only the statistical uncertainties, provide a lower limit to the actual agreement between the presented experimental data and the theoretical model curves being tested, and we mostly use them to judge the relative agreement of the various theoretical model curves.

Depending on the complexity of the model itself, the model calculations for an entire grid can be very intensive in computing power. For instance, one of the simplest SSC scenarios, involving only one emission zone with an electron energy distribution with one spectral break, already leads to a grid spanning a nine-dimensional parameter space. With the ranges and grid spacings we are using in this work, the number of model curves to calculate and evaluate amounts to tens of million. For this reason, the

access to cluster computing becomes essential for this grid-scan modeling approach. The model calculations in this work have been performed using the computing farms at SLAC⁹ and TU Dortmund¹⁰.

After the evaluation of all models regarding their level of agreement with the data, individual models can be chosen for the final set, according to the achieved probability of agreement (derived from the χ^2 and the number of degrees of freedom). These sets of models can then be visualized both in the SED representation and in the space of parameter values defining the models, which could populate non-continuous regions in the parameter space.

One aim of the grid-scan strategy is to keep the range of model parameters as wide as possible. By sampling a large parameter phase space we can reduce the bias which is usually introduced into the model by adopting a set of assumptions or educated choices. In addition to the obvious aim of finding parameter values which describe the data in the best way, another advantage is that the “grid-scan” approach also offers the possibility of investigating the degeneracy of the model-to-data agreement regarding each individual model parameter. In order to do this, sets of models within bands of achieved fit probabilities are compiled and their distributions in each of the model parameters are visualized. Based on such plots, interesting regions in the parameter space can be selected for a deeper search, which leads to models with an even better agreement with the data and to a more thorough study of the degeneracy of individual model parameters. Finally, the grid-scan method can find multiple clusters or regions in the model parameter phase space that could be related to different physical scenarios, which can be equally applicable to the data set at hand, but might be missed by statistical methods aiming at only “one best” solution.

The concept of grid-scan SED modeling has already been presented in Cerruti et al. (2013), where model curves are computed for each point on the parameter space grid, but the assessment of the agreement between model and data is performed in a different way: the authors evaluate the agreement based on seven observables (i.e. the frequency and luminosity of the synchrotron peak, the measured X-ray spectral slope and the GeV and TeV spectral slopes and flux normalizations), which are derived from the model curves and are compared to the data. They also provide a family of solutions involving any uncertainties in the observables. In the work presented here, the model-to-data agreement criterion, which is used to select a set of models, is derived directly from the χ^2 -distances between each data point and each model curve without computing any secondary characteristics of the SED which may introduce additional uncertainties. Cerruti et al. (2013) also determine this distance for the models picked by their algorithm, but apply it only as a posteriori check of their result. Furthermore, the authors have reduced the dimensionality of the parameter space from nine to six, and used only five steps for each parameter, which implies the creation of a grid with $5^6 = 15\,625$ SED realizations. In the work presented here, the smallest grid-scan implies the creation of more than 40×10^6 SED realizations. Additionally, after selecting interesting regions in the various model parameters with the grid-scan, we went one step further and performed a second (dense) grid-scan focused only on those regions, and using a smaller step size.

The objective of finding uncertainty ranges of model parameters has also been addressed by Mankuzhiyil et al. (2011)

⁹ <https://www.slac.stanford.edu/comp/unix/unix-hpc.html>

¹⁰ <http://www.cs.tu-dortmund.de/nps/en/Home/>

and Zabalza (2015). Here, a Markov chain Monte Carlo procedure is used to fit emission model curves (for a number of different emission models) to the observational results. While this approach delivers uncertainties or probability distribution functions for the particle distribution parameters, this is done only for one particular solution. Disjointed regions of equally good model configurations, i.e. “holes” in the probability distribution for the individual parameters, are not found following this method.

A three-dimensional parameter grid with 9504 ($48 \times 22 \times 9$) steps was used by Petry et al. (2000) to find the most suitable model parameter set to describe weekly averaged SEDs of Mrk 501, where the “best” model was selected as the one with the smallest data-model difference, quantified with a χ^2 approach. Although a parameter grid was used, the goal and merits of that work differ from those of the methodology presented here. While Petry et al. (2000) used the three-dimensional parameter grid to find the best model (as in Mankuzhiyil et al. 2011, with a χ^2 minimization procedure), in this work the nine-dimensional grid is used to find the family (or families) of parameter values that give a good representation of the broadband SED, and to show the large degeneracy of the model parameters to describe the SED.

For the theoretical SED modeling of the two flaring states of Mrk 501, following the grid-scan strategy outlined above, the parameter ranges given in Tables 5 and 6 have been investigated for the one-zone and two-zone scenarios described at the beginning of this section. Given that we aim to sample a wide range of parameter values with a relatively coarse step (for each parameter), we denote these scans as “coarse grid-scans”. The general orientation for the choice of parameter ranges is based on previous works on modeling of the SED of Mrk 501, e.g. Albert et al. (2007a), Anderhub et al. (2009), Abdo et al. (2011a), Mankuzhiyil et al. (2012). Based on these values¹¹, one-zone SSC models have been built and second zones for the two-zone scenario as well. In the latter, the first zone is described by the model reproducing the average emission seen over the entire campaign (see Abdo et al. 2011a), while only the second zone is varied as described by the model parameters from the grid presented here. The phase space of the grid-scan could have been reduced by imposing a relation between the locations of the breaks (γ_{break}) and the size R and magnetic field B values, and by forcing the change of index before and after the breaks to be one (i.e. $\Delta\alpha = 1$). However, cooling breaks with a spectral change two times larger than the canonical value of one were necessary to describe the broadband SED of Mrk 421 within a SSC homogeneous model scenario (see Sect. 7.1 of Abdo et al. 2011b), and the breaks needed by the SSC models are not always related to the cooling of the electrons, but instead could be related to the acceleration mechanism, as reported for Mrk 501 in Abdo et al. (2011a). Internal breaks (related to the electron acceleration) have been reported for various blazars (e.g. Abdo et al. 2009; Abdo et al. 2010a). The origin of these internal breaks, as well as large spectral changes at the EED breaks, may be related to variations in the global field orientation, turbulence levels sampled by particles of different energy, or gradients in the physical quantities describing the system. These characteristics are not taken

¹¹ Many of the works in the literature use $\gamma_{\text{min}} = 1$ (e.g. Tavecchio et al. 2001b; Albert et al. 2007a; Mankuzhiyil et al. 2012), but we decided to follow here the approach used in Abdo et al. (2011a), where a $\gamma_{\text{min}} \gg 1$ had to be used in order to properly describe the simultaneous GeV data from *Fermi*-LAT and the high-frequency radio observations from SMA and VLBA, which did not exist in the previous publications parameterizing the broadband SED of Mrk 501.

Table 5. Grid of SSC model parameters that is probed for one-zone models within the coarse grid-scan.

Coarse grid											
one-zone	γ_{\min}	γ_{\max}	$\gamma_{\text{break},1}$	$\gamma_{\text{break},2}$	α_1	α_2	α_3	n_e	B/mG	$\log\left(\frac{R}{\text{cm}}\right)$	δ
min	1×10^2	1×10^6	1×10^4	1×10^5	1.7	2.1	3.6	1×10^3	5	14.0	1
max	1×10^4	1×10^8	1×10^5	3.2×10^6	2.3	3.3	4.8	1×10^6	250	16.0	60
# of steps	3	3	4	4	7	7	4	7	9	5	7
Spacing	log	log	log	log	lin	lin	lin	log	log	lin	log

Notes. For each parameter the probed range is given by a minimum and a maximum value, and the number of tested values is given by the number of steps between (and including) these limits. The number of SSC models required to realize this grid-scan amounts to 62 million.

Table 6. Grid of SSC model parameters that is probed for two-zone models within the coarse grid-scan.

Coarse grid										
two-zone	γ_{\min}	γ_{\max}	γ_{break}	α_1	α_2	n_e	B/mG	$\log\left(\frac{R}{\text{cm}}\right)$	δ	
min	1×10^2	1×10^5	1×10^4	1.7	2.0	100	5	14.0	1	
max	1×10^6	1×10^8	1×10^7	2.3	4.8	1×10^6	250	18.0	60	
# of steps	5	4	7	7	8	9	9	9	7	
Spacing	log	log	log	lin	lin	log	log	lin	log	

Notes. In two-zone models only the second zone is defined by the parameters given here, while the first zone is given by the model derived in [Abdo et al. \(2011a\)](#) and reported in Table 4. The number of SSC models required to realize this grid-scan amounts to 40 million.

into account in the relatively simple homogenous SSC models, and argue for more sophisticated theoretical scenarios like the ones mentioned above. In order to keep the range of allowed model parameter values as broad as possible, in this exercise we did not impose constraints on the location of the EED breaks or in the index values before or after the breaks. The hardest index we use in this study is 1.7, which is harder than the canonical index values >2 derived from shock acceleration mechanisms and used very often to parameterize the broadband SEDs of blazars. But this is actually not a problem as various authors have shown that indices as hard as 1.5 can be produced through stochastic acceleration (e.g. [Virtanen & Vainio 2005](#)) or through diffusive acceleration in relativistic magnetohydrodynamic shocks, as reported in [Stecker et al. \(2007\)](#), [Summerlin & Baring \(2012\)](#) and [Baring et al. \(2016\)](#). We also use γ_{\min} values extending up to 10^6 , substantially higher than those used in conventional SSC models (which typically go up to $\sim 10^3$), but such high γ_{\min} values have already been used by various authors (e.g. [Katarzyński et al. 2006](#); [Tavecchio et al. 2009](#); [Lefa et al. 2011a,b](#)).

In the evaluation of the models, we used two other constraints in addition to the requirement of presenting a good agreement with the SED data points. Equipartition arguments impose the condition that the energy densities held by the electron population (u_e) and the magnetic field (u_B) should be of comparable order. Typically, the parameterization of the broadband SED of Mrk501 (and all TeV blazars in general) within SSC theoretical scenarios require $u_e \sim 10^{2-3} u_B$, which implies higher energy in the particles than in the magnetic field, at least locally, where the broadband blazar emission is produced (see e.g. [Tavecchio et al. 2001b](#); [Abdo et al. 2011a](#); [Aleksić et al. 2015b](#)). There is no physical reason for any specific (somewhat arbitrary) cut value in the quantity u_e/u_B ; however, driven by previous works in the literature, in this study we only consider models fulfilling the requirement of $u_e/u_B < 10^3$. Secondly, the observed variability timescales have to be taken into account. Following causality arguments, the observed variability should not happen on timescales that are shorter than the time needed

to distribute information throughout the emitting region. Based on the given Doppler factor δ and the size of the emitting region R , the implied minimum variability timescale quantity for each model is derived according to

$$t_{\text{var},\min} \simeq \frac{(1+z)R}{\delta c}. \quad (5)$$

For the first flare we observed large flux changes (up to factors of ~ 4) within 0.5 h ([Pichel & Paneque 2011](#); [Aliu et al. 2016](#)); instead, the second flare shows substantial flux changes (~ 2) on timescales of several days. Consequently, we consider only models that yield a minimum variability timescale of $t_{\text{var},\min} \leq 0.25$ h and $t_{\text{var},\min} \leq 1$ day for the first and second VHE flare, respectively.

4.2. First VHE flare

All spectral points that were obtained at the time or close to the time of the VHE flare measured by VERITAS and the *Whipple* 10 m telescope at MJD 54952 are shown in the top panel of Fig. 9 (see Sects. 3.1.1 and 3.1.1 for details on the individual observation times).

The attempt to apply the grid-scan to the broadband SED from this flaring episode is affected by the flux variability on sub-hour timescales and the lack of strictly-simultaneous multi-wavelength observations, as discussed in the previous sections. Therefore, the SED reported in this section is not necessarily a good representation of the true SED for this flaring episode, and hence any modeling results have to be regarded as inconclusive.

In this SED modeling exercise, the data used are the measurements from *Swift* (UV and X-rays), *Fermi*-LAT (two-day spectrum), and *Whipple* 10 m very high state. The optical and infrared, as well as the radio points, are not taken into account for the evaluation of the agreement of the SSC model curves with the data. The first two are strongly dominated by emission from the host galaxy, and the last only serve as upper limits for the SSC flux as the radio emission shows substantially lower variability timescales and is widely assumed to stem from a larger

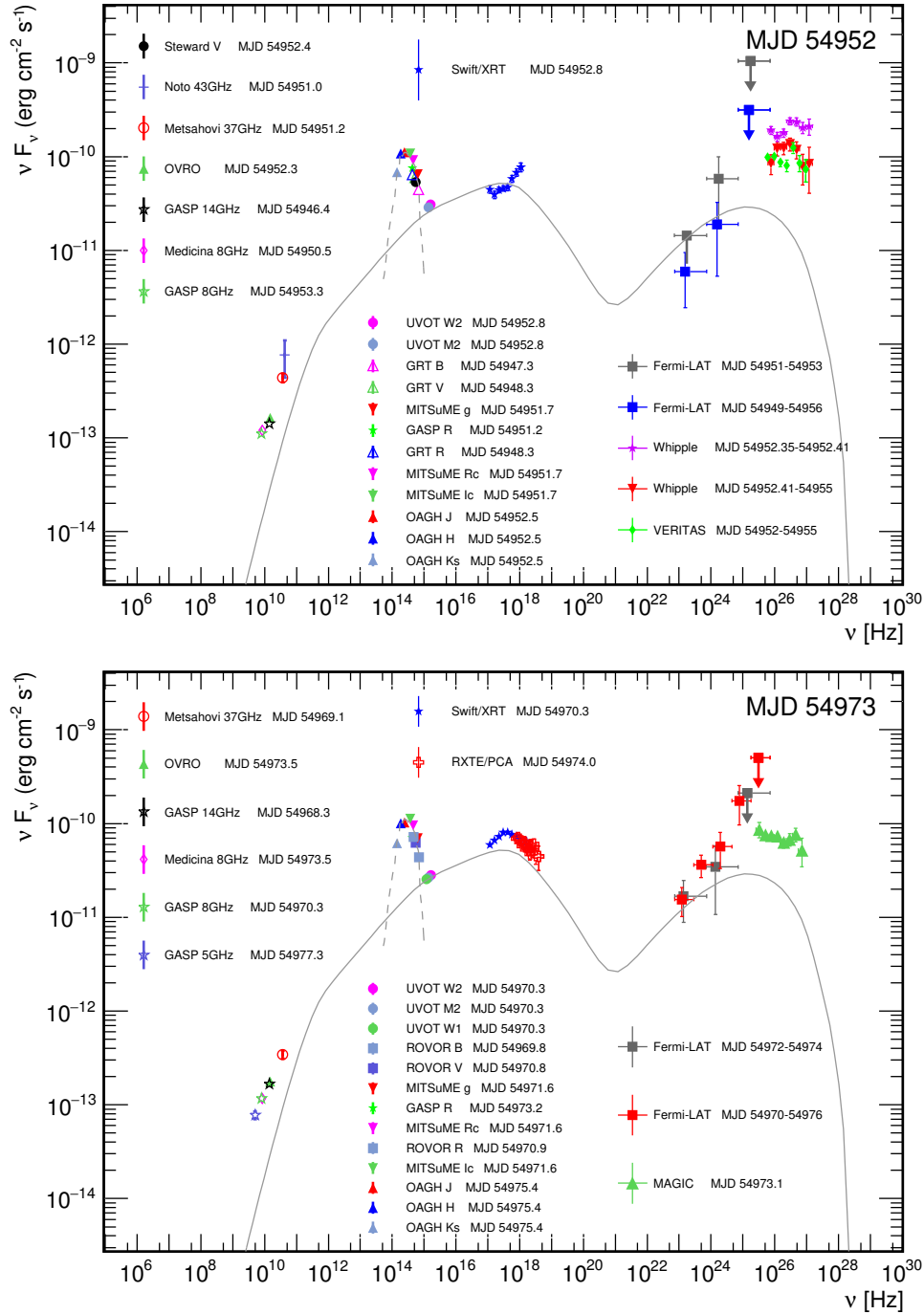


Fig. 9. Broadband SED of Mrk 501 during the two VHE high states observed within the campaign (*upper panel*: MJD 54952, *lower panel*: MJD 54973). See text for details regarding the included spectral measurements. The data points have been corrected for EBL absorption according to the model by Franceschini et al. (2008). The emission of the host galaxy parameterized according to Silva et al. (1998) is shown with a gray dashed line, while the one-zone SSC model describing the average broadband SED over the entire campaign (see Abdo et al. 2011a) is depicted with a gray solid line.

region than the emitting blob responsible for the few-day long flaring activity.

Exploiting the entire parameter grid space, neither the one-zone SSC model nor the two-zone SSC model can reconstruct the measured broadband SED, with the data-model agreement quantified with $\chi^2/\text{d.o.f.} > 300/20$, which would imply a probability of agreement P (or p -value)¹² between the SSC model

¹² The conversion between $\chi^2/\text{d.o.f.}$ and probability values assumes that the χ^2 distribution (for the given degrees of freedom) is also valid for χ^2 values that are very far away from the central value, which is not

curves and the data points of $P < 10^{-50}$. When removing the tight constraint given by the cut in $t_{\text{var, min}}$, the best agreement obtained with the one-zone SSC scenario from the grid-scan defined by Table 5 is $\chi^2/\text{d.o.f.} = 180/20$ ($P \sim 10^{-27}$). The two-zone scenario with the quiescent emission characterized by the

necessarily correct. In any case, when the model-to-data agreement is very bad (i.e. the χ^2 value is very high) the precise knowledge of the P value is not relevant for the discussion, and hence the inaccuracy of the conversion between χ^2 values and probabilities does not critically impact the results discussed in the paper.

model parameters from the average SED reported in Table 4 and the (spatially independent) region responsible for the flaring activity modeled based on the coarse grid parameter values shown in Table 6 provides at best an agreement given by $\chi^2/\text{d.o.f.} = 225/20$ ($P \sim 10^{-36}$). Since the X-ray spectrum at low energies is already accounted for with the “quiescent” zone, the contribution from the “flaring” zone (which is needed to explain the increase in the flux at VHE) exceeds the measured flux at X-ray energies, and hence yields a bad agreement with the data points.

In addition to trying with the grid-scan defined in Table 5, we also evaluated the model-to-data agreement when using a one-zone scenario with the grid-scan defined in Table 6, which provides a simpler theoretical scenario (only one break in the EED instead of two), but with somewhat extended ranges probed for the parameters γ_{\min} , γ_{\max} , γ_{break} , n_e , and $\log(\frac{R}{\text{cm}})$. We found a few models with data-model agreement given by $\chi^2/\text{d.o.f.} = 95/20$ ($P \sim 10^{-11}$). But as soon as the requirement for fast variability is applied, all these models (mostly featuring large emission regions with $R \geq 10^{16.5}$) are no longer applicable, and the agreement between the SSC model curves and the data points become $\chi^2/\text{d.o.f.} > 300/20$.

One of the difficulties in modeling these data with a one-zone scenario is that it is difficult to describe the emission in the UV and the X-ray range with a synchrotron component. These UV flux points cannot be modeled only with the host galaxy template, and the one-zone models that could potentially describe well the shape of the X-ray spectrum would produce a flux that is many times below the measured UV flux, and hence would give a very bad data-model agreement. Contrary to the mentioned caveat of a time offset between the X-ray and VHE γ -ray observations, the UV and the X-ray observations were performed simultaneously and thus should be reconstructed consistently. The difficulty in modeling the UV and X-ray measurements in a consistent way suggests that a more complex scenario is needed to explain this emission. In Aliu et al. (2016), the host galaxy was modeled using a different template with respect to the one in Abdo et al. (2011a) that is used in this paper. The host galaxy template used in Aliu et al. (2016) describes approximately the measured UV flux level from the three-day broadband SED considered in Aliu et al. (2016), but it would not be consistent with the variability in the data set presented here. Figure 1 shows the relative variations in the UV flux of more than 50% (peak to peak), which cannot occur if this UV emission is dominated by the steady emission from the host galaxy.

4.3. Second VHE flare

The SED of Mrk 501 built from spectra around the time of the second flux increase seen by MAGIC on May 22 (MJD 54973) is shown in the bottom panel of Fig. 9 (see Sects. 3.1.2 and 3.1.1 for details on the individual observation times). The data related to the second flare were not taken strictly simultaneously. However, here the resulting caveat is not as strong as for the first flare. On the one hand, the observed variability occurs on timescales of days, rather than tens of minutes, and the RXTE/PCA measurements were performed within a day of the VHE observations. While this is not true for the *Swift*/XRT measurements, the overall flux changes are relatively small, and the derived *Swift*/XRT spectrum is in very good agreement with the one derived from RXTE/PCA, as can be seen in the bottom panel of Fig. 9.

The results obtained for the one-zone scenario following the grid-scan from Table 5 gave a best probability of agreement

with the data points of $P_{\text{best}} \approx 4 \times 10^{-10}$ ($\chi^2/\text{d.o.f.} \approx 123/41$). We found that there are 14 additional SSC model curves with a model-to-data probability higher than 0.1% of the best-matching model (i.e. $P > 10^{-3} \times P_{\text{best}}$), which we set as a generous probability threshold to consider the model-to-data agreement comparable. Given that $P_{\text{best}} \approx 4 \times 10^{-10}$, even those models with a best agreement of $P > 10^{-3} \times P_{\text{best}}$ do not adequately describe the measured broadband SED, yet this relatively bad model-to-data agreement is not worse than some of the agreements between (simple) models and SED data shown in some studies (e.g. Abdo et al. 2010b; Giommi et al. 2012; Domínguez et al. 2013; Ahnen et al. 2016). This occurs because, in most studies involving broadband SEDs, the models are adjusted “by eye” to the data without any rigorous mathematical procedure that quantifies the model-to-data agreement. Differences on the order of 20–30% in a log-log plot spanning many orders of magnitude do not “appear to be problematic”, although these differences could be (statistically) significant owing to the small errors from some of the data points (e.g. optical/UV and X-ray). If the differences between the data and model are not substantial (regardless of the statistical agreement), the models are considered to approximately describe the data and can be used to extract some physical properties of the source and its environment.

Figure 10 depicts the best SSC model curves from the one-zone scenario, with the model featuring the best agreement to the data shown with a red curve, and the other 14 SSC models with comparable (down to 0.1%) model-to-data agreement shown with dark gray curves. Given the very low number of SSC model curves in this group, we decided to also depict those SSC models with model-to-data probability of agreement higher than $10^{-6} \times P_{\text{best}}$ and $10^{-9} \times P_{\text{best}}$ with lighter gray shades (see legend), which increased the number of SSC model curves depicted to 34. The thresholds used of $10^{-6} \times P_{\text{best}}$ and $10^{-9} \times P_{\text{best}}$ are somewhat arbitrary, and could be changed without any major qualitative impact on the reported results. The inclusion of these additional 20 models in the figure helps illustrate the behavior of the SSC model curves that start being worse than the best-matching model. To guide the eye, the SSC model describing the average state is also shown (from Abdo et al. 2011a, dash-dotted black line): the most significant deviations of the model curves from the data points stem from the *Swift* region. Therefore, while the hard X-ray and γ -ray bands can be satisfactorily modeled with a one-zone SSC scenario, this model realization fails at reconstructing both the soft X-ray data points and the UV emission at the same time. Figure 11 displays how many model curves produced for each point on the parameter grid yield a model-to-data agreement probability P better than $10^{-3} \times P_{\text{best}}$, which are the models that are considered to be comparable. This is shown for each of the parameters separately. Some parameters are more constrained than others: e.g. $\gamma_{\text{break},1}$, $\gamma_{\text{break},2}$, and α_2 show a narrower distribution than, for instance, γ_{max} or α_3 , which lead to equally good models over essentially the entire range of values probed. Additionally, as done for Fig. 10, with lighter gray shades we also report the parameter values for $P > 10^{-6} \times P_{\text{best}}$ and $P > 10^{-9} \times P_{\text{best}}$. The SSC models that are not comparable to the best-matching model (i.e. those with $P < 10^{-3} \times P_{\text{best}}$) have a similar distribution for those parameters that are not constrained, like γ_{max} or α_3 . On the other hand, of the parameters that can be constrained, like $\gamma_{\text{break},1}$ and α_2 , these additional models extend the range of parameter values with respect to the distributions for the models with $P > 10^{-3} \times P_{\text{best}}$. The parameter $\gamma_{\text{break},2}$ seems to be quite well constrained, and even the models with $P < 10^{-3} \times P_{\text{best}}$ converge to the same value of 3.2×10^5 . The

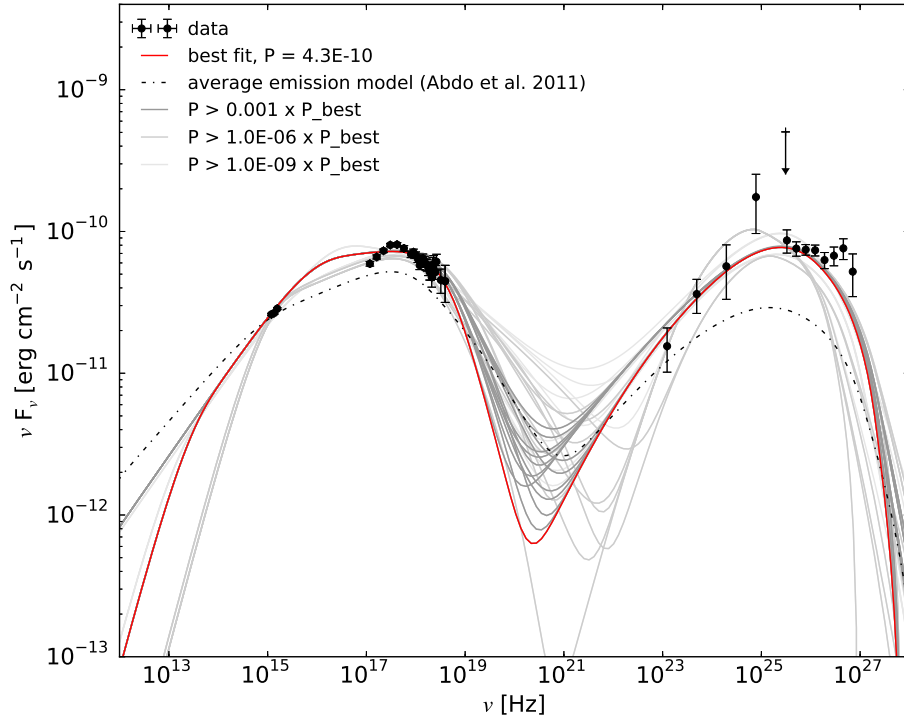


Fig. 10. SED grid-scan modeling results for the flaring episode around MJD 54973 in the scope of a one-zone SSC scenario. Shown are the model curve (red solid line) with the highest probability of agreement with the data as well as model curves within different probability bands. For comparison, the SSC one-zone model found to describe the average state (Abdo et al. 2011a) is also given (black dash-dotted line). Data points have been corrected for EBL absorption according to the model by Franceschini et al. (2008).

implications of these distributions on the possibility to constrain the different model parameters is discussed further in Sect. 5.

We also evaluated the model-to-data agreement for the one-zone scenario that uses the more simple grid-scan defined by Table 6, which is related to a grid of 9 parameters (instead of 11), but with a somewhat extended region for some of these parameters. We found that this grid-scan did not provide any additional SSC model with $P > 10^{-3} \times P_{\text{best}}$, and only five additional SSC models with $P > 10^{-9} \times P_{\text{best}}$. Hence this grid-scan did not bring any practical improvement with respect to that from Table 5, which led to 14 SSC models with $P > 10^{-3} \times P_{\text{best}}$ and 34 SSC models with $P > 10^{-9} \times P_{\text{best}}$.

When using the above-mentioned two-zone SSC scenario, with the quiescent emission characterized by the model parameters from the average SED reported in Table 4 and the spatially independent region responsible for the flaring activity modeled based on the coarse grid parameter values reported in Table 6, we find a substantial improvement with respect to the one-zone models in describing the measured broadband SED (including the UV emission), with a best model-to-data probability of $P_{\text{best}} \approx 2.5 \times 10^{-3}$ ($\chi^2/\text{d.o.f.} \approx 71/41$). The two-zone model provides a better description of the SED than the one zone model, but it still does not reproduce the data perfectly.

Figure 12 displays the 69 SSC model curves with model-to-data agreement probability P better than $10^{-3} \times P_{\text{best}}$, which is the generous probability threshold that we adopted to consider the probability of agreement comparable. Because of the relatively large number of SSC model curves (in comparison to those surviving the same selection criteria in the one-zone scenario), we decided to split those models into three groups according to their model-to-data probability P being better than $10^{-1} \times P_{\text{best}}$, $10^{-2} \times P_{\text{best}}$, and $10^{-3} \times P_{\text{best}}$. Since $P_{\text{best}} \approx 0.25\%$, these models start providing an acceptable representation of the

data, with the different bands reporting slightly different levels of success in the model-to-data agreement. The parameter values for these models are depicted in Fig. 13. As occurred for the one-zone scenario, some parameters are better constrained than others; for example, γ_{break} shows a narrow distribution, while γ_{min} and γ_{max} show a rather flat distribution. Although the parameter γ_{min} was probed up to 10^6 , the highest γ_{min} values used in the SSC models that can adequately describe the broadband SED only go up to 10^4 , which for the highest B field values reported in Fig. 13 (~ 0.15 G) relate to a cooling time of 3.5×10^6 s. This is one order of magnitude longer than the dynamical timescale set by the highest R values reported in Fig. 13 (10^{16} cm), hence ensuring the existence of a low-energy cutoff. See Sect. 5 for further discussions of this topic.

In order to refine the adjustment of the different model parameters even further, a second iteration of the grid-scan modeling, referred to as a dense grid-scan, is performed. The dense grid-scan focuses on the parameter ranges that provide the best model-to-data agreement in the coarse grid-scan, which are depicted in Fig. 13. Following this strategy, the chosen parameter ranges can be narrowed in favor of a smaller step size in the individual parameters, while keeping the computing time at a reasonable amount. The new dense grid ranges and number of steps for each of the parameters are given in Table 7.

The model with the highest probability of model-to-data agreement in the dense grid-scan yields $P_{\text{best}} \approx 6.6 \times 10^{-2}$ ($\chi^2/\text{d.o.f.} \approx 55.4/41$), which implies an order of magnitude improvement with respect to the best-matching model obtained with the coarse grid-scan. If this model curve had been obtained through a regular mathematical fit, and conservatively considering that the nine dimensions of the grid relate to nine independent and free parameters in the fitting procedure, we would have obtained a p -value $\approx 6.3 \times 10^{-3}$ ($\chi^2/\text{d.o.f.} \approx 55.4/32$). The

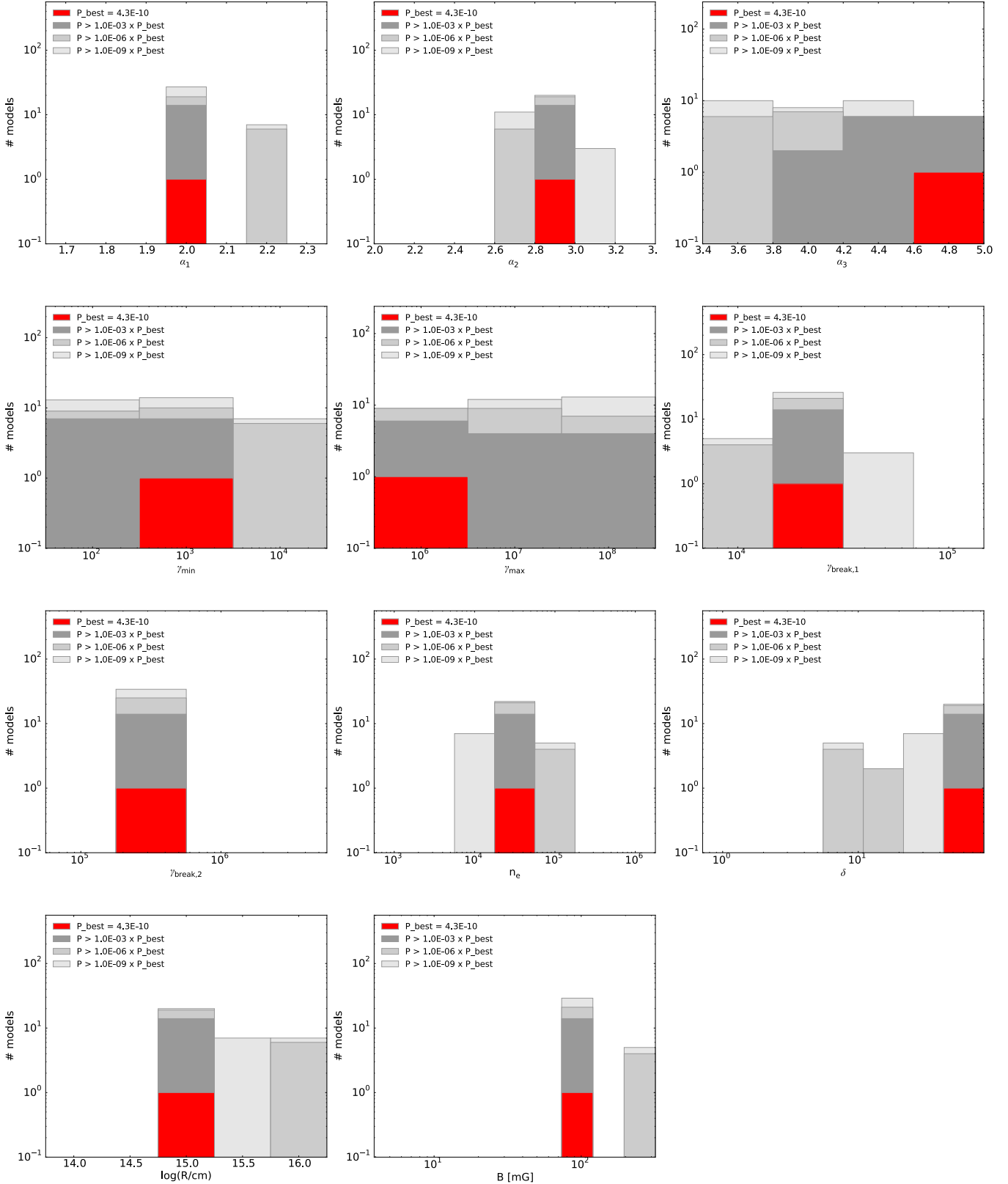


Fig. 11. Number of SSC model curves with a fit probability above the given limits vs. each probed value of each model parameter. Given are the results for the coarse parameter grid within a one-zone scenario for MJD 54973. The X-axis of each plot spans the probed range for each parameter. The figure shows the model with the highest probability of agreement to the data (red) and all models within several probability bands (gray shades, see legend).

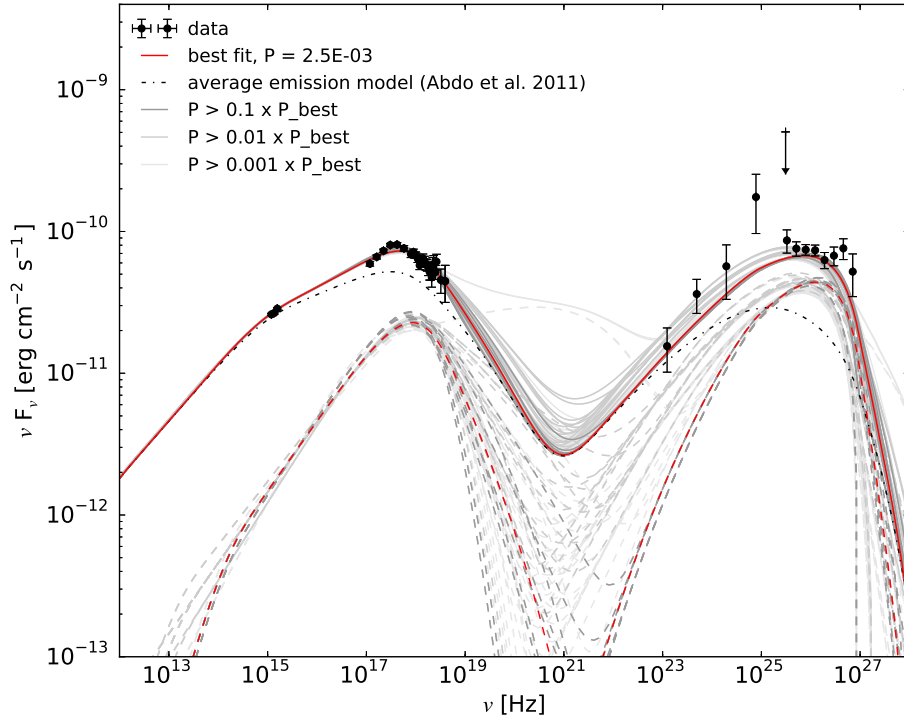


Fig. 12. SED grid-scan modeling results for the flaring episode around MJD 54973 in the scope of a two-zone SSC scenario. The total emission (solid lines) is assumed to stem from a first quiescent region (black dot-dashed lines) responsible for the average state (Abdo et al. 2011a) plus a second emission region (dashed lines). The model with the highest probability of agreement with the data is highlighted in red. Model curves underlaid in gray show the bands spanned by models with a fit probability better than $0.1 \times P_{\text{best}}$, $0.01 \times P_{\text{best}}$, and $0.001 \times P_{\text{best}}$, respectively. Data points have been corrected for EBL absorption according to the model by Franceschini et al. (2008).

dense grid-scan focused on relatively good regions of the parameter space, which yielded a large number of SSC curves with a good model-to-data agreement although the parameter values of this dense grid-scan still vary widely (implying very different physical conditions in the source). Because of the large number of model curves, we can be more demanding with the probability threshold for considering the probability of agreement comparable to that of the best-matching model: a probability threshold of $0.1 \times P_{\text{best}}$ still keeps 1684 SSC models, which is a large increase in statistics, in comparison to the results obtained with the coarse scan. Given that $P_{\text{best}} \approx 6.6\%$, all the models above this probability threshold provide a decent representation of the data. We split these models into three groups according to their model-to-data agreement being $P > 0.9 \times P_{\text{best}}$, $P > 0.5 \times P_{\text{best}}$, and $P > 0.1 \times P_{\text{best}}$, hence reporting somewhat different levels of success in describing the measured broadband SED.

Here too we investigate the spread – or degeneracy – of the different models within the dense grid space of model parameters. Figure 14 shows again the distribution of the best model (red) and the models with $P > 0.9 \times P_{\text{best}}$, $P > 0.5 \times P_{\text{best}}$, and $P > 0.1 \times P_{\text{best}}$ over the entire dense grid parameter space. In comparison to Fig. 13, an apparent larger degree of degeneracy can be seen; the distributions have entries in most of the probed parameter ranges depicted in the figure. The wider spread in the parameter values shown in Fig. 14 is caused by the selected parameter range, which is narrower and intentionally only covers regions with an already reasonable agreement between model and data, as derived from the coarse grid-scan. Despite the large spread, one can see that there are regions with slightly better model-to-data agreement, like the region around $\gamma_{\text{break}} \sim 5 \times 10^5$ or the region around $\alpha_1 \sim 1.9$. The results are discussed further in Sect. 5.

The SED models that were picked as a result of the dense grid-scan for two-zone SSC models are presented in Fig. 15. The figure highlights three SSC model curves: the model that gave the best agreement with the SED data points, a model featuring a prominent high-energy component in the EED, and a model that features a low Doppler factor of $\delta = 5$. The parameter values for these three specific SSC model curves are given in Table 8, showing once more that three very distinct sets of SSC model parameters can provide comparable agreement with the experimental data.

5. Discussion

5.1. Variability and correlations

For Mrk 501, an increase in the fractional variability with energy has been reported in the past within the X-ray and VHE band (Gliozzi et al. 2006; Albert et al. 2007a; Aliu et al. 2016). In the work presented here, we extend this trend throughout all wavelengths from radio to VHE γ rays, showing that the source is relatively steady at radio/optical frequencies, but variable ($F_{\text{var}} \geq 0.2$) and very variable ($F_{\text{var}} \geq 0.4$) in the X-ray and VHE γ -ray bands, respectively, with a clear increase in the fractional variability with energy (observed in all the bands we can measure). A similar variability pattern was reported in Aleksić et al. (2015b) and, during the preparation of this study, also in Ansoldi et al. (in prep.) in relation to the extensive campaigns on Mrk 501 performed in 2008 and 2012, respectively. This suggests that this variability vs. energy behavior is an intrinsic characteristic in Mrk 501. On the other hand, Furniss et al. (2015) has recently reported a different fractional variability vs. energy pattern based on observations taken in 2013 where the observed variability at X-rays is similar to that at VHE.

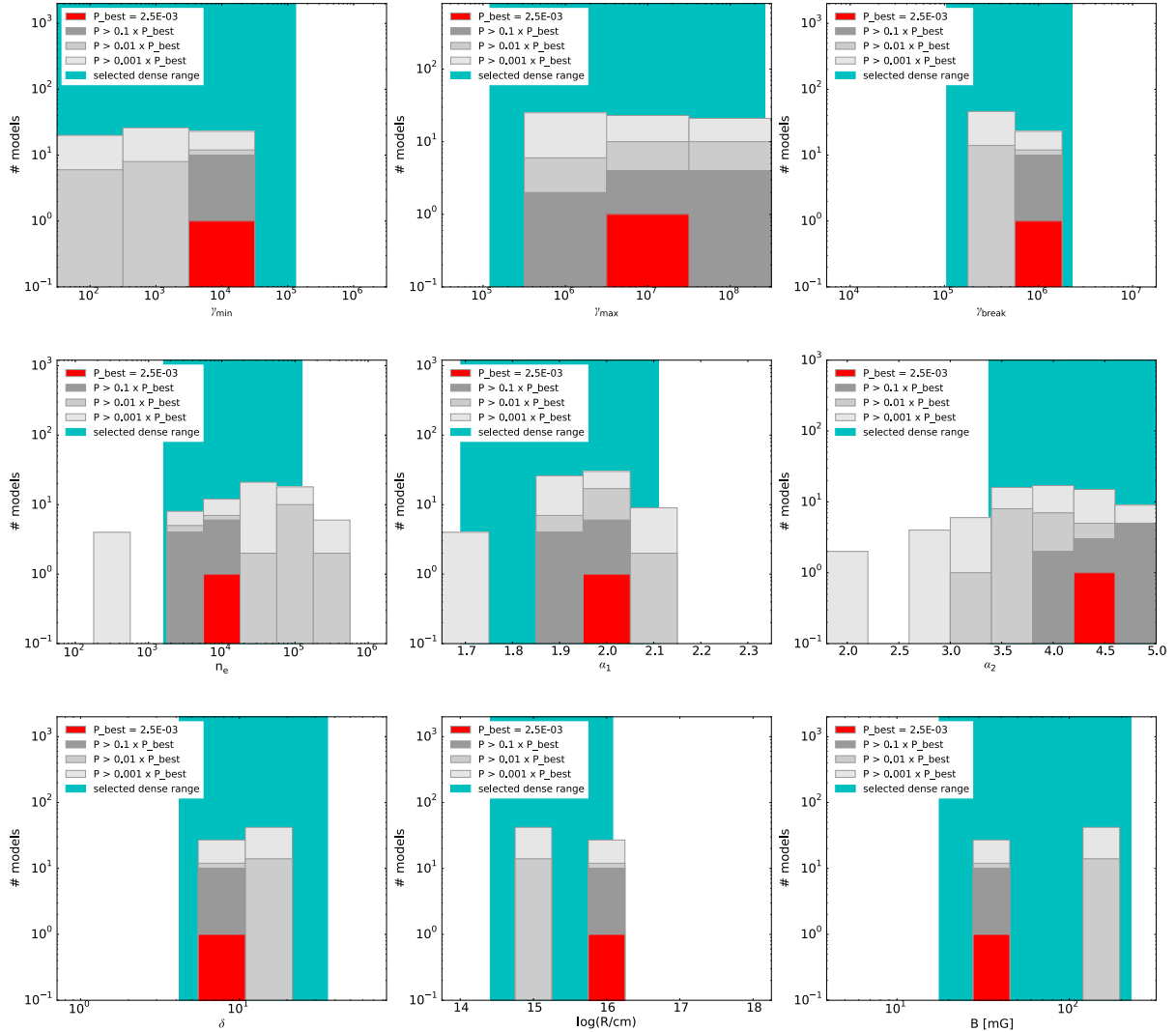


Fig. 13. Number of SSC model curves which fulfill the given limits for the fit probability vs. each probed value of each model parameter. Shown are results for the coarse parameter grid-scan within a two-zone scenario for MJD 54973. The X-axis of each plot spans the probed range for each parameter. Given are the model with the highest probability of agreement with the data and all models within the given probability bands (see legend). The parameter ranges chosen for the dense scan are also shown in each plot.

Table 7. Grid parameter space probed for two-zone models within the dense grid-scan applied to the flare around MJD 54973.

Dense grid	γ_{\min}	γ_{\max}	γ_{break}	α_1	α_2	n_e	$\frac{B}{\text{mG}}$	$\log\left(\frac{R}{\text{cm}}\right)$	δ
two-zone									
min	2.1×10^1	3.2×10^5	1.2×10^5	1.7	3.5	2×10^3	20	14.5	5
max	5×10^4	1×10^8	2×10^6	2.1	5.0	1×10^5	200	16.0	30
# of steps	5	4	12	21	7	10	10	10	6
Spacing	log	log	log	lin	lin	log	log	lin	lin

Notes. The number of SSC models required to realize this grid-scan amounts to 212 million. See text for further details.

The multiband variability pattern that has been observed in Mrk 501 is quite different from that observed in Mrk 421 during the multi-instrument campaigns from 2009, 2010, and 2013, as reported in Aleksić et al. (2015a, 2015c) Baloković et al. (2016). In these works a double-bump structure in the fractional variability plot was found (instead of a continuous increase with energy) which relates to the two bumps in the broadband SED, and where the highest variability occurs at X-rays and VHE at comparable levels.

A clear correlation of the X-ray and VHE γ -ray emission was observed during the large and long γ -ray activity from 1997 (e.g. Pian et al. 1998; Gliozzi et al. 2006), but this correlation was only marginally detected during the γ -ray flare observed in 2005 (Albert et al. 2007a). The low significance in the X-ray-to-VHE correlation during the flares in 2005 was ascribed to the lack of sensitive X-ray measurements during this observing campaign; only RXTE/ASM data, which has limited sensitivity to detect Mrk 501, was available for this study. A positive

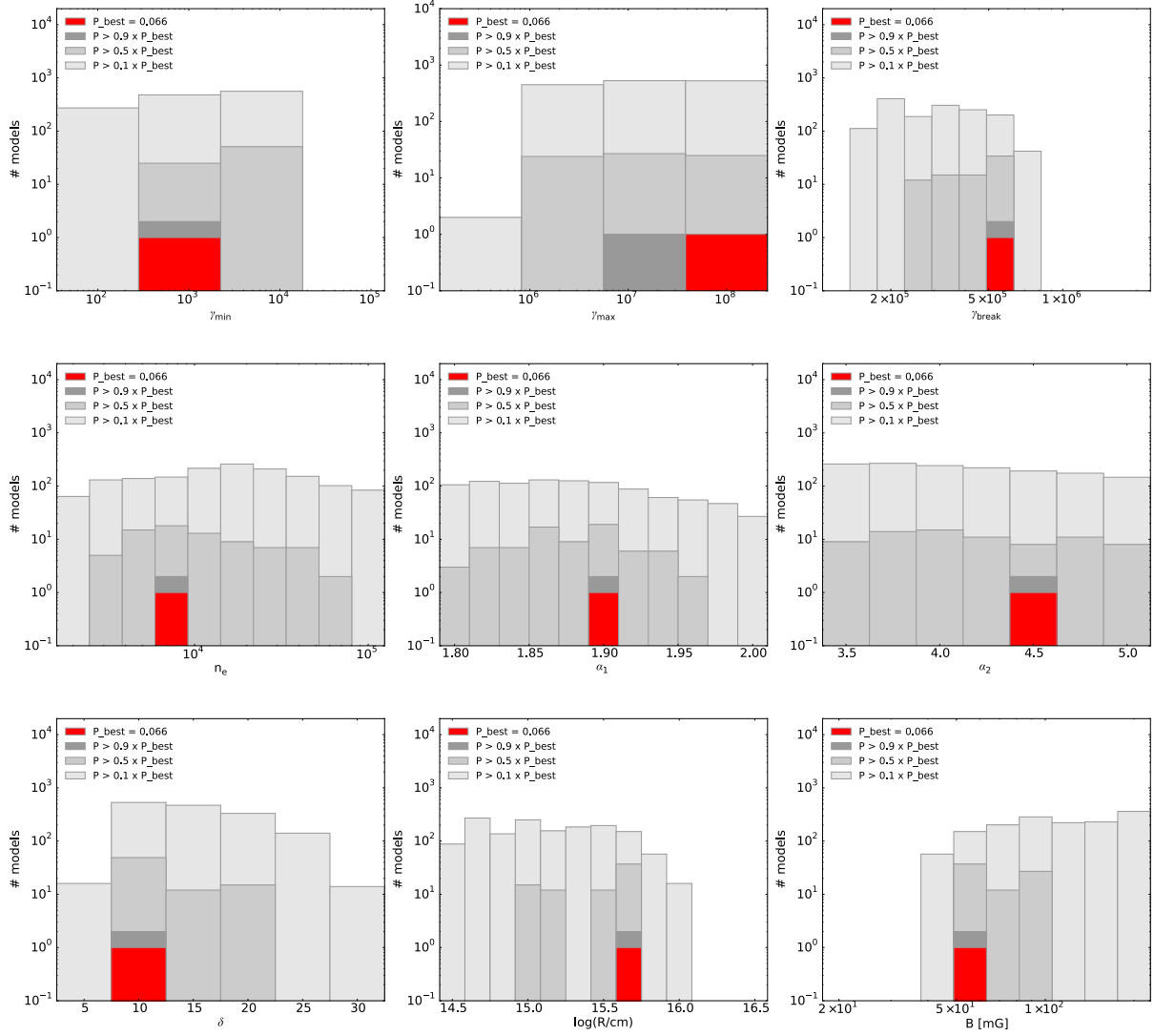


Fig. 14. Distributions of the investigated models in the individual model parameters for the dense parameter grid and a two-zone scenario for MJD 54973. The X-axis of each plot spans the probed range for each parameter. Shown are the model with the highest probability of agreement with the data and all models that populate the given probability bands (see legend).

Table 8. Results of the dense grid-scan SED modelling of the flaring episode around MJD 54973 in the scope of a two-zone SSC scenario.

Selected models	γ_{\min}	γ_{\max}	γ_{break}	α_1	α_2	n_e	$\frac{B}{\text{mG}}$	$\log\left(\frac{R}{\text{cm}}\right)$	δ	$\frac{\chi^2}{\text{d.o.f.}}$	$\frac{P}{P_{\text{best}}}$	$\frac{u_e}{u_B}$	$\frac{t_{\text{varmin}}}{\text{h}}$
Best χ^2	1×10^3	1.0×10^8	5.6×10^5	1.90	4.5	7.4×10^3	56	15.7	10	55.4/41	1.00	933	4
HE comp	1.0×10^3	1.5×10^7	4.3×10^5	1.86	3.5	4.8×10^3	56	15.7	10	57.5/41	0.68	919	4
Low δ	1.5×10^2	1.5×10^7	5.6×10^5	1.82	3.5	2.0×10^3	72	16.0	5	64.2/41	0.18	424	19

Notes. Quoted here are the three models highlighted in Fig. 15: the model with the best agreement to the data, a model with a prominent high-energy electron component, and a model with a remarkably low Doppler factor ($\delta = 5$). Besides the model parameters, the reduced χ^2 values, the fit probability compared to the best achieved fit probability, the departure from equipartition and the implied minimum variability timescale are also reported.

correlation between X-ray and VHE γ rays was also reported – for the first time – during very low X-ray and VHE activity, but only at a 99% confidence level (Aleksić et al. 2015b). The marginally significant correlation observed during this low activity, using data from the multi-instrument campaign in 2008, was ascribed to the very low variability during that campaign, where the measured F_{var} values were about 0.1 for X-rays and 0.2 for

VHE. As reported above, during the multi-instrument campaign in 2009, Mrk 501 was mostly in its low/typical state, but we also measured two flaring activities in May 2009. The measured F_{var} is about 0.3 for X-rays and 0.8 for VHE, while if we exclude the two flaring episodes we obtain F_{var} values of about 0.2 for X-rays and 0.5 for VHE. However, despite the larger variability observed in 2009 (with respect to 2008), we did not

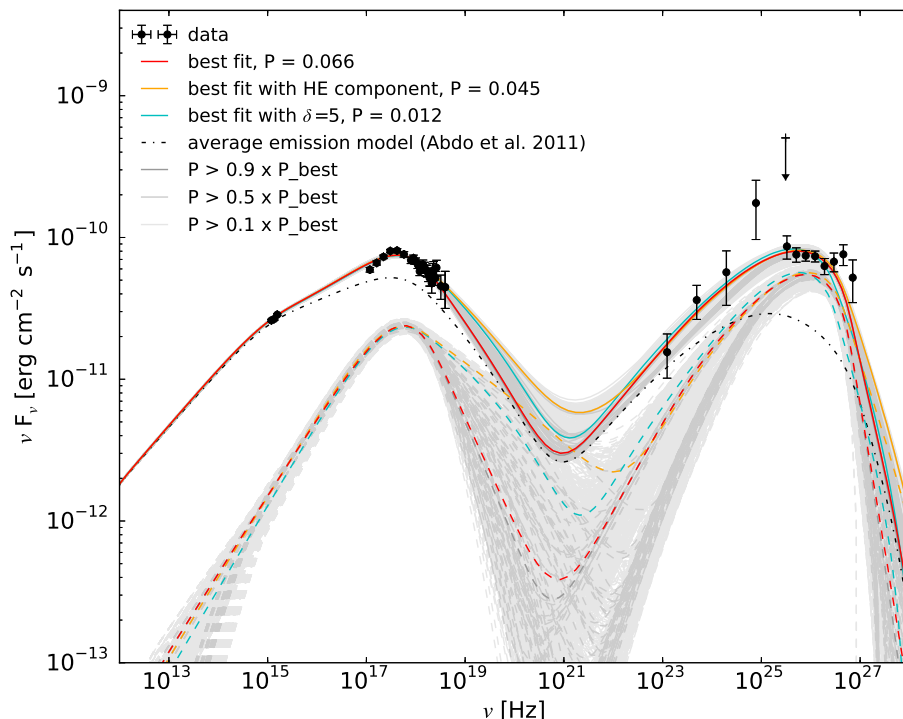


Fig. 15. Modelling of the SED of Mrk 501 compiled from measurements collected during the high state observed around MJD 54 973. Two-zone SSC models have been inspected following the grid-scan strategy. The total emission (solid lines) is assumed to stem from a first quiescent region (black dot-dashed lines) responsible for the average state (Abdo et al. 2011a) plus a second emission region (dashed lines). Highlighted are the model with the highest probability of agreement with the data (red), a model featuring a prominent high-energy component in the EED (orange), and a model with low Doppler factor (cyan, $\delta = 5$). Model curves underlaid in grey show the bands spanned by models with a fit probability better than $0.9 \times P_{\text{best}}$, $0.5 \times P_{\text{best}}$ and $0.1 \times P_{\text{best}}$, respectively. The data points have been corrected for EBL absorption according to the model by Franceschini et al. (2008).

observe any significant correlation between the X-ray and the VHE emission (including and excluding the flaring episodes). This may appear to be a controversial result, but we would like to stress that a very significant correlation with past data was only observed during the very large and long flare in 1997. Recently, Furniss et al. (2015) reported a significant X-ray-to-VHE correlation using data from the multi-instrument campaign in 2013. This correlation is dominated by the large X-ray and VHE activity observed over four consecutive days in July 2013, although it still remains at 2σ (for the 0.3–3 keV energy band) and 5σ (for the 3–7 keV band) when removing the flaring activity. In conclusion, some multi-instrument campaigns on Mrk 501 do not show a clear X-ray-to-VHE correlation when the source is not flaring strongly or persistently high. However, for the other archetypal TeV blazar, Mrk 421, the X-ray-to-VHE correlation is significantly detected during both low- (e.g. Aleksić et al. 2015a; Baloković et al. 2016) and high-activity states (e.g. Fossati et al. 2008; Acciari et al. 2011a; Aleksić et al. 2015c).

The X-ray-to-VHE correlation and the fractional variability vs. energy pattern observed in Mrk 421 suggests that the X-ray and VHE emissions are produced by the same electrons within the framework of SSC scenarios, and that the highest variability is produced by the highest energy and most-variable electrons that dominate the emission at the keV and the TeV bands, respectively. Instead, in Mrk 501 we observe a continuous increase in the variability with energy and absence of persistent correlation between the keV and TeV emissions. This suggests that the highest energy electrons, in the framework of SSC scenarios, are not responsible for the keV emission, while they are responsible (at least partially) for the TeV emission. Alternatively, there

could be an additional (and very variable) component contributing to the γ -ray emission in addition to that coming from the SSC scenario, like inverse-Compton of the high-energy electrons off some external low-energy photon fields (Dermer et al. 1992; Sikora et al. 1994; Finke 2016).

5.2. VHE flaring state SEDs

The first flaring event (MJD 54 952) is characterized by a fast and large outburst in the VHE band, which was apparently not accompanied by a substantial increase in the X-ray flux, and hence appeared to be like an “orphan flare” (see e.g. Krawczynski et al. 2004). In fact, based on these observations, this event was tentatively categorized as an orphan flare event (Pichel & Paneque 2011; Neronov et al. 2012), which would substantially challenge the currently favored SSC emission models (for HBLs). However, a detailed look at the SED of the flaring episode reveals a hardening of the X-ray spectrum measured by *Swift*/XRT (see Sect. 3), which more likely corresponds to a shift of the synchrotron bump towards higher energies. During the outstanding activity in 1997, the synchrotron peak was shifted to beyond 100 keV, as accurately measured by *BeppoSax* (Pian et al. 1998). Such a large increase in the location of the synchrotron peak position could have occurred in the MJD 54 952 flare discussed here. Additionally, the peak of the high-energy γ -ray bump at the time of this flare also appears to shift towards higher energies, as occurred in 1997. This suggests a more general appearance of such phenomena, and that – even though the measured keV and TeV flux are not correlated during this flaring activity – the overall broadband X-ray and VHE emission may still be correlated,

which could have been measured if X-ray observations at several tens of keV had been available during this flaring episode. Such a shift of the entire SED has been interpreted as a shift in the energy distribution of the radiating electron population (e.g. Pian et al. 1998; Albert et al. 2007a). In this context, the small change in the inverse Compton peak position compared to that of the synchrotron peak location could be ascribed to Klein-Nishina effects. High-energy electrons can efficiently produce high-energy synchrotron photons; however, they are not able to upscatter photons as effectively as the lower-energy electrons because the Klein-Nishina cross-section is smaller than the Thomson cross-section (Tavecchio et al. 1998; Acciari et al. 2011b).

We tried to parameterize the broadband SED during this first flare (MJD 54952) using a wide range of SSC emission scenarios following the grid-scan strategy defined in Sect. 4.1, allowing for models with one or two (independent) emission zones and covering a wide range in the space of model parameters. We found that none of the tested models could satisfactorily reproduce the changes observed in the spectral distribution. This broadband SED can be explained with more sophisticated theoretical models, like the inhomogeneous time-dependent models reported in Ghisellini et al. (2005), Graff et al. (2008), Chen et al. (2011, 2015, 2016), which provide a more elaborate physical scenario, at the expense of an increase in the number of degrees of freedom of the model. However, a caveat has to be taken into account when interpreting these results, which is the lack of strict simultaneity of the different data sets, in particular the Swift/XRT and the VHE γ -ray data. The individual exposure times are separated by seven hours, while we see flux changes of a factor of ~ 4 on sub-hour timescales, as reported in Pichel & Paneque (2011) and Aliu et al. (2016). Therefore, it is somewhat uncertain whether the measurements of the synchrotron peak and the high-energy peak probe the same source state. In the recent study reported in Aliu et al. (2016), the broadband SED derived for the three-day time interval MJD 54952–55 could be satisfactorily parameterized with a one-zone SSC scenario that differs from the one used here and in Abdo et al. (2011a) in various aspects, including the template used to describe the host galaxy contribution.

Compared to the first flaring event, the second flare (\approx MJD 54973) occurs during VHE flux changes of factors of ~ 2 on timescales of a few days, and hence the lack of strict simultaneity in the X-ray/VHE observations is a much smaller caveat than for the first flaring event. In this case, again following the grid-scan modeling approach, one-zone SSC models were unable to describe the measured SED (reaching best probabilities of agreement $\sim 10^{-10}$). The two-zone SSC models were able to reproduce the experimental observations better (reaching best probabilities of agreement $\sim 10^{-3}$). Therefore, the two-zone scenario appears to be favored compared to the one-zone scenario considered here. Building on the range of two-zone model parameters providing decent data-model agreement, a fine grid-scan was performed, yielding hundreds of two-zone SSC models with probabilities of agreement $\sim 10^{-2}$. The obtained set of two-zone SSC models providing the best agreement comprises several setups with quite different implications for the parameters defining the EED and the surrounding region of the second emission region (see Sect. 4.3).

Comparing the configurations obtained for the emission region responsible for the second flare with the parameter values describing the emission region assumed to create the quiescent emission, some general trends can be stated: while the parameters describing the EED and the Doppler factor are found to

populate roughly the same ranges of values, the electron density n_e is increased by 1–2 orders of magnitude, the magnetic field is larger by ≈ 1 order of magnitude, and the size of the emission region R is found to be smaller by 1–2 orders of magnitude. The last result is affected by the requirement of a minimum variability timescale of a day in order to account for the variability seen in the data.

In addition to the general observations made above, some interesting model configurations stand out from the set of adequate scenarios: models that feature a prominent high-energy component in the EED and models with Doppler factors as low as $\delta = 5$ can be used to adequately model the flaring SED. In the paragraphs below we discuss the benefits of these two families of models.

Synchrotron self-Compton models with a strong high-energy component are interesting not only to explain the SED collected during the presented campaign, but also in the context of other observations of Mrk 501. During the extreme flare seen in 1997, a strong increase in the regime of hard X-rays, around 100 keV, was observed (Bradbury et al. 1997). This increase can be interpreted as the emergence of a strong high-energy component adding to the overall SED, which only sometimes becomes visible during extreme flaring states. Moreover, Cherenkov telescope observations often give hints of an additional hard component in the EED during flaring times: in Albert et al. (2007a) a significant spectral hardening during flaring states was observed and reported for the first time, and in the course of several more observational campaigns this “harder when brighter” behavior has been established as typical for Mrk 501. Ultimately, a tendency for this behavior was also seen during the campaign presented in this paper. In this light, SSC models with such a high-energy contribution to the EED could be favored as they can also explain such mentioned observations. Naturally, with the data set at hand and the lack of hard X-ray observations above ≈ 20 keV, they can neither be confirmed nor discarded.

The finding that models with $\delta = 5$ can also adequately reconstruct the data is particularly interesting. Quite high values (above $\delta = 10$, up to $\delta = 50$ or more) are usually required to model the SEDs of blazars (Tavecchio et al. 1998; Krawczynski et al. 2001; Saugé & Henri 2004). These high Doppler factors are in tension with regard to expectations from the small (typically less than $2c$) apparent velocities observed in the 43 GHz radio emission of various high-peaked BL Lac objects, and particularly with that measured for Mrk 501 (Edwards & Piner 2002; Piner & Edwards 2004; Piner et al. 2010). This has posed a common problem for TeV sources, which has been dubbed the “bulk Lorentz factor crisis” (Henri & Saugé 2006), and requires the radio and TeV emission to be produced in regions with different bulk Lorentz factors. Debates on this problem (see e.g. Georganopoulos & Kazanas 2003; Levinson 2007; Stern & Poutanen 2008) have led to a series of sophisticated models, for example the “spine-sheath” model from Ghisellini et al. (2005), in which the jet is structured transverse to its axis into a fast “spine” that produces the high-energy emission, and a slower “layer” which dominates the radio emission. The modeling results presented in this paper show that it is actually possible to model the SED of a flaring activity of Mrk 501 using a relatively small Doppler factor to describe the flaring emission, hence alleviating the tension with the radio interferometric observations. Naturally, such low Doppler factors cannot be used for broadband SEDs related to periods with fast (sub-hour) variability, such as the one from MJD 54952, but they can be used for broadband SEDs related to flaring activities

with day timescales, such as the one from MJD 54 973, which are more commonly observed in high-peaked BL Lac objects.

In addition to individual models which give a good reproduction of the data, the degree of degeneracy of well-fitting models in the individual parameters has also been studied, revealing a wide range of equally good models in the SSC parameter space, and showing that some model parameters can be constrained much better than others. While this can be seen already for the one-zone SSC models, where $\gamma_{\text{break},1}$ and $\gamma_{\text{break},2}$ show a narrower distribution than γ_{max} or α_3 , it is particularly interesting to study this for the more applicable two-zone scenario, which is the one that suitably describes the data. We find that for both the coarse and the dense grid-scan, the distribution of parameter values giving a good agreement with the data is quite well constrained for some parameters, such as the Lorentz factor at the break energy of the electrons γ_{break} , while other parameters show a rather broad distribution, like γ_{max} or the index of the EED after the break α_2 , which points to a real degeneracy in these parameters. To some extent this degeneracy can be explained by the unequal sampling of the SED: the density and accuracy of measurements at or around the positions of the synchrotron and the IC peak is rather dense, which leads to a good definition of the spectral break in the EED. However, moving from the peak positions up to higher energies, the uncertainties of the measurements increase (especially for the synchrotron peak) and parameters such as the spectral index after the break α_2 or the Lorentz factor where the EED is cut off γ_{max} cannot be constrained equally well.

This result has several implications for the modeling of SEDs in general. On the one hand, it shows that an actual fitting procedure, which moves along the direction of the steepest gradient in the parameter space towards a minimum in the χ^2 of the model-to-data agreement, does not necessarily reveal the entire picture of possible descriptions of the data in the context of the applied model. Usually one best solution is quoted as the result, while most of the time a wide range of models explain the data equally well. We also see that in order to be able to put stronger constraints on the parameters defining SED models, we need data sets that are characterized by a better coverage in energy and by smaller uncertainties in flux. We see in Fig. 15 that especially the hard X-ray regime, but also the HE and VHE γ -ray regime, allow for a wide range of possible model curves.

Unfortunately, the exercise presented here indicates that the SED modeling results that are performed for less constrained data sets, e.g. for “weak sources” that are sampled with a smaller energy coverage and with spectral measurements with larger statistical uncertainties, should be taken with caution because they are likely to have substantial degeneracies in the model parameters. Such modeling exercises can demonstrate that a particular scenario (e.g. one-zone or two-zone SSC) is capable of reproducing the measured data, but they certainly cannot claim the exclusiveness or even the prominence of the particular set of parameter values that has been chosen or found to be “best”.

5.3. Change in optical polarization during VHE γ -ray flare

The first VHE flare (MJD 54 952) was found to coincide with an observed change in the optical polarization. While simulations of turbulent processes in blazar jets show that a rotation of this dimension can be ascribed to random behavior (Marscher 2014), the coinciding occurrence of the change in rotation and a flare of the VHE γ -ray flux suggests a common origin of these events. Such combined events have already been seen in low-frequency peaked BL Lac-type sources (LBL) and flat spectrum

radio quasars (FSRQ), but it was observed for the first time for an HBL in the course of the 2009 campaign, and already reported in Pichel & Paneque (2011) and Aliu et al. (2016).

These observations show similarities to double or multiple flaring events seen in the LBL BL Lacertae in 2005 and in the FSRQ PKS 1510-089 in 2009, which were discussed by Marscher et al. (2008) and Marscher et al. (2010), respectively.

Exhibiting different peak frequencies for the synchrotron and the IC bump, the optical variability seen in BL Lac could be seen as corresponding to the X-ray variability in Mrk 501. While a strong flare in the VHE band was observed during the first flare of Mrk 501, BL Lac gives hints for activity in that band during the first optical outburst (Albert et al. 2007b). A coincidence of a flaring event and a change in the optical polarization is seen in all three data sets. The observed degree in optical polarization in Mrk 501 of $\approx 5\%$ appears smaller than that in BL Lacertae (up to 18%). Still, the optical flux in Mrk 501 is strongly dominated by the host galaxy, so that the jet contribution amounts to only $\sim 1/3$. Therefore, the measured degree of polarized light in Mrk 501 corresponds to a fraction of $\approx 15\text{--}20\%$ of polarized emission from the jet, which is comparable to BL Lacertae. The second episode of high activity in both Mrk 501 and BL Lac was characterized by an increased flux at the synchrotron bump over a longer time span.

In the case of BL Lac, Marscher et al. (2008) suggested that the first flare and the change in polarization may have occurred when a blob of highly energetic particles traveled along the last spiral arm of a helical path within the acceleration and collimation zone of the jet, and finally left this zone to enter a more turbulent region. The second flare seen in BL Lac has been identified with the passage of the feature through the shocked region of the radio core. The observed behavior of Mrk 501 suggests that the discussed scenario could be applicable here. Despite the lack of simultaneous interferometric radio observations during the two flares, an enhancement of the activity in the VLBA 43 GHz core emission in May 2009 (with respect to the previous months) was observed, supporting the interpretation of the blob traversing a standing shock region during the second flaring episode.

The polarization data collected during this campaign could also hint at a different physical scenario. After the VHE flare on MJD 54 952, not only did the EVPA rotation stop, but it also started rotating in the reverse direction during the following two days, and the polarization degree did not drop to the “typical low-state values” of about 1–2%, but only decreased from 5.4% to 4.5% (see the bottom two panels of Fig. 1). The characteristics of the polarization data after the VHE flare may be better explained as resulting from light-travel-time effects in a straight shock-in-jet model with helical magnetic fields, as proposed by Zhang et al. (2014, 2015). This shock-in-jet model, which uses a full three-dimensional radiation transfer code and takes into account all light-travel-time and other geometric effects (for some assumed geometries), may be more successful in explaining the broadband SED (and variability patterns) observed during the VHE flare from MJD 54 952, which could not be explained with the relatively simple one-zone and two-zone SSC scenarios described in Sect. 4. However, the lack of strictly simultaneous X-ray/VHE data during the MJD 54 952 VHE flare, and the relatively scarce polarization observations after the VHE flare would be an important limitation in the full application of this theoretical scenario to the multi-instrument data set presented here.

6. Summary and concluding remarks

We presented a detailed study of the MWL variability of the HBL Mrk 501, based on a multi-instrument campaign that was conducted over 4.5 months in 2009, with the participation of MAGIC, VERITAS, the *Whipple* 10 m, *Fermi*-LAT, RXTE, *Swift*, GASP-WEBT, and several optical and radio telescopes. Mrk 501 shows an increase in the fractional variability with energy, from a steady flux at radio and optical frequencies to fast and prominent flux changes in the VHE γ -ray band. Overall, no significant correlation was found between any of the measured energy bands, particularly no correlation was seen between X-rays and VHE γ rays despite the relatively large variability measured in these two energy bands. This suggests that the highest energy (and most variable) electrons that are responsible for the VHE γ rays measured by MAGIC, VERITAS, and *Whipple* 10 m do not have a dominant contribution to the ~ 1 keV emission measured by *Swift*/XRT. These high-energy electrons may have a dominant contribution to the hard X-ray emission above 10–50 keV where the instrumentation used in this campaign did not provide sensitive data. Alternatively, there could be a component contributing to the VHE γ -ray emission in addition to the component coming from the SSC scenario (e.g. external Compton), which is highly variable and further increases the variability of Mrk 501 at VHE γ rays with respect to that expected from the pure SSC scenario.

This paper discusses two prominent flaring events at VHE γ rays with different characteristics that were seen during the campaign. The first flare is dominated by a fast outburst in the VHE range, which does not appear to be accompanied by a large flux increase in the X-ray band, but shows a hardening in the X-ray spectrum that can be associated with a shift of the synchrotron bump to higher energies. On the other hand, the second flare is characterized by a flux increase in both the VHE and the X-ray band. For the parameterization of the broadband SEDs from these two VHE γ -ray flares, we applied a novel variation of the *grid-scan* approach in the space of model parameters. For the two theoretical scenarios investigated, the one-zone and two-zone SSC models, we probed multi-dimensional grids with the various model parameters, evaluating the model-to-data agreement for tens of millions of SSC models. This strategy allowed us to identify disjointed regions of equally good model configurations, and provided a quantification of the degeneracy in the model parameters that describe the measured broadband SEDs. The presented methodology provides a less biased interpretation than the commonly used “single-curve model adjustment procedure” typically reported in the literature.

A lack of strict simultaneity in the X-ray/VHE observations of the first flare, which is characterized by large VHE flux changes in sub-hour timescales, does not permit us to draw final conclusions on the underlying mechanism; but the SED modeling with the grid-scan suggests that a simple one-zone or two-independent-zone SSC model is not sufficient to explain the measured broadband emission. The broadband SED derived for the second flare also lacks strictly simultaneous observations, but the flux changes here are smaller and on longer timescales, and hence substantially less problematic than for the first flare. The overall SED from the second flare cannot be properly described by a one-zone SSC model (with an EED with two spectral breaks), while it can be reproduced satisfactorily within a two-independent-zone SSC scenario. In the two-zone models applied here, one zone is responsible for the quiescent emission from the averaged 4.5-month observing period, while the other one, which is spatially separated from the first, dominates

the flaring emission occurring at X-rays and VHE γ rays. The grid-scan shows that there is a large number of SSC model realizations that describe the broadband SED data equally well, and hence that there is substantial degeneracy in the model parameters despite the relatively well-measured broadband SEDs. For instance, regarding the features of the EED, the position of the break(s) appear to be well constrained, while the highest Lorentz factor and the high-energy spectral index vary more strongly within the best-fitting model realizations. While the few models with the best relative agreement to the data feature Doppler factors δ in the range 10–20, the data can also be reproduced using substantially lower Doppler factors of $\delta = 5$ while still reaching fit probabilities higher than 10% P_{best} . This shows that it is possible to reproduce the observed SED from Mrk 501 assuming boost factors well below the usually required values of $\delta \approx 10$ –50, which may loosen a bit the tension posed between large values of δ required for modeling and low values imposed from radio velocity measurements, which has been dubbed the “bulk Lorentz factor crisis”.

A change in the rotation of the EVPA was measured in temporal coincidence with the first VHE flare, at MJD 54 952, as reported in Pichel & Paneque (2011) and Aliu et al. (2016). Here we also show that during the first VHE flare, the degree of polarization increased by a factor of ~ 3 with respect to the polarization measured before and after this flaring activity. This is the first time that this behavior was observed in Mrk 501, or in any other HBL object, and suggests a common origin of the VHE flare and the optical polarized emission. With the coincidence seen of a VHE flare and changes in the trend of the optical polarization, this two-flare event resembles prior events observed in the LBL BL Lacertae and the FSRQ PKS 1510-089, which were discussed in Marscher et al. (2008) and Marscher et al. (2010), respectively. The common features suggest a similar interpretation of the flaring event of Mrk 501 as an emission region which is traveling upstream of the radio core along a spiral path in a helical magnetic field, entering a region of turbulent plasma and crossing the standing shock region of the radio core. After the VHE flare at MJD 54 952, the polarization degree decreased from 5.4% to only 4.5% (instead of the typical low-state value of 1–2%), and there is also a small EVPA rotation in the reverse direction during the following two days, which may be difficult to explain with the typical helical pattern motions mentioned above; they may be better explained as light-travel-time effects in a shock-in-jet model in a straight, axisymmetric jet embedded in a helical magnetic field, as reported in Zhang et al. (2014, 2015). Beyond the interpretation of the flaring event itself, the observational results obtained in the course of this MWL campaign reveal phenomena that have not been seen for any HBL before, but have already been studied for LBLs and FSRQs. This gives a strong indication of the intrinsic similarity of these blazar subclasses, even though they show different jet characteristics in general, such as apparent jet speed and the overall power output. Observations of rapid variability in the LBL BL Lacertae (Arlen et al. 2013) support this further, as such fast flux changes had only been seen in HBL observations.

Additional multi-instrument observations of Mrk 501 will be crucial to confirm and extend several of the observations presented here. First of all, the large degeneracy in the model parameter values providing an acceptable description of the broadband SED is largely dominated by the poor coverage at hard X-rays, as well as the somewhat limited resolution at VHE γ rays. Since mid-2012, NuSTAR¹³ provides excellent sensitivity

¹³ <http://www.nustar.caltech.edu>

above 10 keV, which narrows the large gap in the SED between soft X-rays and the *Fermi*-LAT regime for campaigns from 2012 onwards. In the coming years, observations with ASTROSAT¹⁴ will also be possible, hence facilitating a much more accurate characterization of the evolution of the synchrotron bump of Mrk 501, including the determination of hard components in the EED whose synchrotron emission may peak at 50 or 100 keV. Moreover, in the regime of VHE γ rays, data sets of much higher quality are already being collected, yielding a better resolution and an extended energy coverage. This is achieved on the one hand by the operation of the MAGIC telescopes as a stereo system, which gave a remarkable improvement in the overall performance compared to the mono mode which was still operational during the campaign reported in this paper (Aleksić et al. 2012). On the other hand, both MAGIC and VERITAS underwent major upgrades in the years 2011 and 2012, which gave a further substantial push to the performance (Aleksić et al. 2016a,b; Zitzer et al. 2013). In the future, the Cherenkov Telescope Array (CTA) promises to deliver further substantial improvement both in terms of the energy coverage and the resolution of the flux measurement (Actis et al. 2011). Additionally, the temporal coverage extending over many years will permit variability studies (including many flares) over large portions of the electromagnetic spectrum and with good sensitivity, which will permit an evaluation of whether the association of EVPA rotations and polarization degree changes with VHE γ -ray flares are rare or regular events, whether these events occur together with a second flaring activity with contemporaneous enhancement of the VLBA radio core emission, and whether the measured multiband variability and lack of 1 keV–1 TeV correlation is a typical characteristic in Mrk 501 that is repeated over time.

Acknowledgements. The authors thank the anonymous referee for providing a very detailed and constructive list of remarks that helped us to clarify and improve some of the results reported in the manuscript. The MAGIC Collaboration would like to thank the Instituto de Astrofísica de Canarias for the excellent working conditions at the Observatorio del Roque de los Muchachos in La Palma. The financial support of the German BMBF and MPG, the Italian INFN and INAF, the Swiss National Fund SNF, the ERDF under the Spanish MINECO (FPA2015-69818-P, FPA2012-36668, FPA2015-68278-P, FPA2015-69210-C6-2-R, FPA2015-69210-C6-4-R, FPA2015-69210-C6-6-R, AYA2013-47447-C3-1-P, AYA2015-71042-P, ESP2015-71662-C2-2-P, CSD2009-00064), and the Japanese JSPS and MEXT is gratefully acknowledged. This work was also supported by the Spanish Centro de Excelencia “Severo Ochoa” SEV-2012-0234 and SEV-2015-0548, and Unidad de Excelencia “María de Maeztu” MDM-2014-0369, by grant 268740 of the Academy of Finland, by the Croatian Science Foundation (HrZZ) Project 09/176 and the University of Rijeka Project 13.12.1.3.02, by the DFG Collaborative Research Centers SFB823/C4 and SFB876/C3, and by the Polish MNiSzW grant 745/N-HESS-MAGIC/2010/0. VERITAS is supported by grants from the US Department of Energy Office of Science, the US National Science Foundation and the Smithsonian Institution, by NSERC in Canada, by Science Foundation Ireland (SFI 10/RFP/AST2748), and by STFC in the UK. The VERITAS collaboration acknowledges the excellent work of the technical support staff at the Fred Lawrence Whipple Observatory and at the collaborating institutions in the construction and operation of the instrument. The *Fermi* LAT Collaboration acknowledges support from a number of agencies and institutes for both development and the operation of the LAT as well as scientific data analysis. These include NASA and DOE in the United States; CEA/Irfu and IN2P3/CNRS in France; ASI and INFN in Italy; MEXT, KEK, and JAXA in Japan; and the K. A. Wallenberg Foundation, the Swedish Research Council, and the National Space Board in Sweden. Additional support from INAF in Italy and CNES in France for science analysis during the operations phase is also gratefully acknowledged. We acknowledge the use of public data from the *Swift* and RXTE data archive. The Metsähovi team acknowledges the support from the Academy of Finland to our observing projects (numbers 212656, 210338, 121148, and others). This research has made use of data obtained from the National Radio Astronomy Observatory’s Very Long Baseline Array (VLBA), projects BK150, BP143, and MOJAVE.

¹⁴ <http://astrosat.iucaa.in>

The St. Petersburg University team acknowledges support from Russian RFBR grant 15-02-00949 and St. Petersburg University research grant 6.38.335.2015. AZT-24 observations are made within an agreement between the Pulkovo, Rome, and Teramo observatories. The Abastumani Observatory team acknowledges financial support by the Shota Rustaveli National Science Foundation under contract FR/577/6-320/13. This research is partly based on observations with the 100 m telescope of the MPIFR (Max-Planck-Institut für Radioastronomie) at Effelsberg, as well as with the Medicina and Noto telescopes operated by INAF-Istituto di Radioastronomia. The Submillimeter Array is a joint project between the Smithsonian Astrophysical Observatory and the Academia Sinica Institute of Astronomy and Astrophysics and is funded by the Smithsonian Institution and the Academia Sinica. The OVRO 40 m program was funded in part by NASA Fermi Guest Investigator grant NNX08AW31G, and the NSF grant AST-0808050, and the Steward observatory by the NASA Fermi Guest Investigator grant NNX08AW56G.

References

- Abdo, A. A., Ackermann, M., Ajello, M., et al. 2009, *ApJ*, 699, 817
 Abdo, A. A., Ackermann, M., Ajello, M., et al. 2010a, *ApJ*, 710, 1271
 Abdo, A. A., Ackermann, M., Agudo, I., et al. 2010b, *ApJ*, 716, 30
 Abdo, A. A., Ackermann, M., Ajello, M., et al. 2011a, *ApJ*, 727, 129
 Abdo, A. A., Ackermann, M., Ajello, M., et al. 2011b, *ApJ*, 736, 131
 Acciari, V. A., Aliu, E., Arlen, T., et al. 2011a, *ApJ*, 738, 25
 Acciari, V. A., Arlen, T., Aune, T., et al. 2011b, *ApJ*, 729, 2
 Acero, F., Ackermann, M., Ajello, M., et al. 2015, *Ap&SS*, 218, 23
 Acero, F., Ackermann, M., Ajello, M., et al. 2016, *ApJS*, 223, 26
 Actis, M., Agnetta, G., Aharonian, F., et al. 2011, *Experim. Astron.*, 32, 193
 Aharonian, F., Akhperjanian, A., Barrio, J., et al. 2001, *ApJ*, 546, 898
 Ahnen, M. L., Ansoldi, S., Antonelli, L. A., et al. 2016, *MNRAS*, 459, 3271
 Albert, J., Aliu, E., Anderhub, H., et al. 2007a, *ApJ*, 669, 862
 Albert, J., Aliu, E., Anderhub, H., et al. 2007b, *ApJ*, 666, L17
 Albert, J., Aliu, E., Anderhub, H., et al. 2008, *ApJ*, 674, 1037
 Aleksić, J., Alvarez, E. A., Antonelli, L. A., et al. 2012, *Astropart. Phys.*, 35, 435
 Aleksić, J., Ansoldi, S., Antonelli, L. A., et al. 2014, *A&A*, 572, A121
 Aleksić, J., Ansoldi, S., Antonelli, L. A., et al. 2015a, *A&A*, 576, A126
 Aleksić, J., Ansoldi, S., Antonelli, L. A., et al. 2015b, *A&A*, 573, A50
 Aleksić, J., Ansoldi, S., Antonelli, L. A., et al. 2015c, *A&A*, 578, A22
 Aleksić, J., Ansoldi, S., Antonelli, L. A., et al. 2016a, *Astropart. Phys.*, 72, 61
 Aleksić, J., Ansoldi, S., Antonelli, L. A., et al. 2016b, *Astropart. Phys.*, 72, 76
 Aliu, E., Archambault, S., Archer, A., et al. 2016, *A&A*, 594, A76
 Anderhub, H., Antonelli, L. A., Antoranz, P., et al. 2009, *ApJ*, 705, 1624
 Arévalo, P., Uttley, P., Lira, P., et al. 2009, *MNRAS*, 397, 2004
 Arlen, T., Aune, T., Beilicke, M., et al. 2013, *ApJ*, 762, 92
 Baloković, M., Paneque, D., Madejski, G., et al. 2016, *ApJ*, 819, 156
 Baring, M. G., Boettcher, M., & Summerlin, E. J. 2017, *MNRAS*, 464, 4875
 Bradbury, S. M., Deckers, T., Petry, D., et al. 1997, *A&A*, 320, L5
 Catanese, M., Bradbury, S. M., Breslin, A. C., et al. 1997, *ApJ*, 487, L143
 Cerruti, M., Boisson, C., & Zech, A. 2013, *A&A*, 558, A47
 Chen, X., Fossati, G., Liang, E. P., & Böttcher, M. 2011, *MNRAS*, 416, 2368
 Chen, X., Pohl, M., & Böttcher, M. 2015, *MNRAS*, 447, 530
 Chen, X., Pohl, M., Böttcher, M., & Gao, S. 2016, *MNRAS*, 458, 3260
 Dermer, C. D., Schlickeiser, R., & Mastichiadis, A. 1992, *A&A*, 256, L27
 Djannati-Atai, A., Piron, F., Barrau, A., et al. 1999, *A&A*, 350, 17
 Domínguez, A., Primack, J. R., Rosario, D. J., et al. 2011, *MNRAS*, 410, 2556
 Domínguez, A., Finke, J. D., Prada, F., et al. 2013, *ApJ*, 770, 77
 Edelson, R. A., & Krolik, J. H. 1988, *ApJ*, 333, 646
 Edwards, P. G., & Piner, B. G. 2002, *ApJ*, 579, L67
 Finke, J. 2016, ArXiv e-prints [[arXiv:1602.05965](https://arxiv.org/abs/1602.05965)]
 Finke, J. D., Razzaque, S., & Dermer, C. D. 2010, *ApJ*, 712, 238
 Fomin, V. P., Stepaniana, A. A., Lamb, R. C., et al. 1994, *Astropart. Phys.*, 2, 137
 Fossati, G., Buckley, J. H., Bond, I. H., et al. 2008, *ApJ*, 677, 906
 Franceschini, A., Rodighiero, G., & Vaccari, M. 2008, *A&A*, 487, 837
 Furniss, A., Noda, K., Boggs, S., et al. 2015, *ApJ*, 812, 65
 Georganopoulos, M., & Kazanas, D. 2003, *ApJ*, 594, L27
 Ghisellini, G., Tavecchio, F., & Chiaberge, M. 2005, *A&A*, 432, 401
 Giannios, D., Uzdensky, D. A., & Begelman, M. C. 2009, *MNRAS*, 395, L29
 Giommi, P., Polenta, G., Lähteenmäki, A., et al. 2012, *A&A*, 541, A160
 Giroletti, M., Giovannini, G., Cotton, W. D., et al. 2008, *A&A*, 488, 905
 Gliozzi, M., Sambruna, R. M., Jung, I., et al. 2006, *ApJ*, 646, 61
 Graff, P. B., Georganopoulos, M., Perlman, E. S., & Kazanas, D. 2008, *ApJ*, 689, 68
 Henri, G., & Saugé, L. 2006, *ApJ*, 640, 185
 Horan, D., Atkins, R. W., Badran, H. M., et al. 2007, *ApJ*, 655, 396
 Kataoka, J., Mattox, J. R., Quinn, J., et al. 1999, *Astropart. Phys.*, 11, 149

- Katarzyński, K., Ghisellini, G., Tavecchio, F., Gracia, J., & Maraschi, L. 2006, *MNRAS*, **368**, L52
- Koyama, S., Kino, M., Doi, A., et al. 2015a, *PASJ*, **67**, 67
- Koyama, S., Kino, M., Giroletti, M., et al. 2015b, ArXiv [arXiv:1505.04433]
- Krawczynski, H., Sambruna, R., Kohnle, A., et al. 2001, *ApJ*, **559**, 187
- Krawczynski, H., Hughes, S. B., Horan, D., et al. 2004, *ApJ*, **601**, 151
- Larionov, V. M., Jorstad, S. G., Marscher, A. P., et al. 2008, *A&A*, **492**, 389
- Lefa, E., Aharonian, F. A., & Rieger, F. M. 2011a, *ApJ*, **743**, L19
- Lefa, E., Rieger, F. M., & Aharonian, F. 2011b, *ApJ*, **740**, 64
- Levinson, A. 2007, *ApJ*, **671**, L29
- Mankuzhiyil, N., Ansoldi, S., Persic, M., & Tavecchio, F. 2011, *ApJ*, **733**, 14
- Mankuzhiyil, N., Ansoldi, S., Persic, M., et al. 2012, *ApJ*, **753**, 154
- Marscher, A. P. 2014, *ApJ*, **780**, 87
- Marscher, A. P., Jorstad, S. G., D'Arcangelo, F. D., et al. 2008, *Nature*, **452**, 966
- Marscher, A. P., Jorstad, S. G., Larionov, V. M., et al. 2010, *ApJ*, **710**, L126
- Massaro, E., Perri, M., Giommi, P., Nesci, R., & Verrecchia, F. 2004, *A&A*, **422**, 103
- Mattox, J. R., Bertsch, D. L., Chiang, J., et al. 1996, *ApJ*, **461**, 396
- Moretti, A., Campana, S., Mineo, T., et al. 2005, *UV, X-ray and γ -ray Space Inst. for Astron., Proc. SPIE*, **5898**, 360
- Neronov, A., Semikoz, D., & Taylor, A. M. 2012, *A&A*, **541**, A31
- Nilsson, K., Pasanen, M., Takalo, L. O., et al. 2007, *A&A*, **475**, 199
- Padovani, P., & Giommi, P. 1995, *ApJ*, **444**, 567
- Petty, D., Böttcher, M., Connaughton, V., et al. 2000, *ApJ*, **536**, 742
- Pian, E., Vacanti, G., Tagliaferri, G., et al. 1998, *ApJ*, **492**, L17
- Pichel, A., & Paneque, D. 2011, Proc. 32nd Int. Cosmic Ray Conf. (ICRC 2011), **8**, 173
- Piner, B. G., & Edwards, P. G. 2004, *ApJ*, **600**, 115
- Piner, B. G., Pant, N., & Edwards, P. G. 2008, *ApJ*, **678**, 64
- Piner, B. G., Pant, N., Edwards, P. G., & Wiik, K. 2009, *ApJ*, **690**, L31
- Piner, B. G., Pant, N., & Edwards, P. G. 2010, *ApJ*, **723**, 1150
- Poutanen, J., Zdziarski, A. A., & Ibragimov, A. 2008, *MNRAS*, **389**, 1427
- Protheroe, R. J., Bhat, C. L., Fleury, P., et al. 1997, ArXiv e-prints [astro-ph/9710118]
- Quinn, J., Akerlof, C. W., Biller, S., et al. 1996, *ApJ*, **456**
- Quinn, J., Bond, I. H., Boyle, P. J., et al. 1999, *ApJ*, **518**, 693
- Sambruna, R. M., Aharonian, F. A., Krawczynski, H., et al. 2000, *ApJ*, **538**, 127
- Saugé, L., & Henri, G. 2004, *ApJ*, **616**, 136
- Schlegel, D. J., Finkbeiner, D. P., & Davis, M. 1998, *ApJ*, **500**, 525
- Sikora, M., Begelman, M. C., & Rees, M. J. 1994, *ApJ*, **421**, 153
- Silva, L., Granato, G. L., Bressan, A., & Danese, L. 1998, *ApJ*, **509**, 103
- Smith, P. S., Montiel, E., Rightley, S., et al. 2009, ArXiv e-prints arXiv:0912.3621]
- Stecker, F. W., Baring, M. G., & Summerlin, E. J. 2007, *ApJ*, **667**, L29
- Stern, B. E., & Poutanen, J. 2008, *MNRAS*, **383**, 1695
- Summerlin, E. J., & Baring, M. G. 2012, *ApJ*, **745**, 63
- Takami, H. 2011, *MNRAS*, **413**, 1845
- Tavecchio, F., Maraschi, L., & Ghisellini, G. 1998, *ApJ*, **509**, 608
- Tavecchio, F., Maraschi, L., Pian, E., et al. 2001a, *ApJ*, **554**, 725
- Tavecchio, F., Maraschi, L., Pian, E., et al. 2001b, *ApJ*, **554**, 725
- Tavecchio, F., Ghisellini, G., Ghirlanda, G., Costamante, L., & Franceschini, A. 2009, *MNRAS*, **399**, L59
- Uttley, P., Edelson, R., McHardy, I. M., Peterson, B. M., & Markowitz, A. 2003, *ApJ*, **584**, L53
- Vaughan, S., Edelson, R., Warwick, R. S., & Uttley, P. 2003, *MNRAS*, **345**, 1271
- Villata, M., & Raiteri, C. M. 1999, *A&A*, **347**, 30
- Villata, M., Raiteri, C. M., Lanteri, L., Sobrito, G., & Cavallone, M. 1998, *A&AS*, **130**, 305
- Villata, M., Raiteri, C. M., Larionov, V. M., et al. 2008, *A&A*, **481**, L79
- Villata, M., Raiteri, C. M., Gurwell, M. A., et al. 2009, *A&A*, **504**, L9
- Virtanen, J. J. P., & Vainio, R. 2005, *ApJ*, **621**, 313
- Zabalza, V. 2015, ArXiv e-prints [arXiv:1509.03319]
- Zhang, H., Chen, X., & Böttcher, M. 2014, *ApJ*, **789**, 66
- Zhang, H., Yan, H., & Dong, L. 2015, *ApJ*, **804**, 142
- Zitser, B., et al. 2013, ArXiv e-prints [arXiv:1307.8360]
- ⁹ Inst. de Astrofísica de Canarias, 38200 La Laguna, Tenerife, Universidad de La Laguna, Dpto. Astrofísica, 38206 La Laguna, Tenerife, Spain
- ¹⁰ University of Łódź, 90236 Lodz, Poland
- ¹¹ Deutsches Elektronen-Synchrotron (DESY), 15738 Zeuthen, Germany
- ¹² Institut de Física d'Altes Energies (IFAE), The Barcelona Institute of Science and Technology, Campus UAB, 08193 Bellaterra (Barcelona), Spain
- ¹³ Universität Würzburg, 97074 Würzburg, Germany
- ¹⁴ Università di Padova and INFN, 35131 Padova, Italy
- ¹⁵ Institute for Space Sciences (CSIC/IEEC), 08193 Barcelona, Spain
- ¹⁶ Technische Universität Dortmund, 44221 Dortmund, Germany
- ¹⁷ Finnish MAGIC Consortium, Tuorla Observatory, University of Turku and Astronomy Division, University of Oulu, Finland
- ¹⁸ Unitat de Física de les Radiacions, Departament de Física, and CERES-IEEC, Universitat Autònoma de Barcelona, 08193 Bellaterra, Spain
- ¹⁹ Universitat de Barcelona, ICC, IEEC-UB, 08028 Barcelona, Spain
- ²⁰ Japanese MAGIC Consortium, ICRR, The University of Tokyo, Department of Physics and Hakubi Center, Kyoto University, Tokai University, The University of Tokushima, KEK, Japan
- ²¹ Inst. for Nucl. Research and Nucl. Energy, 1784 Sofia, Bulgaria
- ²² Università di Pisa, and INFN Pisa, 56126 Pisa, Italy
- ²³ ICREA and Institute for Space Sciences (CSIC/IEEC), 08193 Barcelona, Spain
- ²⁴ Now at Centro Brasileiro de Pesquisas Físicas (CBPF/MCTI), R. Dr. Xavier Sigaud, 150 – Urca, Rio de Janeiro – RJ 22290-180, Brazil
- ²⁵ NASA Goddard Space Flight Center, Greenbelt, MD 20771, USA
- ²⁶ Humboldt University of Berlin, Institut für Physik Newtonstr. 15, 12489 Berlin, Germany
- ²⁷ Also at University of Trieste, 34127 Trieste, Italy
- ²⁸ Now at École Polytechnique Fédérale de Lausanne (EPFL), Lausanne, Switzerland
- ²⁹ Now at Max-Planck-Institut für Kernphysik, PO Box 103980, 69029 Heidelberg, Germany
- ³⁰ Also at Japanese MAGIC Consortium, ICRR, The University of Tokyo, Japan
- ³¹ Now at Finnish Centre for Astronomy with ESO (FINCA), Turku, Finland
- ³² Also at INAF – Trieste and Dept. of Physics & Astronomy, University of Bologna, 40126 Bologna, Italy
- ³³ Also at ISDC – Science Data Center for Astrophysics, 1290 Versoix, Geneva, Switzerland
- ³⁴ Also at Department of Physics and Department of Astronomy, University of Maryland, College Park, MD 20742, USA
- ³⁵ Department of Physics and Astronomy, University of Utah, Salt Lake City, UT 84112, USA
- ³⁶ Physics Department, McGill University, Montreal, QC H3A 2T8, Canada
- ³⁷ Department of Physics, Washington University, St. Louis, MO 63130, USA
- ³⁸ Fred Lawrence Whipple Observatory, Harvard-Smithsonian Center for Astrophysics, Amado, AZ 85645, USA
- ³⁹ School of Physics, University College Dublin, Belfield, Dublin 4, Ireland
- ⁴⁰ Department of Physics and Astronomy, University of California, Los Angeles, CA 90095, USA
- ⁴¹ School of Physics, National University of Ireland Galway, University Road, Galway, Ireland
- ⁴² Department of Physics and Astronomy, Purdue University, West Lafayette, IN 47907, USA
- ⁴³ Department of Physics and Center for Astrophysics, Tsinghua University, Beijing 100084, PR China
- ⁴⁴ Department of Physics and Astronomy, Iowa State University, Ames, IA 50011, USA
- ⁴⁵ Department of Astronomy and Astrophysics, 525 Davey Lab., Pennsylvania State University, University Park, PA 16802, USA
- ¹ ETH Zurich, 8093 Zurich, Switzerland
- ² Università di Udine, and INFN Trieste, 33100 Udine, Italy
- ³ INAF National Institute for Astrophysics, 00136 Rome, Italy
- ⁴ Università di Siena, and INFN Pisa, 53100 Siena, Italy
- ⁵ Croatian MAGIC Consortium, Rudjer Boskovic Institute, Univ. Rijeka, Univ. Split and Univ. of Zagreb, Croatia
- ⁶ Saha Institute of Nuclear Physics, 1/AF Bidhannagar, Salt Lake, Sector-1, Kolkata 700064, India
- ⁷ Max-Planck-Institut für Physik, 80805 München, Germany
- ⁸ Universidad Complutense, 28040 Madrid, Spain

- ⁴⁶ School of Physics and Astronomy, University of Minnesota, Minneapolis, MN 55455, USA
- ⁴⁷ Astronomy Department, Adler Planetarium and Astronomy Museum, Chicago, IL 60605, USA
- ⁴⁸ Department of Physics and Astronomy and the Bartol Research Institute, University of Delaware, Newark, DE 19716, USA
- ⁴⁹ Physics Department, Columbia University, New York, NY 10027, USA
- ⁵⁰ Department of Physics and Astronomy, University of Iowa, Van Allen Hall, Iowa City, IA 52242, USA
- ⁵¹ Department of Physics and Astronomy, DePauw University, Greencastle, IN 46135-0037, USA
- ⁵² Department of Physics and Astronomy, Barnard College, Columbia University, NY 10027, USA
- ⁵³ Enrico Fermi Institute, University of Chicago, Chicago, IL 60637, USA
- ⁵⁴ Instituto de Astronomia y Física del Espacio, Casilla de Correo 67 – Sucursal 28, (C1428ZAA) Ciudad Automa de Buenos Aires, Argentina
- ⁵⁵ Institute of Physics and Astronomy, University of Potsdam, 14476 Potsdam-Golm, Germany
- ⁵⁶ Department of Physical Sciences, Cork Institute of Technology, Bishopstown, Cork, Ireland
- ⁵⁷ School of Physics and Center for Relativistic Astrophysics, Georgia Institute of Technology, 837 State Street NW, Atlanta, GA 30332-0430, USA
- ⁵⁸ Santa Cruz Institute for Particle Physics and Department of Physics, University of California, Santa Cruz, CA 95064, USA
- ⁵⁹ Argonne National Laboratory, 9700 S. Cass Avenue, Argonne, IL 60439, USA
- ⁶⁰ Department of Physics, University of Johannesburg, PO Box 524, Auckland Park 2006, South Africa
- ⁶¹ INAF–Osservatorio Astrofisico di Torino, 10025 Pino Torinese (TO), Italy
- ⁶² Department of Astronomy, University of Michigan, Ann Arbor, MI 48109-1042, USA
- ⁶³ Astronomical Institute, St. Petersburg State University, Universitetskij Pr. 28, Petrodvorets, 198504 St. Petersburg, Russia
- ⁶⁴ Pulkovo Observatory, St. Petersburg, Russia
- ⁶⁵ Department of Physics and Institute for Plasma Physics, University of Crete, 71003 Heraklion, Greece
- ⁶⁶ Foundation for Research and Technology – Hellas, IESL, Voutes, 71110 Heraklion, Greece
- ⁶⁷ Circolo Astrofili Talmassons, 33030 Campofornido (UD), Italy
- ⁶⁸ Osservatorio Astrofisico della Regione Autonoma Valle d’Aosta, Italy
- ⁶⁹ Abastumani Observatory, Mt. Kanobili, 0301 Abastumani, Georgia
- ⁷⁰ Engelhard Astronomical Observatory, Kazan Federal University, Tatarstan, Russia
- ⁷¹ Center for Astrophysics, Guangzhou University, Guangzhou 510006, PR China
- ⁷² Graduate Institute of Astronomy, National Central University, 300 Zhongda Road, Zhongli 32001, Taiwan
- ⁷³ Department of Physics and Mathematics, College of Science and 952 Engineering, Aoyama Gakuin University, 5-10-1 Fuchinobe, Chuoku, Sagamihara-shi Kanagawa 252-5258, Japan
- ⁷⁴ Department of Physics, University of Colorado Denver, Denver, Colorado, CO 80217-3364, USA
- ⁷⁵ Department of Physics and Astronomy, Brigham Young University, Provo, Utah 84602, USA
- ⁷⁶ Department of Physics, Tokyo Institute of Technology, Meguro City, Tokyo 152-8551, Japan
- ⁷⁷ Instituto Nacional de Astrofísica, Óptica y Electrónica, Tonantzintla, Puebla 72840, Mexico
- ⁷⁸ Instituto de Astronomia y Meteorología, Dpto. de Física, CUCEI, Universidad de Guadalajara, Mexico
- ⁷⁹ Department of Physics and Astronomy, University of Denver, Denver, CO 80208, USA
- ⁸⁰ Steward Observatory, University of Arizona, Tucson, AZ 85721, USA
- ⁸¹ Space Science Institute, Boulder, CO 80301, USA
- ⁸² Harvard-Smithsonian Center for Astrophysics, Cambridge, MA 02138, USA
- ⁸³ Department of Physics and Astronomy, Pomona College, Claremont, CA 91711-6312, USA
- ⁸⁴ Department of Physics and Astronomy, University of Leicester, Leicester, LE1 7RH, UK
- ⁸⁵ ASI Science Data Center, via del Politecnico snc, 00133 Roma, Italy
- ⁸⁶ INAF–Osservatorio Astronomico di Roma, via di Frascati 33, 00040 Monteporzio, Italy
- ⁸⁷ Department of Physics, University of Trento, 38050 Povo, Trento, Italy
- ⁸⁸ Center for Research and Exploration in Space Science and Technology (CRESST), USA
- ⁸⁹ Universities Space Research Association (USRA), Columbia, MD 21044, USA
- ⁹⁰ Astro Space Center of Lebedev Physical Institute, Profsoyuznaya 84/32, 117997 Moscow, Russia
- ⁹¹ Max-Planck-Institut für Radioastronomie, Auf dem Hügel 69, 53121 Bonn, Germany
- ⁹² Observatori Astronòmic, Universitat de València, Parc Científic, C. Catedrático José Beltrán 2, 46980 Paterna, València, Spain
- ⁹³ Departament d’Astronomia i Astrofísica, Universitat de València, C. Dr. Moliner 50, 46100 Burjassot, València, Spain
- ⁹⁴ Crimean Astrophysical Observatory, 98409 Nauchny, Crimea
- ⁹⁵ Sternberg Astronomical Institute, M.V. Lomonosov Moscow State University, Universitetskij prosp. 13, Moscow 119991, Russia
- ⁹⁶ Institute of Astronomy, Astrophysics, Space Applications and Remote Sensing, National Observatory of Athens, Vas. Pavlou & I. Metaxa, 15 236 Penteli, Greece
- ⁹⁷ Department of Physics and Astronomy, Whittier College, Whittier, CA, USA
- ⁹⁸ Aalto University Metsähovi Radio Observatory, 02540 Kylmäla, Finland
- ⁹⁹ INAF Istituto di Radioastronomia, Sezione di Noto, Contrada Renna Bassa, 96017 Noto (SR), Italy
- ¹⁰⁰ INAF Istituto di Radioastronomia, Stazione Radioastronomica di Medicina, 40059 Medicina (Bologna), Italy
- ¹⁰¹ INAF Osservatorio Astrofisico di Catania, via S. Sofia 78, 95123 Catania, Italy
- ¹⁰² Cahill Center for Astronomy and Astrophysics, California Institute of Technology, Pasadena, CA 91125, USA



Multiwavelength Stellar Polarimetry of the Filamentary Cloud IC5146. I. Dust Properties

Jia-Wei Wang¹, Shih-Ping Lai², Chakali Eswaraiah^{2,3,4}, Dan P. Clemens⁵, Wen-Ping Chen³, and Anil K. Pandey⁴

¹Institute of Astronomy, National Tsing Hua University, 101, Section 2, Kuang-Fu Road, Hsinchu 30013, Taiwan, R.O.C; jwwang@gapp.nthu.edu.tw

²Institute of Astronomy & Department of Physics, National Tsing Hua University, 101, Section 2, Kuang-Fu Road, Hsinchu 30013, Taiwan, R.O.C; slai@phys.nthu.edu.tw

³Institute of Astronomy, National Central University, 300 Jhongda Road, Taoyuan 32001, Taiwan, R.O.C; eswarbramha@gmail.com, wchen@gm.astro.ncu.edu.tw

⁴Aryabhata Research Institute of Observational Sciences (ARIES), Manora-peak, Nainital, Uttarakhand-state, 263002, India; pandey@aries.res.in

⁵Institute for Astrophysical Research, Boston University, 725 Commonwealth Avenue, Boston, MA 02215, USA; clemens@bu.edu

Received 2017 August 9; revised 2017 September 22; accepted 2017 October 5; published 2017 November 10

Abstract

We present optical and near-infrared stellar polarization observations toward the dark filamentary clouds associated with IC5146. The data allow us to investigate the dust properties (this paper) and the magnetic field structure (Paper II). A total of 2022 background stars were detected in the R_c , i' , H , and/or K bands to $A_V \lesssim 25$ mag. The ratio of the polarization percentage at different wavelengths provides an estimate of λ_{\max} , the wavelength of the peak polarization, which is an indicator of the small-size cutoff of the grain size distribution. The grain size distribution seems to significantly change at $A_V \sim 3$ mag, where both the average and dispersion of P_{R_c}/P_H decrease. In addition, we found $\lambda_{\max} \sim 0.6\text{--}0.9 \mu\text{m}$ for $A_V > 2.5$ mag, which is larger than the $\sim 0.55 \mu\text{m}$ in the general interstellar medium (ISM), suggesting that grain growth has already started in low- A_V regions. Our data also reveal that polarization efficiency (PE $\equiv P_\lambda/A_V$) decreases with A_V as a power law in the R_c , i' , and K bands with indices of -0.71 ± 0.10 , -1.23 ± 0.10 , and -0.53 ± 0.09 . However, H -band data show a power index change; the PE varies with A_V steeply (index of -0.95 ± 0.30) when $A_V < 2.88 \pm 0.67$ mag, but softly (index of -0.25 ± 0.06) for greater A_V values. The soft decay of PE in high- A_V regions is consistent with the radiative alignment torque model, suggesting that our data trace the magnetic field to $A_V \sim 20$ mag. Furthermore, the breakpoint found in the H band is similar to that for A_V , where we found the P_{R_c}/P_H dispersion significantly decreased. Therefore, the flat PE- A_V in high- A_V regions implies that the power-index changes result from additional grain growth.

Key words: dust, extinction – ISM: clouds – ISM: individual objects (IC5146) – ISM: magnetic fields – ISM: structure – polarization

Supporting material: machine-readable table

1. Introduction

The linearly polarized background starlight observed in early studies (Hall 1949; Hiltner 1949a) was suggested to result from dichroic absorption by nonspherical dust grains aligned to B fields (Hiltner 1949b). Hence, polarized starlight is commonly used as a tracer of the B-field structure in the plane of sky (e.g., Chapman et al. 2011; Clemens et al. 2012c; Eswaraiah et al. 2012). The first theory to explain dust alignment used a paramagnetic mechanism (DG alignment; Davis & Greenstein 1951). However, later studies revealed timescale and efficiency problems, so other alignment mechanisms were offered, including superparamagnetic grains (Jones & Spitzer 1967) and superthermal rotation rates (Purcell 1979). Nevertheless, most of these mechanisms are only efficient for particular physical conditions, and fail to explain the polarization observed across a wide variety of environments (see review in Andersson et al. 2015).

The model of radiative alignment torques (RATs; Dolginov & Mitrofanov 1976; Draine & Weingartner 1996, 1997; Lazarian & Hoang 2007) can currently best explain how dust grains align with B fields. The RATs theory assumes an anisotropic radiation field impacting nonspherical dust grains. The radiation field can generate net torque on the grains and induce both spin of the grains and precession about the B field. For typical interstellar radiation fields, the RATs alignment timescale is much faster than DG alignment (Lazarian & Hoang 2007), and superthermal rotation tends to enhance RATs alignment more than DG

alignment (Hoang & Lazarian 2009). In addition, RATs is efficient across a variety of environments, and thus more likely dominates the grain alignment process.

A key prediction of the RATs theory is the decreasing polarization efficiency (PE, P_λ/A_V) with increasing A_V , because the radiation field required to align the dust grains is decreased through extinction (Lazarian et al. 1997). In order to examine whether the RATs theory can explain observed polarizations, Whittet et al. (2008) performed a numerical simulation based on RATs theory and assuming a starless core with only an external radiation field and a fixed dust grain size distribution for all A_V . Their simulation results matched their K -band polarimetry data toward Taurus up to at least $A_V \sim 10$ mag; the K -band polarization degree varied with A_V as a power law, with $P_\lambda/\tau_K \propto A_V^{-0.52}$. In addition, their simulation predicted that the RATs mechanism would cease as A_V approached 10 mag, since the radiation that can penetrate to such high column densities has wavelengths too long to effectively align the grains. However, the single power-law matched their data over the $A_V = 0\text{--}30$ mag range well, which was inconsistent with the predicted cessation of alignment at $A_V \sim 10$ mag. To explain the inconsistency, Whittet et al. (2008) argued that the RAT mechanism may still work in high- A_V regions if (1) the dust grains have undergone significant growth and so can couple to longer wavelength radiation, or (2) embedded stars are present to provide radiation at shorter wavelength to enhance the alignment of small dust grains.

To further test the RATs theory in dense clouds, Jones et al. (2015) used both infrared and submillimeter polarimetry data to trace the variation of polarization efficiency (PE) up to $A_V \sim 100$ mag within starless cores. They found a change of power-law index for PE versus extinction from -0.5 to -1 at $A_V \sim 20$ mag, consistent with the cessation of alignment predicted by Whittet et al. (2008). In addition, Jones et al. (2016) found a deeper break point at $A_V \sim$ hundreds mag and a reversed trend such that the power-law index of PE versus A_V changed from -1 to -0.5 within the Class 0 YSO G034.43+00.24 MM1. The opposite trends shown in these two cases suggest that dust alignment in dense clouds could be strongly affected by environmental effects.

In the RATs paradigm, the polarization degree is expected to be wavelength dependent because the cloud extinction penetration is wavelength dependent and because the highest alignment efficiency occurs at wavelengths similar to the sizes of the grains (Cho & Lazarian 2005; Lazarian & Hoang 2007). Therefore, the polarization wavelength-dependence is determined by both the extinction and the size of dust grains, resulting in a polarization spectrum exhibiting a single peak (λ_{\max}). Kim & Martin (1995) showed that λ_{\max} is sensitive to the small-size cutoff of the grain size distribution, since the dust size distribution is a power law and the small-size cutoff will effectively determine the mean size of the dust grains. Whittet et al. (2008) calculated the λ_{\max} variation with A_V using a RATs model with a fixed grain size distribution over A_V , and showed that the RATs theory can explain their observed dependence of λ_{\max} increasing with A_V to ~ 6 mag, but that RATs predicts that λ_{\max} flattens for higher A_V in the Taurus cloud.

Recent observational results are mostly consistent with the RATs theory (Whittet et al. 2008; Alves et al. 2014; Cashman & Clemens 2014), although the dust alignment efficiency varies from source to source. As an extreme case, Goodman et al. (1995) found a constant near-infrared polarization degree toward L1755 for A_V of 1–10 mag, and argued that near-infrared polarization can only trace the B field on the surfaces of dark clouds. In contrast, other observations mostly showed a polarization degree increasing with A_V , such as $P \propto A_V^{0.48}$ toward Taurus (Whittet et al. 2008) and $P \propto A_V^{0.26}$ toward the L204 cloud 3 (Cashman & Clemens 2014), suggesting that the constant polarization degree found in Goodman et al. (1995) represented a special case and was not the norm.

It is still unclear why the P – A_V relation found in L1755 is different from the relation found for other clouds. Whittet et al. (2008) reanalyzed the L1755 polarimetry data with a better background star selection and extinction estimation, but still found the same relation. They speculated that this unique relation might result from a lack of the typical physical conditions leading to grain alignment inside this cloud or a reduction of observed polarization that is due to the complex B-field structure within the L1755 filaments. To examine these possibilities, more polarimetry observations covering both a wider area and more wavebands could help to reveal the alignment conditions for dust grains with different sizes and to probe the detailed B-field structure. In addition, since the Goodman et al. (1995) polarization detections only spanned a small range of A_V (2–8 mag), it would be of interest to perform polarization observations with higher sensitivity to investigate this relation to higher A_V values.

An ideal target for a detailed testing of the RATs paradigm is the system of dark cloud filaments associated with the

reflection and emission nebula IC5146, a nearby (~ 460 pc) star-forming region in Cygnus. The system consists of a young cluster inside an H II region and a long main dark cloud filament with several subfilaments branching out from the main filament. The *Herschel* Gould Belt Survey (Arzoumanian et al. 2011) revealed a complex network of filaments within the long dark cloud, highlighting the locations of young forming stars. The *Planck* polarization map of IC5146 (Planck Collaboration et al. 2016c) revealed that the B field is nearly uniform, with the millimeter-wavelength-traced B field oriented perpendicular to the elongation orientation of the main filament. This apparently uniform B field gives the IC5146 dark cloud system an advantage for testing the RATs model because the high angular resolution of stellar polarizations can be used to test for, and quantify, complex B fields along the multiple line of sights.

In a series of papers, we will report measurements and analyses of the polarizations of stars behind the IC5146 filamentary cloud. The polarimetry of background starlight was performed at both optical and infrared wavelengths to probe the large-scale B field in the cloud. In this paper, we focus on the dust properties and the dust alignment conditions revealed by our data in order to identify where the B fields were accurately probed by our observations. The observations and data reduction are described in Section 2. In Section 3 we present the polarization measurements toward IC5146. Section 4 presents an initial analysis of the data to show how the dust grain alignment conditions vary with A_V and regions. In Section 5 we discuss the evolution of dust grains and how the dust properties influence the PE. The consequences of these results for the investigations of the role of B fields in cloud evolution will be offered in the forthcoming Paper II.

2. Observations and Data Reduction

We measured the polarization of background stars toward the IC5146 filamentary cloud system with several instruments: the Aryabhata Research Institute of Observational Sciences (ARIES) Imaging Polarimeter (AIMPOL; Rautela et al. 2004) and Triple-Range (g' , r' , i') Imager and POLarimeter (TRIPOL; S. Sato et al. 2017, in preparation) provided optical R_c - and i' -band polarimetry data, respectively. Mimir (Clemens et al. 2007) measured the H - and K -band polarizations at near-infrared wavelengths. Figure 1 shows the target fields for each instrument overlaid on the *Herschel* archive $250 \mu\text{m}$ image (Griffin et al. 2010; Arzoumanian et al. 2011). The dust continuum map shows an east-west main filament connected to the bright cluster complex, known as the Cocoon Nebula. Numerous “subfilaments” are extended from the main filament, with the largest subfilament located on the northwest side of the main filament. Almost all parts of the cloud were observed with Mimir, while the fields observed with AIMPOL were chosen to be mainly in the edge of the cloud in order to cover as many optically bright stars as possible. The TRIPOL observations focused on the northwestern region, with longer exposure time, where bright stars are rare at both optical and infrared wavelengths. The detailed information of the observations with the different instruments is described below.

2.1. AIMPOL Polarimetry

The R_c -band ($0.67 \mu\text{m}$, bandwidth = $0.14 \mu\text{m}$) polarimetric observations were carried out toward the IC5146 filamentary

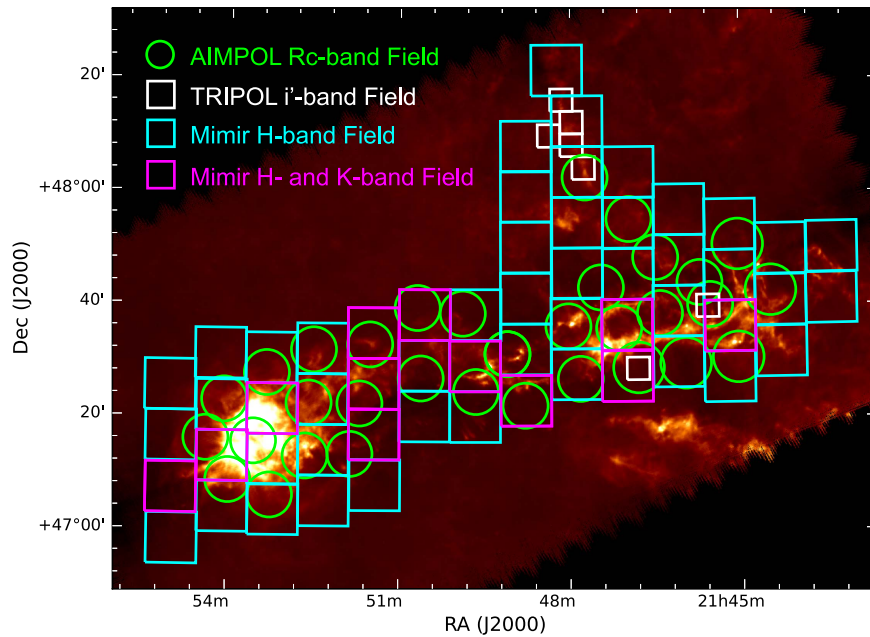


Figure 1. IC5146 fields surveyed in our polarization observations overlaid on the *Herschel* 250 μm image. The fields observed with TRIPOL and AIMPOL are labeled with white boxes and green circles, respectively. The magenta boxes show the fields observed with Mimir using the *H* and *K* bands, and the cyan boxes show the fields observed with Mimir using only the *H* band.

cloud system using AIMPOL, which is mounted at the Cassegrain focus of the 104 cm Sampurnanand telescope of the ARIES, Nainital, India. AIMPOL consisted of a half-wave plate (HWP) modulator and a Wollaston prism beam-splitter illuminating a fraction (370×370 pixel²) of the Tektronics 1024×1024 pixel² CCD camera. The pixel size of the CCD was $1.73''$ and the typical seeing was $\sim 2''$. The observations spanned the nights of 2011 November 4–8 and 2012 November 8–15 and covered 37 fields (see Figure 1), with each field having a useful diameter of $\sim 8'$. In order to obtain Stokes Q and U , we took images at four independent HWP orientations (0° , $22^\circ.5$, 45° , and $67^\circ.5$; Schaefer et al. 2007). The Wollaston prism analyzer produced offset, but simultaneous, ordinary and extraordinary overlapping images for each HWP orientation. Hence, each image resulted in one measurement of Stokes Q or U . The integration time was set to 10 minutes for each HWP orientation, so the total integration time for each field was 40 minutes.

The polarization measurements were calibrated for instrumental polarization and offset angle by observing standard polarized and unpolarized stars drawn from Schmidt et al. (1992). The data were reduced using standard IRAF procedures.⁶ The fluxes in the ordinary and extraordinary beams for each observed source were extracted using standard aperture photometry. Sources with stellar overlap, fewer than 10% of the total sources, were excluded. The polarization degree and angle for each star were derived from the relative fluxes in the ordinary and extraordinary beams. We removed the Ricean bias with the asymptotic estimator

$$P = \sqrt{(U^2 + Q^2) - \sigma_P^2}, \quad (1)$$

where P is the debiased degree of polarization, Q and U are normalized Stokes Q and U , and σ_P is the uncertainty in the

polarization percentage (Wardle & Kronberg 1974). The details of the observing facility and procedures used to estimate the polarization degree and polarization angles (P.A.) are described in Eswaraiah et al. (2011, 2012).

2.2. TRIPOL Polarimetry

Polarimetric observations focused on the northwestern region of IC5146 in the i' bands ($0.77 \mu\text{m}$, bandwidth $0.15 \mu\text{m}$) on 2012 July 27–28 and 2014 July 6 with TRIPOL installed on the Lulin-One-meter Telescope in Lulin Observatory, Taiwan. Seven fields, each with a size of $4' \times 4'$, were observed (see Figure 1). TRIPOL consisted of dichroic mirrors and three ST-9 512 \times 512 pixel² CCD cameras, which enabled simultaneous observations in the g' , r' , and i' bands; however, only the i' -band data were able to detect background stars behind this dark cloud. The pixel sizes of the CCDs were 0.5 arcsec and the average seeing was $\sim 1''.5$. A rotatable achromatic half-wave plate and a fixed wire-grid were used to analyze the incoming light. Each field was measured at four HWP orientations (0° , $22^\circ.5$, 45° , and $67^\circ.5$, with pairs of images yielding stellar Stokes Q and U values.). The integration time for each position angle was 22.5 minutes, so each field required a total of 1.5 hours.

Standard reduction procedures were applied using IRAF, and the photometry of each background star was obtained using Source Extractor (Bertin & Arnouts 1996). The debiased polarization degree and angle for each background star were derived from the fluxes measured through each of the four HWP orientation angles and calibrated against observations of polarized and unpolarized standard stars from Schmidt et al. (1992).

2.3. Mimir Polarimetry

We carried out *H*- ($1.6 \mu\text{m}$) and *K*-band ($2.2 \mu\text{m}$) polarization observations toward IC5146 on 2013 September 17–27,

⁶ IRAF is distributed by the National Optical Astronomy Observatory, which is operated by the Association of Universities for Research in Astronomy (AURA) under a cooperative agreement with the National Science Foundation.

using the Mimir instrument (Clemens et al. 2007), which is mounted on the 1.8 m Perkins telescope located near Flagstaff, AZ, and operated by Lowell Observatory. Fifty-seven fields covering the IC5146 cloud were observed in the H band, and 12 fields were observed in the K band toward the dense regions (see Figure 1). The pixel size of the InSb detector array was 0.58 arcsec and the average seeing was $\sim 1''.5$. The field of view was $10' \times 10'$ for Mimir, and we set $1'$ overlap between adjacent fields. Each field was observed in six sky-dither positions where images were taken at 16 orientation angles of the HWP. A total of 96 (16×6) images were taken for each field with 10 sec of integration time for each image for both the H and K bands, and thus the total integration time was 16 minutes for each field. We took an additional short integration for fields with bright stars, which took 4 minutes per field.

In order to calibrate the nonlinearities of the InSb detector array, a series of images were taken with an increasing exposure time toward an illuminated flat-field screen, and the response curve of each pixel was fitted with a polynomial model to obtain a linearity correction. Flat fields for each HWP position were taken using a lights-on/lights-off method toward a flat-field screen inside the closed dome during the observation run. The data were calibrated using the Mimir Software Package Basic Data Processing (MSP-BDP), and the Photo POLarimetry tool (MSP-PPOL) was used to extract Stokes Q and U values for each observed source from the calibrated data. The detailed processes used in the Mimir Software Package are described in Clemens et al. (2012a, 2012b, 2012c).

3. Results

3.1. The Polarization Catalog

We matched the polarization data to the 2MASS catalog (Skrutskie et al. 2006) to obtain positions accurate to 0.5 arcsec. Table 1 lists all the observed polarization properties as well as photometric magnitudes from 2MASS and *WISE* (Wright et al. 2010). Column 1 lists the star number, and columns 2 and 3 list the R.A. and decl. The measured Stokes Q , U , debiased P , and position angle P.A. in the R_c , i' , H , and K bands with their uncertainties are listed in columns 4–35. The J -, H -, K -, $W1$ -, and $W2$ -band magnitudes and uncertainties are listed in columns 36–45. Column 46 presents the estimated visual extinction described in Section 4.1. Column 47 present the Usage Flag (UF; stars with UF = 1 were selected for further analyses, and stars with UF = 0 were not used). The usage data were selected with the polarization degree divided by its uncertainty $P/\sigma_p \geq 3$ for the R_c and i' bands, and $P/\sigma_p \geq 2$ and $\sigma_p < 5\%$ for the H and K bands; the selection criteria were relaxed for near-infrared data, since the number of 3σ near-infrared detections was too small for adequate statistics.

In total, 2022 independent background stars have polarization detections in at least one of the four bands, 239 stars were detected in two bands, 24 stars were detected in three bands, and only 3 stars were detected in all four bands. About 71% of the background stars were detected in the H band, 24% in the R_c band, 10% in the i' band, and 8% in the K band.

Figure 2 shows all of the polarization measurements on the *Herschel* SPIRE 250 μm image. The inferred B field is seemingly perpendicular to the main filament on large scales but parallel to the subfilaments. The bimodal perpendicular or parallel alignment is similar to that seen in previous polarimetry work toward filamentary clouds, and has been ascribed to

B-field confinement of sub-Alfvénic turbulence or gravitational contraction channeled by strong B fields (Li et al. 2013). We will discuss the B-field structure in detail and estimate the B-field strengths with the Chandrasekhar-Fermi method to determine the dynamical importance of the B fields in Paper II.

3.2. Consistency in P.A. between Multiple Wavelengths

To test whether the results from AIMPOL, TRIPOL, and Mimir were consistent and thereby capable of revealing wavelength-dependent effects in the probed dust columns, we selected the stars that had detections at multiple wavelengths, and we examine their P.A.s in the different wavelengths in Figure 3. In total, 143, 31, and 65 stars were selected in R_c - i' , R_c - H , and H - K band pairs. The mean P.A. differences in these three band pairs were $-4^\circ.6 \pm 0^\circ.8$, $6^\circ.2 \pm 0^\circ.8$, and $-2^\circ.9 \pm 1^\circ.6$, respectively. The standard deviation of the measured P.A. differences were $8^\circ.7$, $16^\circ.3$, and $26^\circ.6$ for the R_c - i' , R_c - H , and H - K band pairwise samples. The average expected uncertainties of P.A. difference, propagated from observational uncertainties ($\sigma_{P.A.,\lambda_1-\lambda_2} = \sqrt{\sigma_{P.A.,\lambda_1}^2 + \sigma_{P.A.,\lambda_2}^2}$), were $4^\circ.2$, $9^\circ.3$, and $12^\circ.3$ for the R_c - i' , R_c - H , and H - K band pairwise samples. The P.A. difference standard deviations obtained from these sets are 1–2 times to the propagated instrumental uncertainties, which are acceptable values since the P.A.s may be intrinsically different at different wavelengths because they may trace the polarizations to different depths.

3.3. Negligible Foreground Contamination

We attempted to identify and exclude foreground stars whose polarizations do not trace the B field of the IC5146 cloud system. To obtain enough star samples to represent the foreground polarization near IC5146, we selected stars with known distances and V -band polarization measurements from van Leeuwen (2007) and Heiles (2000), within a 10° radius sky area near IC5146. Figure 4 shows the V -band polarization degree (P_V) versus distance for these 41 stars. The distance of 460_{-60}^{+40} pc to the IC5146 cloud system (Lada et al. 1999) was used to separate these stars into foreground and background groups. The polarization degree rises significantly at a distance of ~ 400 pc, which is possibly due to nearby clouds in the Gould Belt. For most of the stars with distances smaller than 400 pc, the polarization degrees are below 0.3%. This value was chosen as the upper limit of the foreground V -band polarization for the sky area near IC5146.

In the interstellar medium (ISM), the polarization in the V band is greater than that in the R_c , H , or K bands (Serkowski 1973). Hence, based on the foreground star values in Figure 4, the foreground polarization in the R_c , H , and K bands is expected to be lower than $\sim 0.3\%$. This foreground polarization upper limit is similar to the instrumental uncertainties of our data ($\sim 0.2\%$ – 0.5%). Hence, any foreground stars were likely to have been already excluded by our selection criteria ($P/\sigma_p > 3$ for the R_c and i' bands and $P/\sigma_p > 2$ for the H and K bands). Thus, we concluded that contamination by foreground stars was negligible in our sample set, and furthermore, that no foreground polarization correction to the remaining data was necessary.

Table 1
Measured Polarization Properties of Stars Probing the IC5146 Dark Cloud Complex

ID	R.A. (deg)	Decl. (deg)	R_c -band Polarimetry								i' -band Polarimetry				
			Q_{R_c} (%)	$\sigma_{Q_{R_c}}$ (%)	U_{R_c} (%)	$\sigma_{U_{R_c}}$ (%)	P_{R_c} (%)	$\sigma_{P_{R_c}}$ (%)	PA_{R_c} (deg)	$\sigma_{PA_{R_c}}$ (deg)	$Q_{i'}$ (%)	$\sigma_{Q_{i'}}$ (%)	$U_{i'}$ (%)	$\sigma_{U_{i'}}$ (%)	$P_{i'}$ (%)
(1)	(2)	(3)	(4)	(5)	(6)	(7)	(8)	(9)	(10)	(11)	(12)	(13)	(14)	(15)	(16)
8327	326.3935	47.6311	1.68	0.32	1.94	0.33	2.54	0.34	24.51	3.44	1.59	0.07	2.18	0.07	2.70
12997	326.6920	47.4848	0.98	0.24	0.90	0.24	1.31	0.25	21.34	4.86	0.54	0.05	1.40	0.05	1.50
13793	326.7371	47.4965	2.11	0.18	1.40	0.18	2.53	0.18	16.75	1.97	2.16	0.05	1.75	0.05	2.78

H -band Polarimetry											K -band Polarimetry						
$\sigma_{i'}$ (%)	$PA_{i'}$ (deg)	$\sigma_{PA_{i'}}$ (deg)	Q_H (%)	σ_{Q_H} (%)	U_H (%)	σ_{U_H} (%)	P_H (%)	σ_{P_H} (%)	PA_H (deg)	σ_{PA_H} (deg)	Q_K (%)	σ_{Q_K} (%)	U_K (%)	σ_{U_K} (%)	P_K (%)	σ_{P_K} (%)	PA_K (deg)
(17)	(18)	(19)	(20)	(21)	(22)	(23)	(24)	(25)	(26)	(27)	(28)	(29)	(30)	(31)	(32)	(33)	(34)
0.07	26.90	0.70	0.41	0.11	0.65	0.11	0.76	0.11	28.62	4.28	0.03	0.22	0.53	0.20	0.49	0.20	43.34
0.05	34.46	0.97	0.47	0.23	0.47	0.22	0.62	0.23	22.28	10.49	0.31	0.25	0.44	0.16	0.51	0.20	27.36
0.05	19.55	0.50	0.98	0.21	0.70	0.23	1.19	0.22	17.82	5.33	0.37	0.24	0.36	0.13	0.48	0.19	21.98

2MASS Catalog							WISE Catalog					A_V^a (mag)	UF
σ_{PA_K} (deg)	J (mag)	σ_J (mag)	H (mag)	σ_H (mag)	K (mag)	σ_K (mag)	$W1$ (mag)	σ_{W1} (mag)	$W2$ (mag)	σ_{W2} (mag)	(46)		
(35)	(36)	(37)	(38)	(39)	(40)	(41)	(42)	(43)	(44)	(45)			
11.76	10.861	0.019	9.727	0.028	9.352	0.017	9.163	0.023	9.314	0.019	5.00	1	
11.20	11.483	0.025	10.745	0.03	10.462	0.023	10.257	0.022	10.35	0.021	3.03	1	
11.66	11.205	0.023	10.333	0.028	10.075	0.022	9.894	0.022	9.961	0.021	3.16	1	

Note.

^a The uncertainties of A_V are 0.93 mag, estimated in Section 3.1.

(This table is available in its entirety in machine-readable form.)

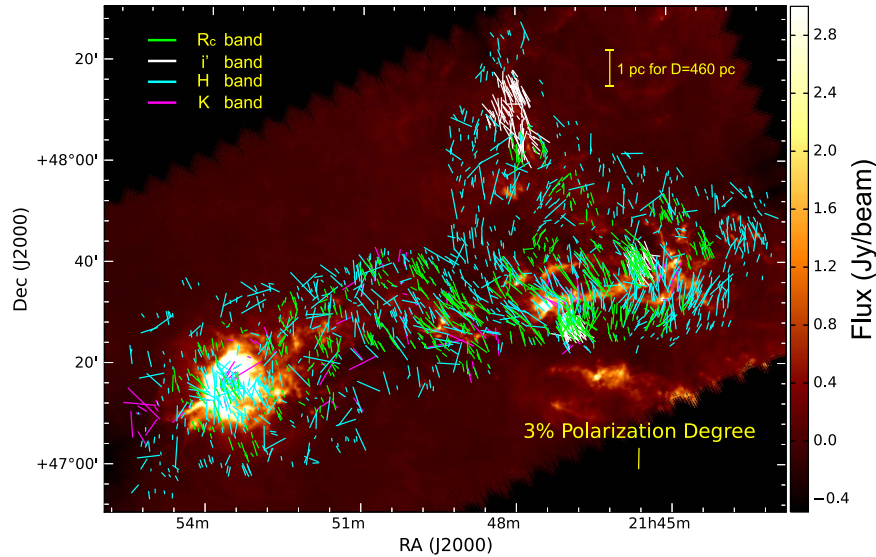


Figure 2. Map of IC5146 stellar polarizations overlaid on the *Herschel* 250 μm image, with an FWHM beamsize of $17''_6$. The detections in the TRIPOL i' band, AIMPOL R_c band, and Mimir H and K band are labeled in white, green, cyan, and magenta.

4. Analysis

4.1. NICER Extinction

Visual extinction provides an estimate of how many dust grains are responsible for the observed starlight polarization, and thus is required for estimating dust alignment efficiency and testing the RATs theory. We used the technique called

near-infrared color excess revisited (NICER; Lombardi & Alves 2001)⁷ to calculate the visual extinction over the IC5146 cloud system. The NICER technique uses multiband colors to obtain extinction for a target field, using extinction coefficients derived from Indebetouw et al. (2005). We selected a total of

⁷ Using the PNICER python package developed by Meingast et al. (2017).

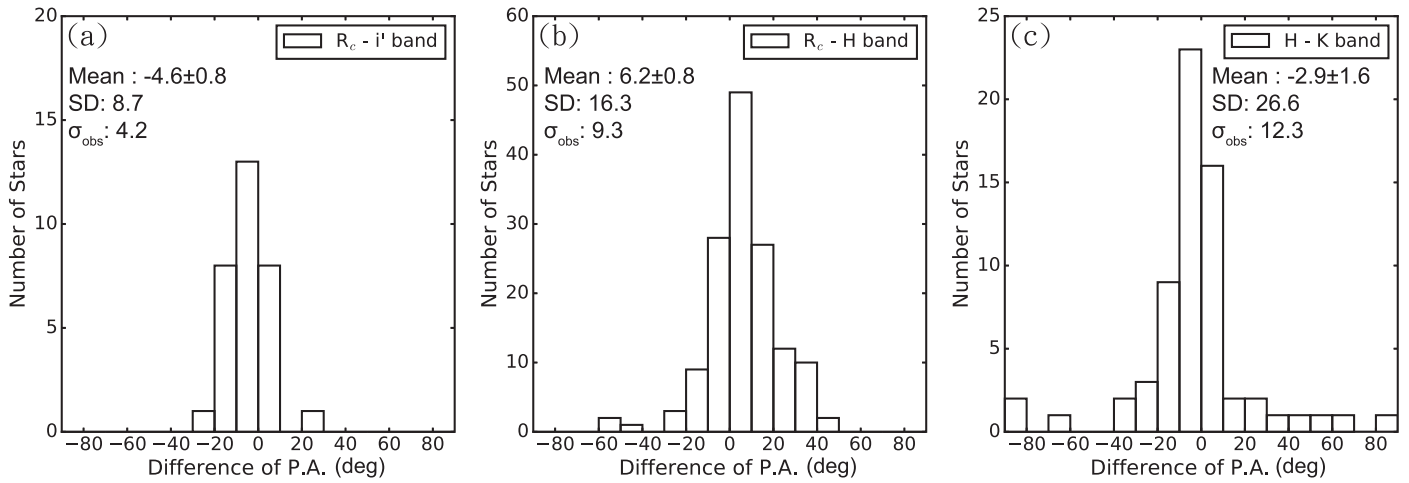


Figure 3. Examination of the P.A. consistency of the data for stars with polarization detections in multiple bands. The differences of P.A.s detected in different band pairs are shown in the histograms with the mean, standard deviation, and averaged instrumental uncertainty (σ_{obs}) of the P.A.s for each band pair, listed in degrees. The comparisons between the R_c - and i' -band number of stars, R - and H -band number of stars, and H - and K -band number of stars are shown in panels (a), (b), and (c), respectively. Although small offsets and larger dispersions are shown in these band pairs compared to the instrumental uncertainties, about 90% of the stars are distributed within $3\sigma_{\text{ins}}$.

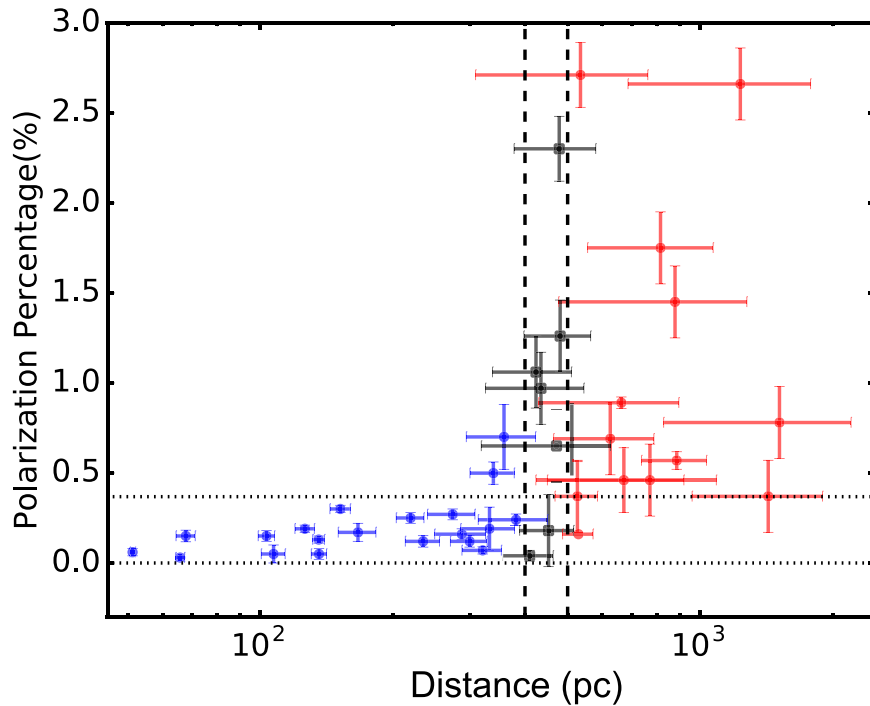


Figure 4. Polarization degree vs. distance for stars within 10° of IC5146 with distance measurements in the *Hipparcos* catalog (van Leeuwen 2007) and polarization measurements in Heiles (2000). The black vertical dashed lines represent the 1σ upper and lower boundary of the distance of the IC5146 dark cloud estimated by Lada et al. (1999). The blue, black, and red dots identify the stars as classified by distance zone. The blue dot stars were used to estimate the foreground polarization to the IC5146 cloud system. The horizontal dotted lines show the estimated foreground polarization of 0%–0.3%.

186,319 stars from the 2MASS catalog and 46,100 stars from the *WISE* catalog that cover the IC5146 cloud system. To estimate the stellar intrinsic colors, a square control field, centered at R.A. = $330^\circ.153$, decl. = $+47^\circ.794$ with a side length of $15'$, was compared to the target field.

To examine the quality of the estimated extinctions, the NICER extinction map shown in Figure 5 was created and compared with the *Herschel* map. The extinction map was created from the variance-weighted mean of NICER extinction of each individual star within a pixel grid with a pixel size of $30''$. The pixel grid was smoothed using a Gaussian weighting kernel with an FWHM of $90''$. The black contours in Figure 5

show the *Herschel* $250\ \mu\text{m}$ data. The morphology of the extinction map is almost identical to that of the $250\ \mu\text{m}$ map.

Figure 6 shows the histogram of A_V values derived from the NICER analysis. The uncertainties in A_V arise both from the uncertainties of the spectral types and from the propagated photometric uncertainties. In order to estimate the overall uncertainty of A_V , we selected all the stars that NICER assigned with negative A_V , and assumed that the negative A_V values were only due to A_V uncertainties. This negative A_V portion of the full distribution was duplicated and reflected about $A_V = 0$ to generate a new pseudo- A_V distribution. Fitting this with a Gaussian centered at $A_V = 0$, we derived a standard deviation

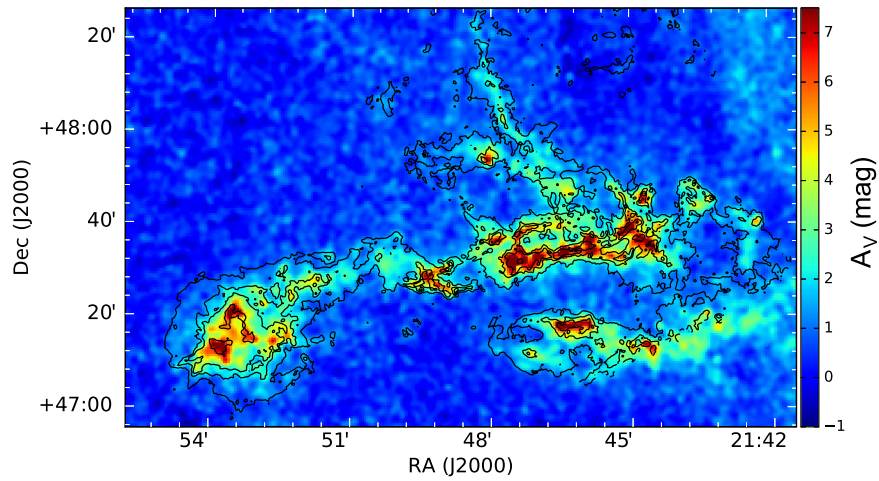


Figure 5. NICER extinction map across the IC5146 dark cloud. Visual extinction, in magnitudes of A_V , is displayed in color, and the black contour lines represent *Herschel* 250 μm intensities with levels of 0.1, 0.5, and 1.5 mJy/beam. The FWHM of the Gaussian smoothing kernel used to create the extinction map was $90''$, and the FWHM beam size of *Herschel* 250 μm image is $18''$. The extinction morphology and 250 μm intensity distribution are in close agreement.

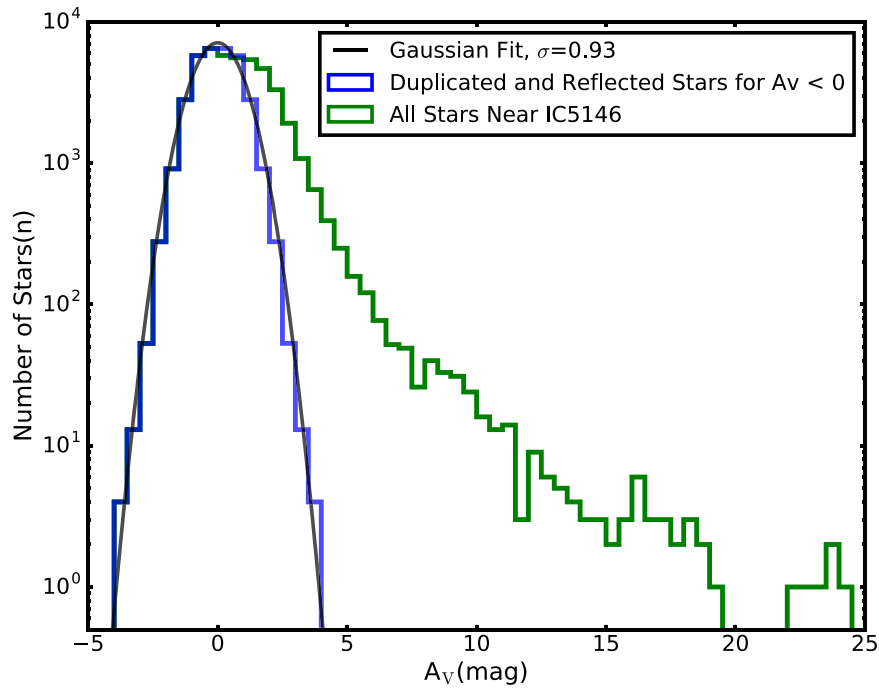


Figure 6. Histogram of A_V for the stars near IC5146 from the NICER analysis. In order to estimate the A_V uncertainty, the negative portion of the A_V distribution was duplicated and reflected about $A_V = 0$ to generate the pseudo-distribution shown in green. The best-fitting Gaussian, plotted in black, indicates a 1σ uncertainty of 0.93 mag.

of 0.93 mag. Because this includes uncertainties from both spectral typing and observations, we adopted this value as our A_V uncertainty.

4.2. Polarization Efficiency

To test whether the polarization measurements trace the magnetic field structure inside the IC5146 cloud system, we examined whether embedded dust grains align with the B fields via estimating how the degree of polarization varied with extinction. PE is defined as polarization percentage divided by A_V . It describes how much polarization is contributed by dust grains in the line of sight. We used PE versus A_V to test whether the dust grains are better aligned in the diffuse region, as predicted by the RATs model.

Figure 7 shows PE versus A_V for the R_c -band data. The data probability density over the PE- A_V space, represented by the contours, was calculated using the kernel density estimation (Rosenblatt 1956; Parzen 1962); for each source, the probability distribution function was described by a Gaussian kernel, and the width of the Gaussian kernel was determined by the uncertainties of PE and A_V . The probability density for the entire data set was represented by the summation of the Gaussian kernels.

To reduce the uncertainty from A_V and also avoid the bias due to uneven sampling over A_V , the variance-weighted means of PE and A_V were calculated in bins of width $\log(A_V) = 0.1$. The uncertainties of the weighted mean of PE and A_V for each bin were propagated from the instrumental uncertainty and A_V uncertainty for each sample. Stars that

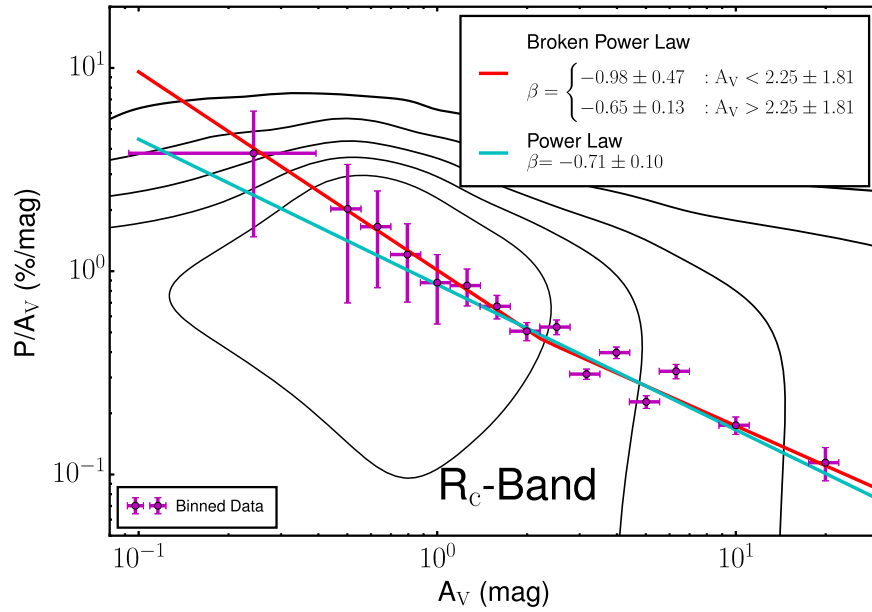


Figure 7. Polarization efficiency (PE) vs. A_V for R_c -band data. Black contours are drawn at 1%, 10%, 30%, 50%, and 70% of the peak data density. The purple points show the weighted mean PE in bins of width $\log(A_V) = 0.1$. The uncertainties of PE for each bin are propagated from instrumental uncertainties, and the uncertainties of A_V are propagated from 0.93 mag for each source. Bins with $A_V < 0.5$ mag were merged to further reduce the uncertainties. The red and cyan lines plots the best-fit single power-law and broken power-law models to the binned data, respectively.

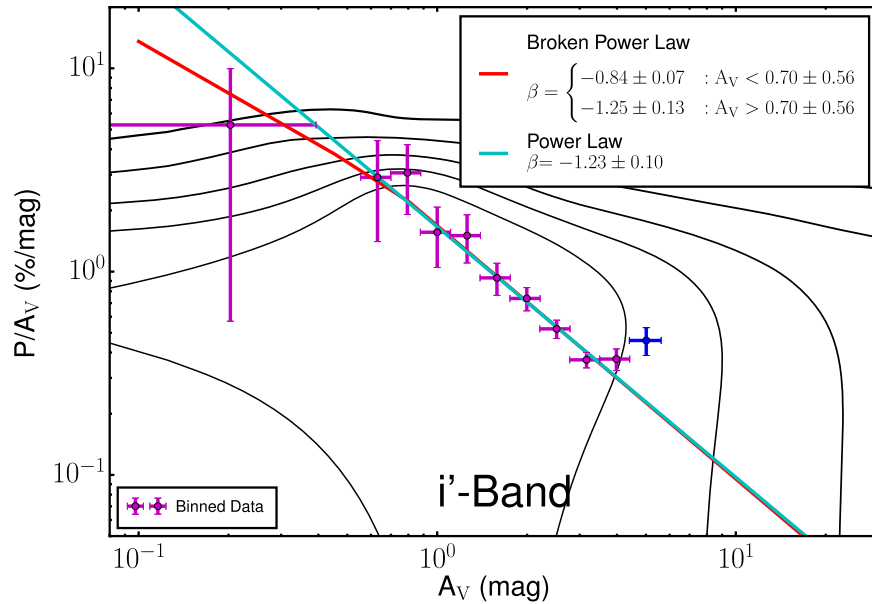


Figure 8. Same as Figure 7, but for i' -band data. The bin with the highest A_V , plotted in blue, contains only two stars that seem to have uncommonly high PE, and thus the bin was excluded from fitting.

NICER assigned with negative A_V were not used for PE determination, since their extinctions were negligible.

Similarly, PE versus A_V plots for the i' , H , and K bands are shown in Figures 8, 9, and 10, respectively. In the i' band, the last bin ($A_V = 5$ mag) was found to have significantly higher PE and the bin only contained two stars. This bin was judged to be an outlier, and was excluded from further analysis. In the four bands, PE always decreased with A_V , but with different slopes. In addition, the PE at $A_V \sim 20$ mag is still half of the PE at $A_V \sim 4$ mag, suggesting that the dust grains in high- A_V regions are still being aligned with some degree of efficiency.

The power-law behavior of PE- A_V has been shown in previous studies (e.g., Whittet et al. 2008; Chapman et al. 2011; Cashman & Clemens 2014) and appears to match the prediction of the RATs theory well. However, recent studies have also discovered changes in the index of the power law for high-extinction regions (Alves et al. 2014; Andersson et al. 2015). To test whether in the IC5146 dark cloud system the power-law index changes with A_V , we fit P_λ/A_V versus A_V with both a single power law (hereafter, Model 1),

$$P_\lambda/A_V = \alpha A_V^\beta, \quad (2)$$

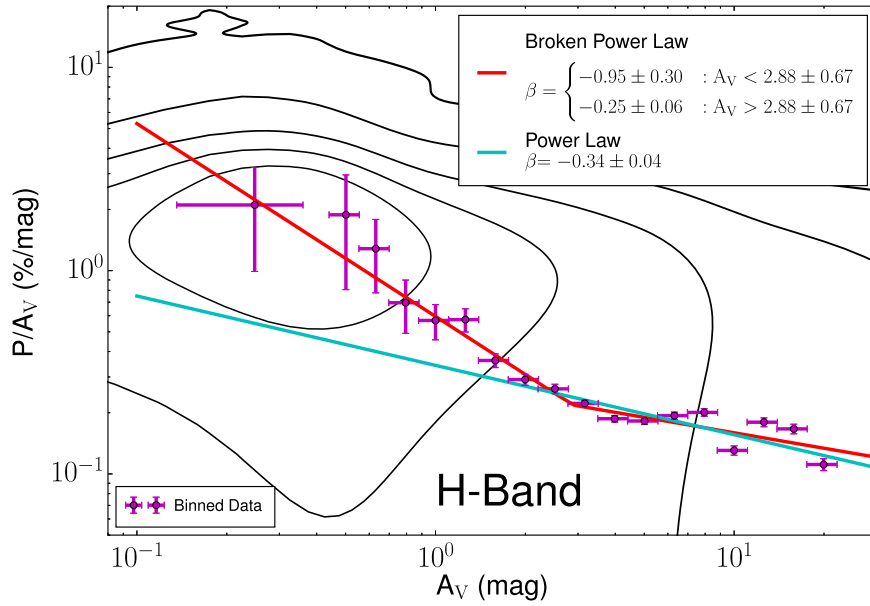


Figure 9. Same as Figure 7, but for H -band data.

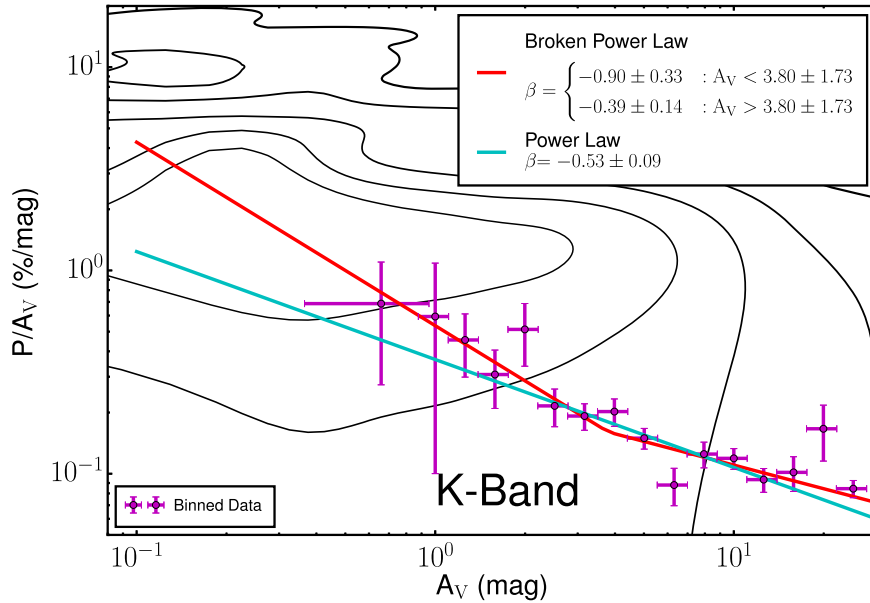


Figure 10. Same as Figure 7, but for K -band data. Bins with $A_V < 1.0$ mag were merged to further reduce the uncertainties.

and with a broken power law (hereafter, Model 2),

$$P_\lambda/A_V = \begin{cases} \alpha_1 A_V^{\beta_1} & : A_V \leq BP \\ \alpha_2 A_V^{\beta_2} & : A_V > BP \end{cases} \quad (3)$$

where $\alpha_2 = \alpha_1 BP^{\beta_1 - \beta_2}$. The four parameters α_1 , β_1 , and β_2 , and BP were all taken as free parameters in the fit to Model 2.

The goodness-of-fit on the binned data to the two models was examined using the F-test and the bias-corrected Akaike information criterion (AICc, Akaike 1974; Sugiura 1978). The two different model comparison methods may exhibit different preferences. For example, Ludden et al. (1994) used Monte Carlo simulations to examine the performance of these methods, finding that the F-test tends to choose the simpler model more often than does the AICc, even when the more complex model is correct. To avoid possible bias, we used both

methods to compare the model fits, and the preferred model was chosen to be the one for which (1) the F-test probability was below 0.05 (95% confidence level) and (2) had the lower AICc value. The results of the fitting and model comparisons are listed in Table 2. Both the F-test and AICc show consistent results; the broken power law is the better model for H bands, and the single power law is the better model for the R_c , i' , and K bands.

The $PE-A_V$ relations were empirically found to be insensitive to observing wavelengths (e.g., Andersson et al. 2015, and references therein), although our observed $PE-A_V$ relations might be expected to show some differences among the observing bands, since each data set covered different A_V and spatial ranges. The R_c - and i' -band data mostly probed the regions with $A_V \lesssim 4$ mag, and thus the derived PE indices mainly characterize the low- A_V regions. The power index of -0.71 ± 0.10 for the R_c band is very different from the index

Table 2
Fitting Results for PE vs. A_V

Band	F -value (model 1 \rightarrow model 2)	p -value	AICc (model 1)	AICc (model 2)	Preferred Model
R_c	0.30	0.75	22.30	30.00	$PE = (0.86 \pm 0.12)A_V^{(-0.71 \pm 0.10)}$
i'	0.40	0.68	-5.64	5.74	$PE = (1.66 \pm 0.17)A_V^{(-1.23 \pm 0.10)}$
H	3.95	0.04	40.68	39.92	$PE = \begin{cases} (0.60 \pm 0.13)A_V^{(-0.95 \pm 0.30)} & : A_V < 2.88 \pm 0.67 \\ (0.29 \pm 0.07)A_V^{(-0.25 \pm 0.06)} & : A_V > 2.88 \pm 0.67 \end{cases}$
K	1.13	0.36	8.90	14.57	$PE = (0.36 \pm 0.06)A_V^{(-0.53 \pm 0.09)}$

Note. The preferred model is determined by (1) a p value from the F-test below 0.05 (95% confidence level) or (2) a lower AICc value.

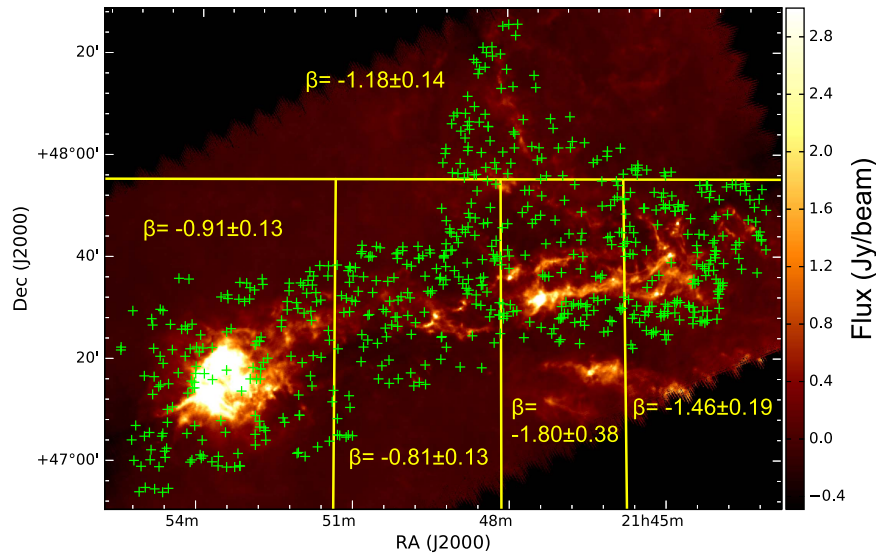


Figure 11. PE- A_V relations for the $A_V < 3$ mag stars in particular regions. The green crosses represent the stars with H -band polarization detections and $A_V < 3$ mag. These stars were separated into five zones, defined by the yellow lines, and the PE power-law β index was calculated for each zone by fitting a single power law. The β values vary with region from -0.81 ± 0.13 to -1.80 ± 0.38 .

for the i' band, namely -1.23 ± 0.10 . In addition, the power index of -0.95 ± 0.30 for the H band for low- A_V values is in between the indices for the R_c band and the i' band. For high- A_V regions, the index of -0.25 ± 0.06 for the H band is softer than the index for the K band (-0.53 ± 0.09), and both are flatter than all of the indices characterizing low- A_V regions. This finding may indicate that the physical properties of grains, as well as their alignment efficiencies, change significantly beyond $A_V \sim 3$ –4 mag (see Section 5.4).

The R_c , i' -, and H -band data all covered the $A_V \lesssim 4$ mag regime; however, the power-law indices for these three bands were all different. One major difference between the R_c -, i' -, and H -band data was that the H -band observations covered almost all of the IC5146 cloud system, while the R_c -band observations mostly covered the main filament, and the i' -band observations only probed the northwest filament (see Figure 1).

To test whether the indices characterizing low- A_V regions differ from region to region, the stars with H -band detections and $A_V < 3$ mag were assigned to one of the five zones delineated in Figure 11. Within each zone, single power-law indices were derived, and they are shown in Figure 11. Power-law indices ranging from -0.81 ± 0.13 to -1.80 ± 0.38 were fit to the assigned H -band data within the different zones. The indices were significantly softer in the eastern part of the cloud than in the western and northern part. In addition, the index

derived within the northern zone was -1.18 ± 0.14 , nearly identical to the index for the i' band, namely -1.23 ± 0.06 , covering a substantially similar region. Hence, the PE- A_V relation varies by region in the low-extinction regions. The different indices derived for the different wavelengths for the whole cloud could then merely arise from the combination of a variety of PE- A_V relations. The possible origin of the diverse PE relation is discussed further in Section 5.3.

4.3. Wavelength Dependence of Polarization using the Serkowski Relation

The polarization of starlight is known to be wavelength dependent, resulting in a polarization spectrum. Since this wavelength dependence originates from dust properties and alignment conditions, the polarization spectrum can be used to investigate the evolution of dust grains. The polarization spectrum is well-fit by the empirical ‘‘Serkowski relation,’’

$$P(\lambda) = P_{\max} \cdot \exp\{-K \cdot \ln^2(\lambda_{\max}/\lambda)\}, \quad (4)$$

where P_{\max} is the peak polarization degree at wavelength λ_{\max} (Serkowski 1973). In later studies, the parameter K was shown to follow the relation $K = -0.1 + c\lambda_{\max}$ (Wilking et al. 1982), where c was found to depend on dust properties, such as

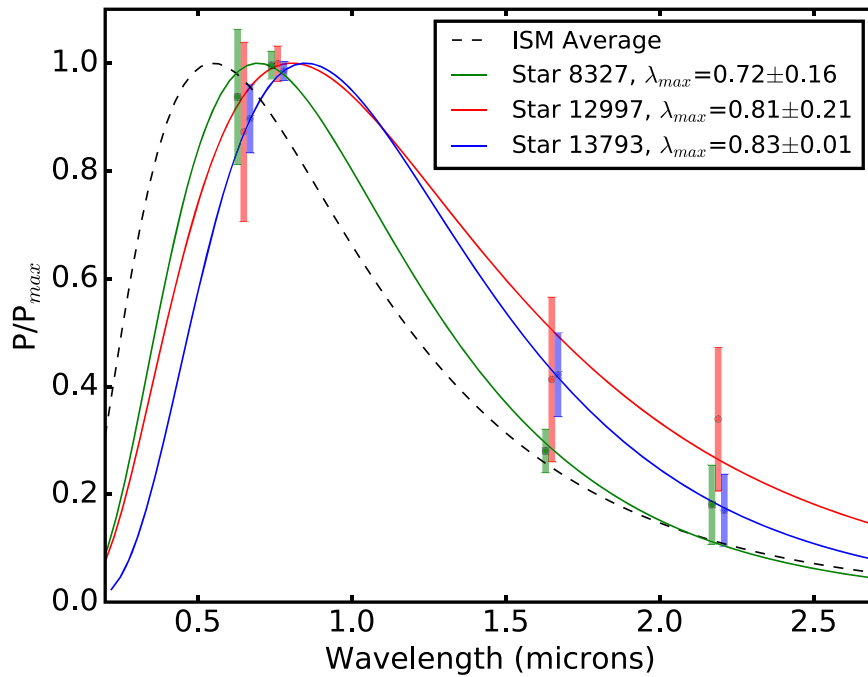


Figure 12. Polarization spectra for the three stars with polarization detections in four bands. Colored curves overplot the best-fit Serkowski relation. Wavelengths of the data points and error bars for stars 8327 and 13793 were slightly shifted to avoid overlapping. The black dashed spectrum represents the typical ISM average with λ_{\max} of $0.55 \mu\text{m}$. All three stars have higher λ_{\max} values than the ISM average.

geometric shape (e.g., Voshchinnikov et al. 2013; Voshchinnikov & Hirashita 2014).

To fit the Serkowski relation for its three parameters, detections in at least four bands are required to obtain uncertainties in the parameters. However, it is difficult to do so in the presence of high extinction. Thus, most of the previous studies have been limited to low-extinction regions. Even in our data, only three stars were detected in all four wavebands. The Serkowski relation fit results for these stars are shown in Figure 12. The range of fitted λ_{\max} is $\sim 0.72\text{--}0.83 \mu\text{m}$, significantly greater than the typical value $\sim 0.55 \mu\text{m}$ characterizing the general diffuse interstellar medium (Serkowski et al. 1975).

4.4. “Polarization Color” as a Constraint on λ_{\max}

It is difficult to obtain the necessary multiple wavelength polarization detections needed to fit Serkowski relations in the presence of strong extinction. In order to have more samples to constrain λ_{\max} , we examined the “polarization color” (the ratio of polarization degrees at two bands) as a partial descriptor of the polarization spectrum. Polarization color can be easily obtained from a limited set of wavebands without presumption of the spectrum shape. The Serkowski relation has been suggested to be only valid for a limited wavelength range, mostly UV through optical. Martin (1989) found that the polarization spectrum between 1.6 and $5 \mu\text{m}$ wavelength behaved more like a power law than like the Serkowski relation, and Clayton et al. (1992) found that the polarization spectrum in the ultraviolet showed an excess with respect to the Serkowski relation.

In the wavelengths where the Serkowski relation is valid, polarization color can constrain λ_{\max} . Following the Serkowski relation, the ratio of the polarization degree of a star at two

wavelengths can be written as

$$\frac{P(\lambda_1)}{P(\lambda_2)} = \frac{\exp\{-K \cdot (\ln^2(\lambda_{\max}/\lambda_1))\}}{\exp\{-K \cdot (\ln^2(\lambda_{\max}/\lambda_2))\}}. \quad (5)$$

To reduce the free parameters, we also assumed the relation $K = -0.1 + c\lambda_{\max}$, where c is expected to be a constant over A_V . Via Equation (5) and the assumptions regarding K , the polarization color (ratio) is determined by only one free parameter, λ_{\max} . Thus, only one polarization color is required to constrain λ_{\max} , although for wavebands right near λ_{\max} , the uncertainties will be large. Clemens et al. (2016) used this approach with Mimir H - and K -band data to identify grain growth in the moderate- to high-extinction regions of L1544, finding λ_{\max} in the $1.0\text{--}1.2 \mu\text{m}$ range.

The polarization color P_{R_c}/P_H versus A_V values shown in Figure 13 reveal how the polarization spectrum varies with A_V . The observed P_{R_c}/P_H distribution seems diverse and can hardly be described with a simple function. To try to find some order, we separated the stars into four A_V groups by eye, based on the similarities in the distribution. They span A_V ranges of <1 , $1.0\text{--}2.5$, $2.5\text{--}4.0$, and >4.0 mag, labeled as regions A, B, C, and D, respectively. The blue horizontal lines show the unweighted average \pm standard deviation (STD) of P_{R_c}/P_H for each group. The intrinsic dispersions of P_{R_c}/P_H were derived using $\sigma_{\text{intrinsic}} = \sqrt{\text{STD}^2 - \sigma_{\text{obs}}^2}$, where σ_{obs} was the average observational uncertainty. The statistical properties of P_{R_c}/P_H for each group are presented in Table 3.

Group A had significantly lower mean P_{R_c}/P_H than the other regions. Since the A_V of this region was comparable to the expected foreground extinction <0.3 mag (Lada et al. 1994), the depolarization due to any foreground medium might significantly affect the polarization spectrum. Thus, the polarization color in this group might not accurately trace the dust properties. The average P_{R_c}/P_H values for groups B, C,

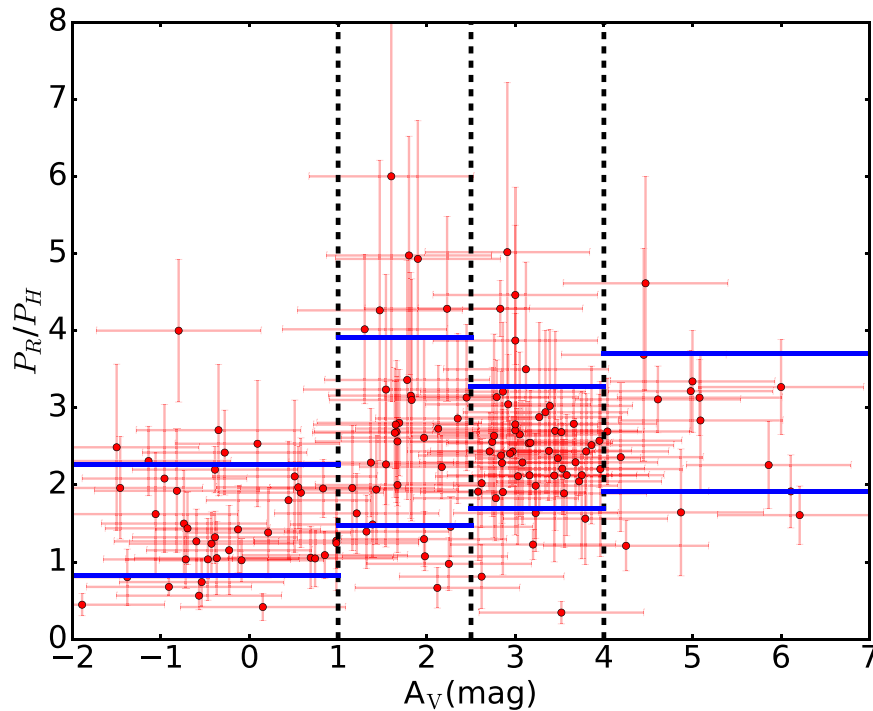


Figure 13. P_{R_c}/P_H vs. A_V from the stars with R_c - and H -band polarization detections. These stars were separated into four groups, based on their A_V values as defined by the black dashed lines. The blue horizontal lines show the $\pm 1\sigma$ excursions above and below the average of P_{R_c}/P_H for each group. The distribution of P_{R_c}/P_H is narrowest when $A_V = 2.5$ – 4 mag. The stars with negative A_V values have negligible extinction: these values result from uncertainties in the NICER extinction estimation.

Table 3
Variation of P_{R_c}/P_H with A_V

Group	A_V Range (mag)	P_{R_c}/P_H			σ_{obs}	Intrinsic Dispersion ^b	$\langle \lambda_{\text{max}} \rangle^a$ (μm)
		Mean	STD				
A	–2.0–1.0	1.54 ± 0.09	0.72 ± 0.11		0.53	0.54 ± 0.15	0.92 ± 0.02
B	1.0–2.5	2.69 ± 0.20	1.22 ± 0.30		0.97	0.73 ± 0.50	0.75 ± 0.03
C	2.5–4.0	2.48 ± 0.12	0.79 ± 0.17		0.80	...	0.78 ± 0.02
D	>4.0	2.81 ± 0.22	0.90 ± 0.29		0.78	0.44 ± 0.59	0.73 ± 0.03

Notes.

^a The λ_{max} calculated from the mean P_{R_c}/P_H . Uncertainties were calculated from the means and the propagated uncertainties of the means, assuming $c = 2.3$.

^b The intrinsic dispersions and the uncertainties of the dispersions. The intrinsic dispersion cannot be defined if the observed dispersion is lower than the instrumental uncertainty.

and D were similar to each other, although significant intrinsic dispersion was found for group B.

The value of P_{R_c}/P_H directly determines the value of λ_{max} if the parameter c in Equation (5) is known. The variance-weighted mean c of 2.3 was derived from the four-band fitting to the three stars shown in Figure 12. This c value was higher than the value of 1.66 found in Wilking et al. (1982) and the value of 1.86 found in Whittet et al. (1992). Figure 14 shows how P_{R_c}/P_H maps to λ_{max} for different value of c . The black horizontal dashed lines delimit the span of the distribution of P_{R_c}/P_H values found in Figure 13. The curves in Figure 14 characterized by $c \leq 2.1$ cannot cover the full range of the distribution of observed P_{R_c}/P_H values, suggesting that the parameter c value in the IC5146 cloud system is likely higher than it is in other clouds. Hence, we assumed $c = 2.3$ to estimate the λ_{max} from observed P_{R_c}/P_H .

The range of λ_{max} versus A_V , for $c = 2.3$, is shown in Figure 15. The mean λ_{max} for the mean P_{R_c}/P_H in each of the

four A_V groups is listed in Table 3. For each P_{R_c}/P_H , two possible λ_{max} solutions from the Serkowski relation are possible, as can be seen in Figure 14. These two solution regions were colored in gray for the lower λ_{max} values and in red for the greater λ_{max} values. If we assume that λ_{max} across the cloud system does not dramatically change within a few magnitudes of extinction, then only one set of solutions is likely to be true. Since the values of λ_{max} derived from the four-band fitting to the three stars shown in Figure 12 were all in the range of 0.72 – $0.83 \mu\text{m}$, $\lambda_{\text{max}} > 0.4 \mu\text{m}$ selects the better solutions.

Hence, the average P_{R_c}/P_H values correspond to λ_{max} of 0.75 , 0.78 , and $0.73 \mu\text{m}$ for groups B, C, and D, respectively. These λ_{max} are all greater than the average value for the ISM of $0.55 \mu\text{m}$ (Serkowski et al. 1975), suggesting that the dust grains across most of the IC5146 cloud system have grown significantly with respect to dust grains in the diffuse ISM. In addition, the large dispersion of λ_{max} in group B implies that

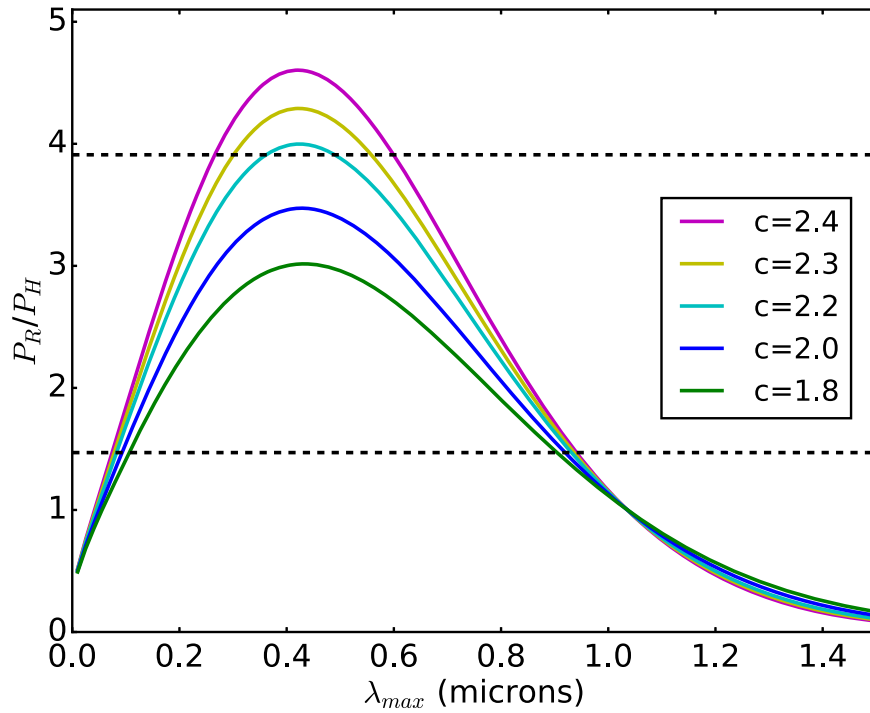


Figure 14. Relations between P_{R_c}/P_H and λ_{max} predicted by the Serkowski relation assuming $K = c\lambda_{max}$. The horizontal dashed lines represent the range of observed P_{R_c}/P_H , seen as the range spanned by the blue horizontal lines shown in Figure 13. Only the relation characterized by $c \geq 2.2$ can cover the range of observed P_{R_c}/P_H . The yellow curve shows the relation for $c = 2.3$, which was used to convert P_{R_c}/P_H into λ_{max} .

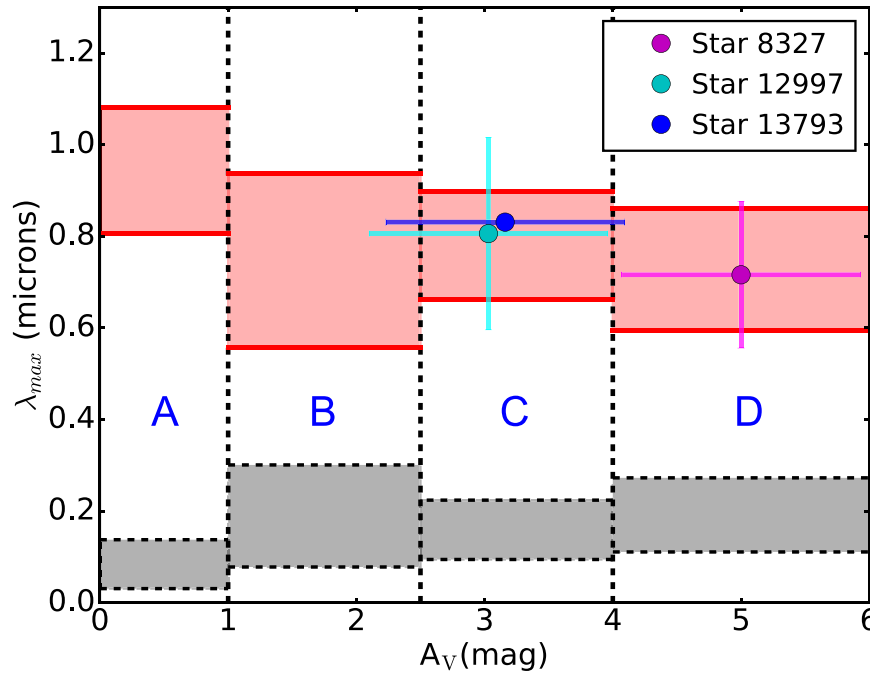


Figure 15. Ranges of λ_{max} with A_V group. The colored regions represent the ranges of the distributions of λ_{max} values in each A_V group, estimated from the observed P_{R_c}/P_H values, the Serkowski relation, and the $c = 2.3$ curve from Figure 14. The red and gray sets of zones identify the two degenerate sets of solutions to the Serkowski relation. The three stars whose four-band polarimetry data were fitted to the Serkowski relation (see Figure 12) are plotted as filled colored circles with error bars and are consistent with the set of red zone solutions corresponding to greater values of λ_{max} .

the dust grain size distributions are more diverse in this A_V range than in the other extinction regions.

Similarly, we plot P_H/P_K versus A_V in Figure 16 to trace the variation in polarization spectrum in the infrared. The data were separated into five groups, in a fashion similar to Figure 13 ($A_V < 1$, 1.0–2.5, 2.5–4.0, 4.0–10.0, and >10.0 mag, labeled

as A, B, C, D, and E, respectively). The statistical properties of P_H/P_K for these groups are listed in Table 4. The average P_H/P_K changes significantly with A_V , with the greatest value found in group B.

The values of λ_{max} converted from P_H/P_K were listed in Table 4. The range of λ_{max} derived from the group averaged

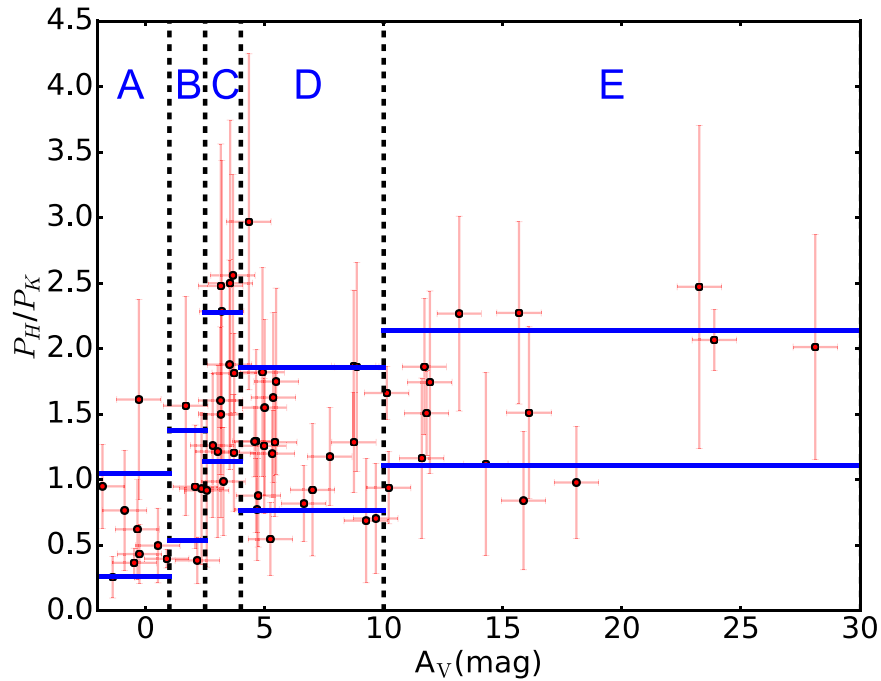


Figure 16. Same as Figure 13, but for P_H/P_K vs. A_V . The dispersions of P_H/P_K are almost the same over the different A_V groups, while the P_H/P_K means appear to change with A_V .

Table 4
Variation of P_H/P_K with A_V

Group	A_V Range (mag)	P_H/P_K			Intrinsic Dispersion ^b	$\langle \lambda_{\max} \rangle^a$ (μm)	Power-law Index
		Mean	STD	σ_{obs}			
A	−2.0–1.0	0.66 ± 0.12	0.39 ± 0.21	0.31	0.27 ± 0.30	$2.20^{+0.13}_{-0.12}$	-1.38 ± 0.60
B	1.0–2.5	0.96 ± 0.20	0.42 ± 0.31	0.52	...	$1.93^{+0.17}_{-0.15}$	-0.14 ± 0.69
C	2.5–4.0	1.71 ± 0.21	0.57 ± 0.24	0.72	...	$1.40^{+0.14}_{-0.13}$	1.78 ± 0.41
D	4.0–10.0	1.31 ± 0.13	0.54 ± 0.20	0.54	...	$1.67^{+0.09}_{-0.08}$	0.90 ± 0.33
E	>10.0	1.63 ± 0.16	0.51 ± 0.19	0.58	...	$1.46^{+0.11}_{-0.11}$	1.62 ± 0.33

Notes.

^a The λ_{\max} calculated from the mean P_{R_c}/P_H . Uncertainties were calculated from the means and the propagated uncertainties of the means, assuming $c = 2.3$.

^b The intrinsic dispersions and the uncertainties of the dispersions. The intrinsic dispersion cannot be defined if the observed dispersion is lower than instrumental uncertainty.

P_H/P_K was 1.46–1.93 μm , significantly higher than the 0.73–0.78 μm range derived from P_{R_c}/P_H . The inconsistency implies that the Serkowski relation may not describe the polarization spectrum at near-infrared wavelengths well. Martin (1989) suggested that the near-infrared polarization spectrum can be better described by a power law

$$P(\lambda) \propto \lambda^{-\beta}, \quad (6)$$

where $\beta \simeq 1.6$ –2.0. In the infrared, polarization color can still constrain the power-law index by

$$\frac{P_H}{P_K} = 0.74^{-\beta}. \quad (7)$$

The β derived from our data are listed in Table 4. These indices probably vary with A_V and have a peak at $A_V \approx 2.5$ –4 mag, as shown by Figure 16. Kim & Martin (1995) showed that the index could depend on the amount of micron-sized dust grains. Our results indicate that the

population of micron-sized dust grains might evolve with A_V , and a significant change occurs at A_V of 2.5–4 mag.

5. Discussion

5.1. Evolution of Dust Grains

The derived λ_{\max} values obtained in previous studies (e.g., Whittet & van Breda 1978; Wilking et al. 1982) are expected to be related to the small-size cutoff of the grain size distribution. Whittet & van Breda (1978) found that λ_{\max} is related to the ratio of total to selective extinction ($R_V = A_V/(E_{B-V})$) by an empirical relation $R_V = (5.6 \pm 0.3)\lambda_{\max}$, tracing the reddening changes with grain size distribution changes. However, with more observations, Andersson & Potter (2007) found no correlation between λ_{\max} and R_V for individual clouds; the empirical relation could only be recovered by combining the data for all of their observed clouds. They further argued that λ_{\max} may depend on both grain size distributions and dust alignment conditions.

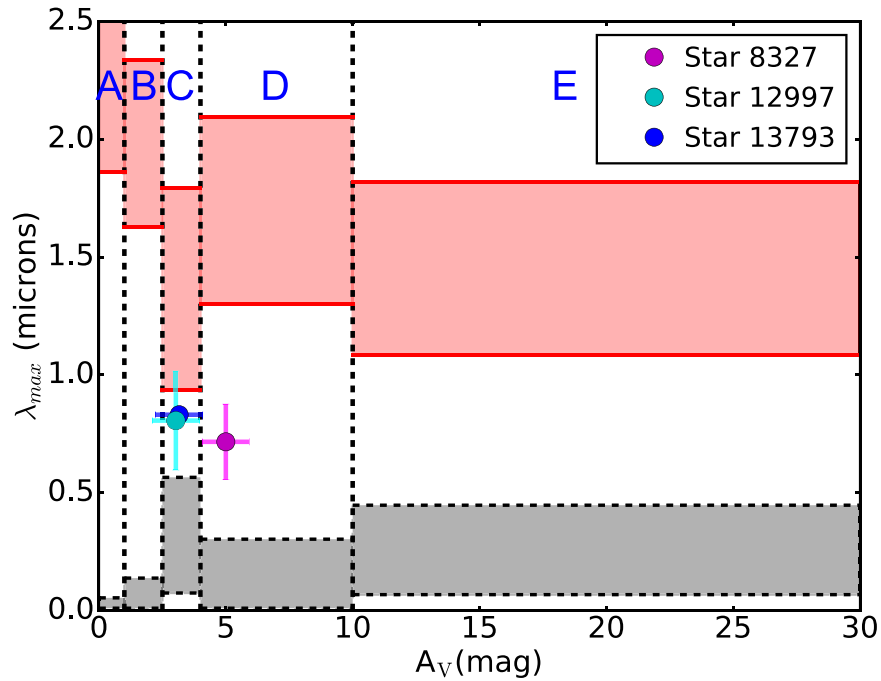


Figure 17. (a) Same as Figure 15, but the λ_{\max} range was estimated from P_H/P_K using the Serkowski relation with $c = 2.3$. The λ_{\max} values derived from P_H/P_K are much greater than the λ_{\max} values derived from P_{R_c}/P_H shown in Figure 15. In addition, the distribution of λ_{\max} is inconsistent with the best-fit Serkowski relations to the three stars with four-band polarimetry data shown in Figure 12, suggesting that the Serkowski relation may not be valid, at least in the K band.

Whittet et al. (2008) showed in their RATs simulations with constant grain size distribution that λ_{\max} increases with A_V because small dust grains become less well aligned as a result of the decaying and reddening of the external radiation field by extinction. Their model predicts a smooth increase of λ_{\max} from 0.45 to 0.75 μm as A_V increases from 0 to 6 mag. However, our derived λ_{\max} values, 0.73–0.78 μm , do not significantly change with A_V . In addition, our data show a significant decrease of the intrinsic dispersion of λ_{\max} from 0.11 ± 0.08 ($A_V = 1.0\text{--}2.5$ mag) to <0.07 ($A_V = 2.5\text{--}4.0$ mag), possibly due to changes of the grain size distribution.

The change in the dispersion of λ_{\max} implies that the grain size distribution in the dense regions could be more uniform than in the diffuse regions. We speculate that the difference is due to the evolution of the dust grain size. In grain-grain collision models (Jones et al. 1996; Hirashita & Yan 2009; Ormel et al. 2009), the grain size distributions are expected to be modified by the competing effects of fragmentation and coagulation. Steady-state grain size distributions are eventually reached when these two effects achieve equilibrium. As a result, the apparent uniform grain size distribution in the dense regions may indicate the existence of stabilized grain-grain collision processes. Together with the increase of λ_{\max} , this non-evolution of grains in the dense regions favors the notion that grain growth has already taken place before A_V reaches 2.5–4.0 mag.

In Figure 17 we show that the λ_{\max} derived from a Serkowski relation based on an analysis of P_H/P_K yielded an average λ_{\max} of 1.46–1.93 μm . This was inconsistent with λ_{\max} derived from P_{R_c}/P_H , which yielded an average λ_{\max} of 0.73–0.78 μm . To reach a λ_{\max} of 0.73–0.78 μm , P_H/P_K would need to be >2.3 , which is much higher than the observed range of mean values from 0.96 ± 0.28 to 1.71 ± 0.21 . This indicates that at least the measured K -band infrared polarization exceeds the predictions of the Serkowski relation. This excess

infrared polarization was also found in early studies (e.g., Jones 1990; Martin & Whittet 1990; Nagata 1990) and is better fit by a power law (Equation (7)). We found that a power law with β ranging from -0.14 ± 0.69 to 1.78 ± 0.41 can explain our data for different A_V . The β index appears to vary with A_V and has its highest value for $A_V = 2.5\text{--}4.0$ mag. Our β are similar to, or smaller than, the value of 1.6 ± 0.2 measured toward ScO-Oph and CyG OB2 (Martin et al. 1992), and 1.76 ± 0.25 measured toward the Galactic center (Hatano et al. 2013).

Two models have tried to explain the physical origin of the excess infrared polarization over the Serkowski relation. Kim & Martin (1995) showed that a model with a dust grain mixture with sizes of 0.3 μm and 0.6–1 μm can reproduce the observational Serkowski relation while also exhibiting a power-law excess infrared polarization. Li & Greenberg (1997) showed that an organic refractory-mantled dust grain model with a Gaussian grain size distribution could reproduce the observed excess infrared polarization without requiring a high abundance of micron-sized dust grains. Our results show that the observed power-law index might vary with A_V , providing new constraints for future models.

5.2. How Deep Into a Cloud Can Polarization Be Used to Reveal B fields?

PE has been used to indicate how deep into a cloud, in A_V , the dust grains remain aligned. Goodman et al. (1995) found a PE- A_V power-law index of -1 in L1755 in the JHK bands. This constancy of P with A_V was used to argue that near-infrared polarization does not trace the B field within dense clouds. In contrast, Whittet et al. (2008) found an index of -0.52 in Taurus at the K band, showing that polarization can trace the B field, at least up to $A_V \sim 10$ mag.

The power-law PE versus A_V indices characterizing these two cases can be found in our data, but for different A_V ranges. The power index of -0.95 ± 0.30 measured for the H band in

low- A_V regions is similar to the results found in L1755 at the R band (Goodman et al. 1995) for $A_V < 8$ –10 mag. Our index of -0.53 ± 0.09 for the K band is close to the value found in Taurus at the K band (-0.52 ± 0.07) by Whittet et al. (2008) and the value found in numerous starless cores at the K band (~ -0.5) for $A_V < 20$ mag by Jones et al. (2015). In addition, the intermediate index -0.71 ± 0.10 found in the R_c band is similar to the results found in Pipe-109 using the R band (-0.76 ± 0.14 , Alves et al. 2014) and in L204 using the H band (-0.74 ± 0.07 , Cashman & Clemens 2014). We found our steepest index, of -1.23 ± 0.10 , in the i' band and our softest index, of -0.25 ± 0.06 , in the H band in high- A_V regions.

The softer indices of -0.25 to -0.53 are only found in high- A_V regions in the H and K bands, while a variety of steeper indices are found in low- A_V regions. The ~ -0.5 indices match predictions of RATs models with constant grain size distributions (Whittet et al. 2008). The same models predicts a steepening of PE as A_V approaches 10 mag, caused by the strong extinction of external radiation. Here, however, the indices we measure for high- A_V regions show that the dust with A_V up to ~ 20 mag still contributes to the measured polarization: the PE at $A_V = 20$ mag is only a factor of ~ 2 lower than that at $A_V = 4$ mag. Thus, the notion that only the dust on the surfaces of clouds is aligned, as concluded by Goodman et al. (1995), is not supported here.

5.3. The Diverse PE in Low- A_V Regions

It is interesting that a variety of PE versus A_V power-law behaviors are seen across the IC5146 cloud system. We showed that the indices derived using the H band varied with region location in Figure 11. The diverse PE- A_V relations likely depend more on A_V and region choice and less on wavelength, as the indices derived from i' and H bands in the same region are almost the same. If all the stellar values from all of the low- A_V regions are combined into a single plot and fitted, the location dependence of the PE- A_V relation would be mixed and thereby lost. The index of -0.95 derived from the H band using all data with low- A_V is merely the average from the mixed PE- A_V relation shown in Figure 11. This is different from the suggestion by Goodman et al. (1995) that a power-law index of ~ -1 indicates that starlight polarization only traces the dust grains on the surfaces of clouds.

Three possibilities could explain the origin of the wide variation of the PE- A_V relation.

(i) The grain size distributions could be diverse and vary greatly from region to region for low A_V . In Section 4.3 we showed that the dispersion of λ_{\max} , estimated from P_R/P_H , is significantly larger for $A_V < 2.5$ mag, suggesting that grain size distributions are diverse. This diversity is likely region-dependent, since the different λ_{\max} values were derived from different sightlines. The grain size distribution is a key element of the RATs theory; radiation can efficiently align dust grains with sizes comparable to its wavelength, and wavelength determines radiation penetration ability.

(ii) Depolarization effects may occur if multiple polarizing layers exist. In Figure 11 we showed that the PE versus A_V indices derived in the western part of the IC5146 cloud were steeper than -1 , hence the polarization percentage must decrease with A_V . This may be a result of depolarization. If a multiple layer structure, in which the layers have different B-field orientations, exists along a line of sight, the net transferred polarization from the different layers would be

reduced. Arzoumanian et al. (2011) found rich and hierarchical filamentary structure in the IC5146 cloud system. These filaments can naturally produce a multiple layer structure if the projections of such structures overlap along the line of sight. In addition, they further found that most of the filaments in the western part of the IC5146 cloud system were supercritical, which might twist to cause complex B fields. This could explain the steeper indices found in the western part of the cloud.

(iii) The degree of dust alignment may be affected by one or more bright illuminators, such as the stars in the Cocoon Nebula. Cashman & Clemens (2014) found a possible dependence of PE- A_V index for regions in the L204 cloud 3 with distance from a nearby illuminator. Brighter stellar radiation can boost alignment of the dust, and the alignment efficiency will mainly depend on the optical depth to the illuminator. In IC5146, the Cocoon Nebula stellar cluster could be a strong illuminator that is able to affect grain alignment. However, the radiation from the Cocoon Nebula is also highly shadowed by the main filament structure, making the optical depth from the Cocoon Nebula to the other regions difficult to estimate.

5.4. The Breakpoint in PE- A_V Relations

In Section 4.2 we showed that PE decays with A_V and a breakpoint (BP) of $A_V = 2.88 \pm 0.67$ mag separates two different power-law slopes of A_V in the H band. Breakpoints of PE near $A_V \sim 2$ –3 mag are rarely seen. Pipe-109 shows a breakpoint at 9.5 mag with power index changing from -1.00 to -0.34 (Alves et al. 2014). LDN 183 shows a breakpoint at $A_V \sim 20$ mag with power index changing from -0.6 to -1 (Crutcher 2004; Clemens 2012; Andersson et al. 2015). Jones et al. (2015) also found a break point at $A_V \sim 20$ mag with power index changing from -0.5 to -1 toward several starless cores. Jones et al. (2016) found an break point at very high A_V , \sim hundreds mag in the Class 0 YSO G034.43+00.24 MM1 with a change of power index from -1 to -0.5 .

Three mechanisms could change the power-law indices with A_V , although in opposite directions. Radiation into the deepest regions could be too faint to align the dust grains, so the power-law index for high- A_V regions should steepen (Whittet et al. 2008). If grains grow at higher A_V , however, the alignment efficiency will be higher for dust with sizes comparable to the wavelength (Lazarian & Hoang 2007), hence the power-law index will become flatter in the dense regions where only radiation with longer wavelengths can penetrate and the dust grains are believed to grow. In addition to the change of dust properties, internal radiation fields from embedded sources within dense clouds could also enhance dust alignment and flatten the power-law index.

Andersson et al. (2015) suggested that the origin of the breakpoint found in LDN 183 is likely due to the extinction of external radiation because their power-law index in low- A_V regions, of -0.6 , is consistent with prediction of the RATs model assuming constant grain size (Whittet et al. 2008). Similar trends were also found within several starless cores by Jones et al. (2015), and they further showed that the RATs theory can explain the break point of ~ 20 mag, where the dust optical depth, for the wavelength comparable to the maximum grain size, becomes optically thick.

Our results showed an opposite trend as compared to the case of LDN183: steeper indices ranging from -0.71 to -1.23

were found in low- A_V regions, while flatter indices ranging from -0.25 to -0.53 , consistent with the Whittet et al. (2008) model, were found in high- A_V regions for all observed wavebands. The results from Alves et al. (2014) toward Pipe-109 and Jones et al. (2016) in G034.43+00.24 MM1 show similar trends as ours, but with different breakpoints. The flattened slopes in high- A_V regions more likely originate from efficient grain alignment due to either grain growth or internal radiation fields. Because Pipe-109 is a starless object but G034.43+00.24 MM1 is a Class 0 YSO, the change of slope for the former likely results mainly from grain growth, while internal radiation might play an important role in the latter. Since the breakpoint of $A_V \sim 2.8$ mag shown in our data is consistent with the A_V of the regions where the intrinsic dispersion of λ_{\max} drops significantly ($A_V = 2.5\text{--}4.0$ mag), our observed trend is more likely caused by grain growth.

An open question is why the breakpoint we measure is so different from the 9.5 mag value in Alves et al. (2014), although both breakpoints likely result from grain growth. The difference could originate from two possible reasons. First, Alves et al. (2014) lacked samples in low- A_V regions, and thus a broken power law with breakpoint at $A_V \sim 3$ mag would be difficult to identify. Second, the difference may come from different grain growth conditions. Ormel et al. (2009) simulated the evolution of dust grain size, based on grain-grain collisions. They found that dust grains with ice-coatings are more likely to aggregate and grow than are grains without ice-coatings, due to the increased surface stickiness. Chiar et al. (2011) found that H₂O-ice in IC5146 only exists in regions exhibiting extinctions exceeding $A_V \sim 4$ mag, a value quite similar to the breakpoint we found. Thus, H₂O-ice mantling could induce a breakpoint via enhanced grain growth. Similarly, Whittet et al. (2001) found that the observed R_V in Taurus changed from $R_V \sim 3$ to 4 around $A_V = 3.2$ mag, coincident with the extinction threshold for H₂O-ice mantling in Taurus, and suggested that mantle growth is an important process in initial grain growth. We conclude that such mantling also enables greater efficiency of dust grain alignment, permitting magnetic field to be traced deeper into clouds than if such mantling is not present.

6. Conclusions

We performed optical and infrared polarimetry observations toward background stars seen through the IC5146 dark cloud system using AIMPOL at the ARIES Observatory, TRIPOL at the Lulin Observatory, and Mimir at the Lowell Observatory Perkins Telescope. A total of 2022 stars showed significant polarization detection in at least one of the four wavebands observed. From the analysis of these data, we found the following results.

1. The polarization efficiency ($PE \equiv P_\lambda/A_V$) decreases with A_V as a power law or broken power law. The values of the power-law indices likely depend more on the choice of targeted regions and local extinction, and less on observing wavelength.
2. A cloud-averaged power-law index of -0.95 for PE versus A_V was found in the H band for low A_V , the same as the index found in L1755 by Goodman et al. (1995). However, we showed that the index of -0.95 resulted from the admixture of a variety of PE- A_V relations, whose local-regional indices varied from -0.8 to -1.8 , different from the suggestion by Goodman et al. (1995)

that the index of ~ -1 indicates that background starlight polarization only traces the dust grains on the surface of clouds.

3. A broken power law relation for PE versus A_V in the H band exhibits a breakpoint at about $A_V \sim 2\text{--}3$ mag. The power-law index in high- A_V regions is shallow and consistent with predictions from RATs models (Whittet et al. 2008), while the indices in low- A_V regions are steeper and vary with region. The shallow index in high- A_V regions is likely due to grain growth.
4. Excess infrared polarization, over that predicted by the Serkowski relation, was observed in P_H/P_K , possibly resulting from abundance enhancements of large micron-sized dust grains. The average P_H/P_K varies with A_V from 0.96 ± 0.20 to 1.71 ± 0.21 , and exhibits its highest value of 1.71 ± 0.21 for A_V in the $2.5\text{--}4.0$ mag range. This implies that the abundance of such micron-sized dust grains might change with A_V .
5. The polarization color (P_{R_c}/P_H) is a useful tool to constrain λ_{\max} , the peak of the Serkowski relation, which may trace the small-size cutoff of the grain size distribution. We found that both the average and dispersion of P_{R_c}/P_H decreased from the $1.0 < A_V < 2.5$ mag range to the $2.5 < A_V < 4.0$ mag range. These variations suggest that the small-size cutoffs of grain size distributions are most likely due to efficient grain-grain collisions, and thus indicate that grain growth could already take place by $A_V \sim 2.5\text{--}4.0$ mag, possibly enhanced at this relatively low- A_V range by the presence of ice mantles on the grains.

In conclusion, this study revealed that dust grains in the diffuse molecular regions ($A_V < 2.5$ mag) of the IC5146 dark cloud system have diverse size distributions. As A_V approaches ~ 3 mag, submicron dust grains grow significantly due to grain-grain collisions. The size distributions may also become more uniform as A_V increases as a balance is reached between fragmentation and coagulation. In addition, the larger micron-sized grains likely already exist in the diffuse regions, and their abundances and sizes likely change with A_V . In the next paper of this series, we will use these polarization data to characterize the magnetic field morphology and strength across this system of filamentary dark molecular clouds associated with IC5146.

We acknowledge support from the Aryabhata Research Institute of Observational Sciences and Lulin Observatory concerning the data collected using AIMPOL and TRIPOL. This research was conducted in part using the Mimir instrument, jointly developed at Boston University and Lowell Observatory and supported by NASA, NSF, and the W.M. Keck Foundation. This work and the analysis software for Mimir data were developed under NSF grants AST 06-07500, 09-07790, and 14-12269 to Boston University. We thank Brian Taylor, Tao-Chung Ching, and Lauren Cashman for their help in the smooth operations of Mimir observations. This research has made use of the Herchel Science Archive (HSA), and the data are based on the observations performed with the ESA *Herschel* Space Observatory (Pilbratt et al. 2010). J.W.W., S.P.L., and C.E. are grateful for the support from the Ministry of Science and Technology (MOST) of Taiwan through grants NSC 99-2923-M-008-002-MY3, NSC 101-2119-M-007-004, MOST 102-2119-M-007-004-MY3, 105-2119-M-007-022-MY3, and 105-2119-M-007-024.

Facilities: ARIES:ST, LO:1m, Perkins.

Software: IRAF, Source Extractor (Bertin & Arnouts 1996), Mimir Software Package (Clemens et al. 2012c), PNICER (Meingast et al. 2017), Astropy (Astropy Collaboration et al. 2013), NumPy (van der Walt et al. 2011), SciPy (Jones et al. 2001), APLpy (Robitaille & Bressert 2012).

ORCID iDs

Jia-Wei Wang  <https://orcid.org/0000-0002-6668-974X>
 Shih-Ping Lai  <https://orcid.org/0000-0001-5522-486X>
 Chakali Eswaraiah  <https://orcid.org/0000-0003-4761-6139>
 Dan P. Clemens  <https://orcid.org/0000-0002-9947-4956>
 Wen-Ping Chen  <https://orcid.org/0000-0003-0262-272X>

References

- Akaike, H. 1974, *ITAC*, **19**, 716
- Alves, F., Frau, P., Girart, J. M., et al. 2014, *A&A*, **569**, A1
- Andersson, B.-G., Lazarian, A., & Vaillancourt, J. E. 2015, *ARA&A*, **53**, 501
- Andersson, B.-G., & Potter, S. B. 2007, *ApJ*, **665**, 369
- Arzoumanian, D., André, P., Didelon, P., et al. 2011, *A&A*, **529**, L6
- Astropy Collaboration, Robitaille, T. P., Tollerud, E. J., et al. 2013, *A&A*, **558**, A33
- Bertin, E., & Arnouts, S. 1996, *A&AS*, **117**, 393
- Cashman, L. R., & Clemens, D. P. 2014, *ApJ*, **793**, 126
- Chapman, N. L., Goldsmith, P. F., Pineda, J. L., et al. 2011, *ApJ*, **741**, 21
- Chiar, J. E., Pendleton, Y. J., Allamandola, L. J., et al. 2011, *ApJ*, **731**, 9
- Cho, J., & Lazarian, A. 2005, *ApJ*, **631**, 361
- Clayton, G. C., Anderson, C. M., Magalhaes, A. M., et al. 1992, *ApJL*, **385**, L53
- Clemens, D. P. 2012, *ApJ*, **748**, 18
- Clemens, D. P., Pavel, M. D., & Cashman, L. R. 2012a, *ApJS*, **200**, 21
- Clemens, D. P., Pinnick, A. F., & Pavel, M. D. 2012b, *ApJS*, **200**, 20
- Clemens, D. P., Pinnick, A. F., Pavel, M. D., & Taylor, B. W. 2012c, *ApJS*, **200**, 19
- Clemens, D. P., Sarcia, D., Grabau, A., et al. 2007, *PASP*, **119**, 1385
- Clemens, D. P., Tassis, K., & Goldsmith, P. F. 2016, *ApJ*, **833**, 176
- Crutcher, R. M. 2004, *Ap&SS*, **292**, 225
- Davis, L., Jr., & Greenstein, J. L. 1951, *ApJ*, **114**, 206
- Dolginov, A. Z., & Mitrofanov, I. G. 1976, *Ap&SS*, **43**, 291
- Draine, B. T., & Weingartner, J. C. 1996, *ApJ*, **470**, 551
- Draine, B. T., & Weingartner, J. C. 1997, *ApJ*, **480**, 633
- Eswaraiah, C., Pandey, A. K., Maheswar, G., et al. 2011, *MNRAS*, **411**, 1418
- Eswaraiah, C., Pandey, A. K., Maheswar, G., et al. 2012, *MNRAS*, **419**, 2587
- Goodman, A. A., Jones, T. J. B., Lada, E. A., & Myers, P. C. 1995, *ApJ*, **448**, 748
- Griffin, M. J., Abergel, A., Abreu, A., et al. 2010, *A&A*, **518**, L3
- Hall, J. S. 1949, *Sci*, **109**, 166
- Hatano, H., Nishiyama, S., Kurita, M., et al. 2013, *AJ*, **145**, 105
- Heiles, C. 2000, *AJ*, **119**, 923
- Hiltner, W. A. 1949a, *ApJ*, **109**, 471
- Hiltner, W. A. 1949b, *Sci*, **109**, 165
- Hirashita, H., & Yan, H. 2009, *MNRAS*, **394**, 1061
- Hoang, T., & Lazarian, A. 2009, *ApJ*, **695**, 1457
- Indebetouw, R., Mathis, J. S., Babler, B. L., et al. 2005, *ApJ*, **619**, 931
- Jones, A. P., Tielens, A. G. G. M., & Hollenbach, D. J. 1996, *ApJ*, **469**, 740
- Jones, E., Oliphant, E., Peterson, P., et al. 2001, SciPy Open Source Scientific Tools for Python (<http://www.scipy.org>)
- Jones, R. V., & Spitzer, L., Jr. 1967, *ApJ*, **147**, 943
- Jones, T. J. 1990, *AJ*, **99**, 1894
- Jones, T. J., Bagley, M., Krejny, M., Andersson, B.-G., & Bastien, P. 2015, *AJ*, **149**, 31
- Jones, T. J., Gordon, M., Shenoy, D., et al. 2016, *AJ*, **151**, 156
- Kim, S.-H., & Martin, P. G. 1995, *ApJ*, **444**, 293
- Lada, C. J., Alves, J., & Lada, E. A. 1999, *ApJ*, **512**, 250
- Lada, C. J., Lada, E. A., Clemens, D. P., & Bally, J. 1994, *ApJ*, **429**, 694
- Lazarian, A., Goodman, A. A., & Myers, P. C. 1997, *ApJ*, **490**, 273
- Lazarian, A., & Hoang, T. 2007, *MNRAS*, **378**, 910
- Li, A., & Greenberg, J. M. 1997, *A&A*, **323**, 566
- Li, H.-b., Fang, M., Henning, T., & Kainulainen, J. 2013, *MNRAS*, **436**, 3707
- Lombardi, M., & Alves, J. 2001, *A&A*, **377**, 1023
- Ludden, T. M., Beal, S. L., & Sheiner, L. B. C. 1994, *Journal of Pharmacokinetics and Biopharmaceutics*, **22**, 431
- Martin, P. G., Adamson, A. J., Whittet, D. C. B., et al. 1992, *ApJ*, **392**, 691
- Martin, P. G., & Whittet, D. C. B. 1990, *ApJ*, **357**, 113
- Martin, P. G. 1989, in IAU Symp. 135, *Interstellar Dust*, ed. L. J. Allamandola & A. G. G. M. Tielens (Dordrecht: Kluwer), 55
- Meingast, S., Lombardi, M., & Alves, J. 2017, *A&A*, **601**, A137
- Nagata, T. 1990, *ApJL*, **348**, L13
- Ormel, C. W., Paszun, D., Dominik, C., & Tielens, A. G. G. M. 2009, *A&A*, **502**, 845
- Parzen, E. 1962, *Ann. Math. Statist.*, **33**, 1065
- Planck Collaboration, Ade, P. A. R., Aghanim, N., et al. 2016, *A&A*, **586**, A138
- Purcell, E. M. 1979, *ApJ*, **231**, 404
- Pilbratt, G. L., Riedinger, J. R., Passvogel, T., et al. 2010, *A&A*, **518**, L1
- Rautela, B. S., Joshi, G. C., & Pandey, J. C. 2004, *BASI*, **32**, 159
- Robitaille, T., & Bressert, E. 2012, APLpy: Astronomical Plotting Library in Python Astrophysics Source Code Library, ascl:1208.017
- Rosenblatt, M. 1956, *Ann. Math. Statist.*, **27**, 832
- Schaefer, B., Collett, E., Smyth, R., et al. 2007, *AmJPh*, **75**, 163
- Schmidt, G. D., Elston, R., & Lupie, O. L. 1992, *AJ*, **104**, 1563
- Serkowski, K. 1973, in IAU Symp. 52, *Interstellar Dust and Related Topics*, ed. J. M. Greenberg & H. C. van de Hulst (Dordrecht: Reidel), 145
- Serkowski, K., Mathewson, D. S., & Ford, V. L. 1975, *ApJ*, **196**, 261
- Skrutskie, M. F., Cutri, R. M., Stiening, R., et al. 2006, *AJ*, **131**, 1163
- Sugiura, N. 1978, *Comm. Statist.*, **A7**, 13
- van der Walt, S., Colbert, S. C., & Varoquaux, G. 2011, *CSE*, **13**, 22
- van Leeuwen, F. 2007, *A&A*, **474**, 653
- Voshchinnikov, N. V., Das, H. K., Yakovlev, I. S., & Il'in, V. B. 2013, *AstL*, **39**, 421
- Voshchinnikov, N. V., & Hirashita, H. 2014, *MNRAS*, **445**, 301
- Wardle, J. F. C., & Kronberg, P. P. 1974, *ApJ*, **194**, 249
- Whittet, D. C. B., Gerakines, P. A., Hough, J. H., & Shenoy, S. S. 2001, *ApJ*, **547**, 872
- Whittet, D. C. B., Hough, J. H., Lazarian, A., & Hoang, T. 2008, *ApJ*, **674**, 304
- Whittet, D. C. B., Martin, P. G., Hough, J. H., et al. 1992, *ApJ*, **386**, 562
- Whittet, D. C. B., & van Breda, I. G. 1978, *A&A*, **66**, 57
- Wilking, B. A., Lebofsky, M. J., & Rieke, G. H. 1982, *AJ*, **87**, 695
- Wright, E. L., Eisenhardt, P. R. M., Mainzer, A. K., et al. 2010, *AJ*, **140**, 1868



Confirmation of Large Super-fast Rotator (144977) 2005 EC₁₂₇

Chan-Kao Chang¹, Hsing-Wen Lin¹, Wing-Huen Ip^{1,2}, Zhong-Yi Lin³, Thomas Kupfer³, Thomas A. Prince³,
Quan-Zhi Ye^{3,4}, Russ R. Laher⁴, Hee-Jae Lee^{5,6}, and Hong-Kyu Moon⁶

¹Institute of Astronomy, National Central University, Jhongli, Taiwan; rex@astro.ncu.edu.tw

²Space Science Institute, Macau University of Science and Technology, Macau

³Division of Physics, Mathematics and Astronomy, California Institute of Technology, Pasadena, CA 91125, USA

⁴Infrared Processing and Analysis Center, California Institute of Technology, Pasadena, CA 91125, USA

⁵Department of Astronomy and Space Science, Chungbuk National University, 1, Chungdae-ro, Seowon-Gu, Cheongju, Chungbuk 28644, Korea

⁶Korea Astronomy and Space Science Institute, 776, Daedeok-daero, Yuseong gu, Daejeon 305-348, Korea

Received 2017 April 2; revised 2017 April 24; accepted 2017 April 27; published 2017 May 10

Abstract

(144977) 2005 EC₁₂₇ is a V-/A-type inner-main-belt asteroid with a diameter of 0.6 ± 0.1 km. Asteroids of this size are believed to have rubble-pile structure, and therefore cannot have a rotation period shorter than 2.2 hr. However, our measurements show that asteroid 2005 EC₁₂₇ completes one rotation in 1.65 ± 0.01 hr with a peak-to-peak light-curve variation of ~ 0.5 mag. Therefore, this asteroid is identified as a large super-fast rotator. Either a rubble-pile asteroid with a bulk density of $\rho \sim 6$ g cm⁻³ or an asteroid with an internal cohesion of 47 ± 30 Pa can explain 2005 EC₁₂₇. However, the scenario of high bulk density is very unlikely for asteroids. To date, only six large super-fast rotators, including 2005 EC₁₂₇, have been reported, and this number is very small when compared with the much more numerous fast rotators. We also note that none of the six reporting large SFRs are classified as C-type asteroids.

Key words: minor planets, asteroids: individual (144977) 2005 EC₁₂₇

1. Introduction

The large (i.e., a diameter of a few hundreds of meters) super-fast rotators (SFRs) are of interest for understanding asteroid interior structure. Because asteroids of sub-kilometer size are believed to have rubble-pile structure (i.e., gravitationally bounded aggregations) and cannot have super-fast rotation, defined as a rotation period shorter than 2.2 hr (Harris 1996).⁷ However, the first large SFR, 2001 OE84, a near-Earth asteroid of ~ 0.7 km in size and completing one rotation in 29.19 minutes (Pravec et al. 2002), cannot be explained by rubble-pile structure, and consequently, internal cohesion was proposed to be a possible solution (Holsapple 2007). Although several attempts were made to discover large SFRs with extensive-sky surveys (Masiero et al. 2009; Dermawan et al. 2011), this asteroid group was not confirmed until another large SFR, 2005 UW163, was found by Chang et al. (2014b). Up to now, five large SFRs have been reported, additionally including 1950 DA (Rozitis et al. 2014), 2000 GD65 (Polishook et al. 2016), and 1999 RE88 (Chang et al. 2016). However, the population size of large SFRs is still not clear. Compared with the 738 large fast rotators (i.e., diameters between 0.5 and 10 km and rotation periods between 2–3 hr) in the up-to-date Asteroid Light Curve Database (LCDB⁸; Warner et al. 2009), large SFRs are rare. Either the difficulty of discovering them due to their sub-kilometer sizes (i.e., relatively faint) or the intrinsically small population size of this group could lead to this rarity in detection. Therefore, a more comprehensive survey of asteroid rotation period with a wider sky coverage and a deeper limiting magnitude, such as the ZTF,⁹ could help in finding more large SFRs. With more

SFR samples, a thorough study of their physical properties could be conducted, and therefore further insights about asteroid interior structure are possible. To this objective, the TANGO project¹⁰ has been conducting asteroid rotation-period surveys since 2013 using the iPTF¹¹ (for details, see Chang et al. 2014a, 2015, 2016). From these surveys, 2 large SFRs and 27 candidates were discovered. Here, we report the confirmation of asteroid (144977) 2005 EC₁₂₇ as a new large SFR. The super-fast rotation of (144977) 2005 EC₁₂₇ was initially and tentatively identified in the asteroid rotation-period survey using the iPTF in 2015 February (Chang et al. 2016), and then later confirmed in this work by follow-up observations using the Lulin One-meter Telescope in Taiwan (LOT; Kinoshita et al. 2005).

This Letter is organized as follows. The observations and measurements are given in Section 2, the rotation period analysis is described in Section 3, the results and discussion are presented in Section 4, and a summary and conclusions can be found in Section 5.

2. Observations

The iPTF, LOT, and spectroscopic observations that support the findings in this work are described in this section. The details of each of these observation runs are summarized in Table 1.

2.1. iPTF Observations

The iPTF is a follow-up project of the PTF, a project whose aim is to explore the transient and variable sky synoptically. The iPTF/PTF employ the Palomar 48 inch Oschin Schmidt Telescope and an 11-chip mosaic CCD camera with a field of view of ~ 7.26 deg² (Law et al. 2009; Rau et al. 2009). This

⁷ The 2.2 hr spin barrier was calculated for an asteroid with a bulk density of $\rho = 3$ g cm⁻³.

⁸ <http://www.minorplanet.info/lightcurvedatabase.html>

⁹ Zwicky Transient Facility; <http://ptf.caltech.edu/ztf>.

¹⁰ Taiwan New Generation OIR Astronomy.

¹¹ Intermediate Palomar Transient Factory; <http://ptf.caltech.edu/iptf>.

Table 1
Observational Details

Telescope	Date	Filter	R.A. (°)	Decl. (°)	N_{exp}	Δt (hr)	α (°)	r (au)	Δ (au)	m (mag)	H (mag)
PTF	2015 Feb 25–26	R'	154.04	10.12	43	28.3	1.3	2.45	1.46	20.3	17.3
LOT	2016 Sept 24	r'	23.81	2.81	84	7.3	2.5	2.03	1.03	19.2	17.3
P200	2016 Oct 4	Spec.: $0.4 - 0.9 \mu\text{m}$	23.65	2.21	3	0.5	7.7	2.05	1.07	19.5	

Note. Δt is observation time span and N_{exp} is the total number of exposures.

wide field of view is extremely useful in collecting a large number of asteroid light curves within a short period of time. Four filters are currently available, including a Mould- R , Gunn- g' , and two different $H\alpha$ bands. The exposure time of the PTF is fixed at 60 s, which routinely reaches a limiting magnitude of $R \sim 21$ mag at the 5σ level (Law et al. 2010). All iPTF exposures are processed by the IPAC-PTF photometric pipeline (Grillmair et al. 2010; Laher et al. 2014), and the Sloan Digital Sky Survey fields (York et al. 2000) are used in the magnitude calibration. Typically, an accuracy of ~ 0.02 mag can be reached for photometric nights (Ofek et al. 2012a, 2012b). Since the magnitude calibration is done on a per-night, per-filter, per-chip basis, small photometric zero-point variations are present in PTF catalogs for different nights, fields, filters, and chips.

In the asteroid rotation-period survey conducted on 2015 February 25–26, we repeatedly observed six consecutive PTF fields near the ecliptic plane, in the R -band with a cadence of ~ 10 minutes. Asteroid 2005 EC₁₂₇ was observed in the PTF field centered at R.A. = 154°04 and decl. = 10°12 when it was approaching its opposition at a low phase angle of $\alpha \sim 1.3$. After all stationary sources were removed from the source catalogs, the light curves for known asteroids were extracted using a radius of $2''$ to match with the ephemerides obtained from the JPL/HORIZONS system. The light curve of 2005 EC₁₂₇ contains 42 clean detections from this observation run (i.e., the detections flagged as defective by the IPAC-PTF photometric pipeline were not included in the light curve).

2.2. LOT Observations

The follow-up observations to confirm the rotation period of 2005 EC₁₂₇ were carried out on 2016 September 24, using the LOT when 2005 EC₁₂₇ had a magnitude of $r' \sim 19.2$ at its low phase angle of $\alpha \sim 2.6$. The average seeing during the observations was $\sim 1.3''$. All images were taken in the r' -band with a fixed exposure time of 300 s using the Apogee U42 camera, a $2K \times 2K$ charge-coupled device with a pixel scale of $0.35''$. We acquired a total of 84 exposures over a time span of ~ 440 minutes, and the time difference between consecutive exposures was ~ 5 minutes. The image processing and reduction included standard procedures of bias and flat-field corrections, astrometric calibration using *astrometry.net*,¹² and aperture photometry using SExtractor (Bertin & Arnouts 1996). The photometric calibration was done against Pan-STARRS1 point sources of $r' \sim 14$ – 22 mag (Magnier et al. 2016) using linear least-squares fitting, which typically achieved a fitting residual of ~ 0.01 mag. We improved the photometric accuracy by employing the trail-fitting method (Vereš et al. 2012; Lin et al. 2015) to accommodate the streaked image of 2005 EC₁₂₇ as a result of asteroid motion over the 300 s exposure time.

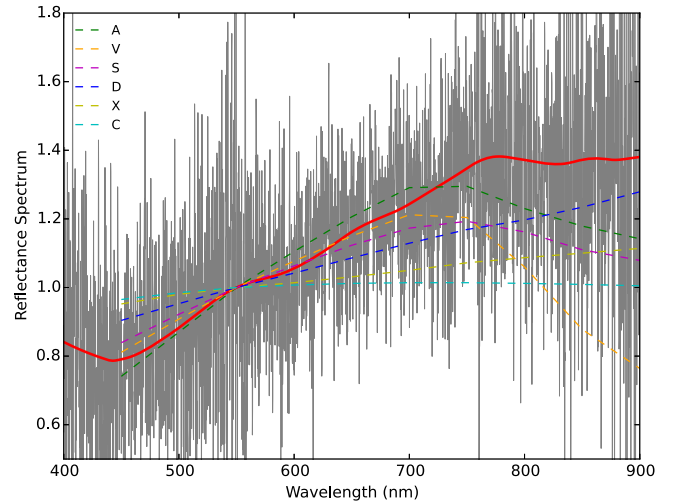


Figure 1. Reflectance spectrum of 2005 EC₁₂₇ taken by the P200. The gray line is the original reflectance spectrum and the red line is the running average using locally weighted scatter-plot smoothing (LOWESS; Cleveland 1979). The colored dashed lines are the reference spectra of A-type (green), V-type (orange), S-type (magenta), D-type (blue), X-type (yellow), and C-type (cyan) asteroids obtained from DeMeo et al. (2009). All spectra are normalized at wavelength 500 nm.

2.3. Spectroscopic Observations

To determine the taxonomic type for 2005 EC₁₂₇, its optical spectra were obtained using the Palomar 200 inch Hale Telescope (hereafter P200) and the Double-beam Spectrograph (Oke & Gunn 1982) in low-resolution mode ($R \sim 1500$). Three consecutive exposures were taken on 2016 October 4, with an exposure time of 300 s each. An average bias frame was made out of 10 individual bias frames and a normalized flat-field frame was constructed out of 10 individual lamp flat-field exposures. For the blue and red arms, respectively, FeAr and HeNeAr arc exposures were taken at the beginning of the night. Both arms of the spectrograph were reduced using a custom PyRAF-based pipeline¹³ (Bellm & Sesar 2016). The pipeline performs standard image processing and spectral reduction procedures, including bias subtraction, flat-field correction, wavelength calibration, optimal spectral extraction, and flux calibration. The average spectrum of 2005 EC₁₂₇ was constructed by combining all individual exposures, and then it was divided by the solar spectrum¹⁴ to obtain the reflectance spectrum of 2005 EC₁₂₇ (Figure 1). The trend of the reflectance spectrum suggests a V-/A-type asteroid for 2005 EC₁₂₇, according to the Bus-DeMeo classification scheme (DeMeo et al. 2009).

¹³ <https://github.com/ebellm/pyraf-dbsp>

¹⁴ The solar spectrum was obtained from Kurucz et al. (1984) and was then convolved with a Gaussian function to match the resolution of the spectrum of 2005 EC₁₂₇.

¹² <http://astrometry.net>

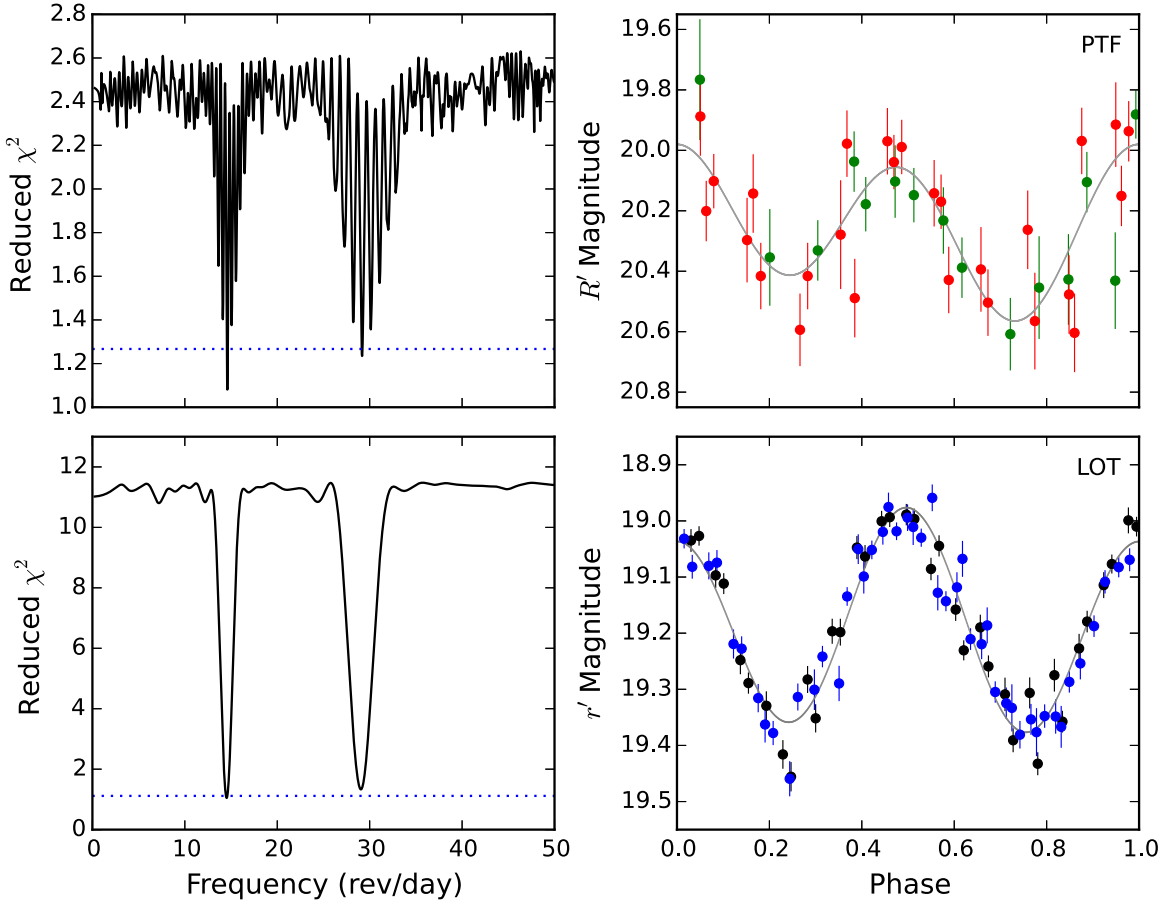


Figure 2. Periodograms (left) and folded light curves (right) for 2005 EC₁₂₇ obtained from iPTF (upper) and LOT (lower) observations. The blue dotted lines in the periodograms indicate the uncertainties in the derived rotation periods. The gray lines in the light curves are the fitted results. The green and red filled circles in the PTF light curve are data points obtained from 2015 February 25 and 26, respectively. The black and blue filled circles in the LOT light curve are data points of the even and odd rotation cycles, respectively.

3. Rotation-period Analysis

Before measuring the synodic rotation period for 2005 EC₁₂₇, the light-curve data points were corrected for light-travel time and were reduced to both heliocentric (r) and geocentric (Δ) distances at 1 au by $M = m + 5 \log(r\Delta)$, where M and m are reduced and apparent magnitudes, respectively. A second-order Fourier series (Harris et al. 1989) was then applied to search for the rotation periods:

$$M_{i,j} = \sum_{k=1,2}^{N_k} B_k \sin \left[\frac{2\pi k}{P} (t_j - t_0) \right] + C_k \cos \left[\frac{2\pi k}{P} (t_j - t_0) \right] + Z_i, \quad (1)$$

where $M_{i,j}$ is the reduced magnitude measured at the light-travel-time-corrected epoch, t_j ; B_k and C_k are the Fourier coefficients; P is the rotation period; t_0 is an arbitrary epoch; and Z_i is the zero point. For the PTF light curve, the fitting of Z_i also includes a correction for the small photometric zero-point variations mentioned in Section 2.1 (for details, see Polishook et al. 2012). To obtain the other free parameters for a given P , we used least-squares minimization to solve Equation (1). The frequency range was explored between 0.25 and 50 rev day⁻¹ with a step of 0.001 rev day⁻¹. To estimate the

uncertainty of the derived rotation periods, we calculated the range of periods with χ^2 smaller than $\chi_{\text{best}}^2 + \Delta\chi^2$, where χ_{best}^2 is the chi-squared value of the picked-out period and $\Delta\chi^2$ is obtained from the inverse chi-squared distribution, assuming $1 + 2N_k + N_i$ degrees of freedom.

The rotation period of 1.64 ± 0.01 hr (i.e., 14.6 rev day⁻¹) of 2005 EC₁₂₇ was first identified using the PTF light curve (Chang et al. 2016). Although the derived frequency of 14.6 rev day⁻¹ is significant in the periodogram calculated from the PTF light curve, the corresponding folded light curve is relatively scattered (see the upper panels of Figure 2). Therefore, we triggered the follow-up observations using the LOT. The rotation periods of 2005 EC₁₂₇ derived from the LOT light curve is 1.65 ± 0.01 hr (i.e., 14.52 rev day⁻¹), which is in good agreement with the PTF result (see the lower panels of Figure 1). Both folded light curves show a clear double-peak/valley feature for asteroid rotation (i.e., two periodic cycles). The peak-to-peak variations of the PTF and LOT light curves are ~ 0.6 and ~ 0.5 mag, respectively. This indicates that 2005 EC₁₂₇ is a moderately elongated asteroid and rules out the possibility of an octahedral shape for 2005 EC₁₂₇, which would lead to a light curve with four peaks and an amplitude of $\Delta m < 0.4$ mag (Harris et al. 2014). Moreover, we cannot morphologically distinguish between the even and odd cycles in the LOT light curve. Therefore, we believe that 1.65 hr is the true rotation period for 2005 EC₁₂₇.

4. Results and Discussion

To estimate the diameter, D , of 2005 EC₁₂₇, we use

$$D = \frac{1329}{\sqrt{p_v}} 10^{-H/5} \quad (2)$$

(see Harris & Lagerros 2002, and references therein). Since the phase angle of the asteroid had a small change during our relatively short observation time span, the absolute magnitude of 2005 EC₁₂₇ is simply calculated using a fixed G slope of 0.15 in the H - G system (Bowell et al. 1989). We obtain $H_{R'} = 17.27 \pm 0.22$ and $H_V = 17.30 \pm 0.02$ mag from the PTF and LOT observations, respectively.¹⁵ Because the absolute magnitude derived from the LOT observation has a smaller dispersion, we finally adopt $H_V = 17.30$ mag for 2005 EC₁₂₇. We use $(V - R) = 0.516$ in the conversion of $H_{R'}$ to H_V (DeMeo et al. 2009; Pravec et al. 2012) and then obtain $H_V = 17.82$ for 2005 EC₁₂₇. Assuming an albedo value of $p_v = 0.36 \pm 0.10$ for V-type and $p_v = 0.19 \pm 0.03$ for A-type asteroids (Masiero et al. 2011; DeMeo & Carry 2013), diameters of $D \sim 0.6 \pm 0.1$ and $\sim 0.8 \pm 0.1$ km, respectively, are estimated for 2005 EC₁₂₇, where the uncertainty includes the residuals in light-curve fitting and the range of assumed albedos. Even when an extreme albedo value of $p_v = 1.0$ is applied, a diameter of 0.4 km is still obtained for 2005 EC₁₂₇. Since A-type asteroids are relatively uncommon in the inner main belt, we therefore assume an V-type asteroid for 2005 EC₁₂₇ in the following discussion. As shown in Figure 4, 2005 EC₁₂₇ lies in the rubble-pile asteroid region and has a rotation period shorter than 2 hr. Therefore, we conclude that 2005 EC₁₂₇ is a large SFR.

If 2005 EC₁₂₇ is a rubble-pile asteroid, a bulk density of $\rho \sim 6 \text{ g cm}^{-3}$ would be required to withstand its super-fast rotation (see Figure 3). This would suggest that 2005 EC₁₂₇ is a very compact object, i.e., composed mostly of metal. However, such high bulk density is very unusual among asteroids. Moreover, 2005 EC₁₂₇ is probably a V-type asteroid. Therefore, this is a very unlikely scenario indeed.

Another possible explanation for the super-fast rotation of 2005 EC₁₂₇ is that it has substantial internal cohesion (Holsapple 2007; Sánchez & Scheeres 2014). Using the Drucker-Prager yield criterion,¹⁶ we can estimate the internal cohesion for asteroids. Assuming an average $\rho = 1.93 \text{ g cm}^{-3}$ for V-type asteroids (Carry 2012), a cohesion of 47 ± 20 Pa results for 2005 EC₁₂₇.¹⁷ This modest value is comparable with that of the other large SFRs (see Table 2) and is also nearly in the cohesion range of lunar regolith, i.e., 100–1000 Pa (Mitchell et al. 1974).

As shown by Holsapple (2007), the size-dependent cohesion would allow large SFRs to be present in the transition zone between monolithic and rubble-pile asteroids. However, only six large SFRs have been reported to date (including this work). This number is very small when compared with the number of

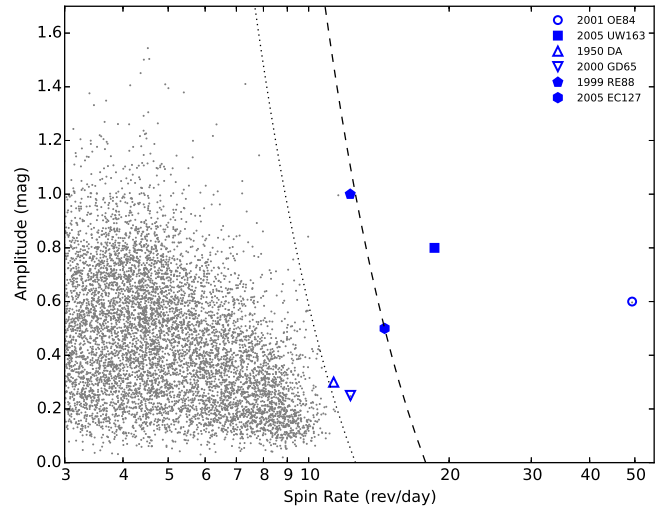


Figure 3. Asteroid light-curve amplitude vs. spin rate. The gray dots are LCDB objects with reliable rotation periods. The blue symbols denote the six reported large SFRs, where the filled symbols were discovered by the iPTF. The dashed and dotted lines represent the estimated spin rate limits for rubble-pile asteroids of bulk densities of $\rho = 6$ and 3 g cm^{-3} , respectively, using $P \sim 3.3\sqrt{(1 + \Delta m)/\rho}$ hr, where Δm is the light-curve amplitude (Harris 1996). Assuming a rubble-pile structure, the estimated bulk density of 2005 EC₁₂₇ (blue hexagon) would be $\sim 6 \text{ g cm}^{-3}$.

large fast rotators (i.e., 738 objects in the LCDB). The reason for the rarity in detecting large SFRs from previous studies (i.e., the sparse number of large SFRs in the transition zone in Figure 4) could be that (a) the rotation periods are difficult to obtain for large SFRs due to their small diameters (i.e., faint brightness) or (b) the population size of large SFRs is intrinsically small. Therefore, a survey of asteroid rotation period with a larger sky coverage and deeper limiting magnitude can help to resolve the aforementioned question. If it is the latter case, these large SFRs might be monoliths, which have relatively large diameters and unusual collision histories.

We also note that none of the six reported large SFRs is classified as C-type asteroids. Therefore, any discovery of a large C-type SFR would fill out this taxonomic vacancy and help to understand the formation of large SFRs. In addition, the determination of the upper limit of the SFR diameter is also important for understanding asteroid interior structure since this can constrain the upper limit of the internal cohesion of asteroids.

5. Summary and Conclusions

(144977) 2005 EC₁₂₇ is consistent with a V-/A-type inner-main-belt asteroid, based on our follow-up spectroscopic observations, with a diameter estimated to be 0.6 ± 0.1 km from the standard brightness/albedo relation. Its rotation period was first determined to be 1.64 ± 0.01 hr from our iPTF asteroid rotation-period survey and then was confirmed as 1.65 ± 0.01 hr by the follow-up observations reported here using the LOT. We categorize 2005 EC₁₂₇ as a large SFR, given its size and since its rotation period is less than the 2.2 hr spin barrier.

Considering its 0.6 km diameter, 2005 EC₁₂₇ is most likely a rubble-pile asteroid. For 2005 EC₁₂₇ to survive under its super-fast rotation, either an internal cohesion of 47 ± 20 Pa or an unusually high bulk density of $\rho \sim 6 \text{ g cm}^{-3}$ is required. However, the latter case is very unlikely for large asteroids, and more so for V-/A-type asteroids, as 2005 EC₁₂₇ has been classified. Only six large SFRs have been reported in the

¹⁵ A G slope of 0.24 for S-type asteroids (Pravec et al. 2012) would make the H magnitude ~ 0.03 mag fainter, which is equivalent to a ~ 0.01 km diameter difference, and within the uncertainty of our estimation.

¹⁶ The detailed calculation is given in Chang et al. (2016). This method has been widely used, e.g., in Holsapple (2007), Rozitis et al. (2014), and Polishook et al. (2016).

¹⁷ For an A-type asteroid with average density $\rho = 3.73 \text{ g cm}^{-3}$ (Carry 2012), the cohesion would be 52 Pa.

Table 2
Confirmed Large SFRs to Date

	Asteroid	Tax.	Per. (hr)	Δm (mag)	Dia. (km)	H (mag)	Coh. (Pa)	a (au)	e	i ($^{\circ}$)	Ω ($^{\circ}$)	ω ($^{\circ}$)	Reference
(144977)	2005 EC ₁₂₇	V/A	1.65 \pm 0.01	0.5	0.6 \pm 0.1	17.8 \pm 0.1	47 \pm 30	2.21	0.17	4.75	336.9	312.8	This work
(455213)	2001 OE ₈₄	S	0.49 \pm 0.00	0.5	0.7 \pm 0.1	18.3 \pm 0.2	\sim 1500 ^a	2.28	0.47	9.34	32.2	2.8	Pravec et al. (2002)
(335433)	2005 UW ₁₆₃	V	1.29 \pm 0.01	0.8	0.6 \pm 0.3	17.7 \pm 0.3	\sim 200 ^a	2.39	0.15	1.62	224.6	183.6	Chang et al. (2014b)
(29075)	1950 DA	M	2.12 \pm 0.00	0.2 ^b	1.3 \pm 0.1	16.8 \pm 0.2	64 \pm 20	1.70	0.51	12.17	356.7	312.8	Rozitis et al. (2014)
(60716)	2000 GD ₆₅	S	1.95 \pm 0.00	0.3	2.0 \pm 0.6	15.6 \pm 0.5	150–450	2.42	0.10	3.17	42.1	162.4	Polishook et al. (2016)
(40511)	1999 RE ₈₈	S	1.96 \pm 0.01	1.0	1.9 \pm 0.3	16.4 \pm 0.3	780 \pm 500	2.38	0.17	2.04	341.6	279.8	Chang et al. (2016)

Notes. The orbital elements were obtained from the MPC website, <http://www.minorplanetcenter.net/iau/mpc.html>.

^a The cohesion is adopted from Chang et al. (2016).

^b Δm is adopted from Busch et al. (2007).

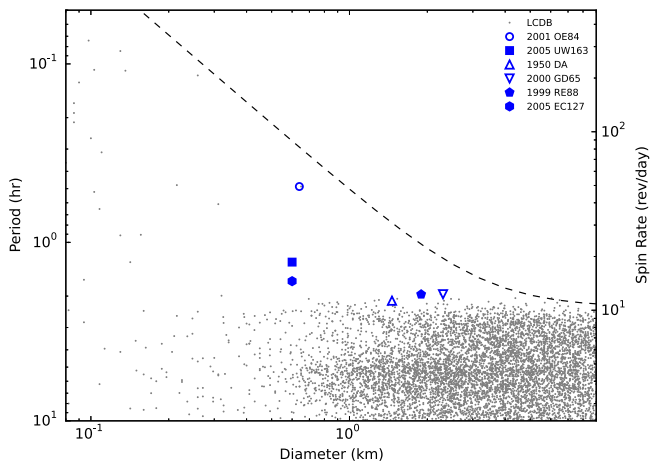


Figure 4. Asteroid rotation period (spin rate) vs. diameter. The symbol assignments are the same as used in Figure 3. The large SFRs have somewhat smaller periods than the spin barrier at 2.2 hr. The dashed line is the predicted spin limit with cohesion $\kappa = k\bar{r}^{-1/2}$, where the strength coefficient $k = 2.25 \times 10^7$ dynes $\text{cm}^{-3/2}$ and \bar{r} is the mean radius (Holsapple 2007).

literature, including 2005 EC₁₂₇, the subject of this work. This number is very small compared with the number of existing large fast rotators. Therefore, future surveys will help to reveal whether this rarity in detection is due to the intrinsically small population size of large SFRs. Moreover, none of the known SFRs have been classified as C-type asteroids, and the discovery of a large SFR of this type in future work would be an interesting development to further our understanding of the formation of large super-fast rotators.

This work is supported in part by the Ministry of Science and Technology of Taiwan under grants MOST 104-2112-M-008-014-MY3, MOST 104-2119-M-008-024, and MOST 105-2112-M-008-002-MY3, and also by Macau Science and Technology Fund No. 017/2014/A1 of MSAR. We are thankful for the indispensable support provided by the staff of the Lulin Observatory and the staff of the Palomar Observatory. We thank the anonymous referee for useful suggestions and comments.

References

Bellm, E. C., & Sesar, B. 2016, pyraf-dbsp: Reduction pipeline for the Palomar Double Beam Spectrograph, Astrophysics Source Code Library, ascl:1602.002
 Bertin, E., & Arnouts, S. 1996, *A&AS*, **117**, 393

Bowell, E., Hapke, B., Domingue, D., et al. 1989, in *Asteroids II* (Tucson, AZ: Univ. Arizona Press), 524
 Busch, M. W., Giorgini, J. D., Ostro, S. J., et al. 2007, *Icar*, **190**, 608
 Carry, B. 2012, *P&SS*, **73**, 98
 Chang, C.-K., Ip, W.-H., Lin, H.-W., et al. 2014a, *ApJ*, **788**, 17
 Chang, C.-K., Ip, W.-H., Lin, H.-W., et al. 2015, *ApJS*, **219**, 27
 Chang, C.-K., Lin, H.-W., Ip, W.-H., et al. 2016, *ApJS*, **227**, 20
 Chang, C.-K., Waszczak, A., Lin, H.-W., et al. 2014b, *ApJL*, **791**, LL35
 Cleveland, W. S. 1979, *J. Am. Stat. Assoc.*, **74**, 829
 DeMeo, F. E., Binzel, R. P., Slivan, S. M., & Bus, S. J. 2009, *Icar*, **202**, 160
 DeMeo, F. E., & Carry, B. 2013, *Icar*, **226**, 723
 Dermawan, B., Nakamura, T., & Yoshida, F. 2011, *PASJ*, **63**, 555
 Grillmair, C. J., Laher, R., Surace, J., et al. 2010, in *ASP Conf. Ser.* 434, *Astronomical Data Analysis Software and Systems XIX*, ed. Y. Mizumoto, K.-I. Morita, & M. Ohishi (San Francisco, CA: ASP), 28
 Harris, A. W., & Lagerros, J. S. V. 2002, in *Asteroids III*, ed. W. F. Bottke Jr., et al. (Tucson, AZ: Univ. Arizona Press), 205
 Harris, A. W., Pravec, P., Galád, A., et al. 2014, *Icar*, **235**, 55
 Harris, A. W., Young, J. W., Bowell, E., et al. 1989, *Icar*, **77**, 171
 Harris, A. W. 1996, *LPSC*, **27**, 493
 Holsapple, K. A. 2007, *Icar*, **187**, 500
 Kinoshita, D., Chen, C.-W., Lin, H.-C., et al. 2005, *ChJAA*, **5**, 315
 Kurucz, R. L., Furenlid, I., Brault, J., & Testerman, L. 1984, *National Solar Observatory Atlas* (Sunspot, NM: National Solar Observatory)
 Laher, R. R., Surace, J., Grillmair, C. J., et al. 2014, *PASP*, **126**, 674
 Law, N. M., Dekany, R. G., Rahmer, G., et al. 2010, *Proc. SPIE*, **7735**, 77353M
 Law, N. M., Kulkarni, S. R., Dekany, R. G., et al. 2009, *PASP*, **121**, 1395
 Lin, H. W., Yoshida, F., Chen, Y. T., Ip, W. H., & Chang, C. K. 2015, *Icar*, **254**, 202
 Magnier, E. A., Schlafly, E. F., Finkbeiner, D. P., et al. 2016, arXiv:1612.05242
 Masiero, J., Jedicke, R., Ďurech, J., et al. 2009, *Icar*, **204**, 145
 Masiero, J. R., Mainzer, A. K., Grav, T., et al. 2011, *ApJ*, **741**, 68
 Mitchell, J. K., Houston, W. N., Carrier, W. D., & Costes, N. C. 1974, *Apollo Soil Mechanics Experiment S-200 Final Report 7285* (Berkeley, CA: Univ. California)
 Ofek, E. O., Laher, R., Law, N., et al. 2012a, *PASP*, **124**, 62
 Ofek, E. O., Laher, R., Surace, J., et al. 2012b, *PASP*, **124**, 854
 Oke, J. B., & Gunn, J. E. 1982, *PASP*, **94**, 586
 Polishook, D., Moskovitz, N., Binzel, R. P., et al. 2016, *Icar*, **267**, 243
 Polishook, D., Ofek, E. O., Waszczak, A., et al. 2012, *MNRAS*, **421**, 2094
 Pravec, P., Harris, A. W., Kušnirák, P., Galád, A., & Hornoch, K. 2012, *Icar*, **221**, 365
 Pravec, P., Kušnirák, P., Šarounová, L., et al. 2002, in *Asteroids, Comets, and Meteors: ACM 2002*, ed. B. Warmbein (ESA SP-500; Noordwijk: ESA), 743
 Rau, A., Kulkarni, S. R., Law, N. M., et al. 2009, *PASP*, **121**, 1334
 Rozitis, B., MacLennan, E., & Emery, J. P. 2014, *Nature*, **512**, 174
 Sánchez, P., & Scheeres, D. J. 2014, *M&PS*, **49**, 788
 Vereš, P., Jedicke, R., Denneau, L., et al. 2012, *PASP*, **124**, 1197
 Warner, B. D., Harris, A. W., & Pravec, P. 2009, *Icar*, **202**, 134
 York, D. G., Adelman, J., Anderson, J. E., Jr., et al. 2000, *AJ*, **120**, 1579

Study of Molecular Clouds, Variable Stars and Related Topics at NUU and UBAI

Alisher S. Hojaev

National University of Uzbekistan (NUU), Ulugh Beg Astronomical Institute (UBAI), Tashkent, Uzbekistan; hojaev@yahoo.com, ash@astrin.uz

Abstract. The search of young PMS stars made by our team at Maidanak, Lulin and Beijing observatories, especially in NGC 6820/23 area, as well as monitoring of a sample of open clusters will be described and results will be presented. We consider physical conditions in different star forming regions, particularly in TDC and around Vul OB1, estimate SFE and SFR, energy balance and instability processes in these regions. We also reviewed all data on molecular clouds in the Galaxy and in other galaxies where the clouds were observed to prepare general catalog of molecular clouds, to study physical conditions, unsteadiness and possible star formation in them, the formation and evolution of molecular cloud systems, to analyze their role in formation of different types of galaxies and structural features therein.

Outside
GCN IAUCs
Other
ATel on Twitter and Facebook ATELstream ATel Community Site MacOS: Dashboard Widget

The Astronomer's Telegram

[Post](#) | [Search](#) | [Policies](#)
[Credential](#) | [Feeds](#) | [Email](#)

6 Apr 2017; 08:49 UT

This space for free for
your conference.



[[Previous](#)]

MAXI J1807+132: Lulin observations find substantial optical variability during the X-ray fading phase

ATel #10245; *A. K. H. Kong (NTHU & Oxford), R. Jin, C.-H. Tseng, E.-T. Lin (NTHU)*
on 6 Apr 2017; 08:09 UT

Credential Certification: *Albert Kong (akong@phys.nthu.edu.tw)*

Subjects: Optical, X-ray, Black Hole, Neutron Star, Transient

Tweet Recommend 1

Following the reports of decaying X-ray and optical flux of the X-ray transient MAXI J1807+132 (ATel #[10223](#),#[10224](#),#[10227](#)), we observed the source from 2017 March 30 to April 5 with the 1m telescope at the Lulin Observatory in Taiwan. The source is clearly detected in all observations and shows night-to-night variability. In particular, the last observation taken on April 5 suggests a rebrightening and a bluer object.

By comparing with the AAVSO Photometric All-Sky Survey (APASS) data, we estimated the following magnitudes in the g and r bands.

MJD	g-band	r-band
57842.7322		20.18+/-0.17 (with thin clouds)
57844.8121	20.94+/-0.07	20.60+/-0.07
57845.8122	21.09+/-0.05	20.93+/-0.05
57846.8487	20.93+/-0.05	20.61+/-0.05
57847.8480	21.49+/-0.07	21.00+/-0.06
57848.8334	19.27+/-0.01	19.18+/-0.02

We notice on April 5 (MJD 57848.6506; roughly 5 hours before our optical observation), there is a 950-sec Swift observation. The source is not detected with the XRT. Assuming a hydrogen column of $2.3e21 \text{ cm}^{-2}$ and a photon index of 2.5 (ATel #[10224](#)), we derived a 3-sigma 0.3-10 keV unabsorbed flux limit of $9.8e-13 \text{ erg/s/cm}^2$, a factor of 20 fainter than that of March 29.

We strongly encourage multi-wavelength follow-up observations to monitor the evolution of the outburst of this source.

[[Telegram Index](#)]

R. E. Rutledge, Editor-in-Chief

Derek Fox, Editor

Mansi M. Kasliwal, Co-Editor

rrutledge@astronomerstelegram.org

dfox@astronomerstelegram.org

mansi@astronomerstelegram.org

- Related**

10245 [MAXI J1807+132: Lulin observations find substantial optical variability during the X-ray fading phase](#)

10227 [ASAS-SN Optical Observations of MAXI J1807+132](#)

10224 [MAXI J1807+132 is fading in both X-rays and optical wavelengths](#)

10223 [MAXI J1807+132: MITSuME Akeno Optical Observation](#)

10222 [Swift/XRT spectral analysis of MAXI J1807+132: possibility of a faint low mass X-ray binary](#)

10221 [MAXI J1807+132: GTC spectroscopy reveals a LMXB-like optical spectrum.](#)

10217 [MAXI J1807+132: archival optical variability of Swift counterpart](#)

10216 [MAXI J1807+132: UV/Optical counterpart, further XRT observations](#)

10215 [MAXI J1807+132: Swift/XRT localization](#)

10208 [MAXI/GSC detection of a long-term soft X-ray flaring event MAXI J1807+132](#)

Dissecting the long-term emission behaviour of the BL Lac object Mrk 421

M. I. Carnerero,¹★ C. M. Raiteri,¹ M. Villata,¹ J. A. Acosta-Pulido,^{2,3}
 V. M. Larionov,^{4,5} P. S. Smith,⁶ F. D’Ammando,^{7,8} I. Agudo,⁹ M. J. Arévalo,^{2,3}
 R. Bachev,¹⁰ J. Barnes,¹¹ S. Boeva,¹⁰ V. Bozhilov,¹² D. Carosati,^{13,14} C. Casadio,¹⁵
 W. P. Chen,¹⁶ G. Damjanovic,¹⁷ E. Eswaraiyah,¹⁶ E. Forné,¹⁸ G. Gantchev,¹²
 J. L. Gómez,⁹ P. A. González-Morales,^{2,3} A. B. Griñón-Marín,^{2,3} T. S. Grishina,⁴
 M. Holden,¹⁹ S. Ibryamov,^{10,20} M. D. Joner,¹⁹ B. Jordan,²¹ S. G. Jorstad,^{4,22}
 M. Joshi,²² E. N. Kopatskaya,⁴ E. Koptelova,¹⁶ O. M. Kurtanidze,^{23,24,25}
 S. O. Kurtanidze,²³ E. G. Larionova,⁴ L. V. Larionova,⁴ G. Latev,¹⁰ C. Lázaro,^{2,3}
 R. Ligustri,²⁶ H. C. Lin,¹⁶ A. P. Marscher,²² C. Martínez-Lombilla,^{2,3} B. McBreen,²⁷
 B. Mihov,¹⁰ S. N. Molina,⁹ J. W. Moody,¹⁹ D. A. Morozova,⁴ M. G. Nikolashvili,²³
 K. Nilsson,²⁸ E. Ovcharov,¹² C. Pace,²⁹ N. Panwar,¹⁶ A. Pastor Yabar,^{2,3}
 R. L. Pearson,¹⁹ F. Pinna,^{2,3} C. Protasio,^{2,3} N. Rizzi,³⁰ F. J. Redondo-Lorenzo,^{2,3}
 G. Rodríguez-Coira,^{2,3} J. A. Ros,¹⁸ A. C. Sadun,³¹ S. S. Savchenko,⁴ E. Semkov,¹⁰
 L. Slavcheva-Mihova,¹⁰ N. Smith,³² A. Strigachev,¹⁰ Yu. V. Troitskaya,⁴
 I. S. Troitsky,⁴ A. A. Vasilyev⁴ and O. Vince¹⁷

Affiliations are listed at the end of the paper

Accepted 2017 August 21. Received 2017 August 21; in original form 2017 January 23

ABSTRACT

We report on long-term multiwavelength monitoring of blazar Mrk 421 by the GLAST-AGILE Support Program of the Whole Earth Blazar Telescope (GASP-WEBT) collaboration and Steward Observatory, and by the *Swift* and *Fermi* satellites. We study the source behaviour in the period 2007–2015, characterized by several extreme flares. The ratio between the optical, X-ray and γ -ray fluxes is very variable. The γ -ray flux variations show a fair correlation with the optical ones starting from 2012. We analyse spectropolarimetric data and find wavelength-dependence of the polarization degree (P), which is compatible with the presence of the host galaxy, and no wavelength dependence of the electric vector polarization angle (EVPA). Optical polarimetry shows a lack of simple correlation between P and flux and wide rotations of the EVPA. We build broad-band spectral energy distributions with simultaneous near-infrared and optical data from the GASP-WEBT and ultraviolet and X-ray data from the *Swift* satellite. They show strong variability in both flux and X-ray spectral shape and suggest a shift of the synchrotron peak up to a factor of ~ 50 in frequency. The interpretation of the flux and spectral variability is compatible with jet models including at least two emitting regions that can change their orientation with respect to the line of sight.

Key words: galaxies: active – BL Lacertae objects: general – BL Lacertae objects: individual: Mrk 421 – galaxies: jets.

1 INTRODUCTION

The active galactic nuclei (AGNs) known as ‘blazars’ are the ideal sources to study extragalactic jets, since in these objects one of the two jets coming out from the central black hole points towards us and its emission is thus enhanced by Doppler beaming. The low-energy

* E-mail: maribel@oato.inaf.it

radiation that we observe from the radio to the optical–X-ray frequencies is ascribed to synchrotron radiation from relativistic electrons, while the highest energy radiation is most likely produced by inverse-Compton scattering on the same relativistic electrons. The photon seeds for the latter process can come either from the jet itself [synchrotron self-Compton (SSC) models] or from the disc, broad line region or torus [external Compton (EC) models]. High-energy radiation can also be produced by hadronic processes (Böttcher et al. 2013). At low frequencies, we can measure the degree and angle of polarization of blazar emission. The study of their variability and possible wavelength dependence is important to infer the jet properties because the polarization is tied to the jet magnetic field structure (e.g. Smith 1996; Visvanathan & Wills 1998).

Mrk 421 at $z = 0.031$ (Ulrich et al. 1975) is one of the best monitored blazar over the entire electromagnetic spectrum. It is classified as a high-energy-peaked BL Lac (HBL), which means that the synchrotron peak (and usually also the inverse-Compton peak) in its spectral energy distribution (SED) is positioned at relatively high frequencies.

It was the first blazar that was detected at energies $E > 500$ GeV (Punch et al. 1992), and many observing campaigns have recently been organized to analyse the source behaviour at TeV frequencies, usually including multiwavelength data (e.g. Aharonian et al. 2005; Albert et al. 2007; Donnarumma et al. 2009; Abdo et al. 2011; Aleksić et al. 2012, 2015a,b; Ahnen et al. 2016b; Baloković et al. 2016). It was observed by the Energetic Gamma Ray Experiment Telescope onboard the *Compton Gamma-Ray Observatory* with an average flux at $E > 100$ MeV of $(13.9 \pm 1.8) \times 10^{-8}$ photons $\text{cm}^{-2} \text{s}^{-1}$ and a photon index $\Gamma = 1.57 \pm 0.15$ (Hartman et al. 1999). The *Fermi* Large Area Telescope (LAT) Third Source Catalog (Acero et al. 2015) reports a γ -ray flux of $\sim 18 \times 10^{-8}$ photons $\text{cm}^{-2} \text{s}^{-1}$ between 100 MeV and 100 GeV, and a photon index $\Gamma = 1.77 \pm 0.08$. The source is very bright and variable at X-rays. In particular, a strong X-ray flare was observed in 2013 (Pian et al. 2014; Paliya et al. 2015; Sinha et al. 2015; Kapanadze et al. 2016). Optical observations have been available since 1899 (Miller 1975) and show that large-amplitude, rapid variability is a distinctive feature also in the optical band. The radio morphology reveals a bright nucleus and a one-sided jet with stationary or subluminal components (Piner, Pant & Edwards 2010; Blasi et al. 2013). An extreme radio flare was observed in 2012, possibly connected with preceding γ -ray flares (Hovatta et al. 2015). Possible radio– γ correlation was also found in 2011 by Lico et al. (2014).

In this paper, we analyse the Mrk 421 long-term flux and polarization behaviour. Very preliminary results were reported in Carnerero et al. (2016). We present the optical and near-infrared (near-IR) data obtained by the GLAST-AGILE Support Program (GASP) of the Whole Earth Blazar Telescope (WEBT) collaboration.¹ We compare the optical and near-IR flux variations with the X-ray and ultraviolet (UV) light curves obtained by the *Swift* satellite and with the γ -ray light curve from the *Fermi* satellite, by means of a cross-correlation analysis on the full data set available from 2007 to 2015. Moreover, we analyse the photopolarimetric behaviour and the spectropolarimetric data acquired at the Steward Observatory in the framework of the monitoring programme in support to the *Fermi* mission.² Finally, broad-band SEDs are built from the near-IR to

the X-ray energies to investigate the source spectral variability in the synchrotron part of the spectrum.

2 OPTICAL PHOTOMETRY

Optical observations in *R* band for the GASP-WEBT were performed with 34 telescopes in 26 observatories around the world: Abastumani (Georgia), AstroCamp (Spain), Belogradchik (Bulgaria), Calar Alto³ (Spain), Castelgrande (Italy), Crimean (Russia), L’Ampolla (Spain), Lowell (Perkins, USA), Lulin (Taiwan), New Mexico Skies (USA), Pulkovo (Russia), ROVOR (USA), Roque de los Muchachos (KVA and Liverpool, Spain), Rozhen (Bulgaria), SAI Crimean (Russia), Sabadell (Spain), Sirio (Italy), Skinakas (Greece), St. Petersburg (Russia), Talmassons (Italy), Teide (BRT, IAC80 and STELLA-I, Spain), Tjarafa (Spain), Torino (Italy), Tuorla (Finland), Astronomical Station Vidojevica - ASV (Serbia) and West Mountain (USA). Further *R*-band data were provided by the Steward Observatory (USA). Calibration of the source magnitude was obtained with respect to the reference stars 1, 2 and 3 by Villata et al. (1998).

The light curve in *R* band was built by carefully assembling the data sets coming from the different telescopes. Moreover, binning was used to reduce the noise of data acquired close in time by the same telescope. Offsets among different GASP data sets caused by partial inclusion of the host galaxy were minimized by adopting the same prescriptions for the photometry, i.e. an aperture radius of 7.5 arcsec. The Steward photometry was obtained with an extraction aperture of 7.6×10 arcsec², so that we had to add 2 mJy to the source flux density to make the Steward data match the GASP data.

The final light curve is shown in Fig. 1, where different symbols and colours highlight data from the various telescopes. It includes 5591 data points in the period from 2007 November 8 (JD = 2454412.7) to 2015 July 23 (JD = 2457227.4). They represent observed magnitudes, with no correction for the Galactic extinction and host-galaxy contribution. Strong variability characterizes the entire period on a large variety of time-scales.

3 NEAR-INFRARED PHOTOMETRY

The near-IR light curves of Mrk 421 in the period 2011–2015 are shown in Fig. 2 in *J*, *H* and *K* bands. The GASP-WEBT observations were performed by the 1.5-m TCS telescope in the Teide observatory.

The source calibration was obtained with respect to stars in the source field of view (FOV), whose magnitudes were adopted from the Two Micron All-Sky Data Release⁴ (2MASS; Skrutskie et al. 2006). Because of the small FOV (4×4 arcsec²) and consequent small number of reliable reference stars, we found a systematic offset between the zero-points of the Mrk 421 images with respect to the zero-points derived from the other fields images. We corrected for this difference and further checked that the inferred colour indices of the source were consistent with those reported in the 2MASS-point source catalogue.

As in the case of the optical data, the near-IR light curves were carefully checked and cleaned by reducing the data scattering through the binning of data close in time. These light curves are

¹ <http://www.oato.inaf.it/blazars/webt/>

² <http://james.as.arizona.edu/~psmith/Fermi/>

³ Calar Alto data was acquired as part of the MAPCAT project: <http://www.iaa.es/~iagudo/iagudo/MAPCAT.html>.

⁴ <http://www.ipac.caltech.edu/2mass/>

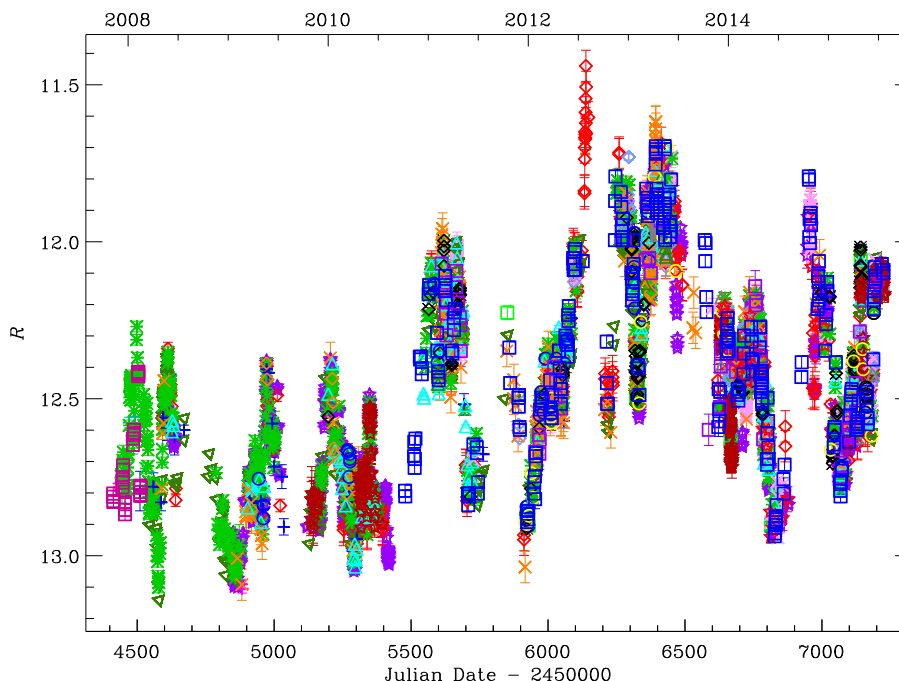


Figure 1. Optical light curve of Mrk 421 built with data from the GASP-WEBT collaboration and Steward Observatory in R band. Different colours and symbols highlight data from different telescopes. No correction for the host-galaxy contribution and Galactic extinction has been applied.

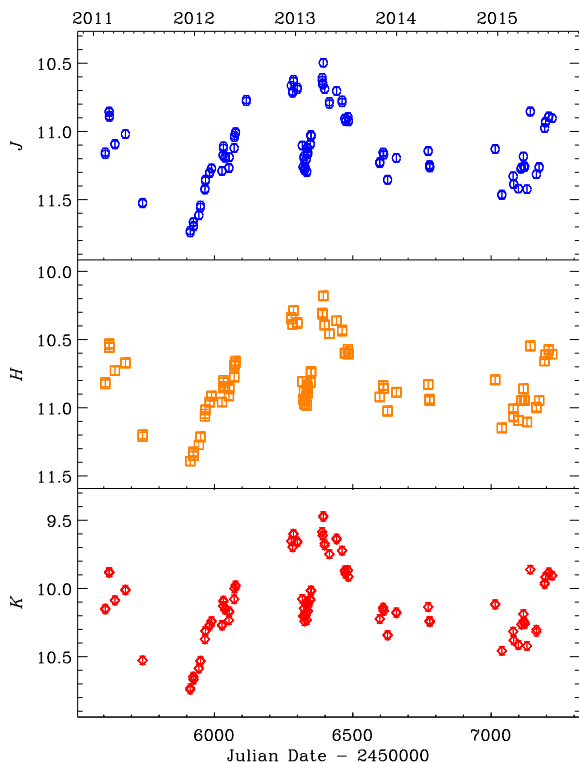


Figure 2. Near-IR light curves of Mrk 421 built with data from the GASP-WEBT collaboration in J , H and K bands. No correction for the host-galaxy contribution and Galactic extinction has been applied.

generally undersampled for a detailed comparison with the optical data, but where sufficient sampling has been achieved, they indicate that a close correspondence exists, as expected if the near-IR and optical emissions are produced by the same mechanism in the same

jet region. We note that the amount of variability is nearly the same in the three near-IR bands.

4 REMOVAL OF THE HOST GALAXY CONTRIBUTION

The Mrk 421 host galaxy is relatively bright in optical bands, very strong in the near-IR, while its flux is small in UV bands. To remove the host-galaxy contribution, we used a de Vaucouleurs profile, as done by Raiteri et al. (2010) for BL Lacertae:

$$I(r) = I_e e^{-7.67[(r/r_e)^{0.25} - 1]},$$

where r_e is the effective radius, i.e. the radius of the isophote containing half of the total luminosity, and I_e is the surface brightness at the effective radius. We used $r_e = 8.2 \pm 0.2$ arcsec and $R_{\text{host}} = 13.18$ mag (Nilsson et al. 2007) to estimate that the host galaxy contribution to the observed fluxes is $p = 48$ per cent of the whole galaxy flux with an aperture radius $r_a = 7.5$ arcsec, as used by the WEBT observers. We also estimated $p = 37$ per cent for $r_a = 5.0$ arcsec, the value that we will use in Section 6.1 for analysing the UV data (see Table 1).

In the R band, we found that 7.86 mJy must be subtracted from the observed photometric flux densities to isolate the non-thermal continuum of the active nucleus. We then calculated the host-galaxy contribution in the other bands by applying the colour indices determined by Mannucci et al. (2001) for elliptical galaxies to the de-reddened R -band magnitude. We adopted a Galactic extinction value of $A_R = 0.041$ mag from Schlegel, Finkbeiner & Davis (1998) and derived extinction in the other bands through the Cardelli, Clayton & Mathis (1989) laws, setting $R_V = A_V/E(B - V) = 3.1$, the mean value for the interstellar medium.

The optical and near-IR host magnitudes were converted into flux densities using the zero-mag fluxes given by Bessell, Castelli & Plez (1998). The whole galaxy flux densities were multiplied by

Table 1. UV, optical and near-IR observing bands with the corresponding Galactic extinction values A_λ , photometry aperture radius r_a , percentage of the host-galaxy flux included in the given aperture $p(r_a)$, host-galaxy flux density contribution to the source photometry F_{gal} , and median observed flux density (F_v^{obs}), including both Mrk 421 and the host galaxy.

Filters	A_λ (mag)	r_a (arcsec)	$p(r_a)$ (per cent)	F_{gal} (mJy)	(F_v^{obs}) (mJy)
<i>w2</i>	0.112	5.0	37	0.039	12.011
<i>m2</i>	0.118	5.0	37	0.067	14.305
<i>w1</i>	0.095	5.0	37	0.122	13.922
<i>U</i>	0.083	5.0	37	0.497	–
<i>R</i>	0.041	7.5	48	7.862	31.615
<i>J</i>	0.014	7.5	48	22.613	54.241
<i>H</i>	0.009	7.5	48	26.786	46.071
<i>K</i>	0.006	7.5	48	20.409	56.102

the $p(r_a)$ values to derive the contribution to the source photometry within the aperture radius. The results are shown in Table 1.

In the UV case, we used the template of a 13 Gyr elliptical galaxy that is available from the SWIRE project⁵ (Polletta et al. 2007). We scaled the template in order to have the host-galaxy flux expected in the *U* filter. Galactic extinction in the UV bands was estimated by convolving the Cardelli et al. (1989) laws with the filter effective area and source spectrum. The results are in Table 1. As can be seen, the host galaxy contribution is relevant in the near-IR, whereas it is negligible in the UV.

We checked that using the SWIRE Template method to calculate the host galaxy contribution at lower frequencies gives the same results obtained by the colour indices method within a few mJy.

5 COLOUR ANALYSIS

Analysis of colour variations is an important tool to investigate the spectral behaviour of the source and, in turn, the nature of its emission.

In Fig. 3, we show the *J*-band light curve (top panel) together with the corresponding $J - K$ colour indices as a function of time (middle panel) and brightness level (bottom panel). The colour indices were calculated by selecting *J*- and *K*-data points with small errors and taken within at most 15 min. We obtained that the average $J - K$ value is 1.12, with a standard deviation of 0.05. The data were corrected for the host galaxy contribution as explained in Section 4.

It can be seen that, in general, the values of $J - K$ decrease with increasing flux, which is more evident in the bottom panel, where the behaviour of the colour index with brightness is displayed. We observe a bluer-when-brighter trend, as expected for a BL Lac object (e.g. Ikejiri et al. 2011), with a linear Pearson’s correlation coefficient of 0.79 and Spearman’s rank correlation coefficient of 0.77.

6 OBSERVATIONS BY SWIFT

In this section, we analyse the *Swift* satellite data on Mrk 421 obtained with the UV/Optical Telescope (UVOT; Roming et al. 2005) and X-ray Telescope (XRT; Burrows et al. 2005) instruments. During the 2007–2015 period, the source was observed by *Swift* in 727 epochs.

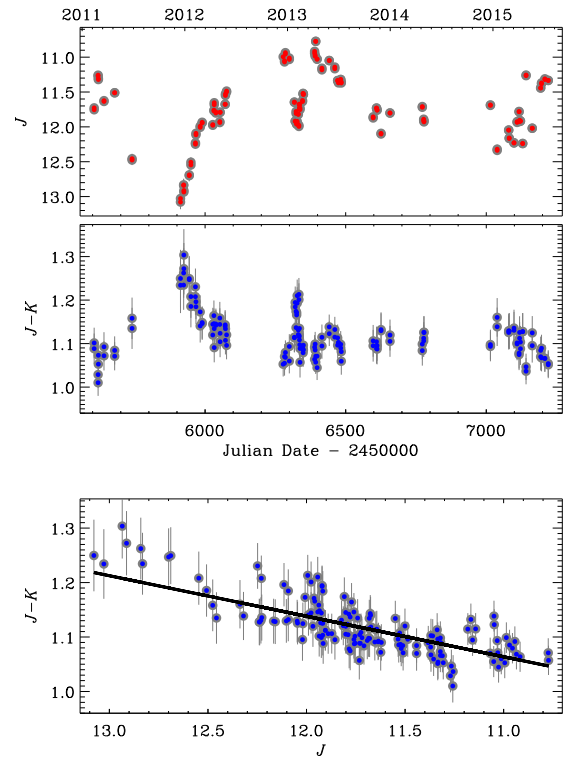


Figure 3. The *J*-band light curve in the 2011–2015 period (top panel); the corresponding $J - K$ colour index as a function of time (middle panel) and brightness level (bottom panel). In the bottom panel, the solid line represents a linear fit to the data. The data have been corrected for the host galaxy contribution.

6.1 UVOT

The UVOT instrument on board *Swift* observed Mrk 421 mostly in the UV bands *w1*, *m2* and *w2*, and sometimes also in the optical bands *v*, *b*, *u*. We downloaded these data from the NASA’s High Energy Astrophysics Science Archive Research Center (HEASARC)⁶ and reduced them with the HEASOFT package version 6.17 and the calibration release 20150717 of the CALDB data base available at HEASARC. For each epoch, multiple images in the same filter were first summed with the task `uvotimsum` and then aperture photometry was performed with `uvotsource`. We extracted source counts from a circular region with 5 arcsec radius centred on the source and background counts from a circle with 15 arcsec radius in a source-free field region.

The UVOT light curves are shown in Fig. 4. They confirm the general behaviour shown by the ground-based optical and near-IR curves in Figs 1 and 2.

6.2 XRT

We processed the XRT data with the HEASOFT package version 6.17 and the CALDB calibration files updated 20150721. The task `XRTPIPELINE` was executed with standard screening criteria. Only observations performed in pointing mode and with more than 50 counts were selected for further analysis. In the 2007–2015 period, we were left with 710 observations in windowed timing (WT) mode

⁵ http://www.iasf-milano.inaf.it/polletta/templates/swire_templates.html

⁶ <http://heasarc.nasa.gov>

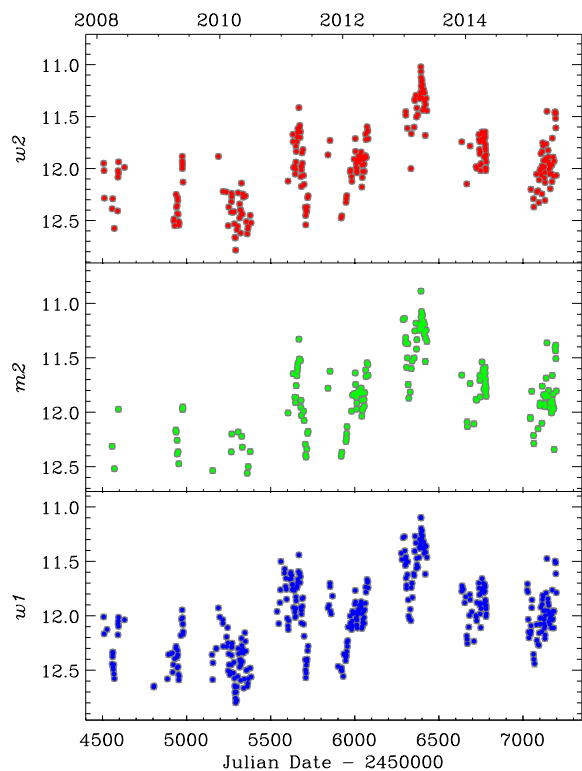


Figure 4. UV light curves of Mrk 421 built with *Swift*-UVOT data.

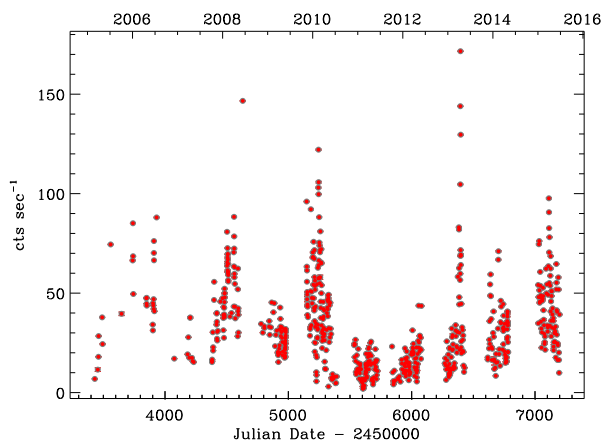


Figure 5. X-ray light curve of Mrk 421 obtained from data collected by the XRT instrument onboard the *Swift* satellite in the period 2007–2015.

and only 16 in photon counting mode, so that we concentrated on the former.

We selected event grades 0–2 and used a circular region with 70-arcsec radius centred on the source to extract the source counts, and a similar region shifted away from the source along the window to extract the background counts. We verified that the background is negligible, as background counts are in average 1.5 per cent and at maximum 5 per cent of the source counts, so we did not correct for it. Only three observations in WT mode have a mean rate greater than 100 counts s^{-1} , implying pile-up. To correct for pile-up, we discarded the inner 3-pixel radius circle in the source extraction region.

We used the `XRTMKARF` task to generate ancillary response files (ARF), which account for different extraction regions, vignetting

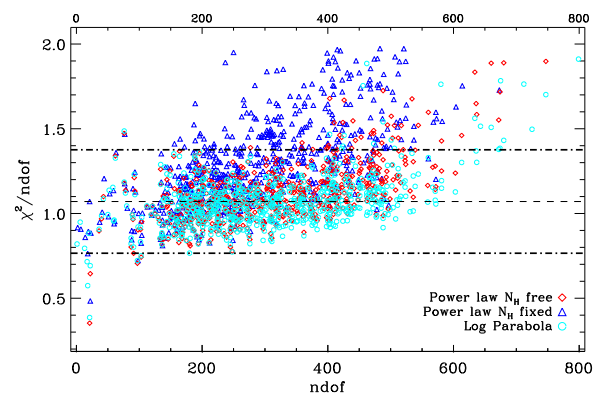


Figure 6. Reduced χ^2 versus the ndof for the different models applied to the XRT spectra of Mrk 421. Blue triangles represent the results of the power-law model with N_H fixed to the Galactic value, red diamonds those of the power-law model with N_H free and the cyan circles those of the log-parabola model with Galactic N_H .

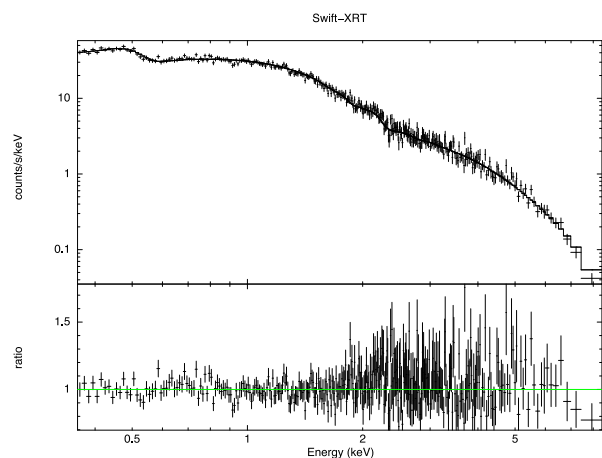


Figure 7. The XRT spectrum of Mrk 421 on 2008 February 13. The best fit was obtained with a log-parabola model. The bottom panel shows the ratio of the data to the folded model.

and PSF corrections. The X-ray light curve is shown in Fig. 5 and is discussed in the next Section.

By means of the task `grppha`, we associated the source spectra with the ARF and CALDB redistribution matrix function files, and binned the source spectra in order to have a minimum of 20 counts in each bin for the χ^2 statistics. These grouped spectra were then analysed with the `XSPEC` package, using the energy channels greater than 0.35 keV to improve the goodness of the fit.

We applied three different models for the spectral fitting: (1) an absorbed power-law model, where absorption is modelled according to Wilms, Allen & McCray (2000) and the hydrogen column is fixed to the Galactic value $N_H = 1.61 \times 10^{20} \text{cm}^{-2}$, as derived from the 21-cm measure by Lockman & Savage (1995); (2) an absorbed power-law model with N_H free; and (3) an absorbed log-parabola model with N_H fixed to the Galactic value. We favoured the third model, whose χ^2 is usually smaller than that of the other models, and that produces results with smaller errors. In Fig. 6, we show the χ^2 versus the number of degrees of freedom (ndof). The χ^2 is more stable when the log-parabola model is applied, but it increases with ndof. This is possibly due to a pronounced curvature. Fig. 7 shows an example of XRT spectrum. It was best fitted with a log parabola.

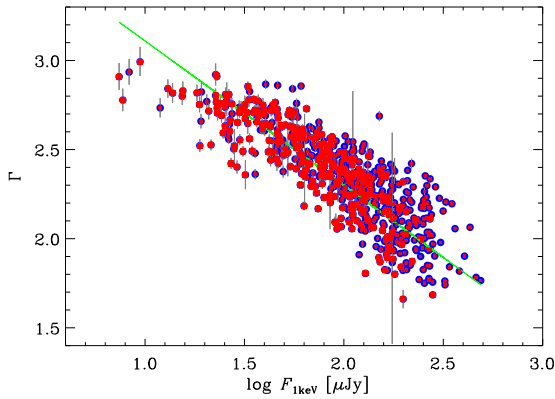


Figure 8. The X-ray photon index Γ as a function of the unabsorbed flux density at 1 keV. Data with error less than 30 per cent of the flux are shown. Red squares refer to the best-fitted cases, where the reduced χ^2 is in the range 0.8–1.2 and the ndof is >10 . The solid line represents a linear fit to the data.

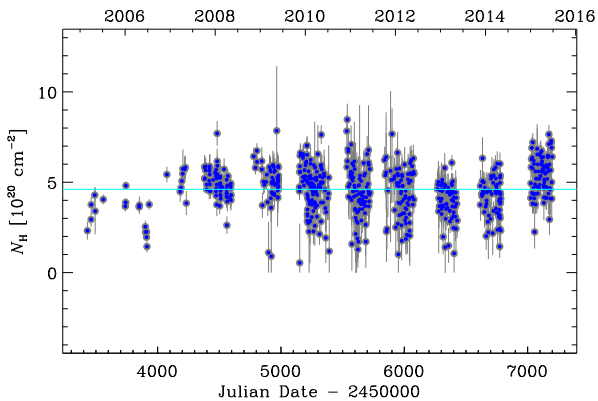


Figure 9. The Galactic hydrogen column N_{H} as a function of time when a power-law model with free absorption is applied to the XRT spectra. The cyan line marks the average value.

In the case of a power-law model with fixed N_{H} , the photon index Γ ranges from 1.66 to 2.99, indicating a spectrum that oscillates from hard to soft. The average value is 2.34, with standard deviation of 0.26. To understand whether these spectral changes correspond to real variations or are due to noise, we recall the definition of the mean fractional variation $F_{\text{var}} = \sqrt{\sigma^2 - \delta^2}/\langle f \rangle$ (Peterson 2001), which is commonly used to characterize variability. Here, $\langle f \rangle$ is the mean value of the variable we are analysing, σ^2 its variance and

δ^2 the mean square uncertainty. In our case, $F_{\text{var}} = 0.11$, so we conclude that the variations reflect genuine source variability rather than noise. Fig. 8 displays the photon index Γ as a function of the flux density at 1 keV. We note that the lowest Γ values correspond to the highest fluxes, in agreement with the harder-when-brighter trend often observed in blazars. However, this model produces statistically unacceptable fits (see Fig. 6).

On the other hand, the power-law model with N_{H} free implies a large spread of N_{H} values, which very unlikely corresponds to a physical scenario (see Fig. 9). We note that in this case the mean value of N_{H} exceeds the Galactic value by a factor of ~ 3 , suggesting that the spectrum is curved.

The log-parabola model has largely been used to fit the X-ray spectrum of this source (e.g. Massaro et al. 2004; Sinha et al. 2015). It offers a statistically better fit to the data in case of a curved spectrum. In this model, the photon index Γ is replaced by two parameters: α , the photon index, and β , the spectral curvature. We obtained α values in the range from 1.58 to 2.99, similar to that found for Γ in the power-law case. The average value is 2.27, with standard deviation of 0.28. The mean fractional variation is $F_{\text{var}} = 0.12$. The β parameter goes from -0.09 to 0.66, with an average value of 0.24 and standard deviation of 0.10. The mean fractional variation is $F_{\text{var}} = 0.29$. The large range of β values indicates strong curvature changes. However, large uncertainties affect the most extreme β values, demanding caution.

In Fig. 10, we show the trend of the α and β parameters of the log-parabola model applied to the X-ray spectra of Mrk 421 as a function of the source flux. While α behaves similarly to Γ (Fig. 8), confirming the harder-when-brighter spectral property, no clear correlation between β and flux is recognizable. We obtained a linear Pearson's correlation coefficient of 0.86/0.20 and Spearman's rank correlation coefficient of 0.88/0.16 for the α/β cases.

7 OBSERVATIONS BY *FERMI*

The LAT (Atwood et al. 2009) instrument onboard the *Fermi* satellite observes in the 20 MeV–300 GeV energy range. In this paper, we considered data between 2008 August 4 (JD = 2454683.15) and 2015 September 10 (JD = 2457275.50). We used Pass 8 data (Atwood et al. 2013), based on a complete revision of the entire LAT event-level analysis. We adopted the `SCIENCETOOLS` software package version v10r0p5 and followed the standard reduction procedure, as done in Carnerero et al. (2015). We considered a region of interest of radius 30° , a maximum zenith angle of 90° and only ‘Source’ class events (evclass=128, evtype=3). The spectral

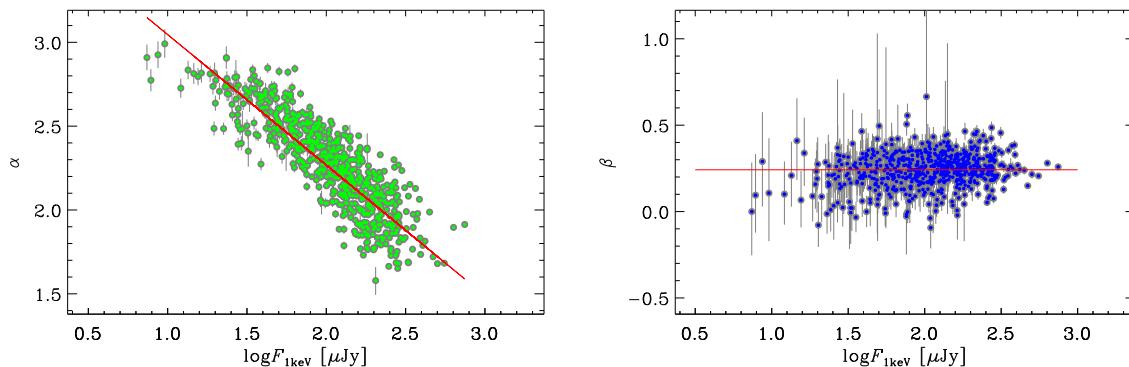


Figure 10. The behaviour of the α (left-hand panel) and β (right-hand panel) parameters of the log-parabola model applied to the XRT spectra of Mrk 421 as a function of the unabsorbed flux density at 1 keV. The solid lines represent linear fits to the data.

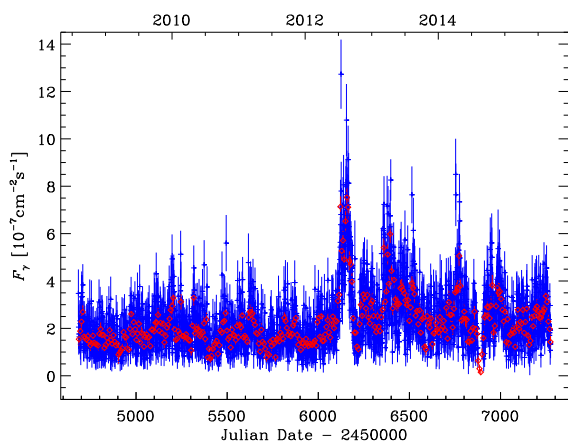


Figure 11. The *Fermi*-LAT 0.1–300 GeV fluxes (10^{-7} photons $\text{cm}^{-2} \text{s}^{-1}$) derived with different time bins in the 2008–2015 period (red symbols refer to weekly binned data and blue symbols to daily binned data).

analysis was performed with the science tool `gtlike` and the response function `P8R2_SOURCE_V6`. Background was modelled with isotropic (`iso_source_v06.txt`) and Galactic diffuse emission (`gll_iem_v06.fit`) components.

As in the 3FGL catalogue, we used a power-law model for the Mrk 421 spectrum. A first maximum likelihood analysis was performed over the whole period to remove from the model the sources having Test Statistics⁷ less than 10. A second maximum likelihood was run on the updated source model.

Integrating over the whole period, the fit gives $\text{TS} = 111714$ in the 0.1–300 GeV energy range, with an integrated average flux of $(2.18 \pm 0.02) \times 10^{-7}$ photons $\text{cm}^{-2} \text{s}^{-1}$ and a photon index $\Gamma = 1.77 \pm 0.01$. The high statistical significance allowed us to obtain weekly binned and even daily binned light curves, which are displayed in Fig. 11. The spectral indices of Mrk 421 and all sources within 10° were frozen to the values resulting from the likelihood analysis over the entire period.

8 MULTIWAVELENGTH BEHAVIOUR

Fig. 12 compares the time evolution of the Mrk 421 flux at different frequencies in the 2007–2015 period. The 2013 outburst was observed at all frequencies, while the X-ray outbursts in 2008 and 2010 lack a major optical counterpart (and the latter also a γ counterpart) and are difficult to identify in UV because of sparse sampling. In contrast, in 2011, we notice a flare in UV, optical and near-IR, but not in X-rays and γ -rays. In γ -rays, a major outburst is observed in 2012, at the same time of the strongest optical event. Other noticeable γ -ray flares were detected in 2013 and 2014. In general, the source behaviour at γ energies appears similar to that observed in the optical band, while the X-ray light curve seems quite different (see also Donnarumma et al. 2009).

In Fig. 13, we compare the source behaviour in X-ray and *R* band. The long-term trend is traced by means of cubic spline interpolations through the 15-d binned light curves. The ratio between the X-ray and optical splines is displayed in the bottom panel and highlights that the X-ray emission strongly dominates from 2007 June to 2009 June, its importance decreases from 2009 June to 2010 July, and

⁷ This is defined as: $\text{TS} = 2(\log L_1 - \log L_0)$, where L_1 and L_0 are the likelihood of the data when the model includes or excludes the source, respectively (Mattox et al. 1996).

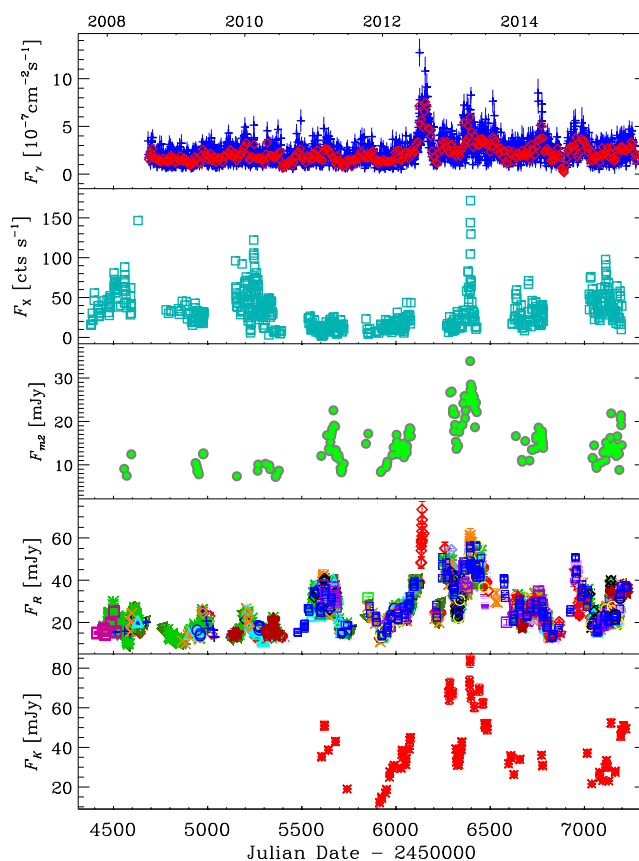


Figure 12. Multiwavelength emission behaviour of Mrk 421 as a function of time. From the top to bottom: the γ -ray fluxes in the 100 MeV–300 GeV energy range from *Fermi*, red diamonds/blue plus signs refer to weekly/daily binned data; the X-ray count rate from *Swift*-XRT; the *Swift*-UVOT observed flux densities in the *m2* band (mJy); the *R*-band observed flux densities (mJy); and the *K*-band observed flux densities (mJy). Data in the *m2*, *R* and *K* filters were cleaned from the host-galaxy light contamination.

reaches a minimum in 2010 October–2012 June, when the source is very active in the optical band. Starting from 2013, the ratio appears to moderately increase again.

In HBLs, the optical and X-ray emissions are thought to be both produced by synchrotron process. The variability of the X-ray-to-optical flux ratio in Mrk 421 then may indicate that the jet zones from where the X-ray and optical radiations are emitted do not coincide and are characterized by their own short-term variability. Moreover, the fact that periods of X-ray flux dominance alternate with periods of optical flux dominance suggests that the corresponding emitting regions belong to a curved jet whose orientation changes may alternatively favour the Doppler enhancement of one region with respect to the other (e.g. Villata et al. 2009a,b). An alternative explanation would be that of a one-zone model where the jet parameters change so that the synchrotron peak frequency shifts, modifying the ratio between the X-ray and optical fluxes. However, this kind of model met some difficulties in explaining the behaviour of Mrk 421 during the 2008 active state (e.g. Aleksić et al. 2012).

9 VARIABILITY OF THE OPTICAL POLARIZATION

As mentioned in the Introduction, the polarized blazar emission shows a variable degree of linear polarization (P) and electric

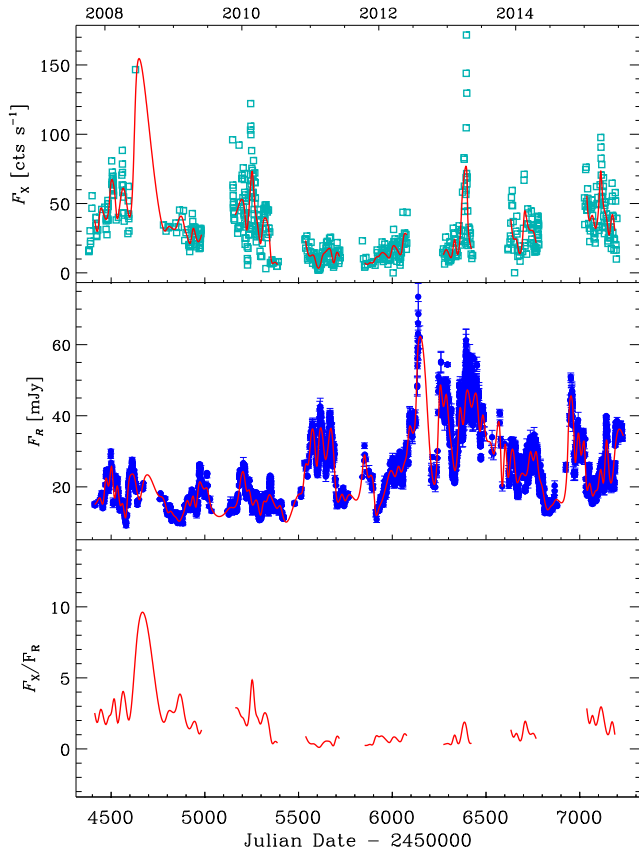


Figure 13. Top panel: the X-ray count rate from *Swift*-XRT. Middle panel: the *R*-band flux densities (mJy). In both panels cubic spline interpolations through the 15-d binned light curves are shown. Bottom panel: the ratio between the X-ray and the optical spline fits.

vector polarization angle (EVPA; e.g. Smith 1996). We analyse the polarimetric behaviour of Mrk 421 by means of 1430 optical data acquired as *R*-band photo-polarimetry by the Lowell (Perkins), Crimean, Calar Alto observatories, and as spectropolarimetry by the Steward Observatory. In the latter case, the values of P and EVPA are derived from the median of the normalized Stokes' parameters $q = Q/I$ and $u = U/I$ in the 5000–7000 Å bandpass, whose effective wavelength is close to the Cousins' *R* band. A description of the data acquisition and reduction procedures is given in Jorstad et al. (2010), Larionov et al. (2008) and Smith et al. (2003).

The time evolution of the observed P and EVPA is shown in Fig. 14. A cubic spline interpolation through the 15-day binned percentage polarization curve is drawn to highlight the long-term behaviour.

In order to determine the degree of polarization intrinsic to the jet, the unpolarized contribution of the galaxy must be subtracted. The intrinsic polarization is computed using the following expression:

$$P_{\text{jet}} = \frac{F_{\text{pol}}}{F_{\text{jet}}} = \frac{P_{\text{obs}} \times F_{\text{obs}}}{F_{\text{obs}} - F_{\text{gal}}}. \quad (1)$$

This is compared to the γ -ray and *R*-band light curves in Fig. 15.⁸ The $\pm 180^\circ n$ (where n is an integer number) ambiguity in EVPA was treated by choosing at each epoch that angle among EVPA,

⁸ The number of P data points in Fig. 15 is smaller than in Fig. 14 because to calculate P_{jet} we need F_{obs} (see equation 1), which was not always available.

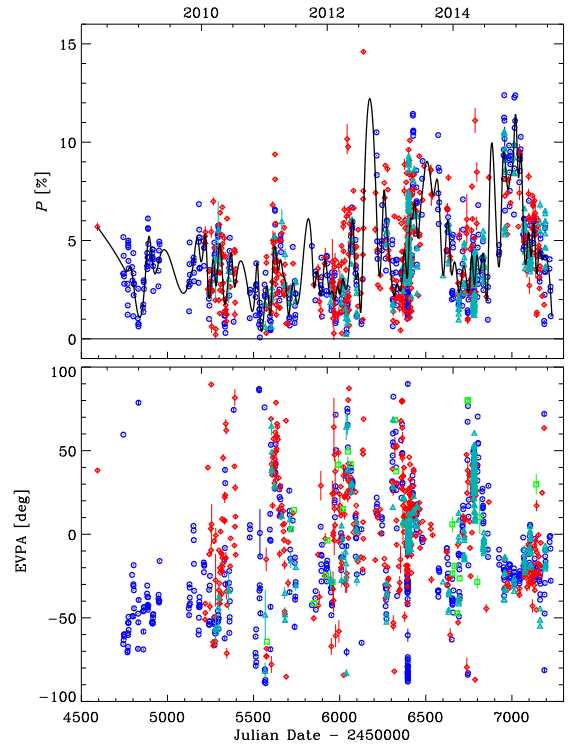


Figure 14. Top panel: the observed degree of polarization as a function of time; the black line represents a cubic spline interpolation through the 15-d binned data. Bottom panel: the observed EVPAs in the -90° and $+90^\circ$ range. Data are from the Calar Alto (green squares), Crimean (red diamonds), Lowell (cyan triangles) and Steward (blue circles) Observatories.

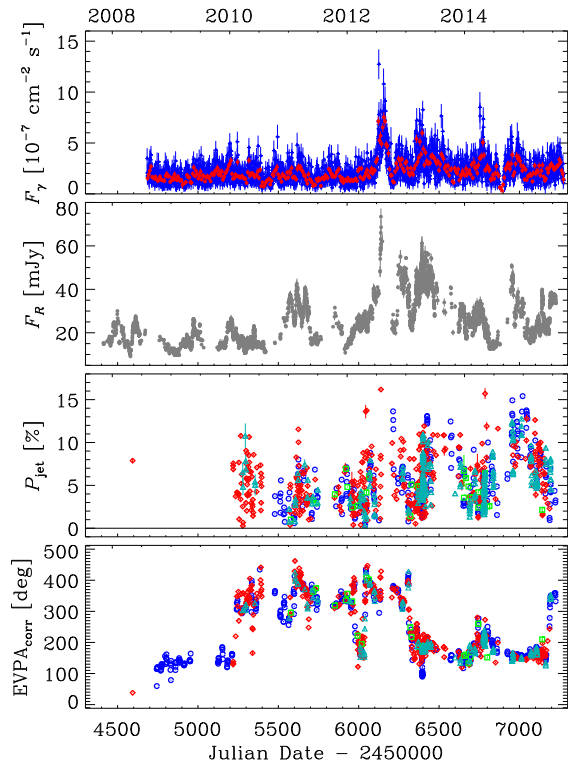


Figure 15. From the top to bottom: the γ -ray fluxes between 100 MeV and 300 GeV; the *R*-band flux densities cleaned from the host-galaxy light contamination; the degree of polarization of the jet emission; the EVPA after fixing the $\pm 180^\circ n$ ambiguity. Symbols and colours as in Fig. 14.

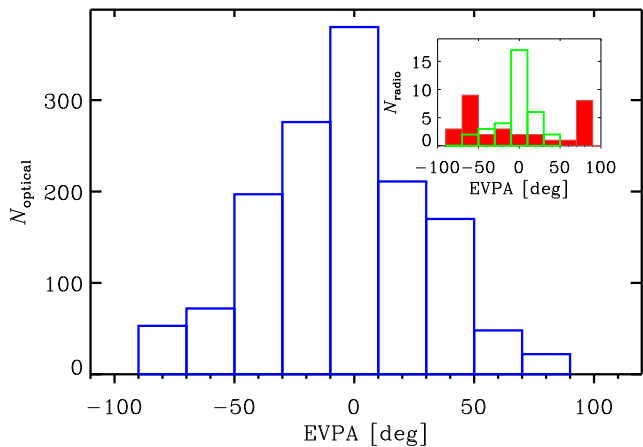


Figure 16. The distribution of the optical EVPAs; the inset displays those of the radio EVPAs at 43 GHz (green line) and at 15 GHz (red histogram).

EVPA+180° and EVPA−180° that leads to a minimum angle difference with respect to the previous epoch. In this choice, we also considered the errors on the EVPAs.

The polarization degree ranges between 0.07 and 14.6 per cent, with a mean value of about 4 per cent. The fractional variability F_{var} (see Section 6.2) for P is ~ 0.56 , significantly larger than that of both optical and γ -ray fluxes, which is ~ 0.40 . This suggests that polarization is likely to be dominated by shorter time-scale effects than the optical and γ -ray flux variability. In any case, the figure shows that there are periods where a high flux corresponds to a high polarization degree, but this is not a general rule.

The EVPA values cluster around a mean value of $\sim 4^\circ$ (see Fig. 16), but wide rotations appear after arranging the angles to fix the $\pm 180^\circ n$ ambiguity. Fig. 16 also shows the distribution of radio EVPAs at 43 and 15 GHz from the Boston University Blazar Group⁹ and MOJAVE Project¹⁰ (Lister et al. 2009), respectively. The number of radio data is small, but they suggest that the direction of the 43 GHz polarization is aligned with the optical one, while the 15 GHz emission, likely coming from an outer jet region, has a transverse polarization angle. A flip by 90° in EVPA usually means that there is a change from optically thin to optically thick properties of the region that most likely has happened between 43 and 15 GHz. In Fig. 17, we plot enlargements of Fig. 15 in different periods to better distinguish the variability properties. We warn that in some cases wide rotations may derive from EVPA shifts performed when the angle difference between subsequent points was around 90° . Though we have considered the angle uncertainties, it is clear that an underestimate of the error in these cases could lead to an apparent wider rotation. This happens in the following dates: JD = 2455234, 2455340 and 2455974. In contrast, there are cases where the rotation appears quite robust. In particular, around JD = 2456040, we observe a counter-clockwise rotation of $\sim 250^\circ$ in about 10 d. This happens when P reaches a local maximum of ~ 10 per cent and the flux is rising towards the peak of 2012 July and August. Another noticeable episode occurred in the last observing season. The EVPA remained stable for several months, and then rotated by $\sim 180^\circ$ in a counter-clockwise direction in about one month around JD = 2457180. We note that P experienced a local minimum at about half-way of the rotation and two symmetric

maxima at the beginning and at the end of the rotation. This behaviour has already been observed in 3C 279 and was interpreted by Nalewajko (2010) in terms of an emitting blob encountering a major bending while travelling in the jet. If we apply that model to our case, assuming a Lorentz factor $\Gamma_{\text{jet}} = \Gamma_{\text{blob}} = 10$, we find a minimum angle between the blob velocity vector and the line of sight of 3.4° , a curvature radius of the trajectory of about 6.6×10^{14} cm, and a distance covered by the blob between the minimum and maximum of P of about 5.3×10^{13} cm. As in the case of 3C 279, the lack of a simultaneous optical flare at the time of the minimum P would mean that the blob gives only a very small contribution to the total observed flux.

In Fig. 18, we show both P_{obs} versus F_{obs} and P_{jet} versus F_{jet} . It can be noticed that in both cases no apparent correlation exists between the two quantities.

Fig. 19 shows the distribution of the Stokes' parameters of Mrk 421 in the u versus q plot, highlighting the EVPA rotation that occurred in 2015 May and June. To this aim, subsequent points have been connected with a cubic spline interpolation. The distance of the spline from the origin, together with the wideness of the spline and the persistence of the direction of rotation, confirms the genuine nature of the rotation.

10 SPECTROPOLARIMETRIC OBSERVATIONS

We analysed 603 spectra from the Steward Observatory data base to investigate the optical spectropolarimetric variability properties of Mrk 421. Fig. 20 shows the source spectra corresponding to the brightest and faintest states. They lack emission lines and point out a bluer-when-brighter behaviour. In the fainter spectrum, we can recognize the Mg I and Na I absorption lines from the host galaxy.

Fig. 21 shows the optical colour of Mrk 421 as a function of the R -band flux density. The colour is determined as the ratio between the median flux in the range 4000–5000 Å ('blue') and that in the 5800–6800 Å range ('red').¹¹ Here, again we note a bluer-when-brighter trend.

We then investigated the wavelength dependence of the optical polarization. We did not find correlation between the degree of optical linear polarization P and the ratio between the blue and the red fluxes (see Fig. 22).

Fig. 23 shows flux densities and polarization percentages for the two wavelength ranges. The blue side is characterized by higher flux variability and polarization degree than the red one, consistently with the larger contribution of the host galaxy light in the red range.

Fig. 24 shows the flux ratio between the blue and the red bins plotted against the ratio of the observed polarization in the same bins. As the blazar becomes fainter (redder), the polarization in the blue tends to be higher than in the red because of the increasing contribution from the red and unpolarized host galaxy light. However, in the faint states, the low levels of polarization result in relatively large uncertainties in $P_{\text{blue}}/P_{\text{red}}$. Fig. 24 also shows the difference between the polarization position angles determined in the two continuum bins. The plot suggests that there is no wavelength dependence in EVPA.

⁹ <https://www.bu.edu/blazars/research.html>

¹⁰ <http://www.physics.purdue.edu/MOJAVE/>

¹¹ We could not use the reddest part of the spectra (from 6800 to 7550 Å) because it includes terrestrial oxygen and water absorption features.

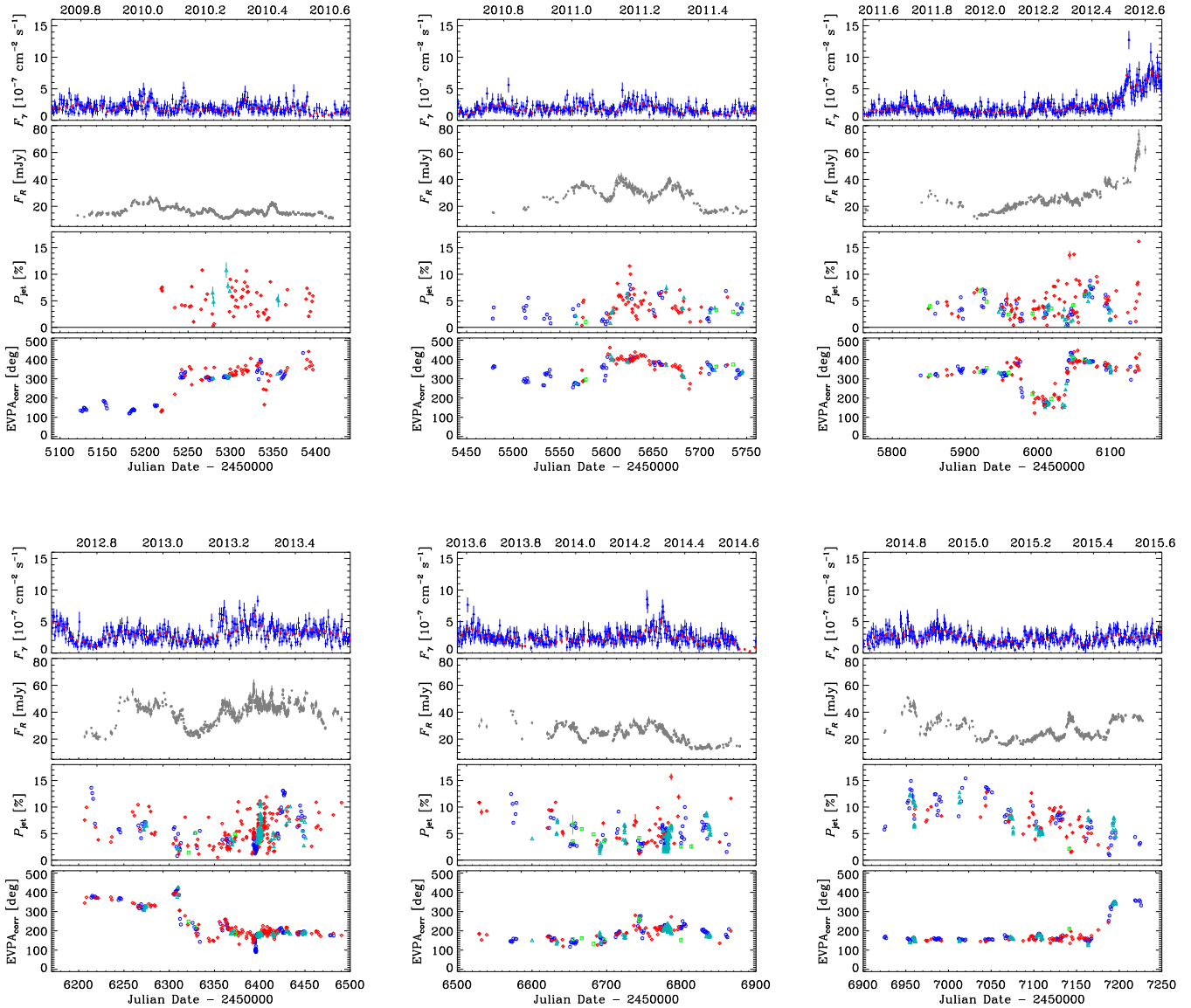


Figure 17. Enlargements of Fig. 15 to appreciate short-term variability.

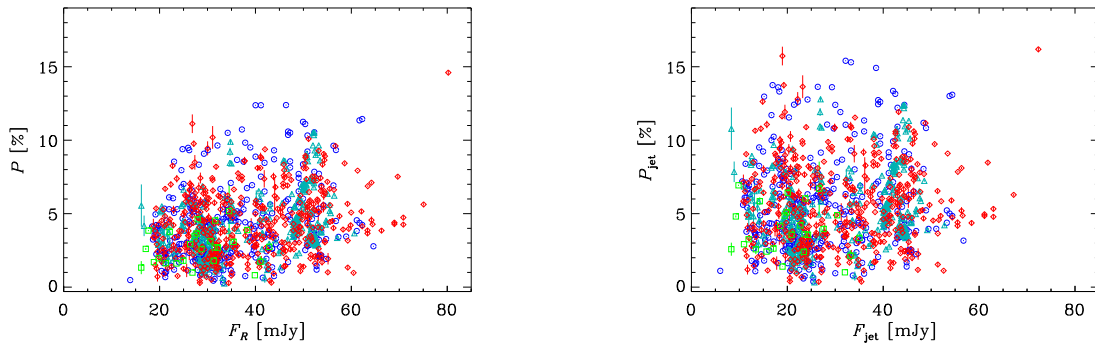


Figure 18. Left-hand panel: The observed degree of polarization as a function of the observed *R*-band flux density. Right-hand panel: The same plot after correcting for the host contribution.

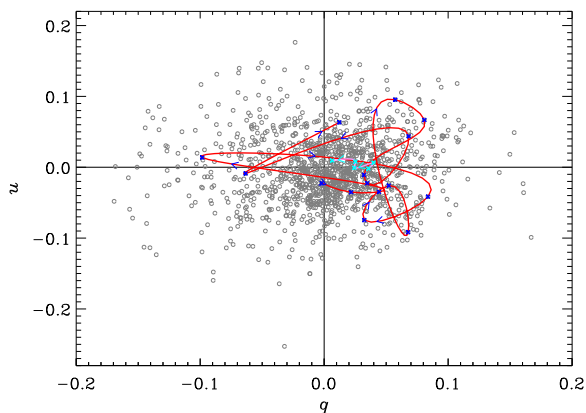


Figure 19. Distribution of the Stokes' parameters in the u versus q plot. The red line highlights the EVPA rotation that occurred in 2015 May and June and was obtained by connecting subsequent points with a cubic spline interpolation. The arrows indicate the time evolution.

11 DISCRETE CORRELATION FUNCTION

We apply the discrete correlation function (DCF) analysis to the data shown in Fig. 12 in order to investigate the existence of characteristic time-scales of variability and the correlation between the γ -ray, X-ray and optical fluxes. This method is suitable to treat unevenly sampled data sets (Edelson & Krolik 1988; Hufnagel & Bregman 1992). Correlation/anticorrelation produces a positive/negative peak of the DCF. The correlation is strong if the peak value approaches or even exceeds one.

The DCF between the X-ray and R -band light curves over the whole 2007–2015 period is shown in Fig. 25. The lack of a strong signal suggests that the X-ray and optical variations are, in general, not correlated. The two low peaks at about -130 and -260 d indicate optical events preceding X-ray ones and likely refer to the major flares in 2012–2015.

In the same figure, we show the DCF between the daily binned γ -ray and the X-ray light curves. The central low peak is likely produced by the match of the major X-ray flare of 2013 with a contemporaneous γ -ray flare. Another low peak at a time lag of ~ 250 d comes from the correspondence between the major 2012 optical and 2013 X-ray flares. However, the value of the DCF always maintains low, implying that the correlation is weak.

Finally, Fig. 25 displays the DCF between the daily binned γ -ray and the optical fluxes over the whole data trains. The value of the DCF at the central maximum is 0.48 and indicates fair cor-

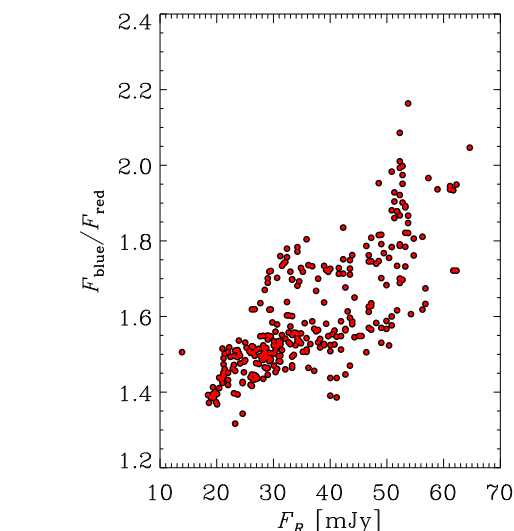
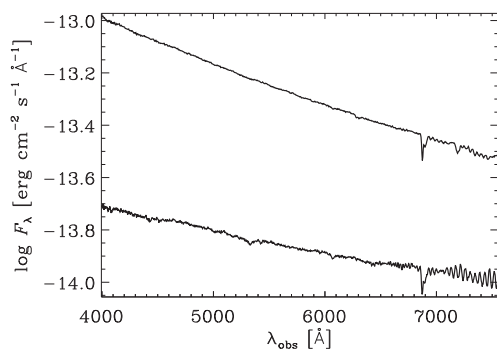


Figure 21. The Mrk 421 optical colour ('blue' to 'red' flux ratio) as a function of the source brightness (observed R -band flux density in mJy).

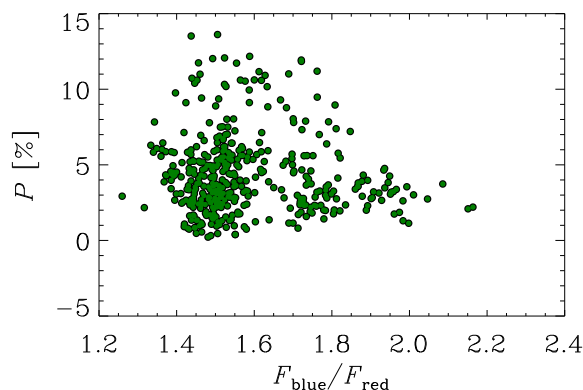


Figure 22. The observed degree of polarization plotted against the optical colour of Mrk 421. The polarization and flux ratio measurements are simultaneous.

relation between the flux variations in the γ -ray and optical bands. The central maximum is broad, possibly because of the superposition of different signatures. To check this, we divided the considered period in three subperiods: the time interval before the big 2012 γ -optical outburst (JD < 2456000), the time interval after

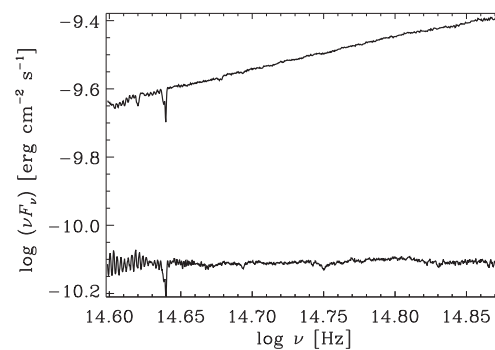


Figure 20. Left-hand panel: the brightest and faintest spectra in the Steward Observatory data base. Their flux density ratio is ~ 5 . Right-hand panel: the same spectra in the $\log(\nu F_\nu)$ versus $\log \nu$ representation used for the SED.

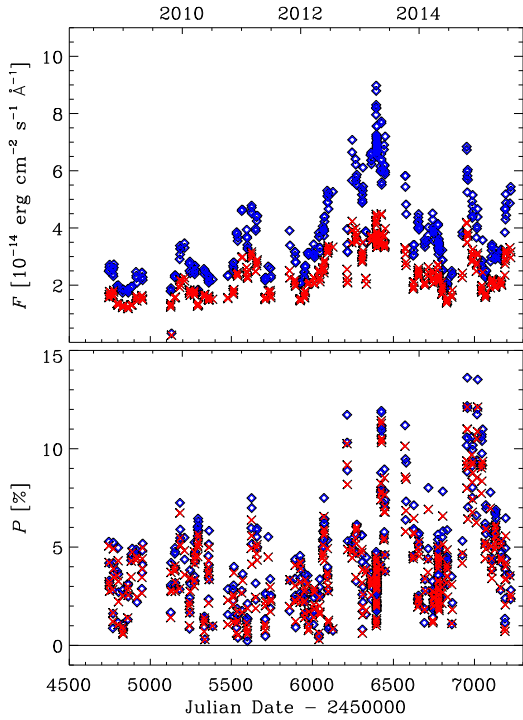


Figure 23. The observed optical flux density (top panel) and polarization percentage (bottom panel) as a function of time in the blue and red bins defined in the text.

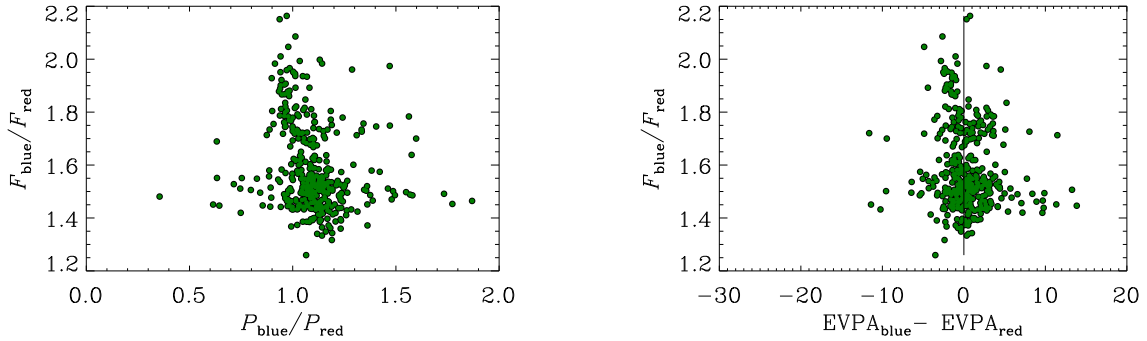


Figure 24. Left-hand panel: the relationship between the ratio of observed polarization in the blue and red bins and the colour defined as in Fig. 21. Right-hand panel: colour versus the difference between the polarization position angles in the blue and red bins.

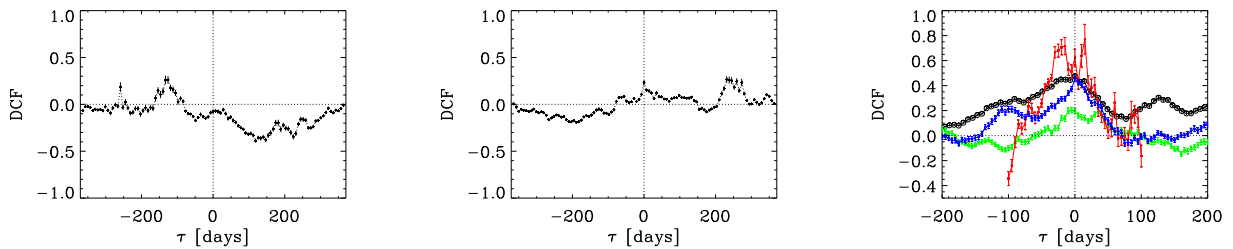


Figure 25. DCF between the X-ray and R-band light curves (left-hand panel); the daily binned γ -ray and X-ray light curves (middle panel); the daily binned γ -ray and R-band light curves (right-hand panel, empty black circles) over the whole 2007–2015 period. In the last panel, we also show the results of the DCF run on the three subperiods corresponding to the time intervals before the 2012 outburst (green triangles), after the outburst (blue diamonds) and around the outburst (red squares).

the outburst ($JD > 2456200$) and the time interval including the outburst ($2456000 < JD < 2456200$). We then calculated the γ -optical cross-correlation for the three periods separately. Before the big outburst, the DCF value is always very low, indicating a poor correlation; after the outburst, the strength of the correlation increases and the central peak (DCF = 0.46) suggests a fair correlation with essentially no time delay. Around the outburst, the correlation is strong, as expected, but the timing is badly defined, with γ variations that can either precede or follow the optical ones. This ambiguity is essentially due to the lack of optical data during the 2012 solar conjunction, when the γ -ray outburst was still at its highest levels.

The optical, X-ray and γ -ray auto correlation functions (ACFs) are plotted in Fig. 26. The peaks are low and their lags reflect the time separation between flares in the corresponding light curves. None of these time-scales can be considered as a periodicity. A recent detailed periodicity analysis on the γ and optical light curves of Mrk 421 by Sandrinelli et al. (2017) found no periodic signals.

12 BROAD-BAND SPECTRAL VARIABILITY

We built IR-to-X-ray SEDs to investigate the spectral variability of Mrk 421 around the synchrotron peak. In order to be able to reliably characterize and model the region of the SED around the synchrotron peak, we considered all the observing epochs where strictly simultaneous data in the K, H, J, R bands from the WEBT Collaboration and at UV and X-ray frequencies from the *Swift*

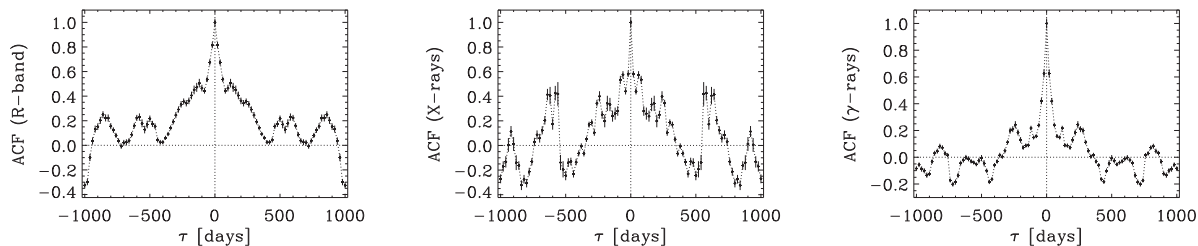


Figure 26. ACF for the galaxy-subtracted optical flux densities (left-hand panel), X-ray count rates (middle panel) and γ -ray fluxes (right-hand panel).

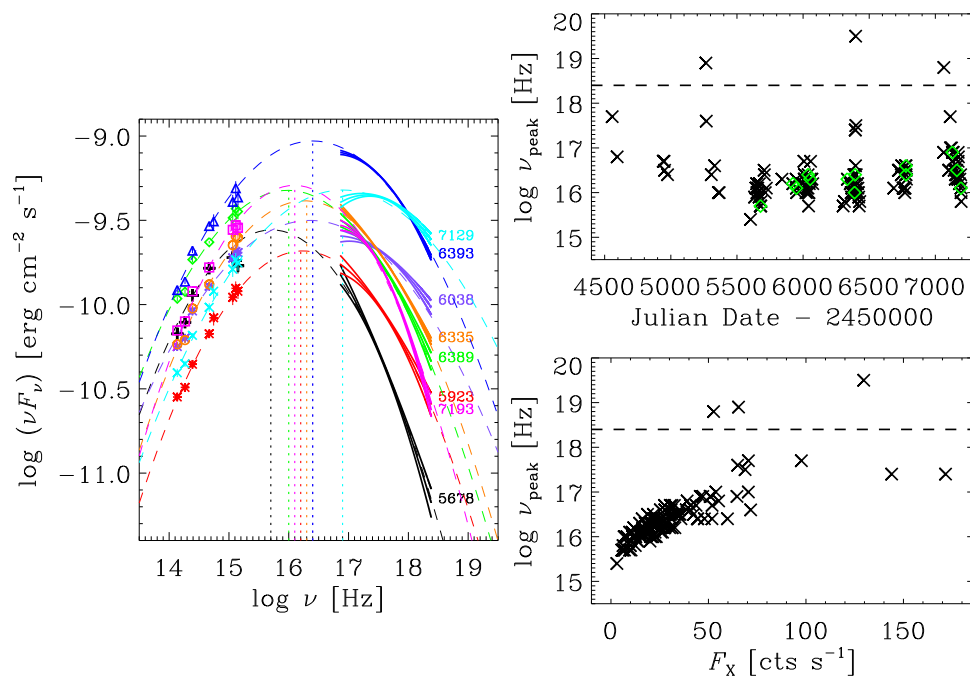


Figure 27. Left-hand panel: broad-band SEDs of Mrk 421 at eight different epochs (identified on the right with their JD – 2450000) where simultaneous near-IR, optical, UV and X-ray data are available. Right-hand panels: The synchrotron peak frequency versus time (top panel) and X-ray flux (bottom panel). The horizontal lines correspond to 10 keV, the upper limit of the energy range covered by XRT. In the top panel, the diamonds represent the cases where also near-IR data were available and included in the SED fit.

satellite were available. Eight of these SEDs¹² are shown in Fig. 27, covering a wide range of brightness states. In three cases, we also found UVOT data in the ν band. The errors in the near-IR and optical flux densities are typically around 3 per cent and are included in the symbol size, while we conservatively assumed a 10 per cent error on the UVOT data. The X-ray spectra are the result of a log-parabola model fitting, including the uncertainties on the flux normalization and α and β parameters.

We also show log-parabolic fits to the broad-band SEDs and the position of the synchrotron peak they identify. The X-ray spectral variability is quite strong and suggests that the frequency of the synchrotron peak can shift over a large range, from $\log \nu \sim 15.7$ to 16.9 [Hz]. Taking into account the curvature of the X-ray spectra alone, the range could be even broader, up to $\log \nu \sim 17.4$ of the JD = 2457129 SED, i.e. a factor 50 in frequency. From these few SEDs, the relationship between the brightness state and the

synchrotron peak frequency appears confused. In particular, the highest peak frequency (JD = 2457129) does not correspond to the highest X-ray flux (JD = 2456393). To better investigate this point, we built SEDs of all epochs with contemporaneous *Swift* and *R*-band data and fit them with a log-parabolic model. The results are shown in Fig. 27. There is a general indication that the synchrotron peak frequency follows the X-ray activity, shifting towards higher values when the X-ray flux increases. The increase is fast below ~ 30 counts s^{-1} , then the curve flattens. Values of $\log \nu_{\text{peak}}$ larger than 17 are reached only if the X-ray count rate is greater than 50 counts s^{-1} . Beyond this general behaviour, there are specific cases with peculiar spectral shapes. There are three cases where the X-ray spectrum is hard so that ν_{peak} falls beyond the 10 keV upper limit of the XRT energy range.

The only steep UV spectrum is shown by the SED on JD = 2455678, corresponding to the faintest and softest X-ray spectrum. We also note that its near-IR and optical part fairly matches that observed at JD = 2457193, but the latter has much brighter UV and X-ray states. If the UV spectrum steepness on JD = 2455678 were real and not due to data uncertainties, its extrapolation to the

¹² The other five SEDs overlap with them and were omitted for sake of clarity.

higher energies would not meet the X-ray spectrum, raising the question whether more than one component is contributing to the source synchrotron flux. The same issue was encountered when comparing the optical and X-ray light curves in Section 8. Similar mismatches in the SED have already been found for this source (Massaro et al. 2004) and were sometimes observed in other HBLs, like PG 1553+113 (Raiteri et al. 2015) and H1722+119 (Ahnen et al. 2016a). In these two cases, they have been interpreted in terms of orientation variations in an inhomogeneous helical jet.

Another pair of SEDs having the same near-IR and optical flux, but a different UV flux and very different X-ray spectra are those on JD = 2456038 and 2456335. Here, a higher UV state corresponds to a softer and less curved X-ray spectrum.

13 SUMMARY AND CONCLUSIONS

In this paper, we have analysed 8 yr of multiwavelength data on the HBL Mrk 421. The GASP-WEBT Collaboration and Steward Observatory provided the near-IR and optical photometric and polarimetric data. Information in the UV and X-ray bands was acquired from the *Swift* satellite and in γ -rays from the LAT instrument on-board *Fermi*. We have also exploited the spectropolarimetric data taken at the Steward Observatory to investigate a possible wavelength dependence of the polarization degree P and angle EVPA. We have calculated the host galaxy contribution to the source photometry in the near-IR, optical and UV bands and subtracted it to analyse the jet emission.

The source showed unceasing activity at all frequencies over all the 2007–2015 period we considered. Variability in the near-IR, UV and γ -ray flux appears well correlated with the optical one, showing prominent flares in 2012–2013. In contrast, the behaviour in X-rays does not follow the same path and X-ray flares occurred in 2008, 2010 and 2013. In γ -rays, the most noticeable event occurred in 2012, while significant flares were also observed in 2013–2014. DCF analysis suggests the lack of a persistent X-ray–optical correlation while indicates a fair correlation between the γ -ray and optical flux changes since 2012.

The spectral variability increases with frequency: Broad-band SEDs show that the near-IR to optical spectral shape is rather stable for different brightness states, while the upturn towards the UV can be more or less pronounced, and this corresponds to a different X-ray spectral form. Indeed, X-ray spectra exhibit a large variety of slopes and curvatures and suggest that the synchrotron peak may cover a large range of frequencies and, in general, shifts towards higher energies when the X-ray flux increases.

The energy output from Mrk 421 has often been interpreted with one-zone SSC models (e.g. Aleksić et al. 2012) or with leptohadronic models involving proton synchrotron radiation and/or photopion interactions (e.g. Böttcher et al. 2013). In these models, the variations of the SED shape are obtained by changing the parameters determining the jet physics. In particular, these changes can produce a shift of the synchrotron peak frequency and, in turn, a lack of correlation between the optical and X-ray emission, even if these two emissions are physically connected. Alternatively, we propose the existence of at least two emitting regions in the jet to explain the different behaviour of the optical and X-ray fluxes. These regions are disjointed and experience independent short-term variability. Moreover, their orientation can likely change in time, so that periods of high X-ray activity would be observed when the part of the jet producing this radiation is more closely aligned with the line of sight. Similarly, when the viewing angle of the optical

emitting region decreases, the optical flux would be more Doppler enhanced.

We have analysed polarimetric data to look for episodes where the behaviour of P and EVPA can suggest that the source variability is due to geometrical effects, like a curved motion of a blob in a helical jet (Nalewajko 2010). We found a possible candidate in the last part of the campaign, and derived the minimum angle between the blob velocity vector and the line of sight, the curvature radius of the trajectory and the distance covered by the blob during that event. Apart from this case, we have not found any correlation between the source flux, and the P and EVPA changes, which strongly suggests that turbulence may play a major role in determining the source polarimetric properties (Marscher 2014; Blinov et al. 2016; Kiehlmann et al. 2016; Raiteri et al. 2017).

ACKNOWLEDGEMENTS

We are grateful to an anonymous referee for useful comments and suggestions. The data collected by the WEBT collaboration are stored in the WEBT archive at the Osservatorio Astrofisico di Torino – INAF (<http://www.oato.inaf.it/blazars/webt/>); for questions regarding their availability, contact the WEBT President Massimo Villata (villata@oato.inaf.it). This article is partly based on observations made with the telescopes IAC80 and TCS operated by the Instituto de Astrofísica de Canarias in the Spanish Observatorio del Teide on the island of Tenerife. The IAC team acknowledges the support from the group of support astronomers and telescope operators of the Observatorio del Teide. Based (partly) on data obtained with the STELLA robotic telescopes in Tenerife, an AIP facility jointly operated by AIP and IAC. The Steward Observatory blazar monitoring programme is funded by NASA through Fermi Guest Investigator grants NNX08AW56G, NNX09AU10G, NNX12AO93G and NNX15AU81G. The Abastumani team acknowledges financial support by Shota Rustaveli NSF under contract FR/577/6-320/13. The research at BU was supported in part by US National Science Foundation grant AST-1615796 and NASA Fermi Guest Investigator grant NNX14AQ58G. This study makes use of 43 GHz VLBA data from the VLBA-BU Blazar Monitoring Program (VLBA-BU-BLAZAR; <http://www.bu.edu/blazars/VLBAproject.html>), funded by NASA through the Fermi Guest Investigator Program. The PRISM camera at the Lowell Observatory was developed by K. Janes et al. at the BU and Lowell Observatory, with funding from the NSF, BU and Lowell Observatory. This research has made use of data from the MOJAVE data base, which is maintained by the MOJAVE team (Lister et al. 2009). The St. Petersburg University team acknowledges support from Russian RFBR grant 15-02-00949 and St. Petersburg University research grant 6.38.335.2015. This paper is partly based on observations carried out at the German-Spanish Calar Alto Observatory, which is jointly operated by the MPIA and the IAA-CSIC. IA research is supported by a Ramón y Cajal grant of the Spanish Ministerio de Economía y Competitividad (MINECO). Acquisition of the MAPCAT data was supported in part by MINECO through grants AYA2010-14844, AYA2013-40825-P and AYA2016-80889-P, and by the Regional Government of Andalucía through grant P09-FQM-4784. This research was partially supported by the Scientific Research Fund of the Bulgarian Ministry of Education and Sciences under grants DO 02-137 (B13/09) and DN 08/1. The Skinakas Observatory is a collaborative project of the University of Crete, the Foundation for Research and Technology – Hellas and the Max-Planck-Institut für Extraterrestrische Physik. GD and OV gratefully acknowledge the observing grant support from the Institute of Astronomy and Rozhen National

Astronomical Observatory, Bulgaria Academy of Sciences, via the bilateral joint research project ‘Observations of ICRF radio-sources visible in optical domain’ (the head is Dr G. Damjanovic). This work is a part of the Projects No 176011 (‘Dynamics and kinematics of celestial bodies and systems’), No 176004 (‘Stellar physics’) and No 176021 (‘Visible and invisible matter in nearby galaxies: theory and observations’) supported by the Ministry of Education, Science and Technological Development of the Republic of Serbia. The Serbian station is the Astronomical Station Vidojevica (ASV) with the 60-cm ASV telescope (and from this year, the 1.4-m ASV one). This research was supported partly by funds of the project RD-08-81 of the Shumen University.

REFERENCES

- Abdo A. A. et al., 2011, *ApJ*, 736, 131
 Acero F. et al., 2015, *ApJS*, 218, 23
 Aharonian F. et al., 2005, *A&A*, 437, 95
 Ahnen M. L. et al., 2016, *MNRAS*, 459, 3271
 Ahnen M. L. et al., 2016, *A&A*, 593, A91
 Albert J. et al., 2007, *ApJ*, 663, 125
 Aleksić J. et al., 2012, *A&A*, 542, A100
 Aleksić J. et al., 2015, *A&A*, 576, A126
 Aleksić J. et al., 2015, *A&A*, 578, A22
 Atwood W. B. et al., 2009, *ApJ*, 697, 1071
 Atwood W. et al., 2013, in Brandt T. J., Omodei N., Wilson-Hodge C., eds., Proc. of the 4th Fermi Symposium, Monterey, California
 Baloković M. et al., 2016, *ApJ*, 819, 156
 Bessell M. S., Castelli F., Plez B., 1998, *A&A*, 333, 231
 Blasi M. G. et al., 2013, *A&A*, 559, A75
 Blinov D. et al., 2016, *MNRAS*, 462, 1775
 Böttcher M., Reimer A., Sweeney K., Prakash A., 2013, *ApJ*, 768, 54
 Burrows D. N. et al., 2005, *Space Sci. Rev.*, 120, 165
 Cardelli J. A., Clayton G. C., Mathis J. S., 1989, *ApJ*, 345, 245
 Carnerero M. I. et al., 2015, *MNRAS*, 450, 2677
 Carnerero M., Raiteri C., Villata M., Acosta Pulido J., Smith P., Larionov V., 2016, *Galaxies*, 4, 61
 Donnarumma I. et al., 2009, *ApJ*, 691, L13
 Edelson R. A., Krolik J. H., 1988, *ApJ*, 333, 646
 Hartman R. C. et al., 1999, *ApJS*, 123, 79
 Hovatta T. et al., 2015, *MNRAS*, 448, 3121
 Hufnagel B. R., Bregman J. N., 1992, *ApJ*, 386, 473
 Ikejiri Y. et al., 2011, *PASJ*, 63, 639
 Jorstad S. G. et al., 2010, *ApJ*, 715, 362
 Kapanadze B. et al., 2016, *ApJ*, 831, 102
 Kiehlmann S. et al., 2016, *A&A*, 590, A10
 Larionov V. M. et al., 2008, *A&A*, 492, 389
 Lico R. et al., 2014, *A&A*, 571, A54
 Lister M. L. et al., 2009, *AJ*, 137, 3718–3729
 Lockman F. J., Savage B. D., 1995, *ApJS*, 97, 1
 Mannucci F., Basile F., Poggianti B. M., Cimatti A., Daddi E., Pozzetti L., Vanzì L., 2001, *MNRAS*, 326, 745
 Marscher A. P., 2014, *ApJ*, 780, 87
 Massaro E., Perri M., Giommi P., Nesci R., 2004, *A&A*, 413, 489
 Mattox J. R. et al., 1996, *ApJ*, 461, 396
 Miller H. R., 1975, *ApJ*, 201, L109
 Nalewajko K., 2010, *Int. J. Mod. Phys. D*, 19, 701
 Nilsson K., Pasanen M., Takalo L. O., Lindfors E., Berdyugin A., Ciprini S., Pforr J., 2007, *A&A*, 475, 199
 Paliya V. S., Böttcher M., Diltz C., Stalin C. S., Sahayanathan S., Ravikulmar C. D., 2015, *ApJ*, 811, 143
 Peterson B. M., 2001, in Arétxaga I., Kunth D., Mújica R., eds., *Advanced Lectures on the Starburst-AGN Connection*. World Scientific, Singapore, p. 3
 Pian E. et al., 2014, *A&A*, 570, A77
 Piner B. G., Pant N., Edwards P. G., 2010, *ApJ*, 723, 1150
 Polletta M. et al., 2007, *ApJ*, 663, 81
 Punch M. et al., 1992, *Nature*, 358, 477
 Raiteri C. M. et al., 2010, *A&A*, 524, A43
 Raiteri C. M. et al., 2015, *MNRAS*, 454, 353
 Raiteri C. M. et al., 2017, *MNRAS*, 466, 3762
 Roming P. W. A. et al., 2005, *Space Sci. Rev.*, 120, 95
 Sandrinelli A. et al., 2017, *A&A*, 600, A132
 Schlegel D. J., Finkbeiner D. P., Davis M., 1998, *ApJ*, 500, 525
 Sinha A., Shukla A., Misra R., Chitnis V. R., Rao A. R., Acharya B. S., 2015, *A&A*, 580, A100
 Skrutskie M. F. et al., 2006, *AJ*, 131, 1163
 Smith A. G., 1996, in Miller H. R., Webb J. R., Noble J. C., eds., *ASP Conf. Ser.*, Vol. 110, *Blazar Continuum Variability*. Astron. Soc. Pac., San Francisco, p. 3
 Smith P. S., Schmidt G. D., Hines D. C., Foltz C. B., 2003, *ApJ*, 593, 676
 Ulrich M.-H., Kinman T. D., Lynds C. R., Rieke G. H., Ekers R. D., 1975, *ApJ*, 198, 261
 Villata M., Raiteri C. M., Lanteri L., Sobrito G., Cavallone M., 1998, *A&AS*, 130, 305
 Villata M. et al., 2009, *A&A*, 504, L9
 Villata M. et al., 2009, *A&A*, 501, 455
 Visvanathan N., Wills B. J., 1998, *AJ*, 116, 2119
 Wilms J., Allen A., McCray R., 2000, *ApJ*, 542, 914
- ¹INAF, Osservatorio Astrofisico di Torino, via Osservatorio 20, I-10025 Pino Torinese, Italy
²Instituto de Astrofísica de Canarias (IAC), La Laguna, E-38200 Tenerife, Spain
³Departamento de Astrofísica, Universidad de La Laguna, La Laguna, E-38205 Tenerife, Spain
⁴Astronomical Institute, St. Petersburg State University, Universitetsky pr. 28, Petrovovoye, 198504 St. Petersburg, Russia
⁵Pulkovo Observatory, 196140 St. Petersburg, Russia
⁶Steward Observatory, University of Arizona, Tucson, AZ 85721, USA
⁷INAF, Istituto di Radioastronomia, via Gobetti 101, I-40129 Bologna, Italy
⁸DIFA, Università di Bologna, Viale B. Pichat 6/2, I-40127 Bologna, Italy
⁹Instituto de Astrofísica de Andalucía, CSIC, Apartado 3004, E-18080 Granada, Spain
¹⁰Institute of Astronomy and NAO, Bulgarian Academy of Sciences, 72 Tsarigradsko shosse Blvd., 1784 Sofia, Bulgaria
¹¹Department of Physics, Salt Lake Community College, Salt Lake City, UT 84070, USA
¹²Department of Astronomy, Faculty of Physics, Sofia University, BG-1164 Sofia, Bulgaria
¹³EPT Observatories, Tifarite, E-38780 La Palma, Spain
¹⁴INAF, TNG Fundación Galileo Galilei, E-38712 La Palma, Spain
¹⁵Max-Planck-Institut für Radioastronomie, Auf dem Hügel, 69, D-53121, Bonn, Germany
¹⁶Graduate Institute of Astronomy, National Central University, 300 Jhongda Road, Jhongli City, Taoyuan County 32001, Taiwan, Republic of China
¹⁷Astronomical Observatory, Volgina 7, 11060 Belgrade, Serbia
¹⁸Agrupació Astronòmica de Sabadell, E-08200 Sabadell, Spain
¹⁹Department of Physics and Astronomy, Brigham Young University, Provo, UT 84602, USA
²⁰Department of Theoretical and Applied Physics, University of Shumen, 9712 Shumen, Bulgaria
²¹School of Cosmic Physics, Dublin Institute For Advanced Studies, D02 XF86, Dublin 2, Ireland
²²Institute for Astrophysical Research, Boston University, 725 Commonwealth Avenue, Boston, MA 02215, USA
²³Abastumani Observatory, Mt. Kanobili, 0301 Abastumani, Georgia
²⁴Engelhardt Astronomical Observatory, Kazan Federal University, 422526 Zelenodolsky region, Tatarstan, Russia

²⁵*Center for Astrophysics, Guangzhou University, Guangzhou 510006, China*

²⁶*Circolo Astrofili Talmassons, I-33030 Talmassons, Italy*

²⁷*UCD School of Physics, University College Dublin, Dublin 4, Ireland*

²⁸*Finnish Centre for Astronomy with ESO (FINCA), University of Turku, FI-21500 Piikkiö, Finland*

²⁹*Department of Physical Science, Southern Utah University, Cedar City, UT 84721, USA*

³⁰*Osservatorio Astronomico Sirio, Piazzale Anelli, I-70013 Castellana Grotte, Italy*

³¹*Department of Physics, University of Colorado Denver, CO 80217-3364 USA*

³²*Cork Institute of Technology, Bishopstown, T12 P928 Cork, Ireland*

This paper has been typeset from a \TeX/L\AA\TeX file prepared by the author.

Synchrotron emission from the blazar PG 1553+113. An analysis of its flux and polarization variability

C. M. Raiteri,^{1★} F. Nicastro,^{2★} A. Stamerra,^{1,3,4★} M. Villata,¹ V. M. Larionov,^{5,6} D. Blinov,^{5,7,8} J. A. Acosta-Pulido,^{9,10} M. J. Arévalo,^{9,10} A. A. Arkharov,⁶ R. Bachev,¹¹ G. A. Borman,¹² M. I. Carnerero,¹ D. Carosati,^{13,14} M. Cecconi,¹⁴ W.-P. Chen,¹⁵ G. Damjanovic,¹⁶ A. Di Paola,² Sh. A. Ehgamberdiev,¹⁷ A. Frasca,¹⁸ M. Giroletti,¹⁹ P. A. González-Morales,^{9,10} A. B. Griñon-Marín,^{9,10} T. S. Grishina,⁵ P.-C. Huang,¹⁵ S. Ibryamov,^{11,20} S. A. Klimanov,⁶ E. N. Kopatskaya,⁵ O. M. Kurtanidze,^{21,22} S. O. Kurtanidze,²¹ A. Lähteenmäki,^{23,24} E. G. Larionova,⁵ L. V. Larionova,⁵ C. Lázaro,^{9,10} G. Leto,¹⁸ I. Liodakis,^{7,8} C. Martínez-Lombilla,^{9,10} B. Mihov,¹¹ D. O. Mirzaqulov,¹⁷ A. A. Mokrushina,⁶ J. W. Moody,²⁵ D. A. Morozova,⁵ S. V. Nazarov,¹² M. G. Nikolashvili,²¹ J. M. Ohlert,^{26,27} G. V. Panopoulou,^{7,8} A. Pastor Yabar,^{9,10} F. Pinna,^{9,10} C. Protasio,^{9,10} N. Rizzi,²⁸ A. C. Sadun,²⁹ S. S. Savchenko,⁵ E. Semkov,¹¹ L. A. Sigua,²¹ L. Slavcheva-Mihova,¹¹ A. Strigachev,¹¹ M. Tornikoski,²³ Yu. V. Troitskaya,⁵ I. S. Troitsky,⁵ A. A. Vasilyev,⁵ R. J. C. Vera,^{23,24} O. Vince¹⁶ and R. Zanmar Sanchez¹⁸

Affiliations are listed at the end of the paper

Accepted 2016 December 19. Received 2016 December 19; in original form 2016 October 17

ABSTRACT

In 2015 July 29–September 1, the satellite *XMM-Newton* pointed at the BL Lac object PG 1553+133 six times, collecting data for 218 h. During one of these epochs, simultaneous observations by the *Swift* satellite were requested to compare the results of the X-ray and optical–UV instruments. Optical, near-infrared and radio monitoring was carried out by the Whole Earth Blazar Telescope (WEBT) collaboration for the whole observing season. We here present the results of the analysis of all these data, together with an investigation of the source photometric and polarimetric behaviour over the last 3 yr. The 2015 EPIC spectra show slight curvature and the corresponding light curves display fast X-ray variability with a time-scale of the order of 1 h. In contrast to previous results, during the brightest X-ray states detected in 2015 the simple log-parabolic model that best fits the *XMM-Newton* data also reproduces reasonably well the whole synchrotron bump, suggesting a peak in the near-UV band. We found evidence of a wide rotation of the polarization angle in 2014, when the polarization degree was variable, but the flux remained almost constant. This is difficult to interpret with deterministic jet emission models, while it can be easily reproduced by assuming some turbulence of the magnetic field.

Key words: galaxies: active – BL Lacertae objects: general – BL Lacertae objects: individual: PG 1553+113.

1 INTRODUCTION

The active galactic nuclei known as ‘blazars’ include flat-spectrum radio quasars and BL Lac objects. They show strong flux variability over all the electromagnetic spectrum, high and variable

* E-mail: raiteri@oato.inaf.it (CMR); fabrizio.nicastro@oa-roma.inaf.it (FN); stamerra@oato.inaf.it (AS)

polarization, superluminal motion of the radio knots, brightness temperatures exceeding the Compton limit. These properties are explained by assuming that blazar emission comes from a plasma jet oriented close to the line of sight, implying relativistic beaming of the radiation (Blandford & Königl 1979). This is produced by synchrotron and likely inverse-Compton processes at low and high energies, respectively (Königl 1981).

The source PG 1553+113 is a high-energy peaked BL Lac object (HBL), which means that its spectral energy distribution (SED) shows a synchrotron bump extending from the radio to the X-rays, and an inverse-Compton bump from X-rays to TeV energies. For these sources, the inverse-Compton radiation is usually assumed to originate from the scattering of synchrotron photons by the same relativistic electrons that produce the synchrotron emission (SSC models; e.g. Mastichiadis & Kirk 1997). The redshift of PG 1553+113 has been investigated in several ways, but has not been firmly established yet. Constraints derived from the analysis of the intergalactic absorption features set it in the range $0.43 < z < 0.58$ (Danforth et al. 2010). Lower limits to the redshift were also obtained from spectroscopy, $z > 0.12$ (Shaw et al. 2013) and $z > 0.3$ (Landoni et al. 2014). Studies of the very-high-energy (VHE, $E > 100$ GeV) spectrum suggested $z < 0.5$ (Orr 2011), $z = 0.49 \pm 0.04$ (Abramowski et al. 2015) or $z \sim 0.4$ (Aleksić et al. 2015). The source has recently gained particular attention because of the ~ 2 yr quasi-periodicity of its flares (Ackermann et al. 2015) and because of its possible association with neutrino signals detected by IceCUBE (e.g. Padovani et al. 2016; Righi, Tavecchio & Guetta 2016).

The SED modelling has produced different results. Abdo et al. (2010) obtained satisfactory fits to the broad-band source SED, from the radio to the VHE band, with a one-zone SSC model where the energy distribution of the electrons producing the synchrotron radiation is modelled by a three-component power law. Different source states were accounted for by only changing the parameters determining this law, while Aleksić et al. (2012) had to fine-tune six parameters to explain the noticeable SED variations. A one-zone SSC model was also applied to the broad-band SED observed during the 2012 flaring state by Aleksić et al. (2015).

In 2013, the Whole Earth Blazar Telescope¹ (WEBT) coordinated a multiwavelength campaign on PG 1553+113 in support of MAGIC observations. The results of the WEBT radio-to-optical monitoring were presented in Raiteri et al. (2015) and used together with observations by *Swift* and *XMM-Newton* to analyse the source synchrotron emission. The picture that emerged was enigmatic because the connection between the UV and X-ray spectra seemed to require a double curvature. Possible interpretations were discussed, favouring variations of the viewing angle of the jet emitting regions, whose effects were tested with an inhomogeneous SSC helical jet model (Villata & Raiteri 1999; Raiteri et al. 2009). Different SED shapes corresponding to various brightness states were matched by changing only three parameters defining the jet geometry.

In 2015, nearly 218 h of *XMM-Newton* observing time on PG 1553+113 were awarded to investigate the warm-hot intergalactic medium (WHIM; e.g. Nicastro et al. 2013, and references therein). At the same time, this offered an extraordinary opportunity to study in detail the emission of the blazar itself and, in particular, the problem of the spectral connection between the UV and X-ray regions discussed by Raiteri et al. (2015). To maximize the scientific output, the WEBT organized a new multifrequency campaign involving optical, near-infrared and radio observing facilities. Moreover, *Swift*

Table 1. Logbook of the *XMM-Newton* GO observations of PG 1553+113 in 2015 (PI: F. Nicastro).

Rev.	Start	End	Duration (s)
2864	2015-07-29 19:57:33	2015-07-31 10:24:13	138 400
2866	2015-08-02 19:40:00	2015-08-04 10:15:00	138 900
2867	2015-08-04 19:32:00	2015-08-06 10:07:00	138 900
2869	2015-08-08 19:12:07	2015-08-10 09:47:07	138 900
2873	2015-08-16 18:52:06	2015-08-17 19:52:06	90 000
2880	2015-08-30 17:52:29	2015-09-01 08:29:09	139 000

target of opportunity observations simultaneous to one of the *XMM-Newton* pointings were activated to check for cross-calibration between the optical-UV and X-ray detectors. MAGIC observations were also scheduled in the first half of August. Their results will be reported elsewhere.

In this paper, we present the results of the six *XMM-Newton* guest-observer (GO) pointings at PG 1553+113 in 2015 (Section 2), together with those of the *Swift* observations (Section 3) and WEBT continuous monitoring (Section 4) in the same period. We discuss the SEDs built with contemporaneous data in the six *XMM-Newton* epochs (Section 5). Moreover, we analyse the long-term (2013–2015) optical photometric and polarimetric behaviour of the source in conjunction with that observed in the X-ray band (Section 6) and discuss a possible interpretation (Section 7). Summary and conclusions are outlined at the end (Section 8).

2 OBSERVATIONS BY *XMM-NEWTON*

Six long GO observations of PG 1553+113 were performed by *XMM-Newton* in 2015, between July 29 and September 1 (PI: F. Nicastro). Their logbook is given in Table 1. The total observing time was 784 100 s.

2.1 EPIC

The European Photon Imaging Camera (EPIC) onboard *XMM-Newton* carries three detectors: MOS1, MOS2 (Turner et al. 2001) and pn (Strüder et al. 2001). During the GO observations of PG 1553+113 in 2015, the pn detector was set in full-frame mode² with thin filter; MOS1 operated in small-window mode with thick filter, and MOS2 in small-window mode with thin filter. We ran the `emproc` and `epproc` tasks of the `SAS` package, version 14.0.0, to reduce the data.

2.1.1 Spectra

Good time intervals with low background counts were selected by asking that the count rate of high-energy events (>10 keV) was less than 0.35 and 0.40 counts s^{-1} on the MOS and pn detectors, respectively. We extracted source counts from a circular region with 25–35 arcsec radius and the background counts from a source-free circle with 50–70 arcsec radius. The `epatplot` task was used to verify the presence of pile-up. This was not a problem for the MOS detectors, but in the case of the pn data, we had to pierce the source counts extraction region, excluding a central circle with 10 arcsec radius.³ We selected only single and double events (`PATTERN<=4`), which

² With the only exception of the observation on August 16–17, when it was set to small window.

³ This was not necessary for the August 16–17 data.

¹ <http://www.oato.inaf.it/blazars/webt/>

Table 2. Results of the EPIC spectral fitting with a power-law model with free absorption.

Date	N_{H} (10^{20} cm^{-2})	Γ	$F_{1\text{keV}}$ (μJy)	χ_{red}^2 (d.o.f.)
July 29–31	5.02 ± 0.11	2.565 ± 0.006	3.260 ± 0.016	1.09 (2671)
August 2–4	5.20 ± 0.11	2.564 ± 0.006	2.995 ± 0.015	1.08 (2787)
August 4–6	5.04 ± 0.10	2.560 ± 0.006	3.010 ± 0.015	1.05 (2832)
August 8–10	4.57 ± 0.11	2.551 ± 0.006	2.693 ± 0.015	1.00 (2657)
August 16–17	4.92 ± 0.09	2.594 ± 0.005	3.678 ± 0.018	1.08 (2865)
Aug 30–Sep 1	5.65 ± 0.10	2.595 ± 0.005	3.912 ± 0.017	1.08 (2948)

Table 3. Results of the EPIC spectral fitting with a log-parabolic model with absorption fixed at the Galactic value $N_{\text{H}} = 3.72 \times 10^{20} \text{ cm}^{-2}$.

Date	α	β	$F_{1\text{keV}}$ (μJy)	χ_{red}^2 (d.o.f.)
July 29–31	2.487 ± 0.004	0.104 ± 0.010	3.179 ± 0.012	1.13 (2671)
August 2–4	2.476 ± 0.004	0.115 ± 0.010	2.909 ± 0.011	1.14 (2787)
August 4–6	2.482 ± 0.003	0.101 ± 0.009	2.931 ± 0.012	1.10 (2832)
August 8–10	2.501 ± 0.004	0.057 ± 0.010	2.645 ± 0.013	1.04 (2657)
August 16–17	2.521 ± 0.003	0.102 ± 0.008	3.596 ± 0.016	1.12 (2865)
Aug 30–Sep 1	2.481 ± 0.003	0.151 ± 0.009	3.767 ± 0.013	1.18 (2948)

are the best calibrated ones, and rejected events next to either the edges of the CCDs or bad pixels (FLAG==0). We produced effective area files with the task `arfgen` and redistribution matrices files with `rmfgen`. We used the task `grppha` of the `HEASOFT` package to bin each spectrum and associate it with the corresponding background, redistribution matrix (`rmf`) and ancillary (`arf`) files. We set a binning of at least 25 counts for each spectral channel to use the χ^2 statistic. All spectra were analysed with `XSPEC` version 12.9.0 between 0.3 keV and 10 keV in the case of MOS, and between 0.3 keV and 12 keV in the pn case. We fitted the three EPIC spectra of each observation first separately and then together. In the latter case, we allowed for some offset between detectors and normalized with respect to MOS1.

The spectra were fitted with both an absorbed power law $N(E) = N_0 E^{-\Gamma}$, where N_0 represents the number of photons $\text{keV}^{-1} \text{ cm}^{-2} \text{ s}^{-1}$ at 1 keV, and an absorbed log-parabolic model

$$N(E) = N_0 (E/E_s)^{[-\alpha - \beta \log(E/E_s)]},$$

where E_s is a scale parameter that we fixed equal to 1 keV. In all cases, we adopted the Wilms, Allen & McCray (2000) elemental abundances. An absorbed power law with N_{H} fixed at the Galactic value of $3.72 \times 10^{20} \text{ cm}^{-2}$ (from the LAB survey; Kalberla et al. 2005) gave statistically bad fits, with χ_{red}^2 of 1.25, 1.29, 1.21, 1.07, 1.27 and 1.49 for the six epochs. We obtained good fits with a power law with free absorption and acceptable fits with a log-parabola with absorption fixed at the Galactic value. The results of the spectral fitting with these two models are shown in Tables 2 and 3.

The power-law fits are statistically better, but suggest an absorption that is 23–52 per cent higher than the Galactic value. This may indicate a spectral curvature that, according to the log-parabolic fits, is however not very pronounced. Indeed, the β parameter ranges between 0.06 on August 8–10 and 0.15 on August 30–September 1. We note that the minimum/maximum curvature corresponds to the minimum/maximum flux density, respectively.

For illustrative purposes, Fig. 1 shows the three EPIC spectra acquired on August 8–10, with the absorbed log-parabolic model folded and data-to-model ratio.

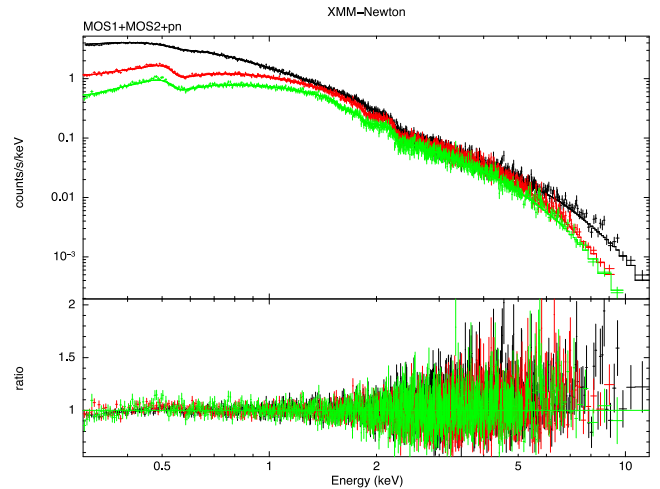


Figure 1. X-ray spectra of PG 1553+113 acquired by the EPIC instruments onboard *XMM-Newton* on 2015 August 8–10. Black, red and green symbols represent MOS1, MOS2 and pn data, respectively. The folded model, an absorbed log parabola with $N_{\text{H}} = 3.72 \times 10^{20} \text{ cm}^{-2}$, is shown by solid lines of the same colour. The ratio between the data and the folded model is plotted in the bottom panel.

2.1.2 Light curves

We checked the EPIC data for possible fast variability, which can put constraints on the size of the emitting region. We built MOS1, MOS2 and pn light curves following standard prescriptions.⁴ We performed a barycentric correction on the event files with the `barycen` task. Source and background light curves were extracted in the 0.2–10 keV energy range from the same regions used for the spectral analysis. For the pn, we considered single and double events only, while for the MOS we also included triples and quadruples. The task `epicldccorr` was finally run to obtain background-subtracted light curves, after performing both absolute (energy-dependent) and relative (time-dependent) corrections. Fig. 2 shows the corrected light curves. Some variability can be recognized especially during

⁴ <http://www.cosmos.esa.int/web/xmm-Newton/sas-thread-timing>

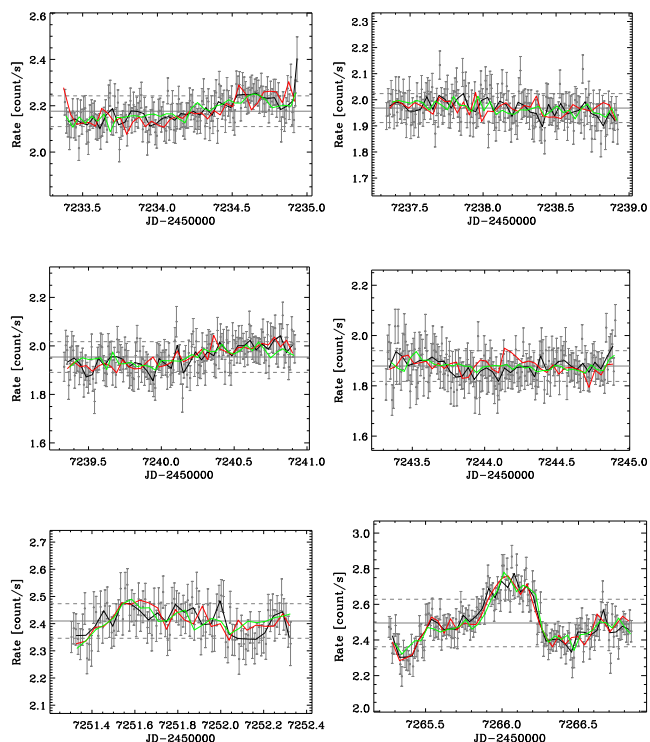


Figure 2. X-ray background-corrected light curves from the EPIC detectors during the *XMM-Newton* pointings. Grey plus signs correspond to the MOS1 rates obtained with a binning of 900 s, while the black line shows the result of a binning over 3600 s. The red and green lines represent 3600 s binning on the MOS2 and pn data, respectively, properly scaled so that the mean values of the three data sets match.

the last *XMM-Newton* pointing, on a hourly time-scale. This suggests that the size of the emitting region is $R \lesssim \delta \times 10^{14}$ cm, where δ is the Doppler beaming factor and typically ranges between 4 and 35 in blazars (Savolainen et al. 2010).

2.2 OM

During each *XMM-Newton* observation, the Optical Monitor (OM; Mason et al. 2001) instrument acquired many exposures in the optical and UV wide-band filters *V*, *B*, *U*, *W1*, *M2* and *W2*. For each filter, one exposure in imaging mode (5000 s long) is followed by one exposure in fast, imaging mode (usually 4400 s long); the sequence ends with a number (4–14) of fast exposures in *W2* band, for a total integration time of 6–17 h in this band.

We processed the data with the pipelines `omichain` and `om-chain` of the `SAS` package, and analysed the results with the `omsources` task. Source magnitudes corresponding to the imaging mode are shown in Fig. 3. Flux densities were obtained by multiplying the count rates for the conversion factors derived from observations of white dwarf standard stars.⁵ We conservatively assumed a 10 per cent uncertainty on the count rates for all filters.

2.3 Joint EPIC-OM spectral fitting

The exceptional quality of the *XMM-Newton* data encouraged us to try a joint fit of the EPIC and OM data. We thus used the `SAS` task `om2pha` to convert the OM data into ‘spectra’ that can be read into

⁵ <http://xmm.esac.esa.int/sas/8.0.0/watchout/>

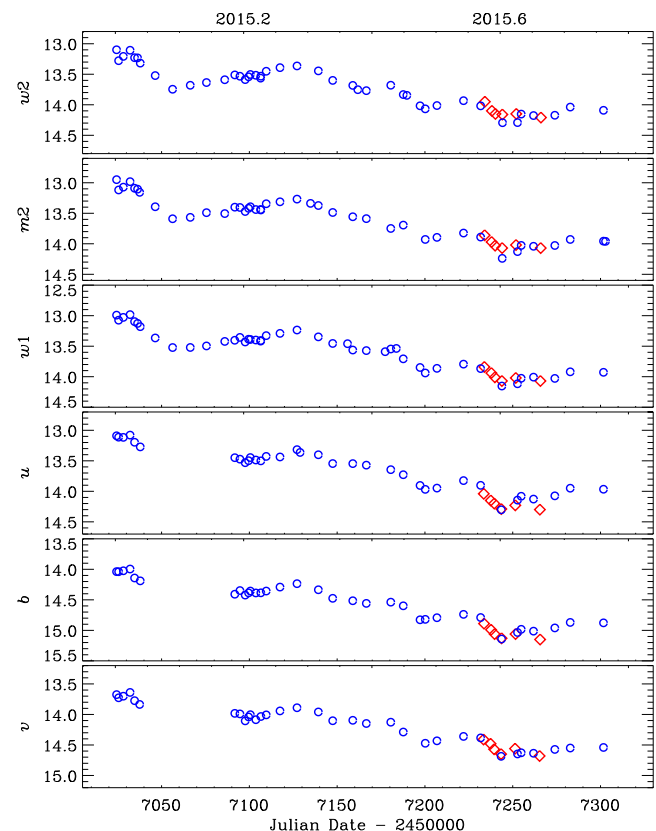


Figure 3. UV-optical observed magnitudes obtained from *Swift*-UVOT data (blue circles) and *XMM-Newton*-OM observations in imaging mode (red diamonds). Errors are smaller than the symbol size.

Table 4. Results of the joint OM+EPIC spectral fitting with a log-parabolic model with free reddening and absorption.

Date	$E(B - V)$ (10^{-2} mag)	N_{H} (10^{20} cm^{-2})	χ_{red}^2 (d.o.f.)	r/r_{MW}
July 29–31	3.32 ± 0.07	4.30 ± 0.05	2.36 (2669)	2.6
August 2–4	3.74 ± 0.08	4.40 ± 0.05	1.51 (2786)	2.4
August 4–6	3.49 ± 0.08	4.27 ± 0.05	1.75 (2830)	2.5
August 8–10	2.88 ± 0.09	3.56 ± 0.05	1.71 (2655)	2.5
August 16–17	5.02 ± 0.09	3.81 ± 0.04	1.32 (2859)	1.5
Aug 30–Sep 1	4.20 ± 0.08	4.47 ± 0.05	1.52 (2947)	2.2

`XSPEC`. The fitting model must be curved since we are considering a broad frequency range that goes through the synchrotron peak. We adopted a log-parabolic model (Landau et al. 1986; Massaro et al. 2004), with reddening applied to the OM data and absorption to the EPIC data (`reden*tbabs*logpar`). Galactic reddening was set to $E(B - V) = 0.05$ (see Raiteri et al. 2015). Fixing both $E(B - V)$ and N_{H} to their Galactic values results in a poor fit, which in general improves significantly when thawing the reddening parameter, but not so much when thawing N_{H} . Leaving both parameters free to vary gives an even slightly better fit, but its goodness is still questionable ($\chi^2/\nu = 1.3$ – 2.4 , see Table 4). In general, a free $E(B - V)$ gives a value smaller than the Galactic one, while a free N_{H} goes in the opposite direction, both results suggesting a gas/dust ratio $r = N_{\text{H}}/E(B - V)$ higher than the average value in the Milky Way, r_{MW} . Assuming $r_{\text{MW}} = 4.93 \times 10^{21} \text{ cm}^{-2} \text{ mag}^{-1}$ from Diplax & Savage (1994), we obtain gas/dust ratios from 1.5 to 2.6 times the Galactic value. The other parameters of the model, i.e. α , β and

the normalization, do not change much when freezing or thawing reddening and absorption.

We conclude that the log-parabolic model does not give a statistically acceptable description of the OM+EPIC spectrum. The above attempts indicate that the OM values for the source brightness are too high to allow for a fair connection between the optical–UV and X-ray spectra. However, we have to consider that these joint fits are strongly constrained by the large number of degrees of freedom (d.o.f.) of the X-ray spectra that give a heavy weight to the X-ray data. A comparison with optical–UV and X-ray data by *Swift* as well as with the WEBT data from the ground is crucial to assess whether the low goodness of the joint fits is due to data uncertainties or if it has to do with the source spectral properties.

3 OBSERVATIONS BY SWIFT

The *Swift* satellite carries three instruments: the Ultraviolet/Optical telescope (UVOT; Roming et al. 2005), the X-ray Telescope (XRT; Burrows et al. 2005) and the BAT telescope. Data were reduced with the HEASOFT⁶ package version 6.18 available at the NASA’s High Energy Astrophysics Science Archive Research Center (HEASARC).

3.1 XRT

We reduced the XRT data with the CALDB calibration release 20160121. The task `xrtpipeline` was run on the observations performed in pointing mode with standard screening criteria, selecting events with grades 0–12 for the PC mode and grades 0–2 for the WT mode. We retained all the PC and WT observations with exposure time greater than 1 min and 30 s, respectively. Data acquired in PC mode were affected by pile-up, so we extracted the source counts from an annular region with inner and outer radius of 10 and 75 arcsec, respectively, while the background counts were derived from an annulus with radii of 100 and 150 arcsec. For the observations performed in WT mode, we extracted the source counts in a circular region with 70 arcsec radius, and the background counts in the same annulus used for the PC mode. The task `xrtmkarf` was used to create ancillary response files to correct for hot columns, bad pixels and the loss of counts caused by using an annular extraction region in the pile-up case. We binned each spectrum and associated it with the corresponding background, redistribution matrix (rmf) and ancillary (arf) files with the task `grppha`, setting a binning of at least 20 counts for each spectral channel in order to use the χ^2 statistic. We fitted the XRT spectra with the same models adopted for the EPIC spectra (see Section 2.1.1). When the number of degrees of freedom was less or equal to 10, we checked the results with the Cash’s *C* statistic. The X-ray light curves will be presented and discussed in Section 6.

3.2 UVOT

UVOT observed PG 1553+113 with the *v*, *b* and *u* optical filters and *w1*, *m2* and *w2* UV filters. Data were processed with the calibration release 20160321 of the CALDB data base accessible from the HEASARC. For each epoch, we summed multiple images in the same filter with the task `uvotimsum` and then performed aperture photometry with `uvotsource`. Source counts were extracted from a circular region with 5 arcsec radius centred on the source, while background counts were obtained from a circle with 20 arcsec radius

Table 5. The optical, near-IR and radio observatories participating in the 2015 WEBT campaign on PG 1553+113.

Observatory	Country	Bands
<i>Optical</i>		
Abastumani	Georgia	<i>R</i>
AstroCamp	Spain	<i>R</i>
Belogradchik	Bulgaria	<i>BVRI</i>
Catania	Italy	<i>BVRI</i>
Crimean ¹	Russia	<i>BVRI</i>
Lulin ¹	Taiwan	<i>g, r, i</i>
Michael Adrian	Germany	<i>RI</i>
Mt. Maidanak ²	Uzbekistan	<i>BVRI</i>
New Mexico Skies	USA	<i>R</i>
ROVOR	USA	<i>RV</i>
Rozhen ²	Bulgaria	<i>BVRI</i>
Siding Spring	Australia	<i>R</i>
Sirio	Italy	<i>R</i>
Skinakas ¹	Greece	<i>BVRI</i>
St. Petersburg ¹	Russia	<i>BVRI</i>
Teide ²	Spain	<i>VR</i>
Tijarafe	Spain	<i>BR</i>
ASV ³	Serbia	<i>BVRI</i>
<i>Near-infrared</i>		
Campo Imperatore	Italy	<i>JHK</i>
Roque de los Muchachos (TNG)	Spain	<i>JHK</i>
Teide	Spain	<i>JHK</i>
<i>Radio</i>		
Medicina	Italy	5, 8 GHz
Metsähovi	Finland	37 GHz

Notes. ¹photometry and photopolarimetry

²two telescopes

³Astronomical Station Vidojevica

located in a source-free field region close to the source. The results were checked against the results of aperture photometry on the single images. We also investigated the occurrence of small scale sensitivity effects⁷ due to the possibility that the source falls on the small areas of the detector with lower throughput.

Fig. 3 displays the optical and UV magnitudes derived from the UVOT data as well as those coming from the OM observations in imaging mode. The comparison between the results of the two instruments shows a fair agreement, as the OM data points lie on the path traced by the UVOT data points, and the differences between simultaneous data are within the uncertainties. The light curves present a general decreasing trend, with the *XMM–Newton* observations occurring when the source was in its faintest state.

De-reddened flux densities were obtained from UVOT data by following the prescriptions of Raiteri et al. (2015).

4 WEBT DATA

The WEBT campaign on PG 1553+113 in 2015 was motivated by and focused on the giant amount of *XMM–Newton* time awarded in July–September. Nonetheless, we collected data from the whole optical observing season. Table 5 lists the participating observatories, together with their country and observing bands.

⁶ <http://heasarc.nasa.gov/heasoft/>

⁷ http://swift.gsfc.nasa.gov/analysis/uvot_digest/sss_check.html

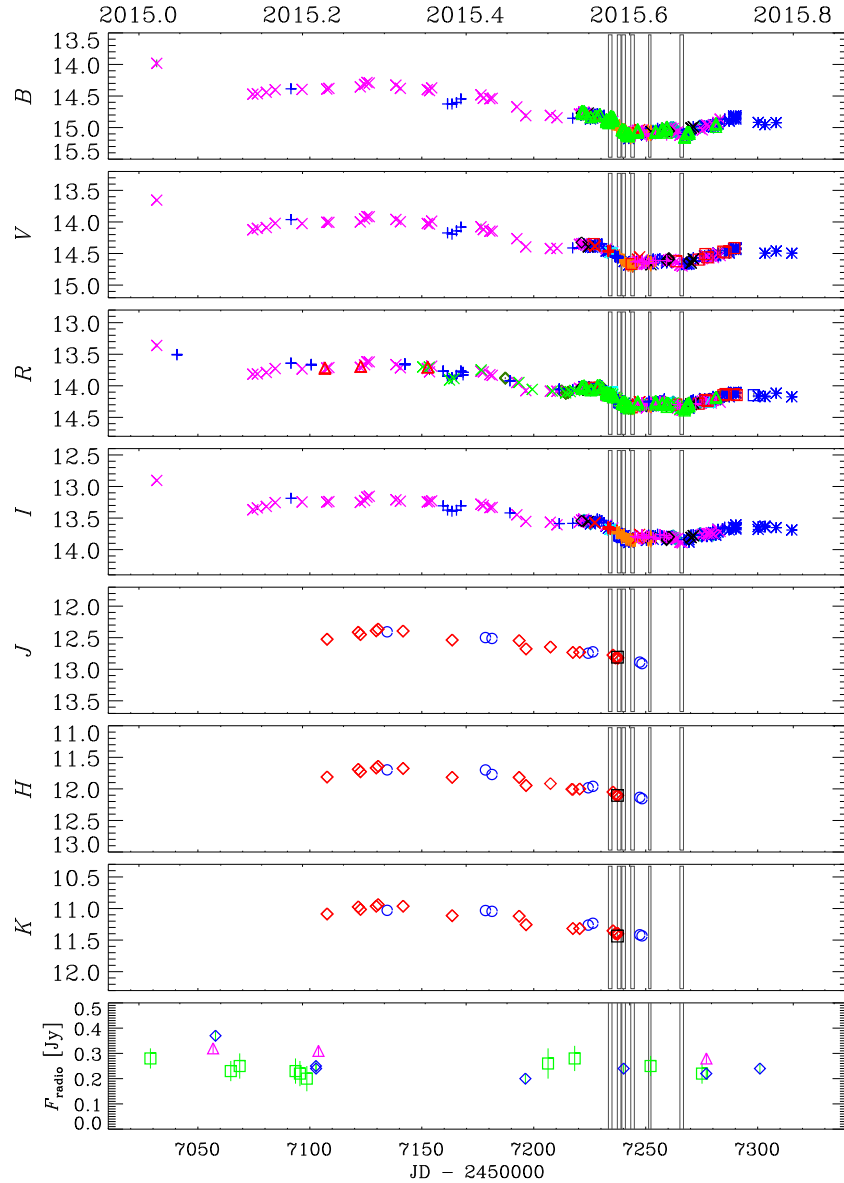


Figure 4. Final *BVRIJHK* light curves of PG 1553+113 obtained by the WEBT collaboration. Different colours and symbols highlight data from different telescopes. Grey boxes indicate the *XMM–Newton* observations. In the bottom panel flux densities at 5 GHz (purple triangles), 8 GHz (blue diamonds) and 37 GHz (green squares) are shown.

In the optical band, 21 telescopes in 18 observatories acquired data for the campaign. The calibration of the source magnitude was obtained with respect to the photometric sequence published by Raiteri et al. (2015). We collected 3120 data points in the Johnson–Cousins’ *B*, *V*, *R*, *I* bands,⁸ which were carefully assembled to obtain homogeneous and reliable light curves. In particular, overlapping of different data sets sometimes revealed offsets that were corrected by shifting deviant data sets to make them match the common trend traced by the others. Moreover, the scatter of dense but noisy data sets was reduced either by binning data points close in time or by deleting points that lie more than 1 standard deviation out of the night average, if no trend is recognizable. Finally, we discarded data with large errors (larger than 0.1 mag)

⁸ Lulin’s data were acquired in the SDSS *g*, *r*, *i* filters and transformed into *B*, *V*, *R*, *I* values with the Chonis & Gaskell (2008) calibrations.

or standing clearly out of the location defined by the bulk of the other points. The cleaning process is facilitated by the simultaneous inspection of the multifrequency light curves. The final light curves are displayed in Fig. 4. They show the same decreasing trend already seen in the *Swift*–UVOT light curves in Fig. 3. The sampling is denser during the core of the campaign, centred on the *XMM–Newton* observations.

Near-infrared observations were performed at the Campo Imperatore, Roque de los Muchachos (TNG), and Teide Observatories. Data reduction and analysis procedures are described in Raiteri et al. (2014). The *JHK* flux densities are plotted in Fig. 4 and show a course similar to that observed in the optical bands.

Radio data were acquired at 5 GHz and 8 GHz with the 32-m dish of the Medicina Radio Astronomical Station and at 37 GHz with the 14-m radio telescope of the Metsähovi Radio Observatory. Data are processed as explained in D’Ammando et al. (2012) and Teräsanta et al. (1998). The radio flux variability is modest.

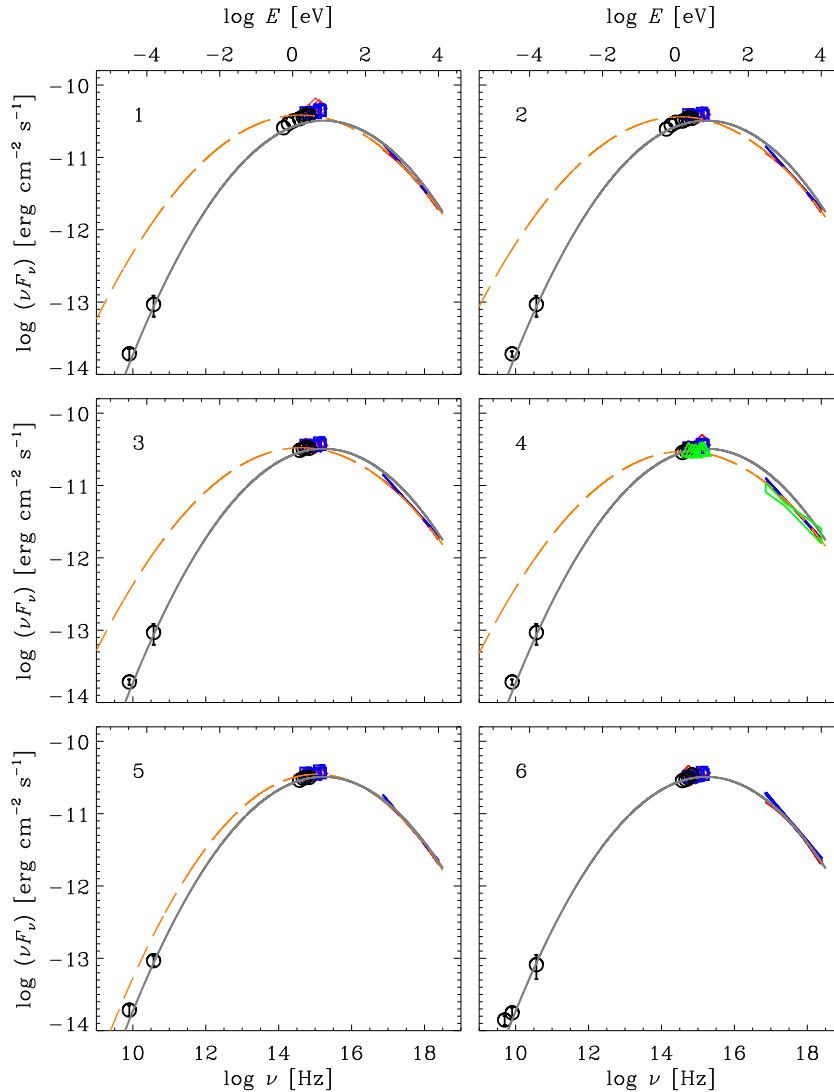


Figure 5. SEDs of PG 1553+113 during the six *XMM-Newton* pointings in 2015 July–September. Both the power-law (blue) and log-parabolic (red) fits to the MOS1, MOS2 and pn spectra analysed together are shown. The OM data acquired in imaging mode are plotted as blue squares, while red diamonds display data taken in fast, imaging mode. Black circles represent WEBT data points. On August 8–10, a simultaneous *Swift* observation was performed; its results are plotted in green. The grey continuous line represents the log-parabolic fit to the joint OM+EPIC data of the last *XMM-Newton* pointing; it is reported in all panels to guide the eye. The log-parabolic fits to the joint OM+EPIC data of each epoch are shown as orange long-dashed lines.

5 SPECTRAL ENERGY DISTRIBUTION

Fig. 5 shows the broad-band SEDs of the source during the six *XMM-Newton* pointings. In X-rays, both fits to the EPIC data (power law with free absorption and log-parabola with Galactic absorption) are plotted. A zoom into the near-infrared-to-UV frequency range is displayed in Fig. 6. In both figures imaging and fast, imaging OM data are plotted separately.

The August 8–10 SED also includes the *Swift* data obtained simultaneously to the *XMM-Newton* pointing. They indicate a slightly lower flux in the UV and a bit harder X-ray spectrum than the *XMM-Newton* data. The UVOT spectrum also shows a less pronounced curvature with respect to those analysed by Raiteri et al. (2015).

Simultaneous optical and near-infrared data taken during the WEBT campaign are added. Flux densities were corrected for Galactic absorption according to the prescriptions given by Raiteri et al. (2015). The WEBT data are in agreement, within errors, with the space data in the overlapping spectral range. In the

radio band, we plotted the nearest data in time, with a tolerance of a couple of weeks.

In each panel, we show the result of the log-parabolic fit to the joint OM and EPIC data of each epoch, together with that of the sixth *XMM-Newton* pointing (see Section 2.3). While in the first five epochs the joint OM+EPIC fits overproduce the WEBT data (radio+near-infrared in the first two cases, radio only in the other three), the fit obtained in the sixth epoch also matches the contemporaneous radio data and suggests that the synchrotron peak lies in the near-UV band. It is also consistent with the broad-band SED of the fifth pointing, while slightly overproduces the X-ray flux of the other epochs and slightly underproduces the UV flux of the first one.

In Fig. 7, we compare this log-parabolic model with the fits to a high, intermediate and low X-ray state of the source obtained by Raiteri et al. (2015) with an inhomogeneous SSC helical jet model (Villata & Raiteri 1999; Raiteri et al. 2009). The 2015 UV-to-X-ray flux is in between those characterizing the intermediate and low

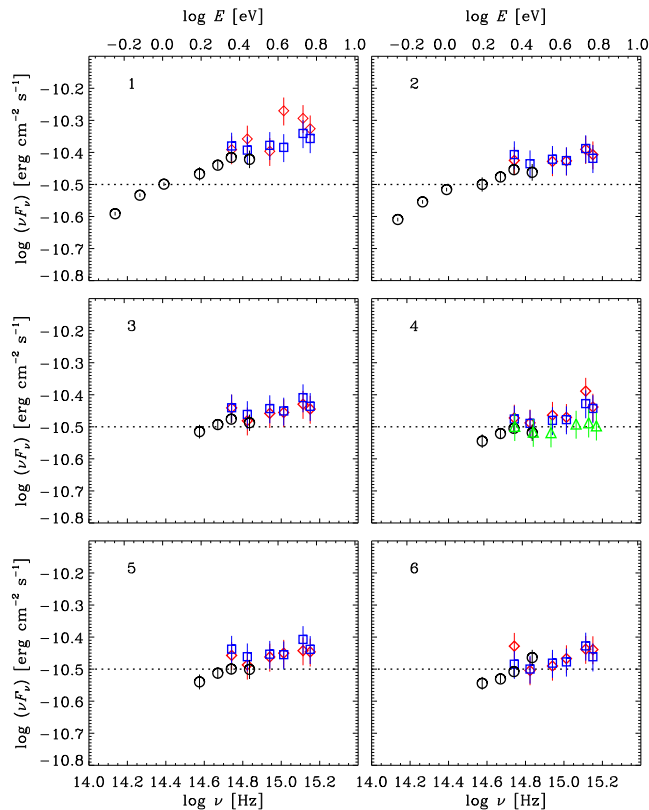


Figure 6. A zoom into the near-IR-to-UV frequency range of the SEDs reported in Fig. 5. The dotted line is drawn to guide the eye through the flux changes.

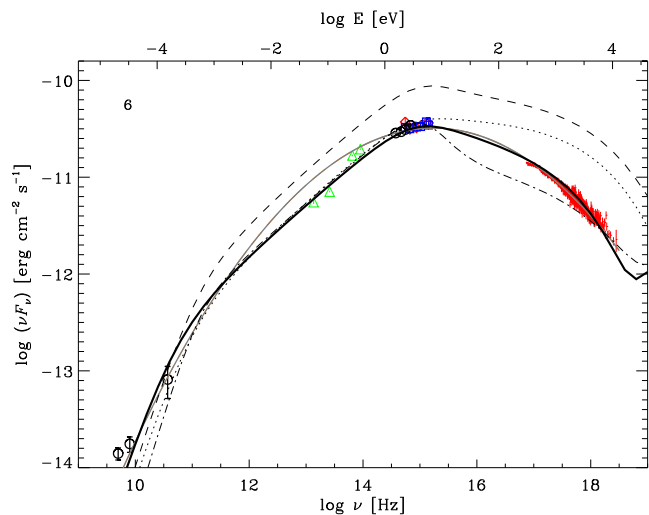


Figure 7. SEDs of PG 1553+113 during the sixth *XMM-Newton* pointing of 2015 August 30–September 1. Symbols are as in Fig. 5. The EPIC-pn spectrum obtained with a log-parabolic fit is shown in red. Infrared data from the AllWISE Source Catalog are plotted as green triangles. The grey continuous line represents the log-parabolic fit to the joint OM+EPIC data. The dashed, dotted and dot-dashed lines show the three fits to high, intermediate and low X-ray states of the source obtained by Raiteri et al. (2015) with an inhomogeneous SSC helical jet model. The black solid line represents a fit to the 2015 August 30–September 1 SED with the same model.

states, and the X-ray spectrum appears softer, while the radio flux is higher. We also show a realization of the same jet model that can satisfactorily reproduce the SED of 2015 August 30–September 1. With respect to the Raiteri et al. (2015) fits, it was obtained by changing the three parameters defining the jet orientation, and by lowering the emitted minimum and maximum frequencies at the jet apex. The new parameters are $a = 75^\circ$, $\psi = 24^\circ$, $\phi = 18^\circ$ and $\log \nu' = 15.4\text{--}18.2$ (rest frame). All the other model parameters are fixed to the values used in Raiteri et al. (2015). The largest separation between the log-parabolic and the jet model fits occurs in the infrared, so in Fig. 7, we added the *WISE* data downloaded from the AllWISE Source Catalog.⁹ Although the *WISE* data are not contemporaneous with the other data, they suggest a power-law shape of the SED in that wavelength range, more in agreement with the jet model.

In conclusion, the 2015 SEDs indicate an intermediate UV-to-X-ray state as compared to those analysed by Raiteri et al. (2015). Moreover, the smaller curvature of the UV and X-ray spectra in 2015 allows for a better connection between the UV and X-ray spectra, so that in first approximation a simple log-parabolic fit appears suitable to describe at least the SEDs with the highest X-ray fluxes. However, a more detailed analysis requires a more complex model, like the inhomogeneous SSC helical jet model that has already been applied to previous, more problematic SEDs of this source.

6 LONG-TERM PHOTOMETRIC AND POLARIMETRIC BEHAVIOUR

The long-term (2013–2015) optical and X-ray light curves are presented in Fig. 8 and compared with the behaviour of the polarization percentage P and of the electric vector position angle (EVPA). Fig. 9 shows an enlargement of the period including the *XMM-Newton* pointings examined in this paper and the corresponding WEBT campaign.

A prominent flare was detected in the X-ray band at the very end of 2014–very beginning of 2015, which was characterized by a rapid fall and was followed by a minor flare. The ratio between the maximum and the minimum flux is ~ 13 . The decreasing part of the X-ray major flare was observed also in the optical band, where it was probably more contained. The maximum observed flux density in the *R* band was only ~ 2.6 times higher than the minimum in 2015. The optical counterpart of the X-ray second, minor flare appears to be more extended in time.

Optical polarimetric data were acquired at the Crimean, Lulin, Skinakas and St Petersburg observatories. Two points with large error ($\sigma_P/P > 2$) were removed. The $\pm n\pi$ ($n \in \mathbb{N}$) ambiguity on the EVPA was treated by minimizing the difference between adjacent points. The value of P rapidly oscillates between ~ 1 per cent and ~ 10 per cent in a way that does not appear to be correlated with the optical (see also Fig. 10) or X-ray brightness behaviour. The first polarimetric datum in 2015, when the source flux was still high, does not reveal particularly high polarization. Instead, P reached the highest values in 2014, when the flux was rather stable and relatively low.

The EVPA is quite variable too. It increases during all the 2014 observing season and makes a rotation of 350° in about six months, with a mean rate of $\sim 60^\circ$ per month, while it remains more or less stable after the major flare. Notice, however, that the jump at JD = 2456794 is $\sim 86^\circ$, i.e. very close to 90° . Therefore, at that epoch

⁹ <http://irsa.ipac.caltech.edu/cgi-bin/Gator/nph-dd>

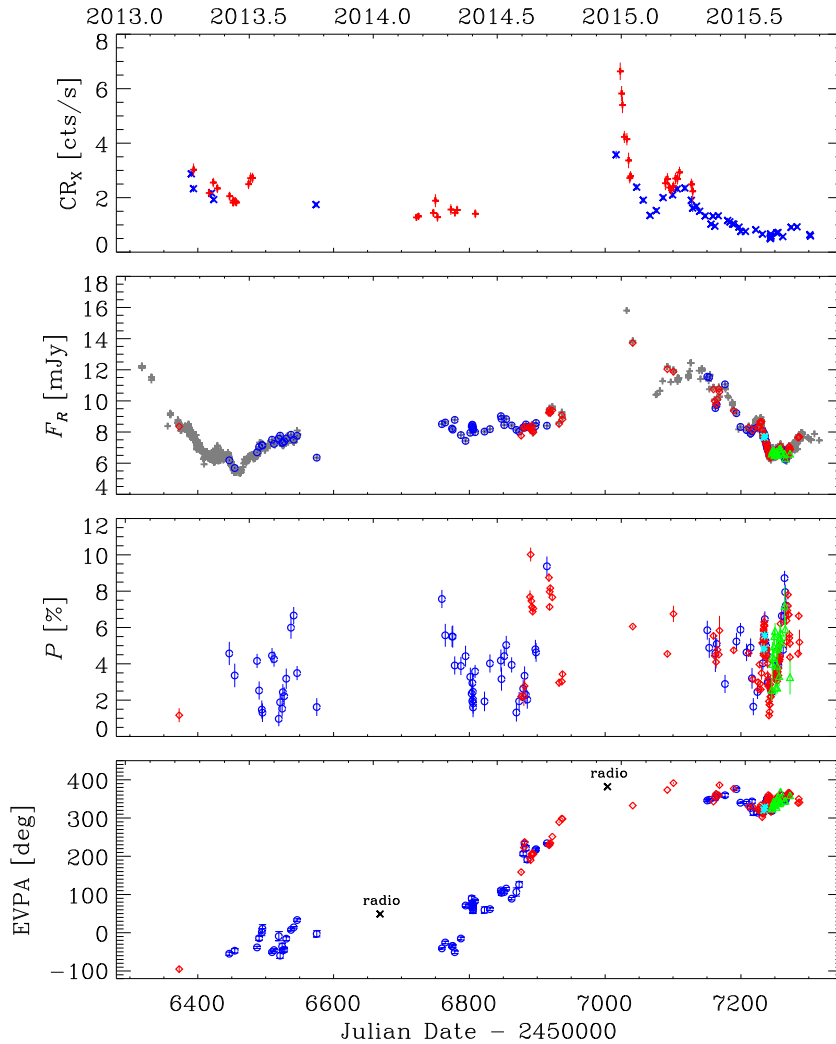


Figure 8. From top to bottom: time trend of the X-ray count rate (top panel), de-absorbed flux density in R band, percentage polarization P and electric vector polarization angle EVPA. In the top panel, red plus signs indicate *Swift*-XRT observations performed in WT mode, while blue crosses those in PC mode. In the other panels, red diamonds, cyan asterisks, blue circles and green triangles refer to data from the Crimean, Lulin, Skinakas and St Petersburg observatories, respectively. Grey plus signs in the second panel indicate the whole *WEBT* data set in the R band, while the black crosses in the last panel correspond to VLBA measurements at 15 GHz obtained by the *MOJAVE* Project.

the EVPA minimizing procedure sets the rotation counter-clockwise (increasing EVPA) instead of clockwise (decreasing EVPA) because of a difference of a few degrees only. This is of the same order of the overall error on the two data points defining the EVPA jump. The opposite choice would produce a smaller total rotation and rate, about 230° in 4.8 months, i.e. $\sim 50^\circ$ per month.¹⁰

Fig. 9 allows us to identify other, smaller rotations of the EVPA corresponding to different behaviours of polarization degree and optical flux. In particular, a nearly 60° change of EVPA was observed in about 10 d, between JD = 2457231 and 2457241, with P reaching a minimum at the rotation inversion point and the optical flux density remaining in a steadily decreasing phase and achieving a minimum just after P .

The *MOJAVE* Project obtained two VLBA polarization measurements¹¹ at 15 GHz in the period we are considering,

yielding radio EVPAs of 49° on 2014 January 11 and 22° on 2014 December 12. These values are plotted in Fig. 8 (the latter augmented by 360°) and show that there may be some displacement between the directions of the optical and radio polarization. The position angle of the structure of the radio source estimated from the *MOJAVE* data is about -40° , so the radio EVPAs are nearly transverse to the jet axis.

7 DISCUSSION

In this paper, we focused on two main issues regarding the spectral and polarimetric behaviour of the HBL PG 1553+113.

In Raiteri et al. (2015), we found a disagreement between the SEDs built with *Swift* and *XMM-Newton* data acquired at a short time distance (about 6 weeks) in 2013. The UVOT spectra showed a pronounced curvature, with a steep UV spectrum whose extrapolation to higher energies did not meet the soft XRT spectrum. On the contrary, the optical–UV spectrum obtained from the OM data was flat and the connection with the EPIC spectrum was less puzzling. To better clarify the matter, in Raiteri et al. (2015), we

¹⁰ For a discussion on the treatment of the EVPA $\pm n\pi$ ambiguity see also Kiehlmann et al. (2016).

¹¹ <http://www.physics.purdue.edu/astro/MOJAVE/>

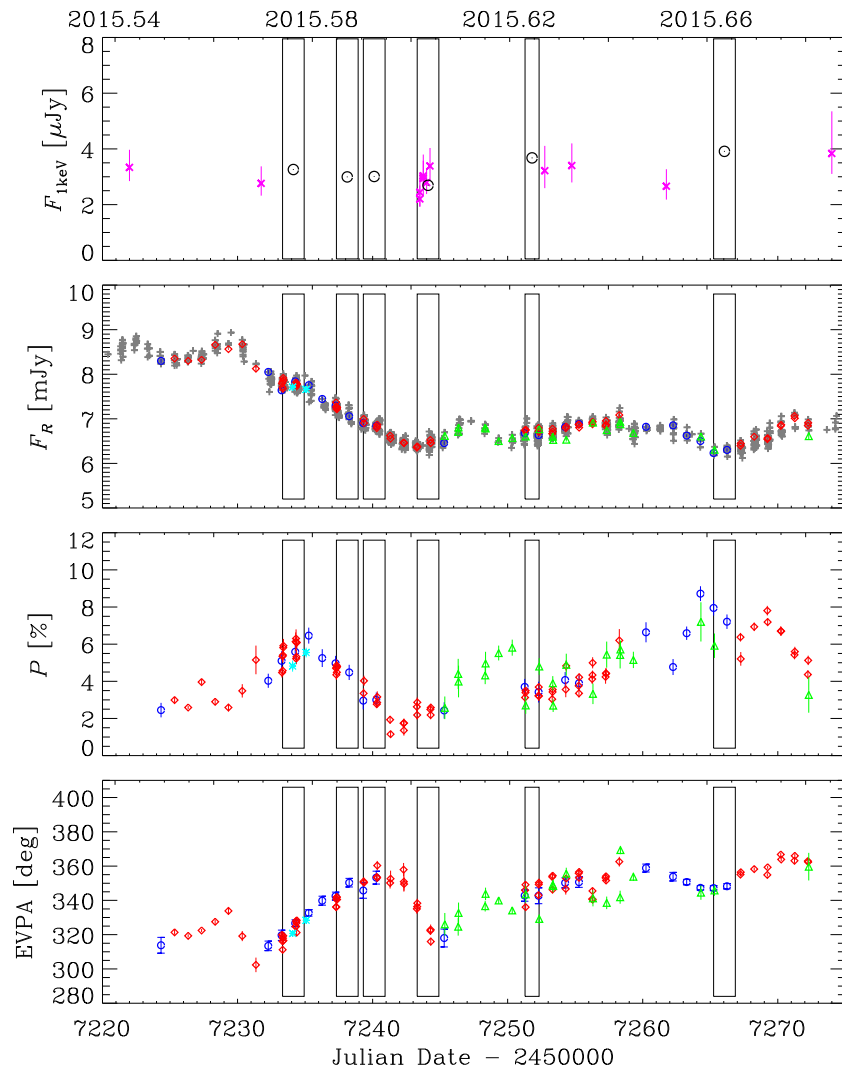


Figure 9. A zoom into the trends shown in Fig. 8. Boxes indicate the epochs of the *XMM-Newton* pointings. In the top panel, the 1 keV flux density is given for both the *Swift*-XRT observations (purple crosses) and the *XMM-Newton*-EPIC ones (black empty circles). They have been obtained by applying an absorbed power-law model with free N_{H} .

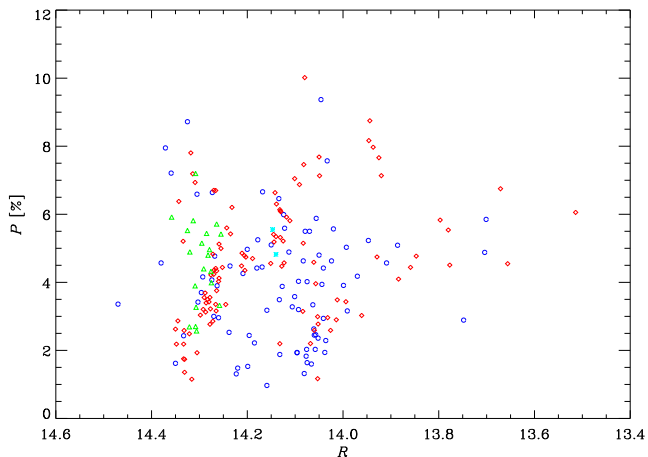


Figure 10. Polarization percentage in the *R* band as a function of the *R*-band magnitude.

compared the 2013 data with previous *Swift*, IUE and HST-COS observations, confirming the UV spectrum steepness showed by the UVOT data. We then fitted the various radio-to-X-ray SEDs with an inhomogeneous SSC helical jet model (Villata & Raiteri 1999; Raiteri et al. 2009), where different X-ray brightness states and spectral shapes are reproduced by changing only three parameters defining the jet geometry and orientation. The 2015 SEDs analysed in this paper found the source in an intermediate UV-to-X-ray brightness state with respect to those discussed by Raiteri et al. (2015). They show a consistency within the uncertainties between the *XMM-Newton* and *Swift* data and smaller optical–UV and X-ray spectral curvatures. The two X-ray brightest SEDs are reproduced reasonably well by the simple log-parabolic model that best fits the OM and EPIC data together, while a possibly better fit is still obtained with the helical jet model. Further *XMM-Newton* long exposures on PG 1553+113 are planned in 2017 when, according to the quasi-periodic behaviour claimed by Ackermann et al. (2015), the source will be in outburst. It will be interesting then to study in detail its spectral variability during the high flux state and compare it with the results obtained in this paper relative to a low flux state.

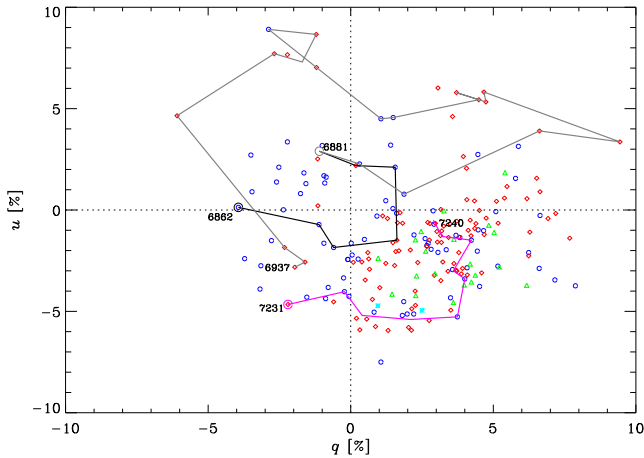


Figure 11. The polarimetric behaviour of PG 1553+113 in the u versus q plot. Red diamonds, cyan asterisks, blue circles and green triangles refer to data from the Crimean, Lulin, Skinakas and St Petersburg observatories, respectively. Solid lines connect daily averages in chronological order in the time intervals delimited by the epochs indicated in the plot. The counter-clockwise rotation from JD = 2456881 to 2457231 (grey) is the continuation of that from JD = 2456862 to 2456881 (black).

As for the polarimetric behaviour, the major point is the interpretation of the ample EVPA rotation observed in 2014. This is also shown in the u versus q plot in Fig. 11. Wide rotations of the radio and optical EVPA have been observed in blazars for more than 30 yr (e.g. Ledden & Aller 1979; Aller, Hodge & Aller 1981; Kikuchi et al. 1988; Larionov et al. 2008; Marscher et al. 2008, 2010; Raiteri et al. 2013; Sasada et al. 2012; Blinov et al. 2015; Carnerero et al. 2015; Larionov et al. 2016). Sometimes they are coincident with γ -ray flares. Many models have been proposed to explain EVPA rotations, based on relativistic aberration or on true physical rotations or curved motions in the source emitting region. Blandford & Königl (1979) analysed the EVPA swing produced in an accelerating source. A more complex model was proposed by Björnsson (1982), considering a 3D magnetic field distribution. Rapid changes of the EVPA are predicted to occur close to a minimum in P and in both models the maximum observable amplitude is 180° . An interpretation for wider rotations was given by Königl & Choudhuri (1985) in terms of shock waves propagating in a relativistic jet with non-axisymmetric magnetic field. This can produce in particular a ‘steplike’ behaviour where minimum P values are expected during the fastest swings (the jumps), as observed in the blazar 0727 – 115 by Aller et al. (1981). Assuming a shock-in-jet model and a helical magnetic field, Zhang, Chen & Böttcher (2014) could explain large EVPA rotations correlated with flux flares, while Zhang et al. (2016) analysed the competition between the shock speed and the magnetization in the emission region and found that in a moderately magnetized environment a fast shock can produce a 180° rotation with only a modest flux increase. The time-scale of the rotation is about a couple of weeks. EVPA swings from emitting blobs propagating on curved trajectories have been investigated by Nalewajko (2010). The maximum rotation rate occurs when the viewing angle is minimum, which implies a minimum in P and a maximum in flux. Larionov et al. (2013) satisfactorily fitted the photopolarimetric behaviour of 0716+714 during the 2011 outburst with a model involving the propagation of a shock in a helical jet, which produces a steplike rotation of the EVPA. Three wide EVPA rotations in different directions were observed by Aleksić et al. (2014) when

analysing the polarimetric behaviour of PKS 1510 – 089 in early 2012. They ascribed this behaviour to turbulence.

The possibility that EVPA rotations are produced by a stochastic process because of the random walk of the polarization vector due to a turbulent magnetic field was investigated by e.g. Marscher (2014), Blinov et al. (2015) and Kiehlmann et al. (2016). They found that wide rotations can be obtained, but they are rare, so it is unlikely that all those observed are produced by this mechanism. Moreover, stochastic and deterministic processes can both be responsible for different events in the same source.

The extremely wide EVPA rotation of PG 1553+113 in 2014 is similar to that observed in the source 0727 – 115 by Aller et al. (1981), though on a different time-scale. There is a general increase, whose finer structure reveals a series of plateaux linked by abrupt jumps. The degree of polarization shows a (possibly double) minimum during the rotation that is much wider than 180° , and the flux density does not show any flare. This questions most of the proposed deterministic models. Hence, it is unlikely that a single emission contribution is responsible for both flux and polarization variability.

Therefore, following the suggestions by D’Arcangelo et al. (2007), Kiehlmann et al. (2013), Blinov et al. (2015) and Kiehlmann et al. (2016), we assumed that some amount of magnetic turbulence is at work in the optical emitting region and we ran Monte Carlo simulations to see whether we can reproduce a photopolarimetric behaviour resembling that shown in Fig. 8. We considered the daily binned R -band light curve made by photopolarimetric data and assumed that the observed flux is equally contributed by $N_{\text{cells}} = 220$ emitting cells with randomly oriented magnetic field. These cells have uniform magnetic field with degree of polarization corresponding to synchrotron radiation from particles with a power-law distribution of energies with index p : $P_{\text{max}} = (p + 1)/(p + 7/3) = 75$ per cent for $p = 3$. At each time step, the flux density is fixed by the observed value, while a number of randomly chosen cells, N_{var} , change the orientation of their magnetic field. This number is crucial to obtain a certain level of ordered behaviour. We set their minimum number to $N_{\text{cells}}/10$ and increased them proportionally to the length of the time step Δt . The overall values of P and EVPA at each epoch can be derived from the Stokes parameters Q and U of the whole emitting region, which are obtained by summing the Q_i and U_i parameters of all cells. We could obtain a variety of different behaviours, with P values statistically close to the observed ones ($P_{\text{min}} = 1$ per cent, $P_{\text{max}} = 10$ per cent, $\langle P \rangle = 4$ per cent, $\sigma(P) \sim 2$ per cent) and sometimes leading to wide EVPA rotations. We show in Fig. 12 the results of one of these simulations, which produces a wide rotation that is similar to that observed in 2014. A full statistical analysis is beyond the scope of this paper; we just want to stress here that the polarimetric behaviour shown by PG 1553+113 is difficult to explain in terms of simple emission models while it is easily accounted for by assuming some turbulence of the magnetic field in the emitting region.

Finally, we noticed that the radio EVPAs measured by the MOJAVE project before and after the 2014 optical EVPA rotation are nearly transverse to the jet axis and possibly present some offset with respect to the optical EVPAs.

8 SUMMARY AND CONCLUSIONS

We have presented an analysis of the huge multiwavelength observing effort on the blazar PG 1553+113 in 2015, which was motivated by the long pointing time spent by *XMM-Newton* during six epochs in July–September.

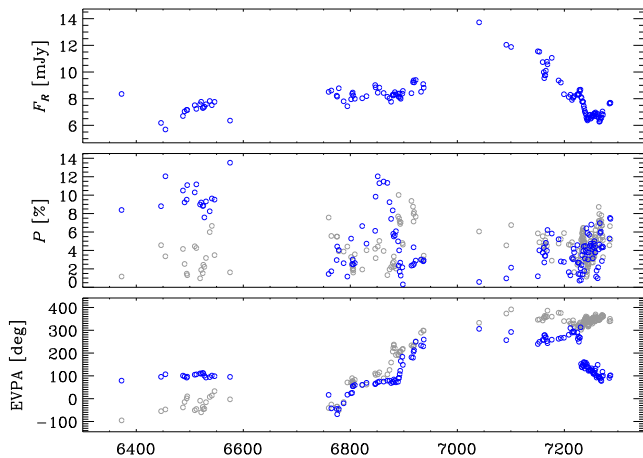


Figure 12. The observed R -band flux density (top) and the simulated P (middle) and EVPA (bottom) time behaviour (blue circles). They are the results of a Monte Carlo simulation with 220 cells having uniform, but randomly oriented magnetic field. Grey circles show the observed P and EVPA values for a comparison. The 2014 EVPA rotation is well reproduced.

The EPIC X-ray spectra are well fitted by a simple power-law model with free absorption, yielding neutral hydrogen column densities from 23 per cent to 52 per cent higher than the Galactic value. Fits with a log-parabolic model with Galactic absorption indicate slight spectral curvature. The long exposures reveal X-ray variability on hourly time-scale. The application of a log-parabolic model with free reddening and absorption to the joint OM+EPIC data suggests a gas/dust ratio that is from 1.5 to 2.6 times higher than in the Milky Way. During the August 8–10 pointing, simultaneous observations by *Swift* were obtained to check inter-calibrations. Both the optical–UV and X-ray data of the two satellites show consistency within the uncertainties.

The radio-to-optical data acquired by the WEBT collaboration complemented the space information at low energies. The optical and near-infrared light curves show a decreasing trend, in agreement with the UVOT and OM data, while the radio flux displays only modest variability.

We have built the radio-to-X-ray SEDs corresponding to the six *XMM–Newton* epochs with simultaneous data from space and ground. We wanted to investigate the properties of the synchrotron emission, and in particular to verify the critical connection between the UV and X-ray spectra that led us to propose an inhomogeneous SSC helical jet model to interpret the SED variability (Raiteri et al. 2015). The new SEDs presented in this paper show less curvature in both the optical–UV and X-ray spectra, and an intermediate UV–X-ray flux, as compared to those analysed by Raiteri et al. (2015). As a consequence, at least the two SEDs corresponding to the brightest X-ray states are satisfactorily reproduced by the simple log-parabolic model that best fits the *XMM–Newton* data. However, the helical jet model is still possibly giving a better fit.

We have also analysed the optical polarimetric behaviour of the source over the last three years, along with the X-ray and optical photometric behaviour. We did not find any clear correlation between the polarization degree and the optical brightness. The EVPA showed an almost complete counter-clockwise rotation in 2014. In the same period, the degree of polarization was very variable and the optical (and possibly the X-ray) flux was rather stable. All together, these pieces of information make an interpretation in terms of simple deterministic emission models quite difficult, while they are more easily explained by a stochastic model that assumes some

turbulence of the magnetic field in the jet emitting region. This is in line with the results of Blinov et al. (2016) and Angelakis et al. (2016), who found that EVPA rotations in high-synchrotron-peaked sources are less frequent than in low-peaked ones and suggested that probably the former are mostly random walk rotations while the latter are due to deterministic processes.

ACKNOWLEDGEMENTS

The data collected by the WEBT collaboration are stored in the WEBT archive at the Osservatorio Astrofisico di Torino – INAF (<http://www.oato.inaf.it/blazars/webt/>); for questions regarding their availability, please contact the WEBT President Massimo Villata (villata@oato.inaf.it). This research has made use of data obtained through the High Energy Astrophysics Science Archive Research Center Online Service, provided by the NASA/Goddard Space Flight Center. This research has made use of the XRT Data Analysis Software (XRTDAS) developed under the responsibility of the ASI Science Data Center (ASDC), Italy. This research was partially funded by the Italian Ministry for Research and Scuola Normale Superiore. This article is partly based on observations made with the telescopes IAC80 and TCS operated by the Instituto de Astrofísica de Canarias in the Spanish Observatorio del Teide on the island of Tenerife. The IAC team acknowledges the support from the group of support astronomers and telescope operators of the Observatorio del Teide. Based (partly) on data obtained with the STELLA robotic telescopes in Tenerife, an AIP facility jointly operated by AIP and IAC. St. Petersburg University team acknowledges support from Russian RFBR grant 15-02-00949 and St Petersburg University research grant 6.38.335.2015. AZT-24 observations are made within an agreement between Pulkovo, Rome and Teramo observatories. GD and OV gratefully acknowledge the observing grant support from the Institute of Astronomy and Rozhen National Astronomical Observatory, Bulgaria Academy of Sciences, via bilateral joint research project ‘Observations of ICRF radio-sources visible in optical domain’ (the head is GD). This work is a part of the Projects No 176011 (‘Dynamics and kinematics of celestial bodies and systems’), No 176004 (‘Stellar physics’) and No 176021 (‘Visible and invisible matter in nearby galaxies: theory and observations’) supported by the Ministry of Education, Science and Technological Development of the Republic of Serbia. The U. of Crete/FORTH group acknowledges support by the ‘RoboPol’ project, which is co-funded by the European Social Fund (ESF) and Greek National Resources, and by the European Commission Seventh Framework Programme (FP7) through grants PCIG10-GA-2011-304001 ‘JetPop’ and PIRSES-GA-2012-31578 ‘EuroCal’. This research was supported partly by funds of the project RD-08-81 of Shumen University. The Abastumani team acknowledges financial support by the by Shota Rustaveli NSF under contract FR/577/6-320/13. This research was partially supported by Scientific Research Fund of the Bulgarian Ministry of Education and Sciences under grant DO 02-137 (BIn-13/09). The Skinakas Observatory is a collaborative project of the University of Crete, the Foundation for Research and Technology – Hellas and the Max-Planck-Institut für Extraterrestrische Physik. The research at Ulugh Beg Astronomical Institute was funded in Uzbekistan Academy of Sciences grants N. F2-FA-F027 and F.4-16. The Metsähovi team acknowledges the support from the Academy of Finland to our observing projects (numbers 212656, 210338, 121148 and others). Based on observations with the Medicina telescope operated by INAF-Istituto di Radioastronomia.

REFERENCES

- Abdo A. A. et al., 2010, *ApJ*, 708, 1310
Abramowski A. et al., 2015, *ApJ*, 802, 65
Ackermann M. et al., 2015, *ApJ*, 813, L41
Aleksić J. et al., 2012, *ApJ*, 748, 46
Aleksić J. et al., 2014, *A&A*, 569, A46
Aleksić J. et al., 2015, *MNRAS*, 450, 4399
Aller H. D., Hodge P. E., Aller M. F., 1981, *ApJ*, 248, L5
Angelakis E. et al., 2016, *MNRAS*, 463, 3365
Björnsson C.-L., 1982, *ApJ*, 260, 855
Blandford R. D., Königl A., 1979, *ApJ*, 232, 34
Blinov D. et al., 2015, *MNRAS*, 453, 1669
Blinov D. et al., 2016, *MNRAS*, 462, 1775
A. Burrows D. N. et al., 2005, *Space Sci. Rev.*, 120, 165
Carnerero M. I. et al., 2015, *MNRAS*, 450, 2677
Chonis T. S., Gaskell C. M., 2008, *AJ*, 135, 264
D'Ammando F. et al., 2012, *MNRAS*, 426, 317
D'Arcangelo F. D. et al., 2007, *ApJ*, 659, L107
Danforth C. W., Keeney B. A., Stocke J. T., Shull J. M., Yao Y., 2010, *ApJ*, 720, 976
Diplas A., Savage B. D., 1994, *ApJ*, 427, 274
Kalberla P. M. W., Burton W. B., Hartmann D., Arnal E. M., Bajaja E., Morras R., Pöppel W. G. L., 2005, *A&A*, 440, 775
Kiehlmann S. et al., 2013, *Eur. Phys. J. Web Conf.*, 61, 06003
Kiehlmann S. et al., 2016, *A&A*, 590, A10
Kikuchi S., Mikami Y., Inoue M., Tabara H., Kato T., 1988, *A&A*, 190, L8
Königl A., 1981, *ApJ*, 243, 700
Königl A., Choudhuri A. R., 1985, *ApJ*, 289, 188
Landau R. et al., 1986, *ApJ*, 308, 78
Landoni M., Falomo R., Treves A., Sbarufatti B., 2014, *A&A*, 570, A126
Larionov V. M. et al., 2008, *A&A*, 492, 389
Larionov V. M. et al., 2013, *ApJ*, 768, 40
Larionov V. M. et al., 2016, *MNRAS*, 461, 3047
Ledden J. E., Aller H. D., 1979, *ApJ*, 229, L1
Marscher A. P., 2014, *ApJ*, 780, 87
Marscher A. P. et al., 2008, *Nature*, 452, 966
Marscher A. P. et al., 2010, *ApJ*, 710, L126
Mason K. O. et al., 2001, *A&A*, 365, L36
Massaro E., Perri M., Giommi P., Nesci R., 2004, *A&A*, 413, 489
Mastichiadis A., Kirk J. G., 1997, *A&A*, 320, 19
Nalewajko K., 2010, *Int. J. Mod. Phys. D*, 19, 701
Nicastro F. et al., 2013, *ApJ*, 769, 90
Orr M., 2011, *Int. Cosmic Ray Conf.*, 8, 121
Padovani P., Resconi E., Giommi P., Arsioli B., Chang Y. L., 2016, *MNRAS*, 457, 3582
Raiteri C. M. et al., 2009, *A&A*, 507, 769
Raiteri C. M. et al., 2012, *A&A*, 545, A48
Raiteri C. M. et al., 2013, *MNRAS*, 436, 1530
Raiteri C. M. et al., 2014, *MNRAS*, 442, 629
Raiteri C. M. et al., 2015, *MNRAS*, 454, 353
Righi C., Tavecchio F., Guetta D., 2016, *A&A*, preprint ([arXiv:1607.08061](https://arxiv.org/abs/1607.08061))
Roming P. W. A. et al., 2005, *Space Sci. Rev.*, 120, 95
Sasada M. et al., 2012, *PASJ*, 64
Savolainen T., Homan D. C., Hovatta T., Kadler M., Kovalev Y. Y., Lister M. L., Ros E., Zensus J. A., 2010, *A&A*, 512, A24
Shaw M. S., Filippenko A. V., Romani R. W., Cenko S. B., Li W., 2013, *AJ*, 146, 127
Strüder L. et al., 2001, *A&A*, 365, L18
Teräsanta H. et al., 1998, *A&AS*, 132, 305
Turner M. J. L. et al., 2001, *A&A*, 365, L27
Villata M., Raiteri C. M., 1999, *A&A*, 347, 30
Wilms J., Allen A., McCray R., 2000, *ApJ*, 542, 914
Zhang H., Chen X., Böttcher M., 2014, *ApJ*, 789, 66
Zhang H., Deng W., Li H., Böttcher M., 2016, *ApJ*, 817, 63
- ¹*INAF, Osservatorio Astrofisico di Torino, via Osservatorio 20, I-10025 Pino Torinese, Italy*
²*INAF, Osservatorio Astronomico di Roma, via di Frascati 33, I-00040 Monte Porzio Catone, Italy*
³*Scuola Normale Superiore, Piazza dei Cavalieri 7, I-56126 Pisa, Italy*
⁴*ASI Science Data Center, via del Politecnico s.n.c., I-00133 Roma, Italy*
⁵*Astronomical Institute, St Petersburg State University, Universitetsky pr. 28, Petrodvoretz, 198504 St Petersburg, Russia*
⁶*Pulkovo Observatory, 196140 St Petersburg, Russia*
⁷*Department of Physics and ITCP, University of Crete, 71003 Heraklion, Greece*
⁸*Foundation for Research and Technology – Hellas, IESL, Voutes, 71110 Heraklion, Greece*
⁹*Instituto de Astrofísica de Canarias (IAC), La Laguna, E-38200 Tenerife, Spain*
¹⁰*Departamento de Astrofísica, Universidad de La Laguna, La Laguna, E-38205 Tenerife, Spain*
¹¹*Institute of Astronomy and NAO, Bulgarian Academy of Sciences, 72 Tsarigradsko shosse Blvd., 1784 Sofia, Bulgaria*
¹²*Crimean Astrophysical Observatory RAS, P/O Nauchny 298409, Russia*
¹³*EPT Observatories, Tijarafe, E-38780 La Palma, Spain*
¹⁴*INAF, TNG Fundación Galileo Galilei, E-38712 La Palma, Spain*
¹⁵*Graduate Institute of Astronomy, National Central University, 300 Zhongda Rd, Zhongli City, Taoyuan County 32001, Taiwan (R.O.C.)*
¹⁶*Astronomical Observatory, Volgina 7, 11060 Belgrade, Serbia*
¹⁷*Ulugh Beg Astronomical Institute, Maidanak Observatory, 33 Astronomicheskaya str., Tashkent, 100052, Uzbekistan*
¹⁸*INAF, Osservatorio Astrofisico di Catania, Via S. Sofia 78, I-95123 Catania, Italy*
¹⁹*INAF, Istituto di Radioastronomia, via Gobetti 101, I-40129 Bologna, Italy*
²⁰*Department of Theoretical and Applied Physics, University of Shumen, 9712 Shumen, Bulgaria*
²¹*Abastumani Observatory, Mt. Kanobili, 0301 Abastumani, Georgia*
²²*Engelhardt Astronomical Observatory, Kazan Federal University, 422526 Zelenodolsky region, Tatarstan, Russia*
²³*Aalto University Metsähovi Radio Observatory, Metsähovintie 114, FI-02540 Kylmälä, Finland*
²⁴*Aalto University Department of Radio Science and Engineering, P.O. BOX 13000, FI-00076 AALTO, Finland*
²⁵*Department of Physics and Astronomy, Brigham Young University, Provo, UT 84602, USA*
²⁶*Michael Adrian Observatorium, Astronomie Stiftung Trebur, D-65468 Trebur, Germany*
²⁷*University of Applied Sciences, Technische Hochschule Mittelhessen, D-61169 Friedberg, Germany*
²⁸*Osservatorio Astronomico Sirio, Piazzale Anelli, I-70013 Castellana Grotte, Italy*
²⁹*Department of Physics, University of Colorado Denver, CO 80217-3364, USA*

This paper has been typeset from a $\text{\TeX}/\text{\LaTeX}$ file prepared by the author.

Blazar spectral variability as explained by a twisted inhomogeneous jet

C. M. Raiteri¹, M. Villata¹, J. A. Acosta–Pulido^{2,3}, I. Agudo⁴, A. A. Arkharov⁵, R. Bachev⁶, G. V. Baida⁷, E. Benítez⁸, G. A. Borman⁷, W. Boschin^{2,3,9}, V. Bozhilov¹⁰, M. S. Butuzova⁷, P. Calcidese¹¹, M. I. Carnerero¹, D. Carosati^{9,12}, C. Casadio^{4,13}, N. Castro–Segura^{3,14}, W.–P. Chen¹⁵, G. Damjanovic¹⁶, F. D’Ammando^{17,18}, A. Di Paola¹⁹, J. Echevarría⁸, N. V. Efimova⁵, Sh. A. Ehgamberdiev²⁰, C. Espinosa⁸, A. Fuentes⁴, A. Giunta¹⁹, J. L. Gómez⁴, T. S. Grishina²¹, M. A. Gurwell²², D. Hiriart⁸, H. Jermak²³, B. Jordan²⁴, S. G. Jorstad^{21,25}, M. Joshi²⁵, E. N. Kopatskaya²¹, K. Kuratov^{26,27}, O. M. Kurtanidze^{28,29,30,31}, S. O. Kurtanidze²⁸, A. Lähteenmäki^{32,33,34}, V. M. Larionov^{5,21}, E. G. Larionova²¹, L. V. Larionova²¹, C. Lázaro^{2,3}, C. S. Lin¹⁵, M. P. Malmrose²⁵, A. P. Marscher²⁵, K. Matsumoto³⁵, B. McBreen³⁶, R. Michel⁸, B. Mihov⁶, M. Mineev¹⁰, D. O. Mirzaqulov²⁰, A. A. Mokrushina^{5,21}, S. N. Molina⁴, J. W. Moody³⁷, D. A. Morozova²¹, S. V. Nazarov⁷, M. G. Nikolashvili²⁸, J. M. Ohlert^{38,39}, D. N. Okhmat⁷, E. Ovcharov¹⁰, F. Pinna^{2,3}, T. A. Polakis⁴⁰, C. Protasio^{2,3}, T. Pursimo⁴¹, F. J. Redondo–Lorenzo^{2,3}, N. Rizzi⁴², G. Rodríguez–Coira^{2,3}, K. Sadakane³⁵, A. C. Sadun⁴³, M. R. Samal¹⁵, S. S. Savchenko²¹, E. Semkov⁶, B. A. Skiff⁴⁴, L. Slavcheva–Mihova⁶, P. S. Smith⁴⁵, I. A. Steele²³, A. Strigachev⁶, J. Tammi³², C. Thum⁴⁶, M. Tornikoski³², Yu. V. Troitskaya²¹, I. S. Troitsky²¹, A. A. Vasiliev²¹ & O. Vince¹⁶

Blazars are active galactic nuclei, which are powerful sources of radiation whose central engine is located in the core of the host galaxy. Blazar emission is dominated by non-thermal radiation from a jet that moves relativistically towards us, and therefore undergoes Doppler beaming¹. This beaming causes flux enhancement and contraction of the variability timescales, so that most blazars appear as luminous sources characterized by noticeable and fast changes in brightness at all frequencies. The mechanism that produces this unpredictable variability is under debate, but proposed mechanisms include injection, acceleration and cooling of particles², with possible intervention of shock waves^{3,4} or turbulence⁵. Changes in the viewing angle of the observed emitting knots or jet regions have also been suggested as an explanation of flaring events^{6–10} and can also explain specific properties of blazar emission, such as intra-day variability¹¹, quasi-periodicity^{12,13} and the delay of radio flux variations relative to optical changes¹⁴. Such a geometric interpretation, however, is not universally accepted because alternative explanations based on changes in physical conditions—such as the size and speed of the emitting zone, the magnetic field, the number of emitting particles and their energy distribution—can explain snapshots of the spectral behaviour of blazars in many cases^{15,16}. Here we report the results of optical-to-radio-wavelength monitoring of the blazar CTA 102 and show that the observed long-term trends of the flux and spectral variability are best explained by an inhomogeneous, curved jet that undergoes changes in orientation

over time. We propose that magnetohydrodynamic instabilities¹⁷ or rotation of the twisted jet⁶ cause different jet regions to change their orientation and hence their relative Doppler factors. In particular, the extreme optical outburst of 2016–2017 (brightness increase of six magnitudes) occurred when the corresponding emitting region had a small viewing angle. The agreement between observations and theoretical predictions can be seen as further validation of the relativistic beaming theory.

The blazar CTA 102 belongs to the subclass of flat-spectrum radio quasars (FSRQs). Its redshift, $z = 1.037$, corresponds to a luminosity distance of about 7,000 Mpc (assuming a flat Universe and a Hubble constant $H_0 = 70 \text{ km s}^{-1} \text{ Mpc}^{-1}$).

The Whole Earth Blazar Telescope (WEBT) Collaboration started to monitor the multiwavelength behaviour of CTA 102 in 2008. Data obtained until January 2013 are reported in ref. 9. In Extended Data Fig. 1 we show the optical and near-infrared light curves acquired in 2013–2017, which were built with data from 39 telescopes in 28 observatories, and in Methods we give some details on these observations.

A period of relatively low activity was recently interrupted by a sudden increase in the source brightness in late 2016, with a jump of 6–7 magnitudes with respect to the minima in the optical and near-infrared bands. The peak of the outburst was observed on 28 December 2016, with an R -band magnitude of 10.82 ± 0.04 (see Fig. 1), which corresponds to a luminosity L_ν at frequency ν of $\log[\nu L_\nu \text{ (erg s}^{-1}\text{)}] = 48.12$

¹INAF, Osservatorio Astrofisico di Torino, I-10025 Pino Torinese, Italy. ²Instituto de Astrofísica de Canarias (IAC), La Laguna, E-38200 Tenerife, Spain. ³Departamento de Astrofísica, Universidad de La Laguna, La Laguna, E-38205 Tenerife, Spain. ⁴Instituto de Astrofísica de Andalucía (CSIC), E-18080 Granada, Spain. ⁵Pulkovo Observatory, 196140 St Petersburg, Russia. ⁶Institute of Astronomy and NAO, Bulgarian Academy of Sciences, 1784 Sofia, Bulgaria. ⁷Crimean Astrophysical Observatory RAS, Nauchny 298409, Russia. ⁸Instituto de Astronomía, Universidad Nacional Autónoma de México, Mexico. ⁹INAF, TNG Fundación Galileo Galilei, E-38712 La Palma, Spain. ¹⁰Department of Astronomy, Faculty of Physics, University of Sofia, BG-1164 Sofia, Bulgaria. ¹¹Osservatorio Astronomico della Regione Autonoma Valle d’Aosta, I-11020 Nus, Italy. ¹²EPT Observatories, Tijarafe, E-38780 La Palma, Spain. ¹³Max-Planck-Institut für Radioastronomie, D-53121 Bonn, Germany. ¹⁴School of Physics and Astronomy, University of Southampton, Southampton SO17 1BJ, UK. ¹⁵Graduate Institute of Astronomy, National Central University, Jhongli City, Taoyuan County 32001, Taiwan. ¹⁶Astronomical Observatory, 11060 Belgrade, Serbia. ¹⁷Dipartimento di Fisica e Astronomia, Università di Bologna, I-40129 Bologna, Italy. ¹⁸INAF, Istituto di Radioastronomia, I-40129 Bologna, Italy. ¹⁹INAF, Osservatorio Astronomico di Roma, I-00040 Monte Porzio Catone, Italy. ²⁰Ulugh Beg Astronomical Institute, Maidanak Observatory, Tashkent 100052, Uzbekistan. ²¹Astronomical Institute, St Petersburg State University, 198504 St Petersburg, Russia. ²²Harvard-Smithsonian Center for Astrophysics, Cambridge, Massachusetts 02138, USA. ²³Astrophysics Research Institute, Liverpool John Moores University, Liverpool L3 5RF, UK. ²⁴School of Cosmic Physics, Dublin Institute For Advanced Studies, Dublin, Ireland. ²⁵Institute for Astrophysical Research, Boston University, Boston, Massachusetts 02215, USA. ²⁶NNLOT, Al-Farabi Kazakh National University, Almaty, Kazakhstan. ²⁷Fesenkov Astrophysical Institute, Almaty, Kazakhstan. ²⁸Abastumani Observatory, Mt Kanobili, 0301 Abastumani, Georgia. ²⁹Engelhardt Astronomical Observatory, Kazan Federal University, Tatarstan, Russia. ³⁰Landessternwarte, Zentrum für Astronomie der Universität Heidelberg, 69117 Heidelberg, Germany. ³¹Center for Astrophysics, Guangzhou University, Guangzhou 510006, China. ³²Aalto University Metsähovi Radio Observatory, FI-02540 Kylmäla, Finland. ³³Aalto University Department of Electronics and Nanoengineering, FI-00076 Aalto, Finland. ³⁴Tartu Observatory, 61602 Tõravere, Estonia. ³⁵Astronomical Institute, Osaka Kyoiku University, Osaka 582-8582, Japan. ³⁶School of Physics, University College Dublin, Dublin 4, Ireland. ³⁷Department of Physics and Astronomy, Brigham Young University, Provo, Utah 84602, USA. ³⁸Michael Adrian Observatorium, Astronomie Stiftung Trebur, 65468 Trebur, Germany. ³⁹University of Applied Sciences, Technische Hochschule Mittelhessen, 61169 Friedberg, Germany. ⁴⁰Command Module Observatory, Tempe, Arizona, USA. ⁴¹Nordic Optical Telescope, E-38700 Santa Cruz de La Palma, Spain. ⁴²Osservatorio Astronomico Sirio, I-70013 Castellana Grotte, Italy. ⁴³Department of Physics, University of Colorado Denver, Denver, Colorado 80217-3364 USA. ⁴⁴Lowell Observatory, Flagstaff, Arizona, USA. ⁴⁵Steward Observatory, University of Arizona, Tucson, Arizona, USA. ⁴⁶Instituto de Radio Astronomía Milimétrica, E-18012 Granada, Spain.

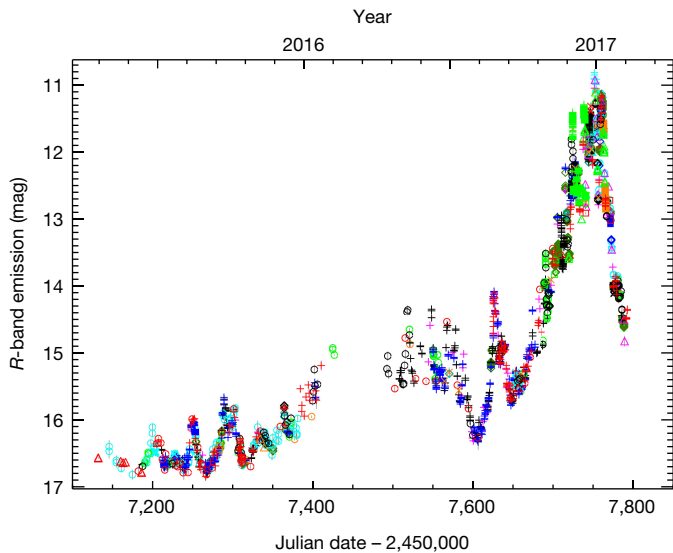


Figure 1 | Observed optical light curve of CTA 102 in the last two observing seasons of the WEBT campaign. *R*-band magnitudes are shown as a function of the Julian date (JD). Different colours and symbols correspond to the various telescopes contributing to the WEBT campaign. Error bars represent 1 s.d. measurement errors. The peak of the 2016–2017 outburst was observed on 28 December 2016 and indicates a brightness increase of about 6 mag with respect to the faintest state.

(corrected for the redshift effect, but without a beaming correction). This represents the most luminous optical blazar state ever detected. The previous record was held by the FSRQ 3C 454.3, which reached $\log[\nu L_\nu \text{ (erg s}^{-1}\text{)}] = 47.54$ during a big outburst¹⁸ observed in 2005.

Inspection of the light curves of CTA 102 reveals that the brightness variation amplitude is larger in the near-infrared than in the optical band. This is a consequence of the source emitting not only synchrotron radiation from the jet, but also thermal radiation from the accretion disk¹⁹ that feeds the super-massive black hole of the active galactic nucleus (AGN). The more stable light from the disk makes a larger contribution to the overall source flux at optical wavelengths than in the near-infrared. Further evidence of thermal radiation from the disk comes from the analysis of colour indices and spectroscopic data (see Methods and Extended Data Figs 3 and 4).

To analyse the synchrotron emission from the jet, we first model the thermal component, usually referred to as the ‘big blue bump’ (BBB). Besides the disk radiation, the BBB includes the contribution of emission lines from the broad-line region of the AGN, in particular, Mg II and H α lines, redshifted to the optical *V* and near-infrared *J* bands, respectively. In the BBB model (details in Methods), we built the spectral energy distribution (SED) of a hypothetical minimum-brightness synchrotron state and then subtracted it from the flux minima in all optical and near-infrared bands to get the BBB contribution. We also added a dust torus emission component in the mid- to far-infrared, as dust emission has been detected in CTA 102 with the IRAS²⁰ and Spitzer²¹ satellites. The results are shown in Fig. 2.

Having modelled the thermal contribution to the source flux, we subtracted it from the near-infrared and optical flux densities to get the jet synchrotron flux. Figure 3 shows the optical *R* band, millimetre-wavelength (230 GHz) and radio (37 GHz) light curves in the period 2008–2017. The optical flux density of the jet ranges from 0.047 mJy to 166 mJy, with a maximum flux ratio higher than 3,500. We note that both the 2012 flare and the 2016–2017 outburst were accompanied by radio activity, but the flux ratios at the peaks of the two events are very different in the various bands. Moreover, in 2012, peaks at lower frequencies followed those at higher frequencies, as is often observed in blazars¹⁴. By contrast, the latest optical outburst was preceded by activity at 37 GHz. Figure 3 also shows that the high flux

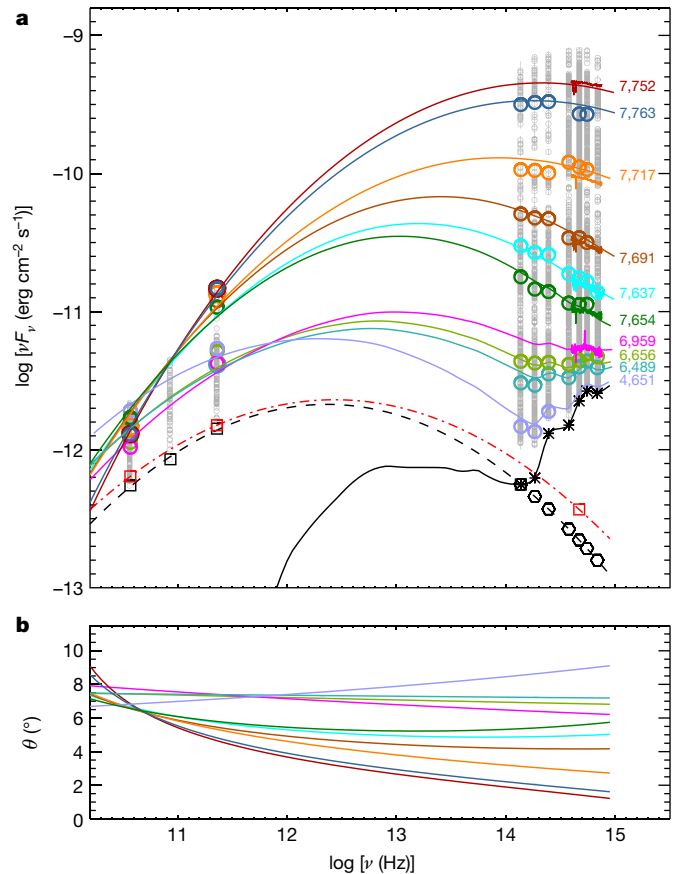


Figure 2 | Spectral energy distributions of CTA 102 and orientation of the emitting regions of the jet. **a**, Small grey circles highlight the observed variability ranges. The black dashed line represents the minimum-brightness synchrotron SED and the black squares (hexagons) the fitted (derived) minimum synchrotron flux densities. The black solid line and asterisks show the thermal emission model and its contributions to the near-infrared and optical bands. The red dot-dashed line represents the base-level synchrotron SED used for the geometric interpretation. Large coloured circles and coloured lines display observed data and spectra and model predictions, respectively, for selected epochs (expressed in JD – 2,450,000). Measurement errors (1 s.d.) are smaller than the symbol size. **b**, Viewing angles of the emitting region producing the (bulk of the) radiation at frequency ν at the epochs shown in **a**.

densities registered at 37 GHz in 2008–2009 correspond to a ‘quiescent’ optical state. This complex optical–radio correlation suggests that the emission in these two bands is produced in different regions of the jet. Explaining the multiwavelength light curves in terms of intrinsic processes would require very different physical conditions along the jet at various epochs, with model parameters chosen ad hoc at any time to reproduce the observed flux levels. Therefore, we propose an alternative scenario, in which the observed source behaviour is ascribed to orientation changes in the jet.

In the light curves of Figs 1 and 3 and Extended Data Fig. 1, especially in the optical and near-infrared bands, we can distinguish fast flares superimposed on a long-term trend. We adopted cubic spline interpolations through the binned data to represent the long-term behaviour of the well-sampled light curves in the *R* band, at 230 GHz and 37 GHz. For the radio and millimetre-wavelength light curves, which are characterized by smooth variations, we used a fixed time bin of 30 days. In the optical band, the fast flares are more rapid and pronounced when the source is brighter. This is expected when the long-term trend is due to a variable Doppler factor δ , which affects both the amplitudes and the timescales of the flux variations. In Methods, we summarize the basic concepts of the relativistic beaming theory and verify the contraction of

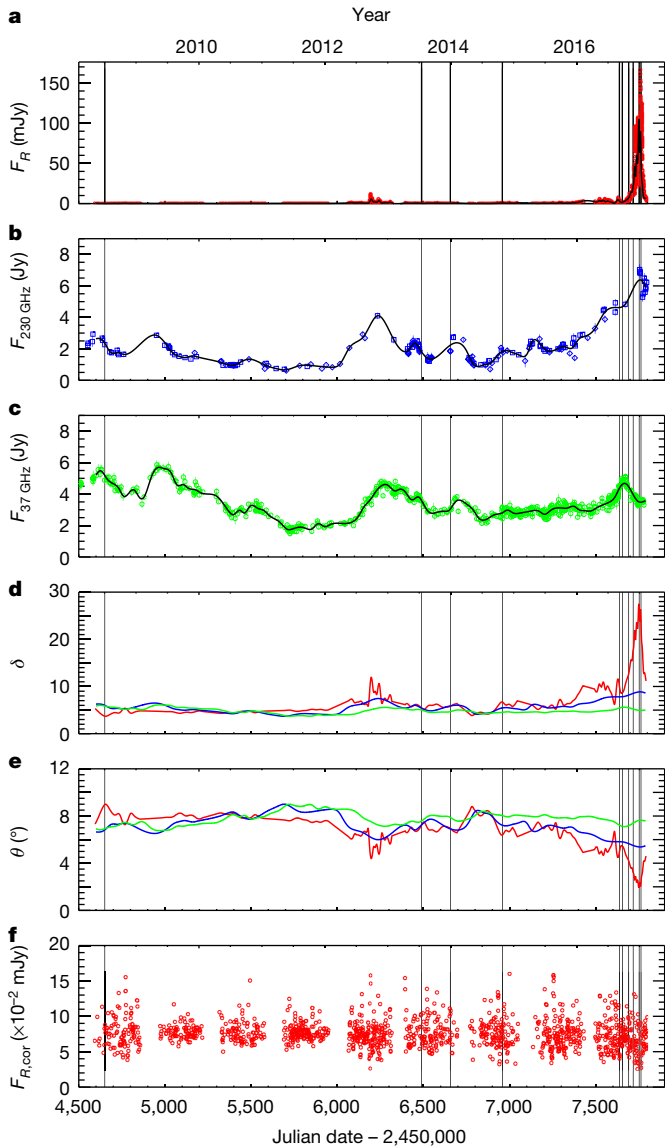


Figure 3 | Multifrequency behaviour of the jet emission of CTA 102 in 2008–2017. **a–c**, The *R*-band (**a**), 230-GHz (**b**) and 37-GHz (**c**) light curves contain 10,462, 170 and 576 flux density points, respectively. Error bars represent 1 s.d. measurement errors. Grey solid lines are cubic spline interpolations through the binned light curves. **d**, **e**, The Doppler factor δ (**d**) and viewing angle θ (**e**) of the optical (red), 230 GHz (blue) and 37 GHz (green) emitting regions according to the geometric model. **f**, *R*-band flux densities obtained for a constant $\delta = \delta_{\text{base}}$, namely, corrected for the variable beaming effect. The vertical lines indicate the epochs considered in Fig. 2.

the flux variation timescales in the brightest optical states. Accordingly, we adopted a variable bin size ranging from 24 days in the low-flux states to 3.4 days in the phases of the 2016–2017 outburst with the most marked changes. The dispersion (root-mean-square) of the optical flux densities around the spline in the various observing seasons changed from 0.03 mJy to 1.1 mJy at the time of the 2012 flare and to 18 mJy during the 2016–2017 outburst. This confirms that fast flares are amplified during high-flux states and strongly indicates that long-term flux changes are probably due to variations in the Doppler factor.

If we accept this, then we can trace the behaviour of δ in time (see Fig. 3) at the three reference frequencies. Because of Doppler beaming, what we observe at a given frequency is emitted by the source at a lower frequency. To correct for this effect, we use the relativistic invariant F_ν/ν^2 (see, for example, ref. 22), where F_ν is the flux density at

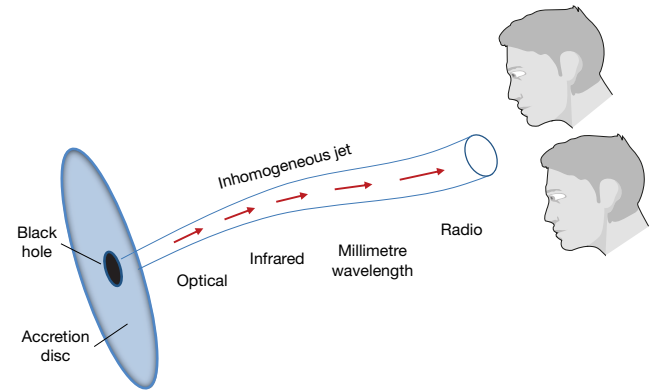


Figure 4 | Schematic representation of the proposed inhomogeneous jet model. Photons of different frequencies come from diverse jet regions. Because of the curvature of the jet, these regions have different orientations. Therefore, the corresponding emission is more (less) enhanced when the region is better (worse) aligned with the line of sight. The jet structure is dynamic, and the orientation of each region changes in time. The two observing eyes on the right represent two different alignments of the line of sight relative to the jet. The upper observer will see enhanced emission in the optical band and relatively low flux between the millimetre-wavelength and radio bands, while for the lower observer the most beamed radiation is the millimetre-wavelength one.

frequency ν . We build a base-level synchrotron spectrum for the long-term flux variations by fitting a log-parabolic model to the spline minima at 37 GHz and in the *R* band (see Fig. 2). This is what we assume to be the source SED for the minimum Doppler factor δ_{base} . Starting from here, for each observed F_ν , we look for the corresponding frequency ν_{base} in the base-level spectrum so that $F_\nu(\nu)/\nu^2 = F_{\nu_{\text{base}}}(\nu_{\text{base}})/\nu_{\text{base}}^2$. Once ν_{base} is found, we can calculate the Doppler factor as $\delta = \delta_{\text{base}}(\nu/\nu_{\text{base}})$. The trends of δ shown in Fig. 3 were obtained assuming typical values²³ for the bulk Lorentz factor ($\Gamma = 20$) and for the maximum viewing angle ($\theta_{\text{max}} = 9^\circ$) so that $\delta_{\text{base}} = 3.7$. Other choices for Γ and θ_{max} do not alter the general findings. The data constrain the ratio $\delta(t)/\delta_{\text{base}}$, whereas the choice of θ_{max} constrains Γ to yield a reasonable θ_{min} . In the light of what is known for blazars (for example, from the study of superluminal radio knots), values of θ_{max} between about 5° and 15° , which correspond to values of Γ between 35 and 10, are possible.

The Doppler factor depends on the bulk Lorentz factor and on the viewing angle. Although changes of Γ both along the jet (see Methods) and in time are in principle possible, they would require large differential accelerations or decelerations of the bulk flow in the various jet regions to explain the extreme flux changes in CTA 102. Instead, we favour the premise that Doppler factor variations are caused by orientation changes, which is also supported by the development of non-axisymmetric instabilities in magnetohydrodynamic jet simulations¹⁷ and by very-long-baseline interferometry observations of CTA 102²⁴ and blazars with swirling jets²⁵ or helical jet structures²⁶ (although on much larger, parsec scales).

Having $\delta(t)$ and a guess for Γ , we can then derive the viewing angle as a function of time. This is shown in Fig. 3 for the three reference bands. Flux enhancements are seen at a given frequency when the corresponding emitting region becomes better aligned with the line of sight. This is observed mainly in the optical band during the 2016–2017 outburst.

If we now correct the flux densities for the variable δ effect (see Methods), we obtain what we would observe if all the emitting regions of the jet had the same orientation, which does not change in time, that is, a constant δ . The residual variability corresponds to fast flares, which are probably caused by intrinsic, energetic processes. The fast flares show similar amplitudes over the whole 2008–2017 period.

The dispersion factor in the various observing seasons is reduced to 2 (0.009–0.022 mJy), compared to the original factor of 600 that should be ascribed to energetic processes within the jet to explain the observed variability.

The above scenario implies that the emission at different frequencies comes from different regions along a continuous jet (that is, the jet is inhomogeneous), which have different orientations with respect to the line of sight that vary in time. A schematic representation of our model is given in Fig. 4.

The variations in θ , δ and the flux (Figs 2 and 3) have smaller amplitudes and are smoother in the radio- and millimetre-wavelength bands compared to those seen at shorter wavelengths. According to the model, this is probably due to the fact that the radio and millimetre-wavelength emitting regions are much more extended along the curved jet than those emitting optical and near-infrared light. Smaller variations would be expected from a larger emission region because the observed emission would be integrated, and thus averaged, over a greater span of angles with respect to the line of sight.

We tested the proposed geometric model by comparing predicted and observed SEDs (Fig. 2). For a given epoch, the predicted SED was obtained by summing the thermal emission model with a synchrotron SED derived by applying the Doppler enhancement to the base-level SED with a frequency-dependent $\delta(\nu)$ (details are given in Methods). The agreement between model and data is very good.

We also analysed optical polarimetric data (see Methods and Extended Data Fig. 6). The polarization fraction shows strong variability throughout the period considered but no general correlation with the flux, suggesting a mainly stochastic process due to turbulence⁵ or a variable jet direction²⁷. On the other hand, the polarization angle undergoes large changes and in some cases its behaviour is consistent with the picture of a rotating twisted jet.

Online Content Methods, along with any additional Extended Data display items and Source Data, are available in the online version of the paper; references unique to these sections appear only in the online paper.

Received 22 June; accepted 6 October 2017.

Published online 4 December 2017.

- Blandford, R. D. & Königl, A. Relativistic jets as compact radio sources. *Astrophys. J.* **232**, 34–48 (1979).
- Ghisellini, G., Celotti, A. & Costamante, L. Low power BL Lacertae objects and the blazar sequence. Clues on the particle acceleration process. *Astron. Astrophys.* **386**, 833–842 (2002).
- Marscher, A. P. & Gear, W. K. Models for high-frequency radio outbursts in extragalactic sources, with application to the early 1983 millimeter-to-infrared flare of 3C 273. *Astrophys. J.* **298**, 114–127 (1985).
- Sikora, M., Błażejowski, M., Begelman, M. C. & Moderski, R. Modeling the production of flares in gamma-ray quasars. *Astrophys. J.* **554**, 1–11 (2001).
- Marscher, A. P. Turbulent, extreme multi-zone model for simulating flux and polarization variability in blazars. *Astrophys. J.* **780**, 87 (2013).
- Villata, M. & Raiteri, C. M. Helical jets in blazars I. The case of Mkn 501. *Astron. Astrophys.* **347**, 30–36 (1999).
- Marscher, A. P. *et al.* The inner jet of an active galactic nucleus as revealed by a radio-to-gamma-ray outburst. *Nature* **452**, 966–969 (2008).
- Abdo, A. A. *et al.* A change in the optical polarization associated with a γ -ray flare in the blazar 3C 279. *Nature* **463**, 919–923 (2010).
- Larionov, V. M. *et al.* Exceptional outburst of the blazar CTA 102 in 2012: the GASP-WEBT campaign and its extension. *Mon. Not. R. Astron. Soc.* **461**, 3047–3056 (2016).
- Casadio, C. *et al.* A multi-wavelength polarimetric study of the blazar CTA 102 during a gamma-ray flare in 2012. *Astrophys. J.* **813**, 51–64 (2015).

- Camenzind, M. & Krockenberger, M. The lighthouse effect of relativistic jets in blazars. A geometric origin of intraday variability. *Astron. Astrophys.* **255**, 59–62 (1992).
- Ostorero, L., Villata, M. & Raiteri, C. M. Helical jets in blazars. Interpretation of the multifrequency long-term variability of AO 0235+16. *Astron. Astrophys.* **419**, 913–925 (2004).
- Rieger, F. M. On the geometrical origin of periodicity in blazar-type sources. *Astrophys. J.* **615**, L5–L8 (2004).
- Villata, M. *et al.* The correlated optical and radio variability of BL Lacertae. WEBT data analysis 1994–2005. *Astron. Astrophys.* **501**, 455–460 (2009).
- Ghisellini, G. & Tavecchio, F. Canonical high-power blazars. *Mon. Not. R. Astron. Soc.* **397**, 985–1002 (2009).
- Marcotulli, L. *et al.* High-redshift blazars through NuSTAR eyes. *Astrophys. J.* **839**, 96 (2017).
- Mignone, A., Rossi, P., Bodo, G., Ferrari, A. & Massaglia, S. High-resolution 3D relativistic MHD simulations of jets. *Mon. Not. R. Astron. Soc.* **402**, 7–12 (2010).
- Villata, M. *et al.* The unprecedented optical outburst of the quasar 3C 454.3. The WEBT campaign of 2004–2005. *Astron. Astrophys.* **453**, 817–822 (2006).
- Raiteri, C. M. *et al.* Infrared properties of blazars: putting the GASP-WEBT sources into context. *Mon. Not. R. Astron. Soc.* **442**, 629–646 (2014).
- Impey, C. D. & Neugebauer, G. Energy distributions of blazars. *Astron. J.* **95**, 307–351 (1988).
- Malmrose, M. P., Marscher, A. P., Jorstad, S. G., Nikutta, R. & Elitzur, M. Emission from hot dust in the infrared spectra of gamma-ray bright blazars. *Astrophys. J.* **732**, 116 (2011).
- Urry, C. M. & Padovani, P. Unified schemes for radio-loud active galactic nuclei. *Publ. Astron. Soc. Pacif.* **107**, 803–845 (1995).
- Savolainen, T. *et al.* Relativistic beaming and gamma-ray brightness of blazars. *Astron. Astrophys.* **512**, A24 (2010).
- Fromm, C. M. *et al.* Catching the radio flare in CTA 102. III. Core-shift and spectral analysis. *Astron. Astrophys.* **557**, A105 (2013).
- Britzen, S. *et al.* A swirling jet in the quasar 1308+326. *Astron. Astrophys.* **602**, A29 (2017).
- Perucho, M., Kovalev, Y. Y., Lobanov, A. P., Hardee, P. E. & Agudo, I. Anatomy of helical extragalactic jets: the case of S5 0836+710. *Astrophys. J.* **749**, 55 (2012).
- Lyutikov, M. & Kravchenko, E. V. Polarization swings in blazars. *Mon. Not. R. Astron. Soc.* **467**, 3876–3886 (2017).

Supplementary Information is available in the online version of the paper.

Acknowledgements The Acknowledgements are listed in the Supplementary Information.

Author Contributions C.M.R. and M.V. managed the WEBT observing campaign, analysed the data, developed the geometric interpretation and wrote the manuscript. J.A.A.-P., A.A.A., M.I.C., N.C.-S., N.V.E., A.D.P., A.G., C.L., F.P., C.P., F.J.R.-L. and G.R.-C. performed near-infrared and optical observations and the related data reduction. I.A., C.C., A.F., J.L.G. and S.N.M. performed photometric and polarimetric optical and radio observations and the related data reduction. E.B., J.E., C.E., T.S.G., D.H., S.G.J., M.J., E.N.K., V.M.L., E.G.L., L.V.L., M.P.M., A.P.M., R.M., A.A.M., J.W.M., D.A.M., S.S.S., Yu.V.T., I.S.T. and A.A.V. acquired and reduced optical photometric and polarimetric data. R.B., G.V.B., G.A.B., V.B., M.S.B., P.C., D.C., W.-P.C., G.D., Sh.A.E., H.J., B.J., K.K., O.M.K., S.O.K., C.S.L., K.M., B.McB., B.Mi., M.M., D.O.M., S.V.N., M.G.N., J.M.O., D.N.O., E.O., T.A.P., N.R., K.S., A.C.S., M.R.S., E.S., B.A.S., L.S.-M., I.A.S., A.S. and O.V. carried out optical observations and the related data reduction. M.A.G., A.L., J.T., C.T. and M.T. performed radio observations and the related data reduction. W.B. acquired and reduced optical spectra. T.P. made optical photometric and spectroscopic observations and the related data reduction. P.S.S. carried out optical photometric, polarimetric and spectroscopic observations and reduced the data. F.D. and all the above authors reviewed and contributed to the manuscript.

Author Information Reprints and permissions information is available at www.nature.com/reprints. The authors declare no competing financial interests. Readers are welcome to comment on the online version of the paper. Publisher's note: Springer Nature remains neutral with regard to jurisdictional claims in published maps and institutional affiliations. Correspondence and requests for materials should be addressed to C.M.R. (raiteri@oato.inaf.it) or M.V. (villata@oato.inaf.it).

METHODS

Observations. Established in 1997, the WEBT Collaboration is an international collaboration of astronomers that monitor blazars in the optical, near-infrared, millimetre-wavelength and radio bands to investigate these highly active objects. Optical data used in this study were acquired at the following observatories: Abastumani (Georgia), AstroCamp (Spain), Belogradchik (Bulgaria), Calar Alto (Spain), Campo Imperatore (Italy), Crimean (Russia), Kitt Peak (USA), Lowell (USA; 70-cm, DCT and Perkins telescopes), Lulin (Taiwan), Michael Adrian (Germany), Mt Maidanak (Uzbekistan), New Mexico Skies (USA), Osaka Kyoiku (Japan), Polakis (USA), Roque de los Muchachos (Spain; Liverpool, NOT and TNG telescopes), ROVOR (USA), Rozhen (Bulgaria; 200- and 50/70-cm telescopes), San Pedro Martir (Mexico), Sirio (Italy), Skinakas (Greece), Steward (USA; Kuiper, Bok and Super-LOTIS), St Petersburg (Russia), Teide (Spain), Tien Shan (Kazakhstan), Tifaraje (Spain), Tucson (USA), Valle d'Aosta (Italy), Vidojevica (Serbia). The source magnitude was calibrated using common photometric standard stars in the source field (Star 1 and Star 2 in ref. 28, with the addition of other stars from ref. 29, when needed). This minimized possible offsets between different data sets. Observations were performed in the Johnson–Cousins *BVRI* bands, except for those at the NOT and Liverpool telescopes. The NOT data were obtained using the *ugriz* filters of the Sloan Digital Sky Survey and then converted with the transformations described in ref. 30. The Liverpool data were taken with the ‘red’ (770–1000 nm), ‘green’ (650–760 nm) and ‘blue’ (350–640 nm) cameras of the RINGO3 instrument and were transformed to the nearest standard (Johnson–Cousins) bands using shifts derived from data-taking periods overlapping with those of other instruments.

Near-infrared data were taken with the *JHK* filters at the Campo Imperatore, Lowell (Perkins) and Teide observatories. The data reduction is described in ref. 19.

Extended Data Fig. 1 shows the optical and near-infrared light curves of CTA 102 in the last four observing seasons. During the phases of the 2016–2017 outburst with the most dramatic variations, some episodes of noticeable and well-sampled intranight variability were observed. Four of them are shown in Extended Data Fig. 2.

Observations in the radio and millimetre-wavelength bands were performed with the 14-m radio telescope of the Metsähovi Radio Observatory (37 GHz) in Finland, the 30-m IRAM telescope (86 GHz and 230 GHz) in Spain and the Submillimetre Array (230 GHz) in Hawaii, USA. For details on the radio data analysis, see refs 31–33.

Spectral behaviour. The optical spectral behaviour of CTA 102 in the period of Extended Data Fig. 1 is shown in Extended Data Fig. 3, where the *B–R* colour indices (and the spectral slopes α of the $F \propto \nu^{-\alpha}$ law) are obtained by coupling data taken by the same telescope within 15-min intervals. A redder-when-brighter trend is observed until $R \approx 15$ (Spearman’s rank correlation coefficient $\rho = -0.82$), which is followed by a slight bluer-when-brighter trend ($\rho = 0.26$) as the source flux increases. This has been previously reported¹⁸ for 3C 454.3; it means that as the source brightens, the disk contribution becomes negligible and then the spectrum becomes bluer again, possibly because of changes in the Doppler factor³⁴. In particular, we note that in faint states, when the source is ‘blue’, the brightness in the *B* band is much more stable than that in the *R* band. This means that the *B*-band flux is dominated by the disk emission, but the *R*-band flux still receives important synchrotron contribution from the jet, which makes the colour index vary considerably in these states.

Spectroscopic observations in the optical band were carried out at the Steward (Kuiper, Bok and MMT telescopes) and Roque de los Muchachos (TNG and NOT telescopes) observatories. A selection of these spectra is shown in Extended Data Fig. 4. The spectra taken during faint states show a prominent, broad Mg II emission feature and a hard spectral shape. As the brightness rises, the lines gradually disappear and the spectra soften as a consequence of the increasing importance of the featureless synchrotron continuum over the BBB. At the highest flux levels the optical spectra harden again, which is consistent with the bluer-when-brighter behaviour discussed earlier.

Modelling the thermal emission component. To model the BBB, whose contribution is assumed to remain constant throughout the observing period, we examined the flux variation ranges in the monitored bands. Figure 2 shows all the data acquired in the 2008–2017 period by WEBT observers in the radio–millimetre (37 GHz, 86 GHz and 230 GHz), near-infrared (*KHJ*) and optical (*IRVB*) bands. When passing from the observed magnitudes to the flux densities, we corrected for Galactic extinction using the recommendations of the NASA/IPAC Extragalactic Database. We built the SED of a hypothetical minimum-brightness synchrotron state by fitting a logarithmic parabolic model to the observed radio–millimetre minimum-flux densities and a minimum synchrotron flux density in the *K* band, which was obtained by assuming that the observed minimum-flux density in that band receives equal synchrotron and thermal contributions. The adequacy of a

logarithmic parabolic model in describing the broadband synchrotron emission of blazars has been previously discussed (for example, in ref. 35), and this model is widely used. The thermal contribution from the BBB in all near-infrared and optical bands was then obtained by subtracting the model-predicted minimum synchrotron flux from the observed flux minima. The result is in agreement with that derived by ref. 19 for the same object using a quasi-stellar object template.

To complete the AGN model towards the mid–far infrared, we also added the emission contribution from the dust torus¹⁹, although it is always negligible, except for the case when the source is very faint.

Relativistic beaming theory. The Doppler factor is defined as $\delta = [\Gamma(1 - \beta \cos\theta)]^{-1}$, where β is the bulk velocity of the emitting source in units of the speed of light, $\Gamma = (1 - \beta^2)^{-1/2}$ is the corresponding Lorentz factor and θ is the viewing angle. Any time interval is shortened in the observer’s frame as $\Delta t = \Delta t'/\delta$, while frequencies are blueshifted as $\nu = \delta\nu'$ (primed symbols refer to quantities in the rest frame of the source). For a continuous jet with isotropic emission in the rest frame, the observed and rest-frame flux densities are linked by $F_\nu(\nu) = \delta^{2+\alpha} F'_{\nu'}(\nu')$, with $F'_{\nu'} \propto (\nu')^{-\alpha}$ (ref. 22). As a consequence, for a given beaming state characterized by a Doppler factor δ , the amplitude of the flux variation due to possible intrinsic processes is $\Delta F_\nu \propto \delta^{2+\alpha}$. Therefore, stronger beaming enhances not only the flux but also the amplitude of the intrinsic variations (fast flares), and shortens the variation timescale. We can correct the observed flux densities at a given frequency for the variable Doppler beaming effect according to $F_\nu^{\text{cor}} = F_\nu(\delta_\nu^{\text{const}}/\delta_\nu^{\text{var}})^{2+\alpha}$, where F_ν^{cor} represents the values that we would observe if the jet had a constant orientation resulting in $\delta_\nu^{\text{const}}$. In Fig. 3, we present F_ν^{cor} in the *R* band for $\delta_\nu^{\text{const}} = \delta_{\text{base}}$.

Variation timescales. Inspection of the optical light curves reveals that variation timescales shorten when the source is brighter, which is a robust indication that the long-term flux changes are due to Doppler factor variations. This can be verified quantitatively by performing time-series analysis, that is, investigating the time structure of flux variations. In order to avoid possible bias due to the long-term trend and related difference in flux amplitude, we applied this analysis to flux densities corrected for the variable relativistic beaming effect (see Fig. 3). We separated the data set in two subsets corresponding to bright ($\delta > \delta_{\text{max}}/2$) and faint ($\delta < \delta_{\text{max}}/2$) states, thus separating the 2016–2017 outburst from the rest of the data. For the two subsets we calculated the structure function³⁶ (SF), which expresses the squared mean difference of the flux densities as a function of the time separation τ between data pairs. The results are shown in Extended Data Fig. 5, where the minimum variability timescale corresponds to the first peak of the SF, which is about 4 days for the bright states and approximately 8 days for the faint ones. This doubling of the timescales matches very well the δ -halving criterion adopted to separate the two subsamples ($\Delta t \propto \delta^{-1}$). We checked the SF results by means of the discrete autocorrelation function³⁷ (ACF; Extended Data Fig. 5b). The timescales are defined by the ACF minima. The shortest timescales for the high (low) flux states are confirmed to be about 4 (8) days.

Finally, we applied the Kolmogorov–Smirnov statistic to check whether the SFs and ACFs of the two subsamples are drawn from the same distribution. The values of the Kolmogorov–Smirnov statistic are 0.67 for the SFs and 0.39 for the ACFs with significance levels 1.1×10^{-6} and 1.0×10^{-4} , respectively; such small values mean that the two distributions are significantly different.

In view of these results and in agreement with the relativistic beaming theory, we modelled the optical long-term trend by setting an adaptive bin size that reduces the time bin by a factor n as the flux increases by a factor $n^{2+\alpha}$, where $n = 2, 3, 4, 5, 6, 7$ and $\alpha = 1.7$ is the slope of the minimum synchrotron spectrum in the *R* band. **Lorentz factor.** We have assumed a single Γ value throughout the jet region of interest. Other scenarios, with Γ varying along or transversally to the jet are in principle possible and have been adopted in some cases. However, the portion of the jet that we are considering (that is, that emitting the bulk of photons from the optical band down to 37 GHz) is inside the inner core of the radio images, so that we can easily guess that the Lorentz factor does not change considerably along this region. On the other hand, transverse velocity gradients, for which there is no observational evidence in the inner zones of blazar jets, are sometimes introduced to explain the properties of high-energy, comptonized radiation^{38,39}, but they would represent an unnecessary complication for the purposes of our model.

Comparison between predicted and observed SEDs. The frequency-dependent trend of the Doppler factor, which is necessary to obtain a model SED for a given epoch, was derived by interpolating or extrapolating the values of δ at 37 GHz, 230 GHz and in the *R* band at that epoch (Fig. 3) in the δ – $\log\nu$ space, after correcting the frequencies for the different beaming affecting the base-level SED and the model SED for the considered epoch. We performed linear interpolation of the Doppler factor in the δ – $\log\nu$ space by minimizing the χ^2 error statistic. When the unreduced χ^2 goodness-of-fit statistic was greater than 1.2, which indicates a poor fit, we also performed a parabolic interpolation and took the average fit

between the two. This occurred three times, for the epochs 7,637, 7,654 and 7,691 (in JD – 2,450,000).

Figure 2 displays ten SEDs that correspond to selected epochs spanning the source variation range. The predicted and observed SEDs are in very good agreement. In particular, the spectral slopes of the calculated SEDs in the optical band match very well those of the observed optical spectra. The offset between the optical and near-infrared data at epoch 7,717 is probably due to non-perfect simultaneity of the observations coupled with strong intranight variability. In Fig. 2, we also show the corresponding viewing angle as a function of frequency for all epochs. The brightest state during the 2016–2017 optical outburst corresponds to the maximum difference of orientation (maximum misalignment) between the radio- and optical-band emitting zones when the optical zone has the best alignment with the line of sight.

Polarization. Optical polarimetric data were acquired by seven observatories: Calar Alto, Crimean, Lowell (Perkins), ROVOR, San Pedro Martir, Steward and St Petersburg. The temporal behaviour of the jet polarization fraction P_{jet} and electric vector polarization angle (EVPA) are shown in Extended Data Fig. 6.

P_{jet} was obtained from the observed polarization degree P by correcting for the dilution effect of the unpolarized BBB emission, $P_{\text{jet}} = P \times F / F_{\text{jet}}$, where F is the de-absorbed flux density and F_{jet} is the same quantity after subtraction of the BBB flux contribution. Extended Data Fig. 6 also shows the mean value of P_{jet} for the whole period and the mean values and standard deviations for each observing season. The EVPA was adjusted for the $\pm n \times \pi$ (n , natural number) ambiguity by requiring that the angle difference between subsequent points in the same observing season is minimum.

Strong variability of P_{jet} and large changes of the EVPA both in the clockwise and anticlockwise directions are observed throughout the period considered. No general correlation is found with the observed flux or with the flux variations that remain after correction for variable Doppler beaming (see Fig. 3). The only hint of correlation between polarization and flux variations is given by the coincidence of the minima in the viewing angle (flux peaks) with either fast changes of the EVPA (at JD \approx 2,457,300) or inversion of its direction (at JD \approx 2,456,200 and JD \approx 2,457,750; that is, during the peaks of the 2012^{9,10} and 2016–2017 outbursts). Both situations may occur when considering a rotating helical jet with a longitudinal magnetic field. As the helix rotates and the emitting region approaches the line of sight, the EVPA undergoes large variations or changes of direction, depending on whether the angle between the line of sight and the helix axis is smaller or larger than the helix pitch angle, respectively. However, some turbulence must be present⁵ to explain the irregular behaviour of P_{jet} . An alternative explanation could be provided by ref. 27, which showed that apparent random behaviour of P (and F) can accompany large EVPA fluctuations in a jet with a helical magnetic field and variable propagation direction.

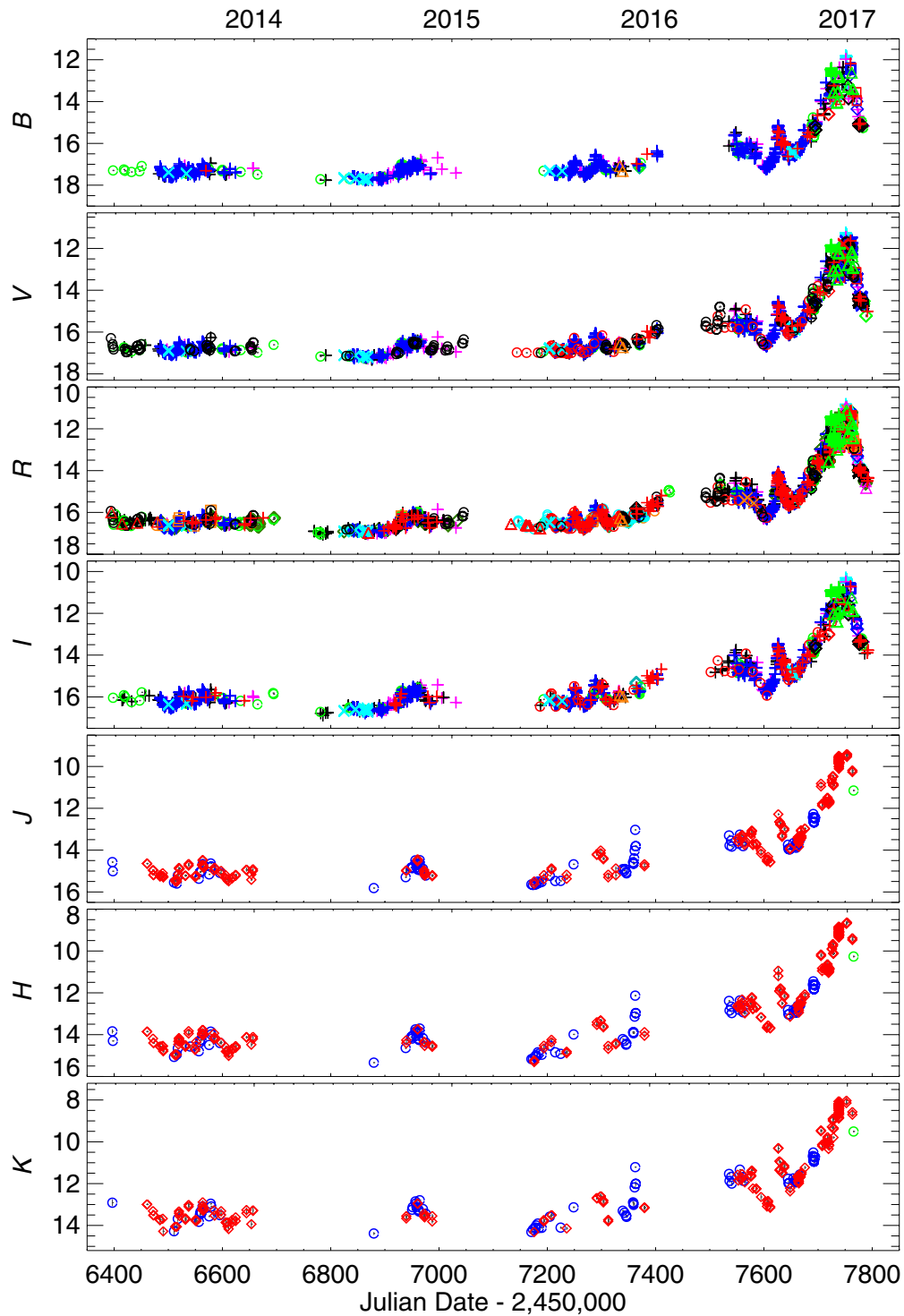
Comparison with a standard one-zone model. We have shown that the long-term multiwavelength flux variability of CTA 102 is well explained by changes of the Doppler factor. We now investigate whether commonly used one-zone models can also explain these spectral changes in the same way. In Extended Data Fig. 7 we present results obtained with the standard one-zone model, proposed in ref. 40. We first fitted the SED at JD = 2,457,637, which represents an intermediate flux level. We used the following physical parameters: radius of the emitting zone $\log[R \text{ (cm)}] = 17.8$; magnetic field $B = 0.08$ G; Doppler factor $\delta = 21.5$; electron

density in the emitting zone $N = 30 \text{ cm}^{-3}$; electron energies between $\log\gamma_{\text{min}} = 1$ and $\log\gamma_{\text{max}} = 5$; and an electron energy distribution expressed by a power law with $\alpha = 2.15$ and a cut-off electron energy $\log\gamma_{\text{cut}} = 3.6$.

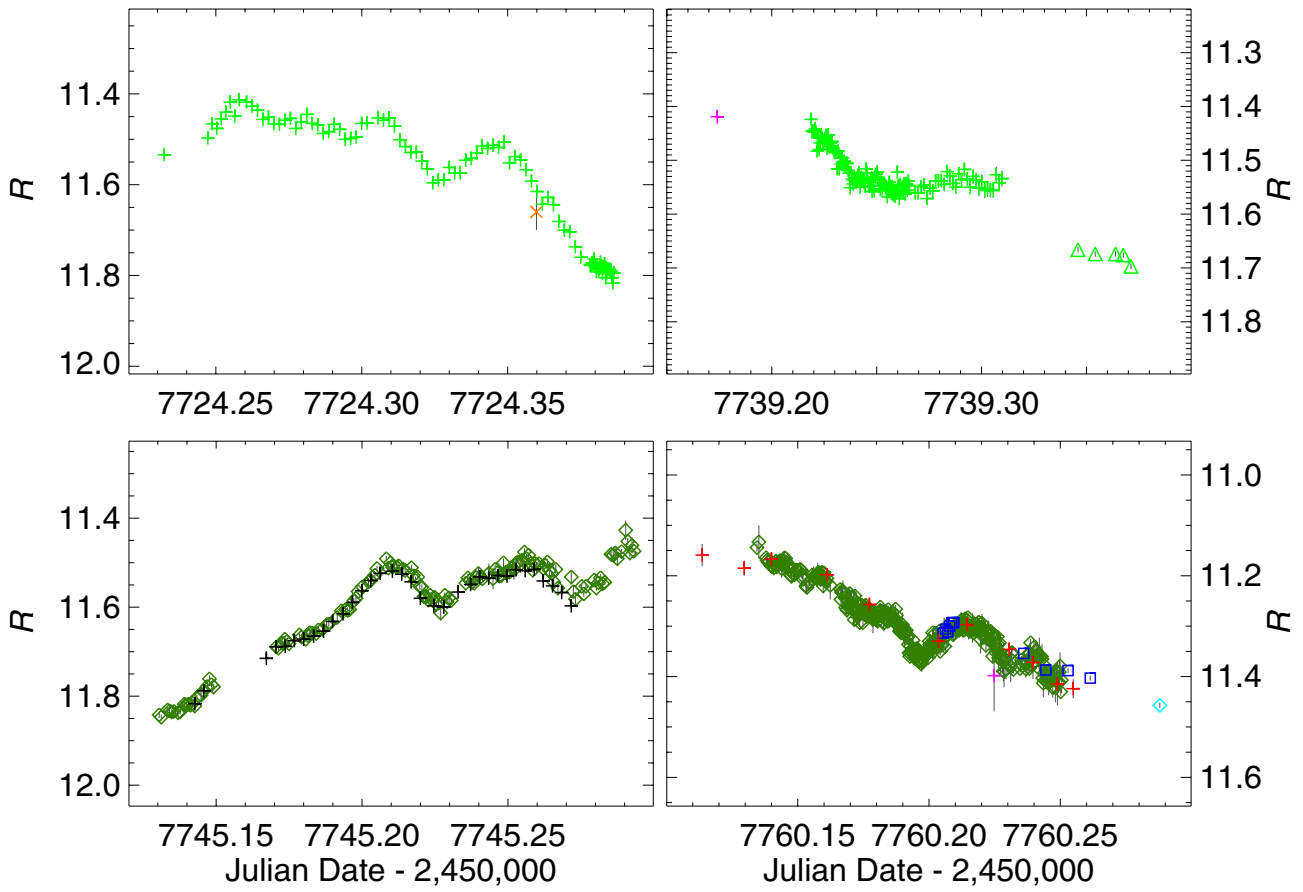
We then tried to fit the highest and the lowest optical levels shown in Fig. 2 by changing only δ . The brightest state requires $\delta = 40$ and the faintest $\delta = 9.5$. However, this model does not fit the lower-frequency data; in particular, the flux in the millimetre-wavelength band is largely over- or under-estimated. Better fits could be obtained with the one-zone model, but at the cost of changing a number of parameters, especially the electron energy distribution. One should then check if a reasonable temporal evolution of all these parameters can be found to explain the multiwavelength light curves.

Data availability. Data taken and assembled by the WEBT Collaboration (optical, near-infrared and radio light curves) are stored in the WEBT archive at the Osservatorio Astrofisico di Torino, INAF (<http://www.oato.inaf.it/blazars/webt/>); they become publicly available one year after publication and can be requested from the WEBT President, M.V. (villata@oato.inaf.it). Optical spectropolarimetric data from the Steward Observatory are publicly available and can be downloaded from <http://james.as.arizona.edu/~psmith/Fermi/>.

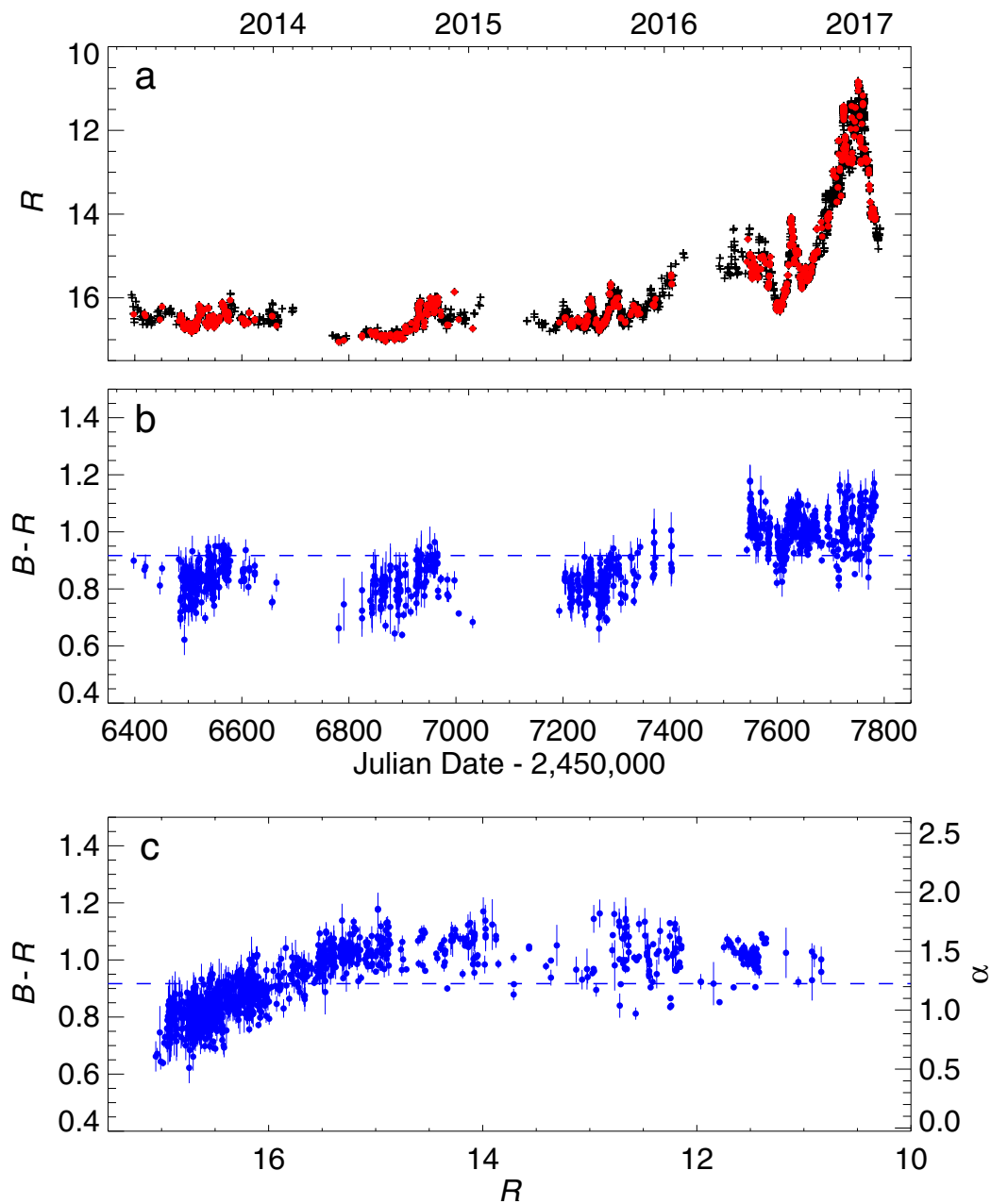
28. Raiteri, C. M., Villata, M., Lanteri, L., Cavallone, M. & Sobrito, G. *BVR* photometry of comparison stars in selected blazar fields. II. Photometric sequences for 9 quasars. *Astron. Astrophys. Suppl. Ser.* **130**, 495–500 (1998).
29. Doroshenko, V. T. *et al.* BVRI CCD-photometry of comparison stars in the fields of galaxies with active nuclei. *V. Astrophysics* **56**, 343–358 (2013).
30. Jordi, K., Grebel, E. K. & Ammon, K. Empirical color transformations between SDSS photometry and other photometric systems. *Astron. Astrophys.* **460**, 339–347 (2006).
31. Teräsraanta, H. *et al.* Fifteen years monitoring of extragalactic radio sources at 22, 37 and 87 GHz. *Astron. Astrophys. Suppl. Ser.* **132**, 305–331 (1998).
32. Agudo, I., Thum, C., Wiesemeyer, H. & Krichbaum, T. P. A. 3.5 mm polarimetric survey of radio-loud active galactic nuclei. *Astrophys. J. Suppl. Ser.* **189**, 1–14 (2010).
33. Gurwell, M. A., Peck, A. B., Hostler, S. R., Darrah, M. R. & Katz, C. A. Monitoring phase calibrators at submillimeter wavelengths. In *From Z-Machines to ALMA: (Sub)Millimeter Spectroscopy of Galaxies (ASP Conf. Ser. 375)* (eds Baker, A. J. *et al.*) 234–237 (Astronomical Society of the Pacific, 2007).
34. Larionov, V. M., Villata, M. & Raiteri, C. M. The nature of optical and near-infrared variability of BL Lacertae. *Astron. Astrophys.* **510**, A93 (2010).
35. Massaro, E., Perri, M., Giommi, P. & Nesci, R. Log-parabolic spectra and particle acceleration in the BL Lac object Mkn 421: Spectral analysis of the complete BeppoSAX wide band X-ray data set. *Astron. Astrophys.* **413**, 489–503 (2004).
36. Simonetti, J. H., Cordes, J. M. & Heeschen, D. S. Flicker of extragalactic radio sources at two frequencies. *Astrophys. J.* **296**, 46–59 (1985).
37. Hufnagel, B. R. & Bregman, J. N. Optical and radio variability in blazars. *Astrophys. J.* **386**, 473–484 (1992).
38. Ghisellini, G., Tavecchio, F. & Chiaberge, M. Structured jets in TeV BL Lac objects and radiogalaxies Implications for the observed properties. *Astron. Astrophys.* **432**, 401–410 (2005).
39. Sikora, M., Rutkowski, M. & Begelman, M. C. A spine-sheath model for strong-line blazars. *Mon. Not. R. Astron. Soc.* **457**, 1352–1358 (2016).
40. Tramacere, A., Giommi, P., Perri, M., Verrecchia, F. & Tosti, G. Swift observations of the very intense flaring activity of Mrk 421 during 2006. I. Phenomenological picture of electron acceleration and predictions for MeV/GeV emission. *Astron. Astrophys.* **501**, 879–898 (2009).



Extended Data Figure 1 | Observed light curves of CTA 102 in the optical *BVRI* and near-infrared *JHK* bands. The curves are built with data from 39 telescopes (marked with different symbols and colours) in 28 observatories participating in the WEBT project. Measurement errors (1 s.d.) are smaller than the symbol size.

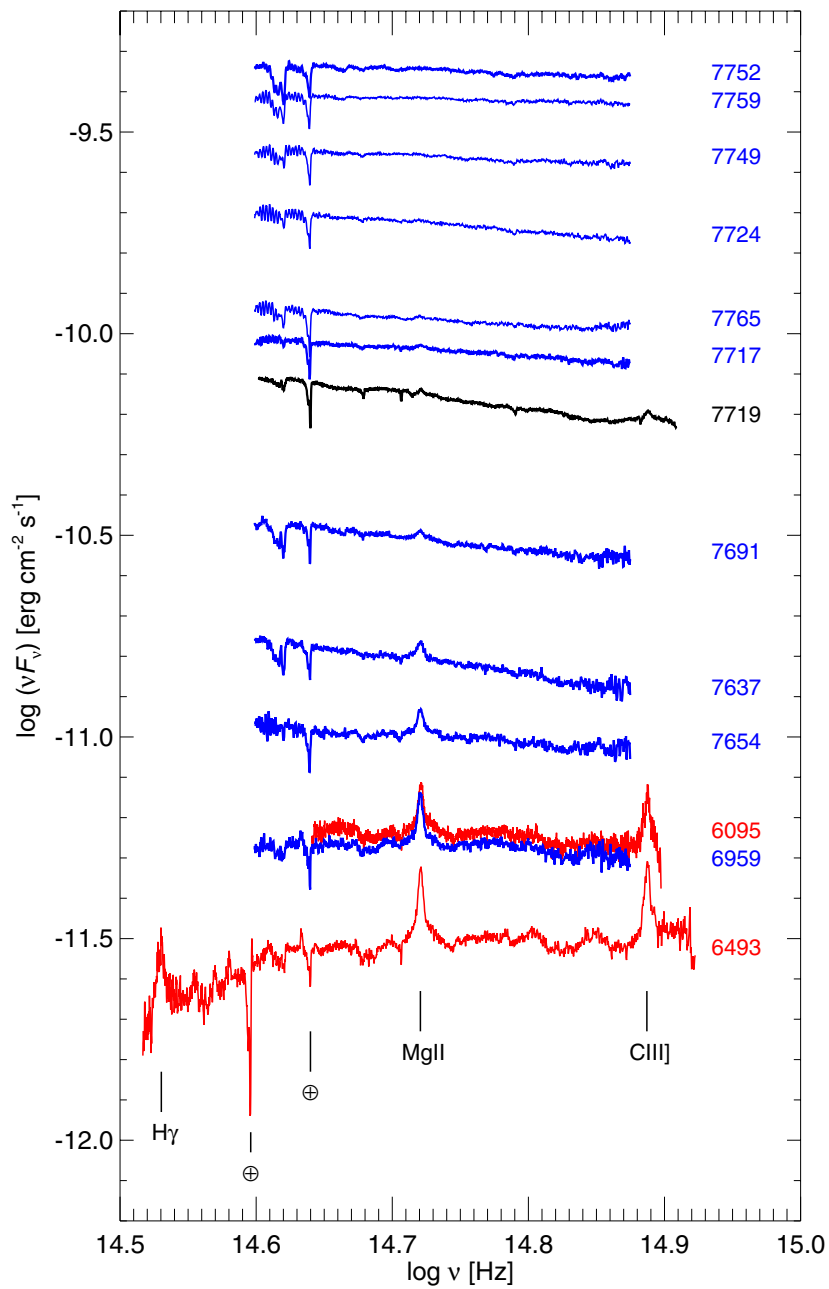


Extended Data Figure 2 | Four episodes of noticeable and well-sampled intranight variability. Magnifications of the *R*-band light curve of Fig. 1 during the phases of the 2016–2017 optical outburst with the most dramatic changes reveal very fast brightness variations. Error bars represent 1 s.d. measurement errors.



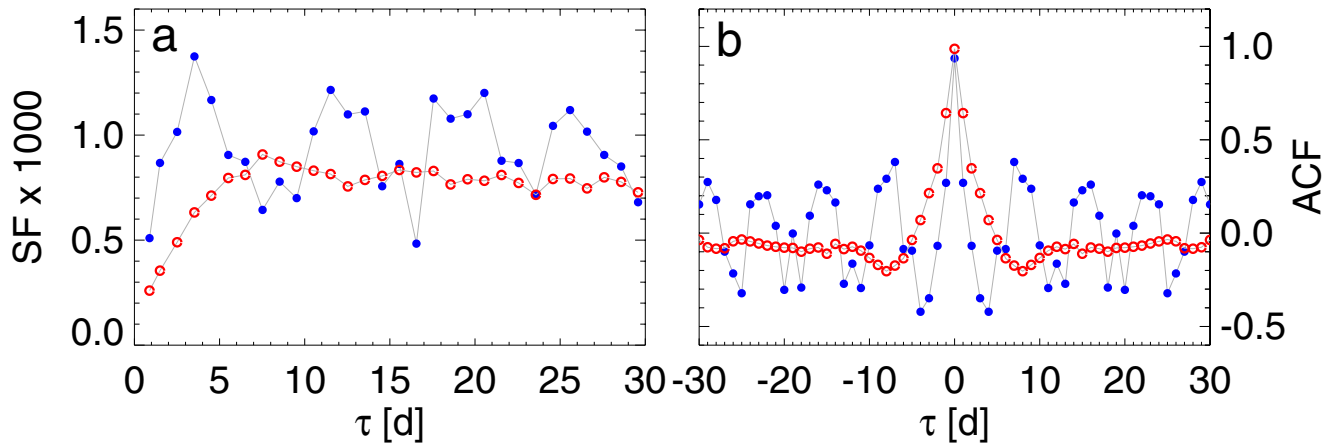
Extended Data Figure 3 | Colour behaviour of CTA 102. **a**, The R -band light curve; red dots represent the data points used to build the colour indices. **b–c**, The $B - R$ colour index as a function of time and R -band magnitude. Error bars were obtained by summing in quadrature the 1-s.d. measurement errors of the corresponding B and R data. The dashed line

indicates the average $B - R$ value. The parameter α is the spectral index of the $F \propto \nu^{-\alpha}$ law. The redder-when-brighter trend that characterizes faint source states ($R > 15$) turns into a slight bluer-when-brighter trend as the source flux increases.



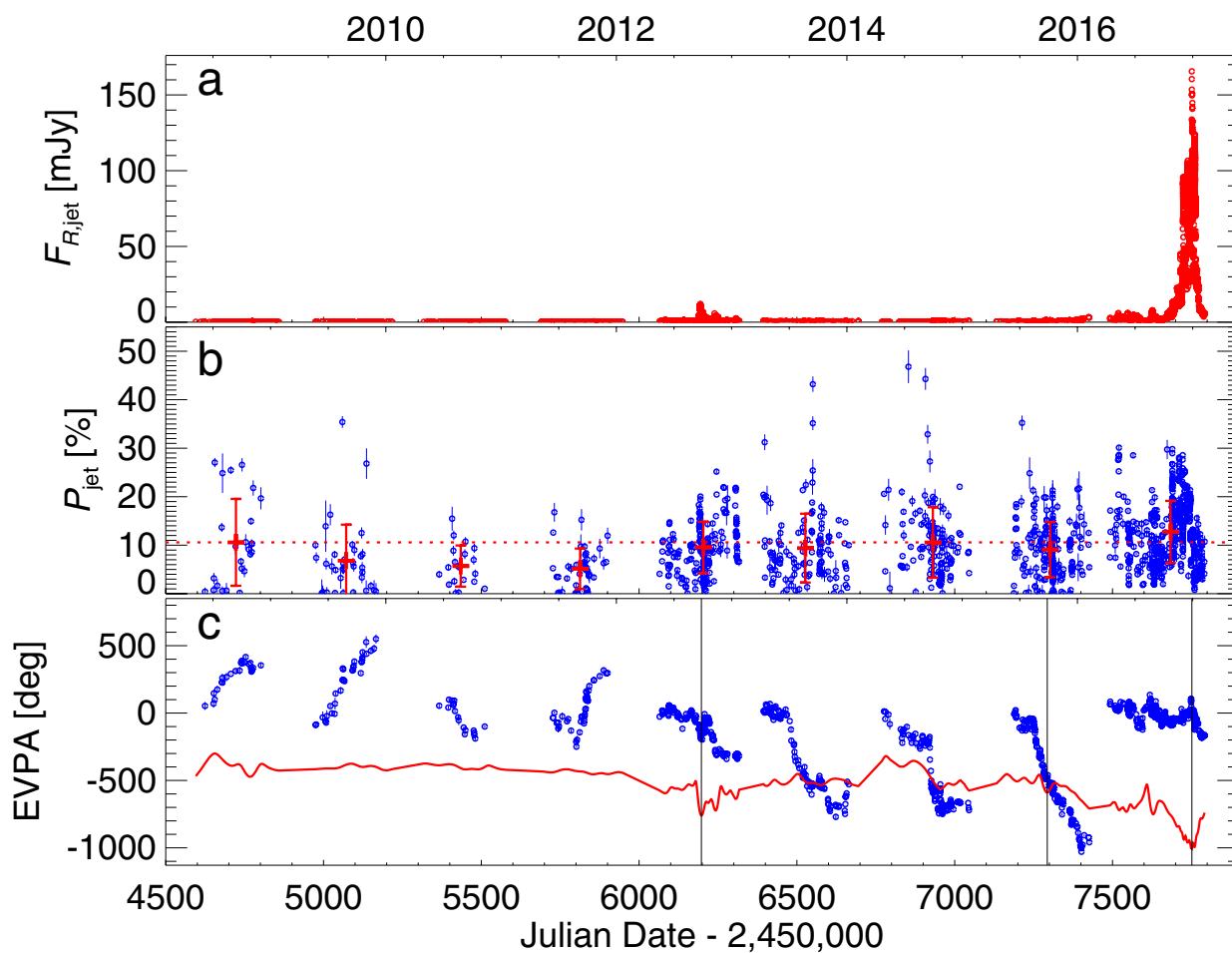
Extended Data Figure 4 | Optical spectra of CTA 102 in different brightness states. Data are from the Steward (blue) and Roque de los Muchachos (TNG and NOT; black and red, respectively) observatories and have been corrected for Galactic extinction. The observing epochs are

given on the right, expressed in JD - 2,450,000. The main broad emission lines (more visible in faint states) are indicated. As the flux increases, the source spectrum first softens (redder-when-brighter trend) and then gradually hardens (bluer-when-brighter).



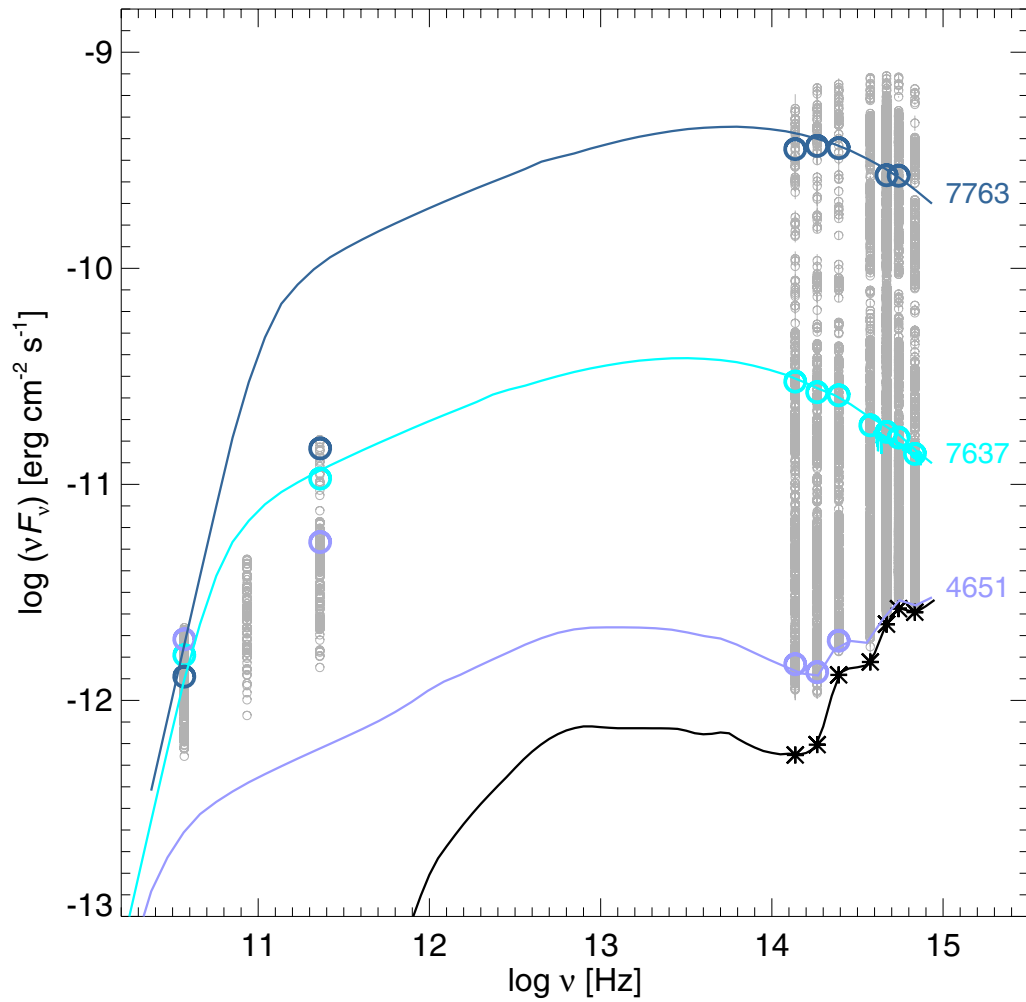
Extended Data Figure 5 | Results of time-series analysis on the optical fluxes. **a**, Structure function of *R*-band flux densities, corrected for the long-term trend due to variable relativistic beaming (see Fig. 3). **b**, Autocorrelation function of the same corrected fluxes. τ is the time

separation between points, expressed in 1-day bins. Filled blue and empty red symbols refer to bright (more beamed) and faint (less beamed) observed states, respectively, and show that variation timescales are halved when the Doppler factor doubles.



Extended Data Figure 6 | Temporal behaviour of the polarization of CTA 102. **a**, The jet optical flux densities. **b**, The jet polarization fraction P_{jet} . The horizontal dotted line indicates the average value over the whole period and crosses show the mean values in each observing season. Error

bars represent 1 s.d. **c**, The electric vector polarization angle. The red solid line displays the trend of the viewing angle in the R band (rescaled to fit in the plot; see Fig. 3) and the vertical lines mark the most interesting events, which are discussed in the text.



Extended Data Figure 7 | One-zone model fits to the SEDs of CTA 102. The standard one-zone model⁴⁰ has been used to fit three SEDs in intermediate-, high- and low-brightness states (see also Fig. 2). Once the physical parameters of the emitting zone are adjusted to reproduce the intermediate-brightness state, the other two model fits are obtained by

changing only the Doppler factor to match the optical data. As a result, the millimetre-wavelength flux is largely over- or under-estimated. In all model fits, the thermal component (accretion disk and torus; black line and symbols) was added to the one-zone model synchrotron component.



Long-term Periodicities of Cataclysmic Variables with Synoptic Surveys

Michael Ting-Chang Yang¹, Yi Chou¹, Chow-Choong Ngeow¹, Chin-Ping Hu², Yi-Hao Su¹, Thomas A. Prince³,
Shrinivas R. Kulkarni³, David Levitan³, Russ Laher⁴, Jason Surace⁵, Andrew J. Drake⁶, Stanislav G. Djorgovski³,
Ashish A. Mahabal³, Matthew J. Graham⁶, and Ciro Donalek³

¹ Graduate Institute of Astronomy, National Central University, Jhongli, Taiwan; mky@astro.ncu.edu.tw

² Department of Physics, The University of Hong Kong, Pokfulam Road, Hong Kong

³ Division of Physics, Mathematics and Astronomy, California Institute of Technology, Pasadena, CA 91125, USA

⁴ Infrared Processing and Analysis Center, California Institute of Technology, Pasadena, CA 91125, USA

⁵ Spitzer Science Center, California Institute of Technology, Pasadena, CA 91125, USA

⁶ California Institute of Technology, Pasadena, CA 91125, USA

Received 2017 May 21; accepted 2017 June 20; published 2017 July 20

Abstract

A systematic study on the long-term periodicities of known Galactic cataclysmic variables (CVs) was conducted. Among 1580 known CVs, 344 sources were matched and extracted from the Palomar Transient Factory (PTF) data repository. The PTF light curves were combined with the Catalina Real-Time Transient Survey (CRTS) light curves and analyzed. Ten targets were found to exhibit long-term periodic variability, which is not frequently observed in the CV systems. These long-term variations are possibly caused by various mechanisms, such as the precession of the accretion disk, hierarchical triple star system, magnetic field change of the companion star, and other possible mechanisms. We discuss the possible mechanisms in this study. If the long-term period is less than several tens of days, the disk precession period scenario is favored. However, the hierarchical triple star system or the variations in magnetic field strengths are most likely the predominant mechanisms for longer periods.

Key words: (stars:) novae – cataclysmic variables – (stars:) binaries (including multiple): close – surveys – catalogs – methods: data analysis – methods: observational

Online material: color figures

1. Introduction

A cataclysmic variable (CV) is an accreting binary system composed of a white dwarf (WD) as primary and a low-mass companion. In general, when the companion fills its Roche lobe, the mass flow stream passing through the inner Lagrangian point (L_1) generates an accretion disk around a non-magnetic WD. On the other hand, only a truncated disk can be formed in an intermediate polar (DQ Her type), a subclass of CVs with a highly magnetic WD. The WD in the polar (AM Her type) system has an even higher magnetic field that can prevent the formation of the accretion disk. The variability on different timescales of CV systems is caused by different mechanisms. The orbital periods of CVs typically range from 70 min to 24 h, which is strictly related to the binary separation and mass ratio. A census on the orbital period distribution of CVs reveals a period gap of approximately 2–3 h (e.g., Warner 1995), which is explained by the evolution scenarios of CVs.

The variation with a timescale longer than a day is typically called the superorbital or long-term variation in CV systems. Long-term variation has been detected in only a few CVs, and this has been neglected in subsequent research. Kafka & Honeycutt (2004) studied 100 CVs using the structure function to characterize the timescales of the long-term variabilities.

However, no further results and the implications behind the long-term variabilities were addressed in this study. Various types of mechanisms were proposed to explain the long-term variations of CVs. For example, Thomas et al. (2010) discovered a long-term modulation with a period of 4.43 ± 0.05 d in cataclysmic variable PX And through eclipse analysis, which was considered to be the disk precession period that triggers the negative superhump in this system. On the other hand, from the analysis of eclipse time variations in eclipsing binary DP Leo, a third body with an elliptical orbit and a period of $P = 2.8 \pm 2.0$ yrs was found by Beuermann et al. (2011). Honeycutt et al. (2014) discovered a period of ~ 25 d oscillations, regarded as the result of accretion disk instability in V794 Aql during its small outbursts. Warner (1988) proposed that the cyclical variations of the orbital periods (on the timescale of years to decades) for some CVs are related to their quiescent magnitudes and outburst intervals, and the variations were inferred as the effect of the solar-type magnetic cycle of the companion. Kalomeni (2012) discovered several polars exhibiting long-term variability with a timescale of hundreds of days, likely caused by the modulation of the mass-transfer rate owing to the magnetic cycles in the companion stars.

Previous studies on the long-term periodicities of CVs are sporadic. With the help of recent large synoptic surveys, we are able to search for and further characterize the long-term variations of the CVs systematically. In Section 2, we introduce the synoptic survey projects we utilized, and the corresponding intensive observations made using the Lulin One-Meter-Telescope (LOT). Descriptions of our analysis method for the long-term periodicity of the sources are presented in Section 3. The possible mechanisms driving the long-term variability and further implications are presented in Section 4. In Section 5, we summarize the long-term periodicities from our results and discuss some of the previous studies related to the sources.

2. CV Catalog, Synoptic Surveys and Observations

The CVs selected for this study are from the catalog by Downes et al. (2006). The data used for this study are from two surveys: the Palomar Transient Factory (PTF) and the Catalina Real-Time Transient Survey (CRTS). In addition, the LOT, a small telescope capable of intensive observations, was utilized for finding the orbital periods of the targets that were unknown before this study.

2.1. CV Catalog for Source Matching

The CV catalog produced by Downes et al. (2006) (hereafter Downes' catalog) is taken as a reference catalog for our study (see Downes et al. 2001 for the catalog description). The latest version of the catalog contains 1830 sources, including 1580 CVs and 250 non-CVs. The catalog used the General Catalog of Variable Stars (GCVS) name as the source identifier. However, some of the sources have no GCVS names, so the constellation name of the sources was adopted as the identifier. In this study, if multiple sources without GCVS names are in the same constellation, then the constellation name with distinct numbers were adopted as the project name of the source (e.g., UMa 01 for one of the CVs in the constellation Ursa Major). We used the Downes' catalog for our matching process and then retrieved the light curves of the matches.

2.2. Palomar Transient Factory

The PTF (Law et al. 2009; Rau et al. 2009) project began observing in 2009.⁷ The Samuel Oschin Telescope, a 48-in Schmidt telescope with Mould R, SDSS g' , and several H- α filters was adopted for the survey. The PTF and its successor intermediate PTF (iPTF) projects were accomplished in 2017 March. A 7.9 square degree field of view (FOV) was achieved with the camera configuration of PTF and iPTF. The next generation of the PTF project, called the Zwicky Transient Facility (ZTF), with its many upgrades in software and hardware, will be operated in mid 2017.

⁷ <http://www.ptf.caltech.edu/>

The software pipelines were readied for the real-time discoveries of transients (Masci et al. 2017) and for the generation of source detections (IPAC pipeline, Laher et al. 2014). The IPAC pipeline was developed by the Infrared Processing and Analysis Center (IPAC),⁸ which reduced the images and generated the detection catalogs on a frame basis. The detection catalogs are stored in the IRSA archive.⁹ We extracted the data from the local copies of the full photometric catalogs in IPAC. Metadata tables with information from the catalog headers were created for accessing the photometric data quickly. The light curve of a specific source could be retrieved out of the total of ~ 24 Terabytes within 2 min via our data-retrieval pipeline.¹⁰ Figure 1 shows a flowchart of the data-retrieval pipeline. A large area of the sky has been observed by the PTF project. The observation numbers in the density map of sky covered by PTF/iPTF are shown in Figure 2.

2.3. Catalina Real-Time Transient Survey

The CRTS project is conducted by analyzing data from the Catalina Sky Survey (CSS), which is originally designed for the study of asteroids. The CRTS team made use of the photometric data for studying the transient sky (Drake et al. 2009; Mahabal et al. 2011; Djorgovski et al. 2012).¹¹ The data was gathered using three telescopes in the Northern and Southern Hemispheres, including the Catalina Sky Survey (CSS, 0.7m), the Mt. Lemmon Survey (MLS, 1.5m), and the Sliding Springs Survey (SSS, 0.5m). No filter was adopted for the survey to maximize the discovery of asteroids. The CRTS data is available to the public through the Catalina Surveys Data Release 2 (CSDR2) website.¹² The calibrated light curves can be accessed by users through the interface.

2.4. Lulin One-Meter Telescope

The orbital periods of the CVs are essential to the discussion on the mechanism of their long-term periodicities. For our sources of interest, only a portion of them have known orbital periods, as presented in Downes et al. (2006) and references therein. To investigate the targets with unknown orbital periods, we used the Lulin One-Meter Telescope, located in central Taiwan, to perform short-cadence observations. The LOT is a telescope with a FOV of $1' \times 1'$. The limiting magnitudes with 5 min exposures are approximately 20–20.5 mag in V and R bands. We used the R-band filter for our short-cadence observations. The 3 sources we observed with LOT are presented in Table 1.

⁸ <http://www.ipac.caltech.edu/>

⁹ <http://irsa.ipac.caltech.edu>

¹⁰ The IPAC web interface with faster data-retrieval process is currently online.

¹¹ <http://crts.caltech.edu>

¹² <http://nessi.cacr.caltech.edu/DataRelease/>

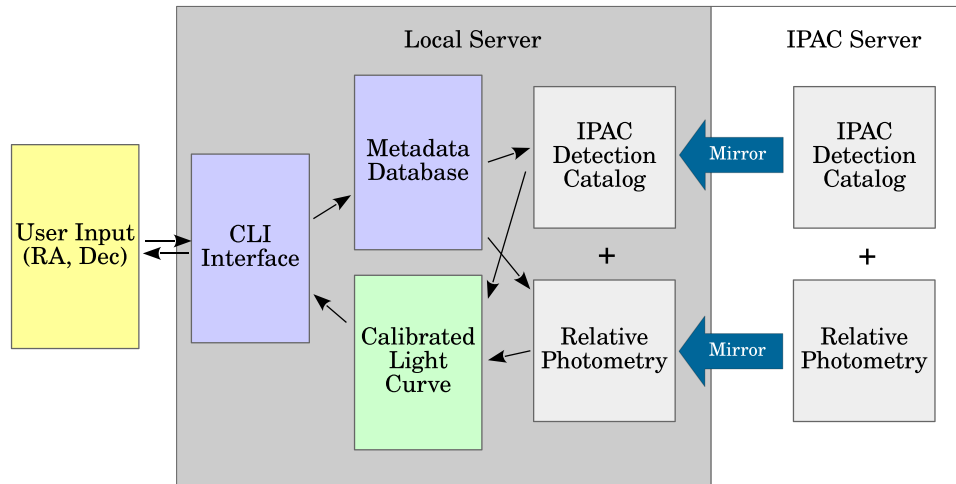


Figure 1. Data flowchart of the light curve retrieval process for PTF. IPAC data-processing pipeline (Laher et al. 2014) reduces the survey images, and generates IPAC detection catalogs and relative photometry for each frame (right panel). Middle panel: programs, metadata database, and mirrors of the processed data in our local server. The metadata database is generated to store the header information of the IPAC detection catalogs, and is used to speed up the data-retrieval process. A command line (CLI) interface was made for users to retrieve the calibrated light curve for a specific source. The speed of the light curve-retrieval process is increased by a significant factor in this implementation.

(A color version of this figure is available in the online journal.)

3. Data Analysis

3.1. Photometric Calibration

The photometric systems of PTF and CRTS are different. The light curves from the PTF repository are in the Mould R-band. The data retrieved from the CSDR2 are in white light (unfiltered). To calibrate the difference between the systems, a linear relation between the PTF and CRTS systems was assumed in our analysis. The linear regression to find the coefficients of the line is described as $M_{\text{PTF}} = A \times M_{\text{CRTS}} + B$, where M_{PTF} is the R-band magnitude measured by the PTF, and M_{CRTS} is the white-light magnitude measured by the CRTS. The slope A and the intercept B were fit across the magnitudes of different reference stars in the nearby regions of the CVs. Most of the resulting fit parameters A and B are consistent across the entire data set. The magnitudes of the CVs were shifted to the PTF photometric system by the linear relation with the best-fit parameters. The photometric results from the relative photometry are sufficient for further temporal analysis. Therefore, global calibration on the photometric systems is not necessary.

3.2. Timing Analysis

We regarded the data from PTF as the major data set, and the data from CRTS as supplemental. We cross-matched the Downes' catalog and the PTF database, and found that 344 CVs have PTF photometric data. The spatial distribution of the matches, along with all the CVs in the Downes' catalog, are shown in Figure 3. About 22% of the CVs in Downes' catalog have a PTF counterpart. This is because the photometric

catalogs of the PTF contain mostly fields in the non-Galactic plane, owing to the difficulties in processing Galactic-plane data and the restrictions inherent to the aperture photometric pipeline.

Matched CVs with only a few observations are not sufficient for studying their timing properties. Therefore, we selected the light curves with more than 100 observations for further investigation. About 100 of the matched CVs satisfied this criterion. These light curves were combined with their corresponding light curves in CRTS. In addition, some of the sources exhibit outbursts in the joint light curves. To avoid the interference from the outbursts, the data points for the outbursts in all the joint light curves were eliminated by visual inspection before the analysis. The dip features that are present in the light curves of cataclysmic variable QZ Ser were eliminated as well, because they are aperiodic. The joint light curves of the 344 selected CVs were then adopted for periodicity analysis. There are 10 CVs found to have long-term periodicities. The joint light curves of these 10 CVs are presented in the upper panels of Figures 4, 5, and 6. The total time span, the data points for timing analysis, and the outburst numbers for the light curves are listed in Table 2.

To study the timing properties of these CVs, the Lomb-Scargle periodogram (LS, Lomb 1976; Scargle 1982) was adopted to search for the periodicities, and the method of Phase-Dispersion Minimization (PDM, Stellingwerf 1978) was used to cross-check the candidate periods. The periods obtained from these two methods are consistent to each other. In this paper, we only present the results from LS. For the same FOV,

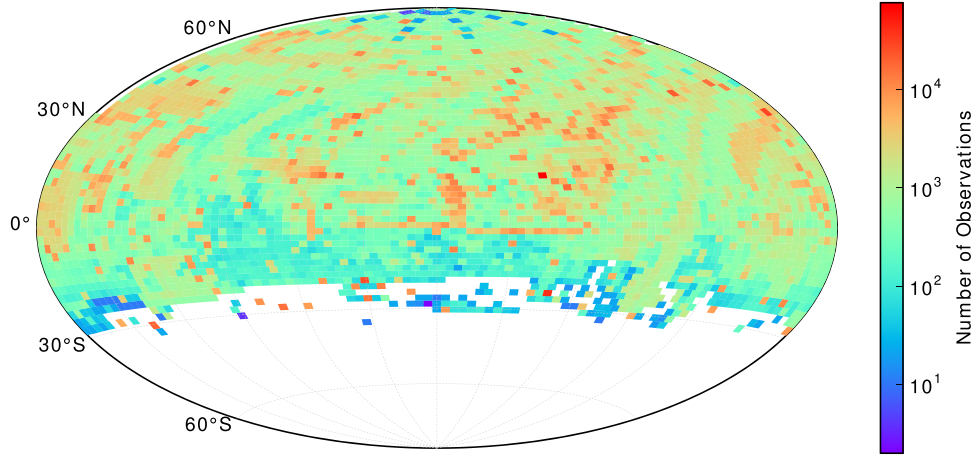


Figure 2. Observational distribution of PTF survey. Each tile in the plot represents a PTF field, and is color coded with the number of observations in the PTF photometric database. Only R-band data are presented. The plot is in equatorial coordinates with the Hammer projection. Observations are absent in the Southern Equatorial Hemisphere (decl. $< -30^\circ$) because of the observing limit of Palomar Mountain site.

(A color version of this figure is available in the online journal.)

Table 1
Observation Log of our LOT observations

Source	Nights (day)	Cadence (second)	Exposure (second)	Filter	N
UMa 01	5	210	200	R	403
CT Boo	4	210	200	R	140
Her 12	2	310	300	R	105

Note. Cadence is the planned observation interval between each of the each frames, and is possibly affected by weather conditions or the instrument. N is the number of the observations.

the observation schedules of PTF and CRTS are not regular and not fixed. Therefore, there are many observation gaps in the light curves. Aliases can be observed in the power spectra owing to the gaps in the observations, and this makes analyzing the light curves difficult. To distinguish and eliminate the aliasing introduced by the windows, the periodogram of the observation windows are plotted against the source periodogram, as demonstrated in the lower graphs of the middle panels in Figures 4, 5, and 6.

A summary of the possible CVs with the long-term periodicities are listed in Table 2. For the LS periodogram, the p -value is frequently adopted to represent the detection significance of a periodic signal. The p -value is defined as the probability that the periodogram power can exceed a given value P_i , expressed as $\text{Prob}(P > P_i)$, and can be expressed as

$$p \equiv \text{Prob}(P > P_i) = \left(1 - \frac{2P_i}{N-1}\right)^{\frac{N-3}{2}}, \quad (1)$$

where N is the total number of observations (Zechmeister & Kürster 2009).

To derive the corresponding uncertainty of the most probable long-term period, Monte Carlo simulations were conducted 10^4 times under the assumption that the observational errors are Gaussian distributed. On the basis of the observed magnitudes and corresponding errors of each CV, we generated 10^4 simulated light curves. The root-mean-square values of the peak values in the power spectra were adopted as the statistic errors of the derived periods. The errors of the periods are also listed in Table 2.

Light curves were folded with the most probable periods in the power spectra, as shown in the lower panels of Figures 4, 5, and 6. To show the profiles of the long-term modulations, we binned the folded light curves into 15 phase intervals, and fit each of them with a two-sinusoidal function, which is given as

$$M = c_1 \sin(2\pi\phi + c_2) + c_3 \sin(4\pi\phi + c_4) + c_5, \quad (2)$$

where ϕ is the phase of the folded light curve, M is the corresponding magnitude, and c_1 through c_5 are the fit coefficients.

The scattering of the points in the folded light curves may be caused by the original photometric uncertainties. However, the variations from shorter timescales, such as the orbital modulations, contribute to the light curves; therefore, these variations cannot be neglected. We tried to fold the original light curves of the CVs with their known constant orbital periods; however, this failed in reconstructing their orbital profiles.

3.3. Lulin One-Meter Telescope Observations

The images we took using the LOT were reduced by NOAO IRAF packages.¹³ The images were processed by subtracting

¹³ <http://iraf.noao.edu/>

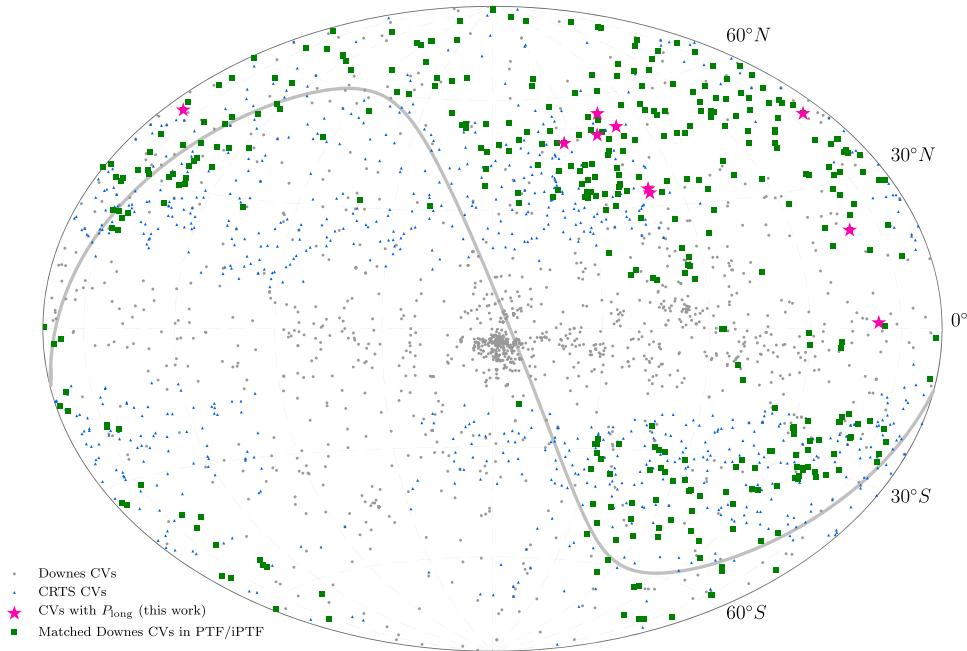


Figure 3. Spatial distribution of Galactic CVs found by various previous studies and in this study. Green squares represent the matched sources in PTF with the catalog from Downes et al. (2006). Gray filled circles are targets in Downes et al. (2006) catalog but not matched in the PTF survey. Blue triangles are the CV candidates with the CRTS project, proposed by Drake et al. (2014). The ecliptic plane is drawn with a gray line. This figure is presented in Galactic coordinates with the Hammer projection.

(A color version of this figure is available in the online journal.)

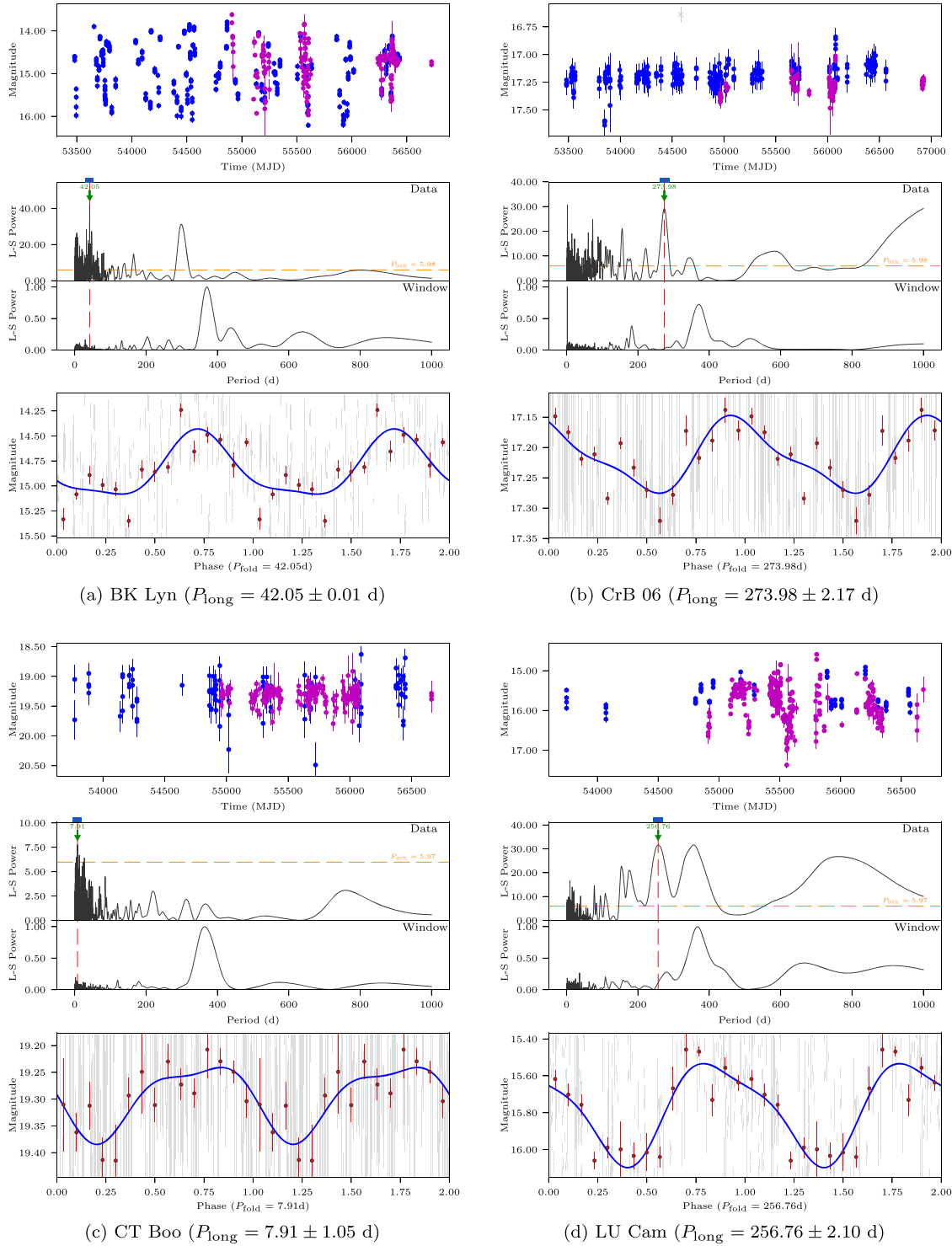
the master bias and dark frames. Then, the flat-field correction was applied for correcting the pixel-dependent instrument response. Point spread function (PSF) fitting was performed on the images using DAOPHOT to obtain accurate photometric results. In the light curves derived from the PSF fitting, different trends exist between different days. The mean value of the data in each day was subtracted for reducing the interference of the trend. The detrended light curves are presented in Figure 7. Moreover, the LS periodogram was applied for searching for periodicities in the light curves. The folded light curves were produced by folding the detrended light curves with the best determined periods. The power spectra and the folded light curves are shown in Figure 7. The significance levels are indicated by the p -values as well. A summary of the results is shown in Table 3.

Intensive observations were conducted for the unknown orbital periods of the CVs with long-term periodicities. In this study, three CVs, namely UMa 01, CT Boo, and Her 12 were observed and analyzed. UMa 01 (a.k.a. 2MASS J09193569+5028261) shows a modulation with a period of 404.10 ± 0.3 min. CT Boo exhibits two significant periodic signals: 229.13 ± 7.02 and 79.55 ± 0.51 min. In addition, two significant periods were found in Her 12 (a.k.a. SDSS J155037.27+405440.0): 75.62 ± 0.008 and 173.65 ± 1.57 min. These

periods for the three CVs are all located in the normal orbital period range of CVs. However, for the CVs with multiple periodicities, further investigation is required to distinguish and confirm the orbital periods. Besides, it is not easy to distinguish them if the modulations in the folded light curves are orbital humps or superhumps (defined below in Section 4.1). We assume that these periods are the possible orbital periods in the discussion that follows.

4. Possible Mechanisms of Long-term Periodicity

Long-term periodicities are not frequently observed in close binary systems. However, some X-ray binaries (XBs) exhibit long-term periodicities. Kotze & Charles (2012) summarized several possible mechanisms for the long-term variability of XBs, and some of the scenarios may also be applicable to CV systems. The distribution of the long-term periodicities in our study is presented in Figure 8. The long-term periods that are associated with the superhumps of other CVs were gathered from different literature, and were plotted for comparison. The long-term periodicities of the low-mass X-ray binaries (LMXBs) in Kotze & Charles (2012) were plotted, as well. In this section, we list and discuss some of the possible mechanisms that cause the long-term variations in CVs.



(a) BK Lyn ($P_{\text{long}} = 42.05 \pm 0.01$ d)

(b) CrB 06 ($P_{\text{long}} = 273.98 \pm 2.17$ d)

(c) CT Boo ($P_{\text{long}} = 7.91 \pm 1.05$ d)

(d) LU Cam ($P_{\text{long}} = 256.76 \pm 2.10$ d)

Figure 4. Upper panel: light curves from PTF and CRTS. Magenta: PTF; blue: CRTS; and gray: data points of outbursts or dips eliminated in the analysis. Middle panel: Lomb-Scargle periodogram of the joint light curve (upper), and the window function (lower, normalized). Blue bar in the top of the panel shows the error from the Monte Carlo simulation. Green arrows show the values of the periods of our interests. Orange dashed line indicates the 95% confidence level ($P_{95\%}$). The red dashed vertical line indicates the period used for the folded light curve in the lower panel. Lower panel: gray: folded light curves; red: binned light curves with 15 bins to address the modulation; and blue: the fit line with two sinusoidal components. (A color version of this figure is available in the online journal.)

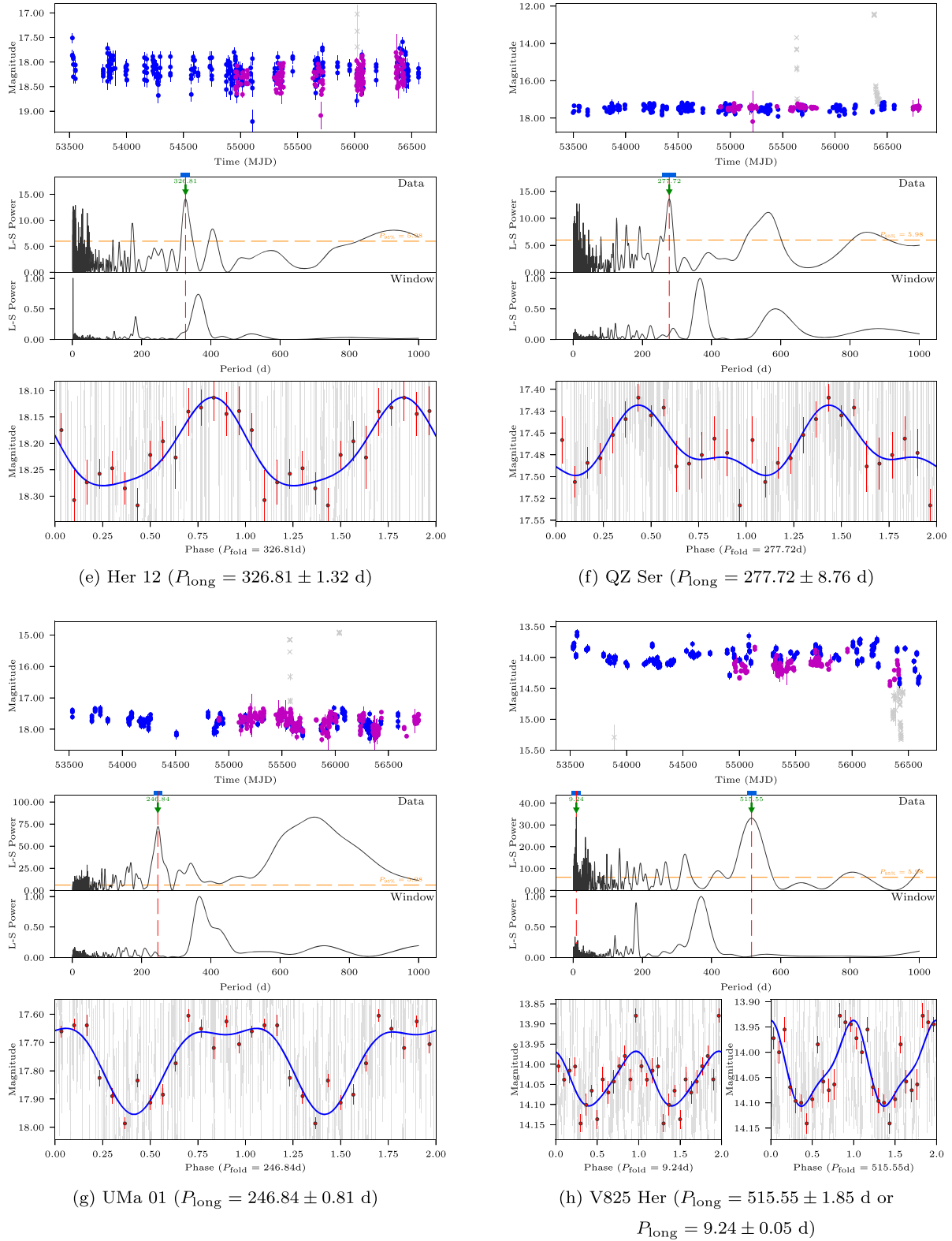


Figure 5. Light curves (upper panel), Lomb-Scargle periodogram of CVs (upper of middle panel) and window function (lower of middle panel), and folded light curves (lower panel) (continued). The descriptions and labels are the same as in Figure 4. (A color version of this figure is available in the online journal.)

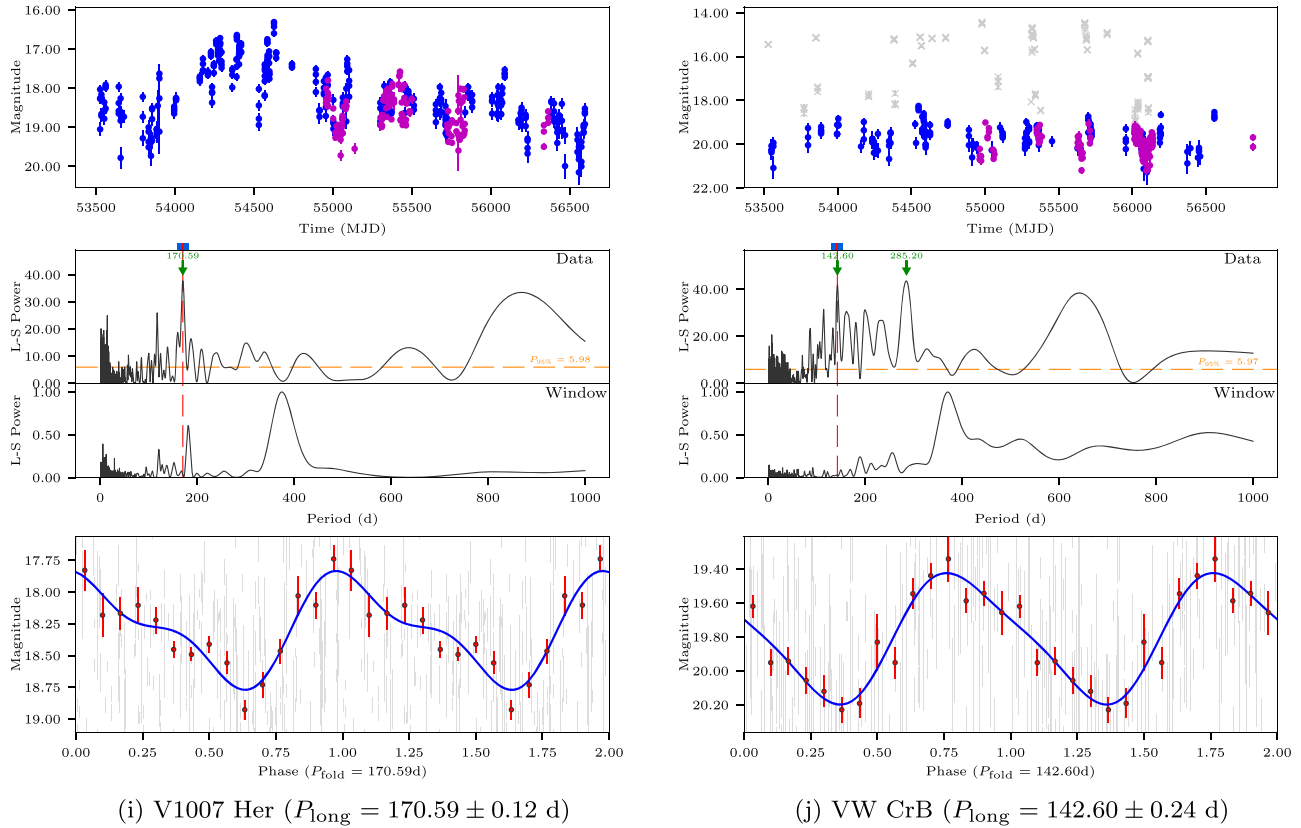


Figure 6. Light curves (upper panel), Lomb-Scargle periodogram of CVs (upper of middle panel) and window function (lower of middle panel), and folded light curves (lower panel) (continued). The descriptions and labels are the same as in Figure 4. (A color version of this figure is available in the online journal.)

4.1. Precession of Accretion Disk

CVs are named for their cataclysmic phenomena. The state change of the accretion disk of CVs may cause their emission flux to change. In addition to the orbital modulations, variations in the periods of a few percent longer or shorter than the orbital periods are called positive and negative superhumps, respectively. Superhump was first found in the SU UMa type (a subtype of dwarf novae (DNe)) of CVs. During the superoutbursts of a SU UMa type star, a periodic hump rather than an orbital hump appears and this was called superhump (Warner 1985; Vogt 1980; Warner 1995). Besides the SU UMa type of CVs, some of the VY Scl type of CVs (or anti-dwarf novae), a subtype of nova-like (NL) CV, were detected to have superhump signals. For example, Kozhevnikov (2007) discovered a negative superhump $P_{\text{sh}} = 3.771 \pm 0.005$ h in KR Aur, a VY Scl NLCV. In addition to the SU UMa and NL systems, superhumps were also observed in the intermediate polar (IP, or DQ Her type of CVs). Woudt et al. (2012) found superhumps in CC Scl, an IP system, with a period of $P_{\text{sh}} = 1.443$ h, $\sim 4.3\%$ longer than its orbital period $P_{\text{orb}} = 1.383$ h.

In general, it is believed that the positive/negative superhump periods are the beat periods of the orbital period and the precession period of the accretion disk. For a positive superhump, the size of the accretion disk is growing as mass transferring from the companion. When the radius of the accretion disk is larger than the 3:1 resonance radius of the binary, the accretion disk becomes asymmetric and exhibits apsidal precession (Whitehurst 1988; Osaki 1989, 1996). Whitehurst & King (1991) proposed that this criterion can be achieved only for CV systems with mass ratio $q \equiv M_d/M_c < 0.25 - 0.33$, where M_c and M_d are the masses of the accretor and donor, respectively. A positive superhump is a consequence of coupling disk apsidal precession and orbital motion with the beat period for these two types of periodic motions. On the other hand, a negative superhump is believed to be the result of coupling between orbital motion and disk nodal precession.

The period excess of a superhump is defined as follows:

$$\epsilon \equiv \frac{P_{\text{sh}} - P_{\text{orb}}}{P_{\text{orb}}}. \quad (3)$$

Table 2
Summary of CVs Having Long-term Periodicities

CV Name ^a	RA (J2000) (hh:mm:ss)	Decl. (J2000) (\pm dd:mm:ss)	Alternative Name ^b	Type ^c	P_{orb} ^d (min)	$\sigma_{P_{\text{orb}}}$ ^e (min)	P_{long} ^f (day)	$\sigma_{P_{\text{long}}}$ ^g (day)	$p(P_{\text{long}})$ ^h	Amp. ⁱ (mag)	T_{span} ^j (day)	N^k (#)	N_{ob}^l (#)
BK Lyn	09:20:11.20	+33:56:42.3	2MASS J09201119+3356423	DN/NL	107.97 ^m	0.07 ^m	42.05	0.01	1.88e-20	0.65	3242.92	514	...
CrB 06	15:32:13.68	+37:01:04.9	2MASS J15321369+3701046	NL	273.98	2.17	1.18e-13	0.11	3443.86	400	1
CT Boo	14:08:20.91	+53:30:40.2	...	NL	230.72	1.78	7.91	1.05	4.11e-04	0.13	2893.00	296	...
					78.65	0.36							
LU Cam	05:58:17.89	+67:53:46.0	2MASS J05581789+6753459	DN	215.95 ⁿ	0.0005 ⁿ	256.76	2.10	3.18e-03	0.62	2934.95	363	...
Her 12	15:50:37.28	+40:54:40.0	SDSS J155037.27+405440.0	CV	75.62	0.008	326.81	1.32	4.97e-07	0.18	3033.88	429	1
					173.65	1.57							
QZ Ser	15:56:54.47	+21:07:19.0	SDSS J155654.47+210719.0	DN	119.75 ^o	0.002 ^o	277.72	8.76	9.18e-07	0.09	3308.01	510	2
UMa 01	09:19:35.70	+50:28:26.2	2MASS J09193569+5028261	CV	404.10	0.30	246.84	0.81	8.01e-20	0.44	3251.05	601	1
V825 Her	17:18:36.99	+41:15:51.2	2MASS J17183699+4115511	NL	296.64 ^p	2.88 ^p	515.55	1.85	3.28e-16	0.16	3069.71	510	...
							9.24	0.05	4.51e-16	0.18			
V1007 Her	17:24:06.32	+41:14:10.1	1RXS J172405.7+411402	AM	119.93 ^q	0.0001 ^q	170.59	0.12	2.13e-18	0.90	3069.71	507	...
VW CrB	16:00:03.71	+33:11:13.9	USNO B1.0 1231-00276740	DN	142.60	0.24	1.92e-21	0.87	3271.19	351	>10

Notes. The numbers in bold face indicate the values derived in this work. Multiple possible orbital periods present in CT Boo and Her 12, and they are listed in the table accordingly.

^a CV name: name designated in this project.

^b Alternative name: the source name in 2MASS, SDSS, *ROSAT* bright source catalog (1RXS) or USNO B1.0 catalogs.

^c Type: the type of CVs designated in Downes et al. (2006) (NL: nova-like, DN: dwarf nova, AM: AM Her (polar)).

^d P_{orb} : orbital periods.

^e $\sigma_{P_{\text{orb}}}$: errors of orbital periods.

^f P_{long} : long-term periods derived in this work.

^g $\sigma_{P_{\text{long}}}$: errors of long-term periods derived in this work.

^h $p(P_{\text{long}})$: the p -value of the long-term period.

ⁱ Amplitude: peak-to-peak magnitude difference from the fit light curve.

^j T_{span} : total time span.

^k N : number of observations excluding outbursts and dips.

^l N_{ob} : number of outbursts observed with PTF and CRTS.

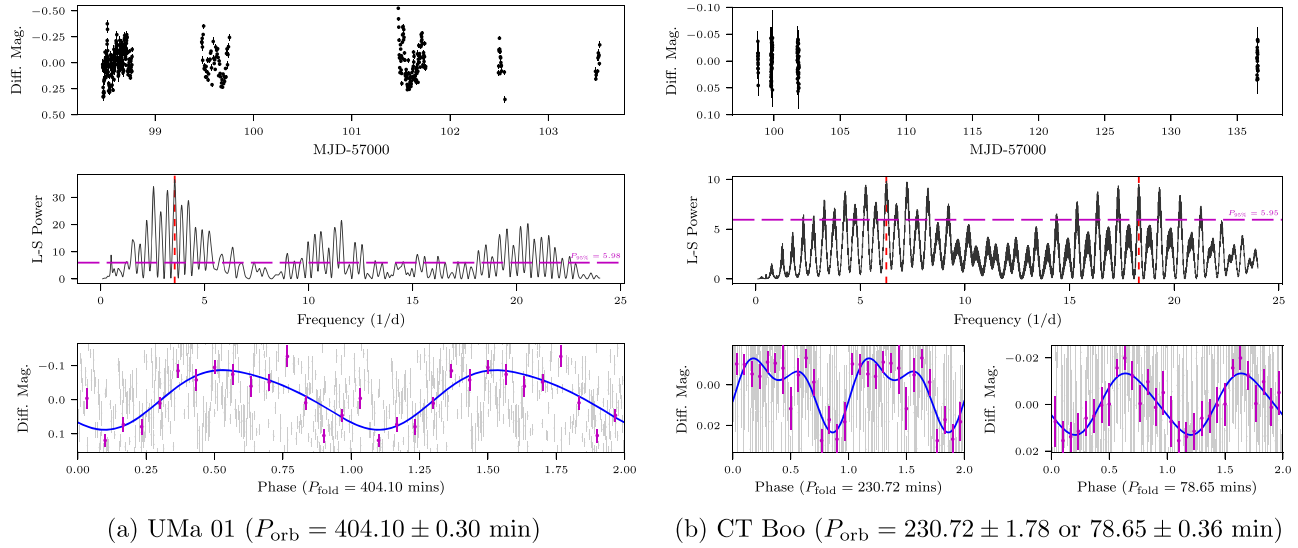
^m Ringwald et al. (1996).

ⁿ Sheets et al. (2007).

^o Thorstensen et al. (2002).

^p Ringwald & Reynolds (2003).

^q Greiner et al. (1998).


 (a) UMa 01 ($P_{\text{orb}} = 404.10 \pm 0.30$ min)

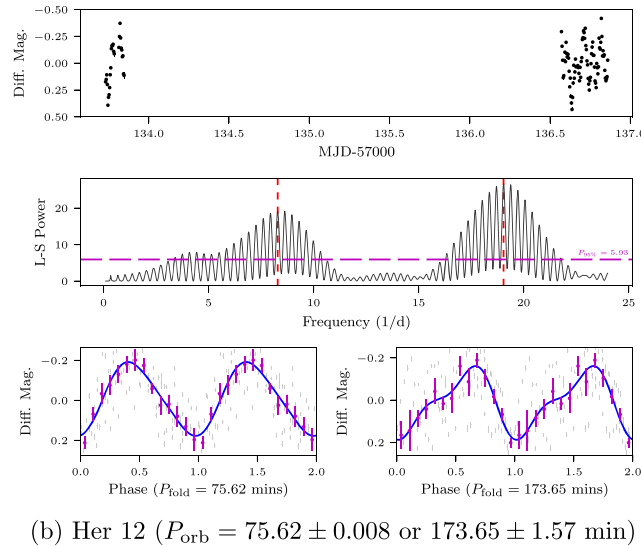
 (b) CT Boo ($P_{\text{orb}} = 230.72 \pm 1.78$ or 78.65 ± 0.36 min)

 (b) Her 12 ($P_{\text{orb}} = 75.62 \pm 0.008$ or 173.65 ± 1.57 min)

Figure 7. Folded short-cadence light curves of (a) UMa 01, (b) CT Boo, and (c) Her 12. Upper panels show the detrended light curves in the available data segments. Middle panels present the Lomb-Scargle periodogram of the CVs. The magenta dashed line denotes the L-S power with 95% confidence level, and red dashed lines denote the periodic signals used for the folded periods. Lower panels show the folded light curves with the best periods in the Lomb-Scargle periodogram. Gray dots are the folded light curves. Purple points indicate the binned light curves and errors. Blue curves represent the modulation trends with fits to a function with two sinusoidal components.

(A color version of this figure is available in the online journal.)

In general, the period excess for a positive superhump is in the range of 1%–7%. The period deficit for a negative superhump is about half of an excess of the positive superhump (Patterson 1999). Therefore, the period ranges of the disk precession can be derived with known P_{orb} and P_{sh} . Figure 9 presents our results in a plot of P_{orb} versus P_{long} .

In general, LMXBs are similar to CVs (Charles 2002). LMXBs have low-mass companions; therefore, some of them possibly satisfy the mass-ratio criterion that introduces the

disk precession. The results of some long-term variability studies on LMXBs (Kotze & Charles 2012) and CVs (see Table 4) were gathered and included with our Figure 9 results for comparison. In Figure 9, the gray area and iris hatched areas denote the possible regions of the long-term periods in the positive ($P_{\text{sh}+}$) and negative superhump ($P_{\text{sh}-}$) systems, respectively. In this study, only the long-term periods of CT Boo and V825 Her are the possible precession periods (see Section 5 for more details).

Table 3
Periodicities in Short-cadence Observations

Source	P_{opt} (min)	$\sigma_{P_{\text{opt}}}$ (min)	P_{peak}	p -value	N
UMa 01	404.10	0.30	36.54	3.74e-18	403
CT Boo	230.72	1.78	9.80	2.99e-05	140
	78.65	0.36	9.49	4.29e-05	140
Her 12	173.65	1.57	26.75	1.00e-16	105
	75.62	0.008	19.22	6.02e-11	105

Note. P_{opt} : optical periods, $\sigma_{P_{\text{opt}}}$: errors in periods by Monte Carlo simulations, P_{peak} : peak power in the power spectrum.

If the long-term period is the disk precession period, the period is confined by its orbital period. For an extreme case of CV, say $P_{\text{orb}} = 1$ day, the maximum apsidal precession period and the maximum nodal precession period are approximately 101 d and 199 d, respectively. We conclude that if the long-term periodicities are longer than 200 d, then the possibility of the long-term period being the disk precession can be completely eliminated.

4.2. Hierarchical Triple Star

Some of the close binaries, such as LMXBs and CVs, were reported in triple or even multiple star systems. Chou & Grindlay (2001) indicated that the superorbital modulation period $P = 171.033 \pm 0.326$ d is found in LMXB 4U 1820-30 with a limit of the period derivative $|\dot{P}| < 1.03 \times 10^{-4} \text{ d d}^{-1}$. The luminosity modulation and its long-term stability suggest that it is a hierarchical triple star system. Beuermann et al. (2011) discovered a third star of mass $M_3 = 6.1 \pm 0.5 M_J$ orbiting the eclipsing binary DP Leo with orbital period $P_3 = 28 \pm 2$ yrs. Potter et al. (2011) studied the eclipsing polar UZ For and found that, except for the binary orbital period $P_{\text{orb}} = 0.088$ d, there are also two long-term cyclic variations: $P_3 = 16 \pm 3$ yrs and $P_4 = 5.25 \pm 0.25$ yrs. Moreover, they were interpreted as two giant exoplanets, with masses of $M_3 = 6.3 \pm 1.5 M_J$ (M_J is the Jovian mass) and $M_4 = 7.7 \pm 1.2 M_J$, being companions to the binary system. Chavez et al. (2012) detected a periodicity of ~ 900 d in the light curves of FS Aur, and then used a numerical simulation of a third body with sub-stellar mass orbiting around the binary to reproduce the long-term modulation in the binary eccentricity variation.

A triple star is expected to form in high number density regions, such as the core of globular clusters, which may aid the capture process by a CV system. Trenti et al. (2008) performed an N-body simulation for investigating the formation of triple systems in star clusters. Their results yielded that the probability of forming triple stars in the center of a star

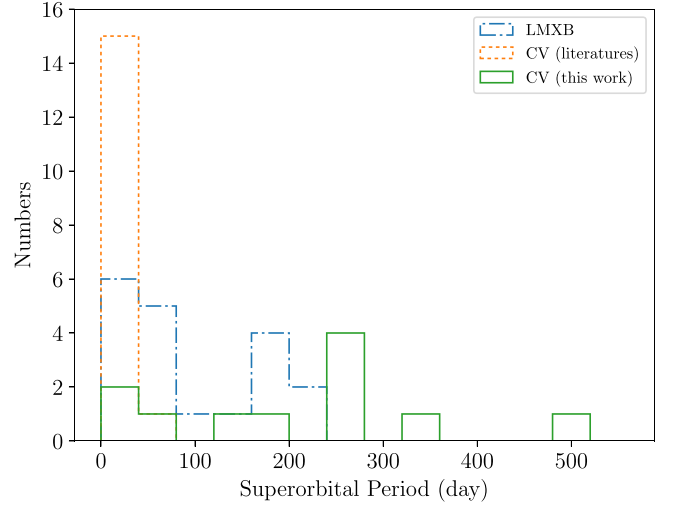


Figure 8. Histogram of known superorbital periods in close binary systems. Blue dashed dots: LMXBs from Kotze & Charles (2012); orange dots: CVs from various studies (see Table 4); and green line: CVs of this study. (A color version of this figure is available in the online journal.)

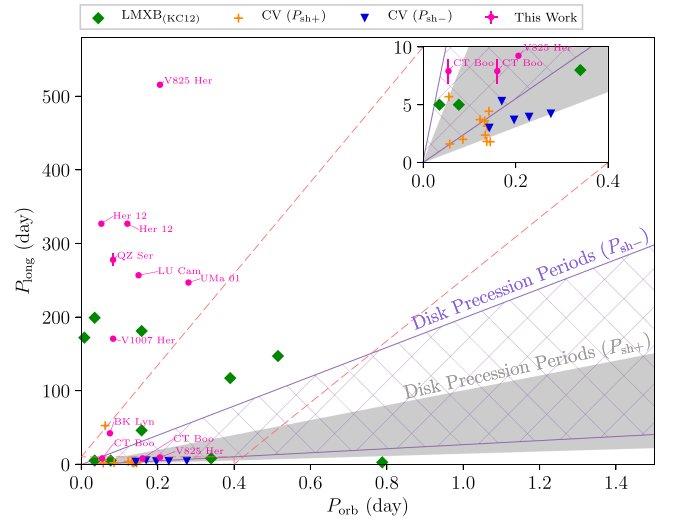


Figure 9. P_{long} vs. P_{orb} relations for LMXBs, and CVs. LMXBs data are shown with green diamonds (see Kotze & Charles (2012) (KC12)). If the long-term periods were provided in ranges, the average values are adopted for the plot. CVs from previous studies with long-term periods, which are related to positive and negative superhumps, are in orange crosses and blue triangles, respectively (as listed in Table 4). The filled magenta circles denote the results from our study. The gray area denotes the possible region of disk precession period P_{prec} with superhump period excess ϵ in 1%–7% range (positive superhump ($P_{\text{sh}+}$)). The iris hatched area represents the region of accretion disk precession period P_{prec} with period excess of superhump (ϵ) between -0.5% and -3.5% (negative superhump ($P_{\text{sh}-}$)). The zoomed-in view of the dashed box is in upper right corner of the plot. Only CT Boo and V825 Her are located in the possible regions related to the superhump phenomenon.

(A color version of this figure is available in the online journal.)

Table 4
Long-term Periodicities in CVs Caused by Superhumps

Name	P_{orb} (hr)	P_{sh} (hr)	P_{long} (day)	Type(sh)	Type	Reference
AH Men	2.95	3.05	3.71	+	Nova	Patterson (1995)
DV UMa	2.06	2.14	2	+	DN	Vanmunster (2006)
CC Scl	1.38	1.44	1.6 ^a	+	Nova	Woudt et al. (2012)
LT Eri	4.08	3.98	5.3	–	CV	Ak et al. (2005a)
LQ Peg	3.22	3.42	2.37	+	Nova	Rude & Ringwald (2012)
MV Lyr	3.19	3.31	3.6	+	Nova	Skillman et al. (1995)
NSV 1907	6.63	6.22	4.21	–	NL	Hümmerich et al. (2017)
PX And	3.41	3.51	4.43	+	CV	Thomas et al. (2010)
RR Pic	3.48	3.78	1.79	+	Nova	Schmidtbreick et al. (2008)
TT Ari	3.30	3.57	1.82	+	Nova	Stanishev et al. (2001)
TV Col	5.50	5.20	3.93	–	DQ Her	Augusteijn et al. (1994)
UX UMa	4.72	4.48	3.68	–	NL	de Miguel et al. (2016)
V1193 Ori	3.43	3.26	2.98	–	Nova	Ak et al. (2005b)
V2051 Oph	1.50	1.54	52.5 ^a	+	DN	Vrielmann & Offutt (2003)
V603 Aql	3.32	3.47	3.15 ^a	+	Nova	Suleimanov et al. (2004)
WZ Sge	1.33	1.37	5.7	+	DN	Patterson et al. (2002)

Note. P_{orb} , P_{sh} , P_{long} are orbital, superhump and long-term disk precession periods, respectively. Type(sh) is the type of superhump: “+” for positive superhumps, “–” for negative superhumps.

^a Average value of multiple periodicities.

cluster is only two orders lower than that of binaries, which is comparably prominent. A small third body could significantly affect the eccentricity of the inner binary, and then result in a mass-transfer-rate change of the CV system. This long-term periodicity is known as Lidov-Kozai oscillation (Lidov 1962; Kozai 1962). The relation between the outer third star and the inner binary can be expressed by the relation proposed by Mazeh & Shaham (1979):

$$P_{\text{long}} = P_{1,2} \left(\frac{a_3}{a_{1,2}} \right) \frac{m_1 + m_2}{m_3}, \quad (4)$$

where P_{long} is the long-term periodicity, $P_{1,2}$ is the inner binary orbital period, m_1 and m_2 are the primary and the secondary masses, m_3 is the mass of the third star, $a_{1,2}$ is the separation of the inner CV, and a_3 is the separation between the CV and the third star. An approximation can be expressed as follows:

$$P_{\text{long}} \approx \alpha \frac{P_3^2}{P_{1,2}} \frac{m_1 + m_2 + m_3}{m_3} (1 - e_{\text{out}})^{3/2}, \quad (5)$$

where e_{out} is the eccentricity between the third star and the inner binary, and α is a dimensionless quantity from the three-body Hamiltonian. When the outer eccentricity is fixed, and there is no mass transfer between the inner binary and outer star, then Equation (5) can be expressed as follows:

$$P_{\text{long}} = K \frac{P_3^2}{P_{1,2}}, \quad (6)$$

where K is a constant of order unity, and Chou & Grindlay (2001) take $K \simeq 1$ as an approximation (for different inclination angles, K taken as a factor of 2 smaller or larger is applicable). For example, in 4U 1820-30, $P_{\text{long}} = 171.033$ d and $P_{\text{orb}} = 685$ s. Using Equation (6), and assuming $K = 1$, this results in $P_3 = 1.18$ d, which is considerably longer than the orbital period of the inner binary, and so the hierarchical order of the triple system is reasonable. Therefore, we could conclude that the hierarchical triple star system is one of the possible scenarios leading to long-term periodicities in CVs.

4.3. Magnetic Variation of the Companion Star

Most companions in CVs are late-type stars. The convective zone in a late-type star (G, K, or M type) yields a strong magnetic field through the well-known dynamo process. The strength of the magnetic field is related to the rotation of the star. Under the same rotation speed, a star of the latter spectral type would yield stronger magnetic field by the dynamo effect (Durney & Robinson 1982; Robinson & Durney 1982). Because of the stronger magnetic field strength, the accretion process in the CV system is possibly affected.

Long-term modulations of orbital period variations have been found and studied in some eclipsing binaries. Applegate (1992) proposed that the torque generated from the magnetic variation of the companion may induce such a long-term periodicity. Meyer-Hofmeister et al. (1996) studied the outburst frequency of dwarf novae and found a cycle of 18 yrs in SS Aur and 7 yrs of SS Cyg. They inferred that these cycles are related

to the magnetic field variation of the companion. Borges et al. (2008) discovered a 36 yr periodic signal in the eclipsing cataclysmic variable HT Cas. The periodicity is likely to be the solar-type magnetic activity of the companion stars. Ak et al. (2001) observed cyclical variations in quiescence magnitude and outburst intervals of 21 dwarf novae, one nova, and one NL star. The probability density functions are peaked at 9.7 yrs for CVs, 7.9 yrs for single main-sequence stars, and 8.6 yrs for all stars.

The distribution of the cycle lengths caused by the magnetic field variations of late-type stars was studied by Suárez Mascareño et al. (2016). Their results reveal that the majority of cycle lengths are in the 2–13 yr range. For our results in Table 2, the longest period is $P_{\text{long}} = 515.52 \pm 1.85$ d in V825 Her, which is marginal relative to the aforementioned magnetic timescale. We cannot completely eliminate the possibility of magnetic variation of the companion as a cause of long-term periodicity in CVs. However, for our targets, the chance of magnetic variation is not high according to the revealed period ranges of our targets.

4.4. Other Possibilities

In addition to the above mechanisms for long-term periodicities in CVs, the superoutburst cycle of the SU UMA type of CV sometimes displays periodic-like signals (e.g., Shears 2009). On the other hand, Šimon (2016) found the periodic-like transition between the high and low states in cataclysmic variable AM Her, and proposed the lifetime of the active region in the companion may contribute to the variation of the accretion rate. In some rare cases, the long-term variation may also possibly be induced by the precession of the jet in XBs (Kotze & Charles 2012), but the existence of jets in CVs is still controversial. However, Körding et al. (2011) first observed the radio emissions of V3885 Sgr, which is a nova-like cataclysmic variable (NLCV), and the radio emission from V3885 Sgr is regarded as synchrotron emissions from the jet.

5. Long-term Modulation for the Individual CVs

We have searched for long-term periodicities in approximately 100 CVs from the PTF database (Section 3.2). It turns out that 10 of the targets exhibit obvious periodic signals. We folded the light curves with their best periods, as shown in Figures 4, 5 and 6. The most convincing CVs that possess long-term periods (P_{long}) are discussed in this section. The long-term periodicities discovered in these CVs provide us with some probable implications for their formation mechanisms (see Section 4). We discuss these CVs in the following subsections.

5.1. BK Lyncis (2MASS J09201119+3356423)

BK Lyn (also PG0917+342), a NLCV, which was discovered by Green et al. (1982), has an orbital period of $P_{\text{orb}} = 107.97 \pm 0.07$ min (Ringwald et al. 1996). Dhillon et al. (2000) found that

its secondary is an M5V star from infrared spectroscopy. The accretion rate was estimated as $\dot{M} \sim 1 \times 10^{-9} M_{\odot}/\text{yr}$ assuming a WD mass of $1.2 M_{\odot}$, or $\dot{M} \sim 1 \times 10^{-8} M_{\odot}/\text{yr}$ for WD mass $M_{\text{WD}} = 0.4 M_{\odot}$ (Zellem et al. 2009). Kemp et al. (2012) studied 20-yr light curves of BK Lyn and detected two sets of superhump signals. One is 4.6% longer and the other is 3.0% shorter than the P_{orb} . The two superhumps were observed in different light curve stages. They are possibly due to the prograde apsidal precession and retrograde nodal precession of its accretion disk. The long-term period found in our study is 42.05 ± 0.01 d, which is considerably longer than the long-term period derived from the superhump periods found by Kemp et al. (2012). This suggests that the periodicity is probably not from the precession of the accretion disk. On the other hand, if the long-term periodicity is driven by a third star orbiting the CV system, then the orbital period of the third star will be $P_3 = 1.78$ d (as calculated by Equation (6)), which is much longer than the orbital period of BK Lyn.

5.2. CT Boötis

CT Boo shows spectra similar to F-G stars, and no emission lines of hot continuum was observed (Zwitter & Munari 1994). If the spectrum is dominated by its companion star, owing to the dynamo effect in the convective layer of a late-type star, the magnetic field will be stronger than for other spectral types of stars. However, the long-term period is $P_{\text{long}} = 7.91 \pm 1.05$ d, which is considerably shorter than the timescale of the stellar magnetic variation (see Section 4.3).

Two possible orbital periods discovered by this study are $P_{\text{orb}} = 230.72 \pm 1.78$ min and $P_{\text{orb}} = 78.65 \pm 0.36$ min. With the positive superhump period excess between 1% and 7% and negative superhump period excess between -0.5% and -3.5% , we calculated the possible accretion disk precession to be 2.45 – 31.88 d for $P_{\text{orb}} = 230.72$ min, and between 0.83 and 10.87 d for $P_{\text{orb}} = 78.65$ min. Therefore, the long-term period found for CT Boo is in good agreement with the disk precession period from the coupling of orbital and superhump periods.

5.3. LU Camelopardalis: 2MASS J05581789+6753459

The orbital period of LU Cam is $P_{\text{orb}} = 0.1499686(4)$ d (Sheets et al. 2007) whereas its long-term modulation period is $P_{\text{long}} = 265.76 \pm 2.10$ d. The possibility of disk precession can be completely eliminated because it exceeds the period limit of 29.84 d for the possible disk precession period. If LU Cam is a hierarchical triple star system, using Equation (6) and assuming $K = 1$, the orbital period of the outer third body is $P_3 \sim 6.20$ d, which is considerably longer than the orbital period of the inner binary. Therefore, the hierarchical triple star is a possible scenario for the long-term periodicity in LU Cam.

5.4. QZ Serpentis: SDSS J155654.47+210719.0

QZ Ser is a dwarf nova system with an orbital period of 0.08316 d, and with a K4 type star as its companion (Thorstensen et al. 2002). If there is superhump-related disk precession, the period should be less than 16.54 d, which is considerably shorter than the long-term period that we obtained ($P_{\text{long}} = 277.72 \pm 8.76$ d). If QZ Ser is a triple star system, the orbital period of the third star would be $P_3 \sim 4.81$ d (through Equation (6)).

5.5. V825 Herculis: 2MASS J17183699+4115511

V825 Her, also named PG117+413 and 2MASS J17183699+4115511, has an orbital period of $P_{\text{orb}} = 4.94$ h discovered by Ringwald (1991). The upper limits of the long-term periods calculated for positive and negative superhump systems are 20.79 d and 40.96 d, respectively. There are two sets of long-term periodicities in the power spectrum of V825 Her. One is $P_{\text{long}} = 9.24 \pm 0.05$ d, and the other one is considerably longer $P_{\text{long}} = 515.52 \pm 1.85$ d. These two periods exhibit convincing variations in the folded light curves, as shown in Figure 5. $P_{\text{long}} = 9.24$ d is plausibly explained as the disk precession period; whereas, $P_{\text{long}} = 515.52$ d is perhaps caused by the magnetic variation of the companion star (see Section 4.3).

5.6. V1007 Her: 1RXS J172405.7+411402

V1007 Her, discovered by Greiner et al. (1998), is a polar system with an orbital period of $P_{\text{orb}} = 119.93 \pm 0.0001$ min. Because it is a polar system, the long-term modulation is impossibly caused by precession of accretion disk. If the long-term periodicity is caused by a third star, then the orbital period of the third star (P_3) is about 3.77 d, much longer than the orbital period of the inner CV, and this becomes a possible mechanism to explain the period of ~ 170 d modulation.

5.7. UMa 01: 2MASS J09193569+5028261

UMa 01 (also 2MASS J09193569+5028261) was identified by Adelman-McCarthy et al. (2006) as a CV. The orbital period discovered in this study is $P_{\text{orb}} = 404.10 \pm 0.30$ min. If there is disk precession in this system, then the precession period would range from 4.29 to 55.84 d. However, the long-term period discovered in this study is $P_{\text{long}} = 246.84 \pm 0.81$ d, which is too large for disk precession. On the other hand, if the long-term periodicity is from a third star orbiting around the CV system, then the orbital period P_3 would be 8.32 d, much longer than the orbital period of the inner CV, and so UMa 01 may be a hierarchical triple system.

5.8. Her 12: SDSS J155037.27+405440.0

Her 12 (also SDSS J155037.27+405440.0) was identified as a CV by Adelman-McCarthy et al. (2006). We proposed two candidates of its orbital period based on the LOT observations,

$P_{\text{orb}} = 75.62 \pm 0.008$ min and $P_{\text{orb}} = 173.65 \pm 1.57$ min. The ranges for the disk precession periods are 0.8 to 10.45 d and 1.84 to 24 d for $P_{\text{orb}} = 75.62$ min and 173.65 min, respectively. The long-term modulation period discovered in this work is $P_{\text{long}} = 43.6 \pm 0.29$ d, exceeding both ranges, and thus, this modulation is unlikely to be caused by accretion disk precession. On the other hand, if this source is a hierarchical triple system, then the orbital period of the third companion is 1.51 d or 2.29 d for the orbital periods of 75.62 min or 173.65 min, respectively. Both of the third-body orbital periods are much larger than the corresponding orbital periods of the CV. Therefore, this triple model is a possible mechanism to explain the long-term variability of Her 12.

5.9. Coronae Borealis 06 and VW Coronae Borealis

CrB 06 (also 2MASS J15321369+3701046) and VW CrB (also USNO-B1.0 1231-00276740) were identified as CVs in Szkody et al. (2006) and Adelman-McCarthy et al. (2006), respectively. Unfortunately, the orbital periods of both CVs remain unknown. Therefore, at the current stage, we cannot speculate on the possible mechanisms of long-term variability for these CVs.

5.10. Summary

We discussed several possible mechanisms to explain the long-term modulations for the CVs that we found in this study. Only the long-term periodicities in CT Boo and V825 Her are possibly caused by the disk precession periods. On the other hand, for the other CVs included in this study, the hierarchical triple systems are conceivable mechanisms for yielding long-term periodicities in CVs. In addition, the magnetic variations of companions in CVs is yet another possible mechanism to cause the long-term variations; nevertheless, the tendency toward longer periods by this mechanism reduces its likelihood as a plausible explanation for the long-term periodicities in this study.

6. Conclusion and Prospect

We presented our study on the long-term variations of CVs in this paper. We matched 344 CVs in the CV catalog of Downes with the PTF photometric database. Approximately 100 CVs have more than 100 observations. Among them, 10 of the CVs exhibited long-term periodicities. The long-term periodicities may be caused by one of the following mechanisms: disk precession, the presence of a hierarchical triple-star system, magnetic variation of the companion star, jet precession, and others. We discussed the likelihood of each possible mechanism with respect to our matched CVs. In addition, we found the possible orbital periods for three of the CVs with the short-cadence optical observations made by LOT.

The ranges of the orbital periods are typical in the orbital period distribution.

With less sparse observations and longer observation time spans, the uncertainties in the long-term periodic signals can be reduced. We look forward to more sophisticated sample of long-term periodicities in CVs when ZTF and other big synoptic surveys are in operation. According to the current plan for ZTF, the Galactic-plane survey will be one of the major parts of the project that may considerably enhance the target number of CVs. We will certainly benefit considerably from next-generation synoptic surveys.

M.T.-C.Y. is grateful to have the anonymous referee for the precious comments and suggestions. M.T.-C.Y. thanks the Ministry of Science and Technology (MOST) of Taiwan for support through the grant MOST 104-2119-M-008-024 (TANGO Project, as the courtesy of W.H.Ip.), NSC 102-2112-M-008-020-MY3, and MOST 105-2112-M-008-012. PTF is a collaboration project in science among the California Institute of Technology, Los Alamos National Laboratory, the University of Wisconsin-Milwaukee, the Oskar Klein Center, the Weizmann Institute of Science, the TANGO Program of the University System of Taiwan, and the Kavli Institute for the Physics and Mathematics of the Universe. C.R.T.S. was supported by the NSF grants of AST-1313422, AST-1413600, and AST-1518308.

References

- Adelman-McCarthy, J. K., Agüeros, M. A., Allam, S. S., et al. 2006, *ApJS*, **162**, 38
- Ak, T., Ozkan, M. T., & Mattei, J. A. 2001 *A&A*, **369**, 882
- Ak, T., Retter, A., Liu, A., & Esenoglu, H. H. 2005a, *PASA*, **22**, 105
- Ak, T., Retter, A., & Liu, A. 2005b, *NewA*, **11**, 147
- Applegate, J. H. 1992, *ApJ*, **385**, 621
- Augusteijn, T., Heemskerck, M. H. M., Zwarthoed, G. A. A., & van Paradijs, J. 1994, *A&AS*, **107**, 219
- Beuermann, K., Buhmann, J., Diese, J., et al. 2011, *A&A*, **526**, A53
- Borges, B. W., Baptista, R., Papadimitriou, C., & Giannakis, O. 2008, *A&A*, **480**, 481
- Charles, P. A. 2002, *The Physics of Cataclysmic Variables and Related Objects*, **261**, 223
- Chavez, C. E., Tovmassian, G., Aguilar, L. A., Zharikov, S., & Henden, A. A. 2012, *A&A*, **538**, A122
- Chou, Y., & Grindlay, J. E. 2001, *ApJ*, **563**, 934
- de Miguel, E., Patterson, J., Cejudo, D., et al. 2016, *MNRAS*, **457**, 1447
- Dhillon, V. S., Littlefair, S. P., Howell, S. B., et al. 2000, *MNRAS*, **314**, 826
- Djorgovski, S. G., Drake, A., Mahabal, A., et al. 2012, in *The First Year of MAXI: Monitoring Variable X-ray Sources—4th International MAXI Workshop*, ed. T. Mihara & M. Serino (Tokyo: RIKEN), 263 Special Publ. IPCR-127
- Downes, R. A., Webbink, R. F., Shara, M. M., et al. 2006, *yCat*, **5123**, 0
- Downes, R. A., Webbink, R. F., Shara, M. M., et al. 2001, *PASP*, **113**, 764
- Drake, A. J., Djorgovski, S. G., Mahabal, A., et al. 2009, *ApJ*, **696**, 870
- Drake, A. J., Gänsicke, B. T., Djorgovski, S. G., et al. 2014, *MNRAS*, **441**, 1186
- Durney, B. R., & Robinson, R. D. 1982, *ApJ*, **253**, 290
- Green, R. F., Ferguson, D. H., Liebert, J., & Schmidt, M. 1982, *PASP*, **94**, 560
- Greiner, J., Schwarz, R., & Wenzel, W. 1998, *MNRAS*, **296**, 437
- Honeycutt, R. K., Kafka, S., & Robertson, J. W. 2014, *AJ*, **147**, 10
- Hümmerich, S., Gröbel, R., Hamsch, F.-J., et al. 2017, *NewA*, **50**, 30
- Kafka, S., & Honeycutt, R. K. 2004, *Revista Mexicana de Astronomia y Astrofisica Conf. Ser.*, **20**, 238
- Kalomeni, B. 2012, *From Interacting Binaries to Exoplanets: Essential Modeling Tools*, **282**, 91
- Kemp, J., Patterson, J., de Miguel, E., et al. 2012, in *Society for Astronomical Sciences Annual Symposium*, **31**, 7
- Kotze, M. M., & Charles, P. A. 2012, *MNRAS*, **420**, 1575 (KC12)
- Kozai, Y. 1962, *AJ*, **67**, 591
- Kozhevnikov, V. P. 2007, *MNRAS*, **378**, 955
- Körding, E. G., Knigge, C., Tzioumis, T., & Fender, R. 2011, *MNRAS*, **418**, L129
- Laher, R. R., Surace, J., Grillmair, C. J., et al. 2014, *PASP*, **126**, 674
- Law, N. M., Kulkarni, S. R., Dekany, R. G., et al. 2009, *PASP*, **121**, 1395
- Lidov, M. L. 1962, *P&SS*, **9**, 719
- Lomb, N. R. 1976, *Ap&SS*, **39**, 447
- Mahabal, A. A., Djorgovski, S. G., Drake, A. J., et al. 2011, *BASI*, **39**, 387
- Masci, F. J., Laher, R. R., Rebbapragada, U. D., et al. 2017, *PASP*, **129**, 014002
- Mazeh, T., & Shaham, J. 1979, *A&A*, **77**, 145
- Meyer-Hofmeister, E., Vogt, N., & Meyer, F. 1996, *A&A*, **310**, 519
- Osaki, Y. 1989, *PASJ*, **41**, 1005
- Osaki, Y. 1996, *PASP*, **108**, 39
- Patterson, J. 1995, *PASP*, **107**, 657
- Patterson, J. 1999, in *Disk Instabilities in Close Binary Systems*, ed. S. Mineshige & C. Wheeler (Tokyo: Academy Press), 61
- Patterson, J., Masi, G., Richmond, M. W., et al. 2002, *PASP*, **114**, 721
- Potter, S. B., Romero-Colmenero, E., Ramsay, G., et al. 2011, *MNRAS*, **416**, 2202
- Rau, A., Kulkarni, S. R., Law, N. M., et al. 2009, *PASP*, **121**, 1334
- Ringwald, F. A., Thorstensen, J. R., Honeycutt, R. K., & Robertson, J. W. 1996, *MNRAS*, **278**, 125
- Ringwald, F. A. 1991, *BAAS*, **23**, 1463
- Ringwald, F. A., & Reynolds, D. S. 2003, *BAAS*, **35**, 44.07
- Robinson, R. D., & Durney, B. R. 1982, *A&A*, **108**, 322
- Rude, G. D., & Ringwald, F. A. 2012, *NewA*, **17**, 453
- Scargle, J. D. 1982, *ApJ*, **263**, 835
- Schmidtobreick, L., Papadaki, C., Tappert, C., & Ederoclitte, A. 2008, *MNRAS*, **389**, 1345
- Shears, J. 2009 *JAVSO*, **37**, 80
- Sheets, H. A., Thorstensen, J. R., Peters, C. J., Kapusta, A. B., & Taylor, C. J. 2007, *PASP*, **119**, 494
- Šimon, V. 2016, *MNRAS*, **463**, 1342
- Skillman, D. R., Patterson, J., & Thorstensen, J. R. 1995, *PASP*, **107**, 545
- Stanishev, V., Kraicheva, Z., & Genkov, V. 2001, *A&A*, **379**, 185
- Stellingwerf, R. F. 1978, *ApJ*, **224**, 953
- Suárez Mascareño, A., Rebolo, R., & González Hernández, J. I. 2016, *A&A*, **595**, A12
- Suleimanov, V., Bikmaev, I., Belyakov, K., et al. 2004, *AstL*, **30**, 615
- Szkody, P., Henden, A., Agüeros, M., et al. 2006, *AJ*, **131**, 973
- Thomas, N. L., Norton, A. J., Pollacco, D., et al. 2010, *A&A*, **514**, A30
- Thorstensen, J. R., Fenton, W. H., Patterson, J., et al. 2002, *PASP*, **114**, 1117
- Trenti, M., Ransom, S., Hut, P., & Heggie, D. C. 2008, *MNRAS*, **387**, 815
- Vanmunster, T. 2006 *JAVSO*, **35**, 132
- Vogt, N. 1980, *A&A*, **88**, 66
- Vrielmann, S., & Offutt, W. 2003, *MNRAS*, **338**, 165
- Warner, B. 1985, in *Interacting Binaries*, ed. P. P. Eggleton & J. E. Pringle (Dordrecht: D. Reidel Publishing Company), 367
- Warner, B. 1988, *Natur*, **336**, 129
- Warner, B. 1995, *CAS*, **28**, 464
- Whitehurst, R. 1988, *MNRAS*, **232**, 35
- Whitehurst, R., & King, A. 1991, *MNRAS*, **249**, 25
- Woudt, P. A., Warner, B., Gulbis, A., et al. 2012, *MNRAS*, **427**, 1004
- Zechmeister, M., & Kürster, M. 2009, *A&A*, **496**, 577
- Zellem, R., Hollon, N., Ballouz, R.-L., et al. 2009, *PASP*, **121**, 942
- Zwitter, T., & Munari, U. 1994, *A&AS*, **107**, 503

Recent work on sprite spectrum in Taiwan

Min-Ruey Lu¹, Pei-Yu Chen¹, Cheng-Ling Kuo^{1,*}, Chien-Chung Chou¹, Bin-Xing Wu², Shinsuke Abe³, Han-Tzong Su⁴, Rue-Ron Hsu⁴, Sheng-Hsiang Wang⁵, Neng-Huei Lin⁵, and Lou-Chuang Lee⁶

¹*Institute of Space Science, National Central University, Taoyuan City, Taiwan*

²*Graduate Institute of Astronomy, National Central University, Taoyuan City, Taiwan*

³*Department of Aerospace Engineering, Nihon University, Funabashi City, Japan*

⁴*Department of Physics, National Cheng Kung University, Tainan City, Taiwan*

⁵*Department of Atmospheric Sciences, National Central University, Taoyuan City, Taiwan*

⁶*Institute of Earth Sciences, Academia Sinica, Taipei City, Taiwan*

Article history:

Received 15 February 2016

Revised 20 August 2016

Accepted 26 August 2016

Keywords:

Sprite, Spectroimager, Lightning

Citation:

Lu, M.-R., P.-Y. Chen, C.-L. Kuo, C.-C. Chou, B.-X. Wu, S. Abe, H.-T. Su, R.-R. Hsu, S.-H. Wang, N.-H. Lin, and L.-C. Lee, 2017: Recent work on sprite spectrum in Taiwan. *Terr. Atmos. Ocean. Sci.*, 28, 625-636, doi: 10.3319/TAO.2016.08.26.02

ABSTRACT

This paper reports on the recent developments in spectroimagers for sprite campaigns in Taiwan. We first introduce two types of spectroimagers, the slit and slitless types, and discuss their advantages and shortcomings. Next we explore the instrument development and procedures undertaken for this study. In 2006, a slit spectroimager was installed for a sprite campaign and on 15 August of that year, two sprite spectra were recorded using the slit spectroimager along with seven sprites, one halo, one ELVES emission and two jets. By the end of 2015, a slitless spectroimager had been successfully constructed and was ready to conduct additional investigations. On 7 May 2016, a sprite spectrum was recorded using the slitless spectroimager. Following an examination of the calibrations (comprising detection region field of view, wavelength calibration, and response curve), data analysis, and additional calibrations (comprising elevation and azimuthal angles, atmospheric transmittance, and theoretical wavelength calculations) performed in this study, we present the results from our observed sprite spectra using the slit and slitless spectroimagers.

1. INTRODUCTION

A research group from the University of Minnesota was the first to demonstrate the existence of upward electrical discharges, called “sprites,” on the night of 22 September 1989 (Franz et al. 1990). Later, during the sprite 1994 aircraft campaign, the first color image of the phenomena was captured, elucidating the luminosity and transient nature of its structure (< 16 ms). Sprites typically have a red body with faint bluish tendrils extending downward, occasionally reaching the cloud top. They usually appear at altitudes of 50 - 90 km above the Earth’s surface. The high-speed imaging of sprites with a time resolution of 0.3 - 1.0 ms, halos, and ELVES emissions has been discussed by Stanley et al. (1999), Barrington-Leigh et al. (2001), and Moudry et al. (2002, 2003). Stanley et al. (1999) determined that sprites usually begin at an altitude of approximately 75 km and

simultaneously expand upward and downward from their point of origin. McHarg et al. (2007) analyzed sub millisecond images of sprites (5000 and 7200 frames s^{-1}) and compiled statistics on the velocities of streamer heads, which varied between 10^6 and 10^7 m s^{-1} . Additionally, Cummer et al. (2006) demonstrated that the long-persisting sprite beads that form at the tips of downward moving sprite streamers are attracted to and collide with other streamer channels. Higher-speed dynamic evolutions of the fine structured streamers in sprites have also been predicted by theoretical streamer models (Pasko et al. 1998; Liu and Pasko 2004, 2005; Liu et al. 2006, 2009), which are consistent with our sprite observations.

Among the main groups of sprite emissions, the molecular nitrogen first positive band (N_2 1P) was the first to be identified using an intensifier charge-coupled device (CCD) spectrograph (Mende et al. 1995). Subsequent studies further determined the vibrational excitement states of N_2 1P

* Corresponding author
E-mail: clkuo@jupiter.ss.ncu.edu.tw

(Green et al. 1996; Hampton et al. 1996), and obtained evidence of the existence of a N_2^+ Meinel band emission (Bucselia et al. 2003). More recently, 1-ms time resolution spectrograph observations were achieved (Stenbaek-Nielse and McHarg 2004). The altitude-resolved spectrum (with a 3-ms temporal resolution and approximately 3-nm spectral resolution, from 640 - 820 nm) revealed that the upper vibrational state population of the N_2 1P bands, $B^3\Pi_g$, varies with the altitude, which is similar to the laboratory afterglow at low pressure (Kanmae et al. 2007, 2010; Parra-Rojas et al. 2013; Stenbaek-Nielsen et al. 2013).

We discuss the recent development in spectroimagers for sprite campaigns in Taiwan. In section 2, we introduce two types of spectroimagers (slit and slitless designed), and discuss the advantages and shortcomings of each. In section 3, we list the sprite spectroimager campaign results, conducted from 2006 to the present. In section 4, we present the spectroimager calibrations (comprising detection region field of view, wavelength calibration, and response curve), data analysis, and additional calibration (comprising elevation and azimuthal angles, atmospheric transmittance, and theoretical wavelength calculations) performed in this study. Section 5 explores the observed sprite and lightning spectra results.

2. INSTRUMENT

In contrast to progressive scanning spectroscopy laboratory experiment applications for obtaining high-resolution wavelength, it was necessary to capture the entire low-intensity spectrum within a condensed time in this study because sprite occurrence is rare and unpredictable. The criteria required for the spectroimager sprite observations were (1) a wide field, (2) low light level, (3) short exposure time, and (4) full wavelength band scanning (visual and infrared). The slit spectrometer was originally designed to avoid the overlap of various spectral regions diffracted from diverse light sources. Conversely, the slitless spectroimager was developed to increase the likelihood of capturing a sprite in the spectroimager's field of view, and has often been used in meteor spectrum observations (Abe et al. 2004a, b; Fujiwara et al. 2004; Passas et al. 2016) because a high-resolution (0.45 nm) spectroimager is required to investigate the spectroscopic features of meteors (Passas et al. 2016).

Slitless spectroimagers have also been frequently used in astronomy and remote sensing (Abe et al. 2004a, b; Fujiwara et al. 2004). They are comprised of a diffracting component (transmittance grating or reflected grating), a light-path component (mirrors or wedges), and a low-light-level sensor. The diffracting component curves the light through the grating at different angles. For a specified angle of light, the constructive wave interference enhances the light within the specified wavelength range. The destructive wave interference cancels the light outside of the specified wavelength

range. The point light source curves the light through the diffracting component to the light intensity within a specified wavelength range of interest. Slitless spectroimagers are valid only for point light sources that generate the spectrum diffracted by a light source external to or within the narrow slit region. Hence, using slitless spectroimagers increases the likelihood of capturing a light point spectrum.

Compared with reflected gratings, transmittance gratings direct the light path along the instrument optical axial direction, which is easily aligned. A wedge prism was used to refract the light along the optical axis in this study because the refracted prism angle on the light path depends on the transmittance grating diffraction angle of the wavelength range of interest. Figures 1a - c illustrate the slitless spectroimager design used in this study. Table 1 presents a summary of the device optical and electrical components. The cost of the full spectroimager suite was approximately US\$1000. A commercial global positioning system module was adopted to provide an accurate timestamp on our recording system.

The slit spectroimager design is presented in Fig. 2a, and depicted schematically in Fig. 2b. One of the advantages of a slit spectroimager is that the sensor rectangular window can be fixed for light source mapping. However, this is also a shortcoming because the slit shrinks the observation window and decreases the likelihood of recording a sprite. As indicated in Fig. 2b, the first two lens components are a collimator and a slit with an adjustable width. The second and third components are the transmission grating and the CCD light sensor, respectively.

The collimator component is composed of three identical Nikon F1.4 50-mm lenses and an adjustable slit. The first lens, portrayed on the left in Fig. 2b, is an object lens that projects the image onto the slit. The adjusted slit component (length, 6.3 mm) is opened from the center. Its size can be expanded from 0 mm (closed) to 6.0 mm (maximum clear opening). The slit width was set at 0.2 mm for this research. The spectrograph had a spectral resolution of approximately 6 nm. The light from the slit, collimated by the second lens, was diffracted by the prism (one prism plus the transmission grating with 300 lines mm^{-1}). The diffracted light was then focused by the third lens and finally recorded by the light sensor.

As illustrated by the dashed line in Fig. 3, the responses of the slit and slitless spectrograph systems covered the sprite infrared emissions (i.e., N_2 1P spectra). An Andor electron multiplying CCD (EMCCD) light sensor was used for the slit spectrograph. The EMCCD is a quantitative digital camera that can detect single photon events while maintaining high quantum efficiency. This is achieved through a unique electron-multiplying structure built into the sensor (see http://www.emccd.com/what_is_emccd/ for more information) and is specifically designed for time-integrated image intensified spectroscopy.

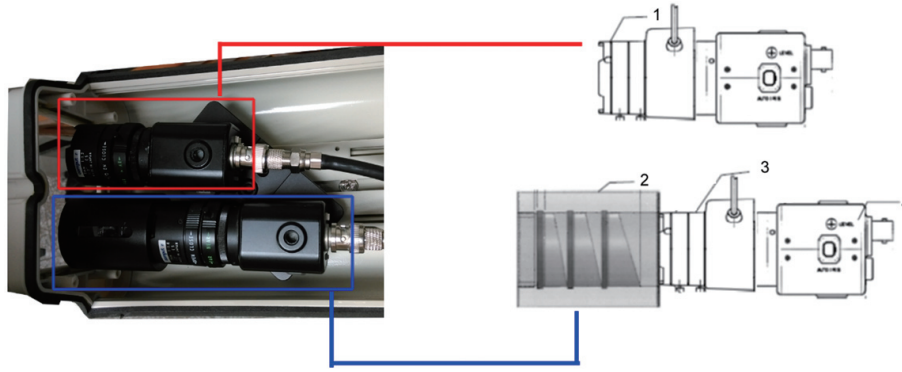


Fig. 1. Slitless spectroimager components. (Color online only)

Table 1. Slitless spectroimager optical components.

Item	Description	Manufacture
1	Optical lens (12 mm)	Computar
2	Diffracting component	Unice E-O
3	Optical lens (8 mm)	Computar
4	Monochrome CCD	Watec

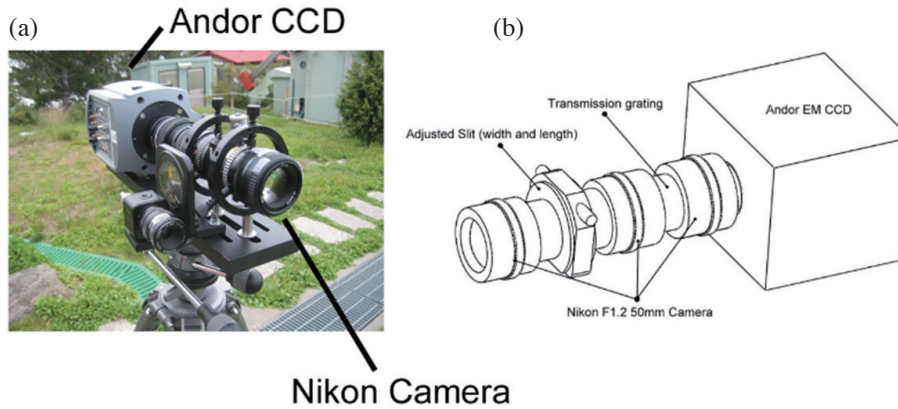


Fig. 2. (a) Photograph of the slit spectroimager, and (b) optical layouts of the slit spectroimager. (Color online only)

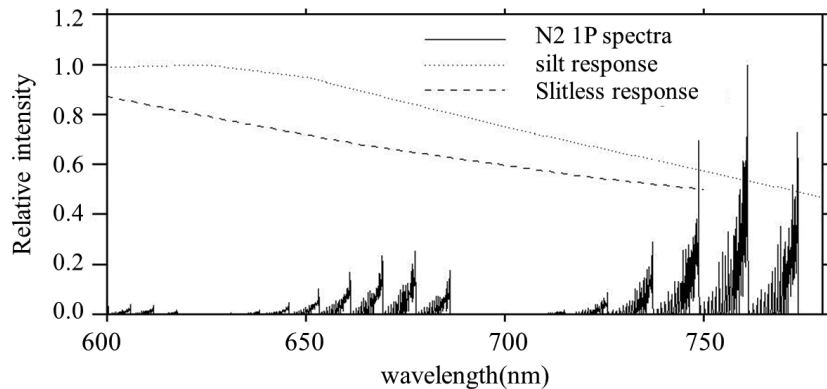


Fig. 3. Simulated spectra for N_2 1P band emissions (solid lines), and relative responses of the slit spectroimager (dotted line) and slitless spectroimager (dash line).

3. OBSERVATIONS

We conducted a sprite campaign at the Lulin Observatory in Taiwan during the summer of 2006. On 15 August 2006, a total of seven sprites, one halo, one ELVES emission, and two jets were recorded using the low-light-level CCD system. Of these events, two sprites and one lightning spectrum were recorded in a slit spectroimager, which has a narrower field of view than do low-light-level CCD systems.

From 2010 - 2012, the ground campaign from Lulin Observatory and the National Central University (NCU) campaign were established and recorded by Shinsuke Abe and BinXing Wu. A total of 158 events were analyzed, with 140 sprites, 6 ELVES emissions, 5 gigantic jets, and 2 blue jets recorded (Table 2); the events per month between 2010 and 2012 are summarized in Table 3. The recording of transient luminous events (TLEs) began in May (Table 3),

coinciding with Taiwan's monsoon season, which starts in early May and ends in late September [Central Weather Bureau (CWB)]. The monsoon season is accompanied with typhoons, especially from June to September, that cause a seasonal wind reversal. Hence, the climate during the monsoon season tends to produce thunderstorms with sprites. According to the CWB, typhoons are most common in August; correspondingly, the number of TLEs recorded in August and September was higher than that in other months. In contrast to our expectations, the number of events in November 2011 was also very high. The projected location of detected TLEs near Taiwan and the spatial distribution of recorded events from 2010 - 2012 at the Lulin Observatory are presented in Fig. 4.

Between 2012 and 2014, the sprite ground observatory was tested from three stations: the NCU station, the NCU Taiwan Coastal Observation and Assessment Station

Table 2. Results of the 2010 - 2012 Lulin Observatory ground campaign.

Type	May	June	July	August	September	October	November	Sum
Blue jets				1			1	2
Elves				4	1	1		6
Gigantic jet				1	4			5
Halos				5	1			6
Sprites	38	1	4	24	29	7	30	133
Sprite + elve					1			1
Sprite + halo				2	3			5
Total	38	1	4	37	39	8	31	158

Table 3. Number of events detected from the Lulin Observatory between 2010 and 2012.

Month	Year			Month total
	2010	2011	2012	
05		17	21	38
06		1		1
07		4		4
08	32	5		37
09	34	5		39
10	2	6		8
11		31		37
Year total	68	69	21	158

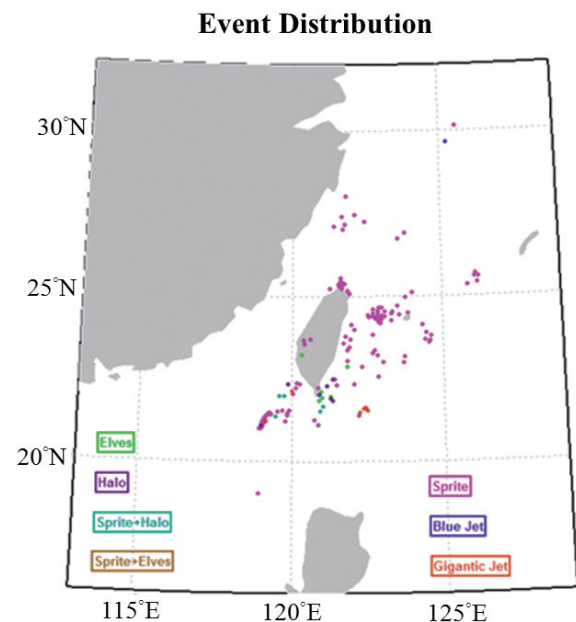


Fig. 4. Spatial distribution of events recorded at the Lulin Observatory from 2010 - 2012. (Color online only)

(TaiCOAST), and the Lulin Observatory. In 2015, the Lulin Observatory was selected for a spectroimager campaign, and a slitless spectroimager with a Watec-910HX detector was installed in April 2015. However, during the first test run, the auto recording system had difficulty recording both a sprite and its spectrum simultaneously; thus, in October 2015; the composite image (picture-in-picture) method using video synthesis was adopted. The images acquired from the slitless spectroimager were displayed on a full screen, and the associated sprite image was displayed in a small window at the lower right-hand corner; this technique successfully enabled synchronous video recording of the sprite and associated spectral images.

4. INSTRUMENT CALIBRATION

4.1 Optical Laboratory for Calibration

Figure 5 illustrates the optical layout for the spectroimager calibration experiment. Table 4 presents the optical components. Halogen lamps were used as the calibrated visual light source, although Hamamatsu Xenon lamps are recommended for future studies. The wideband light was first diffracted into narrowband light using a monochromator. The point light source was next placed on the focal point of the parabolic mirror where the optical flat mirror folds the light path into a shorter length on a small optical board. The parabolic and optical flat mirrors were then used to project the point source from the iris diaphragm to the light source at an infinite distance. subsequently, the source light alignment was tested using the collimator, and the detection region field of view, wavelength, and response curve of the spectroimager were calibrated in the optical laboratory, as described by Harris (2000, 2003).

4.2 Elevation and Azimuthal Angle

The azimuthal and elevation angles of the recorded stars were calibrated in the CCD spectrograph. The uncovered star fields were compared with the star field in the astronomy software Stellarium. Figure 6a depicts the stars that were selected in this study for calibrating the azimuthal and elevation angles. The azimuthal and elevation star angles from Stellarium were subsequently fitted with a linear function to determine the angles of each recorded image frame pixel (Figs. 6b and c).

4.3 Wavelength Calibration

Several methods can be employed to calibrate a spectroimager wavelength. For slitless spectroimagers, the simplest approach to determine the wavelength position on an image frame is to identify the characteristic wavelength of the recorded spectrum, because the expanded spectrum de-

pends on the incident angle of the point light source. The position of the wavelength subsequently changes as a function of this incident angle. For slit spectroimagers, this angle can be limited by the width of the slit. Therefore, wavelength calibrations in a laboratory experiment are consistent with the observed spectrum. For laboratory experiments, a standard lamp (e.g., Newport 6035) is sufficient for calibrating the wavelength of recorded spectra before observation.

4.4 Atmospheric Transmittance

Atmospheric transmittance along the sight line affects the percentage of band emissions (B_k), and is calculated using Lambert's law:

$$T(\lambda, h, L) = \exp\left[-\sum_x \sigma_x(\lambda) D_x(h, L)\right] \quad (1)$$

where $\sigma_x(\lambda)$ is the absorption cross-section for the major atmospheric species, namely O_2 absorption, O_3 absorption, and molecular Rayleigh scattering (N_2, O_2). The data for $O_2, O_3,$ and molecular Rayleigh scattering were retrieved from Jursa (1985) and Minschwaner et al. (1992). In this study, the absorption cross-section of N_2 was minor (185 - 800 nm), and its effect on transmittance was negligible.

Column density [$(D_x(h, L))$] was calculated by integrating the densities of $N_2, O_2,$ and O_3 from the observation site to the assumed altitude (h) of a TLE:

$$D_x(h_{TLE}, L) = \int_{FS-2}^{h_{TLE}} n_x(s) ds \quad (2)$$

where the total length of the path between the observation site and the TLE is L . The N_2 and O_2 densities were computed using the MSIS model (Hedin 1991), whereas the overnight O_3 density profile at an altitude between 18 and 100 km was measured using the Michelson interferometer for passive atmospheric sounding (Verronen et al. 2005). The O_3 region below 100 km accounted for most of the O_3 absorption in the calculated atmospheric extinction. Figure 7 illustrates the distance transmittance (200, 300, 400, and 500 km) between the observation site (altitude approximately 2862 m) and the sprite.

4.5 Theoretical Wavelength Calculation

Atmospheric gas heating produces two problems: cold plasma in the middle atmosphere (in the form of TLEs) and hot plasma (in the form of lightning). Thus, the plasma chemistry model for cold plasma (Sentman et al. 2008; Kuo et al. 2011) was applied to study the associated radiative emissions that accompany atmospheric discharge (N_2 1P/2P/LBH, N_2^+ Meinel/1N, atmospheric $O_2,$ and O_2^+ 1N bands) (Gordillo-Vázquez et al. 2011, 2012). Notably, the

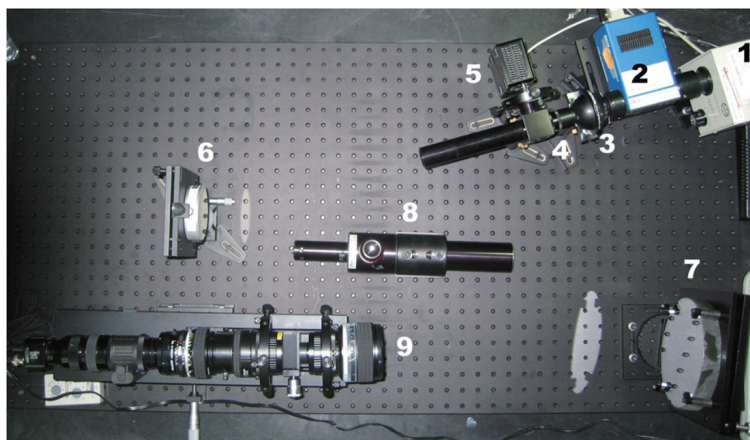


Fig. 5. Optical table to calibrate the field of view, wavelength, and optical response of a spectroimager. The numbers correspond with the optical components listed in Table 4. (Color online only)

Table 4. Optical components used in the optical laboratory for calibration. The number for each component appears in Fig. 5.

Item	Description	Manufacturer
1	Light source	TAIWAN FIBEROPTICS
2	Monochromator	CVI
3	Integrating Sphere	Light Ports
4	Iris Diaphragm	Edmund
5	Calibrated microspectrometer (250 - 950 nm)	BWTEK
6	Optical Flat Mirrors - 3.0"D Dia: 76.2 mm Thickness: 19.1 mm	Edmund
7	Parabolic Mirrors EFL = 1219.2 mm Dia 152.4 mm	Edmund
8	Auto Collimator ± 55 arc min, per 5 arc minute gradations	Edmund
9	Spectroimager	-

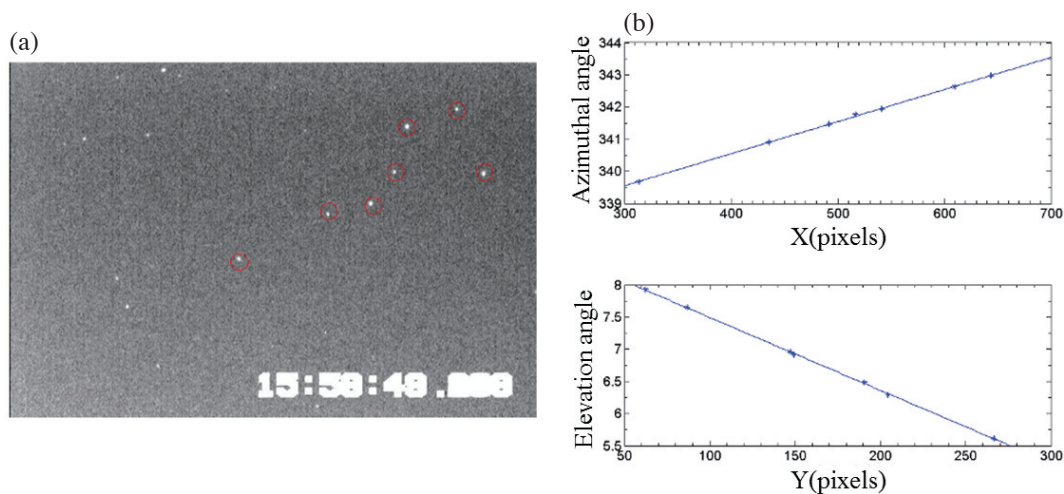


Fig. 6. Calibration of (a) azimuthal and (b) elevation angles using stars selected from Stellarium. (Color online only)

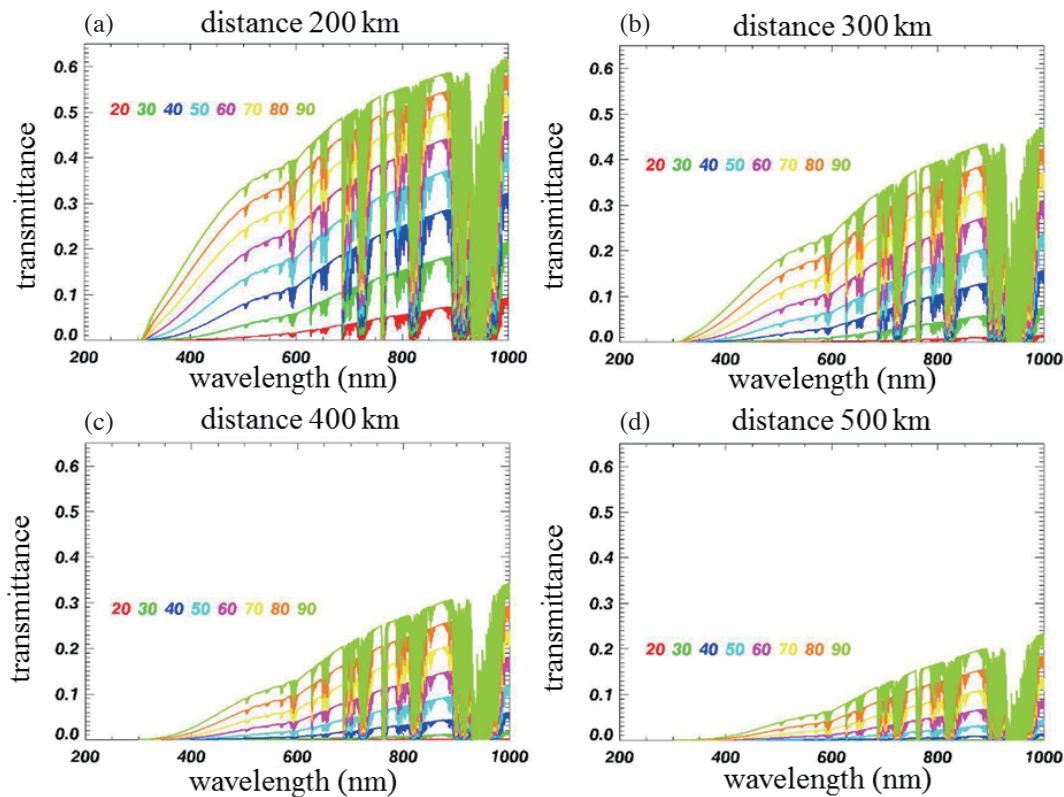


Fig. 7. Atmospheric transmittance at (a) 200 km, (b) 300 km, (c) 400 km, and (d) 500 km between the observation site and the assumed sprite altitude (20 - 90 km, with increments of 10 km), which are labeled with different colors. (Color online only)

specified energy level ($E_{e,v,j}$) of the upper or lower state of a given emission band in N_2 can be expressed as the sum of the electron term energy (T_e), the vibrational term energy [$G(v)$], and the rotational term energy [$F_v(J)$], as follows:

$$\begin{aligned}
 G(v) &\approx \omega_e(v + \frac{1}{2}) - \omega_e x_e(v + \frac{1}{2})^2 + \\
 &\quad \omega_e y_e(v + \frac{1}{2})^3 + \omega_e z_e(v + \frac{1}{2})^4 \\
 F_v(J) &\approx [B_e - \alpha_e(v + \frac{1}{2})]J(J + 1) - \\
 &\quad [D_e + \beta_e(v + \frac{1}{2})]J^2(J + 1)^2
 \end{aligned}
 \tag{3}$$

where $G(v)$ and $F_v(J)$ are fitted using Klein-Dunham polynomial expansions for the specified vibrational quantum number v and the specified rotational quantum number J of the energy level (Lofthus and Krupenie 1977). The formula for calculating the vibrational and rotational term energies $G(v)$ and $F_v(J)$ can be truncated into four and two terms, respectively, and approximating the related parameters (namely, T_e , ω_e , x_e , y_e , z_e , α_e , β_e , B_e , and D_e) for $1PN_2$, $2PN_2$, $1NN_2^+$ (Herzberg 1950; Krupenie 1972; Naghizadeh-Kashani et al. 2002), and N_2 LBH (NIST Chemistry WebBook).

5. RESULTS

5.1 The Slit Spectroimager

Figures 8a and b depict a sprite recorded at 15:58:49 on 15 October 2006, by 12- and 50-mm lenses, respectively, with an exposure time of approximately 17 ms for both image frames. Figure 9a illustrates the possible projected position of a sprite recorded in color and enhanced with infrared imaging using multifunctional transport satellites. The distance between the sprite and the observation site is approximately 400 km. Figure 9b displays additional sprite images recorded using the 50-mm lens, wherein the column sprite heights were estimated to be 50 - 85 km and the spectroimager slit was estimated at a height of 55.4 - 61.4 km. Figure 9c presents a wide-field sprite recording acquired using a 12-mm lens. Figure 9d shows the observed image recorded by the Andor EMCCD. The images indicate that the sprites acquired through the slit were converted into intensity profiles as a function of the wavelength. A recorded sprite spectrum, where the N_2 1P band wavelength is indicated by the difference between the vibrational number of the upper states and that of the lower states, is shown in Fig. 10. The sprite spectrum was measured between 600 and 780 nm, and the observed spectrum included all of the major

N_2 1P band emission characteristics.

Figure 11 shows composite images of the lightning observed at 01:52:34 on 25 October 2006, which was recorded by both the 50-mm lens (Fig. 11a) and the Andor EMCCD camera (Fig. 11b). Figure 11c indicates the possible position of the lightning over the thunderstorm and Fig. 11d depicts the recorded lightning spectrum where the N_2 1P band and the OI line (744.2 and 777.4 nm, respectively) are located.

5.2 The Slitless Spectroimager

Figure 12 depicts a sprite recorded at 02:12:58 on 7 May 2016 (acquired using a 12-mm lens) and the spectra recorded using the slitless spectroimager. The relative spectrum intensity was calibrated according to the Jupiter spectrum wavelength intensity, recorded on the same night and determined by four absorption lines (H_α 656.3 nm, H_β 486.1 nm, H_γ

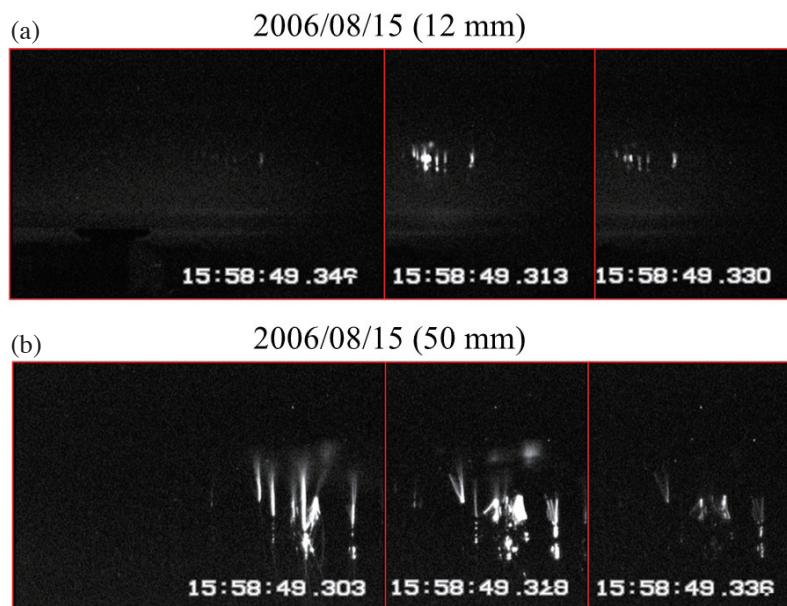


Fig. 8. Sprite recorded at 15:58:49 on 15 October 2006, captured using a (a) 12-mm lens and (b) 50-mm lens. (Color online only)

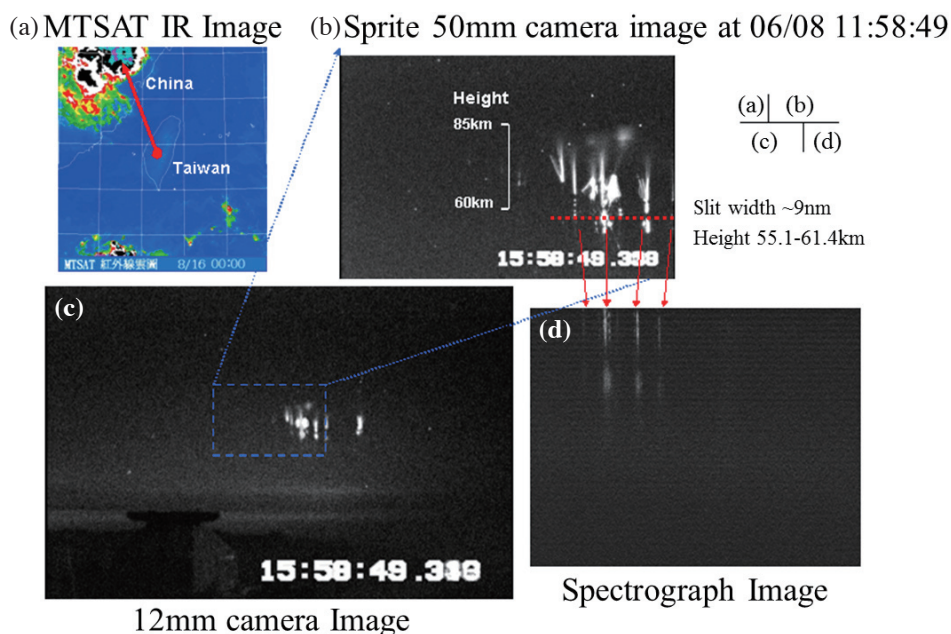


Fig. 9. Lulin Observatory sprite campaign from the summer of 2006 in Taiwan, including (a) the weather map with the location of the Lulin Observatory (red dot), (b) the sprite recorded at 15:58:49 on 15 October 2006, acquired using a 50-mm lens, (c) the same sprite, acquired using a 12-mm lens, and (d) the spectrum recorded by the slit spectroimager. (Color online only)

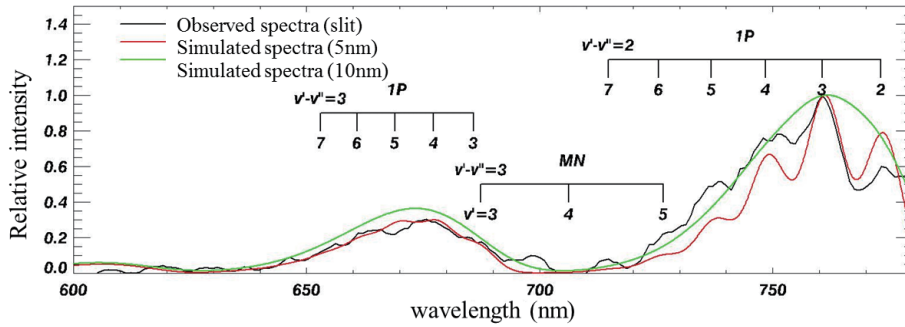


Fig. 10. Sprite spectrum (solid line) recorded by the slit spectroimager. The marks indicate that the vibrational transitions of the N₂ 1P band, and the spectral resolution is approximately 6 nm. (Color online only)

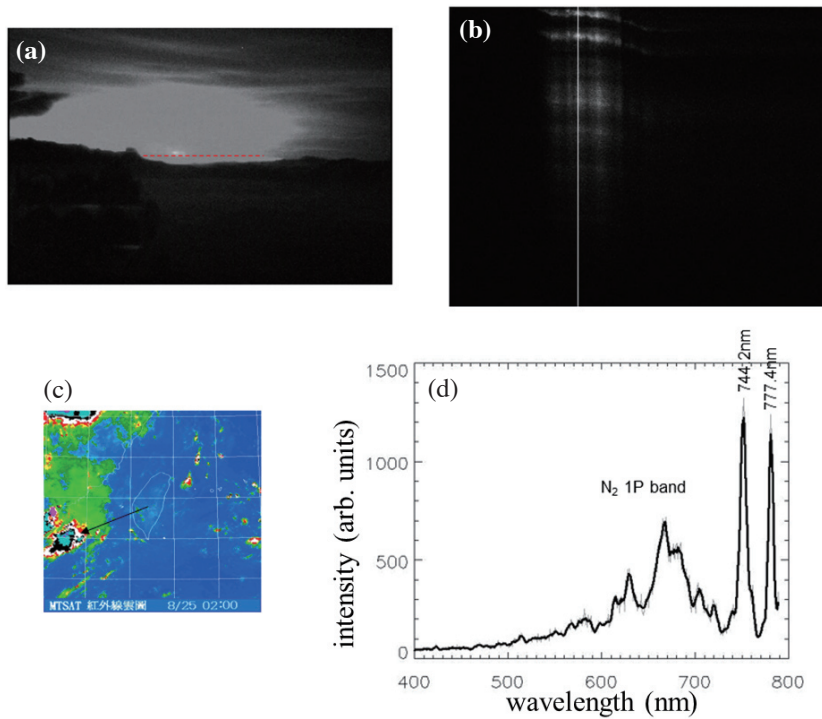


Fig. 11. Lightning recorded at 01:52:34 on 25 October 2006. (a) Lightning image, (b) the spectrum recorded by the slit spectroimager, (c) the weather map (black arrow indicates the direction from the Lulin Observatory to the lightning location), and (d) the recorded spectrum of lightning. (Color online only)

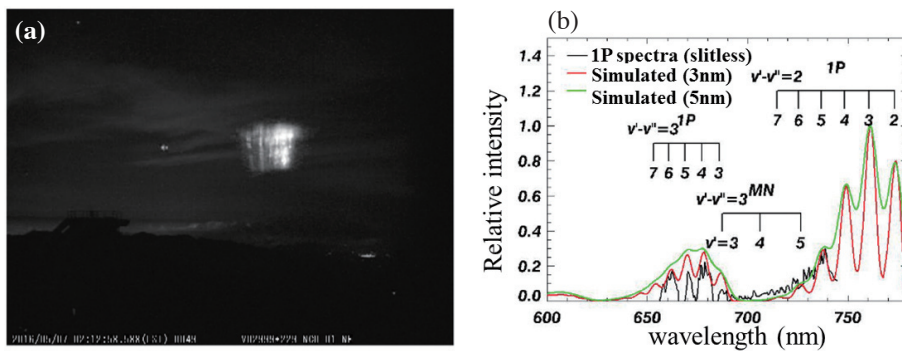


Fig. 12. (a) Sprite image taken acquired using a 12-mm lens at 02:12:58 on 7 May 2016, and (b) spectrum recorded using the slitless spectroimager. (Color online only)

434.1, and H δ 410.2 nm). As indicated by the dashed line in Fig. 3, the slitless spectroimager response can be determined through the modeling Jupiter spectra intensity and the atmospheric transmittance at a specified elevation angle. Notably, the maximum response value is 750 nm because that was the maximum Jupiter spectrum wavelength recorded by our slitless spectrograph. However, the wavelength limit can be improved by integrating more Jupiter spectra image frames to enhance the spectral intensity above 750 nm.

The recorded spectra resolution acquired by the slitless spectroimager was approximately 3 nm, compared with the simulated sprite spectra with two slit functions (widths of 3 and 5 nm). As the recorded sprite spectra presented in Fig. 10 (slit spectrograph) and Fig. 12 (slitless spectrograph) demonstrate, the N $_2$ Meinel band can be mixed with the dominant N $_2$ 1P band emission, which peaks between 650 and 700 nm. Our results are not comparable with the 1-nm wavelength resolution spectra observed by other researchers (Kanmae et al. 2007, 2010; Stenbaek-Nielsen et al. 2013). However, our slitless spectroimager has many advantages including its compact and lightweight size, low cost (US\$1500), and simple, easy assembly process. Additionally, the proposed slitless spectroimager is appropriate for education, particularly among college or high school students conducting sprite research.

6. SUMMARY

In addition to instrument development and sprite observation, the related spectroimager calibration and data analysis work, including optical experiment design, are reported in this paper. The spectroimager calibrations included the detection region field of view, wavelength calibration and spectroimager response curve. The elevation and azimuthal angles of the observation site, atmospheric transmittance and theoretical wavelength calculations for spectrum analysis were discussed.

In addition, we explored the recent development in spectroimagers in Taiwan for sprite campaigns. Notably, a slit spectroimager was developed and used for sprite campaigns in 2006. In that year, two sprite spectra were recorded using our spectroimager along with seven sprites, one halo, one ELVES emission and two jets. By the end of 2015, a slitless spectroimager was ready to conduct additional investigations, and during the subsequent 2016 sprite campaign, a sprite spectrum was successfully recorded using the slitless spectroimager. Slitless spectroimagers are substantially more cost-effective than slit spectroimagers and their assembly process is simple, which are critical advantages for young students conducting their first sprite studies.

Acknowledgements This work was supported in part by grants (MOST 103-2111-M-008-021, MOST 104-2111-M-008-023, and MOST 105-2111-M-008-007) from Ministry

of Science and Technology in Taiwan. We thank Ming-Han Chou, Ying-Xuan Chen, Yen-Chan Chen, and Wei-Chen Lai for their assistance in these observations.

REFERENCES

- Abe, S., J. Borovicka, S. Sugimoto, and M. Yamamoto, 2004a: TV spectroscopy of persistent trains during 2001 Leonid meteor storm over Japan. In: Paillé, J. P. (Ed.), 35th COSPAR Scientific Assembly, 18 - 25 July 2004, Paris, France.
- Abe, S., N. Ebizuka, H. Murayama, K. Ohtsuka, S. Sugimoto, M. Y. Yamamoto, H. Yano, J. I. Watanabe, and J. Borovička, 2004b: Video and Photographic Spectroscopy of 1998 and 2001 Leonid Persistent Trains from 300 TO 930 nm. *Earth Moon Planets*, **95**, 265-277, doi: 10.1007/s11038-005-9031-0. [\[Link\]](#)
- Barrington-Leigh, C. P., U. S. Inan, and M. Stanley, 2001: Identification of sprites and elves with intensified video and broadband array photometry. *J. Geophys. Res.*, **106**, 1741-1750, doi: 10.1029/2000JA000073. [\[Link\]](#)
- Bucsel, E., J. Morrill, M. Heavner, C. Siefing, S. Berg, D. Hampton, D. Moudry, E. Wescott, and D. Sentman, 2003: N $_2$ (B $^3\Pi_g$) and N $_2^+$ (A $^2\Pi_u$) vibrational distributions observed in sprites. *J. Atmos. Sol.-Terr. Phys.*, **65**, 583-590, doi: 10.1016/S1364-6826(02)00316-4. [\[Link\]](#)
- Cummer, S. A., N. Jaugey, J. Li, W. A. Lyons, T. E. Nelson, and E. A. Gerken, 2006: Submillisecond imaging of sprite development and structure. *Geophys. Res. Lett.*, **33**, L04104, doi: 10.1029/2005GL024969. [\[Link\]](#)
- Franz, R. C., R. J. Nemzek, and J. R. Winckler, 1990: Television Image of a Large Upward Electrical Discharge Above a Thunderstorm System. *Science*, **249**, 48-51, doi: 10.1126/science.249.4964.48. [\[Link\]](#)
- Fujiwara, Y., M. Ueda, M. Sugimoto, T. Sagayama, and S. Abe, 2004: TV Observation of the Daytime Meteor Shower. The Arietids. *Earth Moon Planets*, **95**, 595-600, doi: 10.1007/s11038-005-5040-2. [\[Link\]](#)
- Gordillo-Vázquez, F. J., A. Luque, and M. Simek, 2011: Spectrum of sprite halos. *J. Geophys. Res.*, **116**, A09319, doi: 10.1029/2011JA016652. [\[Link\]](#)
- Gordillo-Vázquez, F. J., A. Luque, and M. Simek, 2012: Near infrared and ultraviolet spectra of TLEs. *J. Geophys. Res.*, **117**, A05329, doi: 10.1029/2012JA017516. [\[Link\]](#)
- Green, B. D., M. E. Fraser, W. T. Rawlins, L. Jeong, W. A. M. Blumberg, S. B. Mende, G. R. Swenson, D. L. Hampton, E. M. Wescott, and D. D. Sentman, 1996: Molecular excitation in sprites. *Geophys. Res. Lett.*, **23**, 2161-2164, doi: 10.1029/96GL02071. [\[Link\]](#)
- Hampton, D. L., M. J. Heavner, E. M. Wescott, and D. D. Sentman, 1996: Optical spectral characteristics of sprites. *Geophys. Res. Lett.*, **23**, 89-92, doi: 10.1029/95GL03587. [\[Link\]](#)

- Harris, S., 2000: ISUAL Imager Science Performance Test Report, Space Sciences Laboratory, UCB, Berkeley, CA, Doc. 8988-W7 rev B.
- Harris, S., 2003: ISUAL Spectrophotometer Science Performance Test Report, Space Sciences Laboratory, UCB, Berkeley, CA, Doc. 8998W7 rev B.
- Hedin, A. E., 1991: Extension of the MSIS Thermosphere Model into the middle and lower atmosphere. *J. Geophys. Res.*, **96**, 1159-1172, doi: 10.1029/90JA02125. [[Link](#)]
- Herzberg, G., 1950: Molecular Spectra and Molecular Structure, Van Nostrand, New York.
- Jursa, A. S., 1985: Handbook of Geophysics and the Space Environment, 4th Ed., Air Force Geophysics Laboratory, Hanscom AFB, MA, 25 pp.
- Kanmae, T., H. C. Stenbaek-Nielsen, and M. G. McHarg, 2007: Altitude resolved sprite spectra with 3 ms temporal resolution. *Geophys. Res. Lett.*, **34**, L07810, doi: 10.1029/2006GL028608. [[Link](#)]
- Kanmae, T., H. C. Stenbaek-Nielsen, M. G. McHarg, and R. K. Haaland, 2010: Observation of sprite streamer head's spectra at 10,000 fps. *J. Geophys. Res.*, **115**, A00E48, doi: 10.1029/2009JA014546. [[Link](#)]
- Krupenie, P. H., 1972: The spectrum of molecular oxygen. *J. Phys. Chem. Ref. Data*, **1**, 423-534, doi: 10.1063/1.3253101. [[Link](#)]
- Kuo, C. L., S. C. Chang, L. J. Lee, T. Y. Huang, A. B. Chen, H. T. Su, R. R. Hsu, D. D. Sentman, H. U. Frey, S. B. Mende, Y. Takahashi, and L. C. Lee, 2011: The 762 nm emissions of sprites. *J. Geophys. Res.*, **116**, A01310, doi: 10.1029/2010JA015949. [[Link](#)]
- Liu, N. and V. P. Pasko, 2004: Effects of photoionization on propagation and branching of positive and negative streamers in sprites. *J. Geophys. Res.*, **109**, A04301, doi: 10.1029/2003JA010064. [[Link](#)]
- Liu, N. and V. P. Pasko, 2005: Molecular nitrogen LBH band system far-UV emissions of sprite streamers. *Geophys. Res. Lett.*, **32**, L05104, doi: 10.1029/2004GL022001. [[Link](#)]
- Liu, N., V. P. Pasko, D. H. Burkhardt, H. U. Frey, S. B. Mende, H. T. Su, A. B. Chen, R. R. Hsu, L. C. Lee, H. Fukunishi, and Y. Takahashi, 2006: Comparison of results from sprite streamer modeling with spectrophotometric measurements by ISUAL instrument on FORMOSAT-2 satellite. *Geophys. Res. Lett.*, **33**, L01101, doi: 10.1029/2005GL024243. [[Link](#)]
- Liu, N. Y., V. P. Pasko, K. Adams, H. C. Stenbaek-Nielsen, and M. G. McHarg, 2009: Comparison of acceleration, expansion, and brightness of sprite streamers obtained from modeling and high-speed video observations. *J. Geophys. Res.*, **114**, A00E03, doi: 10.1029/2008JA013720. [[Link](#)]
- Lofthus, A. and P. H. Krupenie, 1977: The spectrum of molecular nitrogen. *J. Phys. Chem. Ref. Data*, **6**, 113-307, doi: 10.1063/1.555546. [[Link](#)]
- McHarg, M. G., H. C. Stenbaek-Nielsen, and T. Kammae, 2007: Observations of streamer formation in sprites. *Geophys. Res. Lett.*, **34**, L06804, doi: 10.1029/2006GL027854. [[Link](#)]
- Mende, S. B., R. L. Rairden, G. R. Swenson, and W. A. Lyons, 1995: Sprite spectra; N21 PG band identification. *Geophys. Res. Lett.*, **22**, 2633-2636, doi: 10.1029/95gl02827. [[Link](#)]
- Minschwaner, K., G. P. Anderson, L. A. Hall, and K. Yoshino, 1992: Polynomial coefficients for calculating O₂ Schumann-Runge cross sections at 0.5 cm⁻¹ resolution. *J. Geophys. Res.*, **97**, 10103-10108, doi: 10.1029/92JD00661. [[Link](#)]
- Moudry, D. R., H. C. Stenbaek-Nielsen, D. D. Sentman, and E. M. Wescott, 2002: Velocities of sprite tendrils. *Geophys. Res. Lett.*, **29**, doi: 10.1029/2002GL015682. [[Link](#)]
- Moudry, D. R., H. C. Stenbaek-Nielsen, D. Sentman, and E. Wescott, 2003: Imaging of elves, halos and sprite initiation at 1 ms time resolution. *J. Atmos. Sol.-Terr. Phys.*, **65**, 509-518, doi: 10.1016/S1364-6826(02)00323-1. [[Link](#)]
- Naghizadeh-Kashani, Y., Y. Cressault, and A. Gleizes, 2002: Net emission coefficient of air thermal plasmas. *J. Phys. D: Appl. Phys.*, **35**, 2925-2934, doi: 10.1088/0022-3727/35/22/306. [[Link](#)]
- Parra-Rojas, F. C., M. Passas, E. Carrasco, A. Luque, I. Tanarro, M. Simek, and F. J. Gordillo-Vázquez, 2013: Spectroscopic diagnostics of laboratory air plasmas as a benchmark for spectral rotational (gas) temperature determination in TLEs. *J. Geophys. Res.*, **118**, 4649-4661, doi: 10.1002/jgra.50433. [[Link](#)]
- Pasko, V. P., U. S. Inan, and T. F. Bell, 1998: Spatial structure of sprites. *Geophys. Res. Lett.*, **25**, 2123-2126, doi: 10.1029/98gl01242. [[Link](#)]
- Passas, M., J. M. Madiedo, and F. J. Gordillo-Vázquez, 2016: High resolution spectroscopy of an Orionid meteor from 700 to 800 nm. *Icarus*, **266**, 134-141, doi: 10.1016/j.icarus.2015.11.020. [[Link](#)]
- Sentman, D. D., H. C. Stenbaek-Nielsen, M. G. McHarg, and J. S. Morrill, 2008: Plasma chemistry of sprite streamers. *J. Geophys. Res.*, **113**, D11112, doi: 10.1029/2007jd008941. [[Link](#)]
- Stanley, M., P. Krehbiel, M. Brook, C. Moore, W. Rison, and B. Abrahams, 1999: High speed video of initial sprite development. *Geophys. Res. Lett.*, **26**, 3201-3204, doi: 10.1029/1999GL010673. [[Link](#)]
- Stenbaek-Nielsen, H. and M. G. McHarg, 2004: Sprite Spectra at 1000 fps, American Geophysical Union, Fall Meeting 2004, abstract #AE51A-08.
- Stenbaek-Nielsen, H. C., T. Kanmae, M. G. McHarg, and R. Haaland, 2013: High-Speed Observations of Sprite Streamers. *Surv. Geophys.*, **34**, 769-795, doi: 10.1007/

s10712-013-9224-4. [[Link](#)]

Verronen, P. T., E. Kyrölä, J. Tamminen, B. Funke, S. Gil-López, M. Kaufmann, M. López-Puertas, T.v. Clarmann, G. Stiller, U. Grabowski, and M. Höpf-

ner, 2005: A comparison of night-time GOMOS and MIPAS ozone profiles in the stratosphere and mesosphere. *Adv. Space Res.*, **36**, 958-966, doi: 10.1016/j.asr.2005.04.073. [[Link](#)]

工作報告

鹿林天文台觀測時數統計(2003-2017)

林宏欽、蕭翔耀、林啟生

鹿林天文台自 2002 年 9 月開始人員常駐，2003 年鹿林一米望遠鏡(LOT)上線，開始有正式觀測時數紀錄，可供瞭解鹿林長期的天氣狀況。依 2003-2017 共 15 年的統計結果，鹿林天文台年平均觀測時數為 1439 小時。一年可分為四個觀測季，

- 最佳觀測季：10-12 月。
- 次佳觀測季：1-3 月。
- 最差觀測季：4-6 月。4 月開始進入雨季，5-6 月受梅雨影響，天氣最差。
- 次差觀測季：7-9 月。主要受颱風及西南氣流影響，天氣變化大。此外夏季晝長夜短，每晚可觀測時間比冬季為短。

詳細統計資料及統計圖如下，

表 1 每月觀測時數統計 (2003-2017)

Month	2003	2004	2005	2006	2007	2008	2009	2010	2011	2012	2013	2014	2015	2016	2017	Average
1	78.75	125	163.25	129	127.32	179	234.52	206.9	90.8	113.42	153.58	269.62	188.55	75.4	160.85	150.072
2	142.5	145.98	94.75	149	128.55	118.25	165.7	100.6	123.8	64.88	183.63	109.8	131.65	60.25	105.3	121.597
3	147.5	163	143	126.05	116.4	138.5	146.75	181.3	75.9	168.23	134.26	78.7	111.1	72.8	96.4	126.599
4	126.5	110.5	144.75	86.8	53.75	85.25	71.8	75.8	151.45	32.75	55.83	135.95	124	82.9	86.9	95.4408
5	129.75	106.25	136.25	59.5	106.6	98.25	167.4	86.05	56.6	74.3	41.02	32.4	64.2	86.05	84.55	86.8746
6	24	133	45	39.3	54	37	81.75	26.5	61.5	35.15	80.14	33.7	146.9	114.05	76.1	62.8608
7	222.5	48	167.75	91.57	128.88	88.4	76.6	99.85	81.75	106.4	88.05	114.65	87.45	123.95	105.25	104.658
8	137.75	142	76	111.65	56.6	118.95	6.8	98.3	97.9	35.7	72.2	110.9	45.1	61	139.9	89.3808
9	142	116	129.25	60.05	69.55	59.8	0	109.95	90.1	117.35	107.84	134.39	93.25	42.85	128.2	96.8138
10	149.25	219.75	210.25	150.6	172.63	191.38	175.6	139.8	136.95	214.51	200.57	232.33	145.4	142.2	187.8	176.903
11	166.5	214.5	216.25	71.75	160.55	152.55	175.8	163.65	87.2	93.81	136.1	166.15	197.05	171.85	134.55	155.405
12	271.5	232.45	129	132	261.09	211.17	169.8	169.65	115.25	132.21	86	137.3	161.2	193.27	156.7	169.315
Total	1738.5	1756.43	1655.5	1207.27	1435.92	1478.5	1472.52	1458.35	1169.2	1188.71	1339.22	1555.89	1495.85	1226.57	1462.5	1439.64

* 2009 年因受莫拉克颱風八八風災影響，自八月八日起至十月初約 2 個月期間道路中斷並停電，無法觀測。所以 2009 年之八、九月觀測時數很少，甚至為 0。

**Average 值為扣除最高及最低值後取平均。

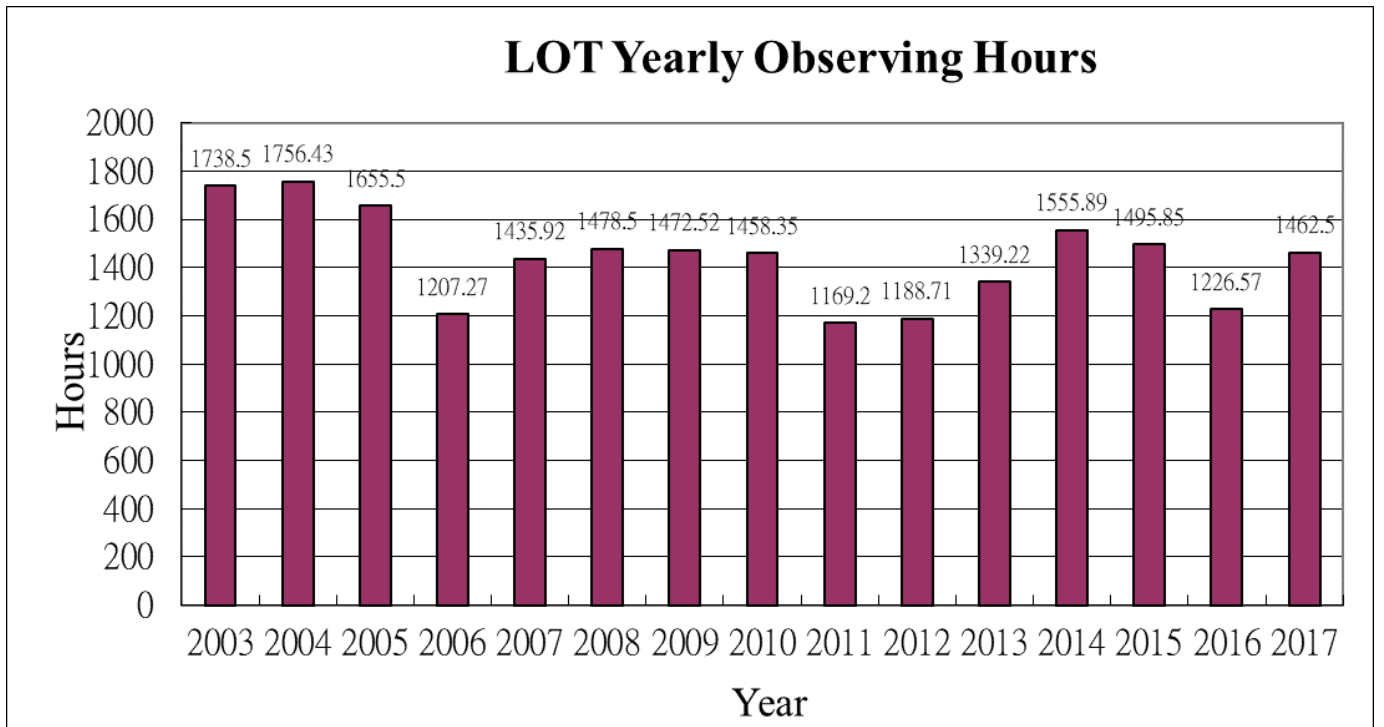


圖 1 鹿林天文台年平均觀測時數統計圖(2003-2017)

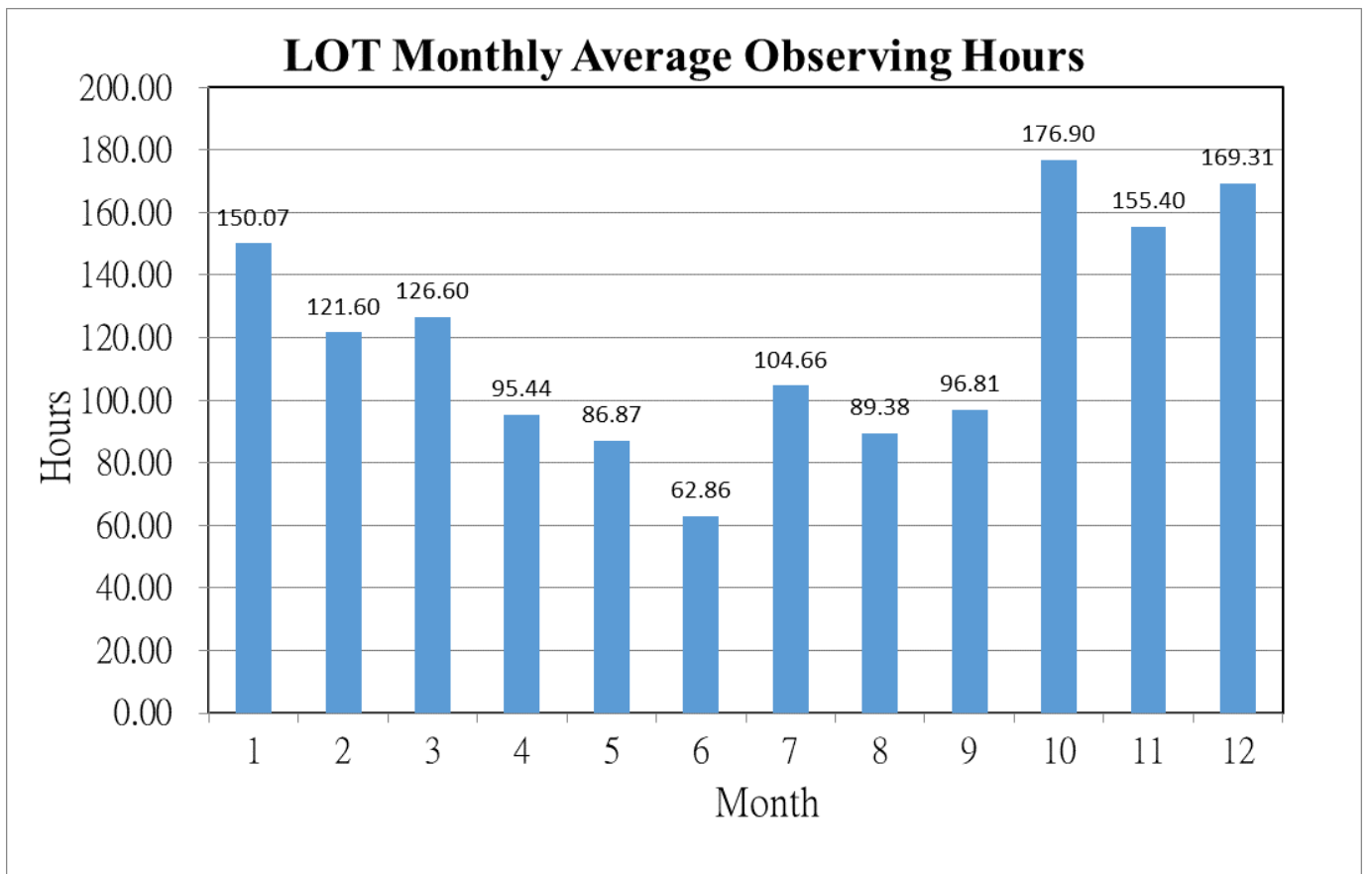
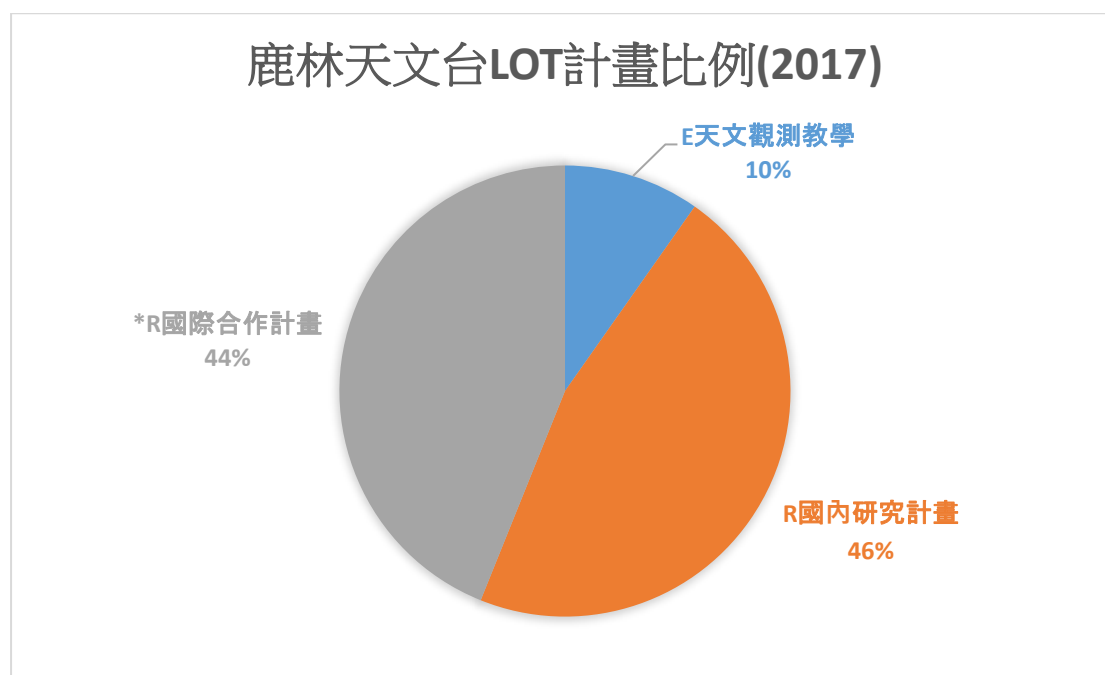


圖 2 鹿林天文台月平均觀測時數統計圖 (2003-2017)

鹿林天文台 LOT 觀測研究計畫統計 (2017)

鹿林天文台一米望遠鏡(LOT)觀測研究計畫時間安排以 4 個月為一個觀測期，一年分為三期 (A = 1-4 月、B = 5-8 月、C = 9-12 月)，其中 E=天文觀測教學、R=國內研究計畫、*R 為國際合作計畫。

2017 年的觀測計畫如下，統計結果：E 天文觀測教學有 4 個，佔 10%。R 國內研究計畫有 19 個，佔 46%。*R 國際合作計畫有 18 個，佔 44%。



LOT 2017A (01 Jan – 30 Apr, 2017)

Education Program:

E01 – Educational Observation for “Advanced Observational Astronomy” Class

PI: Chow-Choong Ngeow (cngew@astro.ncu.edu.tw)

E02 – Student Training for NTHUs Fundamentals of Observational Astronomy Course

PI: Shih-Ping Lai (slai@phys.nthu.edu.tw)

Research Program:

R02 – The rotation period confrmations for large super-fast rotating asteroids

PI: Chan-Kao Chang (rex@astro.ncu.edu.tw)

*R04 – Monitoring the activity of comets 2P, 41P, 45P, C/2015 V2, and C/2015 ER61

PI: Zhong-Yi Lin (zylin@astro.ncu.edu.tw)

*R05 – Multicolor observations of Near-Earth Asteroids

PI: Zhong-Yi Lin (zylin@astro.ncu.edu.tw)

*R06 – Narrow-band Imaging of New Planetary Nebula Selected from LAMOST Database

PI: Chih-Hao Hsia (chhsia@must.edu.mo)

*R08 – The Nature of Unidentified Fermi Objects

PI: Albert Kong (akong@phys.nthu.edu.tw)

R09 – Polarization Follow-up observations for GM Cep and other UX Ori type stars

PI: Po-Chieh Huang (pochiehuang1@gmail.com)

*R10 – Eclipsing binaries in star clusters

PI: Shengbang Qian(qsb@ynao.ac.cn)

R11 – Follow-up Observations of Gravitational Waves Using LOT: I. Reference Images

PI: Po-Chieh Yu (pcyu@astro.ncu.edu.tw)

*R12 – Polarimetric observations of T-Tauri stars

PI: Poshih Chiang (pschiang@gmail.com)

*R13 – Rotationally Resolved Polarization Observations of Main Belt Asteroids

PI: Kang-Shian Pan (m989005@astro.ncu.edu.tw)

R14 – Spetroscopic Observation of Recent Bright Comets

PI: Yu-Chi Cheng (m969005@astro.ncu.edu.tw)

*R15 – Conrming the Be stars in open clusters

PI: Chang-Hsien Yu (m1049002@gm.astro.ncu.edu.tw)

LOT2017B (08 May – 31 Aug, 2017)

Research Program:

R01 – BVRI monitoring of classical Cepheids in M31 for distance scale applications
PI: Chow-Choong Ngeow (cngeow@astro.ncu.edu.tw)

R02 – The rotation period confirmations for large super-fast rotating asteroids
PI: Chan-Kao Chang (rex@astro.ncu.edu.tw)

R05 – Polarization follow-up observations for GM Cep and other UX Ori type stars
PI: Po-Chieh Huang (pochiehuang1@gmail.com)

R06 – The long period variable star and recurrent nova search in M33
PI: Jia-Yu Ou (m1039004@gm.astro.ncu.edu.tw)

*R07 – Multicolor observations and low resolution spectra of near-Earth asteroids
PI: Zhong-Yi Lin (zylin@astro.ncu.edu.tw)

*R08 – Comet observing campaign of comets 41P, C/2015 V2, and C/2015 ER61
PI: Zhong-Yi Lin (zylin@astro.ncu.edu.tw)

*R10 – The nature of unidentified Fermi objects
PI: Albert Kong (akong@phys.nthu.edu.tw)

*R11 – Observations of solar analogue stars for the preparation of asteroid spectroscopy
PI: Daisuke Kinoshita (kinoshita@astro.ncu.edu.tw)

R12 – Follow-up observations of gravitational waves using LOT: I. reference images
PI: Po-Chieh Yu (pcyu@astro.ncu.edu.tw)

*R14 – Rotationally resolved polarimetric observations of 596 Sheila and other main belt asteroids
PI: Kang-Shian Pan (m989005@astro.ncu.edu.tw)

R15 – Spectroscopic observation of recent bright comets

PI: Yu-Chi Cheng (m969005@astro.ncu.edu.tw)

R16 – Rotationally resolved spectra on large asteroids with $D > 200$ km

PI: Yu-Chi Cheng (m969005@astro.ncu.edu.tw)

LOT2017C (01 September – 31 December, 2017)

Education Program:

E01 – Student Training for NTHUs Fundamentals of Observational Astronomy Course

PI: Shih-Ping Lai (slai@phys.nthu.edu.tw)

E02 – Training observation for “Learning Japanese using Popular Science Magazine”

PI: Daisuke Kinoshita (kinoshita@astro.ncu.edu.tw)

Allocated ToO Time: R02 → 1 night, total 8 hours

Research Program:

*R01 – Multicolor observations of Near-Earth Asteroids

PI: Lin Zhong-Yi (zylin@astro.ncu.edu.tw) [Col: YNAO]

R03 – BV RI Monitoring of Classical Cepheids in M31 For Distance Scale Applications

PI: Ngeow Chow-Choong (cngchow@astro.ncu.edu.tw)

R04 – The rotation period confirmations for large super-fast rotating asteroids

PI: Chang Chan-Kao (rex@astro.ncu.edu.tw)

*R05 – The Nature of Unidentified Fermi Objects

PI: Albert Kong (akong@phys.nthu.edu.tw) [Col: MSU, USA and YNAO]

R06 – Polarization Follow-up observations for GM Cep and other UX Ori type stars

PI: Huang Po-Chieh (pochiehhuang1@gmail.com)

R08 – Follow-up Observations of Gravitational Waves Using LOT: I. Reference Images

PI: Yu Po-Chieh (pcyu@astro.ncu.edu.tw)

*R09 – A multi-instrument campaign of (3200) Phaethon

PI: Lin Zhong-Yi (zylin@astro.ncu.edu.tw) [Col: NAOJ and NIHON-U, Japan]

R10 – The long period variable stars in Kepler field distinguish with spectra

PI: Ou Jia-Yu (m1039004@gm.astro.ncu.edu.tw)

R11 – The Long period variable star and recurrent nova search in M33

PI: Ou Jia-Yu (m1039004@gm.astro.ncu.edu.tw)

*R12 – Time-resolved Spectroscopy of Active Near-Earth Asteroid (3200) Phaethon

PI: Daisuke Kinoshita (kinoshita@astro.ncu.edu.tw) [Col: NAOJ]

*R13 – Muti-phase angle polarimetric observations of M-, B- and C-type main belt asteroids

PI: Pan, Kang-Shian (m989005@astro.ncu.edu.tw) [Col: NAOJ]

*R14 – A multi-instrument campaign of (3200) Phaethon

PI: Cheng Yu-Chi (m969005@astro.ncu.edu.tw) [Col: YNAO, NAOJ and NIHON-U, Japan]

R15 – Rotationally Resolved Spectra on Large Asteroids with $D > 200$ km

PI: Cheng Yu-Chi (m969005@astro.ncu.edu.tw)

鹿林天文台工作報告 2017

林宏欽、張明新、張永欣、林啟生、蕭翔耀、郭鎮魁

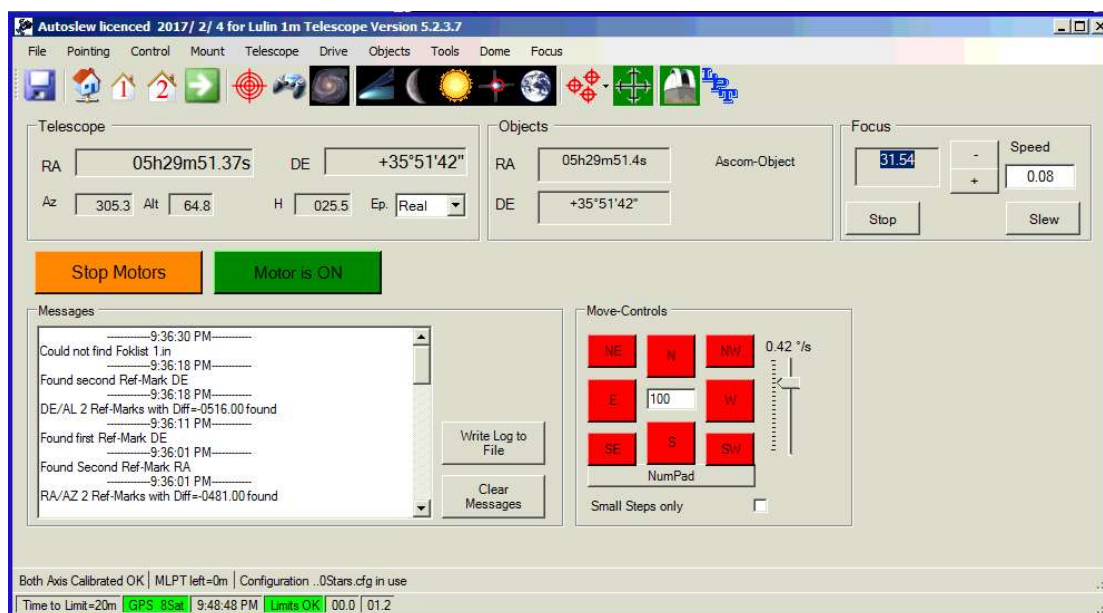
鹿林天文台一米望遠鏡 (LOT) 自 2002 年 9 月開始運作以來已經 15 年，藉著這次鹿林天文台營運之優化計畫將 LOT 望遠鏡軟硬體系統升級，一併將次鏡重鍍、CCD 相機更新，可望大幅提升觀測效率及科學產出。

1 LOT 望遠鏡系統優化及更新升級

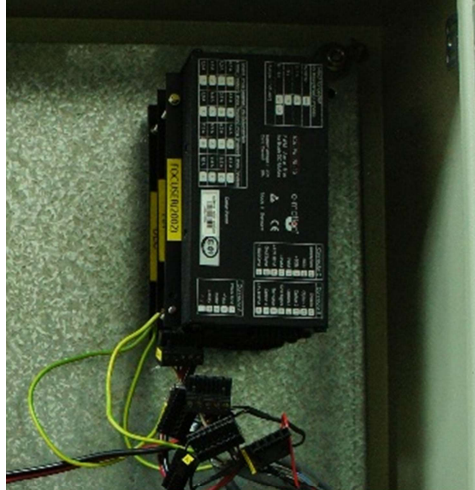
2017 年 2 月 3 日至 2 月 10 日德國技師 Philipp Keller 來台進行一米望遠鏡(LOT)系統優化及更新升級作業，完成主要工作如下，

1.1 LOT 望遠鏡控制系統軟硬體更新及升級

- 安裝 LOT 望遠鏡新控制 PC，新望遠鏡控制軟體 AUTOSLEW V5.2.3



- 安裝新馬達控制器：3 個 Accelnet Controllers (型號：ADP-090-36-S for RA/DEC, 型號：ACJ-055-09-S for FOCUS) 及 KLLUCBC Kvaser Leaf Light USB Can Bus converter

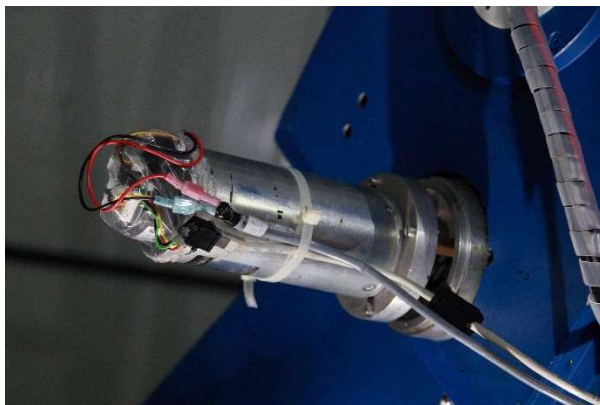


舊馬達控制器 (ISA 介面)



新馬達控制器 (USB 介面)

- 修改舊 RA motor/encoder 線路及接頭，連接新控制器
- 舊 FOCUS motor 加上 Line driver IC AM26LS31，修改線路及接頭，連接新控制器
- 安裝新 DEC motor/encoder，做線路及接頭，連接新控制器



舊馬達及舊編碼器



新馬達及新編碼器

- 望遠鏡主鏡蓋安裝電控馬達
- 安裝電控中央 baffle 蓋
- 安裝鏡蓋控制器(Relaisbox for Controlling the Telescope covers)及相關線路
- AUTOSLEW 軟體測試控制鏡蓋開啟/關閉



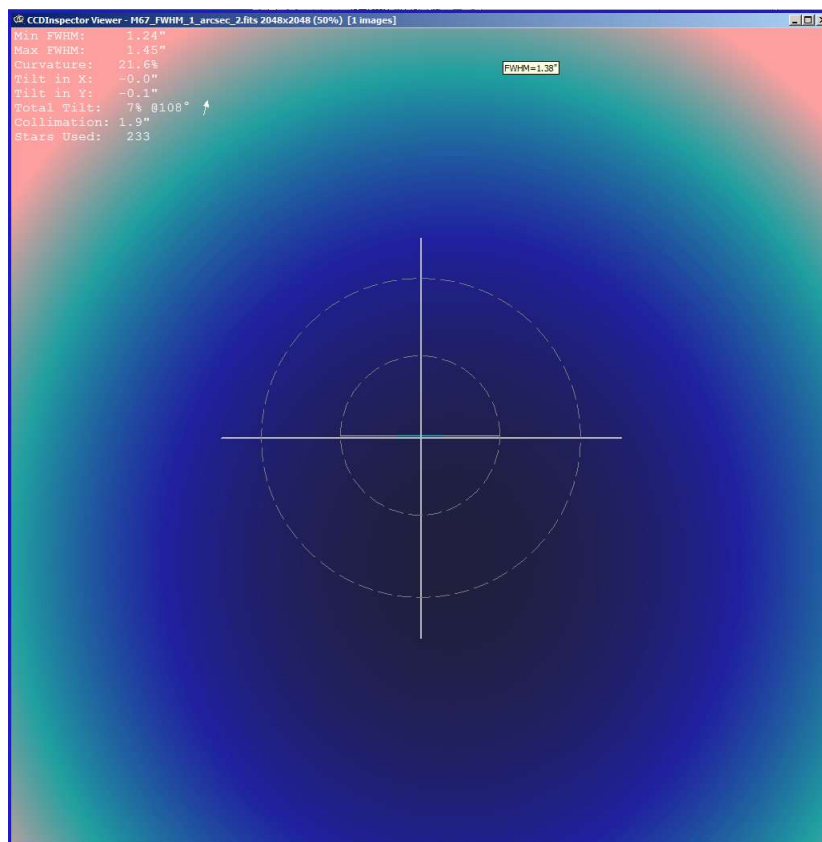
鏡蓋關閉



鏡蓋開啟

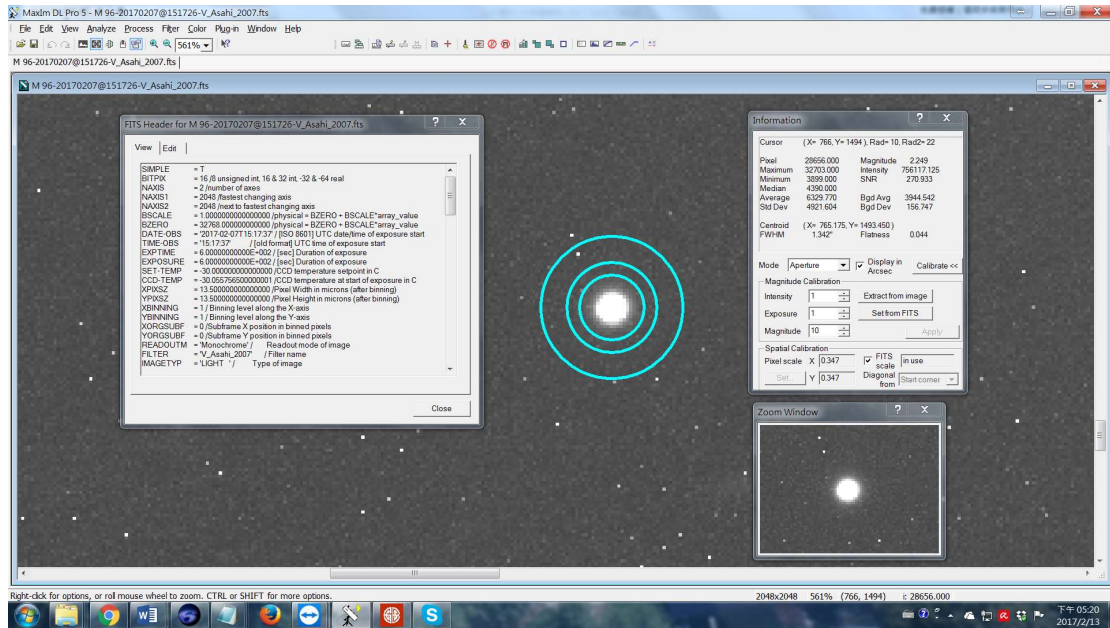
1.2 光軸調整、成像品質優化

- 主鏡側支撐調整
- 主鏡光軸調整
- 星點實測結果如下：最小星點 FWHM=1.24" ，最大星點 FWHM=1.45" ，光軸準直度 (Collimation)=1.9"

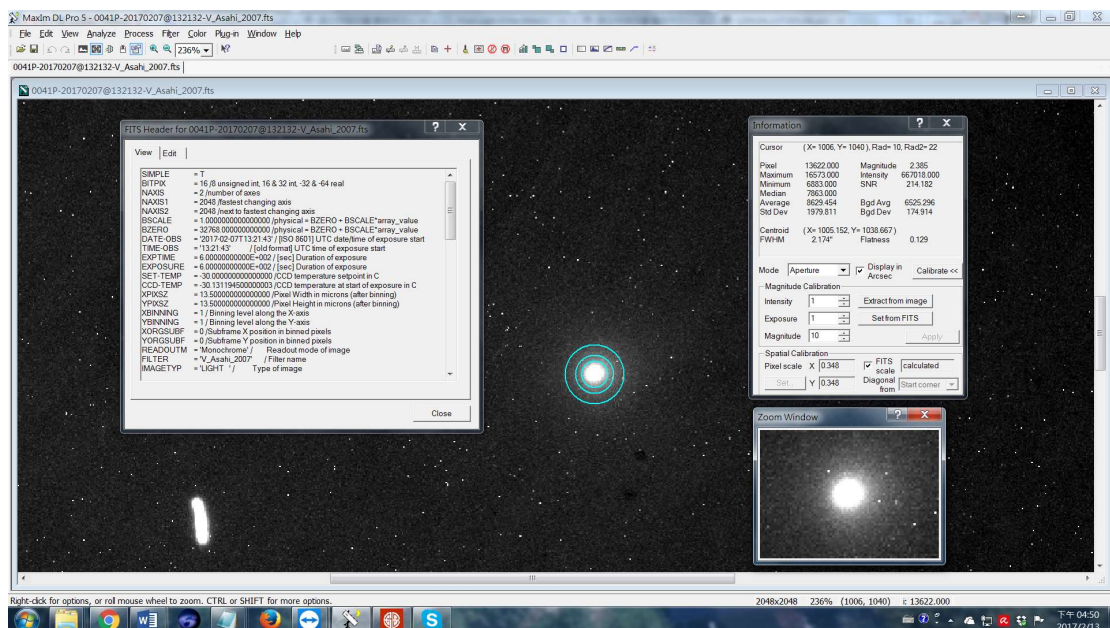


1.3 望遠鏡指向及追蹤精度優化

- 做新的望遠鏡指向修正模型（約 100 點），實測 10 個天區結果：RMS pointing error = 0.376 arcmin.
- 檢查 RA 齒輪齒隙約 40-50"，調整後減小至 10"
- 恆星時自由追蹤 10 分鐘結果：FWHM~1.34"，星點橢度(Flatness)<0.1。

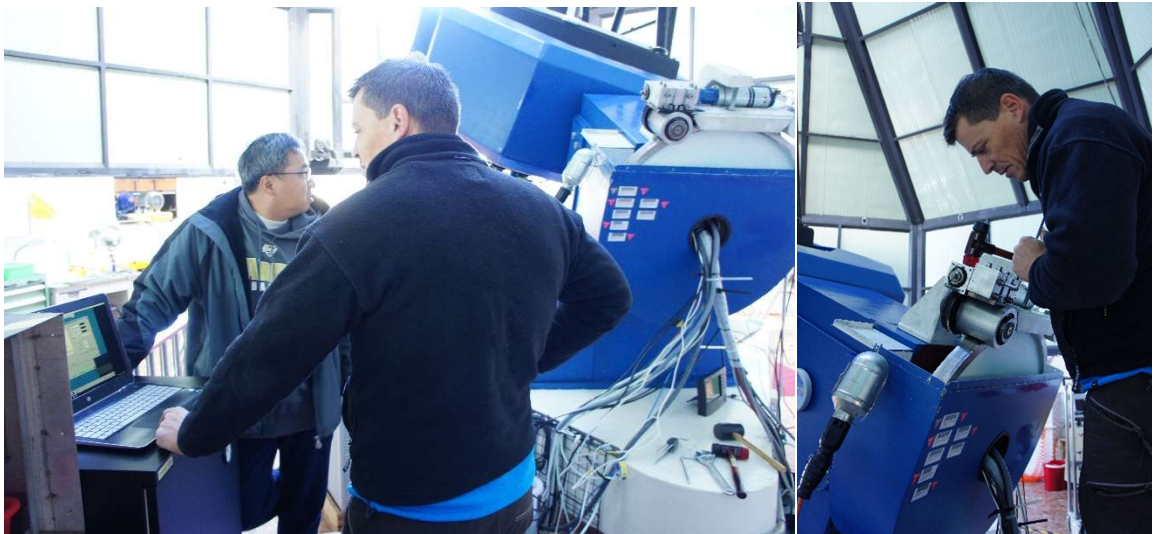


- 追蹤彗星 10 分鐘結果：FWHM~2.2"，星點橢度(Flatness)~0.13。



1.4 其他

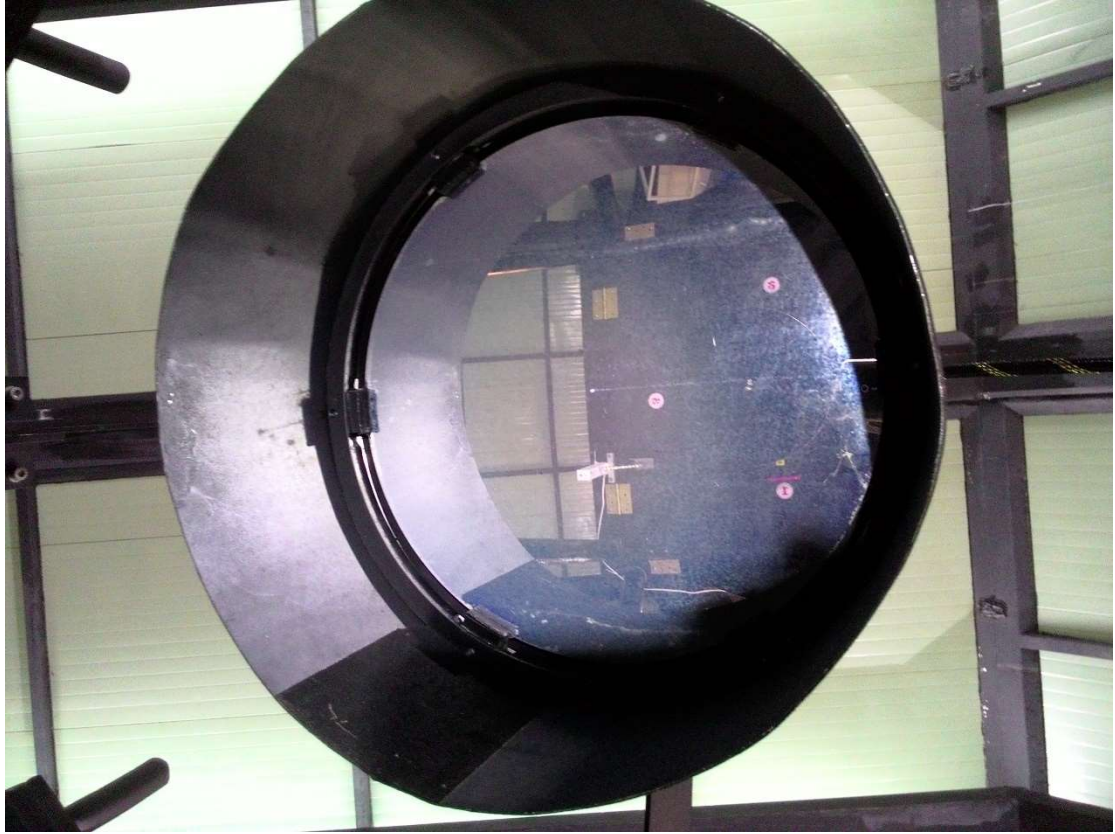
1. 備用 FOCUS motor 加上 Line driver 線路及做接頭
2. 備用 2 個 RA encoder 做接頭
3. 整理舊的 DEC motor/encoder (舊 encoder 有 Line driver) 當備品
4. 檢查 Heidenhain Encoder: RA 正常, DEC 較差, 對 DEC 做了調整
5. 檢查 RA 摩擦輪: 正常
6. 用 CME2 軟體檢查並調整 RA/DEC 兩軸配重平衡
7. 主次鏡鍍膜檢查 OK, 次鏡建議重鍍
8. 檢查圓頂隨動問題, 調整 SmartDome encoder 參數
9. 檢查 ACP plan 執行時 ACE dome slave 未同步就開拍的問題: 改由 AUTOSLEW 統一控制望遠鏡和 DOME 來解決
10. AUTOSLEW PC 做系統完整備份
11. 安裝 Gamepad 無線搖桿作為輔助控制器
12. 各部機件檢查、清掃、調整、測試
13. 解決軟體整合之間的 BUG



Philipp 於鹿林天文台工作情形

2 LOT 次鏡重鍍

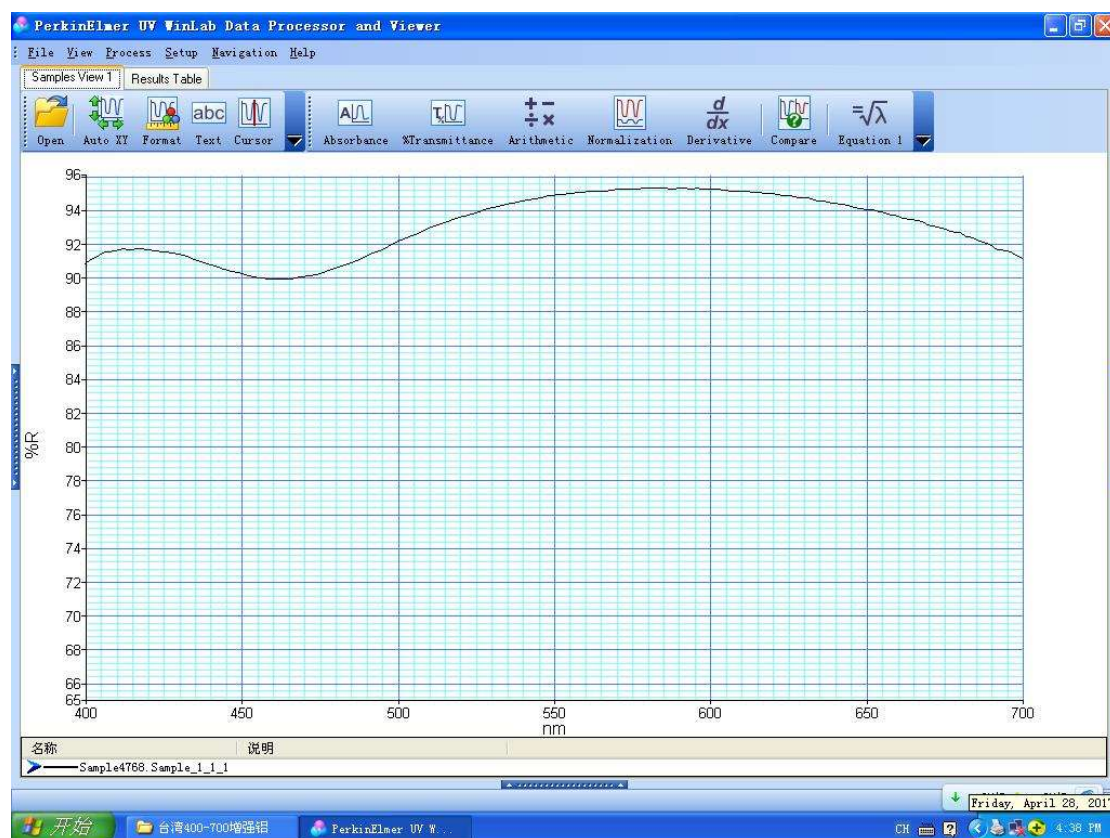
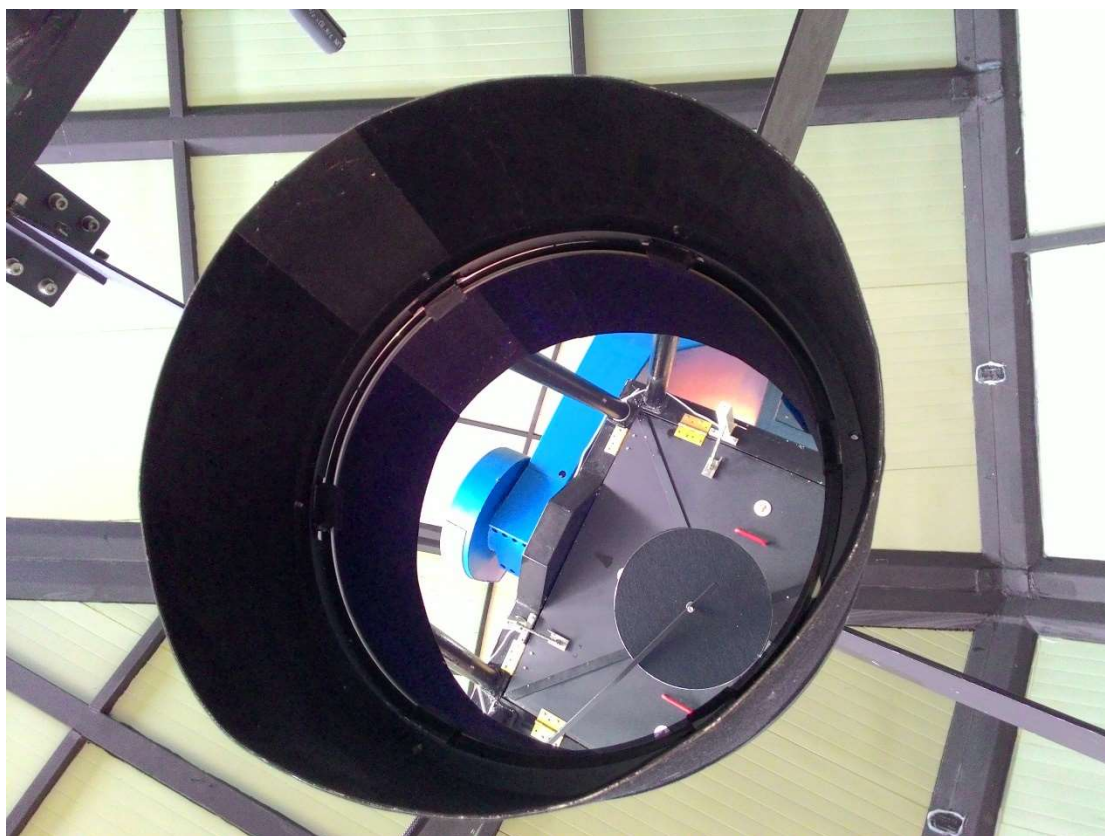
LOT 主次鏡上次重鍍是 2006 年, 迄今使用已逾 10 年。沒有觀測時主鏡有鏡蓋保護, 狀況較好; 次鏡面位置雖然朝下, 但長期暴露在空氣中, 周遭環境較為潮濕, 狀況較差, 即使經過清洗表面還是呈現明顯霧化斑駁現象。



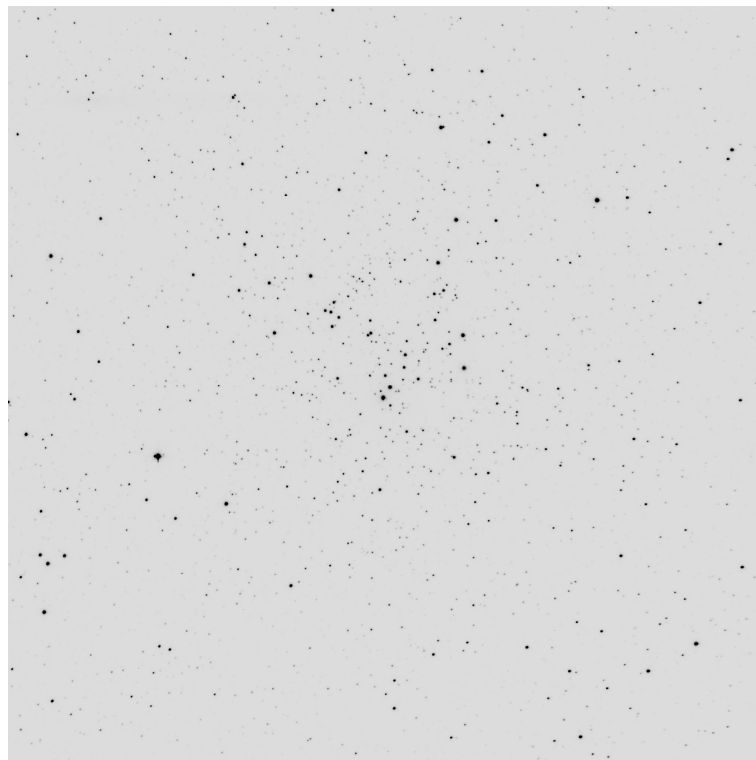
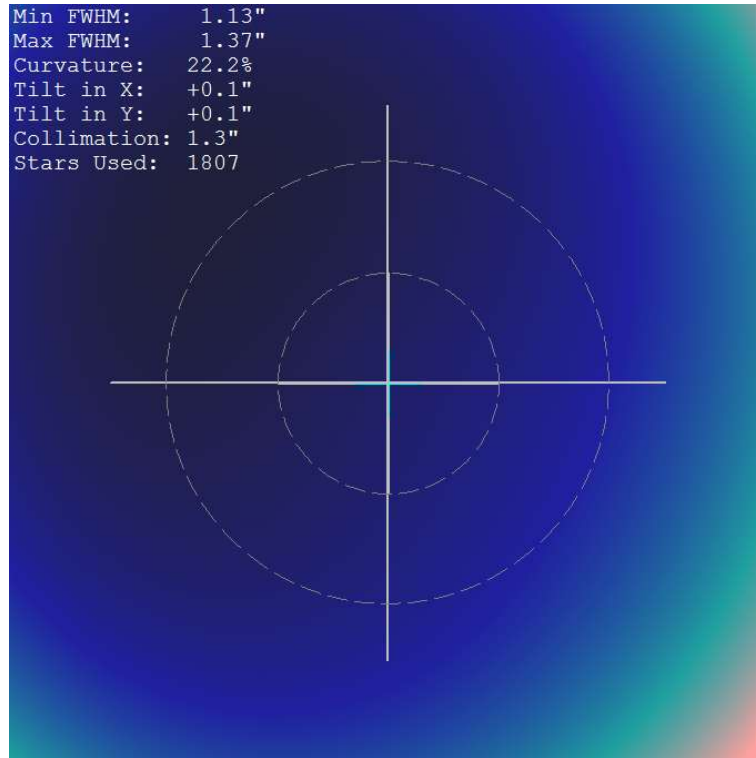
經過評估，2017 年 4 月 26 日送南京天文光學技術研究所重鍍，鍍膜採增強膜，增強鋁的保護層一共 3 層：SiO₂、TiO₂、SiO₂。品質、技術要求如下：

1. 工作波段 400-750nm，最低反射率大於 90%，平均反射率大於 94%。
2. 經高溫膠帶粘附撕扯 20 次，膜層不脫落。
3. 次鏡中心標記直徑 5mm 的中心圓用於裝調。
4. 驗收方法：測試陪鍍片光譜曲線及牢固度。

重鍍完成之次鏡面及（陪鍍片）光譜曲線如下，



5月1日將 LOT 次鏡帶上山安裝，調整光軸，對 NGC6779 以 V 濾鏡曝光 60 秒，1807 顆星的測量結果：FWHM 介於 1.13" ~ 1.37" 之間，有約 1.3" 的 Collimation 誤差，與重鍍之前 Collimation 誤差(1.9") 相近。

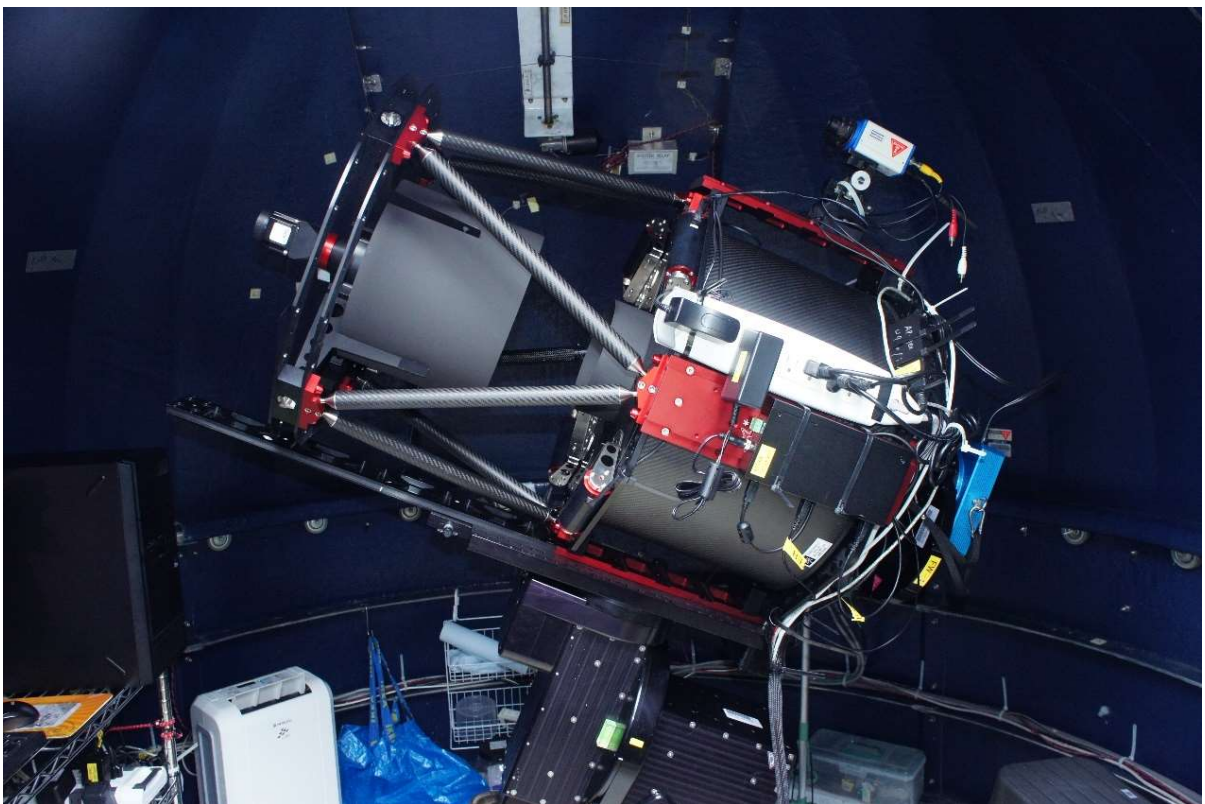


3 其他重要工作

1. LOT CCD 相機更新：已於 2017/5 到貨，驗收測試中
2. LOT 濾鏡更新：已於 2017/5 到貨，準備更新
3. TAOS 中美掩星計畫四台 50cm 望遠鏡吊運下山，準備 2 台送到新疆及 2 台送到墨西哥進行其他合作計畫
4. NCUIRCAM 近紅外相機：完成濾鏡背景漏光改善、與夏威夷 UH88 望遠鏡整合控制軟體及現地試驗觀測

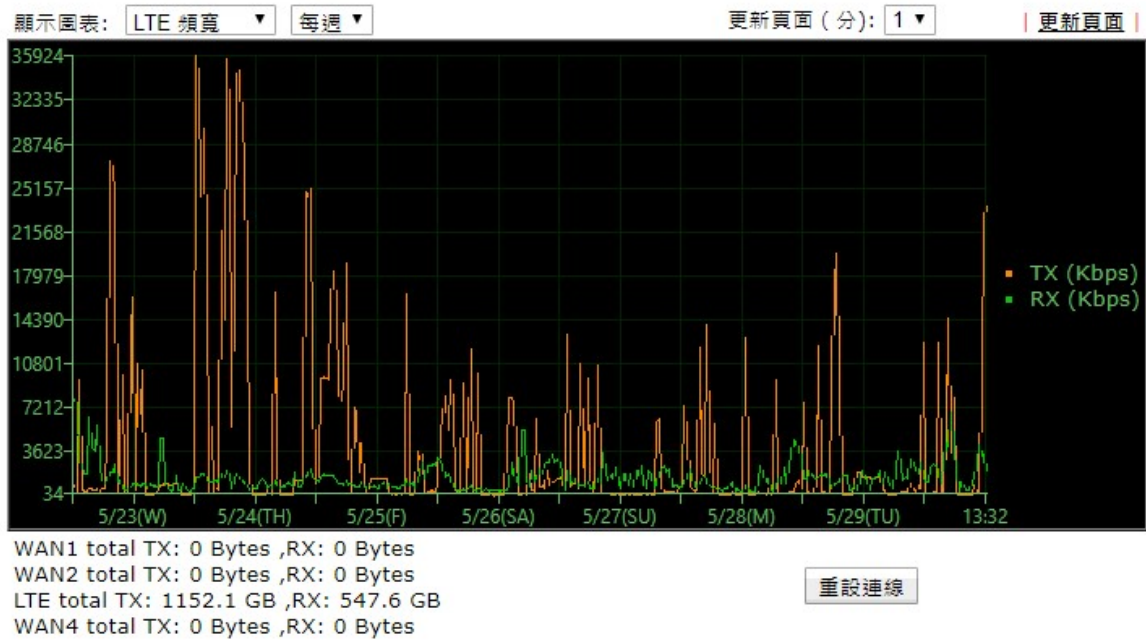
4 LWT 望遠鏡升級

1. RiFAST400 (D=40cm, F3.8)廣視場望遠鏡於 2017/5 到貨，於 2017/10 安裝測試，目前已投入近地小行星及變星之監測工作。
2. LWT 相關的望遠鏡控制 PC、資料分析工作站及資料存儲 NAS 等已設置完成。



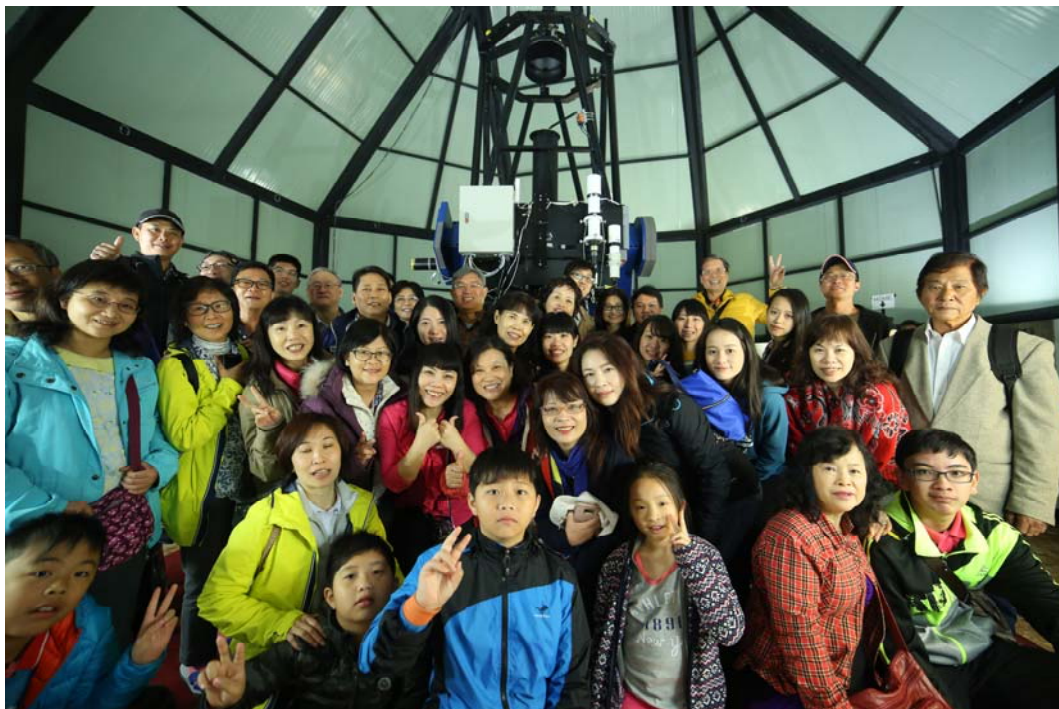
5 鹿林 4G 上網

鹿林天文台原有 E1 網路專線速度只有 2Mbps，既慢又昂貴，2017/5 更換為 4G 上網後，速度提升 10 倍，費用卻只要 E1 的 1/10。歷經一年來測試，鹿林 4G 網路相當穩定，解決了長期以來鹿林大量觀測資料傳輸之網路壅塞問題！



鹿林天文台團體參觀及觀測教學 2017

20170120	清大天文社	20
20170122-24	成功中學教學觀測	21
20170123	北一女+萬芳地科社	25
20170123	台南一中天文社	88
20170124	逢甲大學	25
20170204	麗山高中星宇天文社	41
20170226-27	中原大學教學觀測	31
20170303-04	中央天文所教學觀測	7
20170318	清大教學觀測	15
20170319	清大教學觀測	20
20170325	台北教育大學自然科學系	25
20170325	嘉義大學天文社	20
20170423	李光華副校長中大教授團	40
20170429	中大職工會	40
20170508	玉管處	35
20170623	玉山警察小隊	20
20170703	枋寮高中	34
20170717	林口高中	21
20170722	台北市天文協會	25
20170725	台大天文社	36
20180812	苗栗社大	40
20170812	高雄女中	17
20170819	台灣親子觀星會	17
20171101	溪南國小	44
20171102	一傳十公司	3
20171102	福龜國小	39
20171107	中大第一屆校友	20
20171118	台南社大	45
20171118	竹中天文社	34
20171204	板橋國中	32
20171216	輔大天文社	25
20171217	高師大天文社	25
20171223	興大附中	36



李光華副校長率中大教授參訪



清華大學賴詩萍教授天文觀測教學

SSP-4 近紅外光度計(NIR-photometer)於鹿林一米望遠鏡(LOT)上測試與觀測工作簡報

羅烜玟，國立中央大學天文研究所，2017/03/24

一、簡介

SSP-4 (Single-channel Stellar Photometer generation 4)由 Optec 光學公司所製造，此為該公司唯一配有近紅外線波段的光度計。使用 SSP-4 儀器前，歷經約半年左右(2014/12-2015/6)修復並改裝後，SSP-4 以全新面貌來觀測。這次改裝的部分有：

- (1) 機板升級到 SSP-4A Gen2 version，原手動濾鏡改可用電腦控制自動更換 (Automated Filter Slider w/ 6-position filter slider)。
- (2) 將原本翻轉鏡(Flip-mirror)光路改為冷光鏡(cold-mirror)，此鏡能反射可見光，只讓紅外線頻寬通過，可同時監視目標（可見光）及取得資料（紅外線）。
- (3) 可見光之光路上加裝一台電子 CMOS 相機(2015/09/17 加裝 MINTRON)作為目標監視及確認(2015/10/01 改換 ZWO ASI130MM Monochrome 1.3MP astronomy camera)。
- (4) 控制軟體升級 (Upgrade of SSP4Dataq software to SSP4Dataq2 software)。



(a)

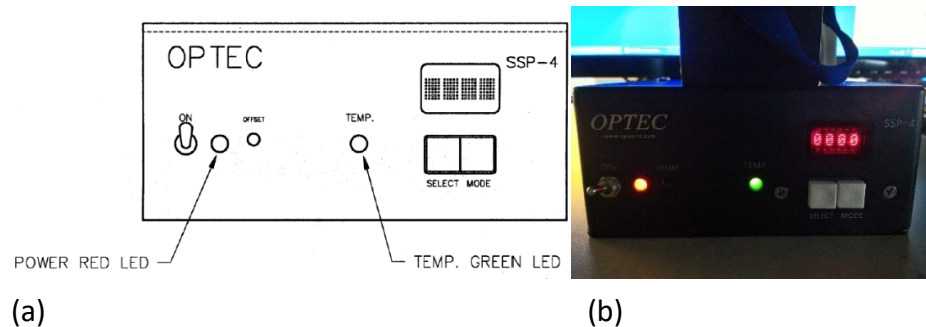
(b)

圖 1. SSP-4 改機前(a)與改機後(b)照片

(圖(a)取自 Optec 官網 <http://www.optecinc.com/astronomy/catalog/ssp/ssp4.htm>)

SSP-4 光度計採用半導體材料砷化鎵銻(InGaAs)為探測元件(Detector)，InGaAs 對長波長光線($0.5 \mu\text{m} \sim 2.6 \mu\text{m}$)具有更高的偵測能力之外，還具有以下優點：探測速度快(high speed)、極靈敏性(high sensitivity)、低噪訊(low noise)等特性。儀器的控制面板只有左側電源鍵和右側分別為 select 和 mode 的兩個按

鈕。在電源鍵在 on 的位置時，電源鍵旁的紅燈會亮起，同時亮起綠燈，顯示儀器溫度正常控制在設定範圍，右側的兩個按鈕可控制上方小型液晶數字面板的切換模式，在未與電腦連線的情況下，才可透過此兩按鈕控制數字面板。



(a) (b)
圖 2. SSP-4 光度計控制板介面示意圖(a)(取自 ssp_4_technical_manual 操作手冊第 8 頁)和實際連線後儀器的狀態照(b)



(a) (b)
圖 3. SSP-4 光度計安裝於 LOT 上(a)遠和(b)近之照片

二、測試與觀測

觀測前約 1 小時就先讓 ssp4 開機，原預設溫度為 -25°C ，廠商建議把 ssp4 儀器溫度降到約 -35°C 或 -40°C ，因讀取數值比較穩定，易合適觀測。若圓頂外天氣(無雨無雲)與濕度(濕度小於 95%)理想，才開圓頂，等待至少 50 分鐘後(操作手冊建議暖機至少 10 分鐘)，再去觀察 ssp4 的 DARK 穩定度。為預防溫度 or 濕度突然陡升 or 驟降，影響 count 數值，在拍 target 前後皆須拍 sky 取平均。在拍攝造父變星的同時，會選取一些不同赤經(R.A.)與赤緯(Dec.)座標位置的標準星，以獲取不同大氣質量(airmass)的數值進行大氣消光的處理，從透過大氣

層所觀測到的儀器星等轉換成視星等。在累積近 20 次視星等數值後，以找出造父變星最合適的光度變化週期。

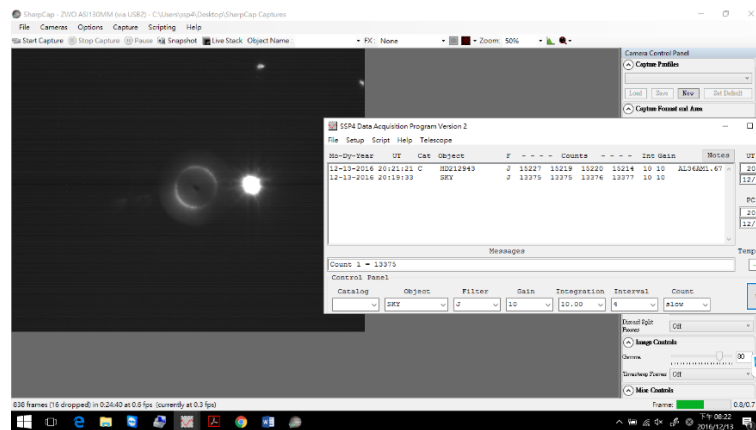
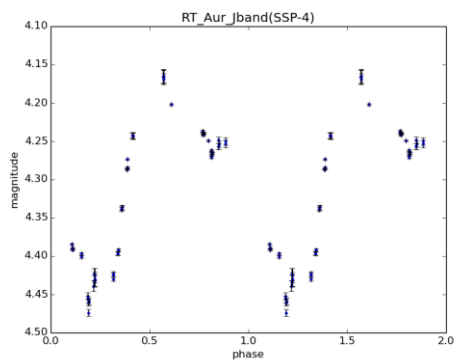
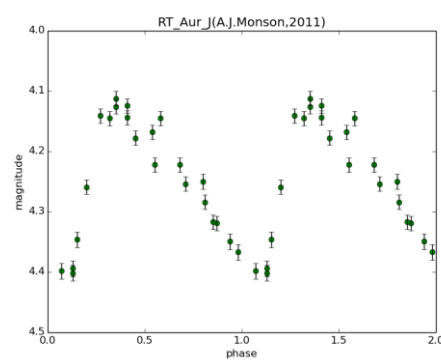


圖 4. 使用 ASI130MMS CMOS 觀看目標位置和 SSP4Dataq2 軟體讀取觀測目標背景數值。



(a) SSP-4 觀測變星 RT Aur 的資料點



(b) CCD 觀測變星 RT Aur 觀測資料點(A.J. Monson, 2011)

圖 5. 造父變星 RT Aur 於 J 波段之觀測資料點 SSP-4(a)與 CCD(b)分布。

Rotationally Resolved Polarization Observations of the M-type Asteroid 16 Psyche

Kang-Shian Pan¹, Yu-Chi Cheng¹ and Win-Huen Ip¹

¹Graduate Institute of Astronomy, National Central University, 300 Jhongda Road, Jhongli, Taoyuan, 32001, Taiwan

Abstract

M-type asteroid is one of asteroid taxonomies which represent a metal-rich surface. Asteroid (16) Psyche is the largest M-type asteroid and also the next space mission of the metallic world. A photometric and polarimetric survey program on M-type asteroid has recently been established with Lulin One-meter Telescope making use of the Triple Range Imager and POLarimeter (TRIPOL) instrument. To study the surface heterogeneity, we observed the selected targets simultaneously. We will have a brief report on the phase-angle v.s. polarimetry curve, the rotationally resolved polarimetric measurements, and photo-polarimetric light-curves of (16) Psyche and other M-type objects.

Introduction

Photo-polarimetric measurements are very useful in characterizing the surface properties of asteroids. It is well known that the opposition effect and the negative linear polarization curves as functions of the phase angle are important diagnostic tools for taxonomic classification of different types of asteroids [1]. The multi-filter polarimeter camera (TRIPOL) at the Lulin Observatory of National Central University is well suited for such observations. A survey program of M-type asteroids with the emphasis on rotationally resolved polarization measurements has been initiated. The first results on 16 Psyche are reported here.

Observation — TRIPOL on LOT of Lulin observatory, and L35

The TRIPOL instrument was designed by Nagoya University. It can make simultaneous CCD images in three wavelengths, namely, g' , r' and i' in the SDSS system. The half-wave plate can be rotated to four different positions: 0° , 22.5° , 45° and 67.5° , sequentially. A sketch of the instrument design is shown in Figure 1. Besides the TRIPOL observations, simultaneous photometric measurements in R-band can be carried out at the Celestron C14 telescope of 35-cm aperture, also, at Lulin.

The observation was made on December 13, 2015 when the V- magnitude of 16 Psyche was 9.5 and the phase angle was 2.5 degrees. Psyche's dimension is $240 \times 185 \times 145$ km and its rotation period is 4.196 hours. The interval of data points was 6~7 mins for 10° rotation. Our three-hour observation therefore does not cover one full rotation.

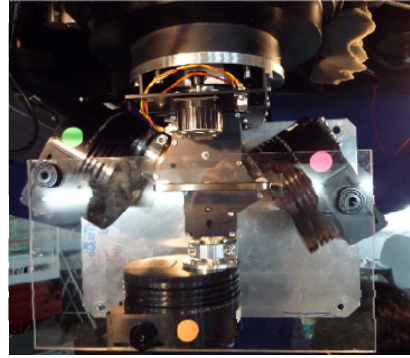
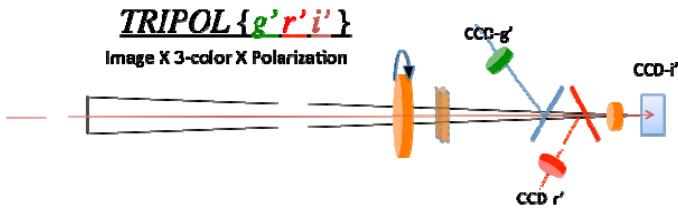


Figure 1.
TRIPOL instrument is composed of three optical CCDs to do simultaneous polarization measurements.

Data Analysis

Both of photo and polarized data was required to process data reduction of the bias, dark and flat to clean the noise from the CCD instruments. Polarimetry measurement is based on the Stokes parameters Q and U. The polarization degree P and position angle θ are expressed via Q and U.

$$P = \sqrt{U^2 + Q^2} \quad \theta = \frac{1}{2} \arctan \frac{U}{Q}$$

$$\sigma_p = \frac{|U \cdot \Delta U + Q \cdot \Delta Q|}{P} \quad \sigma_\theta = \frac{28.65 \cdot \sigma_p}{P}$$

ΔU and ΔQ are errors on the Stokes parameters. The proper coordinate linear polarization degree $P_r(\%)$ and the proper coordinate position angle of polarization θ_r are defined on the scattering plane of the Sun-object-observer. θ_r is derived from $\theta_r = \theta_{\text{obs}} - (\text{PA} \pm 90^\circ)$, where θ_{obs} is measured position angle of polarization, and PA is the position angle of the scattering plane. The polarization quantity P_r has been corrected from $P_r = P_{\text{obs}} \cos(2\theta_r)$, where P_{obs} is measured linear polarization degree. And the final value of $P_r(\%)$ and θ_r are calibrated offset in reference to some unpolarized and polarized standard stars.

Result I — Phase angle and Polarimetry

Table 1.

Asteroid	Date	Phase Angle	Position Angle	Vmag	* $P_r(\%)$ g', r', i'	* $\theta_r(^{\circ})$ g', r', i'	Amplitude of $P_r(\%)$
16 Psyche	2015.11.12	11.7	273.888	9.9	-0.577	90.512	0.563
					-0.504	91.412	0.206
					-0.466	91.512	0.388
16 Psyche	2015.12.13	2.5	41.693	9.5	-0.721	77.237	0.505
					-0.714	76.017	0.322
					-0.797	72.637	0.371
16 Psyche	2017.01.04	16.3	293.008	11.3	-0.475	84.278	0.111**
					-0.435	83.248	0.209**
					-0.284	80.078	0.336**
16 Psyche	2017.03.21	6.3	114.925	10.7	-0.982	85.165	0.423
					-0.807	87.255	0.421
					-0.760	86.365	0.384
216 Kleopatra	2016.06.03	8.4	116.250	12.5	-0.768	89.600	0.547
					-0.389	96.650	0.505
					-0.354	96.700	0.364

* average value ** not completely observed whole rotation

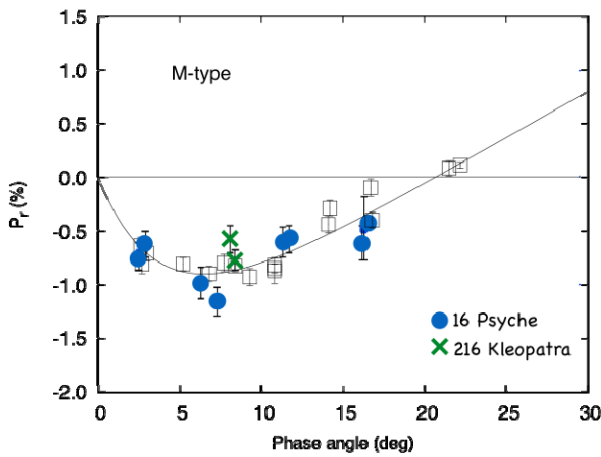


Figure 2.
 Our observation was working on phase angle 2.5-16.3. The blue circle is 16 Psyche and green cross is 216 Kleopatra asteroids. The result is similar with the polarization-phase angle curve of the M-type asteroids.^[2]

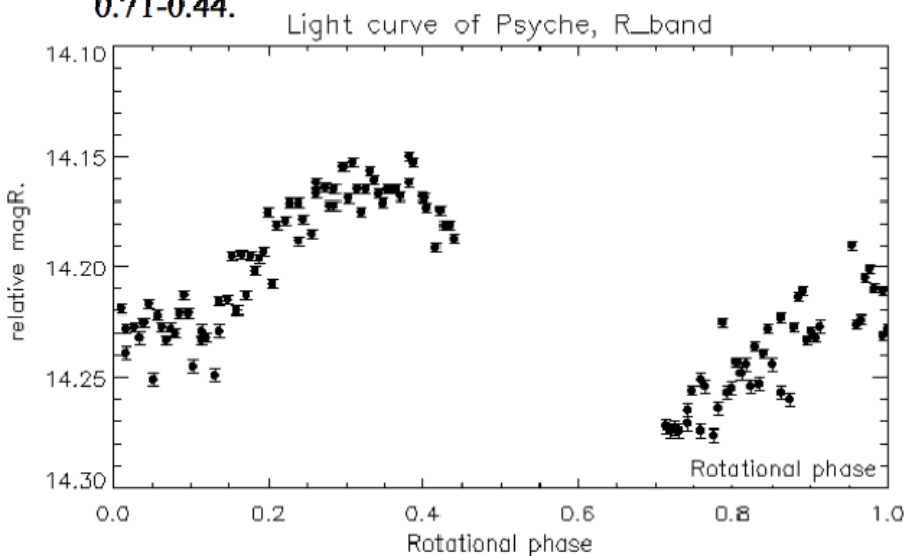
Result II — light curve on photometry and polarimetry

Figure 3. shows the R-band photometric observations with the L35 telescope. The starting point of the rotational phase is set to be zero at HJD time 2445900+6.284 [3]. The rotational phase (ϕ) coverage of the R-band photometry was from 0.71 to 0.44 with a gap between 0.44 and 0.71. The primary peak in the light curve is at $\phi = 0.4$ and a secondary peak at $\phi = 0.95$.

The rotationally resolved $P_r(\%)$ values are shown in Figure 4. Certain variability can be seen (with an amplitude of about 0.51 in g') suggesting the possible existence of surface inhomogeneity either in the form of compositional change or geomorphological difference. The variation in r' and I' are less significant, however. Figure 5 showed the different polarization curves which the surface was observed twice in the night.



Figure 3
R band Light curve of Psyche on 2015.12.13. The rotational period is 4.196hrs. Our data was cover the phase 0.71-0.44.



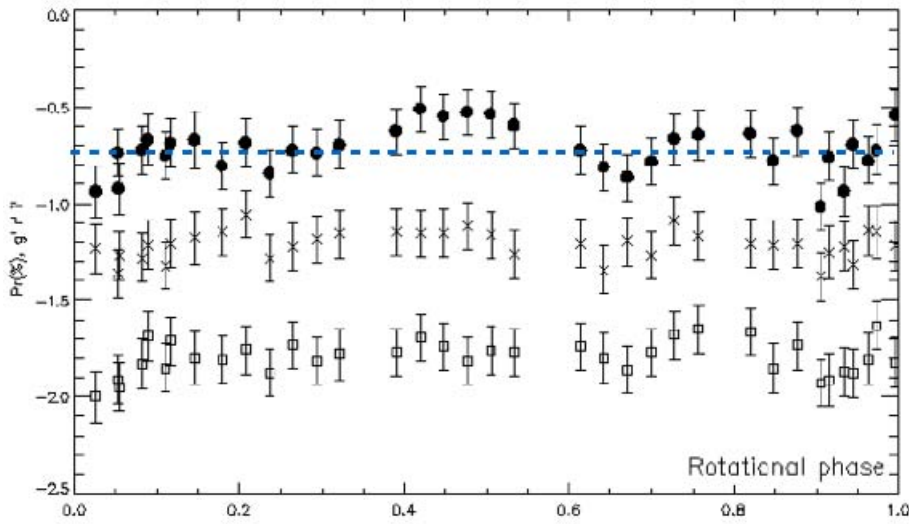


Figure 4
The Pr(%) of g' , $r'-0.5$, $i'-1.0$, in rotational phase variation. We observed 16 Psyche on 2015.12.13. The blue dash line show the average Pr(%) $g' -0.72$.

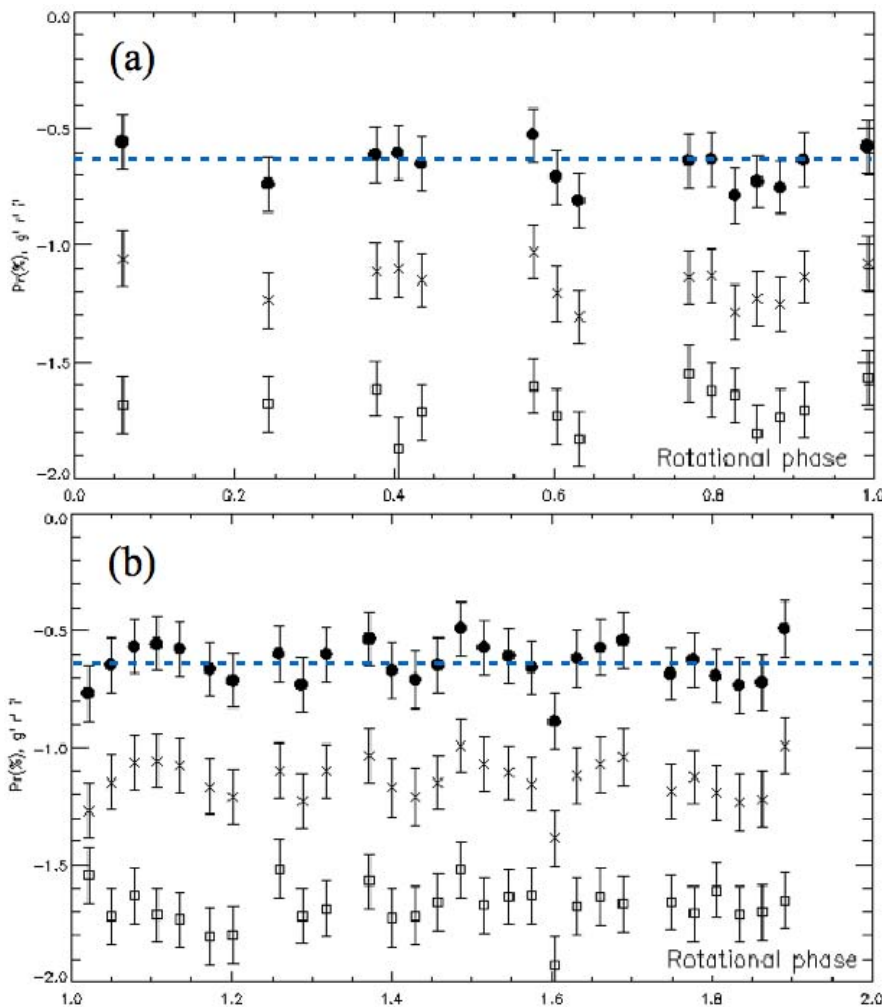


Figure 5 (a, b)

The Pr(%) of g' , $r'-0.5$, $i'-1.0$, in rotational phase variation.

On the next night, 2015.12.14, the Psyche was observed two round of the period. The blue dash line show the average Pr(%) $g' -0.62$. (a) The first rotation (b) the second round.

Synchronous Surveillances of Meteor Events using the Taiwan Meteor Detection System

Bo-Hao Wang¹, Jun-You Liu², Zong-yi Lin³, Jim Lee⁴, Zhong-Yi Lin⁵ and Hsin-Chang Chi⁶

¹*Department of Applied Mathematics, National Dong Hwa University, Hualien, Taiwan 97401*

²*Department of Natural Resources and Environmental Studies, National Dong Hwa University,
Hualien, Taiwan 97401*

³*Department of Physics, National Dong Hwa University, Hualien, Taiwan 97401*

⁴*Taipei Astronomical Museum, Taipei, Taiwan 11160*

⁵*Graduate Institute of Astronomy, National Central University, Taoyuan, Taiwan 32001*

⁶*Department of Physics, National Dong Hwa University, Hualien, Taiwan 97401*

Abstract

Taiwan Meteor Detection System (TMDS) is a developing system under a collaboration among National Dong-Hwa University (NDHU), National Central University (NCU) and Taipei Astronomical Museum (TAM). This system aims at capturing meteor instances in the sky surrounding Taiwan. At present, we have established two sites to perform synchronous observations of meteors in the NE direction: One is located at the Lulin observatory of NCU. The other is at Hutian Elementary school inside Yang Ming Shan National park. To summarize, over the period from Aug. to Oct. in 2016, Lulin stations detected 783 meteor events while Hutian marked 197 events. It is noteworthy that 7 simultaneous events recording a common meteor are justified. We apply the triangulation method to calculate the positions and velocities of simultaneously detected meteors. In consequence, orbits of these meteors are determined using the commercial codes UFO Capture and Orbit. With diffraction gratings implemented, the current TMDS framework is capable of achieving meteor illumination spectra.

Observation Stations

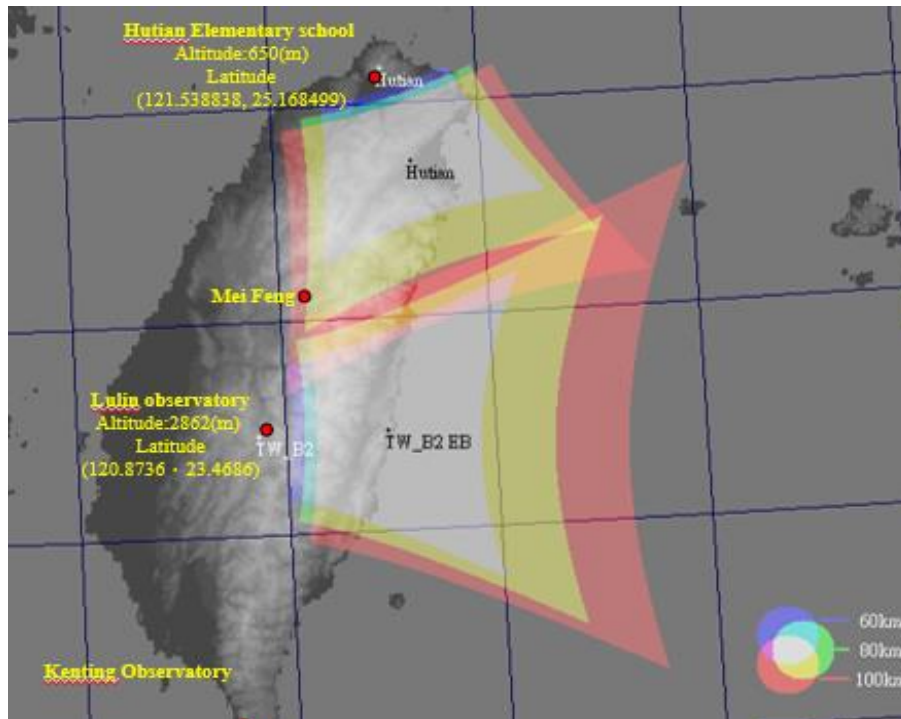
Two Meteor Cameras being operated 200 km apart captured the same meteor.



Hutian elementary school



Lulin observatory



Established :

1. Hutian Elementary School

HUTIAN

Azimuth: 168.89°

Elevation: 42.16°

Fov: 64.3°

2. Lulin observatory

E1A

Azimuth: 91.5865°

Elevation: 51.1938°

Fov: 33.3984°

E1B

Azimuth: 89.4880 °

Elevation: 50.4941°

Fov: 69.4838°

Developing:

1. Keating observatory

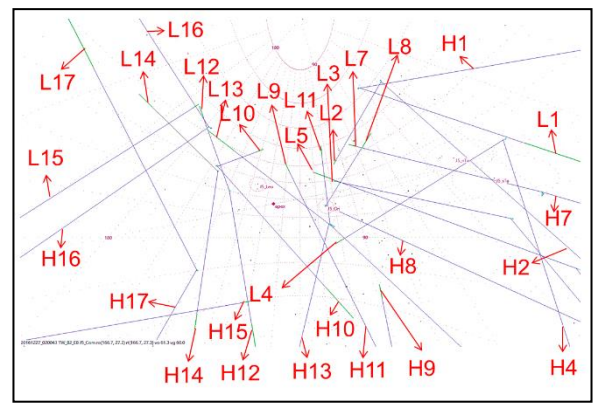
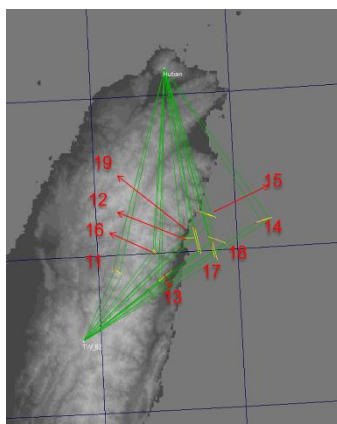
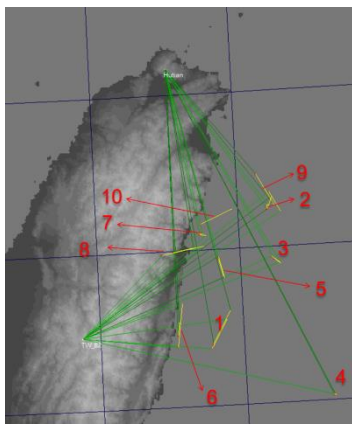
2. Mei Feng Farm

	E1A (Lulin)	E1B (Lulin)	HUTIAN (Hutian)
Camera	Watec 910HX	902H2U	Watec902H2
Len	12mm F1.2CCTV LENS	6mmF0.95	F0.95~F1.2 CCTV
Focus length	FUJINON 2.9-8mm	6 mm	5~12mm
Grating	600 line/mm	Not installed	Not installed
Sensitivity	0.000005 (Lux)	0.0001(Lux)	0.0001(Lux)

Summary and Analyses

1. Meteor Orbit

The triangulation method is applied to calculate the positions and velocities of simultaneously detected meteors. With the position and velocity components of individual meteors obtained, meteor orbits are determined in the solar system.



H=Hutian, L=Lulin

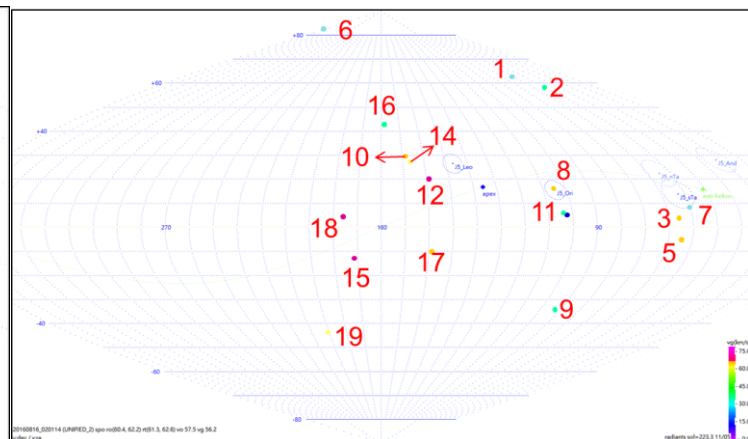
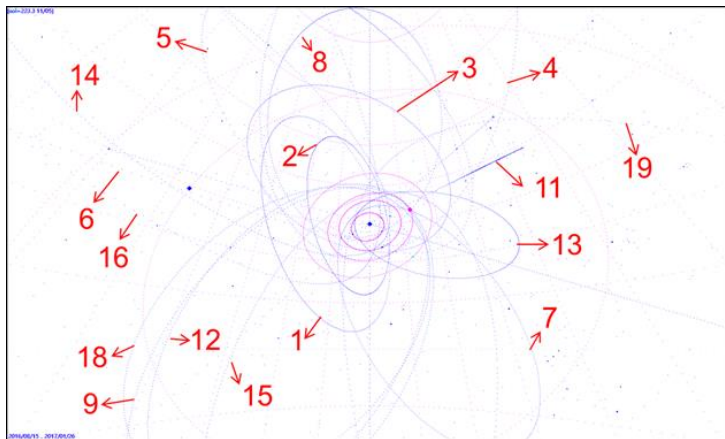
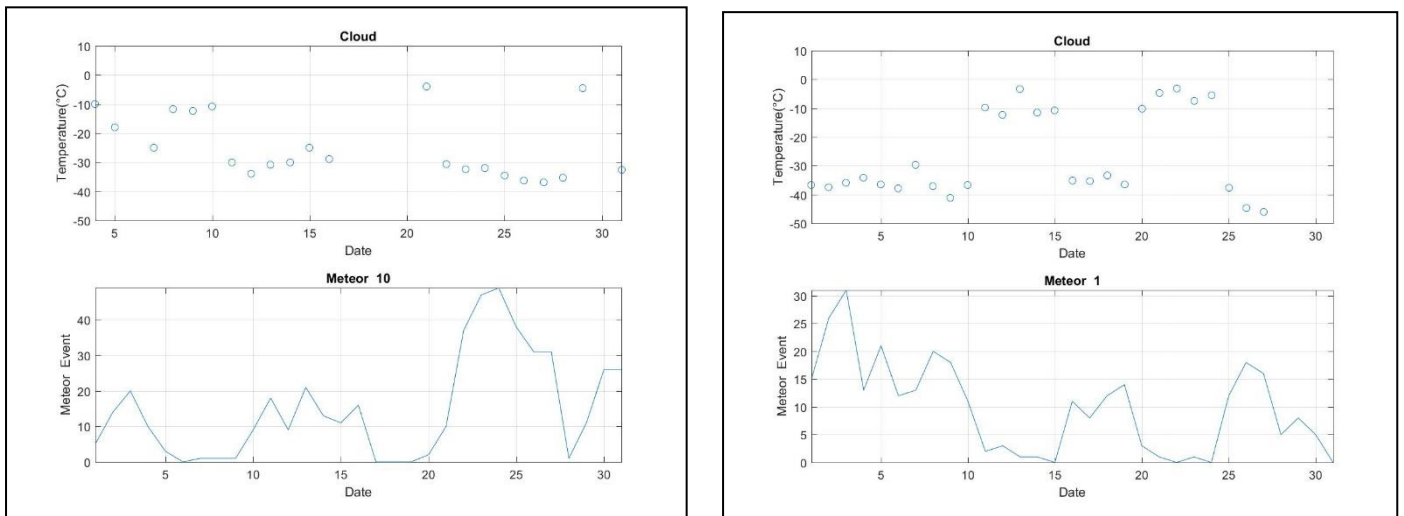


**Table of orbit parameters and geocentric datum of 19
concurrently detected meteors**

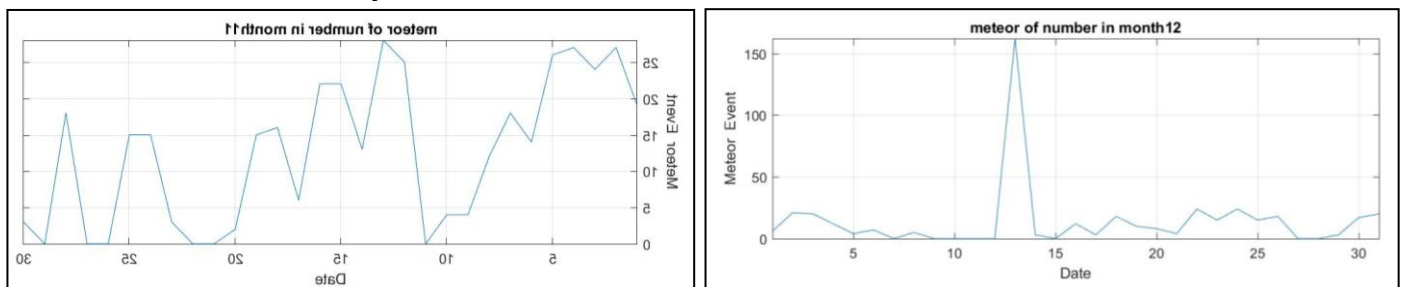
No.	Local time (Date_hms)	Meteor Streams	mag	high of start point (km)	high of end point (km)	duration (sec)	a semi- major axis (au)	q perihelion (au)	e eccentricity	p period (year)	ω argument of perihelion (deg)	Ω longitude of the ascending node (deg)	i inclination (deg)
1	20160816_020114	spo	-2.8	104.8	87.4	0.55	10.1	0.9	0.9	32.2	137.3	143.1	106
2	20160816_035718	J5_Per	-0.8	103.5	91.3	0.28	2.8	0.9	0.7	4.8	146	143.2	111.6
3	20160823_035945	spo	-1	106.1	93.1	0.22	4.8	1	0.8	10.7	22.2	329.9	153.2
4	20160823_043600	spo	-1	108.1	89	0.27	11.5	0.9	0.9	38.8	215.6	149.9	172.2
5	20160823_045811	spo	-4.4	105.8	78.8	0.47	58.3	1	1	446	28.5	329.9	138.2
6	20160922_194446	spo	-0.9	105.6	88.7	0.8	54.7	1	1	405	197.1	179.7	72.2
7	20161104_222435	J5_sTa	0.1	93.7	83.3	0.45	2.8	0.4	0.8	4.8	103.4	42.4	10.2
8	20161104_225421	J5_Ori	-0.4	112.1	101.3	0.48	17.4	0.5	1	72.7	95.6	42.4	164.4
9	20161105_010113	spo	-0.7	101.8	89.8	0.63	6.7	0.9	0.9	17.5	45.3	42.5	70.9
10	20161106_030147	spo	-0.3	110.5	99.5	0.42	---	0.7	1	---	112.2	223.6	135.5
11	20161115_014311	spo	-0.2	103.4	91.6	0.22	---	0.3	1	---	114.5	52.6	130.5
12	20161118_045337	J5_Leo	-0.8	103.3	89	0.22	3.8	0.9	0.8	7.3	152.4	235.7	161.5
13	20161220_022355	J5_Mon	-4	97.1	75.9	0.58	2	0.3	0.8	2.8	115.4	88.1	21.5
14	20161227_020043	J5_Com	-3.5	105.8	88.2	0.35	4.8	0.5	0.9	10.5	272.9	275.2	134.6
15	20170105_013501	spo	1.35	106.1	102.1	0.17	4.4	1	0.8	9.4	354.9	104.3	166.6
16	20170105_060233	spo	-0.8	94	85.7	0.17	6.6	0.6	0.9	16.9	259.1	284.5	96.5
17	20170106_025540	spo	-0.8	107.5	89	0.35	---	0.5	1	---	91.3	105.4	138.9
18	20170110_031233	spo	0.05	113.7	103.4	0.18	3.5	0.9	0.7	6.5	206.9	289.5	161.6
19	20170127_043658	spo	-1	96.8	89.7	0.3	8.2	0.9	0.9	23.4	336.8	126.9	129.5

2. Cloud Sensor Data versus Counted Meteor Events at Lulin Station



The upper panels in the above plots give cloud sensor data monitored at the Lulin observatory with respect to dates. In the lower panels, the corresponding accumulated meteor events are shown. Note that a temperature $< -30^{\circ}\text{C}$ indicates cloudlessness while a temperature $> -10^{\circ}\text{C}$ implies a cloudy climate. Here we use the cloud sensor data at AM 3:00 to represent the weather conditions of each dates. Further scenarios in development with respect to hours are presented in Supplement B.

3. Historical Analysis of Meteor Events

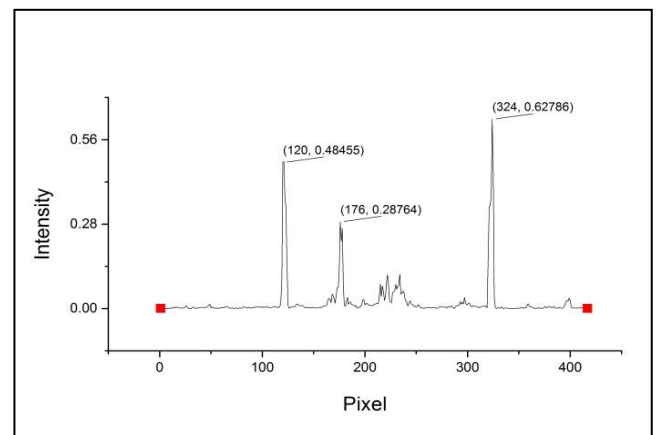


The above figures give the detected meteor events by E1B with respect to dates. The numbers of event detected are directly correlated to important astronomical events such as meteor showers and etc. (Refer to Supplement A for detail information).

4. Detected meteor events from August to December 2016

Month (2016)	Meteor events accumulated (Lulin_E1A/Lulin_E1B/Hutian_HUTIAN)
August	164 / 180 / 104
September	153 / 133 / 16
October	625 / 461 / 33
November	453 / 378 / 47
December	480 / 432 / 86

5. Meteor Spectroscopy at Lulin Station



In the above plots, the left panel presents a detected meteor image showing diffraction pattern by E1A at Lulin station. The occurring is at 00:38:27 on 2016/10/24. As an illustrative example, the right panel gives a raw-data analysis of the diffraction pattern. Spectroscopic identifications of the absolute profiles are under our attempts.

Conclusions

(1) Our observations at the Lulin station show that the time sequence of detected events is strongly interrelated with the cloud sensor data. It is worthwhile to note that further studies of the interrelations may provide approaches to designate desired observation programs for specific purposes.

(2) We have detected 19 simultaneous events recording a common meteor, and the corresponding orbits the meteor is determined. The orbits data may be applied to acquire the activity information of the meteor parent bodies (Near-Earth Asteroids).

(3) It is found that around 2.65% of detected meteor events are concurrently associated with illumination spectra.

(4) We have successfully obtained meteor illumination spectra by using diffraction-grating implementations. We are undertaking attempts to analyze the line profiles of the observed spectra to resolve the compositions of the detected meteors.

Reference

1. Audrey B. & Meenakshi W., 2010, *Nature Geoscience*, 3, 637–641
2. NASA JPL Small Bodies Database Browser (<http://ssd.jpl.nasa.gov/sbdb.cgi#top>)
3. William Stewart *et al*, 2013, “NEMETODE: The Network for Meteor Triangulation and Orbit Determination. System Overview and Initial Results from a UK Video Meteor Network”, *Journal of the IMO*, 41, 84-91
4. Kitchin, C. R. (1995), *Optical Astronomical Spectroscopy*, Series in Astronomy and Astrophysics (Book 3), CRC Press

Acknowledgements

The Ministry of Science and Technology of Taiwan supported this work. The work of Zhong-Yi Lin was supported by Grant No. MOST 105-2112-M-008-002-MY3. The work of Hsin-Chnag Chi was supported under Grant No. MOST 104-2112-M-259-006.

受限於天候，許多重要的天文觀測計畫皆無法在臺灣進行，中美掩星計畫（TAOS）算是其中的異數。1998年提案，2005年於鹿林山正式運作的這個計畫，共建置了四座配備0.5米望遠鏡的全自動觀測系統，總經費卻僅約五十萬美元，曾被國際知名的「自然」期刊形容為「經費少、野心大」的天文計畫。

中美掩星計畫 I · II

文/ 陳筱琪

TAOS望遠鏡與鹿林天文台夜景。（圖片來源：國立中央大學）

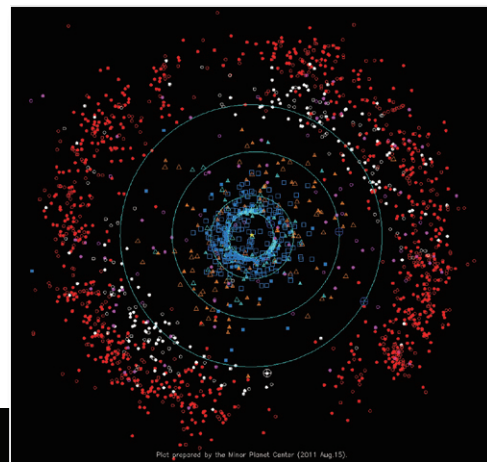


圖一、鹿林天文台，標高2,880公尺，位於玉山國家公園。左上角為TAOS陣列中的其中一台50公分望遠鏡。（圖片來源：TAOS望遠鏡—中研院天文所；2007年鹿林天文台鳥瞰圖—中華民國環保署）

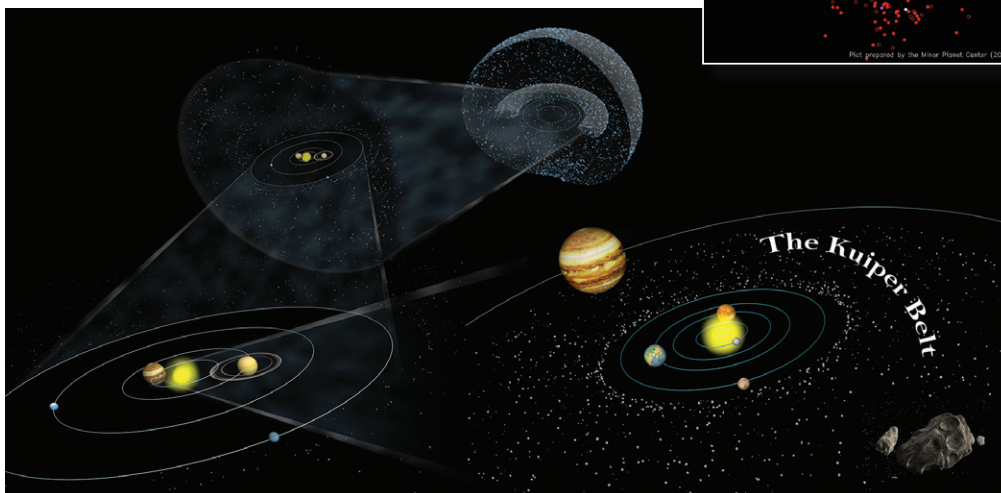
計畫推手中研院李太楓院士表示，此計畫是查理斯·阿卡克（Charles Alcock；現任美國哈佛史密松天文物理中心主任）所提出。當初為籌措經費，阿卡克跨海來臺找中研院天文所籌備處主任魯國鏞（現任美國國家電波天文臺主任），觀測系統也因此決定蓋在臺灣；計畫則由中研院天文所、國立中央大學、哈佛史密松天文物理中心與韓國延世大學，四個機構合作執行。

掩星計畫簡單來說就是利用掩星觀測法來研究太陽系外圍的小天體。這一群小行星與彗星，分布在海王星之外的太陽系邊陲，直徑介於數公尺到數千公里之間，被稱為「古柏帶天體」，其中最大顆、最有名的就是冥王星（圖二、圖

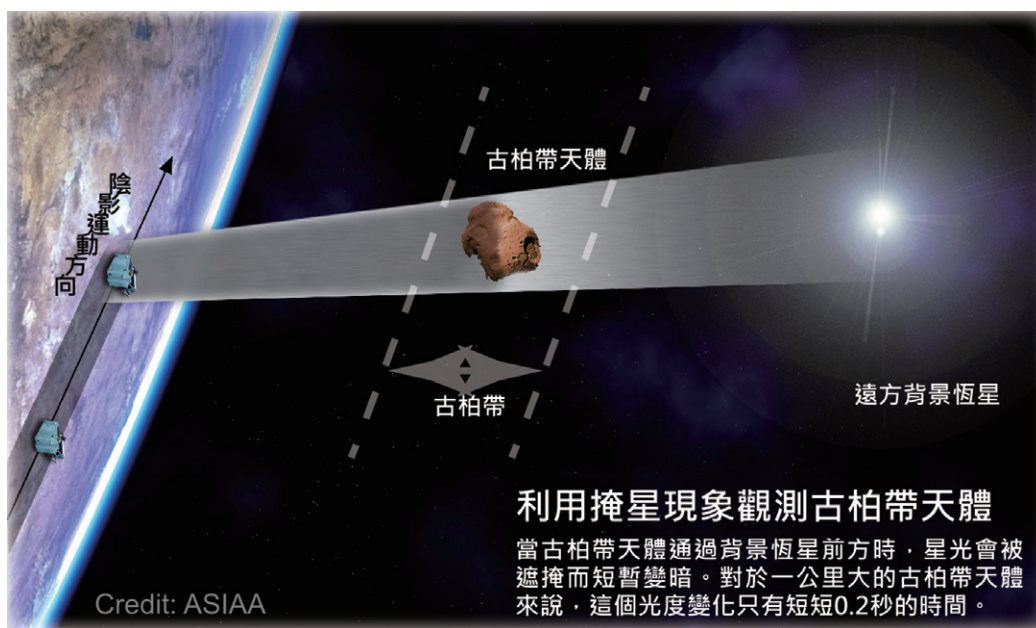
三）。然而直徑30公里以下的小行星與彗星因為距離我們太遙遠、尺寸太小、光度太暗，以致任何現有的地面或太空望遠鏡都無法直接看到，因此其「真相」始終是個謎。為了解開謎底，TAOS藉由監測背景恆星亮度，透過亮度變化的計算來



↑圖二、國際天文聯合會小行星中心的資料，紅色點主要是分佈在海王星外到50天文單位之間的古柏帶天體。（圖片來源：Minor Planet Center/Division F of IAU）



←圖三、太陽系及古柏帶；右下角為古柏帶天體放大範例。（圖片來源：中研院天文所）



圖四、掩星觀測法。
(圖片來源：中研院天文所)

利用掩星現象觀測古柏帶天體

當古柏帶天體通過背景恆星前方時，星光會被遮擋而短暫變暗。對於一公里大的古柏帶天體來說，這個光度變化只有短短0.2秒的時間。

確認掩星事件是否由直徑500公尺到30公里範圍內的古柏帶小天體所造成。那麼，何謂掩星？又，如何利用掩星來觀測古柏帶天體呢？

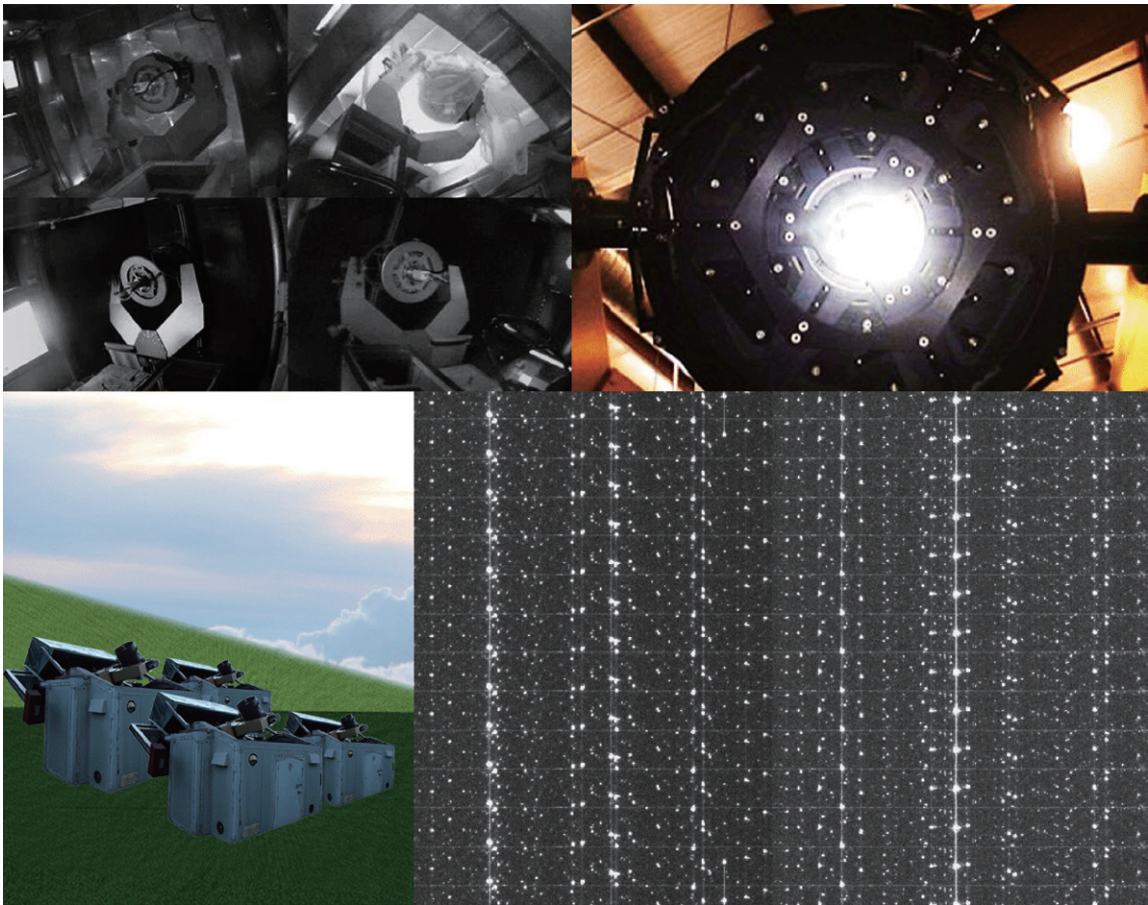
掩星指的是「一個天體被另一個天體遮擋」的過程。夜空中數不清的閃亮星星，當古柏帶天體運行通過我們和這些背景星的中間時，因為遮住了星光，星星亮度會暫時變暗。由於古柏帶天體都很小，所以亮度變化時間極短，平均只有0.2秒，這麼短暫的掩星過程稍縱即逝，偵測速度必須很快才行。此外為了減低誤判機率，必須利用三到四台望遠鏡觀測同一片星空，以每秒至少五次的速度量測視野中星星的亮度。這在一般天文觀測中是很少見的（圖四）。

鹿林山上的四座TAOS全自動觀測系統，利用 $2,048 \times 2,048$ CCD相機（每秒5次測光），每晚監測約1,000顆恆星來蒐尋位於古柏帶的太陽系天體對遠處背景恆星造成的掩星現象。觀測系統的望遠鏡是直徑50公分的小型超廣角望遠鏡，入夜後系統便進行無人全自動觀測，針對排定要觀測的天區進行自動對焦與影像輸出。建構這個系統最大的挑戰在於如何實現全自動及高速測光的要求。為了達成全自動運作的目標，系統中加入許多偵測元件來監控望遠鏡以及天候狀況。每天日落前，控制系統會根據氣象儀器的資料決定是

否自動開啓系統或是關閉遮罩。在每一個觀測天區，這個每秒五次的高速觀測會持續進行1.5個小時，之後再移動至下一個目標天區。每個晴朗的晚上，TAOS可產生超過100GB的資料。

一般天文觀測要求的是長時間的曝光，影像讀取時間通常需要好幾秒鐘。TAOS為了建構高速測光系統，特別採用了拉鍊讀取模式，一次只讀取一小部分影像，以降低影像讀取時間。利用這種方式可以達成5赫茲的取樣速度（圖五）。因而產生的星星影像重疊以及高背景亮度問題，則利用影像處理程式來解決。

負責建構觀測系統的中研院天文所副所長王祥宇表示，TAOS系統的開發涉及光學、機械、電子、軟體等多種科技工程，因此提供相關領域人才不少就業與訓練機會。然而事與願違，掩星計畫在資料收集方面未如預期順利。2005年起至今TAOS在鹿林山上雖已累積超過860億筆的觀測資料，卻沒能發現任何掩星事件。王祥宇指出，除了鹿林當地近年天候多雨霧影響觀測時間、觀測系統偵測與望遠鏡成像不夠靈敏等原因外，古柏帶天體的實際數目有可能也的確比理論推估值少，這些年來天文界其它觀測結果也都支持這個看法；TAOS八年來的觀測結果對太陽系中直徑大於700公尺的古柏帶天體數量設下了非常嚴格的密度上限值。



圖五、TAOS利用網路攝影機同時監看四台望遠鏡的截圖畫面。右上為望遠鏡主鏡支撐機構。下方是以特殊「拉鍊模式」讀取所獲得的影像，圖中由星星拖拉出來的亮線看起來就如同拉鍊般。（圖片來源：中研院天文所）

古柏帶天體的「真相探索」，當然不會因為這些瓶頸而中止。為了解決目前的問題，掩星計畫除了持續提升鹿林山上TAOS望遠鏡的觀測性能，也開始發展海王星外自動掩星普查計畫（TAOS-2），並且為該計畫望遠鏡研發新一代相機系統。針對TAOS各項問題修正的TAOS-2是由中研院天文所主導，與哈佛史密松天文物理中心、國立墨西哥自治大學、中央大學共同合作的計畫。三座1.3米TAOS-2新型望遠鏡台址選在隸屬墨西哥國家天文台(OAN)、海拔2,800公尺的聖白多祿(San Pedro de Martir; SPM)天文台，當地一年中適合進行觀測的天數有300天，是鹿林山的5倍。TAOS-2已於2013年5月在SPM舉行破土典禮（圖六），台址上各項基礎建設一包括道路、電力、網路與房舍的興建，由墨西哥天文台的國立墨西哥自治大

學天文所負責運轉並支付費用。三座望遠鏡計畫於2014年架設至該台址，預期2016年即可全面運轉進行科學觀測。

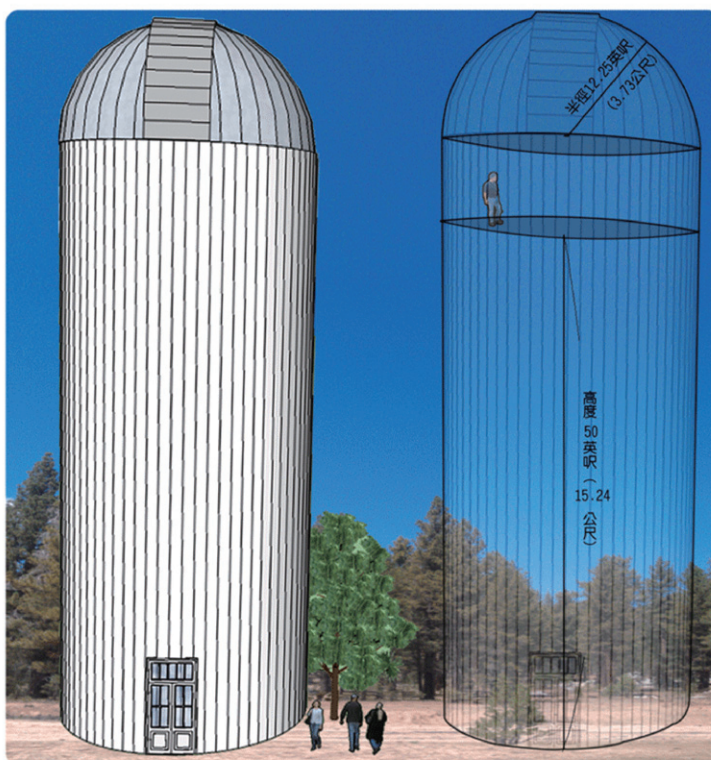


圖六、2013年5月2日TAOS-2破土典禮於墨西哥聖白多祿天文台舉行。右下角人物由左至右分別為：國立墨西哥自治大學校長Carlos Aramburo、國立墨西哥自治大學天文所所長William Lee、中研院天文所所長賀曾樸、哈佛史密松天文物理中心Charles Alcock。（圖片來源：中研院天文所）

TAOS-2所採用的望遠鏡口徑比TAOS更大，相機系統更靈敏、速度更快（圖七、圖八）；以CMOS新偵測器技術為基礎設計的新一代相機，偵測速度至少可提高4倍，將可提供每秒20至40幅超低雜訊（約3個電子等級）的優異影像。整體靈敏度預期將提高兩個數量級，取樣頻率也將提升至20Hz，太陽系小天體可觀測極限將提升10倍，從100天文單位範圍推進至1,000天文單位範圍，TAOS-2觀測系統的整体效能將比TAOS提升至少100倍。加上位於墨西哥天文臺基地這個更理想的觀測台址，TAOS-2將有機會察覺更多、更短暫的掩星事件，找到更小的古柏帶天體。

中研院對於TAOS-2充滿信心。參與中美掩星計畫超過10年的張智威解釋：這些太陽系邊陲的古柏帶天體被認為保存了太陽系形成初期的訊息；掩星觀測倘若成功，除了可以研究古柏帶天體，還可解答太陽系行星如何經由這些天體碰撞而形成的歷史奧秘。

在TAOS-2望遠鏡全面運轉之前，鹿林山上的TAOS仍會持續運轉，作為訓練學生與測試新儀器之用。中研院天文所為四座TAOS望遠鏡安裝了影像暫存相機以改善望遠鏡的效能與古柏帶天體的統計結果；2013年起，新一代觀測系統改採 $1,024 \times 1,024$ CCD相機（每秒10次測光）。目前TAOS運轉良好，可靠度很高。雖然測不到掩星事件，但TAOS望遠鏡的遠端觀測性能及快速驅動系統，已經讓TAOS三次成功偵測到宇宙伽瑪射線爆的光學餘暉，這些餘暉通常是被太空天文望遠鏡在爆發後一分鐘內測得。伽瑪射線爆是宇宙中能量最強的現象，其爆發機制迄今尚未十分明瞭。TAOS在伽瑪射線爆的幾乎同時間即偵測到早期光學餘暉，此成果將成為伽瑪射線爆發生機制極有用的研究參考。未來的TAOS-2一旦提升了偵測靈敏度以及取樣速度，也能加入偵測不同時間範圍內的伽瑪射線爆，預期將可成為解析天體結構的重要工具。



圖七、TAOS-2望遠鏡頂直徑為24.5英呎（7.46公尺），觀測層距離地面約50英呎（15.24公尺），與下層之間以氣閘（air lock）隔開。（圖片來源：中研院天文所）

	TAOS-1	TAOS-2	改善倍數
可觀測天數	50天/年	250天/年	5
口徑	0.5 m	1.3 m	6.2
背景雜訊	16 e ⁻	2 e ⁻	7.28
曝光時間	105 ms	50 ms	0.47
可偵測最小 KBO 大小	0.7 km	0.4 km	2
視野	3 □°	1.4 □°	0.47
Total			≈100

圖八、TAOS-2採用Ritchey-Chretien (RC) 卡塞格林反射式望遠鏡。主鏡焦長為5.2公尺，焦比為F/4，屬於短焦距光學系統，能讓我們一次看到較大的星空。（圖片來源：中研院天文所）

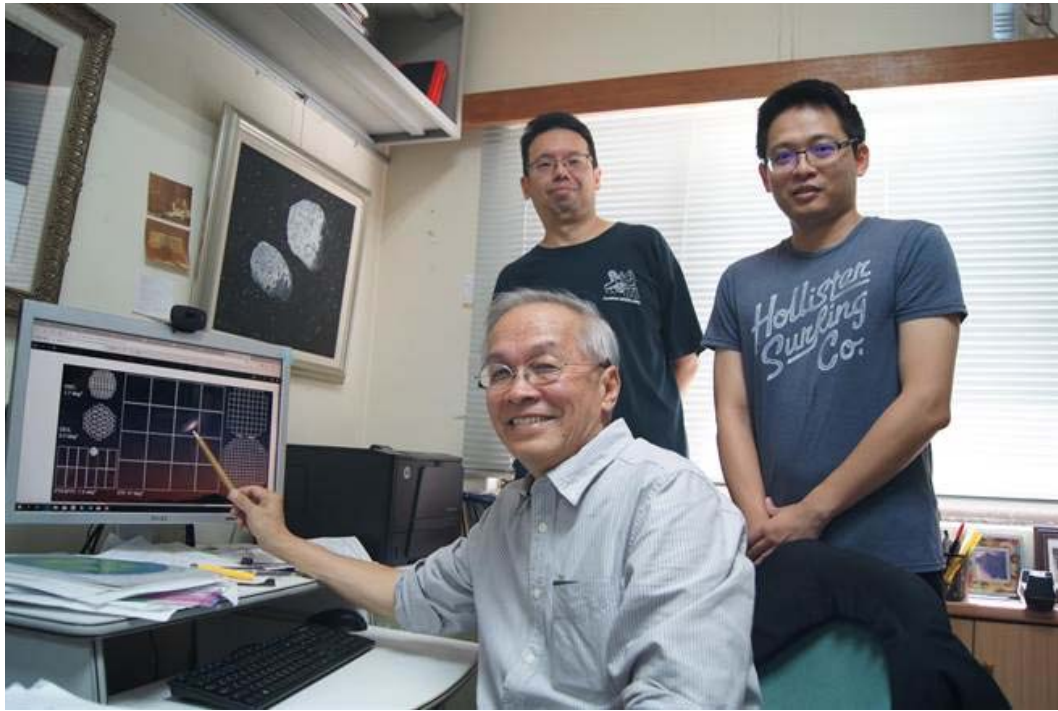
參考資料：

1. Nathan, R. (1997) Taiwan looks to the skies for a boost to its basic research. *Nature*, 390 : 544
2. 中研院天文所掩星計畫網頁<http://taos.asiaa.sinica.edu.tw/>
3. 2013年中研院天文所掩星計畫摺頁簡介
4. 2014年中研院天文所研究成果專刊

陳筱琪：任職於中研院天文所天文教育推廣小組，
天聞季報主編

新聞報導

中大清大超廣角 ZTF 探測器啟動 天文學研究大躍進



中央大學參與的 ZTF 計畫，可達 47 平方度的大視野，將對可見光時域天文學做出重大的科學貢獻。照片前方葉永烜院士，後左饒兆聰教授，後右俞伯傑博士後研究員。（中央大學提供）

2017 年 11 月 15 日 15:25 [旺報](#) [李侑珊](#)



ZTF 擁有 47 平方度視野的超廣角相機，其實際大小如同一台 20 吋螢幕。圖為該相機所使用的濾鏡。(照片由加州理工學院天文台提供)

中央大學及清華大學聯合組成的探高計畫，在科技部支持下，參與由美國加州理工學院所主導的「史維基瞬變探測器」(Zwicky Transient Facility, 簡稱為 ZTF)，將天文研究推進到時間加上空間的 4D 階段，可望對可見光時域天文學作出重大的科學貢獻。

ZTF 計畫前身為「帕洛馬瞬變工廠 Palomar Transient Factory, 簡稱為 PTF」，該計畫於今年初達成階段性任務後功成身退，並將於今年底邁入另一個重要的里程碑，且更名為「史維基瞬變探測器 Zwicky Transient Factory, 簡稱為 ZTF」，原先使用在 PTF 上的 7 平方度廣視野相機將更換成擁有 47 平方度視野的超廣角相機(一幅影像可同時容納 213 個月亮)，加上改良後的儀器和軟體，觀測效率將提高為 10 倍之多，該計畫 11 月 15 日開光後開始進行常規的科學工作，預計每個晚上可巡視北天二次。

中央大學天文所教授葉永烜，擔任探高計畫主持人；他興奮地表示，ZTF 將以前所未有的效率發現超新星，黑洞吞食恆星事件，以及紀錄所有短時間內變動的天體現象。

在找尋重力波的可見光對應天體上，ZTF 因其超廣視野，而擁有無可取代的優勢，一旦重力波被發現後，ZTF 能在數分鐘內，完成相關區域的觀測而到重力波的起源，並提供鹿林天文台和全世界其他望遠鏡，進行更精準後續觀測。

中大天文所博士後研究員俞伯傑解釋，中子星與中子星的合併或中子星與黑洞的合併會產生重力波與電磁波，藉由這類的研究，天文學家可瞭解宇宙中貴金屬與其它重元素的來源。

ZTF 計畫約一半經費由美國自然科學基金會提供，另一半則由加州理工學院領導的國際合作團隊所分擔，除中央大學及清大組成的探高計畫，另外參加的國際研究單位則來自以色列、瑞典及德國等大學與研究單位。

跨校團隊運用超廣角相機 可望記錄黑洞吞食恆星奇景

2017/11/16 udn 聯合新聞網

由國立中央大學及清華大學聯合組成的探高計畫，在科技部的支持下，參與由美國加州理工學院主導的大型國際合作計畫「史維基瞬變探測器 Zwicky Transient Facility，簡稱為 ZTF」，將以 47 平方度的超大廣角視野、前所未有的效率，記錄短時間內的天體變化，邁向天文研究中時間加上空間的 4D 階段里程碑。

該計畫的前身「帕洛馬瞬變工廠計畫」今年初達成階段性任務後，今年底正式更名為「史維基瞬變探測器計畫」，將原先使用的 7 平方度廣角視野相機更換成 47 平方度超廣角相機，等同一幅影像可同時容納 213 個月亮，加上改良後的儀器和軟體，觀測效率將可提高 10 倍之多，今天正式展開常規科學研究工作，預計每晚巡視 2 次。

計畫主持人葉永烜教授興奮地表示，ZTF 將以前所未有的效率發現超新星、黑洞吞食恆星事件，以及紀錄所有短時間內變動的天體現象。執行小行星研究的助理研究員章展誥強調，ZTF 是第一個提供完整時序巡天的計畫，其效率有如把腳踏車換成高鐵，將天文研究推進到時間加上空間的 4D 階段，為「可見光時域天文學」寫下重要的里程碑。

團隊指出，ZTF 擁有超廣角視野的優勢，在找尋重力波的可見光對應天體上有重大功用，一旦重力波被發現後，能在數分鐘內完成相關區域的觀測，進而了解到重力波的起源，使鹿林天文台和全世界其他望遠鏡能更精準地進行後續觀測。中大天文所博士後研究員俞伯傑表示，中子星彼此之間或與黑洞的合併會產生重力波與電磁波，透過此研究，天文學家可瞭解宇宙中各元素的來源。

ZTF 計畫有一半經費由美國自然科學基金會提供，另一半則由加州理工學院領導的國際合作團隊分擔。除中大及清大組成的探高計畫外，參加單位包括以色列的衛斯曼研究所、瑞典斯德哥爾摩大學的奧斯卡·克萊思研究中心、馬利蘭大學、華盛頓大學、德國電子回旋加速器中心、美國洛斯阿拉摩斯國家實驗室、威斯康辛大學及美國柏克萊羅倫斯國家實驗室。詳細內容可參考連結：<http://www.caltech.edu/news/zwicky-transient-facility-opens-its-eyes-volatile-cosmos-80369>

年輕天文學者獎 日本田中雅臣博士榮獲

2017/10/19 HiNet 新聞社群

記者葉志成／桃園報導

由中央大學與台達電子文教基金會共同頒發的「年輕天文學者講座」，2017年秋季得主由日本國家天文台的田中雅臣博士榮獲，其為「時域天文學」專家，特別關注天體如何隨時間快速變化，18日上午接受中央大學周景揚校長頒獎，並將在台灣展開三場演講，首場為當前最熱門的重力波偵測。

此講座表彰國際上在天文學領域有卓越表現之年輕學者，邀請具潛力的學術菁英來台與國內學界互動，並啟發年輕心靈。講座獎金由台達電子文教基金會提供，由國際甄選委員會推薦候選人，並由中央大學天文所執行邀訪活動。獲獎者將在中央大學天文所發表學術演講，與國內學者進行交流，另在台達電子文教基金會，以及台中一中進行科普演講，讓民眾與學生接觸最前沿的天文課題，並藉與講者互動景仰其學術風範。

中央大學天文所所長陳文屏表示，夜空看似靜謐永恆，其實天體隨時都在變化。地球上日夜更迭、四季輪迴；太陽每時每刻都在進行核反應產生光與熱，另方面則以百億年的時間尺度生、老、病、死。

陳文屏說，天體以不同的時間尺度變化，有些長達數十年，需要長期觀察，另外有些現象則非常快速。有些恆星以爆發的方式結束一生，稱為「超新星」，在幾天之內急遽變亮，同時把恆星一生當中進行核反應所產生的複雜元素，撒回星際太空，成為製造下一代恆星的原料。爆發期間釋放大量能量，核融合產生更複雜的元素。近年藉由精密儀器與偵測技術的發展，人們得以認識瞬間產生變化的天體，像是伽瑪射線爆發源，或是黑洞合併以後產生的重力波動，讓人認識宇宙的視野更加寬廣。

田中雅臣博士 (Dr. Masaomi Tanaka)於 2009 年取得東京大學天文學博士學位，目前為日本國家天文台助理教授。他來台發表三場演講，其中學術演講有關重力波的偵測，講題為 ” Hunting for Gravitational Wave Sources” ，10 月 18 日下午 3 點，地點在中央大學天文所健雄館。另外兩場為科普演講，內容是宇宙當中黃金的來源，分別是 10 月 20 日下午 2 點，在台達電子台北總公司； 10 月 21 日上午 9 點在台中一中。其中第二場與第三場備有中文導讀，歡迎參加！

原文轉載自【2017-10-19/HiNet 新聞社群】

日本田中雅臣博士獲「年輕天文學者獎」2017 年秋季得主

更新： 2017 年 10 月 18 日



帥氣的田中雅臣博士（左 2），與中央大學天文所教授們合影。（記者徐乃義／攝影）

【記者徐乃義／桃園報導】中央大學與台達電子文教基金會共同頒發的「年輕天文學者講座」，2017年秋季得主由日本國家天文台的田中雅臣博士榮獲，其為「時域天文學」專家，關注天體如何隨時間快速變化，接受中央大學周景揚校長頒獎，並將在台灣展開3場演講，首場為當前最熱門的重力波偵測。



中大與台達電子文教基金會共同頒發的「年輕天文學者講座」，田中雅臣博士（左）接受中大周景揚校長(右)頒獎。(中大提供)

講座獎金由台達電子文教基金會提供，由國際甄選委員會推薦候選人，並由中央大學天文所執行邀訪活動。獲獎者將在中央大學天文所發表學術演講，與國內學者進行交流，另在台達電子文教基金會，以及台中一中進行科普演講，讓民眾與學生接觸最前沿的天文課題，並藉與講者互動景仰其學術風範。

中大天文所所長陳文屏表示，夜空看似靜謐永恆，其實天體隨時都在變化。地球上日夜更迭、四季輪迴；太陽每時每刻都在進行核反應產生光與熱，另一方面則以百億年的時間尺度生、老、病、死。

陳文屏說，天體以不同的時間尺度變化，有些長達數十年，需要長期觀察，另外有些現象則非常快速。有些恆星以爆發的方式結束一生，稱為「超新星」，在幾天之內急遽變亮，同時把恆星一生當中進行核反應所產生的複雜元素，撒回星際太空，成為製造下一代恆星的原料。爆發期間釋放大量能量，核融合產生更複雜的元素。近年藉由精密儀器與偵測技術的發展，人們得以認識瞬間產

生變化的天體，像是伽瑪射線爆發源，或是黑洞合併以後產生的重力波動，讓人認識宇宙的視野更加寬廣。

田中雅臣博士 (Dr. Masaomi Tanaka)於 2009 年取得東京大學天文學博士學位，目前為日本國家天文台助理教授。◇

2017 年秋季「年輕天文學者獎」 日本田中雅臣博士榮獲

文／天文所



由中央大學與台達電子文教基金會共同頒發的「年輕天文學者講座」，2017 年秋季得主由日本國家天文台的田中雅臣博士（左）榮獲，上午接受中央大學周景揚校長（右）頒獎。石孟佳攝

由中央大學與台達電子文教基金會共同頒發的「年輕天文學者講座」，2017 年秋季得主由日本國家天文台的田中雅臣博士榮獲，其為「時域天文學」專家，特別關注天體如何隨時間快速變化，10 月 18 日上午接受中央大學周景揚校長頒獎，並將在台灣展開三場演講，首場為當前最熱門的重力波偵測。

此講座表彰國際上在天文學領域有卓越表現之年輕學者，邀請具潛力的學術菁英來台與國內學界互動，並啟發年輕心靈。講座獎金由台達電子文教基金會提供，由國際甄選委員會推薦候選人，並由中央大學天文所執行邀訪活動。獲獎者將在中央大學天文所發表學術演講，與國內學者進行交流，另在台達電子文教基金會，以及台中一中進行科普演講，讓民眾與學生接觸最前沿的天文課

題，並藉與講者互動景仰其學術風範。

中央大學天文所所長陳文屏表示，夜空看似靜謐永恆，其實天體隨時都在變化。地球上日夜更迭、四季輪迴；太陽每時每刻都在進行核反應產生光與熱，另方面則以百億年的時間尺度生、老、病、死。

陳文屏說，天體以不同的時間尺度變化，有些長達數十年，需要長期觀察，另外有些現象則非常快速。有些恆星以爆發的方式結束一生，稱為「超新星」，在幾天之內急遽變亮，同時把恆星一生當中進行核反應所產生的複雜元素，撒回星際太空，成為製造下一代恆星的原料。爆發期間釋放大量能量，核融合產生更複雜的元素。近年藉由精密儀器與偵測技術的發展，人們得以認識瞬間產生變化的天體，像是伽瑪射線爆發源，或是黑洞合併以後產生的重力波動，讓人認識宇宙的視野更加寬廣。

田中雅臣博士 (Dr. Masaomi Tanaka)於 2009 年取得東京大學天文學博士學位，目前為日本國家天文台助理教授。他來台發表三場演講，其中學術演講有關重力波的偵測，講題為 ” Hunting for Gravitational Wave Sources” ，10 月 18 日下午 3 點，地點在中央大學天文所健雄館。另外兩場為科普演講，內容是宇宙當中黃金的來源，分別是 10 月 20 日下午 2 點，在台達電子台北總公司；10 月 21 日上午 9 點在台中一中。其中第二場與第三場備有中文導讀，歡迎參加！



帥氣的田中雅臣博士（左三），與中央大學天文所教授們合影，並從 10 月 18 日開始在台灣展開三場演講。石孟佳攝

相關連結：http://www.astro.ncu.edu.tw/ncu_delta/reciNews.php?id=10

陽明山雲頂上有「紅色精靈」快閃 天文館：北台灣 首次紀錄



▲這不是鬼魂，而是罕見的「紅色精靈」。（圖／台北天文館提供）

記者戴榕萱／台北報導

罕見的「紅色精靈」，是一種發生在積雨雲以上的大範圍放電現象，與常見的閃電不同，並不是帶著高溫，而是一種冷電漿的現象，接近螢光燈內的放電物質。台北天文館設立在陽明山湖田國小的自動觀測站，於9月30日凌晨就首度捕獲這罕見的天象，也是北台灣的首次紀錄。

天文館解釋，「紅色精靈」發生在雲頂之上的大範圍放電現象，當積雨雲發出閃電的千分之幾秒後，由雲頂向更高空的放電，時間僅數十分之一秒，因呈橘紅色且瞬間消失，肉眼幾乎無法看見，故稱為「紅色精靈」。

為觀察夜空現象並進行分析研究，台北天文館與東華大學物理系、中央大學天文研究所等單位合作建立觀測網，於全國各地設立自動觀測站。迄今除了記錄

到數千顆流星事件外，亦獲得許多珍貴的觀測記錄，此次紅色精靈就是特殊又珍貴的一例。

紅色精靈在北美洲、中美洲、南美洲、歐洲，及非洲中部（薩伊）、日本海等地都有紀錄，通常在滂沱大雨中的雷暴系統中都會出現。紀錄上可推回 1730 年，被科學家觀察到暴雷雨中的雲頂會有短暫發光的現象，直到 1989 年 7 月 6 日，明尼蘇達大學的科學家用低光攝影機，偶然拍到首張照片；由於此現象消縱即逝，因此才有「精靈」的稱號。

原文網址: [陽明山雲頂上有「紅色精靈」快閃 天文館：北台灣首次紀錄 | ETtoday 新奇 | ETtoday 新聞雲](#)

中大探測重力波揚威 參與研究學者批港大取消天文學系失策



[社會新聞](#)

撰文：潘希橋

2017-10-17 15:01

最後更新日期：2017-10-17 18:14

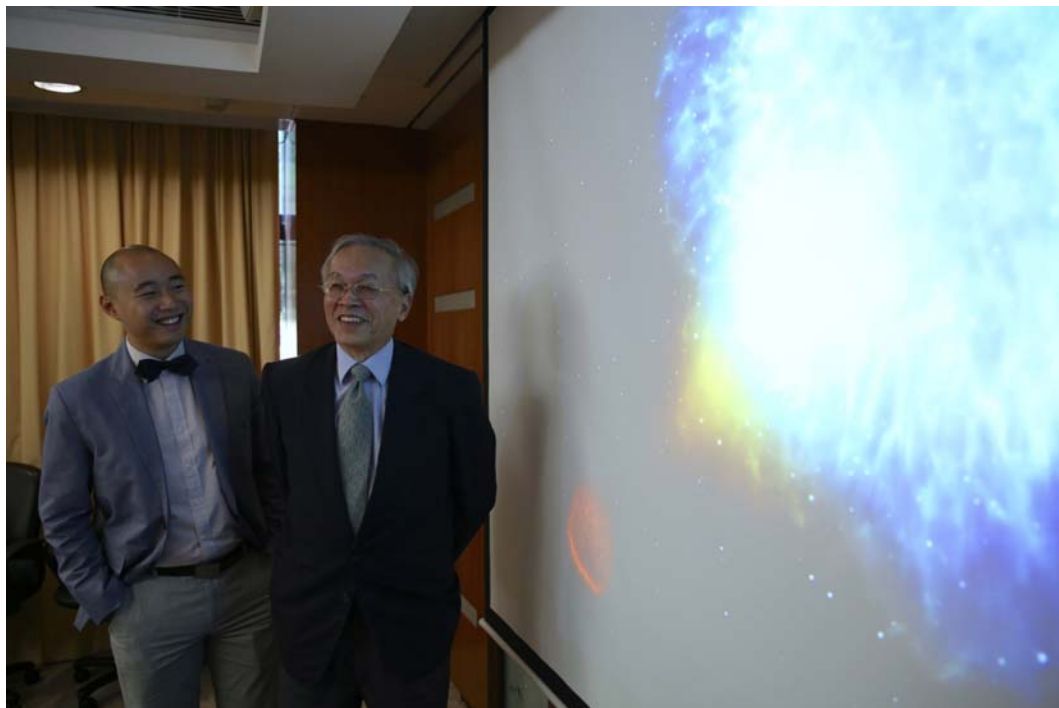
本月（10月）初頒授的諾貝爾物理學獎，由三名成功探測重力波的科學家奪得，當中中文大學亦有份參與研究團隊「LIGO」的工作，令人意識到香港學府科研水平毫不遜色。該團隊聯同其他天文學家合作，昨晚再有新發現，其中有

份參與今次研究的前中大校友、國立中央大學教授葉永烜批評，香港大學取消天文學系非常失策，批評部分人太短視。

葉永烜教授嘆港大取消天文學系失策，港人太短視。

重力波團隊（The Virgo Collaboration）偕同激光干涉儀重力波觀測站（LIGO），昨晚觀測出極具科學價值的重力波，為科學家對相關課題的研究打下強心針。

有份參與觀測的國立中央大學天文所及太空科學研究院國鼎講座教授葉永烜，本身亦是中文大學的前校友，他在講述有關發現的重要性同時，慨嘆港大早前取消天文學主修科的決定「非常失策」，批評管理層和政府太短視：「他們兩三年就想回本，但科研工作並非如此……今屆諾貝爾獎得主，工作了 40 年才有今天的成果。」他又認為，美國和英國的知名學府都位處著名城府中心，質疑香港既然有充分財政資源，為何不能建設更好的基礎吸引人才。



重力波團隊觀測出極具科學價值的重力波。（鍾偉德攝）

早前港大以修讀人數不斷下降為由，擬剔除兩科主修，隨同天文學一起被淘汰的，還有數學/物理主修科，當中畢業生便包括天文台台長岑智明，他從莘莘學子到成為天文台台長過程毫不容易，他今早撰文提及自己兒時經歷，指父親當年希望他做醫生律師等高薪厚職，而在家人壓力外，還要承受視網膜穿洞的雙重打擊，但他堅持夢想修讀物理，最終成為了天文台台長。他早前得悉當年的本科或會被取消後，亦表示「失望及遺憾」，認為是本港科學教育的損失。

同一學系孕育出兩任天文台台長，前天文台台長林超英亦是擬取消的數學/物理學系畢業生，他今年3月得悉有關「殺科」的消息後，批評校方以修生人數經營「業績指標」做法令人難以置信，又認為數學及物理是科學教育的核心部分，他其後更去信港大理學院院長，質疑對方取消學科的做法越權。

人類首次！中央大學參與偵測到中子星合併產生重力波

出版時間：2017/10/17 11:25

美國與歐洲科學家昨天宣布證實，人類首度偵測到由2顆中子星劇烈相撞產生的重力波與光，而中央大學天文所研究團隊參與美國加州理工學院主導的跨國「全球瞬變現象偵測網」，對偵測到重力波結果加以確認來源，此發現再度證實愛因斯坦提出《廣義相對論》中，「重力波是以光速傳播」理論，刊登在新一期的國際頂尖期刊《科學》（Science）上，未來也有助於解開宇宙中黃金等重金屬形成之謎。

百年前愛因斯坦的廣義相對論就預測重力波存在，但是偵測極為困難，只有黑洞、中子星等天體合併才發出足夠的訊號，今年諾貝爾物理獎頒發給萊納·魏斯（Rainer Weiss）、基普·索恩（Kip Thorn）、巴瑞·巴利許（Barry Barish）3人，表彰他們設計建造重力波偵測器 LIGO 以及人類首次偵測到重力波的成功。

科技部指出，LIGO 團隊在 2015 年 9 月 14 號首次探測到由兩個黑洞合併所產生的重力波，之後陸續觀測到合計四次因黑洞合併所產生的重力波，驗證了愛因斯坦廣義相對論的預測，但上述重力波事件只有美國 LIGO 偵測器進行觀測，對於重力波源的定位能力有限，無法得知重力波源自哪一個星系。

中大天文所研究團隊在科技部計畫補助下，參與美國加州理工學院主導的「全球瞬變現象聯測網（GROWTH）」，而 GROWTH 由加州理工學院主導，全球共有台美等 8 國共 14 個研究所（含 18 座天文台）組成的團隊，台灣則由中研院院士葉永烜、中大天文所教授饒兆聰、俞伯傑博士及鹿林天文台 4 所組成團隊，藉由科技部長期補助探高計畫（TANGO）等，投入這次國際天文合作。

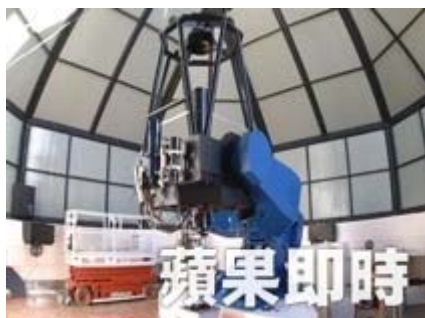
中大天文所博士後研究員俞伯傑表示，今年 8 月 17 日 LIGO 首次偵測到由中子星合併所產生的重力波，位於智利天文台進一步發現重力波來源為可能是編號 NGC4993 星系，於是 GROWTH 團隊在往後 2 周利用全球各波段的望遠鏡，包

含可見光,紅外,無線電,及 X 射線波段，對其做後續追蹤觀測，以觀測結果與中子星合併理論模型進行比較後，發現其重力波與 LIGO 前幾次因黑洞合併造成的重力波事件不同，依此確認這是由兩個中子星碰撞合併所產生的重力波事件。

俞伯傑分析，現今超新星爆炸理論無法解釋宇宙中重金屬的形成，因此包括黃金等重金屬的形成過程還是個謎，而新的理論認為在中子星合併的過程會產生「快中子捕獲過程」，形成比鐵更重的元素，而有助於解釋像黃金這類的重金屬形成，這次偵測到中子星合併所產生的重力波與後續的多波段觀測，將成為重力波天文學的先導，並有助於人類解開宇宙中的重金屬形成的謎題。（許敏溶／台北報導）



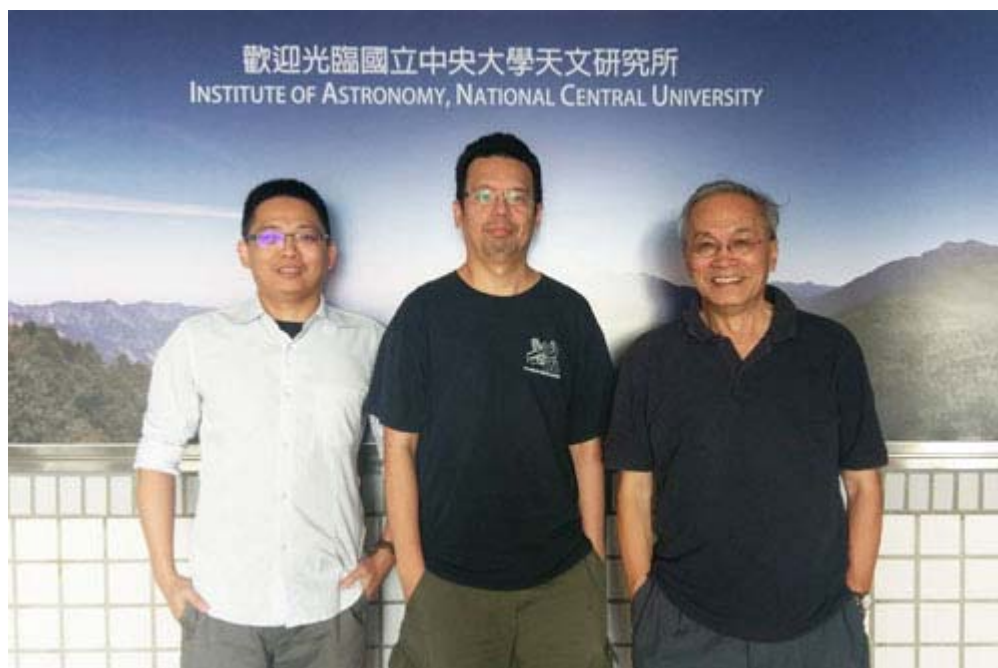
俞伯傑說明偵測到中子星合併產生重力波與光的過程。周永受攝



中大鹿林天文台也參與這次偵測到中子星合併產生重力波與光的過程。中大提供

首次目睹產生重力波的中子星相撞 天文所參與全球聯測成果登上《Science》

文／天文所



中央大學天文團隊與研究成果：探高計畫(TANGO)主持人中央大學葉永烜教授(右)，台灣參與 GROWTH 計畫主持人饒兆聰教授(中)，俞伯傑博士(左)。照片天文所提供

中央大學天文所研究團隊在科技部計畫補助下，參與美國加州理工學院主導之「全球瞬變現象聯測網(Global Relay of Observatories Watching Transients Happen, GROWTH)」，而 GROWTH 對 LIGO 所偵測到之重力波結果加以確認來源之研究成果，則為人類首次之發現！本次發現不但驗證了愛因斯坦廣義相對論，未來也有助於解開宇宙中黃金形成之謎。這項重要成果 “Illuminating Gravitational Waves: A Concordant Picture of Photons from a Neutron Star Merger” 刊載在最新一期的國際頂尖期刊《科學》(Science) 上。

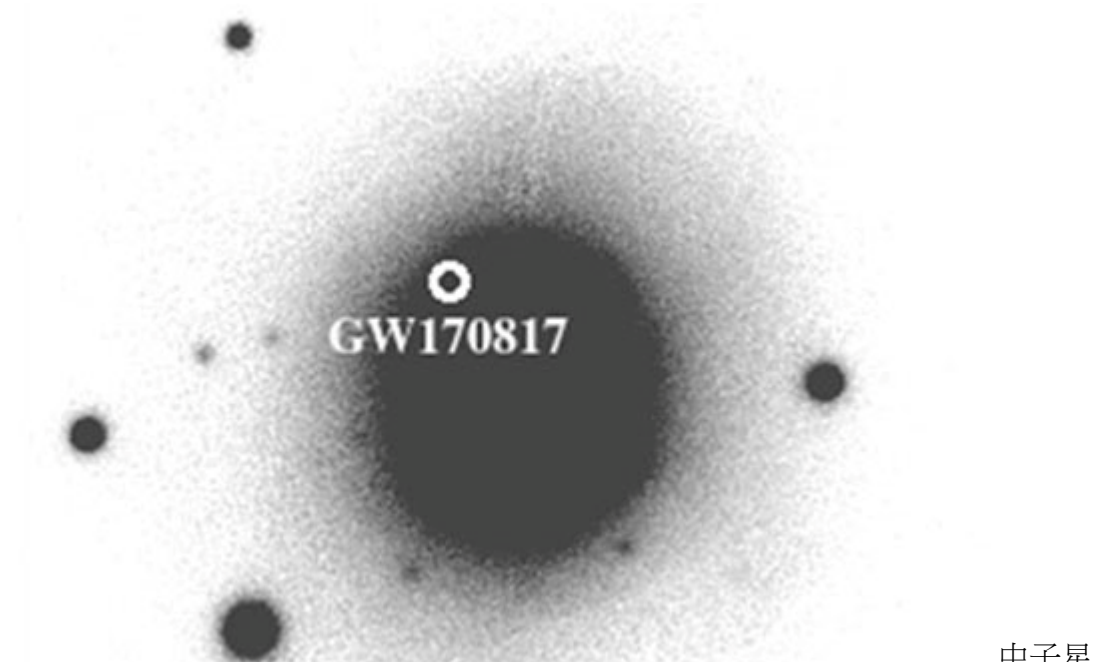
全球瞬變現象聯測網 (GROWTH)」是由美國加州理工學院主導，全球共 8 個國家包含美國、日本、德國、英國、瑞典、以色列、印度及台灣共 14 個研究所(含 18 座天文台)組成的團隊。我國則以科技部計畫補助下之葉永烜院士、饒兆聰教授和俞伯傑博士及鹿林天文台 4 所組成之團隊，藉由科技部長期補助之探高計畫 (TANGO)及參與臺美雙邊 PIRE 國際合作計畫機會加入 GROWTH，以此投入國際天文合作研究。此次成果亦使鹿林天文台再次躍入國際聯測研究舞台。

百年前愛因斯坦的廣義相對論早就預測了重力波存在，但是偵測極為困難，只

有當極度緻密的天體，例如黑洞、中子星等天體合併才發出足夠的訊號。2017年諾貝爾物理獎頒發給萊納·魏斯(Rainer Weiss)、基普·索恩(Kip Thorn)以及巴瑞·巴利許(Barry Barish)，表彰他們設計建造重力波偵測器 LIGO 以及人類首次偵測到重力波的成就。LIGO 團隊在 2015 年 9 月 14 號首次探測到由兩個黑洞合併所產生的重力波，之後陸續觀測到合計四次因黑洞合併所產生的重力波，驗證了愛因斯坦廣義相對論的預測。然而，由於前幾次重力波事件只有美國 LIGO 偵測器進行觀測，對於重力波源的定位能力有限，無法得知重力波源自哪一個星系。

由於歐洲重力波 Virgo 偵測器的加入觀測，在本(2017)年 8 月 17 日 LIGO 首次偵測到由中子星合併所產生的重力波(編號 GW170817)事件中，位於智利 Las Campanas 天文台因此標定重力波來源之可能星系(編號 NGC4993)，並發現一個可能的光學對應體。於是 GROWTH 團隊以其全球聯測網，在往後兩個星期利用全球各波段的望遠鏡，包含可見光,紅外,無線電,及 X 射線波段，對其做後續追蹤觀測，以觀測結果與中子星合併理論模型進行比較後，發現 GW170817 重力波與 LIGO 前幾次因黑洞合併造成的重力波事件不同，依此確認這是由兩個中子星碰撞合併所產生的重力波事件。

由於現今的超新星爆炸理論無法解釋宇宙中重金屬的形成，因此重金屬(例如黃金)的形成過程還是個謎題。而新的理論認為在中子星合併的過程會產生「快中子捕獲過程(r-process)」形成比鐵更重的元素，而有助於解釋像黃金這類的重金屬形成。這次偵測到中子星合併所產生的重力波與後續的多波段觀測，將成為重力波天文學的先導，並有助於人類解開宇宙中的重金屬形成的謎題。



合併發生的地點：位於夏威夷的泛星計畫(Pan-STARRS)望遠鏡所拍攝的星系 NGC4993 可見光影像。白色圓圈為中子星合併發生的地點。照片天文所提供



科技部

舉辦記者會宣布這項重要成果。照片左起中央大學物理系張元翰教授、天文所饒兆聰教授、俞伯傑博士、科技部自然司長吳俊傑、中央大學天文所陳文屏所長。陳如枝攝

相關連結：<http://science.sciencemag.org/content/early/2017/10/13/science.aap9455>

「雲的兩邊」葉永烜油畫展 看見天文學家特有的人間美畫

2017/07/12 台灣好新聞

記者葉志成／桃園報導

集科學家與藝術家於一身的中央大學天文研究所葉永烜院士，今年歡慶七十歲生日。中大天文所於7月10日舉辦一連三天的「太陽系的偶然機遇與超越」國際學術研討會，邀請國際天文學者與會，感念葉院士對天文界之卓越貢獻。另在藝文中心舉辦「雲的兩邊」葉永烜油畫創作展，透過一幅幅真情流露的畫作，讓人看見天文學家特有的人間美畫。

研討會中國內外貴賓雲集，葉教授合作過的學術界先進好友齊聚一堂，包括三

位美國國家科學院院士 Prof. Gary Zank、Prof. David Jewitt 和 Prof. Renu Malhotra。另外，卡西尼計畫相關的 Prof. Linda Spilker 和惠更斯號（Huygens）Prof. Jean-Pierre Lebreton 等，以及世界各國的科學家均遠道而來，表達祝賀之意。

中央大學天文所所長陳文屏在研討會開場介紹葉永烜院士，「認識葉永烜的人都知道，他富創意、精力充沛，永遠都有新點子。」中央大學校長周景揚接者表示，葉教授曾獲美國 NASA 特殊公共服務榮譽勳章、教育部終身國家講座，更於去年獲選中央研究院院士，榮耀輝煌、實至名歸。

台達電子榮譽董事長鄭崇華讚譽葉永烜是一位「好老師，也是優秀的科學家。」鄭崇華認為，人類生命短暫，藉由科學家引領我們認識宇宙的長遠浩瀚，應更懂得珍惜，不該短視近利。他很感謝自 2012 年起葉永烜協助選拔「台達電子年輕天文學者講座」，推展天文學研究和教育。

當初延攬葉永烜回台任教的中大前校長劉兆漢回憶，40 年前在德國與葉永烜的初次相遇也是機緣。他在國際間學術聲望及個人熱忱，促成各項重要計畫開端和豐碩成果，並引薦不少學生及年輕學者參與國際合作，功不可沒。

葉永烜 1982 年與歐美科學家共同提出的「卡西尼探測土星」跨國計畫，為人類史上首次深入探測土星的計畫，1997 年 10 月 15 日發射升空，2004 年抵達土星，預計今年 9 月 15 日任務將圓滿結束。這項長達 20 年的太空船飛行任務，共耗資 34 億美元，全球 5 千多人參與，帶來人類前所未見的天文重大成就，葉教授也成為華人《Nature》和《Science》論文發表之最。

他近期在國家地理雜誌發表的「卡西尼任務的十個突破性發現」，第一項就是泰坦（土衛六）表面有與地球類似，由甲烷驅動的水文作用。第二項土衛二南極冰殼裂縫噴發出大量水氣和冰粒子，冰殼下存在著覆蓋整個衛星的地下海洋，科學家相信那裏可能有生命的存在。

葉教授除卓越科學成就之外，同時也一位業餘畫家，三十年來創作不輟。他在 1987 年在一個偶然的機會開始學畫，差不多同時也被診斷患有青光眼疾，但他逆光飛翔，透過不斷創作，本次在藝文中心展出的「雲的兩邊」創作個展，有五十幅作畫精彩呈現。

當中「卡西尼發射後的早晨」，紀錄 1997 年 10 月 15 日卡西尼太空船成功發射那一天，他徹夜未眠，等到翌日清晨，捕捉那千變萬化灑落在大西洋天空的綺麗朝陽。另有一幅畫作「看見台灣」，畫的是原住民孩童在玉山山頂高歌，期

盼向導演齊柏林致敬，電影的贊助者台達電創辦人鄭崇華董事長也到場，場面溫馨。

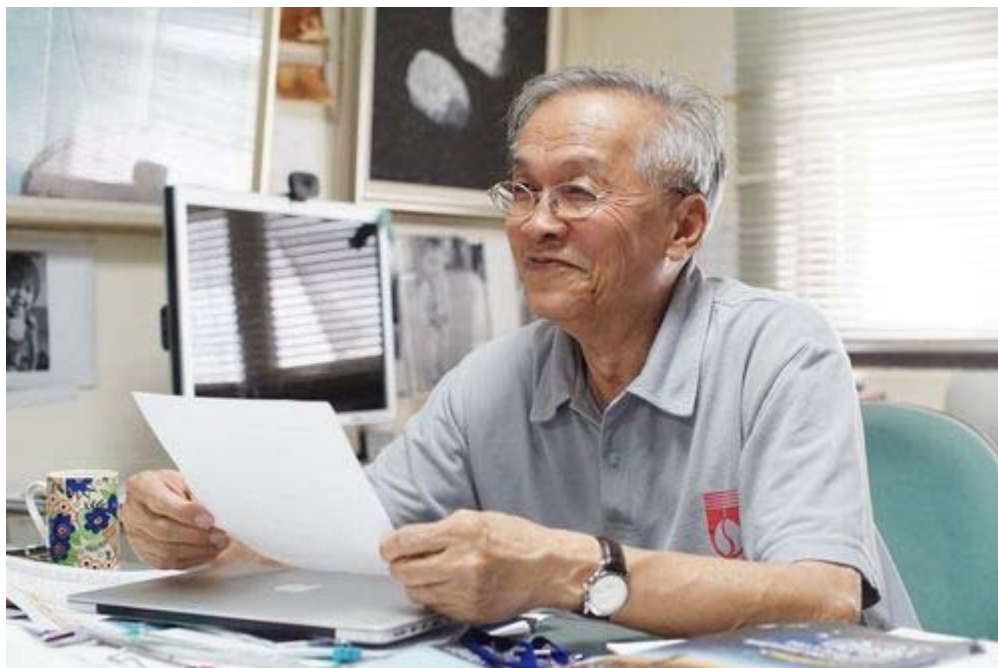
葉教授表示，「雲的兩邊」主題來自他在一次談論中，比較西方油畫與中國水墨畫對「雲」迥然不同的處理方式，另一則來自瓊妮·米歇爾在1968年撰寫一首歌《Both sides now》中的故事。他將本次畫展獻給他在天上的母親，以及和她同樣經歷不朽的偉大女性們，不管在雲的那一邊，她們都和我們在一起。

而能在科學與藝術不同領域游刃有餘，葉永烜分享，其實是來自源源不絕的好奇心。好奇心乃是人類被賦予的無價之寶，取之不盡，用之不竭。探索宇宙天文一輩子，後來發現宇宙70%以上是「暗能量」所組成的，這是我們看不見的，若以人生哲學來看，就象徵著歷史長河，現階段看不見，但卻無形中一直牽引著我們，要懂得從歷史中記取教訓，學習用道德與寬容來處世，才能達到「天人合一」的境地。

原文轉載於【2017-07-12/台灣好新聞】

人生七十才開始 葉永烜院士：好奇心是無價之寶

文／秘書室



理性與感性交融的智慧，葉永烜院士集科學家與藝術家於一身。劉天祺攝

集科學家與藝術家於一身的中央大學天文研究所葉永烜院士，今年歡慶七十歲生日。中大天文所於7月10日一連三天舉辦「太陽系的偶然機遇與超越」國際

學術研討會，邀請國際天文學者與會，感念葉院士對天文界之卓越貢獻。另在藝文中心舉辦「雲的兩邊」葉永烜油畫創作展，透過一幅幅真情流露的畫作，讓人看見天文學家特有的人間美畫。

研討會中國內外貴賓雲集，葉教授合作過的學術界先進好友齊聚一堂，包括三位美國國家科學院院士 Prof. Gary Zank、Prof. David Jewitt 和 Prof. Renu Malhotra。另外，卡西尼計畫相關的 Prof. Linda Spilker 和惠更斯號（Huygens）Prof. Jean-Pierre Lebreton 等，以及世界各國的科學家均遠道而來，表達祝賀之意。

榮耀輝煌 「卡西尼計畫」人類空前成就

中央大學天文所所長陳文屏在研討會開場介紹葉永烜院士，「認識葉永烜的人都知道，他富創意、精力充沛，永遠都有新點子。」中央大學校長周景揚接者表示，葉教授曾獲美國 NASA 特殊公共服務榮譽勳章、教育部終身國家講座，更於去年獲選中央研究院院士，榮耀輝煌、實至名歸。

台達電子榮譽董事長鄭崇華讚譽葉永烜是一位「好老師，也是優秀的科學家。」鄭崇華認為，人類生命短暫，藉由科學家引領我們認識宇宙的浩瀚，因此眼光要放遠。他很感謝自 2012 年起葉永烜協助選拔「台達電子年輕天文學者講座」，推展天文學研究和教育。

當初延攬葉永烜回台任教的中大前校長劉兆漢回憶，40 年前在德國與葉永烜的初次相遇也是機緣。他在國際間學術聲望及個人熱忱，促成各項重要計畫開端和豐碩成果，並引薦不少學生及年輕學者參與國際合作，功不可沒。

葉永烜 1982 年與歐美科學家共同提出的「卡西尼探測土星」跨國計畫，為人類史上首次深入探測土星的計畫，1997 年 10 月 15 日發射升空，2004 年抵達土星，預計今年 9 月 15 日任務將圓滿結束。這項長達 20 年的太空船飛行任務，共耗資 34 億美元，全球 5 千多人參與，帶來人類前所未見的天文重大成就，葉教授也成為華人《Nature》和《Science》論文發表之最。

他近期在國家地理雜誌發表的「卡西尼任務的十個突破性發現」，第一項就是泰坦(土衛六)表面有與地球類似，由甲烷驅動的水文作用。其次是土衛二南極冰殼裂縫噴發出大量水氣和冰粒子，冰殼下存在著覆蓋整個衛星的地下海洋，科學家相信那裏可能有生命的存在。

油畫創作 天文學家特有的人間美畫

葉教授除卓越科學成就之外，同時也一位業餘畫家，三十年來創作不輟。他在1987年在一個偶然的機會開始學畫，差不多同時也被診斷患有青光眼疾，但他逆光飛翔，透過不斷創作，本次在藝文中心展出的「雲的兩邊」創作個展，有五十幅作畫精彩呈現。

當中「卡西尼發射後的早晨」，紀錄1997年10月15日卡西尼太空船成功發射那一天，他徹夜未眠，等到翌日清晨，捕捉那千變萬化灑落在大西洋天空的綺麗朝陽。另有一幅畫作「看見台灣」，畫的是原住民孩童在玉山山頂高歌，期盼向導演齊柏林致敬，電影的贊助者台達電創辦人鄭崇華董事長也到場，場面溫馨。

葉教授表示，「雲的兩邊」主題來自他在一次談論中，比較西方油畫與中國水墨畫對「雲」迥然不同的處理方式，另一則來自瓊妮·米歇爾在1968年撰寫一首歌《Both sides now》中的故事。他將本次畫展獻給他在天上的母親，以及和她同樣經歷不朽的偉大女性們，不管在雲的那一邊，她們都和我們在一起。

而能在科學與藝術不同領域游刃有餘，葉永烜分享，其實是來自源源不絕的好奇心。好奇心乃是人類被賦予的無價之寶，取之不盡，用之不竭。探索宇宙天文一輩子，後來發現宇宙70%以上是「暗能量」所組成的，這是我們看不見的，若以人生哲學來看，就象徵著歷史長河，現階段看不見，但卻無形中一直牽引著我們，要懂得從歷史中記取教訓，學習用道德與寬容來處世，才能達到「天人合一」的境地。



慶祝中央大學葉永烜院士七十歲生日的國際學術研討會，各國天文學者應邀與會，感念葉院士對天文界之卓越貢獻。劉天祺攝



「雲的兩邊」葉永烜油畫創作展，透過一幅幅真情流露的畫作，讓人看見天文學家特有的人間美畫。劉天祺攝

天文學家葉永烜：兩岸學術研究環境有落差

<http://www.CRNTT.com> 2017-07-11 00:37:09



葉永烜。（中評社 黃文杰攝）

中評社桃園 7 月 11 日電（記者 黃文杰）德國籍華人天文學家、台灣中央大學天文所及太空科學所教授葉永烜接受中評社訪問表示，看看大陸砸重金力邀諾貝爾獎得主主持實驗室，提升學術研究成果，反觀台灣的大學只能拼命要“救命錢”，形成強烈對比。他也坦誠，兩岸的學術研究環境與條件確實有落差，台灣的大學國際排名不斷落後，只能說非戰之罪。

葉永烜，1947 年生，原籍廣東梅縣客家人，出生南京，澳門成長，入籍德國，1982 年與歐美科學家共同提出的“卡西尼探測土星”跨國計劃，為人類史上首次深入探測土星的計劃，現為中大天文所教授、澳門科技大學太空科學研究所特聘教授，去年榮獲“中央研究院”第 31 屆院士。

葉教授除卓越科學成就之外，同時也是一位業餘畫家，“雲的兩邊”油畫個展 10 日在校內藝文中心舉行開幕，讓外界看見天文學家特有的人間美畫，會後

接受中評社訪問。

中評社問，今年 4 月，兩位諾貝爾獎科學家實驗室同日落戶香港中文大學（深圳），包括 2013 年諾貝爾化學獎得主阿里耶·瓦謝爾教授領銜的香港中文大學(深圳)瓦謝爾計算生物研究院，以及 2012 年諾貝爾化學獎得主布萊恩·科比爾卡教授領銜的香港中文大學(深圳)科比爾卡創新藥物與轉化醫學研究院，同時在深圳成立。

葉永烜告訴中評社，（大陸）邀請諾貝爾獎得主來主持實驗室，世界各國也是如此，印象沒記錯的話，馬來亞大學也是如此，過去台灣也有這樣的作法，因為找諾貝爾獎得主，這就好像找到“高檔貨”，確實可以提升自己國家學術研究地位。

他說，若從這個角度來看，可以想想，台灣是否沒有展現企圖心？因為沒有企圖心，就不會有動力去推動這樣的學術研究，確實蠻可惜，實際上兩岸環境還是有所差異，光深圳的 GDP(生產毛額) 來看，深圳早就超越台灣，連續 4 年都領先台灣，估計 2018 深圳 GDP 會超越香港。

葉永烜說，把深圳打造世界領先的地位，過去台灣也是擁有這樣的精神，問題在於，這些學者的講法或建議，我們都沒有辦法去實現，自然會抱怨。



天文學者葉永烜，舉辦“雲的兩邊”油畫個展，獲得好評。（中評社 黃文杰攝）

他解釋，台灣不是沒有努力過，尤其爭取人才來台灣，讓大學法令鬆綁是另外一回事，畢竟找人才，都是透過大學而來，可惜的是，台灣的大學沒有錢。

葉永烜指出，參考大陸的大學作法，好比北京、上海或天津，把大筆錢留給大學去運用，讓大陸大學去找最頂尖的學者教授，台灣作法不是這樣，台灣是拼命喊多給“救命錢”，這是強烈對比。

他告訴中評社，確實佩服台灣的教授，在這樣艱苦環境依舊繳出不錯學術研究成績，如果說，政府虧待了我們，只要能夠給更多資源與鼓勵，會做出更好的成績。

葉永烜認為，兩岸的學術研究環境與條件，確實有落差，看到台灣的大學，在國際學術排名不斷落後，也只能說“非戰之罪”，這不是不努力，而是相對其他國家投入教育資源更多，造成台灣沒有競爭力。



天文學者葉永烜，舉辦“雲的兩邊”油畫個展，獲得好評。（中評社 黃文杰攝）



天文學者葉永烜，舉辦“雲的兩邊”油畫個展，獲得好評。（中評社 黃文杰攝）



天文學者葉永烜，舉辦“雲的兩邊”油畫個展，獲得好評。（中評社 黃文杰攝）

以天文學家美感創作 葉永烜中大展 50 幅油畫



葉永烜介紹其畫作。（中大提供）

2017年07月10日 20:09 [中時](#)

楊明峰



葉

永烜紀錄太空船成功發射之「卡西尼發射後的早晨」作品。(中大提供)

知名天文學家、中央大學天文所及太空科學所教授葉永烜，10日起在中大藝文中心舉辦「雲的兩邊」個人油畫創作展，以其天文學家的獨有美感，造就 50 幅藝術創作，包括向已故導演齊柏林致敬的「看見台灣」，還有紀錄無人飛行器成功發射之「卡西尼發射後的早晨」等。

70 歲德國籍華人天文學家葉永烜，1982 年時與歐美科學家共同提出「卡西尼探測土星」跨國計畫，這項人類史上首次深入探測土星的計畫，其無人太空飛行器，1997 年 10 月 15 日發射升空，2004 年抵達土星，預計今年 9 月 15 日任務結束。

葉永烜對天文界的重大貢獻，因此曾獲美國 NASA 特殊公共服務榮譽勳章、台灣教育部終身國家講座、中央研究院院士，也成為華人《Nature》和《Science》論文發表之最。

適逢葉永烜今年 70 歲，中大天文所 10 日起一連三天舉辦「太陽系的偶然機遇與超越」國際學術研討會，邀請國際天文學者與會。另在藝文中心舉辦「雲的兩邊」葉永烜油畫創作展。

縱使罹患青光眼、30 年來仍創作不輟的葉永烜指出，曾比較西方油畫與中國水墨畫對「雲」迥然不同的處理方式，加上歌曲《Both sides now》中的故事，成

就這次畫作「雲的兩邊」之主題。他將本次畫展獻給他在天上的母親，以及和她同樣經歷不朽的偉大女性們，「不管在雲的那一邊，她們都和我們在一起」。

「卡西尼發射後的早晨」畫出大西洋天空的綺麗朝陽，係葉永烜紀錄 1997 年 10 月 15 日卡西尼太空船成功發射當天，徹夜未眠至翌日清晨，看見的美景。而另一幅畫作「看見台灣」，畫出台灣原住民孩童在玉山山頂高歌，以此向齊柏林致敬。

人生七十才開始 葉永烜：好奇心是無價寶

2017/07/11 聯合財經網

經濟日報 曹松清

集科學家與藝術家於一身的中央大學天文研究所葉永烜院士，今年歡慶 70 歲生日。

中大天文所 10 日舉辦一連三天的「太陽系的偶然機遇與超越」國際學術研討會，邀請國際天文學者與會，感念葉永烜對天文界之卓越貢獻。另在藝文中心舉辦「雲的兩邊」葉永烜油畫創作展，透過一幅幅真情流露的畫作，讓人看見天文學家特有的人間美畫。

研討會中國內外貴賓雲集，葉永烜合作過的學術界先進好友齊聚一堂，包括三位美國國家科學院院士 Prof. Gary Zank、Prof. David Jewitt 和 Prof. Renu Malhotra。另外，卡西尼計畫相關的 Prof. Linda Spilker 和惠更斯號（Huygens）Prof. Jean-Pierre Lebreton 等，及世界各國的科學家均遠道而來，表達祝賀之意。

榮耀輝煌 「卡西尼計畫」人類空前成就

中央大學天文所所長陳文屏在研討會開場介紹葉永烜院士，「認識葉永烜的人都知道，他富創意、精力充沛，永遠都有新點子。」中央大學校長周景揚接者表示，葉教授曾獲美國 NASA 特殊公共服務榮譽勳章、教育部終身國家講座，更於去年獲選中央研究院院士，榮耀輝煌、實至名歸。

台達電子榮譽董事長鄭崇華讚譽葉永烜是一位「好老師，也是優秀的科學家。」鄭崇華認為，人類生命短暫，藉由科學家引領我們認識宇宙的長遠浩瀚，應更懂得珍惜，不該短視近利。他很感謝自 2012 年起葉永烜協助選拔「台達電子年輕天文學者講座」，推展天文學研究和教育。

當初延攬葉永烜回台任教的中大前校長劉兆漢回憶，40 年前在德國與葉永烜的初次相遇也是機緣。他在國際間學術聲望及個人熱忱，促成各項重要計畫開端和豐碩成果，並引薦不少學生及年輕學者參與國際合作，功不可沒。

葉永烜 1982 年與歐美科學家共同提出的「卡西尼探測土星」跨國計畫，為人類史上首次深入探測土星的計畫，1997 年 10 月 15 日發射升空，2004 年抵達土星，預計今年 9 月 15 日任務將圓滿結束。這項長達 20 年的太空船飛行任務，共耗資 34 億美元，全球 5000 多人參與，帶來人類前所未見的天文重大成就，葉教授也成為華人《Nature》和《Science》論文發表之最。

他近期在國家地理雜誌發表的「卡西尼任務的十個突破性發現」，第一項就是泰坦(土衛六)表面有與地球類似，由甲烷驅動的水文作用。第二項土衛二南極冰殼裂縫噴發出大量水氣和冰粒子，冰殼下存在著覆蓋整個衛星的地下海洋，科學家相信那裏可能有生命的存在。

油畫創作 天文學家特有的人間美畫

葉永烜除卓越科學成就之外，同時也一位業餘畫家，三十年來創作不輟。他在 1987 年在一個偶然的機會開始學畫，差不多同時也被診斷患有青光眼疾，但他逆光飛翔，透過不斷創作，這次在藝文中心展出的「雲的兩邊」創作個展，有五十幅作畫精彩呈現。

當中「卡西尼發射後的早晨」，紀錄 1997 年 10 月 15 日卡西尼太空船成功發射那一天，他徹夜未眠，等到翌日清晨，捕捉那千變萬化灑落在大西洋天空的綺麗朝陽。另有一幅畫作「看見台灣」，畫的是原住民孩童在玉山山頂高歌，期盼向導演齊柏林致敬，電影的贊助者台達電創辦人鄭崇華董事長也到場，場面溫馨。

葉永烜表示，「雲的兩邊」主題來自他在一次談論中，比較西方油畫與中國水墨畫對「雲」迥然不同的處理方式，另一則來自瓊妮·米歇爾在 1968 年撰寫一首歌《Both sides now》中的故事。他將這次畫展獻給他在天上的母親，以及和她同樣經歷不朽的偉大女性們，不管在雲的那一邊，她們都和我們在一起。

而能在科學與藝術不同領域游刃有餘，葉永烜分享，其實是來自源源不絕的好奇心。好奇心乃是人類被賦予的無價之寶，取之不盡，用之不竭。探索宇宙天文一輩子，後來發現宇宙 70%以上是「暗能量」所組成的，這是我們看不見的，若以人生哲學來看，就象徵著歷史長河，現階段看不見，但卻無形中一直牽引著我們，要懂得從歷史中記取教訓，學習用道德與寬容來處世，才能達到「天人合一」的境地。

原文轉載自【2017-07-11/聯合財經網/經濟日報】

2017 年春季「年輕天文學者獎」得主 文森博士訪台

文／天文所



2017 年

春季獲獎者為德國航空太空中心的文森博士於 24 日訪台。彭國瑛攝

彗星是太陽系最古老、最原始的天體。由國立中央大學與台達電子文教基金會共同頒發的「年輕天文學者講座」，2017 年春季獲獎者為德國航空太空中心的文森博士，於 4 月 24 日起來台接受頒獎，並進行演講，說說前往彗星探險的故事。

此講座表彰國際上在天文學領域有卓越表現之年輕學者，邀請具潛力的學術菁英來台與國內學界互動，並啟發年輕心靈。講座獎金由台達電子文教基金會提供，由國際甄選委員會推薦候選人，並由中央大學天文所執行邀訪活動。獲獎者將在中央大學天文所發表學術演講，與國內學者進行交流，另在台達電子文

教基金會，以及台中一中進行科普演講，讓民眾與學生接觸最前沿的天文課題，並藉與講者互動景仰其學術風範。

彗星由冰和少量岩石組成，它們像化石般紀錄了太陽系初期發生的過程。地球現在生意盎然，很有可能歸功於年幼時期，受到彗星撞擊而帶來有機分子與大量水分子。人類觀察彗星數千年，古代認為不祥之兆，現在除了利用望遠鏡觀測，還派遣太空船就近研究，甚至登陸勘查。2014 年開始「羅賽塔」太空船伴隨著彗星 67P，就近觀察彗星距離太陽由遠而近的變化，以便探討彗核與彗髮、彗尾的交互關連。有如考古學家利用大英博物館中「羅賽塔石碑」，比對已知的古希臘文來破解神秘的象形文字，以瞭解古埃及文化。此任務以「羅賽塔」為名，便是希望透過彗星為基石，來解答太陽系與行星、生命形成的迷團。本季年輕天文學者講座，將由親身參與羅賽塔太空任務的文森博士闡述這解謎的過程。

強·巴蒂斯特·文森 (Jean-Baptiste Vincent) 博士於 2009 年取得德國馬克斯普朗克研究所天文物理博士學位，之後繼續從事博士後研究。2010 年起擔任 ESA 羅賽塔任務可見光與紅外相機(OSIRIS)共同主持人之一，以及 NASA 黎明號(Dawn mission)的研究人員。2016 年底起，文森博士為德國航空太空中心研究員。

文森博士的學術演講，講題為” Rosetta’ s journey to the origin of the Solar System”，時間與場所分別為 (1) 4 月 24 日（週一）下午四點，在東華大學理工一館理一講堂；(2) 4 月 25 日（週二）下午兩點，在台達電子台北總公司（台北市內湖路陽光街 256 號）；(3) 5 月 5 日（週五）下午兩點，在中央大學天文所（健雄館 1013 室）；(4) 5 月 6 日（週六）上午九點，在台中一中（台中市育才街 2 號）；其中第二場與第四場備有中文導讀，歡迎參加。



校長、天文所所長與文森博士等人合影留念。彭國瑛攝

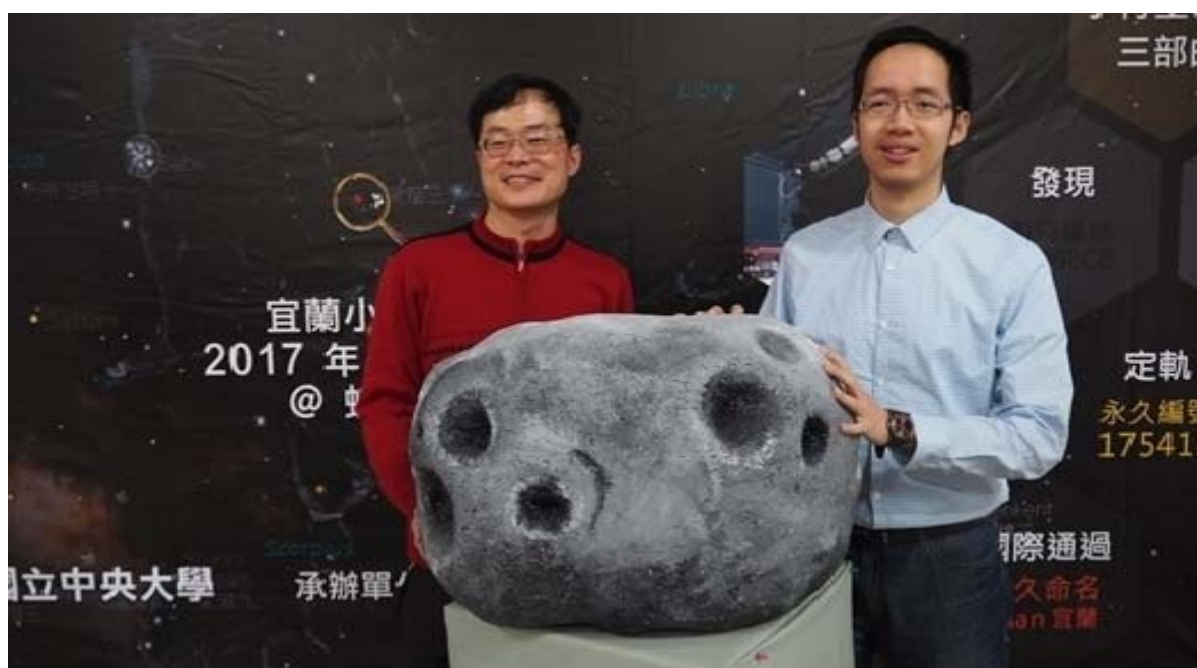


一行人相談甚歡，文森博士將於 5/5 和 5/6 舉辦兩場學術演講。彭國瑛攝

鹿林天文台發現小行星，「宜蘭」躋身宇宙明星之列

作者 [TechNews](#) | 發布日期 2017 年 03 月 06 日 16:30 | 分類 [天文](#) , [自然科學](#)

[學](#) [Follow](#)



國立中央大學鹿林天文台發現的第 175411 號小行星，經國際天文學聯合會（IAU/CSBN）審查通過，命名為「Yilan」，讓宜蘭晉升宇宙明星之一！

宜蘭縣長吳澤成 3 日與國立中央大學校長周景揚共同發表此項天文好消息，正式介紹「Yilan」小行星誕生。

吳縣長表示，宜蘭縣「幸福宜蘭」縣政願景以「生態」、「創意」及「友善」為主軸，縣府每年舉辦「童玩節」活動，都吸引數十萬名親子參與，如今在浩瀚星河裡出現一顆宜蘭小行星，更振奮宜蘭兒童。

周校長說，能與同為中大校友的吳縣長，攜手見證家鄉宜蘭通過小行星命名，意義非凡。而位在玉山國家公園的中大鹿林天文台，不僅是國內最重要的光學天文基地，也是亞洲發現小行星最活躍的地方；這顆「Yilan」是中大以台灣縣市命名的小行星之一。天文所所長陳文屏補充，中大開始計畫性觀測小行星，始於 2006 年啟動的「鹿林巡天計畫（LUlin Sky Survey, LUSS）」，此計畫於

3 年間（2006 年～2009 年）共發現八百多顆小行星、1 顆近地小行星及 1 顆彗星，成效卓著。

「Yilan」小行星發現者鹿林天文台台長林宏欽及加州理工學院葉泉志博士（見首圖）也出席發表會。他們說宜蘭小行星的大小約在 1-3 公里之間，繞行太陽一圈 3.78 年（軌道週期），離太陽最近時（近日點）為 3 億公里，最遠時（遠日點）為 4.2 億公里。這顆「Yilan」是 2006 年 8 月 12 日被發現，當時是在魔羯座附近，目前 2017 年 3 月位置則在蛇夫座。宜蘭繼 1992 年辦理區運會之後，將於今年再度承辦全國運動會，適逢「Yilan」小行星第三度繞行至它被發現的觀測點，似也為「2017 全運會競戰宜蘭」帶來了全宇宙的祝福。

其實不僅中央大學鹿林天文台在尋找小行星，在堅持環保立縣的宜蘭，許多地方例如南澳、大同及太平山，都具備空氣品質佳與低光害等絕佳的天文觀測條件。近年來，宜蘭縣各級學校及社團亦積極發展天文教育及觀星活動，其中，羅東高中更成立天文社，由老師帶著學生積極進行各項天文觀測活動，於 2012 年羅高參與國際天文搜尋聯盟主辦之搜尋小行星活動時，有 3 名學生更發現 5 顆小行星，這也締造當時國內高中學生及高中天文社團觀測並發現小行星最多的紀錄。

「Yilan」小行星的發現讓宜蘭在宇宙中也佔有一席之地，不僅進一步開啟了宜蘭縣各級學校的學生探索天文奧秘的興趣，也為學子心中點亮一盞明燈，當他們探索浩瀚宇宙之際，都能胸懷寰宇卻時刻不忘宜蘭這方故土。

天文小知識——小行星命名

小行星是目前各類天體中唯一可以由發現者進行命名並得到世界公認的天體。發現小行星後，需先通報國際小行星中心（Minor Planet Center, MPC）；經初步確認後，MPC 會按發現時的年份與順序配予暫時編號。當該小行星至少 4 次在回歸中被觀測到，軌道又可以精確測定時，它就會得到一個永久編號。一旦取得永久編號，發現者便擁有該小行星的永久命名權。但因提出的名稱必須經過國際天文學聯合會（IAU）的小天體命名委員會（CSBN）審查通過並公告生效，所以從發現到命名確認往往需時數年。

（首圖來源：[中央大學](#)）

中大天文所發現小行星命名"宜蘭 YILAN"

2017/03/08 人間衛視

記者：吳玉茹 賴志慶 宜蘭報導

一顆由中央大學天文所老師及加州理工學院博士共同發現的小行星，經國際天文學聯合會通過命名，取名為『宜蘭 Yilan』。除了因為中央大學校長周景揚是宜蘭人之外，更為了鼓勵學生參與天文探索，宜蘭縣政府與國立中央大學共同發表這項天文盛事，激發更多台灣學生探索天文奧秘的興趣。

在宇宙運行的星星中，只要是小行星被地球人類新發現，就可以讓發現者命名。

這顆由中央大學天文所鹿林天文台台長林宏欽及加州理工學院葉泉志博士發現的 175411 號小行星，是 2009 年在中央大學位在玉山上的天文站所探察到的，經過漫長的國際命名程序，獲得國際天文學聯合會通過命名為『宜蘭 Yilan』。

中央大學天文研究在國際間相當富有盛名，宇宙中的行星已經有 20 多顆，是中央大學團隊所發現命名，這次命名為『宜蘭』，希望啟發台灣學生多多觀測天文。

宜蘭縣政府與國立中央大學共同發表這項天文盛事，讓更多人引發探索天文奧秘的興趣，鼓勵孩子探索浩瀚宇宙。

原文轉載自【2017-03-08/人間衛視】

等了 11 年 這顆小行星叫宜蘭

電子報紙

【本報宜蘭訊】宇宙間成千上萬顆星系，從今起有一顆叫「宜蘭」。十一年前中央大學天文台發現了編號



宜蘭成為宇宙間小行星的名字，令學生很興奮。圖／張芮瑜

175411 號小行星，經過長期觀測確認它是新的天體後，昨天團隊決定將之命名為「宜蘭」，表示對宜蘭土地的心意。宜蘭縣長吳澤成代表接下這份珍貴的禮物，直呼很高興宜蘭從此在宇宙間占了一席之地。

位於玉山國家公園的中央大學鹿林天文台是國內重要天文基地，也是亞洲發現小行星最活躍的地方。二〇〇六年啟動為期三年的「鹿林巡天計畫」（LUSS），期間內共發現八百多顆小行星、一顆近地行星和一顆彗星，成效卓越。

二〇〇六年八月十二日天文台台長林宏欽和當時只是高中生的葉泉志，在天文望遠鏡中發現宇宙中亮眼小行星，備感興奮，通報國際小行星中心後，左等右盼，小行星中心總算被確認了軌道、獲得永久編號 175411。

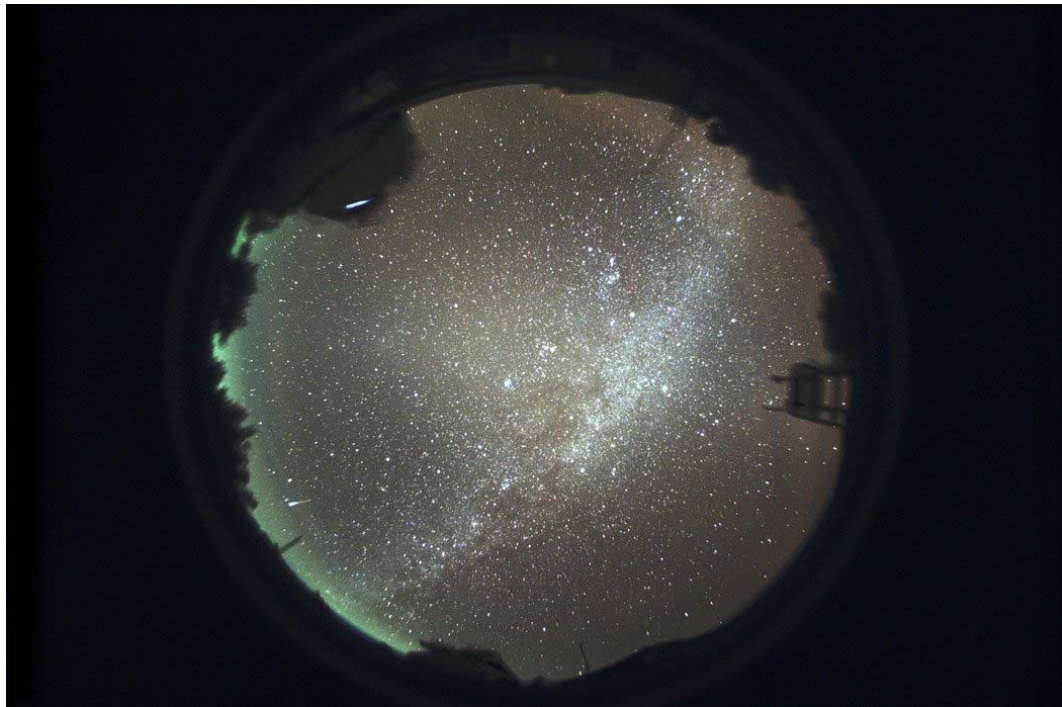
「我們已經發現八百多顆，目前命名了一百多顆。」林宏欽說，小行星是目前各類天體中唯一能由發現者命名的天體，經過日積月累的觀察紀錄，他和如今已經是加州理工學院的博士葉泉志，決定將滿天星星中的其中一顆，獻給宜蘭，就此定名為宜蘭（Yilan）。

中央大學天文所昨天上午在宜蘭成功國小辦理小行星發表會，同為宜蘭人的中央大學校長周景揚也到場；宜蘭縣長吳澤成接下大禮，感謝他們以這麼特別的方式愛台灣、愛宜蘭，同時鼓勵在場的小學生，也能勇於探索未知的宇宙。

林宏欽說，他們發現的小行星，大多以台灣人事物命名，因此不少縣市如桃園、嘉義、南投、屏東等都已成為小行星名稱；對台灣有貢獻的、值得永誌不忘的人物，他們也曾以此為名，如陳樹菊。未來也希望持續以這種方式回饋台灣土地。

哈囉 E.T. 歡迎來到宜蘭…宇宙還有哪些台灣星？

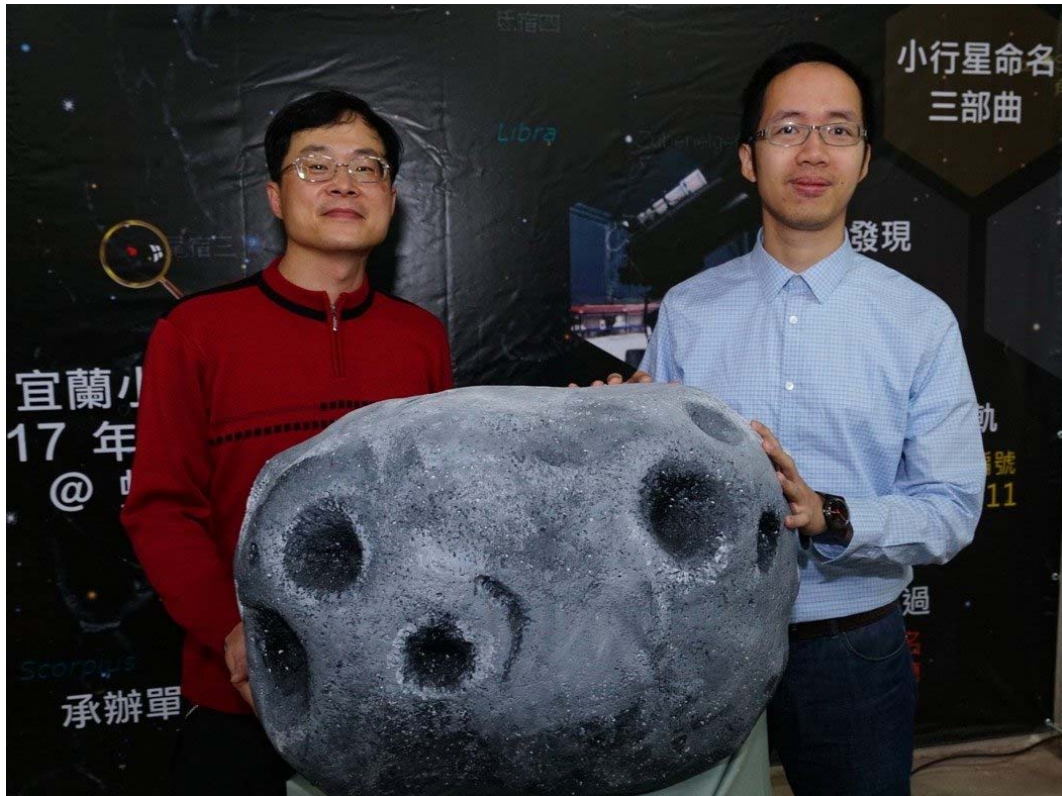
2017-03-04 09:00:00 聯合報 記者張芮瑜／宜蘭報導



鹿林天文台位於鹿林前山，臨近玉山國家公園處，庭院可以望見美麗的夜空。圖／中央大學天文所鹿林天文台提供

宇宙間無數星星，從昨天起有一顆叫「宜蘭」。11年前中央大學天文研究所發現編號 175411 號小行星，經長期觀測確認為新的天體，昨天決定命名為「宜蘭」，向這塊好山好水、堅持環保的土地致敬。

中大天文所昨在宜蘭縣成功國小辦理小行星發表會，同為宜蘭人的校長周景揚，將這顆小行星當成「禮物」送給宜蘭縣政府。代理縣長吳澤成說，從此「宜蘭在宇宙之中也占有一席之地！」感謝中大以這麼特別的方式愛台灣、愛宜蘭。



行星發現者葉泉志（右）、林宏欽將小行星命名為宜蘭。 記者張芮瑜／攝影

● 仰望「宜蘭」星，就在蛇夫座

時空回到 2006 年 8 月 12 日，中大鹿林天文台台長林宏欽和當時只是高中生的葉泉志，在天文望遠鏡中發現宇宙中亮眼小行星，備感振奮，通報國際小行星中心後，左等右盼，小行星中心總算被確認軌道、獲得永久編號 175411。

林宏欽說，當時是宜蘭小行星距離地球最近的一次，因此光芒才會被天文望遠鏡這一端的他們看見；經計算，其軌道周期為 3.78 年，每年只有一次機會較靠近地球，目前位置則在蛇夫座旁。如今想起，他們仍然對這緣分感到振奮。



中央大學天文所將 2006 年發現的小行星命名為「宜蘭」，昨天在宜蘭成功國小舉行命名儀式，令宜蘭學子十分振奮。 記者張芮瑜／攝影

●小行星命名三部曲：發現、定軌、國際通過

小行星是目前唯一可由發現者命名的天體。發現後必須先通報國際小行星中心（MPC）暫時編號，且至少 4 次在回歸中被觀測到，軌道又可以精確測定，才能得到永久編號，發現者便擁有該小行星的永久命名權，經小天體命名委員會（CSBN）審查通過並公告才生效。

林宏欽說，觀測研究員每日觀測星體的移動軌跡，每發現「疑似新的星」便記錄時間、位置等數據，兩三天後得出初步數據，計算軌道後再比對資料庫並通報，但外國很多人也在「追星」，「因此每顆星都得來不易，若晚了一步，便是幫別人的星做白工。」

● 這些小星星 與台灣有關

國際編號

永久命名

中文譯名

145534

Jhongda

中大小行星

申請
理由

台灣首次命名，中央大學天文所發現，中央大學簡稱中大



▲ 中央大學位於中壢，圖為中大正門景觀。

國際編號

永久命名

中文譯名

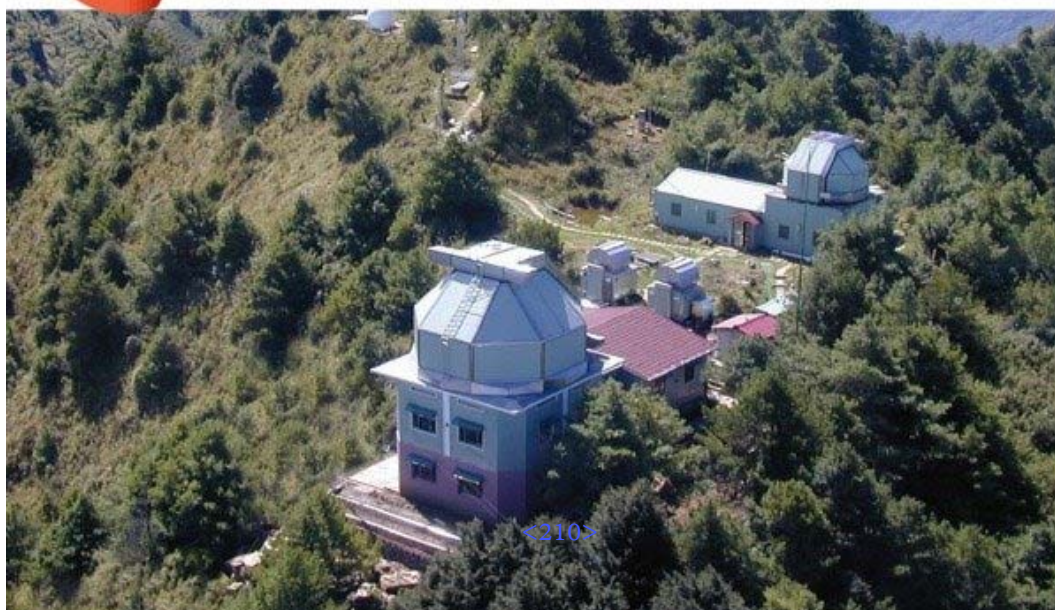
147918

Chiayi

嘉義小行星

申請
理由

首度以台灣縣市命名，因中大在嘉義鹿林設天文台為研究重鎮



位於玉山國家公園的中央大學鹿林天文台是國內重要天文基地，2006 年啟動為期 3 年的鹿林巡天計畫(LUSS)，期間內共發現 800 多顆小行星、1 顆近地行星和 1 顆彗星，目前命名了 100 多顆，成效卓越，國際看得見。

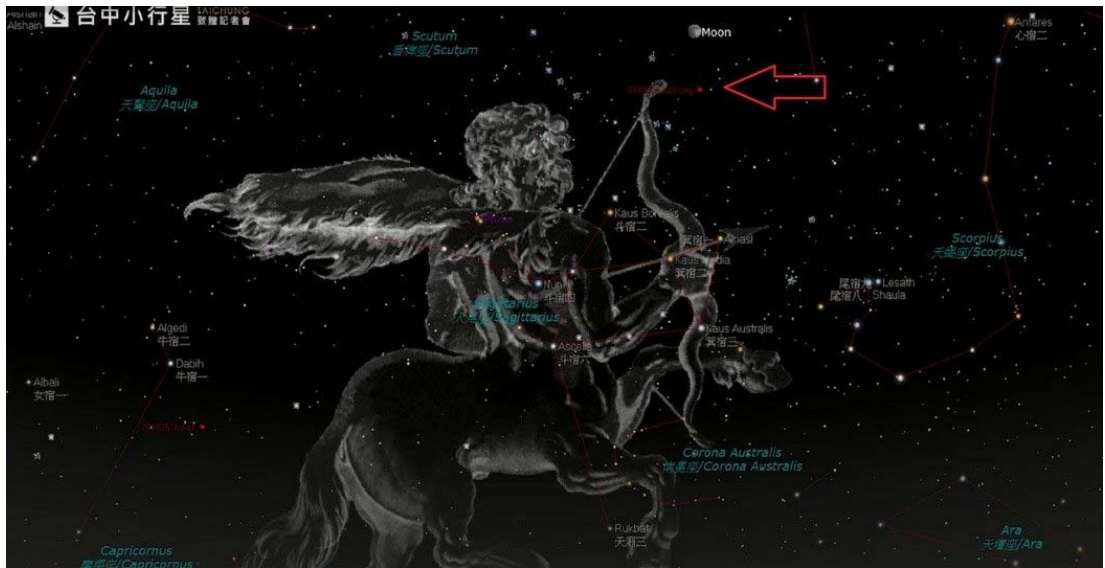
林宏欽說，他們發現的小行星，大多以台灣人事物命名，因此不少縣市如嘉義、台中、屏東等都已成為小行星名稱；對台灣有貢獻的、值得永誌不忘的人物，如陳樹菊、鄭崇華等，也被命名過。未來也希望持續以這種方式回饋台灣土地，「讓每個地方都有自己的一顆星」。



小行星是否掠過地球，人們始終充滿想像。圖／報系資料照

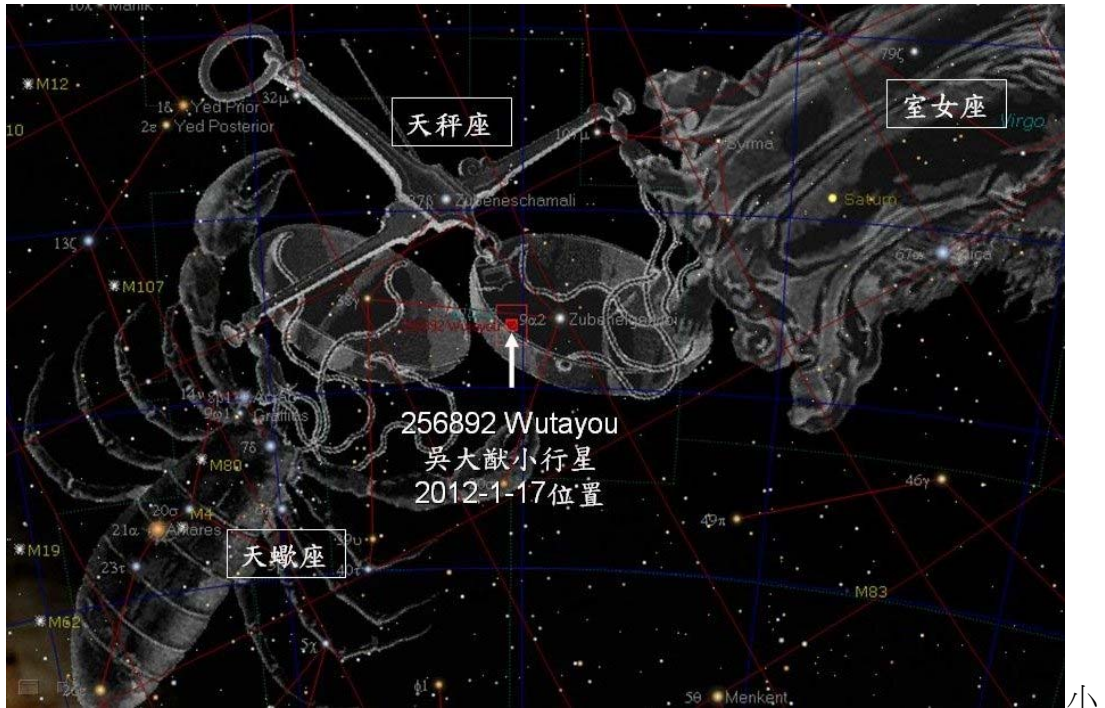
● 浩瀚星空，追星不易

彗星、隕石常成為電影題材，每次有小行星與地球擦身而過，也總引起人們好奇，但小行星的面貌常不如大家想像，在浩瀚天際中也不易搜尋。



「台中」小行星（紅色箭頭指處紅點）2015 年出現在台中市南方天空的人馬座方向。圖／報系資料照

中大天文所表示，體積大的小行星才會是球體，如地球；體積小的小行星因常受碰撞、擠壓，多為不規則狀，充滿坑洞；小行星較易觀測位置也不同，如「台中」小行星在南方天空的人馬座方向，小行星「吳大猷」則在天秤座附近，「都很小」，須專業天文望遠鏡才能發現。



行星「吳大猷」2012 年運行至天秤座附近。圖／中央大學提供

天上的星星叫「宜蘭」小學生做見證

2017/03/04 HiNet 新聞

「宜蘭也在宇宙中占有一席之地！」中央大學今天在宜蘭縣成功國小，舉行第 175411 號小行星命名發布會，在小學生的見證下，小行星正式定名為「宜蘭」。宜蘭縣代理縣長吳澤成盼開啟學生探索天文奧秘的興趣，鼓勵孩子持續探索浩瀚的宇宙，也不要忘了宜蘭這方故土。

175411 號小行星在 2006 年 8 月 12 日由中央大學天文所鹿林天文台台長林宏欽、加州理工學院博士葉泉志發現的，這顆位於太陽系小行星帶的小行星，每 3.78 年才會繞行太陽一次。

發現者決定將小行星命名為宜蘭(Yilan)，上呈國際天文學聯合會(IAU CSBN)後去年才通過，今年是宜蘭小行星被發現後，第三度運行來到被發現者觀察到的位置，吳澤成與同為宜蘭人的中央大學校長周景揚，認為「時機對了」，決定共同發表這項天文好消息，宣布「宜蘭」在宇宙中也占有一席之地。

周景揚說，玉山國家公園的中大鹿林天文台是國內重要天文基地，也是亞洲發現小行星最活躍的地方。

天文所所長陳文屏表示，中大開始計畫性觀測小行星，此計畫在三年間共發現 800 多顆小行星、一顆近地小行星及一顆彗星，這是中大以縣市命名的小行星之一，命名為宜蘭，讓它與眾不同。

星球命名 政治人物 NO

陳文屏說，命名星球必須有其意義，人名、地名都可以，唯獨政治人物不行，台灣的縣市如嘉義、南投、桃園、中壢、苗栗等都曾採用過，屏東是上個被命名的縣市，慈濟和雲門也曾入名。

此外，以人名命名的小行星有鄧雨賢、李國鼎、鄭崇華等，之前還有兩岸四名天文愛好者共同發現的小行星，以知名歌手周杰倫命名。

原文轉載自【2017-03-04 /聯合新聞網】

〈北部〉小行星命名 「宜蘭」喜入星河

2017-03-04

〔記者江志雄／宜蘭報導〕宜蘭縣政府與國立中央大學，昨在羅東鎮成功國小舉辦第一七五四一一號宜蘭小行星發布會，「宜蘭」名字拜小行星所賜，進入浩瀚星河。

二〇〇六年八月，中央大學天文所鹿林天文台長林宏欽、加州理工學院葉泉志博士，在魔羯座附近發現一顆小行星，決定命名為宜蘭（Yilan）；經過多方認證，去年才獲國際天文學聯合會審核通過，校長周景揚、同為中大校友的代理縣長吳澤成，昨共同發表這個好消息；吳澤成鼓勵小朋友充實自我，持續探索天文奧秘。

宜蘭小行星繞行太陽一圈需要三·七八年，目前位置在蛇夫座；中大天文所長陳文屏說，星球命名排除政治人物，通常採地名、人名，南投、嘉義、桃園、屏東等十多個縣市陸續被採用，希望每個縣市至少有一個專屬名稱。

宜蘭縣空氣品質佳、低光害，具有極佳天文觀測條件，南澳、大同、太平山都是觀星好去處；近年縣內各級學校天文社團如雨後春筍，例如國立羅東高中成立天文社，老師帶領學生四處觀測，二〇一二年國際天文搜索聯盟主辦的搜尋小行星活動，羅高有三名學生觀測到五顆小行星，締造當年高中生發現小行星最多的紀錄。

國際天文學聯合會通過宜蘭小行星命名



宜蘭小行星（175411 號小行星）。（曾漢東／大紀元）

【大紀元 2017 年 03 月 03 日訊】（大紀元記者曾漢東台灣宜蘭報導）國立中央大學鹿林天文台發現的第 175411 號小行星，經國際天文學聯合會（IAU/CSBN）審查通過，命名為「Yilan」，讓宜蘭晉升宇宙明星之一。宜蘭縣長吳澤成 3 日與國立中央大學校長周景揚共同發表此項天文好消息，正式介紹「Yilan」小行星誕生。

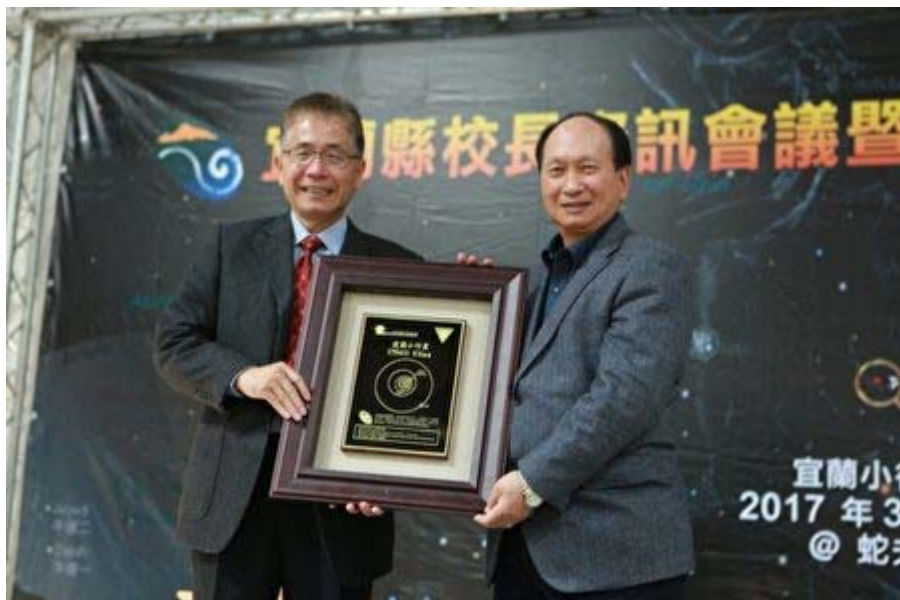
吳縣長表示，宜蘭縣「幸福宜蘭」縣政願景以「生態」、「創意」及「友善」為主軸，縣府每年舉辦「童玩節」活動，都吸引數十萬名親子參與，如今在浩瀚星河裡出現一顆宜蘭小行星，更振奮宜蘭兒童。

周校長說，能與同為中大校友的吳縣長，攜手見證家鄉宜蘭通過小行星命名，意義非凡。而位在玉山國家公園的中大鹿林天文台，不僅是國內最重要的光學天文基地，也是亞洲發現小行星最活躍的地方；這顆「Yilan」是中大以台灣縣市命名的小行星之一。天文所所長陳文屏補充，中大開始計畫性觀測小行星，始於 2006 年啟動的「鹿林巡天計畫（Lulin Sky Survey, LUSS）」，此計畫於三年間（2006 年～2009 年）共發現 800 多顆小行星、1 顆近地小行星及 1 顆彗星，成效卓著。



2006年8月12日中央大學天文所鹿林天文台台長林宏欽（左）及加州理工學院葉泉志博士（右）發現「Yilan」小行星。（曾漢東／大紀元）

「Yilan」小行星發現者鹿林天文台台長林宏欽及加州理工學院葉泉志博士也出席發表會。林宏欽說宜蘭小行星的大小約為1~3公里，繞行太陽一圈3.78年（軌道週期），離太陽最近時（近日點）為3億公里、最遠時（遠日點）為4.2億公里。這顆「Yilan」是2006年8月12日被發現，當時是在魔羯座附近，目前2017年3月位置則在蛇夫座。



宜蘭縣長吳澤成（右）與國立中央大學校長周景揚（左）正式介紹「Yilan」小行星誕生。（曾漢東／大紀元）

宜蘭繼 1992 年辦理區運會之後，將於今年再度承辦全國運動會，適逢「Yilan」小行星第三度遠行至它被發現的觀測點，似也為「2017 全運會競戰宜蘭」帶來了全宇宙的祝福。



宜蘭縣政府吳澤成縣長（右）致贈紀念品給中央大學周景揚校長（左）。（曾漢東／大紀元）

「Yilan」小行星的發現讓宜蘭在宇宙中也占有一席之地，不僅進一步開啟了宜蘭縣各級學校的學生探索天文奧秘的興趣，也為學子心中點亮一盞明燈，當他們探索浩瀚宇宙之際，都能胸懷寰宇卻時刻不忘宜蘭這方故土。



「古第」（右）與[國際天文學聯合會](#)通過宜蘭小行星命名，參加來賓合影。（曾漢東／大紀元）



成功國小美術班小朋友畫出他們心目中的「宜蘭小行星」。(曾漢東／大紀元)

鹿林天文台發現小行星命名「宜蘭」

2017/03/03 中央廣播電台

記者 陳國維 / 報導

國立中央大學校長周景揚今天(3日)與宜蘭縣代理縣長吳澤成共同宣布，由中央大學鹿林天文台發現的第175411號小行星，經國際天文學聯合會(IAU/CSBN)審查通過，命名為「Yilan」，讓「宜蘭」也在宇宙中占有一席之地。

「Yilan」小行星發現者鹿林天文台台長林宏欽及美國加州理工學院博士葉泉志在發表會上表示，「宜蘭」小行星的大小約在1到3公里之間，繞行太陽一圈要3.78年，離太陽最近時為3億公里，最遠時為4.2億公里。這顆「Yilan」是在2006年8月12日被發現，當時是在魔羯座附近，目前的位置在蛇夫座。

周景揚說，能與同為中央大學校友的吳澤成，共同見證家鄉宜蘭通過小行星命名，意義非凡，相信也將進一步開啟宜蘭學子探索天文奧秘的興趣。

原文轉載自【2017-03-03 /中央廣播電台】

鹿林天文台發現小行星 「宜蘭」躋身宇宙明星之列

文／宜蘭縣政府、中大秘書室



周景揚校長與校友吳澤成縣長，一同見證家鄉「宜蘭」的榮耀。林宏欽攝。

國立中央大學鹿林天文台發現的第 175411 號小行星，經國際天文學聯合會（IAU/CSBN）審查通過，命名為「Yilan」，讓宜蘭晉升宇宙明星之一！

宜蘭縣長吳澤成 3 日與國立中央大學校長周景揚共同發表此項天文好消息，正式介紹「Yilan」小行星誕生。

吳縣長表示，宜蘭縣「幸福宜蘭」縣政願景以「生態」、「創意」及「友善」為主軸，縣府每年舉辦「童玩節」活動，都吸引數十萬名親子參與，如今在浩瀚星河裡出現一顆宜蘭小行星，更振奮宜蘭兒童。

周校長說，能與同為中大校友的吳縣長，攜手見證家鄉宜蘭通過小行星命名，意義非凡。而位在玉山國家公園的中大鹿林天文台，不僅是國內最重要的光學天文基地，也是亞洲發現小行星最活躍的地方；這顆「Yilan」是中大以台灣縣市命名的小行星之一。天文所所長陳文屏補充，中大開始計畫性觀測小行星，始於 2006 年啟動的「鹿林巡天計畫（LUlin Sky Survey，LUSS）」，此計畫於三年間（2006 年～2009 年）共發現 800 多顆小行星、1 顆近地小行星及 1 顆彗星，成效卓著。

「Yilan」小行星發現者鹿林天文台台長林宏欽及加州理工學院葉泉志博士也出席發表會。他們說宜蘭小行星的大小約在 1-3 公里之間，繞行太陽一圈 3.78 年（軌道週期），離太陽最近時（近日點）為 3 億公里，最遠時（遠日點）為 4.2 億公里。這顆「Yilan」是 2006 年 8 月 12 日被發現，當時是在魔羯座附近，目前 2017 年 3 月位置則在蛇夫座。宜蘭繼 1992 年辦理區運會之後，將於今年再度承辦全國運動會，適逢「Yilan」小行星第三度繞行至它被發現的觀測點，似也為「2017 全運會競戰宜蘭」帶來了全宇宙的祝福。

其實不僅中央大學鹿林天文台在尋找小行星，在堅持環保立縣的宜蘭，許多地方例如南澳、大同及太平山，都具備空氣品質佳與低光害等絕佳的天文觀測條件。近年來，宜蘭縣各級學校及社團亦積極發展天文教育及觀星活動，其中，羅東高中更成立天文社，由老師帶著學生積極進行各項天文觀測活動，於 2012 年羅高參與國際天文搜尋聯盟主辦之搜尋小行星活動時，有三位學生更發現五顆小行星，這也締造當時國內高中學生及高中天文社團觀測並發現小行星最多的紀錄。

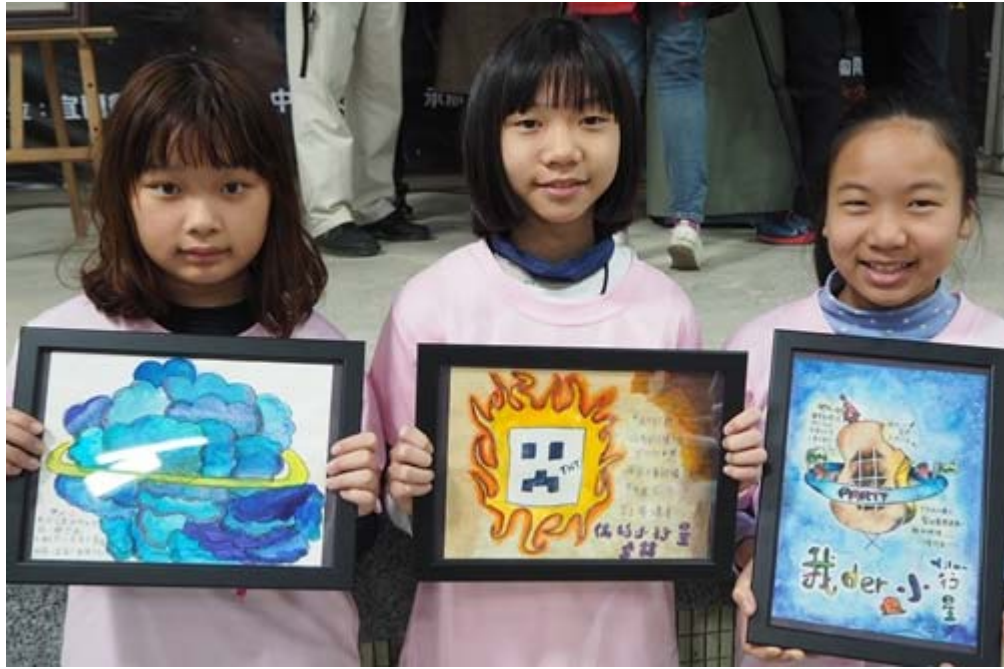
「Yilan」小行星的發現讓宜蘭在宇宙中也占有一席之地，不僅進一步開啟了宜蘭縣各級學校的學生探索天文奧秘的興趣，也為學子心中點亮一盞明燈，當他們探索浩瀚宇宙之際，都能胸懷寰宇卻時刻不忘宜蘭這方故土。

※天文小知識-有關小行星命名

小行星是目前各類天體中唯一可以由發現者進行命名並得到世界公認的天體。發現小行星後，需先通報國際小行星中心（Minor Planet Center，MPC）；經初步確認後，MPC 會按發現時的年份與順序配予暫時編號。當該小行星至少 4 次在回歸中被觀測到，軌道又可以精確測定時，它就會得到一個永久編號。一旦取得永久編號，發現者便擁有該小行星的永久命名權。但因提出的名稱必須經過國際天文學聯合會（IAU）的小天體命名委員會（CSBN）審查通過並公告生效，所以從發現到命名確認往往需時數年。



宜蘭小行星發現者林宏欽台長及葉泉志博士，與成功國小自製的小行星想像模型合影。邱燕淇攝。



宜蘭成

功國小美術班的學生，發揮想像以畫筆勾勒出心目中的宜蘭小行星，巧思十足。邱燕淇攝。

側寫／80 歲鄭崇華熱愛天文 聊星星一秒變小學生



▲年近 70 的鄭崇華一看到博物館新奇的展品，就像個小孩不停發問。（圖／台達電提供）

記者周康玉／台中報導

台達攜手台中科博館打造「物理世界」，除了耗資 3000 萬打造，甚至把台達產線上最尖端的科技搬到展區，兩造的結盟，其實源起於創辦人鄭崇華和台中科博館館長深厚的淵源。

原來，兩人是「以天文會友」，本身就是天文背景出生的孫維新說，20 年前兩人就認識了，[在孫維新眼中這位擁有千億身家的科技創辦人，不僅是個令人無比尊敬的長者，還是個「心裡住著一顆童心」的孩子。](#)

孫維新說，20 多年前他回到中央大學服務，當時鄭崇華捐贈了 2000 多萬給中央大學建置鹿林天文台，也漸漸了解到[鄭崇華喜歡天文是因為從小隻身在外，假日沒飯吃，只能看月亮、數星星這樣令人難過的理由。](#)

孫維新說，也因此對於鄭崇華後來白手創業至今，還持續回饋社會，是件很不容易的事情，在他眼裡，鄭崇華是他無比尊敬的長者，但看到鄭崇華在科博館

看著很多新奇的展品時，仍會像小學生一樣提出很多問題，這時候這位 80 歲的長者，瞬間又變成了孩子。

▼台達電創辦人鄭崇華（左 2）和董事長海英俊（左 3）在台下當學生學習物理。（圖／記者周康玉攝）



鄭崇華：媽媽可能也跟我看同樣的星星

說到高中時候在操場看星星，鄭崇華也回應，當時在台中一中念書，當時空氣好，如果晚上睡不著，看天空、東想西想，**他想著「會不會媽媽也在看著同樣的星星？」一解思親之愁**；看著看著，他就想著，「每天一定不只有一顆流星掉下來」；甚至，**他想到童話故事中的賣火柴女孩說，「每掉下一顆星星，就代表一個人死去」，也看出鄭崇華從小細膩和浪漫的性格。**

鄭崇華說，光是「天上到底有多少星星」，為了找到答案，他還會到台北的圖書館找一堆書來看，也會思索從前的科學和現在的不同，他也直言「科學就是哲學」已經是陳舊的說法了，以希臘哲學家蘇格拉底為例，他連公積、浮力等物理知識都沒有，卻能解釋「石頭為什麼會掉下來？」「煙為什麼會往上飄？」等問題，**因為每個時代的人所能看到的範圍就是這麼多。**

▼鄭崇華（中）與科博館館長孫維新（右）20年前因為天文而結識彼此。（圖／記者周康玉攝）



原文網址: [側寫／80歲鄭崇華熱愛天文 聊星星一秒變小學生 | ETtoday 財經 | ETtoday 新聞雲](https://www.ettoday.net/news/20170220/869780.htm#ixzz5apAhv6ou) <https://www.ettoday.net/news/20170220/869780.htm#ixzz5apAhv6ou>
Follow us: [@ETtodaynet on Twitter](https://twitter.com/ETtodaynet) | [ETtoday on Facebook](#)

2017/03/06



Home > Environment > Top News

Top News

Minor planet named after Yilan County

March 06, 2017 |



NCU President Jou Jing-yang speaks at an event March 3 in Yilan to celebrate the naming of a minor planet after the northeastern Taiwan county. (Courtesy of NCU)

A- A+

A minor planet co-discovered by the Lulin Observatory of National Central University has been named Yilan in tribute to the northeastern Taiwan county's natural beauty and rich culture, Acting Yilan County Magistrate Wu Ze-cheng and NCU President Jou Jing-yang announced March 3.

Jointly discovered Aug. 12, 2006, by Lin Hung-chin, head of the observatory, and California Institute of Technology astronomer Ye Quanzhi, the minor planet is located between the orbits of Mars and Jupiter and classified as a main-belt asteroid. Yilan 2006 PC8 measures between 1 and 3 km in diameter and takes 3.78 years to orbit the sun.

Its closest and farthest distances from the sun are 300 million km and 420 million km, respectively. It was uncovered in a portion of the sky near the Capricornus constellation and this month is close to the Ophiuchus constellation.

The title of Yilan was officially published Sept. 9, 2014, by the Paris-based International Astronomical Union, Lin said, adding that he hopes this will bring further international recognition to the northeastern county.

Wu said at the announcement that the naming of the asteroid has given Yilan "a place among the stars," while encouraging local students to learn more about astronomy and the mysteries of the universe.

According to Jou, the Lulin Observatory, located in Yushan National Park in central Taiwan's Nantou County, is the nation's most important optical astronomy facility and among the most active in Asia with regard to uncovering minor planets.

Established in 1999, the Lulin Observatory discovered around 800 asteroids, one near-Earth asteroid and one comet between 2006 and 2009, NCU's Graduate Institute of Astronomy said. (KWS-E)

Write to Taiwan Today at ttonline@mofa.gov.tw

Popular

THE SCIENTIFIC PAYLOAD
ON FORMOSAT-5.

“FUJI-YUSHAN PEAK-CONQUERING
INTERNATIONAL COLLABORATION PROJECT”.

NCU National Central University NEWSLETTER

THE CONTRIBUTION OF THE GRADUATE INSTITUTE OF ASTRONOMY
AT NCU TO GLOBAL ASTRONOMICAL OBSERVATION RESULTS
WAS PUBLISHED IN *SCIENCE*.

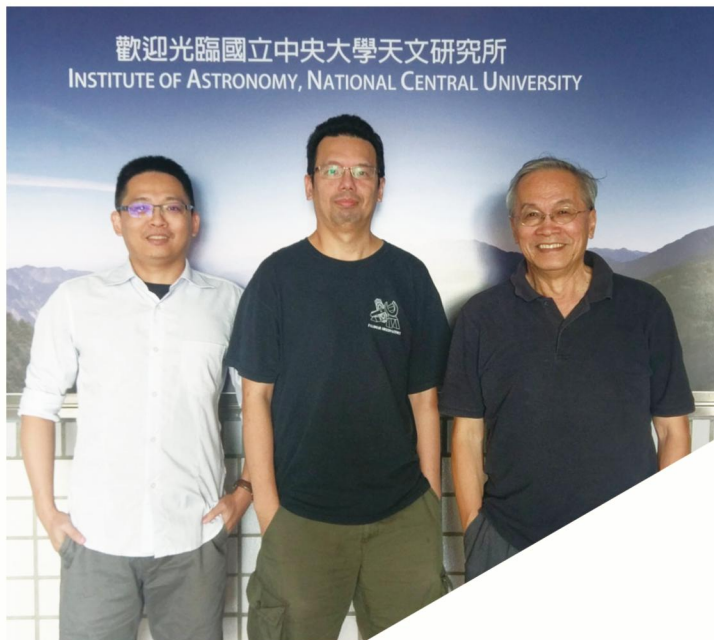


國內郵資已付

印刷品

NO.12

DECEMBER 2017



◀ Research results of the Graduate Institute of Astrology at NCU: Professor. Ip Wing-huen, Organizer of Project TANGO (Right), Professor Ngeow Chow-choong, Director of Project GROWTH in Taiwan (middle), and Dr. Yu Po-chieh (left). (PHOTO: Graduate Institute of Astrology)

WITNESSING A NEUTRON STAR MERGER CAUSING GRAVITATIONAL

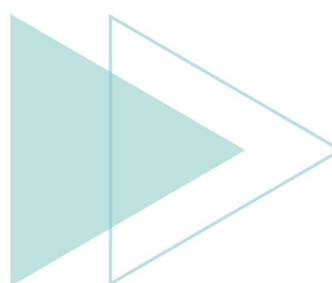
The Contribution of the Graduate Institute of Astronomy at NCU to Global Astronomical Observation Results Was Published in Science.

Sponsored by the Ministry of Science Technology (MOST), the research team from the Graduate Institute of Astronomy (GIA) at NCU participated in the project of Global Relay of Observatories Watching Transients Happen (GROWTH) led by the California Institute of Technology (Caltech) in the United States. Further research results on the confirmation of the origin of the gravitational waves detected by the Laser Interferometer Gravitational-Wave Observatory (LIGO) was an unprecedented discovery. The discovery not only verified the general theory of relativity developed by Albert Einstein but also helped solve the riddle of formation of gold in the universe. This significant research achievement was written in the article “Illuminating Gravitational Waves: A Concordant Picture of Photons from a Neutron Star Merger” and published in the latest world-renowned scientific journal, Science.



▲ A neutron star merger occurs: Pan-STARRS, located in Hawaii, captured the visible light image of the galaxy NGC 4993. The white circle is where the neutron star merger took place. (Photo: Pan-STARRS Project)

GROWTH was a team led by Caltech, and there were 14 research institutes (including 18 observatories) from eight countries participating in the project. The research team from Taiwan included Academician of Academia Sinica Dr. Ip Wing-huen, Associate Professor Dr. Ngeow Chow-choong, Postdoctoral Researcher Yu Po-chieh, and crew members of Lulin Observatory. Through the TANGO project sponsored by the MOST and the PIRE (Partnerships for International Research and Education) collaboration between Taiwan and the United States, our research team thus joined this international astronomical collaborative research. The achievement also put the Lulin Observatory on the international stage for cross-country astronomical observation.



2012.05.30

天文所新發現 行星胚胎形成的關鍵證據

文／陳文屏



中央大學天文所團隊參與國際「Young Exoplanet Transit Initiative 觀測計畫」，取得重要研究成果。圖為天文所研究生胡佳伶（中間，淺紫外套）與指導教授陳文屏（前排，紅外套）在德國天文台與觀測團隊合影。照片胡佳伶提供

由我國學者主導的國際天文團隊，觀測到初誕生恆星周圍形成原始行星的證據，成果刊載於六月一日出版之《天文物理期刊》。中央大學天文所研究生胡佳伶以及指導教授陳文屏，利用鹿林天文台望遠鏡，搭配國際其他望遠鏡數據，取得重要成果。

太陽、地球以及其他行星、衛星來自太空某團雲氣，由於自身萬有引力收縮，導致旋轉越來越快，成為扁平形狀。雲氣由氣體與塵埃組成，收縮後溫度升高，最中央部分最終形成太陽，內部進行核子反應，產生光與熱。周圍盤狀雲氣當中的塵埃彼此凝集，逐漸變大成為小行星、行星。換句話說，行星是形成恆星的副產品，太空中應該有很多行星。天文學家的確在「嬰兒時期」的恆星周圍，觀測到由塵埃構成的盤狀結構，另一方面則在「已經成年」超過數百顆恆星周圍找到具體成形的行星。

胡佳伶任職於台北天文教育館，這個研究是她就讀中大天文所的碩士論文內容，她說道：「很高興有機會使用臺灣的設備，得到不錯的科學成果。」中大團隊參加由國際天文台觀測網，監測 Trumpler 37 這個年輕星團，年齡只有約四百萬年，希望利用「掩星」方式，也就是行星運行到恆星前方所產生的亮度變化，來偵測行星存在。

但是胡佳伶在分析資料時，發現編號為「仙王座 GM」這顆星球的亮度有奇特的變化方式，它大約相隔一年，會變暗長達一個月，這是前所未見的現象。陳文屏強調：「我們原來想找行星，但沒有找到，卻意外偵測到可能是行星胚胎形成的首要步驟。」國際知名行星科學專家、中央大學天文所葉永烜教授說：「行星形成的關鍵，就是恆星周圍的塵埃盤開始變得均勻。在很多年輕恆星周圍可能也有類似現象，值得繼續發掘。」

名為 Young Exoplanet Transit Initiative 的觀測網，簡稱 YETI，英文是「雪怪」的意思，參加的研究機構來自德國、波蘭、保加利亞、立陶宛、美國、敘利亞、斯洛伐克、委內瑞拉、亞美尼亞、印度、日本，以及大陸，利用不同經度的望遠鏡觀測同樣天區，「讓星星不下山，才能取得長時間的數據。此次有關仙王座 GM 星的資料主要來自鹿林天文台望遠鏡，以及中央大學天文所操作、位於美國亞利桑納州的 Tenagra 望遠鏡」胡佳伶跟陳文屏都很感激其他國外合作者提供數據，共同取得這項成果。

2017.11.10

回溫舊夢 大學部首屆45周年返校同學會

文／校友中心駱季青、通訊四蔡秉翰



周景揚校長、林沛練學務長、顏宏元主任、嚴明鉦主任(前排右四至右一)，與大學部首屆校友於校門口建校紀念碑前合影。駱季青攝

時光荏苒，本校第一屆大學部畢業校友已畢業四十五年，今年在何正行、詹文鑫、劉家興、侯永昌校友們的籌備下，寓居各地的校友長姐們在11月3日的下午，回到了母校中央大學，走在綠意盎然的校園中，回憶共同成長的青春年華，連繫與母校間的珍貴情誼。

歡聚秉文堂 回憶美好時光

同學會活動安排在科學館二樓秉文堂，由周景揚校長為同學會開幕致詞，隨後同學會的四位發起人上台餽贈「師恩永懷」紀念牌，母校回以校旗以茲留念。活動在眾位系所師長的蒞臨與分享中，揭開母校近年發展概況，並欣賞校友們當年生活在中大的生活照片，以及他們2007年及2011年返校參觀校史館的活動剪影。在這個承載著校友們當年上週會課與共同科的大教室裡，他們在輕鬆的茶敘時光中，回憶當年一起在秉文堂晚自習，在秉文堂推出校慶公演，誰與誰的故事，都在這個與記憶中相似又些微不同的空間裡沈澱與清晰，於是校歌緩緩揚起，情誼彌足珍惜。溫馨的氣氛喚起種種回憶歷歷在目。

科學一館天文台博物館

離開秉文堂，校友們來到科學一館三樓的天文台博物館，參觀昔日臺灣第一座具有天文研究用大型望遠鏡的天文台，並回顧中大天文領域的學術發展、應用與社會貢獻。科學一館的天文台博物館，不單紀念著中大在天文領域的發展，同時兼具教學功能。自1999年中大於玉山前峰建置鹿林天文台，成就中大擁有全台最高天文台設備，並在全球天文界佔踞高度學術地位。在天文所的支持下，畢業四十五的校友們於11月7日登上鹿林天文台，參訪這一座聞名全球的中大天文基地，來一場山林與知性之旅的邂逅。

校園參訪 重溫在校生活

在離開校園之前，校友們漫步至昔日生活過的學生宿舍（今日國際學生宿舍），一同回憶舊時風貌，同時在林沛練學務長的引領之下，參觀現今學生宿舍，了解學弟妹的住校環境，在青春活潑的氣息裡，重溫美好的住校時光。



校友們參觀完科學一館天文台後，在地科學院門口合影留念。駱季青攝



第一屆的校友們參觀女十四舍，交誼廳中有許多中大學子青春活潑的模樣，好不熱鬧。駱季青攝